

ACS SYMPOSIUM SERIES 975

IONIC LIQUIDS IV

NOT JUST SOLVENTS ANYMORE



EDITED BY
Joan F. Brennecke, Robin D. Rogers,
and Kenneth R. Seddon

Ionic Liquids IV

ACS SYMPOSIUM SERIES **975**

Ionic Liquids IV

Not Just Solvents Anymore

Joan F. Brennecke, Editor
University of Notre Dame

Robin D. Rogers, Editor
The University of Alabama

Kenneth R. Seddon, Editor
The Queen's University of Belfast

**Sponsored by the
Division of Industrial and Engineering Chemistry, Inc.**



American Chemical Society, Washington, DC



Library of Congress Cataloging-in-Publication Data

Ionic liquids IV : not just solvents anymore / Robin D. Rogers, editor , Joan F. Brennecke, editor, Kenneth R. Seddon, editor ; sponsored by the Division of Industrial and Engineering Chemistry, Inc.

p. cm.—(ACS symposium series ; 975)

Includes bibliographical references and index.

ISBN 978-0-8412-7445-7 (alk. paper)

I. Ionic solutions—Congresses. 2. Ionic structure—Congresses. III. Solution (Chemistry)—Congresses.

I. Rogers, Robin D. II. Brennecke, Joan F., 1962- III. Seddon, Kenneth R., 1959- IV. American Chemical Society. Division of Industrial and Engineering Chemistry. V. Title: Ionic liquids 4.

QD540.I582 2005
546'.34—dc22

2007060813

The paper used in this publication meets the minimum requirements of American National Standard for Information Sciences—Permanence of Paper for Printed Library Materials, ANSI Z39.48-1984.

Copyright © 2007 American Chemical Society

Distributed by Oxford University Press

All Rights Reserved. Reprographic copying beyond that permitted by Sections 107 or 108 of the U.S. Copyright Act is allowed for internal use only, provided that a per-chapter fee of \$36.50 plus \$0.75 per page is paid to the Copyright Clearance Center, Inc., 222 Rosewood Drive, Danvers, MA 01923, USA. Reproduction or reproduction for sale of pages in this book is permitted only under license from ACS. Direct these and other permission requests to ACS Copyright Office, Publications Division, 1155 16th Street, N.W., Washington, DC 20036.

The citation of trade names and/or names of manufacturers in this publication is not to be construed as an endorsement or as approval by ACS of the commercial products or services referenced herein; nor should the mere reference herein to any drawing, specification, chemical process, or other data be regarded as a license or as a conveyance of any right or permission to the holder, reader, or any other person or corporation, to manufacture, reproduce, use, or sell any patented invention or copyrighted work that may in any way be related thereto. Registered names, trademarks, etc., used in this publication, even without specific indication thereof, are not to be considered unprotected by law.

PRINTED IN THE UNITED STATES OF AMERICA

Table of Contents

Table of Contents	i
Foreword	x
Preface	xi
Analysis and Environment	1
1 How to Analyze Imidazolium Ionic Liquids in Environmental Samples?	2
Introduction.....	3
Analysis of Ionic Liquids By Liquid Chromatography.....	3
Analysis of Ionic Liquids By Capillary Electrophoresis	6
Solid Phase Extraction of Ionic Liquids From Environmental Samples.....	7
Conclusions	8
Acknowledgement	9
References	9
2 Potential Environmental Impact of Imidazolium Ionic Liquids	10
Introduction.....	11
Molecular Interaction Potential of Ionic Liquid Cations in Environmental Systems.....	12
Sorption and Stability of Ionic Liquids In the Environment	13
Lipophilicity and Ecotoxicology of Ionic Liquids.....	16
Conclusions	18
Acknowledgement	19
References	19
3 ¹³C NMR Relaxation Studies of Ionic Liquids	21
NMR measurements.....	22
Methodology.....	22
¹³ C NMR relaxation studies	22
Nuclear Overhauser effect	23
Spectral densities.....	23
Chemical shift anisotropy (CSA)	23
CSA in aliphatic carbons.....	24
Solution of the Combined Dipolar and NOE equations.....	24
Chemical shift anisotropy (CSA)	25
Basic Assumptions.....	26
Sources of Error	26
Common sources of error in NMR relaxation analysis	26
Analysis of the [EMIM]BSO ₃ ionic liquid	27

NMR relaxation measurements.....	27
Sample analysis	27
13C total relaxation rates for [EMIM] cation and butanesulfonate anion.....	28
13C correlation times for [EMIM] cation and butanesulfonate anion.....	28
Evidence of CSA in Both Cation and Anion of [EMIM]BSO3	29
Evidence of phase changes from viscosity and NMR data	31
NMR correlation time relationship with viscosity	32
Acknowledgments	32
References	33
4 Ionic Liquids for Silica Modification: Assessment by Capillary Zone Electrophoresis	35
Introduction.....	35
Experimental.....	37
Apparatus.....	37
Experimental conditions	38
Reagents.....	38
Capillary coating procedure	38
Results and Discussion	40
Surface characterization	40
Effect of IL concentration in buffer	41
Conclusion.....	45
Acknowledgements	45
References	45
5 Characterization of Phosphonium Ionic Liquids with Emphasis on Mass Spectrometry and Chromatography ...	47
Introduction.....	47
Phosphonium Ionic Liquids.....	48
General Characterization Techniques	49
TGA.....	49
31P NMR spectroscopy	52
Other Traditional Characterization Techniques.....	52
Mass Spectrometry and Chromatographic Techniques	52
Objectives	52
Mass Spectrometry of Phosphonium ILs	55
Cluster Ions.....	55
Chromatography of Phosphonium ILs.....	58
Mobile Phase for HPLC.....	58
Sensitivity and Linearity of LC/MS	61
Identification of IL Anions from MS Cluster Ion	61
Residual Chloride Analysis	63
Conclusion.....	63

Experimental.....	66
Instruments	66
Chromatographic conditions	66
References	67
Theory	69
6 Force Field Refinement and Molecular Simulations of Imidazolium-Based Ionic Liquids	70
1. Introduction.....	70
2. Force Field Development	71
2.1 All-atom (AA) force field	71
2.2 United-atom (UA) force field	73
3. Molecular Dynamics Simulations.....	75
3.1 Pure ionic liquids.....	76
3.1.1 Densities.....	76
3.1.2 Inter-molecular Energies	76
3.2 Mixtures of [bmim][BF ₄] and acetonitrile (CH ₃ CN)	79
3.2.1 Excess volumetric and energetic properties.....	79
3.2.2 Viscosities.....	79
3.2.3 Microscopic structures.....	82
4. Conclusions.....	82
Acknowledgements	82
References	85
7 Intra- and Intermodular Structure of Ionic Liquids: From Conformers to Nanostructures.....	86
Introduction.....	87
Conformational distributions of imidazolium cations in the liquid phase	87
Nanometer-scale structures in ionic liquids.....	93
Solvation structure of nonpolar, polar and associating solutes	97
Conclusion.....	99
References	101
8 Molecular Simulation of Mixtures Containing Imidazolium- and Pyridinium-Based Ionic Liquids and 1-Butanol.....	102
Introduction.....	103
Methodology	103
Results and Discussion	106
Densities	106
Fluid Structure and Local Composition	106
Mixtures with the [BF ₄] anion.....	107
Mixtures with the [Tf ₂ N] anion.....	115
Diffusion	121

Conclusions	123
Acknowledgements	124
References	124
Applications.....	126
9 Carbonylation in Ionic Liquids Using Vapor-Takeoff Reactors.....	128
Development of Vapor Take-off Reactors with Ionic Liquids	129
Conclusions	135
Experimental.....	136
Materials.....	136
Carbonylation reactions	136
References	137
10 Ionic Liquids for Space Propulsion.....	138
Introduction	139
Space Propulsion	140
Space Propulsion Missions	140
Space Propulsion Performance Parameters.....	141
Electric Propulsion	142
Discharge-Free Electric Thrusters: Electrospray Thrusters	144
Electrohydrodynamics of Taylor Cones.....	147
Mass Spectrometry Measurements of Ions Field Evaporated from Ionic Liquids	150
Mass Spectrometric Experiment	150
[Emim][BF ₄]	151
[Emim][Im]	152
[Emim][NO ₃].....	157
Conclusions	158
Acknowledgments	159
References	159
11 Columnar Liquid Crystalline Imidazolium Salts: Self-Organized One-Dimensional Ion Conductors.....	161
Introduction.....	162
Results and Discussion	163
Synthesis and Liquid Crystalline Properties.....	163
Macroscopic Alignment of the Columns.....	166
Anisotropic Ionic Conductivities of Columnar Ionic Liquids (31)	166
Conclusion.....	168
Acknowledgements	169
References	169
12 Ionic Liquids as Versatile Media in Lanthanide Chemistry.....	172
Trivalent lanthanides in ionic liquids - structural	

Trivalent lanthanides in ionic liquids - structural characterizations	173
Optical Properties of Lanthanides in Ionic Liquids.....	176
Low Valent Lanthanides in Ionic Liquids	179
Acknowledgements	182
References	183
13 Electropolishing and Electroplating of Metals Using Ionic Liquids Based on Choline Chloride	186
Introduction	187
Experimental.....	187
Results and Discussion	188
Electropolishing.....	188
Electroplating of Alloys	192
Conclusions	196
Acknowledgements	196
References	196
14 Ionic Liquids as Vehicles for Reactions and Separations.....	198
Experimental.....	199
Nucleophilic Substitution Reactions	199
Physical Property Measurements	200
Results and Discussion	201
Nucleophilic Substitution Reactions	201
Physical Property Measurements	203
Microviscosity using a fluorescent molecular rotor.....	204
Local dielectric using a fluorescent molecular rotor ...	206
Reversible ionic liquids.....	208
Conclusions	209
References	210
15 Mesoscopic Dye Sensitized Solar Cells Using Hydrophobic Ionic Liquid Electrolyte	212
Introduction	213
Experimental.....	213
Results and Discussion	214
Conclusions	218
Acknowledgement	218
References	218
16 The Application of Trialkyl-Imidazolium Ionic Liquids and Salts for the Preparation of Polymer-Clay Nanocomposites	220
Introduction	221
Experimental*	225
Materials.....	225
Instrumentation	225
Results and Discussion	226
Imidazolium treated layered silicates.	226

Polymer Layered Silicate Nanocomposites.....	228
Conclusions	231
Acknowledgements	231
References	231
17 Ionic Liquids as Modifiers for Cationic and Anionic Nanoclays	234
Introduction.....	235
Experimental.....	236
Materials.....	236
Modification of Clays.....	237
Characterization	237
Results and Discussion	239
Cationic clays.....	239
Anionic clays	243
Conclusions	244
References	246
18 Solution Chemistry of Cm(III) and Eu(III)in Ionic Liquids	247
Experimental Section.....	249
Measurements in H ₂ O	249
Measurements in BumimTf ₂ N.....	249
TRLFS.....	250
Results and Discussion	250
Eu(III) and Cm(III) Fluorescence Quenching by Cu(II) in H ₂ O	250
Eu(III) and Cm(III) solvation in BumimTf ₂ N	251
Eu(III) and Cm(III) Fluorescence Quenching by Cu(II) in BumimTf ₂ N	254
References	256
<i>Synthesis and Properties</i>.....	257
19 New Ionic Liquids Based on Anion Functionalization...258	258
Introduction.....	258
Synthesis of functionalized alkylsulfate ionic liquids.....	259
Quaternization step.....	259
Transesterification step.....	260
Kinetics of the transesterification reaction and concepts for scale-up.....	261
Selected physical-chemical properties of functionalized alkylsulfate ionic liquids	263
Viscosity.....	263
Density	264
Synthesis of vinylsulfonate ionic liquids and further functionalization.....	265
Ion exchange in dry acetone.....	266
Ion exchange using an ion exchange resin.....	267

Selected physical-chemical properties of [EMIM]/[BMIM] [vinylsulfonate].....	267
Thermal properties	267
Viscosity	268
Transformations of Vinylsulfonate Ionic Liquids	268
Hydrogenation of vinylsulfonate	269
Hydroformylation of vinylsulfonate	270
Conclusion	270
References	270
20 Spatial Heterogeneity in Ionic Liquids	272
Introduction	273
Models and Methods	274
Polarizable atomistic models.....	275
Heterogeneity Order Parameter	277
Diffusion and local structure.....	279
Molecular Dynamics Procedure	279
Results.....	280
Finite Size Effects	281
Structural, Dynamical, and Thermodynamical Properties.....	285
Spatial Heterogeneity.....	286
Mechanism.....	294
Discussion and Conclusions.....	298
Acknowledgments	299
Appendix.....	300
A1. Isotropic Atomic Polarizabilities	300
A2. Partial Charges of Atoms.....	300
A2.1. C2 and Nitrate	300
A2.2. C4.....	301
A2.3. C6.....	301
A2.4. C8.....	301
A2.5. C10.....	302
A2.6. C12.....	302
A3. Force Field Parameters	303
References	306
21 Taylor Cones of Ionic Liquids as Ion Sources: The Role of Electrical Conductivity and Surface Tension.....	308
Introduction	309
Taylor cones of ionic liquids as sources of ions in vacuum	310
Surface tension measurement.....	313
Ionic Liquids.....	315
Performance of the ionic liquids as ion sources	315
Acknowledgments	317
References	317

22 How to Make Ionic Liquids More Liquid.....	320
Results and Discussion	321
Experimental.....	332
Chemicals	332
Analytical procedures.....	332
Acknowledgement	332
References	333
23 Molecular Dynamics Study of the Mechanism of Cellulose Dissolution in the Ionic Liquid 1-n-Butyl-3-methylimidazolium Chloride	335
1. Introduction.....	336
2. Simulation Details.....	336
3. Neat [C4mim]Cl Simulations.....	338
3.1. Optimization of Non-bonded Parameters.....	338
3.2. Structural Features of Neat [C4mim]Cl	339
3.3. Dynamic Properties of Neat [C4mim]Cl	342
4. Cellobiose/[C4mim]Cl Simulations	343
4.1 Solute-Solvent Interactions	343
4.2. Solvent Structuring in Cellobiose/[C4mim]Cl Solutions	346
4.3. Dynamic Properties of Cellobiose/[C4mim]Cl Solutions	347
5. Conclusions	347
Acknowledgment	348
References	349
24 New Class of Ionic Liquids Synthesized from Amino Acid and Other Bioderived Materials	351
Room temperature ionic liquids composed of amino acid anions	352
Binary mixtures of amino acid ionic liquids.....	354
Zwitterions derived from amino acid.....	355
Fully natural ionic liquids containing amino acids.....	358
Conclusions	359
Acknowledgements	360
References	360
25 Hydrophobic n-Alkyl-N-isoquinolinium Salts: Ionic Liquids and Low Melting Solids	362
Introduction.....	363
Experimental.....	363
Synthesis of [Cnisoq]Cl Salts.....	363
Synthesis of [Cnisoq][X] (X = [PF6]-, [NTf2]-, and [BETA]-) Salts	364
Physical Property Measurements	364
X-ray Diffraction Studies	365
Partitioning Studies	366

Results and Discussion	366
Physical Properties	366
Single Crystal X-ray Diffraction Studies	368
Solvent Properties.....	373
Conclusions	378
Acknowledgements	378
References	379
Author Index.....	383
Subject Index.....	385
Color Figure Insert (Figure 3 from Chapter 10)	409

Foreword

The ACS Symposium Series was first published in 1974 to provide a mechanism for publishing symposia quickly in book form. The purpose of the series is to publish timely, comprehensive books developed from ACS sponsored symposia based on current scientific research. Occasionally, books are developed from symposia sponsored by other organizations when the topic is of keen interest to the chemistry audience.

Before agreeing to publish a book, the proposed table of contents is reviewed for appropriate and comprehensive coverage and for interest to the audience. Some papers may be excluded to better focus the book; others may be added to provide comprehensiveness. When appropriate, overview or introductory chapters are added. Drafts of chapters are peer-reviewed prior to final acceptance or rejection, and manuscripts are prepared in camera-ready format.

As a rule, only original research papers and original review papers are included in the volumes. Verbatim reproductions of previously published papers are not accepted.

ACS Books Department

Preface

This book contains the key papers presented at the American Chemical Society (ACS) national meeting symposium *Ionic Liquids: Not Just Solvents Anymore OR Ionic Liquids: Parallel Futures*, held at the 231st ACS National Meeting in Atlanta, Georgia, March 26–30, 2006. The meeting was split into 10 sessions (Why Are Ionic Liquids Liquid?; Ionic Liquid Structure–Activity Relationships and Modelling; Ionic Liquid Environmental Fate and Toxicity; New Industrial Applications of Ionic Liquids; Really New Ionic Liquids; Ionic Liquids and Education; Ionic Liquids Applications Based on Physical Properties; Functional Ionic Liquids/Ionic Materials; Analytical Applications of Ionic Liquids; Microengineering with Ionic Liquids), running from Sunday morning to Thursday afternoon; more than 80 presentations were delivered. We are indebted to the session organizers (E. J. Maginn, G. A. Lamberti, R. J. Bernot, R. T. Hembre, J. H. Davis Jr., R. D. Singer, J. S. Wilkes, H. Ohno, D. W. Armstrong, and R. W. K. Allen) for helping to deliver such a stimulating program.

The explosion of interest (*see* Figure 1) in the field of ionic liquids has been worldwide and truly interdisciplinary. The intense interest in the field has led to an unprecedented increase in our knowledge of salts in general and specifically in how to manipulate their physical and chemical properties. Such fundamental knowledge has been closely followed by a dramatic increase in the technological application of ionic liquids, as illustrated by the number of published patents using the term “ionic liquid” since 1996 (*see* Figure 2). Page restrictions prevent the publication of all the presentations, but we have selected a representative subset of the papers that illustrate the variety and novelty of topics currently being pursued worldwide.

This symposium would not have been successful without invaluable support from several academic, industrial, and professional organizations. The symposium was hosted and sponsored by three subdivisions of the ACS Division of Industrial and Engineering Chemistry, Inc.: Green Chemistry and Engineering, Separation Science and Technology, and Novel Chemistry with Industrial Applications. Additional financial support for the symposium was received from The University of Alabama Center for Green Manufacturing, The Queen’s University Ionic Liquid Laboratory (QUILL) in Belfast, BASF, Cytec Industries, Inc.,

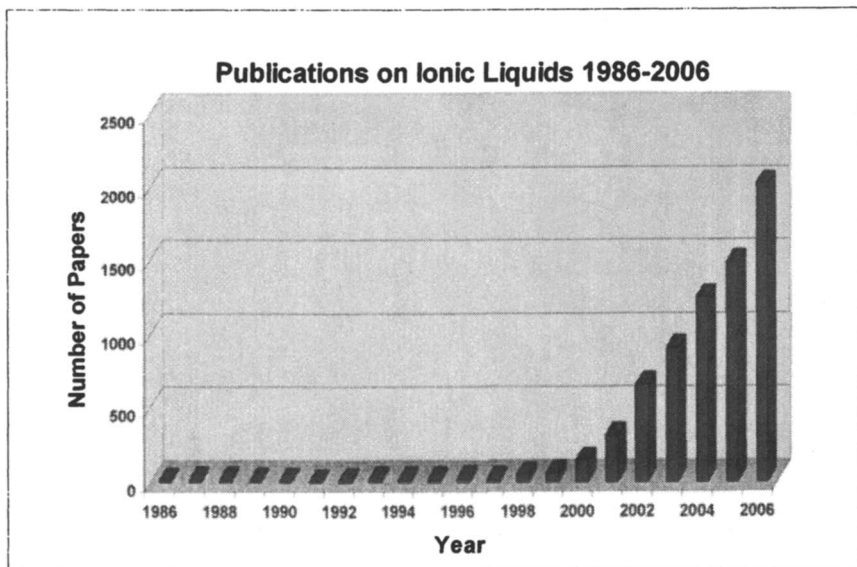


Figure 1. Steeper than exponential growth of ionic liquid publications (M. Deetlefs, U. Hakala, K. R. Seddon, and K. Wähälä, unpublished data, 2006).

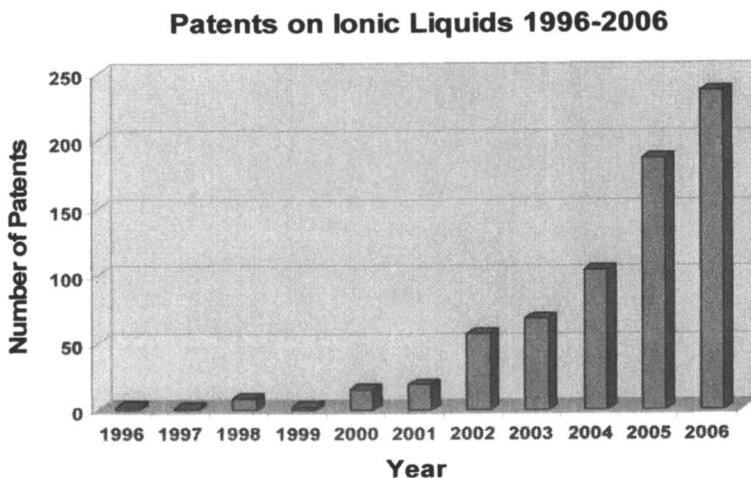


Figure 2. Annual growth of ionic liquid patents (M. Deetlefs, U. Hakala, K.R. Seddon, and K. Wähälä, unpublished data, 2006).

Merck KGaA/EMD Chemicals, 525Solutions, and Solvent Innovations. We are grateful to these organizations and the individuals who represent them, and we look forward to continued work with them as the field develops even further.

Joan F. Brennecke

Department of Chemical and Biomolecular Engineering

University of Notre Dame

South Bend, IN 46556

jfb@nd.edu (email)

1 574 631 5847 (telephone)

1 574 631 8366 (fax)

<http://cbe.nd.edu/faculty/show/jfb/> (URL)

Robin D. Rogers

Center for Green Manufacturing and Department of Chemistry

Box 870336

The University of Alabama

Tuscaloosa, AL 35487

RDRogers@bama.ua.edu (email)

1 205 348 4323 (telephone)

1 205 348 0823 (fax)

<http://bama.ua.edu/~rdrogers/> (URL)

Kenneth R. Seddon

The QUILL Research Centre

The Queen's University of Belfast

Stranmillis Road

Belfast BT9 5AG

Northern Ireland, United Kingdom

k.seddon@qub.ac.uk (email)

+44 28 90975420 (telephone)

+44 28 90665297 (fax)

<http://quill.qub.ac.uk/> (URL)

Ionic Liquids IV

Analysis and Environment

Chapter 1

How to Analyze Imidazolium Ionic Liquids in Environmental Samples?

Piotr Stepnowski

**Faculty of Chemistry, University of Gdansk, ul. Sobieskiego 18,
80–952 Gdansk, Poland (email: sox@chem.univ.gda.pl)**

The development of novel analytical methods for the rapid and reproducible separation and identification of ionic liquids is a prerequisite for future biological and environmental research into these compounds. Analytical methods are also necessary to assess the purity of ionic liquids as well as to determine the type and nature of impurities present in technical chemicals. A number of instrumental techniques have recently been developed that are now ready for application to natural samples. This chapter outlines the preliminary stages in the development of analytical methods for ionic liquids: they involve reversed phase and ionic high performance liquid chromatography, capillary electrophoresis and solid phase extraction.

Introduction

Ionic liquids are considered to be highly promising neoteric solvents. Once they become employed on an industrial scale, small amounts will inevitably find their way into the environment. Therefore, the development of novel analytical methods for the rapid and reproducible separation and identification of ionic liquids is a prerequisite for future biological and environmental research into these substances.

Our group has recently developed a number of instrumental methods that are now ready for testing on natural samples. Alkylimidazolium ionic liquid cations were separated using reversed phase high performance liquid chromatography using UV as well as electrospray ionization mass detection, where mobile phases consisted of methanolic and acetonitrile aqueous solutions modified with variety of buffers and ion pair reagents (1, 2). Also different chromatographic column packings with specific structural properties were examined in order to obtain the best selectivity for the analysis of specific ionic liquids (3, 4). The application of capillary electrophoresis for resolving selected imidazolium ionic liquid cations in standard mixtures was also conducted (5, 6). When applied to environmental samples, however, all these methods are significantly limited by their low sensitivity. This can be substantially improved by performing a pre-concentration step. A selective method for the clean-up and pre-concentration of ionic liquid cations from environmental water samples using cation-exchange solid phase extraction followed by selective elution was also developed (7).

This chapter outlines the preliminary stages in the development of these methods, as well as discuss possibility of their application for environmental samples.

Analysis of Ionic Liquids By Liquid Chromatography

Ionic liquids have already been targeted in the field of chromatographic analysis, not as solutes but as potential replacements for organic solvents in mobile phases and as agents suppressing the deleterious effects of free silanol groups (8-11). Nevertheless, this also implies some serious complications in their direct analysis on a conventional reversed phase columns with a low surface coverage of ligands. We have recently reported the separation of selected 1-alkyl- and 1-aryl-methylimidazolium-based room-temperature ionic liquids using reversed phase HPLC with electrospray ionization mass detection (1). Figure 1 presents isocratic separation of 1-ethyl-3-ethyl-, 1-propyl-3-methyl-, 1-propyl-3-ethyl-, 1-butyl-3-methyl-, 1-benzyl-3-methyl-, 1-amyl-3-methyl-, 1-(2-phenylethyl)-3-methyl-, 1-methylbenzyl-3-methyl-, 1-hexyl-3-methyl-, 1-hexyl-3-ethyl- and 1-heptyl-3-methyl-imidazolium cations numbered from 1 to 11

respectively, obtained with this methodology. Mobile phase composition was optimized for peak resolution, sensitivity and high reproducibility of retention values. Satisfactory results were obtained with methanol – water phase with the addition of 1% acetic acid and 20mM ammonium acetate. Within certain limitations, this simple and selective method was initially validated through the analysis of biological samples used for cytotoxicity studies of the ionic liquid in question.

As outlined in Figure 1, all congeners using this method can be separated in an isocratic system using methanol as the organic modifier of the mobile phase. A routine analytical method was further developed on the basis of this chromatographic procedure and then successfully applied to different environmental and biological matrices.

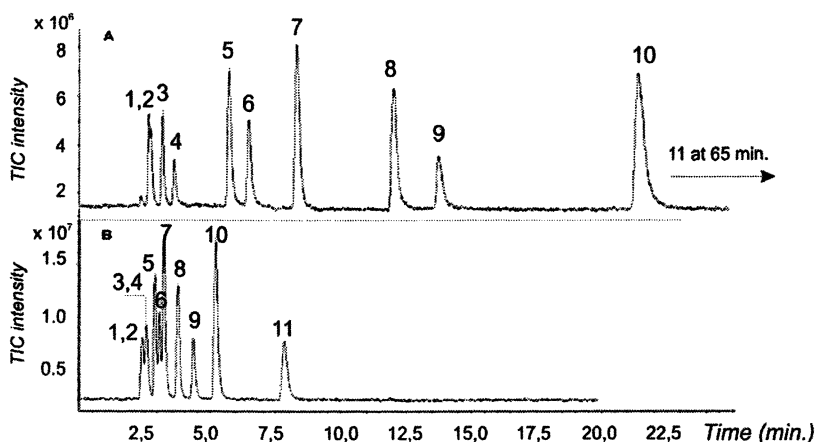


Figure 1. Isocratic separation of imidazolium cations as used in ionic liquids. Concentrations of ionic liquids are in the range from 0.2 to 0.4 mM. Column RP C8 MetaSil Basic (Varian Inc.). Mobile phase A: 10% methanol: water (1% acetic acid /20mM ammonium acetate), B 40% methanol : water (1% acetic acid /20mM ammonium acetate).

- 1) 1-ethyl-3-ethylimidazolium, 2) 1-propyl-3-methylimidazolium,
- 3) 1-propyl-3-ethylimidazolium, 4) 1-butyl-3-methylimidazolium,
- 5) 1-benzyl-3-methylimidazolium, 6) 1-amyl-3-methylimidazolium,
- 7) 1-(2-phenylethyl)-3-methylimidazolium,
- 8) 1-methylbenzyl-3-methylimidazolium, 9) 1-hexyl-3-methylimidazolium,
- 10) 1-hexyl-3-ethylimidazolium, 11) 1-heptyl-3-methylimidazolium cations

Despite its simplicity and selectivity, however, the method cannot yet be proposed as a routine methodology for future applications, since mass detection was used in the total ion current mode. In the further studies (2-5) therefore we have switched to more common but less sensitive UV detection. Additionally, from presented chromatograms it can also be noticed that the short-chain hydrophilic entities (1-ethyl-3-ethyl- and 1-propyl-3-ethylimidazolium salts, numbered 1 and 2 respectively) are poorly separated on this type of columns.

Ion chromatography provides a very useful means of separating quaternary ammonium salts, and is already applied routinely to the analysis of cationic surfactants in industrial and environmental samples (12). Like surfactants, ionic liquids consist of a charged hydrophilic center and a hydrophobic periphery. Therefore a strong stationary-phase cation exchanger was also initially applied in the separation of homologous series of 1-alkyl-methylimidazolium cations with side-chains from -ethyl to -octyl in length (2). During the use of this stationary phase, several interactions occurred with varying strength, depending on the mobile phase composition. Cation exchange, nonspecific hydrophobic interactions and adsorption chromatography behavior were observed. Reversed phase chromatography occurred at low concentrations of acetonitrile in the mobile phase, electrostatic and adsorption interactions at higher organic modifier concentrations. Elevated buffer concentrations decreased retention factors without affecting the selectivity of the alkylimidazolium cations. Appropriate modifications of the mobile phase enable even the smallest, most hydrophilic cations to be separated and analyzed. While using 40-60% of acetonitrile in the mobile phase we have successfully separated hydrophobically similar 1-ethyl-3-ethylimidazolium and 1-butyl-3-methylimidazolium entities. The analytical performance parameters were assessed under optimized chromatographic conditions with an acetonitrile - 30mM K_2HPO_4 (40:60) mobile phase. 1-butyl-3-methylimidazolium was chromatographed in the concentration range 1 - 100 μ M. The correlation coefficient for the resultant calibration plots was 0.998. The reproducibility of the peak area was 1.36% (RSD), and the reproducibility for peak retention was 0.23% (RSD). Limit of detection estimated for the 1-butyl-3-methylimidazolium cation was 20 μ g. The method is directly applicable to the analysis of ionic liquid cations in aqueous environmental or industrial samples. Figure 2 shows a chromatogram of the 1-butyl-3-methylimidazolium entity and its degradation products obtained during the degradation treatment of spiked wastewater.

In another recent study, we investigated different types of columns with specific structural properties (3). We tested packings containing cholesterol ligands chemically bonded to silica (SG-CHOL), and mixed stationary phases (SG-MIX) containing cyanopropyl, aminopropyl, phenyl and octadecyl ligands. There were significant differences in the results: packings containing functional groups bonded to the silica surface and capable of undergoing protonization turned out to be unsuitable for separating ionic liquids under the given analytical

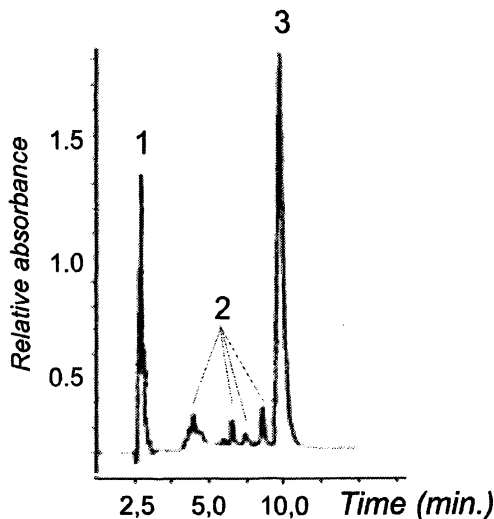


Figure 2. Chromatogram of the 1-butyl-3-methylimidazolium entity (3) and its unidentified degradation products (1-2). Mobile phase: 40% acetonitrile - 30mM K₂HPO₄. Column: Strong Cation Exchanger MetaSil SCX 250 × 4.6 mm ID (Ansys Technologies). UV detection at 218nm

conditions (pH = 4). In this comparison, the butyl and octadecyl stationary phases yielded the best results (RP-18e Innovation Chromolith™ performance and MacroSphere 300 C4 packings respectively). This is most probably due to a lowest heterogeneity of this ligands in comparison to other tested phases. It seems that stationary phases with specific structural properties, among others with cholesterolic and mixed ligands, are unsuitable for the separation of ionic liquid cation mixtures. Figure 3 presents exemplary chromatogram of separation of six ionic liquid cations on SG-C4 packing.

Analysis of Ionic Liquids By Capillary Electrophoresis

In the field of capillary electrophoresis CE, ionic liquids are recognized as electrolyte solutions in non-aqueous CE for the analysis of polar compounds or as capillary modifiers by dynamic coating for the separation of chiral analytes (13-15). We also evaluated a routine capillary electrophoretic method for separating selected imidazolium ionic liquid cations (5). In this study, we successfully separated a series of alkyl and aryl imidazolium ionic liquid cations

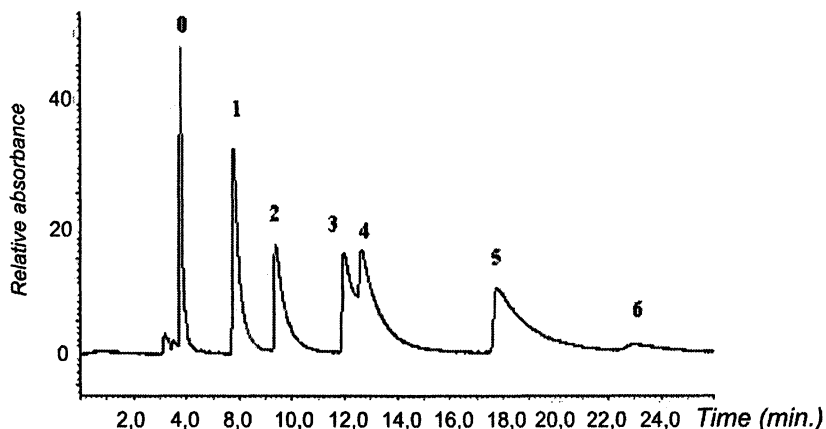


Figure 3. Chromatogram of separation of six ionic liquid cations on SG-C4 stationary phase. Key: 0, unknown compound; 1, PMIM; 2, BMIM; 3, AMIM; 4, MBPy; 5, HMIM; 6, pMBzMIM (analysis conditions: 95% v/v 40 mM KH₂PO₄ pH = 4, 5% v/v MeOH). Reprinted from (3) with the permission of WILEY-VCH Verlag GmbH & Co. KGaA, Weinheim

using citric buffer as the electrolyte solution at a relatively high concentration of 200mM and pH=4. A simple and reliable method, its analytical performance parameters have proved excellent; The relative standard deviation (RSD) of the migration time are in the range from 0.05 to 0.1% whereas the RSD of peak area and corrected peak area are in ranges from 1.30 to 2.55% and 1.24 to 2.48%, respectively. The detection limit of the 1-ethyl-3-methylimidazolium cation obtained with a 500 s injection time was 0.01 $\mu\text{g ml}^{-1}$ (10 ppb). The developed method is also applicable to the various experiments tracking the concentrations of cationic constituents of ionic liquids in aqueous solutions. In the same study, we tested samples obtained during a photodegradation experiment of 1-butyl-3-methylimidazolium tetrafluoroborate: the target solute was well separated from its degradation product (see Figure 4).

Solid Phase Extraction of Ionic Liquids From Environmental Samples

The promising results obtained during the separation of ionic liquids on strong cation exchanger (2) open up new possibilities for the selective extraction of analytes from different liquid media. We found that strong cation exchanger solid phase extraction followed by selective elution could be applied to the preconcentration of 1-alkyl- and 1-aryl-3-methylimidazolium ionic liquids from

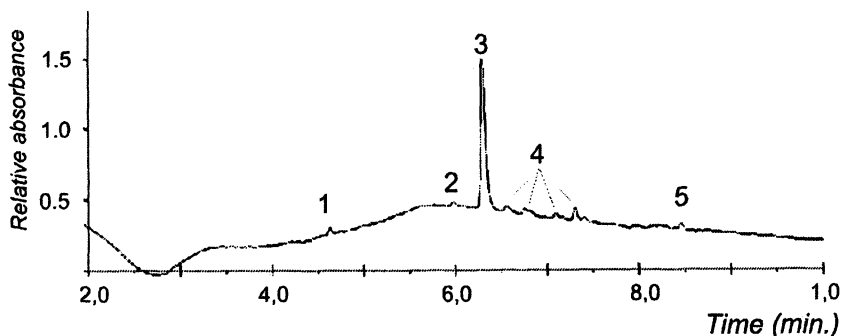


Figure 4. Electropherogram of 1-butyl-3-methyl-imidazolium ionic liquid recorded during the photodegradation experiment. Running electrolyte: 200mM citric buffer, pH = 4.0; temperature: 20°C; separation voltage: 12 kV; injection: 50 s, UV detection at 214 nm. Peaks 1,2,4,5 – unidentified degradation products, 3 - 1-butyl-3-methylimidazolium cation

water samples of environmental origin (7). Both simple and selective, the method is thought to be applicable to imidazolium ionic liquids of the same basic design. It was possible to enrich all the ionic liquids on a strong cation exchange resin with enrichment factor of 100 – 120, and then to elute them selectively with 50% MeOH in NH_4Cl (sat.) (pH=3). Pre-concentration of environmental samples showed that this method could be applied to the analysis of 1-alkyl- and 1-aryl-3-methylimidazolium cations with very good recoveries. In the case of tap water, all the compounds except the AMIM cation were recovered with an excellent yield (> 90%). The best recoveries were with ionic liquids containing the largest functional groups in position 1. All the compounds used to spike the freshwater samples were also recovered at a comparable level (~ 96%), regardless of structural differences. The lowest recovery rates were recorded for ionic liquids extracted from seawater samples (> 90%); clearly, these low rates are due to the higher ionic strength of this environmental matrix.

Conclusions

The chapter presents a preliminary overview of some methods of analyzing ionic liquids, with special emphasis on environmental samples. We are now able to analyze cations with good selectivity using chromatographic and electrophoretic methods. The examples given here are specific to cation analysis; hence, the determination of an ionic liquid's anion should now become one of

the main goals of future analytical research. As regards the preparation of biological and environmental samples, only one method for the preconcentration of natural water samples has been developed so far. Further work should therefore focus on procedures for the selective liquid extraction of ionic liquids (cations and anions) from solid samples such as soils or plant matter.

Acknowledgement

Financial support was provided by the Polish Ministry of Research and Higher Education under grants: 2PO4G 083 29, 2PO4G 118 29 and DS 8390-4-0141-6

References

1. Stepnowski, P.; Müller, A.; Behrend, P.; Ranke, J.; Hoffmann, J.; Jastorff, B. *J. Chromatogr. A* **2003**, 993, 173-178.
2. Stepnowski, P.; Mrozik, W. *J Sep Sci* **2005**, 28, 149-154.
3. Kowalska, S.; Buszewski, B.; Stepnowski, P. *J Sep. Sci.* **2005**, 29, 1116-1125.
4. Stepnowski, P.; Nichthäuser, J.; Mrozik, W.; Buszewski B. *Anal. Bioanal. Chem. (in press)*
5. Markuszewski, M.; Stepnowski, P.; Marszał, M. *Electrophoresis* **2004**, 25, 3450-3454.
6. Qin, W.; Wei, H.; Li, S.F. *Analyst* **2002**, 127, 490-493.
7. Stepnowski, P. *Anal. Bioanal. Chem.* **2005**, 381, 189-193.
8. Armstrong, D.W.; He, L.; Liu, Y-S. *Anal. Chem.* **1999** 71, 3873-3876.
9. He, L.; Zhang, W.; Zhao, L.; Liu, X.; Jiang, S. *J. Chromatogr. A* **2003**, 1007, 39-45.
10. Kaliszan, R.; Marszał, M.P.; Markuszewski, M.J.; Bączek, T.; Pernak, J. *J. Chromatogr. A* **2004**, 1030, 263-271
11. Vaher, M; Koel, M.; Kaljurand, M. *J. Chromatogr. A* **2002**, 979, 27-32
12. Nair, L.; Saari-Nordhaus, R. *J. Chromatogr. A* **1998**, 804, 233-239.
13. Yanes, E.G.; Gratz, S.R.; Baldwin, M.J.; Robison, S.E.; Stalcup, A.M. *Anal. Chem.*, **2001**, 73, 3838-3844.
14. Mwongela, S.M.; Numan, A.; Gill, N.L.; Agbaria, R.A.; Warner, I.M.; *Anal. Chem.* **2003**, 15, 6089-6096.
15. Jiang, T-F.; Gu, Y.-L.; Liang, B.; Li, J-B.; Shi, Y-P.; Ou, Q-Y.; *Anal. Chim. Acta* **2003**, 479, 249-254.

Chapter 2

Potential Environmental Impact of Imidazolium Ionic Liquids

Piotr Stepnowski

Faculty of Chemistry, University of Gdansk, ul. Sobieskiego 18,
80-952 Gdansk, Poland (email: sox@chem.univ.gda.pl)

Excellent, non-volatile solvents for a wide range of applications, and claimed to be environmentally benign, room temperature ionic liquids are generating increasing interest for their potential in different chemical processes. However, the production, application and waste management of ionic liquids will inevitably lead to their accidental discharge into the environment. Therefore, responsible product design should always take into consideration not only technological demands but also the possible health and environmental hazards. This chapter includes data on the photodegradation rates of ionic liquids as well as their sorption to different types of soil and marine sediment. It outlines the toxicological screening of ionic liquids using algae, which takes environmental parameters such as salinity into account, and discusses the theoretical prediction and experimental determination of lipophilicity and possible metabolic pathways. The data presented here provide a preliminary insight into the prospective presence of ionic liquids in the environment.

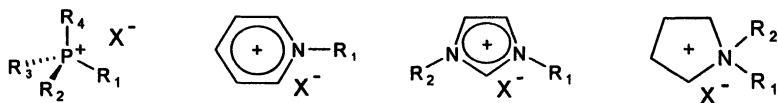
Introduction

In the last ten years ionic liquids have come to be recognized as possible alternative solvents because of their favorable properties. Typically, they are a combination of nitrogen-containing organic cations, and inorganic or organic anions. Figure 1 gives some common examples of ionic liquids. The cation's (or sometimes the anion's) remarkably high degree of asymmetry is responsible for the low crystalline lattice energy, which ensures liquidity over a wide range of low temperatures. Although estimates vary, the number of possible cation and anion combinations that are liquid at room temperature is vast. The variety of possible combinations, and thus, the fine-tuning of their chemical properties, has given the chemical industry new target-oriented reaction media (often called "designer solvents") for synthesis, extraction, catalysis and electrochemistry. Their most important and technologically useful properties are their high ionic conductivity and polarity, physicochemical stability, and wide electrochemical window (1-7). Moreover, since ionic liquids consist entirely of ions, they do not have a significant vapor pressure, and are therefore often regarded as environmentally benign.

The non-volatility of a chemical is insufficient justification for calling a technology "cleaner". Several environmentally related properties, such as toxicity, persistence and degradability, are key issues if we are to understand the consequences of introducing a new industrial chemical on to the market. The modern design of chemical products and processes that take these factors into account, thereby reducing or eliminating the generation of environmental hazards, is the main goal of green chemistry (8).

The production, application and waste management of ionic liquids will inevitably lead to their accidental discharge into the environment. Managing the risks involved with the use of ionic liquids represents a challenge for future environmental research.

This chapter outlines what we know so far about the fate of ionic liquids in different compartments of the environment. Since the most extensively studied group of ionic liquids comprises salts based on the imidazolium head group, our



alkylphosphonium alkylpyridinium Alkylimidazolium alkylpyrrolidinium
 X^- : BF_4^- , PF_6^- , $AlCl_4^-$, SbF_6^- , $CF_3SO_3^-$, $(CF_3SO_2)_2N^-$ etc. R_x : from $-CH_3$ to $-C_9H_{19}$

Figure 1. Common examples of ionic liquid cations and anions

research has focused on imidazolium ionic liquids. Given that a key parameter in understanding the potential of a chemical to cause adverse effects in the environment is its lipophilicity, we have, in all our studies, taken ionic liquid cations to be a congeneric model of imidazolium compounds with different alkyl side chain lengths. The chapter includes data on the photodegradation rates of ionic liquids, as well as their sorption by different types of soil and marine sediment. It then touches upon the toxicological screening of ionic liquids using algae, which takes environmental parameters such as salinity into account. Finally, there is a discussion of the theoretical prediction and experimental determination of the lipophilicity and possible metabolic pathways of ionic liquids.

Molecular Interaction Potential of Ionic Liquid Cations in Environmental Systems

Theoretically, we can predict several molecular interactions that are likely to occur between ionic liquids and different environmental compartments or biomolecules. This prospective analysis is a very important qualitative element when predicting physical and chemical properties for ionic liquids. Potential molecular interactions of ionic liquid cations in environmental systems are shown in the Figure 2.

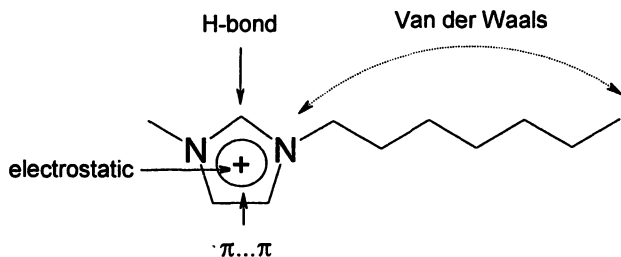


Figure 2. Potential molecular interactions of ionic liquid cations in environmental systems

The high electron acceptor potential of delocalized aromatic systems in the cationic compartments of ionic liquids may be responsible for electrostatic attractions with polar moieties on the surfaces of particles, e.g. of oxides or clay minerals, or on ionized carboxylic functional groups in biomolecules. But since ionic liquids do not retain any non-bonded electrons, the potential reactivity is much reduced. Furthermore, elongating the alkyl chain of ionic liquids will result

in elevated hydrophobicity, which may further affect the partitioning of the molecule to organic matter. Partitioning, moreover, will depend strongly on the anions present in the aqueous phase, with which selected cations will form ion-pairs, thereby enabling phase transfer, and hence partitioning. Since the hydrogen attached to the carbon atom nr 2 of the imidazolium ring has an acidic character, H-bond-like interactions may take place. Deprotonation in this position leading to the carbene formation that can also occur but only in alkalic pH, which is unlikely in most of environmental conditions. Since in neutral and acidic environments alkylimidazolium ionic liquids are rather stable, they will be predominantly bioavailable in ionic rather than neutral form. Also possible are $\pi\cdots\pi$ interactions between the aromatic system in the imidazolium ring and aromatic moieties in biomolecules or environmental compartments (9).

Sorption and Stability of Ionic Liquids In the Environment

The sorption of a substance to soils and sediments is a crucial parameter in the evaluation of the environmental fate of any newly produced chemical. Since the strength of sorption determines the mobility of the chemical in the soil environment, it is possible to predict the risk of ground water contamination with a discharged ionic liquid and its persistence. In a recent study, we conducted several experiments to examine the sorption of ionic liquids to a variety of soils and marine sediments (10, 11); we found that all the compounds were strongly sorbed to all the soils; moreover, sorption was the stronger, the longer the alkyl side chain (Table 1). This positive correlation appears to suggest that the sorption of ionic liquids to soils depends to some extent on interactions with the organic matter in the soil. Furthermore, regardless of the hydrophobic interactions of ionic liquids with organic matter, their non-hydrophobic relations appear to contribute to the sorption. Recently Gorman-Lewis and Fein (12) has measured the adsorption of 1-butyl-3-methylimidazolium chloride onto a range of environmental surfaces. It was found that ionic liquids also interact with mineral montmorillonite, which is solely attributed to electrostatic interaction between the cation and the mineral surface, but also possibly in-between clay mineral layers.

Additionally, we found that all the ionic liquids were strongly sorbed to sediments from the southern Baltic Sea. Sediments from this region are greenish – gray sapropel, a typical mixed mineral suit, which fits the model of “swelling clays” that can dominate the sorption of cationic entities. As was the case with the soil component, K_d was highest ($> 2400 \text{ ml g}^{-1}$) for the compound with the longest alkyl chain (1-hexyl-3-methylimidazolium). Desorption data show that all ionic liquids have an exceedingly strong affinity for both soil and sedimentary matter.

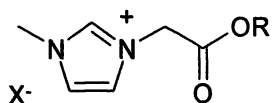
These results give a preliminary insight into the distribution of ionic liquids, should they be discharged into the soil. In most cases they will be strongly and irreversibly bound to most types of soils, so potential ground-water contamination will be limited. The first prediction regarding the aquatic fate of ionic liquids can now be assessed. It seems that ionic liquids will accumulate in sedimentary (and suspended particulate) mineral matter.

Table 1. Sorption coefficients at equilibrium K_d (ml g⁻¹), and desorption characteristics D (%). Data from (10)

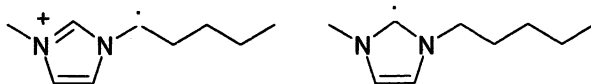
<i>ionic liquid cation</i>	<i>Agricultural</i>	<i>Clayey</i>	<i>Peaty</i>
1-propyl-3-methylimidazolium	14.9(24.4)	6.91(29.9)	2.75(40.3)
1-butyl-3-methylimidazolium	21.0(15.4)	20.1(19.3)	5.8(22.9)
1-amyl-3-methylimidazolium	59.1(5.7)	31.1(10.9)	20.5(18.7)
1-hexyl-3-methylimidazolium	226.3(1.5)	81.5(3.9)	24.0(16.4)

This will probably reduce their overall bioavailability in marine ecosystems. Nonetheless, this poses several questions that future research needs to address: the effect of pH, ionic strength, temperature and biodegradability potential on the sorption and desorption of ionic liquids require the most urgent attention. As we stated earlier, certain amounts of ionic liquids will soon be present in industrial effluents, where, because of their high stability, they could become persistent and break through classical treatment systems into natural waters. In another recent study, we compared the effectiveness of three photodegradation methods (UV, UV/H₂O₂, UV/TiO₂) applied to aqueous solutions of selected imidazolium ionic liquids (13). The fact that all three techniques were successful in degrading a variety of contaminants makes this a good starting point for evaluating the kinetics of ionic liquid degradation. Furthermore, ionic liquids were already targeted in photocatalytic degradation of variety of pollutants, not as targets however but as reaction media (14, 15). These studies revealed that imidazolium ionic liquids are relatively resistant to phototransformation when used as pure phases. In our studies we found the UV/H₂O₂ system to be the most effective for degrading all the ionic liquids. Of the compounds studied in these enhanced photodegradation systems, the 1-ethyl-3-ethylimidazolium species was the most stable. The molecular symmetry of this cation probably reinforces its stability, which in turn significantly decreases its degradability. As far as the other ionic species are concerned, their degradability correlates directly with the length of the n-alkyl substituent. The most stable 1-alkyl-3-methylimidazolium species is the 1-octyl- compound, and the least stable is the 1-butyl- entity. The n-alkyl chain therefore seems to be responsible for the resistance of imidazolium ionic liquids to photodegradation.

The potential persistence of ionic liquids in the environment will also be a function of their biodegradability. Several investigations in this area have recently been conducted by Prof. Scammells' group, which has investigated the baseline biodegradability of ionic liquids, as well as the influence of structural modifications to the alkyl chain and the influence of the type of anion on biodegradation (16, 17). According to recent reports, alkylimidazolium entities are characterized by poor to negligible biodegradability. Incorporating an ester in the side chain, however, significantly enhanced biodegradation. Moreover, the presence of a readily catabolized organic anion, rather than an inorganic one, clearly improved the extent of ultimate biodegradation. Example of biodegradable ionic liquid cation proposed in (16) is presented below:



Biodegradation and abiotic conversions of ionic liquids will produce more or less stable transformation products. Recently, we conducted a computational study of degradation routes during theoretically predicted metabolic reactions using the 1-butyl-3-methylimidazolium cation (BMIM) as the model entity (18). In theory, when an ionic liquid cation enters a cell or is exposed to abiotic degradation activity, it can be oxidized at different positions in the ring or alkyl side chains and be further metabolized. According to our predictions of metabolic routes, based solely on thermodynamic data of the radical intermediates, the energetically most stable radical structure is generated by hydrogen abstraction from the α position of the BMIM cation alkyl chain. Something similar can occur at carbon atom nr 2 in the imidazolium ring, where we know that a very stable carbene entity is formed. This has very recently been confirmed by Kroon et al. (19), who used semi-empirical calculations to follow the decomposition mechanism of ionic liquids in electrochemical processing. The radicals can then undergo further reactions (coupling, disproportionation, etc), resulting in the formation of entirely new compounds, whose environmental impact is unknown (almost like that of ionic liquids). Therefore, even though the prediction regarding the metabolism of ionic liquids is of a preliminary nature, toxicological and ecotoxicological screening of the most stable metabolites should also be undertaken in any prospective hazard assessment. Possible structures of radical transformation products of imidazolium cations are given below (18, 19).



Lipophilicity and Ecotoxicology of Ionic Liquids

The very recent review by Jastorff et al. (20) summarizes the studies of ionic liquid toxicology undertaken so far. The “side chain length effect” with a multitude of combinations of cations and anions was compared for several biological test systems: for all of them the finding was that the shorter the alkyl side chain, the lower the cytotoxicity. The importance of the side chain length (and hence, the lipophilicity) as a factor contributing to the overall observed biological effect was further studied in detail.

In our recent contribution (18) we evaluated lipophilicity by means of reversed phase and immobilized artificial membrane chromatography, then compared our results with calculated data. Two other studies have examined the lipophilicity of imidazolium ionic liquids through the measurement of their octanol-water partition coefficients (21, 22). An ionic liquid was partitioned in the form of associated and dissociated cations and anions: differences due to the various anions used were noted. The results obtained by this procedure, however, cannot be readily extrapolated to environmental conditions. We chose the chromatographic methodology since it yields average values corresponding to a cation partition regardless of the anion present in the native structure of the ionic liquid. It is likely that, after entering the environment, cations and anions will be solvated and to a large extent separated. Therefore, the partitioning of the cation to organic phases is most likely to occur together with the anions prevailing in the environment after some time, and not with those with which it entered the environment.

The experimentally measured and theoretically estimated lipophilicity coefficients obtained for all the ionic liquids studied here generally indicate a relatively low value of this parameter, which implies their preferential partitioning to the aqueous phase. This must be interpreted only in terms of the well solvated, dissociated cation of the ionic liquid, not the ionic liquid in its native, ion-pair form. Moreover, the data obtained on an immobilized artificial membrane does not preclude possible interactions with biological and environmental barriers. This therefore confirms that penetration of a biological membrane is the more likely, the longer the alkyl side chain of imidazolium cations.

Figure 3 shows an example of the theoretical prediction of lipophilicity using fragmental methodology (CLOGP) combined with manual calculations of the geometric bond factor for quaternary ammonium and the electronic bond factor due to the presence of a charge.

Algal assays have become standard ecotoxicological testing systems in environmental impact studies. The use of algae is justified by their ecological role as primary producers in transferring energy to higher trophic levels (23). In addition, algal assays are relatively simple, quick and inexpensive in comparison

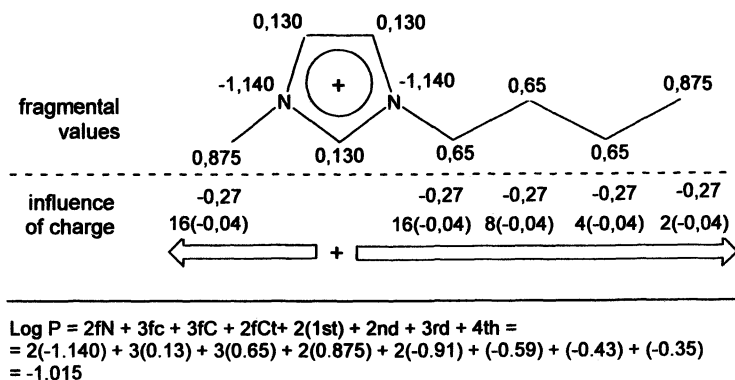


Figure 3. Calculation of lipophilicity of an ionic liquid cation using CLOGP methodology.

with bioassays using other organisms. Our recent assessment of the toxicity of selected imidazolium ionic liquids towards marine algae (24) has revealed significant differences in the responses of the two species studied. *Oocystis submarina* (Figure 4) appeared to acclimatize to the lower concentrations used: after c. 5 days their ability to grow recovered, and initial densities were eventually restored. In the case of *Cyclotella meneghiniana*, growth in batch cultures was effectively inhibited throughout the experiment regardless of the concentration of ionic liquid applied.

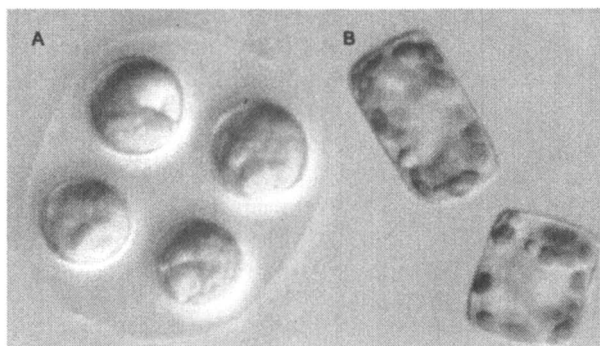


Figure 4. Green algae *Oocystis submarina* (A) and diatom *Cyclotella meneghiniana* (B) used in an ecotoxicological assessment of ionic liquids (photograph: A. Latala)

The observed differences between algal species in their response to exposure to ionic liquids can be initially attributed to structural differences in the cell walls. In the case of green algae, cellulose is the main structural element of the wall, whereas diatoms are surrounded by a siliceous frustule. Additionally, it was found that at higher salinities, the toxicity of the 1-butyl- and 1-hexyl-3-methyl-imidazolium entities towards *O. submarina* was significantly less than at low salinities. The lower toxicity is probably due to the reduced permeability of the algal cell walls to ionic liquid cations. Higher chloride concentrations offer a good ion-pairing environment for imidazolium cations and therefore compete with functional groups in cell walls.

On the basis of the data obtained, it is not possible to precisely calculate any effective concentration values. However it can be roughly estimated that $\log EC_{50}$ values for all analyzed ionic liquids are in the range of 2.4 – 3.0, thus comparable to the values obtained with *Vibrio fischeri* acute bioluminescence inhibition assay (Microtox test) (25)

Conclusions

This is probably the first time that industrial chemicals have been studied so extensively in the context of their effects on health and their environmental properties before being put on the market. Although ionic liquids are not yet present in the environment, a better understanding of their environmental properties and prospective risk assessment have become integral steps in their design. As shown in this chapter, we have already obtained preliminary information about their prospective environmental fate. We know that in most cases ionic liquids will be strongly and irreversibly bound to most types of soils or that they will accumulate in sedimentary matter. We also know that imidazolium ionic liquids, only poorly biodegradable, can be effectively decomposed by advanced oxidation techniques, and that symmetrical molecules exhibit the greatest stability. It is a fact, moreover, that the incorporation of one or more oxygen atoms in the side chain can further enhance degradation; yet we still do not know whether modified cations will be as useful for a vast array of syntheses and separations. The detailed study of lipophilicity has shown that ionic liquids can interact with biological and environmental barriers, which may indicate that the predominant mechanism of toxicity is by disruption of biological membrane, this being the more extensive, the longer the alkyl side chain. We have also learned that certain environmental factors (salinity, but very likely also ionic strength, pH and others) will have a great influence on the toxicity and distribution of ionic liquids.

Acknowledgement

Financial support was provided by the Polish Ministry of Research and Higher Education under grants: 2PO4G 083 29, 2P04G 118 29 and DS 8390-4-0141-6

References

1. Gordon, C. M. *Appl. Catalysis A* **2001**, *222*, 101-117.
2. Sheldon, R. *Chem. Commun.* **2001**, 2399-2407.
3. Wasserscheid, P.; Keim, W. *Angew. Chem.* **2000**, *112*, 3926-3945.
4. Welton, T. *Chem. Rev.* **99** (1999) 2071-2083.
5. Holbrey, J.D.; Seddon, K.R. *Clean Prod. Proc.* **1999**, *1*, 223-236.
6. Olivier-Bourbigou, H.; Magna, L. *J. Mol. Catalysis A: Chemical* **2002**, *182-183*, 419-437.
7. Brennecke, J.F.; Magin, E.J. *AIChE J.* **2001**, *47*, 2384-2389.
8. Anastas, P.T.; Warner, J.C.: *Green Chemistry: Theory and Practice*; Oxford University Press, New York, NY, 1998.
9. Stepnowski, P. In *Proceedings of IEEE International Conference on Technologies for Homeland Security and Safety*; Stepnowski, A. Ed.; Gdańsk, University of Technology: Gdańsk, Poland, 2005, pp 487-492.
10. Stepnowski, P. *Aust. J. Chem.* **2005**, *58*, 170-173.
11. Mrozik, W.; Jungnickel, C.; Stepnowski, P., In *Proceedings of The Second Baltic Symposium on Environmental Chemistry Eco-Tech'05*; Hogland, W.; Broby, T. Ed.; RVFs Utveckingsatsning Deponiering, Kalmar, Sweden, 2005, pp 571-578.
12. Gorman-Lewis D.J.; Fein J.B. *Environ. Sci. Technol.* **2004**, *38*, 2491-2495
13. Stepnowski, P.; Zaleska, A. *J. Photochem. Photobiol. A: Chemistry* **2005**, *170*, 45-50.
14. Yang, Q.; Dionysiou, D.D. *J. Photochem. Photobiol. A: Chemistry* **2004**, *165*, 229-240.
15. Yang, Q.; Dionysiou, D.D. In *Ionic Liquids IIIB: Fundamentals, Progress, Challenges, and Opportunities*; Rogers, R.D., Seddon, K.R. Eds. ACS Symposium Series 902, American Chemical Society 2005, pp 182-198.
16. Gathergood, N.; Garcia, M. T.; Scammells, P.J. *Green Chem.* **2004**, *6*, 166-175.
17. Garcia, M. T.; Gathergood, N.; Scammells, P.J. *Green Chem.* **2005**, *7*, 9-14.
18. Stepnowski, P.; Storoniak, P. *Environ. Sci. Poll. Res.* **2005**, *12*, 199-204.

19. Kroon, M. C.; Buijs, W.; Peters, C.J.; Witkamp, G.-J. *Green Chem.* **2006**, *8*, 241-245.
20. Jastorff, B.; Mölter, K.; Behrend, P.; Bottin-Weber, U.; Filser, J.; Heimers, A.; Ondruschka, B.; Ranke, J.; Schaefer, M.; Schröder, H.; Stark, A.; Stepnowski, P.; Stock, F.; Störmann, R.; Stolte, S.; Welz-Biermann, U.; Ziegert, S.; Thöming, J. *Green Chem.* **2005**, *7*, 362-372.
21. Domańska, U.; Bogel-Lukasik, E.; Bogel-Lukasik, R. *Chem. Eur. J.* **2003**, *9*, 3033-3041.
22. Ropel, L.; Belveze, L.S.; Aki, S.N.V.K.; Stadtherr, M.A.; Brennecke, J.F. *Green Chem.*, **2005**, *7*, 83-90.
23. Wong, P.T.; Couture, P. In *Toxicity screening using phytoplankton*; Dutka, B.J.; Bitton, G. Eds. Florida, FL, CRC Press, 1986, pp. 79-100.
24. Latała, A.; Stepnowski, P.; Nędzi, M.; Mrozik, W. *Aquatic Toxicol.* **2005**, *73*, 91-98.
25. Ranke, J.; Mölter, K.; Stock, F.; Bottin-Weber, U.; Poczobutt, J.; Hoffmann, J.; Ondruschka, B.; Filser, J.; Jastorff, B., *Ecotox. Environ. Safety* **2004**, *28*, 396-404.

Chapter 3

¹³C NMR Relaxation Studies of Ionic Liquids

W. R. Carper¹, P. G. Wahlbeck¹, N. E. Heimer², and J. S. Wilkes²

¹Department of Chemistry, Wichita State University, Wichita, KS 67260

²Department of Chemistry, U.S. Air Force Academy, CO 80840-6230

A new method of obtaining molecular reorientational dynamics from ¹³C spin-lattice relaxation data of aromatic carbons in viscous solutions is applied to the cation and anion of the ionic liquid, 1-ethyl-3-methyl-imidazolium butane-sulfonate ([EMIM]BSO₃). Rotational correlation times are compared with viscosity data and indicate several [EMIM]BSO₃ phase changes over the temperature range from 278 to 328 K. Chemical shift anisotropy values are obtained for the ring and immediately adjacent methylene and methyl carbons in the imidazolium cation and for the three carbon atoms nearest to the sulfonate group in the anion.

The ability of ionic liquids to form supramolecular aggregates has always been suspected by various investigators and recent reports in the literature establish this as factual using mass spectrophotometric, ¹H NMR, conductivity and microcalorimetric methods (1,2). The ability of room temperature ionic liquids to aggregate undoubtedly affects their ability to serve as efficient reaction media and suggests that those methods identifying the aggregations process may prove to be quite useful.

In particular, nuclear relaxation rates often provide valuable information concerning the dynamics and molecular interactions that occur in the liquid state. Use of nuclear spin-lattice relaxation rates to obtain information concerning reorientational dynamics is often restricted to the extreme narrowing region. In this region, the product of the resonance frequency and the rotational correlation time is less than unity. However, many ionic liquid systems of interest are viscous such that one is outside of the region of extreme narrowing and

relaxation rates are frequency dependent. The rotational correlation equations that describe the frequency-dependent region are considerably more complex and analysis is somewhat more difficult.

NMR measurements

The ^{13}C NMR relaxation data were measured on a Varian Unity-Plus spectrometer using a D_2O capillary for a lock. ($B_0 = 4.70$ T, $\nu_0(^{13}\text{C}) = 50.31$ MHz, $\nu_0(^1\text{H}) = 200.10$ MHz). The spin-lattice relaxation times were measured using the inversion-recovery pulse sequence and calculated from the ^1H -broadband-decoupled ^{13}C spectra by a three parameter exponential fit implemented in the spectrometer software. The relaxation data were extracted from the signal heights. The measurements of the spin-lattice relaxation times were repeated at least five times, those for the NOE factors 10 times, and then the average values were used further. The error in the temperature was estimated to be ± 1 K. Chemical shift values were determined using COSY and HETCOR methods.

Methodology

^{13}C NMR relaxation studies

The relaxation of ^{13}C in medium-sized molecules at moderate magnetic fields is usually caused by dipolar interactions with directly bonded protons. When one measures the relaxation times under ^1H decoupling conditions, the cross-relaxation term vanishes. The intramolecular dipolar longitudinal (spin-lattice) relaxation rate ($R_i^{DD} = 1/T_i^{DD}$), for the relaxation of ^{13}C nucleus i by N_H protons j is connected to the molecular reorientations by (3-8):

$$1/T_i^{DD} = [1/20] N_H [2\pi D_{ij}]^2 [J(\omega_C - \omega_H) + 3J(\omega_C) + 6J(\omega_C + \omega_H)] \quad (1)$$

where the dipolar coupling constant is $D_0 = (\mu_0/4\pi)\gamma_C\gamma_H(\hbar/2\pi)r_{ij}^{-3}$, μ_0 is the permeability of vacuum, γ_C and γ_H are the magnetogyric ratios of the ^{13}C and ^1H nuclei, respectively, and r_{ij} is the length of the internuclear vector between i and j ($\text{C-H} = 1.09$ Å). $J(\omega)$ are the spectral densities with ω_C and ω_H the resonance frequencies of the ^{13}C and ^1H nuclei, respectively.

Nuclear Overhauser effect

The nuclear Overhauser (NOE) factor η_j of carbon atom j relaxed by N_H protons j is given by (3-8,9):

$$\eta_i = \gamma_H \sum \sigma_{ij} / \left[\gamma_C \sum (\rho_{ij} + \rho_i^*) \right] \quad (2)$$

where Σ includes from $j = 1$ to N_H , σ_{ij} is the cross-relaxation rate, ρ_{ij} is the dipolar relaxation rate, ρ_i^* the leakage term that represents the contribution of all other relaxation mechanisms to the relaxation of a ^{13}C nucleus i , thus reducing the NOE factor. Usually, intermolecular dipolar contributions can be neglected for ^{13}C nuclei with directly bonded protons. Under ^1H decoupling conditions, the sum of ρ_{ij} over all N_H interacting protons gives the dipolar spin lattice relaxation rate ($R_i^{DD} = R_i^{\text{Dipolar}} = 1/T_i^{\text{Dipolar}}$). The relaxation of ^{13}C exclusively via intramolecular dipolar interaction implies a leakage term $\rho_i^* = 0$. Thus the NOE factor reaches its maximum value and depends only on reorientational molecular dynamics (3-8,9):

$$\eta_{i,\max} = \gamma_H \left[6J(\omega_C + \omega_H) - J(\omega_C - \omega_H) \right] / \gamma_C \left[J(\omega_C - \omega_H) + 3J(\omega_C) + 6J(\omega_C + \omega_H) \right] \quad (3)$$

Spectral densities

Assuming isotropic tumbling, the spectral densities can be connected to the effective correlation times, τ_c , for reorientation of the corresponding internuclear ^{13}C - ^1H vectors by:

$$J(\omega) = 2\tau_c / \left[1 + (\omega\tau_c)^2 \right] \quad (4)$$

In theory τ_c is the time required for a molecule (i.e. vector connecting the interacting nuclei) to rotate through an angle of one radian, however in fact, the correlation time is the integral with respect to time from 0 to ∞ of the normalized autocorrelation function (4,7,8) and is actually τ_2 , the time constant for the exponential decay of the second-rank Legendre polynomial P_2 . In the extreme narrowing case (low viscosity solutions – unlike ionic liquids) the product of $\omega\tau_c$ is much less than unity and $J(\omega) = 2\tau_c$. For this case, $\eta_{i,\max} = 1.988$.

Chemical shift anisotropy (CSA)

Aromatic ^{13}C nuclei relax even in moderate magnetic fields partially via the chemical-shift anisotropy (CSA) mechanism. The corresponding longitudinal

relaxation rate of ^{13}C nucleus i is given by (3-8):

$$R_1^{CSA} = [1/15] \gamma_C^2 H_o^2 (\Delta\sigma_i)^2 [1 + (\eta_{CSA}^2 / 3)] J(\omega_C) \quad (5)$$

with the magnetic field strength H_o , the chemical-shift anisotropy $\Delta\sigma$ for an axially symmetric chemical shift tensor and the asymmetry parameter, η_{CSA} . The $(1 + \eta_{CSA}^2/3)$ term usually represents a correction factor of less than 5% and is therefore ignored.

CSA in aliphatic carbons

Typically, one assumes that aliphatic carbons in ionic liquids undergo only dipolar relaxation, however this is not the case for the [EMIM]BSO₃ ionic liquid as will be shown in the following sections of this report. Unless one uses the CWD method (10-12) of analysis outlined in the following sections, the degree of CSA contribution may well be overlooked. This of course would lead to errors in the determination of rotational correlation times and possibly to incorrect evaluation of possible phase changes.

Solution of the Combined Dipolar and NOE equations

In the case of ring (aromatic) carbons, it is assumed that dipolar relaxation and chemical shift anisotropy make up the overall relaxation rate:

$$R_1^{total} = R_1^{Dipolar} + R_1^{CSA} \quad (6)$$

The dipolar ($R_1^{Dipolar}$) and chemical shift anisotropy (R_1^{CSA}) spin-lattice relaxation rates for aromatic carbons may be obtained by iterations of the following steps (1) through (4), followed by step (5).

(1) The experimental T_1 's are assumed to be completely dipolar and eq 1 is solved for a pseudo rotational correlation time as follows:

$$\tau_c = [10/T_1 N_H (2\pi D_{ij})^2] \times \\ [(1/[1 + (\omega_C - \omega_H)^2 \tau_c^2]) + (3/[1 + \omega_C^2 \tau_c^2]) + (6/[1 + (\omega_C + \omega_H)^2 \tau_c^2])] \quad (7)$$

Values of τ_c were calculated by successive approximation steps by setting τ_c on the right-hand side of eq 7 equal to the previously calculated τ_c value. The initial

value of τ_c was set at 0.01 ns. A constant value of τ_c was obtained after ca. 5 successive steps, however the value after 40 successive steps was utilized.

(2) Eq's 1 and 3 are combined to form eq 8. The experimental T_1 's and the pseudo rotational correlation times from eq 7 were used in eq 8 to calculate η_{max} . If these values of η_{max} were greater than 1.988, η_{max} was set equal to 1.988.

$$\eta_{max} = N_H [T_1^{DD} / 20 (\gamma_H / \gamma_C) (2D_j)^2 [6J_+ - J_-]] \quad (8)$$

where $J_+ = [2\tau_c / [1 + (\omega_C + \omega_H)^2 \tau_c^2]]$ and $J_- = [2\tau_c / [1 + (\omega_C - \omega_H)^2 \tau_c^2]]$.

(3) The η_{max} value is then used to calculate $R_1^{Dipolar}$ from eq 9.

$$R_1^{Dipolar} = (NOE / NOE_{max}) / T_1^{total} \quad (9)$$

(4) $R_1^{Dipolar}$ is used to calculate a new τ_c as outlined in (1) above. The new τ_c is then used as outlined in step (2) above to determine a new η_{max} and the iterative process is repeated until a final self-consistent τ_c and $R_1^{Dipolar}$ are obtained.

(5) Finally, the aromatic carbon chemical shift anisotropy (R_1^{CSAr}) spin-lattice relaxation rates are determined from eq 6. Eq 5 is then used to calculate the chemical shift anisotropy ($\Delta\sigma$) for an axially symmetric chemical-shift tensor (see below).

Chemical shift anisotropy (CSA)

The chemical shift anisotropy (eq 5) is typically defined as:

$$\Delta\sigma = |\sigma_{\parallel} - \sigma_{\perp}| = \sigma_{zz} - (\sigma_{xx} + \sigma_{yy}) / 2 \quad (10)$$

With $|\sigma_{zz}| \geq |\sigma_{yy}| \geq |\sigma_{xx}|$. The asymmetry parameter, η_{csa} , is generally ignored (as mentioned previously) in chemical shift anisotropy analysis as it would normally result in less than a 5-10 % correction as shown in solid state (13) isotropic studies. Using the convention outlined for eq 9, the asymmetry factor is given by (3-8, 13):

$$\eta_{csa} = (3/2)(\sigma_{xx} - \sigma_{yy}) / \Delta\sigma \quad (11)$$

Basic Assumptions

The basic assumption in this analysis is that the maximum value of the ^{13}C NOE in eq 3 is determined by the dipolar rotational correlation time obtained from the measured relaxation rate. This assumption is based on the validity of eq 3, the derivation of which is outlined in numerous references (3-9).

Sources of Error

Sources of error include the possibility of bi-exponential behavior and the use of an isotropic model to describe anisotropic motion. At present, there are no examples of bi-exponential behavior in the literature for viscous solutions of this type. Despite its inherent assumptions, the isotropic model has proved to be reasonably successful in describing a wide range of viscous solutions and providing useful physical information concerning these systems (10-12,14,15).

Other easily detected problems include scalar relaxation and chemical exchange (3-5,8,13,16). Scalar relaxation is generally not a factor as it arises only when (a) the Larmor frequencies are similar (carbon bonded to bromine) or when a slowly relaxing nucleus is bonded to a fast relaxing nucleus (carbon bonded to aluminum). Chemical exchange is generally present when observed NMR peaks are seen to coalesce with increasing temperature as the exchange rate between species is faster than the NMR time scale. Temperature studies of [EMIM]B SO_3 and other ionic liquids discussed herein fail to indicate the presence of any of the above relaxation mechanisms.

Common sources of error in NMR relaxation analysis

- (1) A common error in NMR relaxation analysis is the assumption that one is in the region of "extreme narrowing" where $\omega\tau_c < 1$. This is simply not the case for viscous solutions where τ_c is often in the picosecond to nanosecond range.
- (2) A second error is based on the assumption that CSA is a relatively minor effect. Unfortunately, one often forgets that CSA increases with the square of the magnetic field (see eq 5) and with investigators using 9.40 Tesla and higher field magnets, CSA is likely to exist. By failing to properly evaluate the relative contribution of CSA, the dipolar relaxation rates are over estimated and the dipolar correlation times are in error. This error can lead to incorrect phase change temperatures and other related phenomena as indicated in the following sections.
- (3) Errors (1) and (2) are easily avoided by using the method of analysis described previously and outlined in eq's 1 through 11.

Analysis of the [EMIM]BSO₃ ionic liquid

NMR relaxation measurements

The δ_C chemical shift assignments for [EMIM]BSO₃ are shown in Figure 1 on the next page (16).

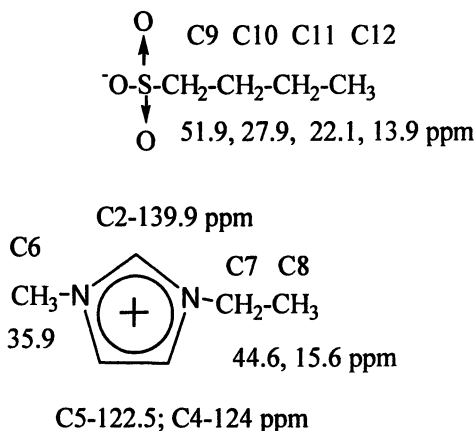


Figure 1. Chemical shift values (¹³C – ppm) and carbon positions for the 1-ethyl-3-methylimidazolium butanesulfonate ionic liquid.

Sample analysis

The following is an example of analyzed data taken from our recent study of the [EMIM]BSO₃ ionic liquid (12). The initial successive approximation process (1) for the C2 carbon at 303 K is shown in Figure 2 (1st iteration solving eq 7) and τ_c changes from 317 to 385 ps. This τ_c value is then used (2) to calculate η_{max} from eq 8. This corrected η_{max} value is used (3) to generate a new value for $R_I^{Dipolar}$ from eq (9). This $R_I^{Dipolar}$ value is then used to solve (1) iteratively for τ_c and the entire process is repeated until the values of $R_I^{Dipolar}$ and τ_c are self-consistent.

The last (7th) cycle of this process results in a τ_c value that increased slightly from 128 to 132 ps as shown in Figure 2. During the seven cycles, the η_{max} value changes from 1.694 to 1.948. Overall, the τ_c value drops from an initial 385 ps to a final value of 132 ps. This result was then used to determine the CSA contribution and a final $\Delta\sigma$ value.

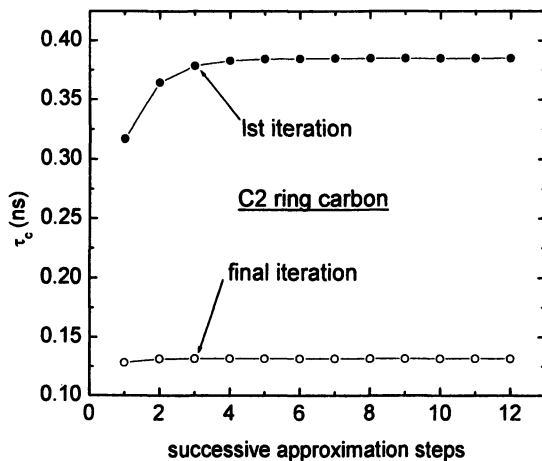


Figure 2. Solution of eq (1) for the C2 carbon in [EMIM]BSO₃.

¹³C total relaxation rates for [EMIM] cation and butanesulfonate anion

The imidazolium ring carbons (C2,C4,C5), the methyl and methylene carbons attached directly to the imidazolium ring (C6,C7) have a maximum R_1 (= T_1 minimum) in the region of 15-20°C as shown in Figure 3. The terminal ring methyl (C8) and the butyl sulfate carbons (C9,C10,C11,C12) have maxima at less than 0°C. These results indicate that the butyl carbons and the methyl carbon in the ring ethyl group are less constrained than those attached directly to the imidazolium ring. Similar results have been obtained for the [BMIM]PF₆ and [MNIM]PF₆ ionic liquids.

¹³C correlation times for [EMIM] cation and butanesulfonate anion

The initial rotational correlation times (τ_c) are determined using steps (1) through (4) followed by (5) (assuming complete dipolar relaxation) as outlined in the methodology section. The corrected rotational correlation times (ps) for the imidazolium ring carbons and other remaining cationic and anionic carbons are shown in Figure 4. The corrected (final) rotational correlation times are shorter (17) than the initial rotational correlation times, and the total relaxation rate is now separated into both dipolar relaxation and a second contribution (chemical shift anisotropy). Correction of the imidazolium ring carbon NOE's results in a correlation time maximum at 40-50°C, a shift of ca. 25°C from the R_1 maximum (= $1/T_1$ minimum) for these same carbons. At the same time, the

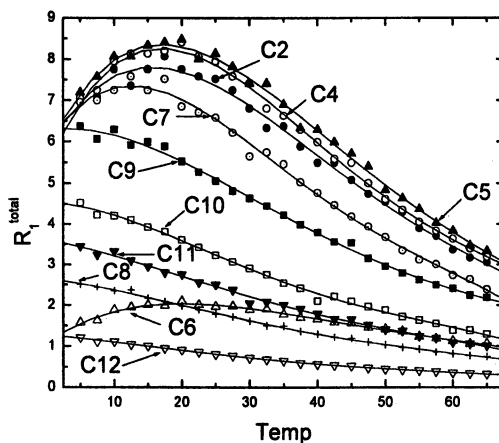


Figure 3. ^{13}C Total spin lattice relaxation rates (s^{-1}) for [EMIM]BSO₃ ionic liquid vs temperature. Imidazolium ring ^{13}C 's: C2-139.9 ppm (●); C4-124.0 ppm (○) and C5-122.5 ppm (▲). Ring methyl ^{13}C : C6-35.9 ppm (◐), ring methylene ^{13}C : C7-44.6 ppm (◑) and terminal methyl ^{13}C : C8-15.6 ppm (+). Butanesulfonate ^{13}C 's: SO₃ methylene ^{13}C : C9-51.9 ppm (■), methylene ^{13}C : C10-27.9 ppm (□), methylene ^{13}C : C11-22.1 ppm (▼) and terminal methyl ^{13}C : C12-13.9 ppm (▽). (Reproduced from reference 12. Copyright 2006 American Chemical Society.)

imidazolium ring methyl group (C6) also has a correlation time maximum at 40–50°C while the imidazolium ring methylene group (C7) has a maximum at a slightly lower temperature of ca. 35°C.

The imidazolium ring carbons (C2,C4,C5), the methyl and methylene carbons attached directly to the imidazolium ring (C6,C7) have a maximum correlation times in the region of 15–20°C as shown in Fig. 4. The terminal ring methyl (C8) and the butyl sulfate carbons (C9,C10,C11,C12) have maxima at less than 0°C. These results indicate that the butyl carbons and the methyl carbon in the ring ethyl group are less constrained than those attached directly to the imidazolium ring. Similar results have been obtained for the [BMIM]PF₆ and [MNIM]PF₆ ionic liquids.

Evidence of CSA in Both Cation and Anion of [EMIM]BSO₃

The imidazolium ring carbon C2 correlation times (τ_c) maximum at $\approx 45^\circ\text{C}$ lies between correlation time maxima of 37 and 52°C for the imidazolium C2

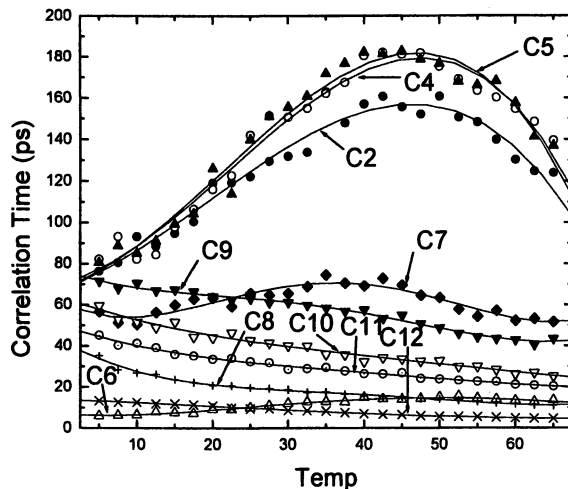


Figure 4. ^{13}C Correlation times (ps) for [EMIM]BSO₃ ionic liquid vs. temperature. Imidazolium ring ^{13}C 's: C2-139.9 ppm (●); C4-124.0 ppm (○) and C5-122.5 ppm (▲). Ring methyl ^{13}C : C6-35.9 ppm (△), ring methylene ^{13}C : C7-44.6 ppm (◆) and terminal methyl ^{13}C : C8-15.6 ppm (+). Butanesulfonate ^{13}C 's: SO₃ methylene ^{13}C : C9-51.9 ppm (▼), methylene ^{13}C : C10-27.9 ppm (▽), methylene ^{13}C : C11-22.1 ppm (○) and terminal methyl ^{13}C : C12-13.9 ppm (×).

carbons in [BMIM]PF₆ and [MNIM]PF₆ ionic liquids (10,11). The results for the methyl and methylene ring carbons are similar to those obtained for the [BMIM]PF₆ and [MNIM]PF₆ ionic liquids (10,11).

Figure 5 contains a plot of ^{13}C CSA vs. temperature for the [EMIM] cation and the butylsulfonate anion in the [EMIM]BSO₃ ionic liquid. In previous studies of [BMIM]PF₆ and [MNIM]PF₆, CSA was observed for the imidazolium carbons and those carbons immediately adjacent to the imidazolium ring. In the case of the [EMIM]BSO₃ ionic liquid, one observes CSA for the ring methyl and ethyl carbons and for the three carbons nearest to the sulfonate group. Only the terminal carbon in the butyl group fails to exhibit CSA dependency. In previous studies of [BMIM]PF₆ and [MNIM]PF₆ ionic liquids (10,11), CSA was present only in either the ring carbons or those carbons immediately adjacent to the imidazolium ring. The [EMIM]BSO₃ ionic liquid exhibits CSA in all of the imidazolium carbons and all butyl carbons with the exception of the terminal methyl carbon. The average $\Delta\sigma$ values for the imidazolium ring and butanesulfonate carbons are C2-136, C4-130, C5-139, C6-251, C7-147, C8-113, C9-167, C10-135 and C11-136 ppm. Unlike the other carbons in both cation and anion, the C12 carbon displays only dipolar relaxation.

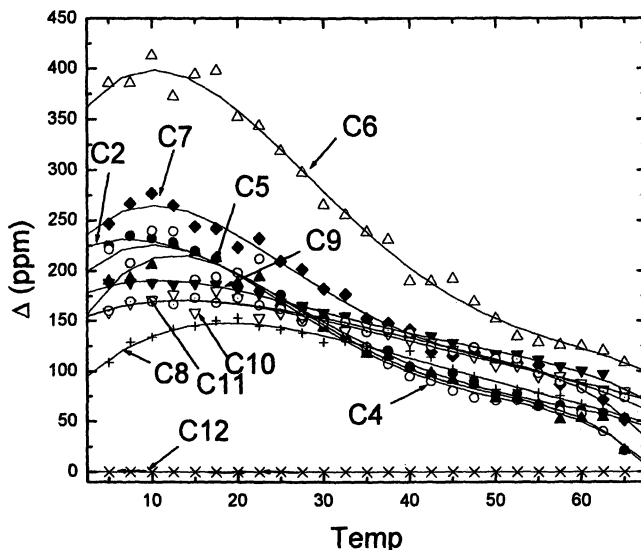


Figure 5. ^{13}C CSA (Δ) for [EMIM]BSO₃ ionic liquid vs. temperature: Imidazolium ring ^{13}C 's: C2-139.9 ppm (●); C4-124.0 ppm (○) and C5-122.5 ppm (▲). Ring methyl ^{13}C : C6-35.9 ppm (△), ring methylene ^{13}C : C7-44.6 ppm (◆) and terminal methyl ^{13}C : C8-15.6 ppm (+). Butanesulfonate ^{13}C 's: SO₃ methylene ^{13}C : C9-51.9 ppm (▼), methylene ^{13}C : C10-27.9 ppm (▽), methylene ^{13}C : C11-22.1 ppm (○) and terminal methyl ^{13}C : C12-13.9 ppm (×).

Evidence of phase changes from viscosity and NMR data

In classical mechanics, the correlation time, τ_c , of spherical particle undergoing isotropic rotation is given by the SED eqn:

$$\tau_c = 4\pi a^3 \eta / 3kT = V\eta / kT \quad (12)$$

For those correlation times determined by NMR, the relationship (19) between τ_c and temperature in the viscosity-dependent region is given by:

$$\tau_c = \tau_o + \eta\tau_{red} / T \quad (13)$$

Where $\tau_{red} = V/k$. The values of the hydrodynamic radius obtained from this type of analysis are typically too small and are often corrected using a nonspherical rotational model (10-12,19).

NMR correlation time relationship with viscosity

Figure 6 contains a plot of [EMIM] ring carbon (C2,C4,C5) NMR correlation times vs. viscosity/K for the [EMIM]BSO₃ ionic liquid. A similar plot was obtained for the more viscous ionic liquid, [MNIM]PF₆ (11). As is the case with [MNIM]PF₆, [EMIM]BSO₃ undergoes several phase changes and the only region where the slope is positive is at the higher temperatures between 35 and 55°C.

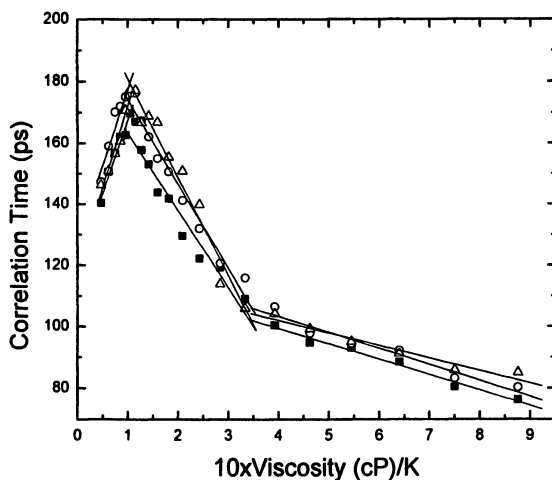


Figure 6. Correlation time (ps) for C2 (■), C4 (○) and C5 (△) vs viscosity/K (cP/K) for [EMIM] in [EMIM]BSO₃. From left to right, temperature ranges include 328-308 K, 308-293 K and 293-278 K. (Reproduced from reference 12. Copyright 2006 American Chemical Society.)

Figure 7 contains a plot of the BSO₃ ¹³C (C9,C10,C11,C12) NMR correlation times vs. viscosity/K for the [EMIM]BSO₃ ionic liquid. Unlike the [EMIM] cation in [EMIM]BSO₃, one observes only a single phase for the BSO₃ anion change in the vicinity of 25-35°C. Furthermore, there are no additional phase changes observed between 5 and 30°C for the BSO₃ anion.

Acknowledgments

W.R.C. thanks the National Research Council for a Summer Research Faculty Fellowship and Professors Andreas Dölle and Manfred Zeidler, RWTH Aachen, Germany for many fruitful discussions.

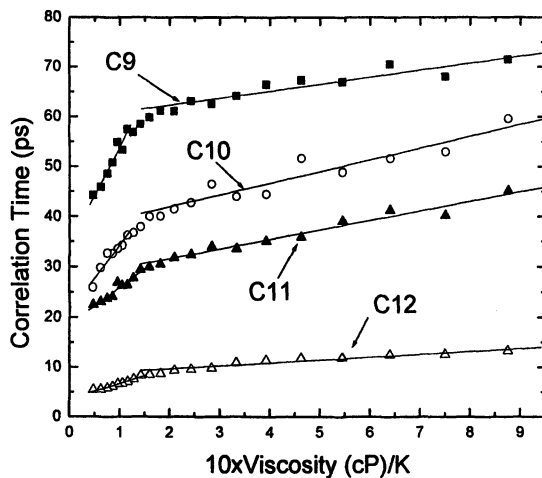


Figure 7. Correlation time (ps) for butyl carbons in BSO_3 in $[\text{EMIM}]\text{SO}_3$ vs viscosity/K (cP/K): C9 (■), C10 (○), C11 (▲) and C12 (△). From left to right, temperature ranges include approx. 328-303 K and 303-278 K.

References

1. Dorbritz, S.; Ruth, W.; Kragl, U. *Adv. Synth. Catal.* **2005**, *347*, 1273-1279.
2. Consorti, C. S.; Suarez, P. A. Z.; de Souza, R. F.; Burrow, R. A.; Farrar, D.; Lough, A. J.; Loh, W.; de Silva, L. H. M.; Dupont, J. *J. Phys. Chem.. B* **2005**, *109*, 4341-4349.
3. Abragam, A. *Principles of Nuclear Magnetism*; Oxford University Press: Oxford, UK, 1961; Chapter 8.
4. Farrar, T. C.; Becker, E. D. *Pulse and Fourier Transform NMR. Introduction to Theory and Methods*; Academic Press: New York, 1971.
5. Spiess, H. W. In *NMR: Basic Principles and Progress*; Diehl, P., Fluck, E., Kosfeld, R., Eds.; Springer-Verlag: Berlin, 1978; Vol. 15, 55.
6. Canet, D.; Robert, J. B. In *NMR: Basic Principles and Progress*; Diehl, P., Fluck, E., Gunther, H., Kosfeld, R., Seelig, J., Eds.; Springer-Verlag: Berlin, 1990; Vol. 25, 46.
7. McConnell, J. *Nuclear Magnetic Relaxation in Liquids*. Cambridge University Press, Cambridge, 1987.
8. Canet, D. *Nuclear Magnetic Resonance: Concepts and Methods*. John Wiley & sons, New York, 1996.
9. Neuhaus D.; Williamson M. P. *The Nuclear Overhauser Effect in Structural and Conformational Analysis*. Wiley-VCH press, New York, 2000.

10. Carper, W. R.; Wahlbeck, P. G.; Dölle, A. *J. Phys. Chem. A* **2004**, *108*, 6096-6099.
11. Antony, J. H.; Dölle, A.; Mertens, D.; Wasserscheid, P.; Carper, W. R.; Wahlbeck, P. G. *J. Phys. Chem. A* **2005**, *109*, 6676-6682.
12. Heimer, N. E.; Wilkes, J. S.; Wahlbeck, P. G.; Carper, W. R. *J. Phys. Chem. A* **2006**, *110*, 868-874.
13. Mehring, M. In *High Resolution NMR Spectroscopy in Solids*; Diehl, P., Fluck, E., Kosfeld, R., Eds.; Springer-Verlag: Berlin-Heidelberg-New York; NMR-Basic Principles and Progress, 1976, Vol 11, 167.
14. Antony, J. H.; Mertens, D.; Dölle, A.; Wasserscheid, P.; Carper, W. R. *ChemPhysChem*, **2003**, *4*, 588-594.
15. Carper, W. R. *Concepts Magn. Reson.* **1999**, *11*, 51-60.
16. Halle, B.; Wennerstrom, H. *J. Magn. Reson.* **1981**, *44*, 89-100.
17. This statement is incorrect in ref. (10) due to an error in legend of Fig. 2 in ref. (10).
18. Parhami, P.; Fung, B. M. *J. Amer. Chem. Soc.* **1985**, *107*, 7304-7306.
19. Boere, R. T.; Kidd, R. G. In *Annual Reports on NMR Spectroscopy*; Webb, G. A., Ed.; Academic Press: New York, 1982; Vol. 13, p. 319.

Chapter 4

Ionic Liquids for Silica Modification: Assessment by Capillary Zone Electrophoresis

Maria Borissova, Mihkel Koel, and Mihkel Kaljurand

**Institute of Chemistry, Akademia tee 15, Tallinn University of Technology,
12 618 Tallinn, Estonia**

Use of Room Temperature Ionic Liquids (RTILs) in capillary electrophoresis as the additives of separation media and/or modifiers of capillary surface is question of great interest. The modified capillary has remarkable benefits: the analyte – silica wall interactions are significantly decreased and the direction of electroosmotic flow can be manipulated by appropriate modifying reagent. In the present study imidazole-based ionic liquid analogs have been permanently bounded to capillary wall. The coated capillaries were examined for use with aqueous as well as with non-aqueous electrolytes. The effectiveness of the coating has been investigated by separating the mixture of phenolic compounds in non-aqueous media. The run-to-run and for day-to-day reproducibility of coated capillaries in terms of neutral marker migration times has been evaluated.

Introduction

Silica xerogels has received much attention as a support material in chromatographic methods, catalysis, photo-catalysis and other areas due to its' many advantages over other inorganic or organic supports. The silica surface is resistant to organic solvents and moderate thermal treatment, modification of silica is easier than any organic polymeric support and is achieved using a great variety of silylating agents [1]. Moreover, silica gel is a very popular, relatively inexpensive and commercially available material.

Silica gels can also be coated along with such reagents as polymers [2], surfactants [3] and amine compounds [4], room-temperature ionic liquids (ILs) have begun to be used. Ionic liquids are widely known as non-volatile, high thermal and chemical stability liquids and as good solvents for various inorganic and organic materials. These properties make them unique choices for different chemical processes, but current emphasis still belongs to organic synthesis [5], electrochemistry [6] and catalyst technology [7]. In the last few years, the application of ionic liquids in separation science has grown progressively and particularly in capillary electrophoresis (CE) [8-11], liquid (LC) [12-14] and gas chromatography (GC) [15].

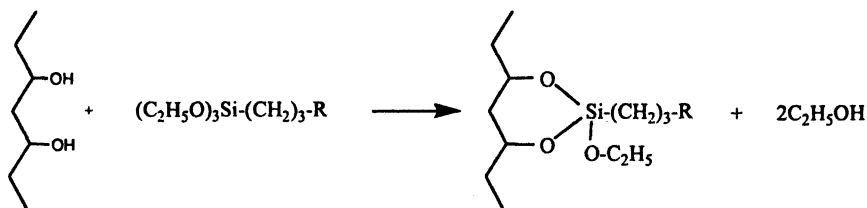
Traditional physical methods, such as X-ray photoelectron spectroscopy [16], photoacoustic IR spectroscopy [17,18], solid-state ^{13}C and ^{29}Si NMR [17], and chemical methods [19, 17] are suitable for the measuring changes on silica surface. In spite of this, CE proved to be a simple and promising technique for characterization of ionic liquid interaction with silanol groups. The determination of the magnitude and the direction of generated electroosmotic flow (EOF) is major characteristic of the new surface. Based on electrophoretic method, changes in charge density and charge type could be easily determined [20]. Behavior of immobilized ionic salt in different organic medias and affect of modified silica on analytes are also could be investigated by this analytical method.

In capillary electrophoresis IL – silica interaction could be examined as adsorption onto activated silica surface or modification without any chemical bonding via weak-forces (physical or ionic forces). Such kinds of surface modification are called dynamic coating. These attract attention due to method simplicity and their renewable properties. The presence of ILs in running buffer acts as coating agent covering the negatively charged surface with positive imidazolium ions and, thus, causing reduced or reversed electroosmotic flow EOF [2, 21].

Yanes and co-workers reported [9] the simple and reliable capillary electrophoretic method for the separation of phenolic compounds using typical ionic liquids (1-alkyl-3-methylimidazolium with different anionic parts). According to these authors, the separation mechanism is based on association between IL cation, presented in bulk buffer solution or and immobilized onto capillary wall, and analyte.

In similar way Jiang et al. [22] solved the problem of positively charged proteins adsorbing on the bare capillary surface by adding imidazolium-based ionic liquids to the running electrolyte in CE system: added salt “masked” the negative charge of fused capillary surface turning it to positive. The ability of ILs to adsorb onto wall surface and affect the EOF was used by Yu et.al [23] for separation of benzoic acid and chlorophenoxy acid herbicides. Rapid and sensitive method for separation of anthraquinones in Chines herb using dynamically adsorbed 1-butyl-3-methylimidazolium-based ionic liquid was reported by Qi et al. [24]

In the case of permanent coating, modifying compound is introduced onto the fused-silica capillary wall via formation of covalent bonds. Covalently bonded capillaries are less intricate in maintenance, but preparation process could be complicated. The most used approach for compound immobilization onto silica surface is organo-silanization through Si-O-Si linkage. Usually, modified silica surface prepared by well-known method which include the silane precursor $X_3\text{Si-A}$ bonding to the pretreated support. The typical reaction is using propyltriethoxysilane group as precursor and can be presented as:



where R is the moiety representing the functional part needed for further modification. Unfortunately, siloxane linkage Si-Q-Si suffers from long-term instability, since the siloxane linkage is prone to hydrolysis in basic conditions [25].

Such permanent coatings have been employed by Qin et al. [26,27] for determination of ammonium and metal ions by CE. Authors used imidazolium-based ionic liquid as the coating reagent and as the component in separation media also.

Chemical modification of the silica surface results in predetermined changes of chemical composition and, thus, properties of resulted support. The knowledge of behaviour of silica – modifying agent interaction is of great importance for the understanding and eventual improvement of their performances. In the present paper we study the interaction of ionic liquid-based modifier with a silica surface and its' behavior on silica coatings. An evaluation of this modifier as a multi-purpose coating for aqueous and non-aqueous capillary electrophoresis is reported as one of the possible applications.

Experimental

Apparatus

CE separations were performed in ISCO Model 3850 electropherograph with a UV absorbance detector. All experiments were carried out in coated fused-silica capillary of 50 μm I.D. with a total length of 67 cm and a distance from injection end to detection window 41 cm. pH values of the buffers were measured using Metrohm 744 pH Meter equipped with combined glass electrode.

Experimental conditions

Mesityl oxide (MO) for non-aqueous and dimethyl sulfoxide (DMSO) for aqueous buffers were used as neutral markers for EOF observation. Previously capillary for the experiments was washed with appropriate buffer till baseline stabilization. All samples were introduced hydrodynamically into capillary with duration of an injection 2-4 sec. The applied voltage was conducted at -18 kV or 18 kV. Separation processes were monitored by light absorbance at 210 nm.

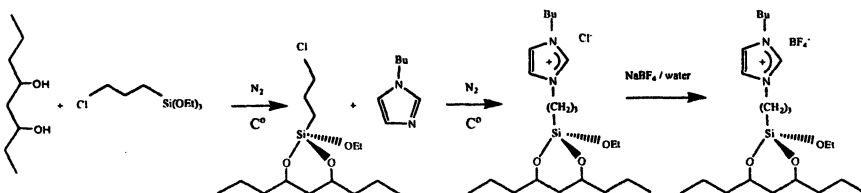
Reagents

N-3-(3-triethoxysilylpropyl)-4, 5-dihydroimidazole was purchased from ABCR GmbH & Co, 1-chlorobutane and sodium tetrafluoroborate were obtained from Aldrich (Germany). All organic solvents (acetonitrile (ACN), acetone, methanol, ethanol, DMSO, propylene carbonate (PC) were analytical reagent grade and were received from Sigma-Aldrich (Germany). 1-butyl-3-methylimidazolium-based ionic liquids with two typical anionic parts: heptafluorobutanoate ($[\text{CF}_3(\text{CF}_2)_2\text{COO}]^-$) and trifluoroacetate ($[\text{CF}_3\text{COO}]^-$) as background buffer components were prepared at the Institute of Chemistry of Tallinn University of Technology following the methods described elsewhere [28]. Phenolic compounds: resorcinole, phloroglycinol, phenol, *p*-cresol were obtained from Sigma-Aldrich (Germany). Deionized water from a Milli-Q water system (Millipore, France) were used for capillary washing and solution preparation.

Capillary coating procedure

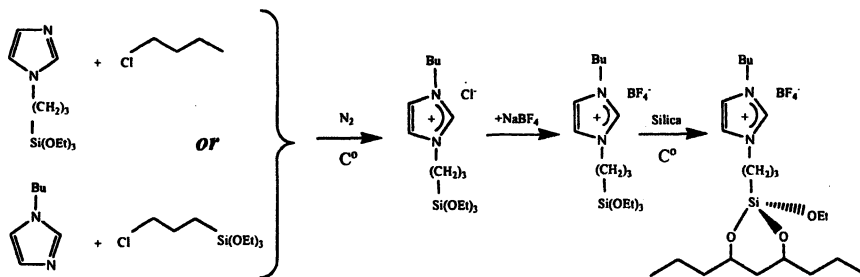
Before coating, the fresh capillary was activated by rinsing with $1M$ NaOH for 2 h and with deionized water for 20 min, with $1M$ HCl for 60 min with further flushing with deionized water in consecutive order. The capillary was washed with methanol for 10 min and then dried at 110°C under the flow of dry nitrogen directly before silanization. Finally the capillary inner surface was modified via different procedures described in [16,17,29,30] which should result in the same final product.

Heterogeneous way (HE)



The pre-treated capillary was filled with 3-chloropropyltriethoxysilane dissolved in *m*-xylene (20 %, v/v). The ends of the capillary were closed and then the capillary was heated in the oven at 150°C for 20 hours. After the reacting time the column was washed with *m*-xylene and dried with nitrogen at 110°C. During the next step butylimidazole was dissolved in *m*-xylene (50%, v/v) and introduced into capillary. The filled and closed column was heated in the oven at 90°C for 48 hours and then washed with xylene and dried under nitrogen flow. The final step of the modification process consisted of anion exchange of coating reagents. The 40mM aqueous solution of NaBF₄ was prepared for that purpose. The column was filled with NaBF₄ solution and both ends of the capillary were also immersed into the same solution. The capillary was held at room temperature for 24 hours and flushed with fresh solution after 12 hours. Finally, the modified column was washed with deionized water.

Homogeneous way (HO)



The coating reagent 1-butyl-3-(3-triethoxysilylpropyl)-4,5-dihydroimidazolium tetrafluoroborate was prepared as follows: chloride complex was synthesized by stirring *N*-3-(3-triethoxysilylpropyl)-4,5-dihydroimidazol with 1-chlorobutane at 78 °C for 21 h. The resulting mixture was cooled and the volatiles evaporated under reduced pressure. The residue was washed several times with pentane and dried. Finally, after dissolving the material into dichloromethane, filtration and the removal of volatile components the chloride was obtained. The same product was received by refluxing of butylimidazol with 3-chloropropyltriethoxysilane at 90°C for 60h. After that unreacting materials were separated by extraction with diethyl ether and the residual ether was evaporated under reduced pressure. All reactions were performed under argon atmosphere because of air- and water sensitivity of compounds. Afterwards chloride was treated with NaBF₄ in ACN at room temperature to form ionic liquid - based modifier. The resulting ionic liquid complex was dissolved in chloroform (50 mg/ml) and introduced into capillary. The filled capillary was placed in the oven and kept there at 90 °C for 1 8h. Later the excess of ionic liquid was removed by bleeding of nitrogen through the capillary. Then a capillary was flushed with acetone and deionized water for 10 and 30 min correspondingly and dried with nitrogen.

Results and Discussion

Surface characterization

In the present study, the modification of the inner surface of a capillary using an imidazolium-based ionic liquid analogs was achieved with both immobilizing methods described above. As experiments show, the final step of the modifying process, Cl^- replacing by BF_4^- , may be excluded because the anion choice has no demonstrable influence on electrophoretic behaviour in the coated capillary. The direction and magnitude of EOF are central parameters which help to characterize the modified capillary surface. The first parameter informs about the charge type on the surface and the second – about the charge density. It was observed that in ACN the direction of EOF in HO and HE capillaries was reversed in comparison to that of bare capillary (towards to cathode) and this confirmed that the negative capillary wall charge was changed to positive. The completeness of modifying processes was determined by measurements of EOF mobilities in ACN in both method coated capillaries (Table 1). Although the two methods nominally lead to the formation of the same coating, the capillary prepared by heterogeneous approach was less effectively covered. This results in low peak resolution, peak broadening and longer analysis time.

The difference in magnitude of the EOF can be explained by charged silanol groups that have not been covered by modifier as well as an indicator of the number of immobilized anchor groups on the wall capillary. This means, that number of blocked OH-groups is greater in the case of the homogeneous method [19]. In other words, anchored imidazolium cations that predominate on the capillary wall, but positive charge density is lower in comparison to the charge density on the capillary wall when prepared by the homogeneous method. The magnitude of reversed EOF is limited by ionisation of uncoated silanol groups.

In spite of this, the first method is easier and less reagent-consumed since all reactions are carried out inside the capillary. Moreover, varying the concentration of 3-chloropropyltriethoxysilane during the first step of surface modification, could lead to total suppression of the EOF. This is due to the resulting balance between negatively charged silanol groups on bare silica and the positive charge induced by the immobilized cations.

Table 1. Comparison of two modified capillaries prepared in different mode.

	EOF mobility ($\cdot 10^{-8} \text{ m}^2 \text{V}^{-1} \text{ s}^{-1}$)	Run-to-run RSD% (n=5)	Day-to-day RSD% (n=3)
Heterogeneous	6,1	2,11	3,43
Homogeneous	10,96	1,17	4,28

Moreover, six organic solvents and water were used to characterize the properties of coated capillary. The variety of different solvents (including water) applied in CE encompass a broad scale of physicochemical properties and, thus, flexibility in electrophoretic selectivity manipulation. It is known, that mobility of the electroosmotic flow (μ_{eof}) strongly depends on the nature of the separation buffer as following:

$$\mu_{eof} = -\varepsilon\xi/\eta \quad (1)$$

where ε is the relative permittivity, η is the viscosity of the buffer and ξ is the zeta-potential [31]. In case of pure solvent the last parameter ξ is predominantly dependent on the charge density on the capillary surface which is influenced by modifications of the inner surface of capillary.

The magnitude of EOF in HO capillary for non-aqueous buffers and water was determined by measuring migration time of neutral marker and the ξ -potential of HO coated capillary surface in all solvents was calculated also (Table 2). As it was reported [32] there is no direct correlation between the zeta potential and EOF mobility. It can be seen from the table that the highest mobility was detected using ACN ($10,96 \times 10^{-8} \text{ m}^2\text{V}^{-1}\text{s}^{-1}$) and slowest in propylene carbonate ($1,57 \times 10^{-8} \text{ m}^2\text{V}^{-1}\text{s}^{-1}$). EOF mobility value in ACN was in accordance with theoretical reasoning taking high ε/η ratio and high zeta potential (-130,9 mV) into account. EOF mobility in DMSO was slow because of the high viscosity of this solvent; nevertheless the zeta potential was higher (-136,9 mV) in compare with other solvents.

Taking into account the above-mentioned reasons and results the homogeneously prepared capillary and acetonitrile as a separation media were chosen for further experiments in non-aqueous electrophoretic system.

Effect of IL concentration in buffer

1-butyl-3-methylimidazolium heptafluorobutanoate (BuMeIm-HPB) and 1-butyl-3-methylimidazolium trifluoroacetate (BuMeIm-TFA) were tested as additives to ACN. The addition of ionic liquid to the separating buffer executes several functions. First of all ionic liquid acts as source of charged components in buffer. The charging mechanism of analyte in ACN (which is poor hydrogen bond donor) is based on analyte ability to donate a hydrogen bond to the ionic liquid anions and thus form negatively charged analyte-anion complexes that could be separated due to the differences in heteroconjugate formation. [35,36] Moreover, addition of salt plays a role of dynamical modification by blocking the uncoated silanol groups of the wall to avoid analyte adsorption and improve migration time reproducibility.

The influence of ionic liquid concentration was evaluated for the separation of four phenolic compounds and is illustrated in Figure 1.

Table 2. Some physiochemical properties of conventional organic solvents [33], EOF migration mobilities and calculated surface zeta-potentials in HO coated capillary using pure solvents as separation media (Conditions as described in 2.1 and 2.2 except values marked with * - applied voltage, -30 kV).

Solvent	Properties of the organic solvents		EOF measurements			
			Coated capillary	Fused capillary ^a		
	Relative Permittivity, ϵ	Viscosity, (mPa·s) η	Mobility, μ , ($10^{-9} \text{ m}^2 \text{ V}^{-1} \text{ s}^{-1}$)	Run-to-run RSD% of μ (n=5)	Mobility, μ , ($10^{-9} \text{ m}^2 \text{ V}^{-1} \text{ s}^{-1}$)	Calculated zeta-potentials ξ , mV
ACN	35.94	0.341	109.6	1.17	20.5	-130.9
H ₂ O	78.36	0.89	69.2	0.62	7.7	-98.77
MeOH	32.66	0.551	33.6	0.69	3.2	-72.05
Acetone	20.72	0.326	27.0	0.69	8,9	-53.4
EtOH	24.55	1.083	19.6	0.46	1.9	-110.8
PC	64.92	2.53	15.7*	1.98	4.2	-74.72
DMSO	46.45	1.991	25.0*	0.88	0.1	-136.9

^a Data from Ref. [34]

It is easy to notice that the usage of BuMeIm-HPB (plot A on figure 1) as buffer additive represents better results in resolution/analysis time ratio. Thus heteroconjugation of the analytes was strongest with this type of ionic liquid anion. BuMeIm-HPB concentration corresponding to the limiting mobility (maximum degree of heteroconjugation) for resorcinol and phenol was found in range of 0,8 mg/ml and for *p*-cresol, phloroglucinol – 1 mg/ml. Further addition of ionic liquid to the running buffer leads only to analysis time increasing due to the changes in viscosity and ionic strength (buffer concentration) value and do not influence on complex formation.

As can be seen in case of BuMeIm-TFA (plot B on figure 1) the analyte mobility dependence from additive concentration is different. Using additive concentration 0,6-0,8 mg/ml no resolution was observed for the *p*-cresol and phloroglucinol. In the same time phenol and resorcinol were successfully separated at IL concentration 0,8 mg/ml. Further increase of ionic liquid content improves the separation of *p*-cresol and phloroglucinol also. Interesting is the fact that phenol and resorcinol are the analytes that exhibit a decrease in mobilities when increasing the concentration of ionic liquid in the buffer. Explanation of that needs further investigations. So BuMeIm-TFA concentration in 1 mg/ml was found to be optimal for achievement sufficient relation between migration time and resolution (selectivity).

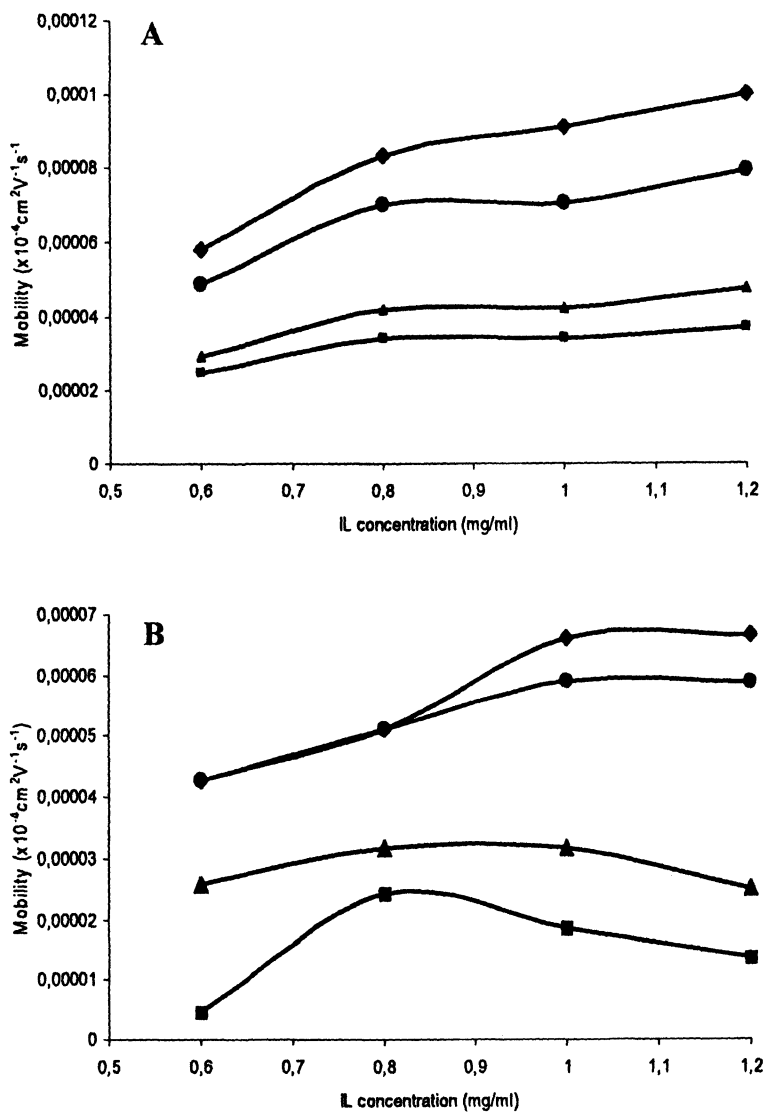


Figure 1. The effect of 1-butyl-3-methyl-imidazolium heptafluorobutanoate (A), 1-butyl-3-methyl-imidazolium trifluoroacetate (B) on the electrophoretic mobility of phenols: (◆) *p*-cresol, (●) phloroglucinol, (▲) phenol, (■) resorcinol.

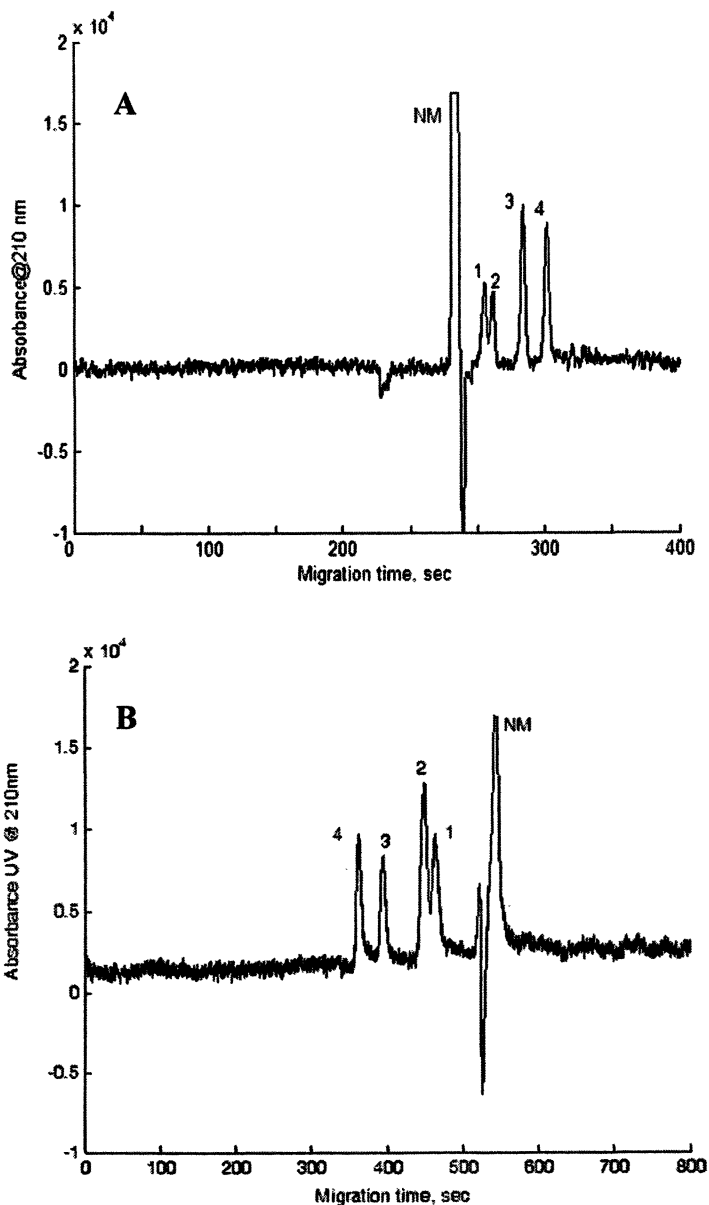


Figure 2. Performance of phenols separation in A) uncoated capillary. Conditions: applied voltage, 18 kV; background electrolyte, BuMeIm-HFB in acetonitrile (1 mg/ml); B) HO coated capillary. Conditions: applied voltage, -18kV; background electrolyte, BuMeIm-HFB in acetonitrile (0,8 mg/ml). Analytes: 1- phloroglucinol, 2 - resorcinol, 3 - p-cresol, 4 - phenol, NM - neutral marker.

Figure 2 presents an example of separation of phenolic compounds when BuMeJmHFB was used as background additive for both untreated and coated capillaries. As it is seen the separation for both systems is realized with the similar resolution and in short analysis time (6-10 min). In uncoated capillary simple addition of ionic liquids (1 mg/ml) does not change the EOF direction. On the other hand the analysis time in the modified capillary is longer. The analytes also migrated in reversed order.

The performance and stability of coated capillary was also tested for aquatic separation media. Si-O-Si linkage stability at pH range 4-7 makes possible (although, with the limitation) the application of coated capillary for separation using aqueous electrolytes.

Stability of coating was examined by measuring of migration time of neutral marker (DMSO). Reproducibility test were performed for run-to-run variation of migration times and resulted in RSD value of 1,88 % (n=5) and day-to-day variation in RSD value of 4,52% (n=3). The last number obviously indicate the degradation of surface coating and it instability in aqueous electrophoretic system.

Conclusion

Capillary electrophoresis is a suitable and simple method for the characterization of a modified capillary silica surface. Two silica capillaries with a covalently anchored imidazolium-based ionic liquid analog were successfully prepared by homogenous and heterogeneous techniques and compared using capillary zone electrophoresis. It was found that homogeneous process of capillary modifying is preferable in terms of stability and positive charge density. Direction of electroosmotic flow in coated capillaries was reversed in case of all background buffers. EOF magnitude and zeta potentials, as principal surface characteristics, were determined for six different electrophoretic solvents. At last, baseline separation of some phenolic compounds, using combination of coated capillary and ionic liquids as background analyte has been successfully achieved.

Acknowledgements

The authors thank the Estonian Science Foundation grant 5610 for financial support.

References

1. Jal, P. K.; Patel, S.; Mishra, B. K. *Talanta* **2004**, *62*, 1005-1028.
2. Belder, D.; Elke, K.; Husmann, H. *J. Microcol. Sep.* **1999**, *11*, 209-213,
3. Melanson, J. E.; Barylka, N. E.; Lucy, C. A. *Tr. Anal. Chem.* **2001**, *20*, 365-374.

4. Righetti, P. G.; Gelfi, C.; Sebastiano, R.; Citterio, A. *J.Chromatogr. A* **2004**, *1053*, 15-26.
5. Rogers, R.D.; Seddon, K.R. *Ionic Liquids as Green Solvents: Progress and Prospects*, ACS, Washington DC, 2003.
6. *Electrochemical Aspects of Ionic Liquids*; Hiroyuki, O.; Wiley & Sons, 2005.
7. Welton, T. *Coordination Chem. Rev.* **2004**, *248*, 2459-1477.
8. Vaher, M.; Koel, M.; Kaljurand, M. *Chromatographia* **2001**, *53*, 302-306.
9. Yanes, E.G.; Gratz, S.R.; Stalcup A.M. *Analyst* **2000**, *125*, 1919.
10. Tian, K.; Qi, S.; Cheng, Y.; Chen, X.; Hu, Z. *J. Chromatogr. A* **2005**, *1078*, 181-187.
11. Vaher, M.; Koel, M.; Kaljurand, M. *J. Chromatogr. A* **2002**, *979*, 27-32.
12. He, L.; Zhang, W.; Zhao, L.; Liu, X.; Jiang, S. *J. Chromatogr. A* **2003**, *1007*, 39-45
13. Xiaohua, X.; Liang, Z.; Xia, L.; Shengxiang, J. *Anal. Chim. Acta* **2004**, *519*, 207-211.
14. Marszałł, M. P.; Bączek, T.; Kaliszczan, R. *Anal. Chim. Acta* **2005**, *547*, 172-178.
15. Anderson, J.L.; Armstrong, D.W. *Anal. Chem.* **2003**, *75*, 4851.
16. Chi, Y. S. *Langmuir* **2004**, *20*, 3024-3027.
17. Valkenberg, M.H.; deCastro, C.; Hölderich, W.F. *Green Chem.* **2002**, *88-93*.
18. Guidotti, B. R.; Herzog, E.; Bangerter, F.; Caseri, W. R.; Suter, U. W. *J. Coll. Interf. Science* **1997**, *191*, 209-215.
19. Prado, A. G. S.; Sales, J. A. A.; Carvalho, R. M.; Rubim, J. C.; Airoidi, C. *J. Non-Cryst. Solids* **2004**, *333*, 61-67.
20. Xu, L.; Feng, Y.; Shi, Z.; Da, S.; Wei, F. *J. Chromatogr. A* **2004**, *1033*, 161-166.
21. Steiner, F.; Hassel, M. *Electrophoresis* **2003**, *24*, 399-407.
22. Jiang, T.; Gu, Y.; Liang, B.; Li, J.; Shi, Y.; Ou, Q. *Anal. Chim. Acta* **2003**, *479*, 249-254.
23. Yu, L.; Qin, W.; Li, S. F. Y. *Anal. Chim. Acta* **2005**, *547*, 165-171
24. Qi, S.; Cui, S.; Chen, X.; Hu, Z. *J. Chromatogr. A* **2004**, *1059*, 191-198
25. Nakatani, M.; Shibukawa, A.; Nakagawa, T. *Electrophoresis* **1995**, *16*, 1451.
26. Qin, W.; Wei, H.; Li, S.F.Y. *J. Chromatogr. A* **2003**, *985*, 447-454.
27. Qin, W.; Li, S. F. Y. *J. Chromatogr. A* **2004**, *1048*, 253-256.
28. Bonhôte, P.; Dias, A.; Papageorgiou, N.; Kalyanasundaram, K.; Grätze, M. *Inorg. Chem.* **1996**, *35*, 1168-1178.
29. Mehnert, C.P. *J. Am. Chem. Soc.* **2002**, *124*, 12932-12933.
30. Liu, C.; Ho, Y.; Pai, Y. *J. Chromatogr. A* **2000**, *897*, 383-392.
31. Geiser, L.; Mirgaldi, M.; Veuthey, J.-L. *J. Chromatogr. A* **2005**, *1068*, 75-81.
32. Valkó, I. E.; Siren, H.; Riekkola, M.-L. *J. Microcol. Sep.* **1999**, *11*, 199.
33. Marcus, Y. *The Properties of Solvents* Wiley, Chichester, 1998.
34. Vaher, M.; Koel, M. *Proc. Estonian Acad. Sci. Chem.* **2004**, *53*, 36-45.
35. Okada, T. *J. Chromatogr. A* **1998**, *804*, 17-28.
36. Porras, S. P.; Kuldvee, R.; Palonen, S.; Riekkola, M.-L. *J. Chromatogr. A*, **2003**, *990*, 35-44.

Chapter 5

Characterization of Phosphonium Ionic Liquids with Emphasis on Mass Spectrometry and Chromatography

**Ted Chang¹, Allan Robertson², Eduardo Kamenetzky¹,
Chermeine Rivera¹, Liying Du¹, Douglas Harris¹, Michael Piquette¹,
Donato Nucciarone², and Christopher Crutchfield¹**

¹Cytec Research Center, Cytec Industries, 1937 West Main Street,
Stamford, CT 06904

²Cytec Canada Inc., 9061 Garner Road, Niagara Falls,
Ontario L2E 6S5, Canada

Introduction

The majority of ionic liquid publications deal the synthesis, properties and applications of ionic liquids. This paper focuses on characterization and analysis of ionic liquids, more specifically on trace analysis. Cytec is a major producer of phosphonium ionic liquids and believes that as industrial applications and demand for ionic liquids continues to grow, so will the needs for accurate analytical methods to determine trace quantities of various ionic liquids in reactions streams as well as impurity ions in the ionic liquids. In this paper, we will address some of these issues.

Product assays usually require identification and analysis to the extent of 0.1% for various impurities-physical properties of ionic liquids are particularly sensitive to low levels of anion impurities¹. In addition, toxic and carcinogenic impurities need to be determined to the ppm level or to the ppb level depending on their chemical/biological toxicity. If ILs are to be used as solvents or as catalysts, their residual amounts in the products have to be analyzed accurately.

In degradation studies, UV measurement alone is not only insufficient but often also includes false positives. The degradation products need to be identified and determined individually. For environmental and toxicology studies, analytical methods are often required with sub-ppm or ppb sensitivity

depending on regulations. In industrial productions, the discharge of waste water to natural water is a highly regulated issue. As ionic liquid manufacturers, we are obligated to develop methods not only to assay the products but also to determine their ultimate fate in the environment. For these reasons, applications of mass spectrometric and chromatographic techniques for the analysis of phosphonium ionic liquids are being investigated.

Phosphonium Ionic Liquids

Phosphonium salts, especially halides, have been available commercially for many years. The main applications being used as phase transfer catalysts, in resin curing or as biocides. They are typically made by quaternizing a tertiary alkylphosphine with a chloro, bromo or iodo alkane. The resulting phosphonium halides can be used as ionic liquids or as usually is the case, they are converted by various metatheses to non-halogen phosphonium ionic liquids. Alternatively, tertiary alkylphosphines can directly react with active esters such as tosylates, sulfates, phosphates or mesylates to form "non-halogenated salts" directly. Detailed procedures for the syntheses of many phosphonium ILs have been summarized by Downard et.al.².

Phosphonium ILs are also the subject of many other researchers. J. Knifton published numerous papers and patents on petrochemical applications using "molten phosphonium salts" as solvents³. Phosphonium salts have been successfully used for Heck, Suzuki and esterification reactions^{4,5,6,7}. Hoffmann reported surprisingly high CO₂ solubility in phosphonium ILs⁸. The Wilkes group demonstrated the unusual ability of alkylphosphonium cations to "liquefy" very high molecular weight salts^{9,10}. More recently, Clyburne demonstrated the surprising stability of phosphonium salts toward strong bases such as Grignard reagents and borane^{11,12}. Pernak has prepared and investigated electrochemical properties of several series of phosphonium salts^{13,14}. Livingston has addressed the important issue of removing trace levels of ionic liquids from reactor products by use of unique "molecular filters"^{15,16,17}. A unique series of phosphonium ILs with amino acids derived anions were reported at the March, 2006 Atlanta ACS Ionic Liquid Symposium by Ohno¹⁸. At the same meeting, McCleskey discussed para-magnetic properties of phosphonium salts containing transition metal anions¹⁹. The all-important aspect of bioactivity has been addressed by Pernak and Stock^{20,21}.

CYPHOS IL[®] is the trade name of Cytec phosphonium ILs. Table 1 lists the phosphonium ILs used in this study. The table includes abbreviations used in the LC/MS study (P1, P2, etc), commercial names (CYPHOS IL 101, CYPHOS IL 102, etc), and cations and their anions. The table also includes imidazolium ILs used in this study.

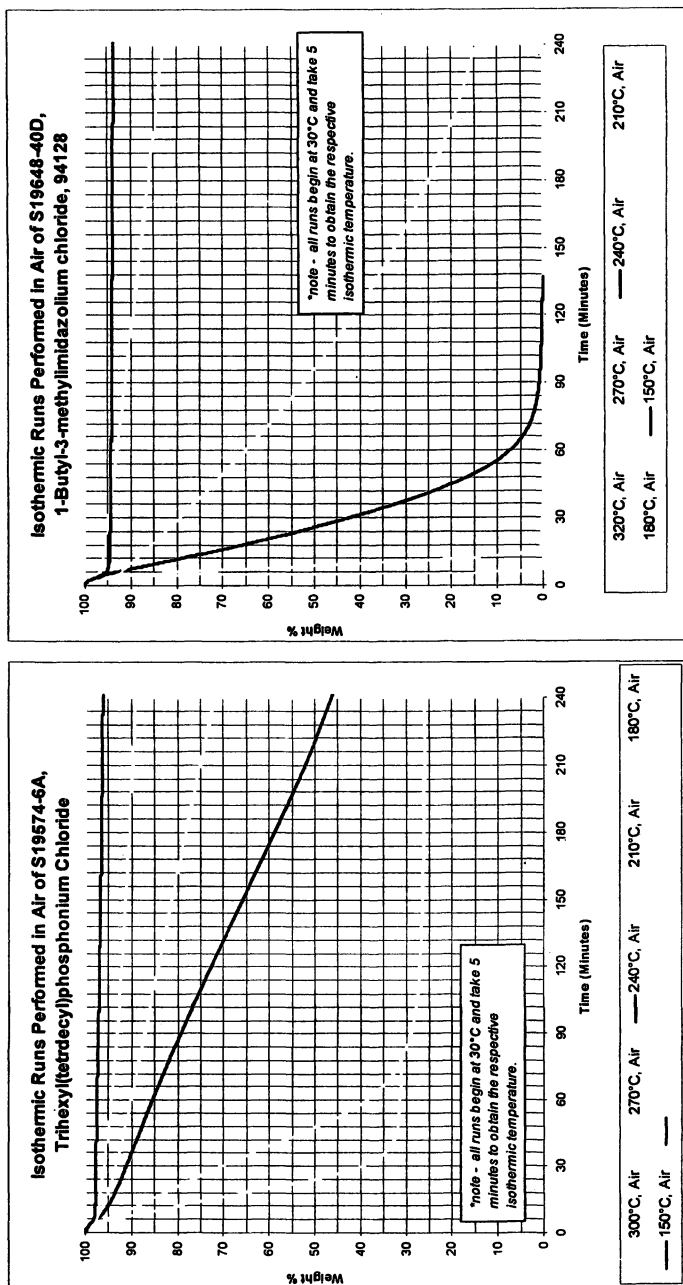
Table I. Ionic Liquids used in this Study

<i>Abbr</i>	<i>CYPHOS IL</i> [®]	<i>R,R,R,R'-P</i>	<i>Anion</i>
P1	IL106	C4,C4,C4,C1-P	tosylate
P2	IL164	C4,C4,C4,C4-P	chloride
P3	IL167	C4,C4,C4,C14-P	chloride
P4	IL101	C6,C6,C6,C14-P	chloride
P5	IL163	C4,C4,C4,C4-P	bromide
P6	IL104	C6,C6,C6,C14-P	(C8,C8)phosphinate
P7	IL109	C6,C6,C6,C14-P	bis(trifluoromethane sulfonyl)amide
P8	IL105	C6,C6,C6,C14-P	dicyanamide
P9	IL162	C4,C4,C4,C16-P	bromide
P10	IL107	C4,C4,C4,C4-P	dibutylphosphate
P11	IL102	C6,C6,C6,C14-P	bromide
P12	IL110	C6,C6,C6,C14-P	hexafluorophosphate
P13	IL202	C6,C6,C6,C14-P	decanoate
Im1		EMIm	chloride
Im2		BMIm	chloride
Im3		EMIm	trifluoromethanesulfonate
Py1		pyridinium	p-toluenesulfonate

General Characterization Techniques

TGA

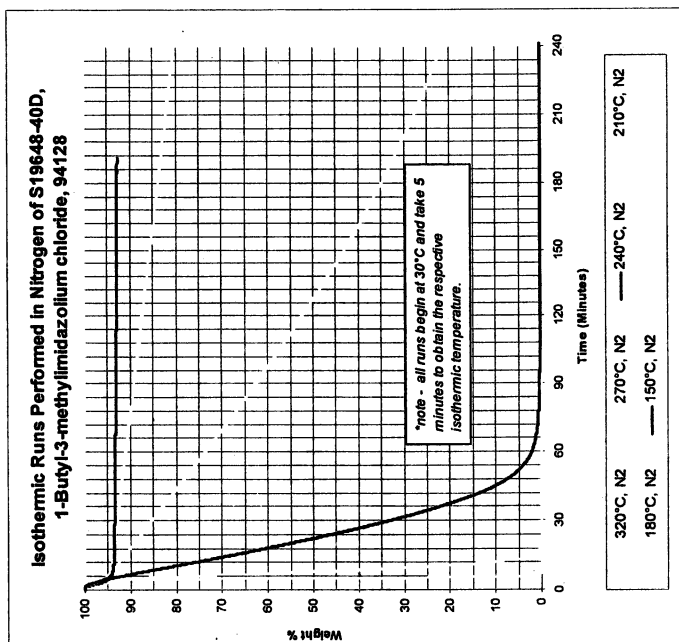
Thermal stability is an important property of ILs, and TGA usually is the first analytical technique employed for characterization. It has been repeatedly pointed out that dynamic TGA does not reflect the true thermal stability of ILs²². Thermal decomposition of a compound commences at the onset of weight loss and not the normally quoted inflection point of the derivative of TGA curve. Static TGA is a better technique to reflect this onset of thermal decomposition, which is typically 80-100°C lower than the inflection point of TGA curve. Figure 1 compares the static TGA of IL101 and BMIm under air and Figure 2 compares the static TGA of IL101 and BMIm in nitrogen. The inflection point of dynamic TGA for IL 101 is 350°C under air and 375°C under nitrogen. However, as can be seen in Figure 1, both IL101 and BMIm lost approximately 10% in 4 hours at 180°C. IL101 was more stable than BMIm at higher



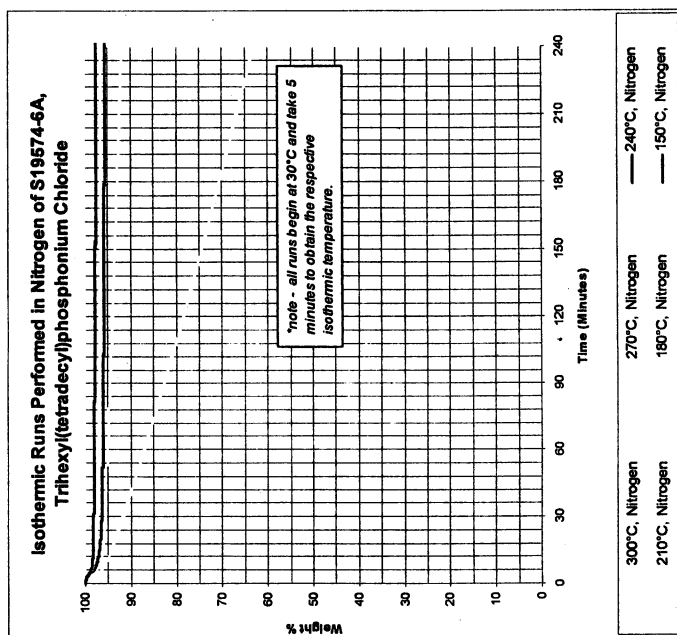
BMIm chloride
Solid lines: 180°C, 240°C

IL101 (P4)
Solid lines: 180°C, 240°C

Figure 1. Thermal Stability, Static TGA under Air



BMIm chloride
White: 180°C, 210°C Solid: 240°C



IL101 (P4)
Solid: 270°C White: 300°C

Figure 2. Thermal Stability, Static TGA under nitrogen

temperatures - at 210°C after 4 hours, IL101 lost 30% versus 85% loss of BMIm; and at 240°C after 4 hours, IL101 lost 55% versus 100% loss of BMIm. Under nitrogen, the stability of IL101 improves dramatically. Its weight loss was less than 10% at 270°C after 4 hours and less than 40% at 300°C after 4 hours. BMIm, on the other hand, showed no noticeable improvement under nitrogen.

³¹P NMR spectroscopy

³¹P NMR spectroscopy is a sensitive and powerful technique for characterization of phosphonium ILs. Because of the mono-isotopic nature of phosphorous atom (100% ³¹P) and high gyromagnetic ratio, its sensitivity is two orders of magnitude greater than ¹³C NMR. In addition, ¹H-decoupled ³¹P NMR spectra are simple, with one spectral peak for each phosphorous atom and no interference from most organic compounds. Figure 3 shows the sensitivity of ³¹P NMR for phosphonium ILs. The sample contains IL101 at a concentration of 400 ppm, with 700 ppm of tripropylphosphonium oxide (TPPO) as an internal quantitation standard. The $T_{1,P}$ relaxation constants can be very long, so 3 mg/mL of the paramagnetic relaxation agent, chromium tri-acetylacetonate was added to reduce the recycle delay between acquisitions required to obtain quantitative spectra. Utilizing a 400 MHz NMR spectrometer equipped with a 5mm BBO (broad band observed) probe, the limits of detection and quantitation in a 30 minute acquisition were found to be approximately 10 and 100 ppm, respectively. Figure 4 shows the ease of detecting impurities using ³¹P NMR spectroscopy. The sample is tris-(n-butyl)decadecylphosphonium chloride dissolved in chloroform. Signal A is attributed to the tris(n-butyl)tetradecylphosphonium ion. Signal B arises from the impurity bis(n-butyl)(isobutyl)phosphonium ion at a 2 mol% relative abundance. The presence of this isomeric compound was confirmed by LC/MS.

Other Traditional Characterization Techniques

Other properties of ILs commonly determined are viscosity, density, solubility, EC window, water content, etc. They are not within the scope of this study.

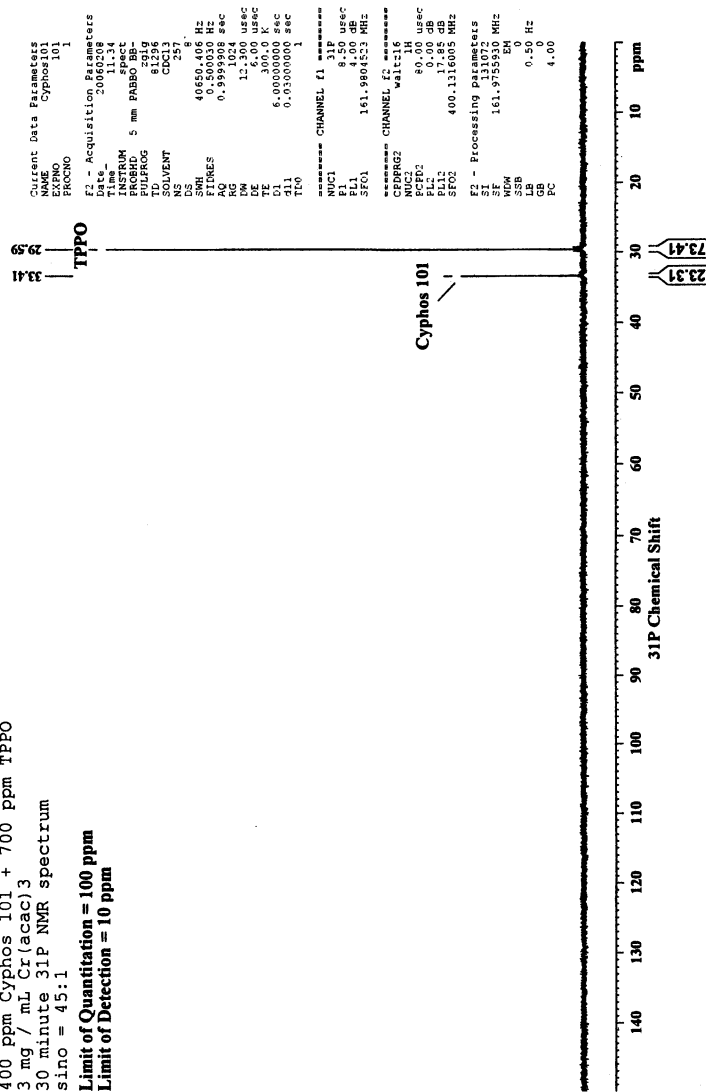
Mass Spectrometry and Chromatographic Techniques

Objectives

The objective of this study is three folds. The first objective is to develop an LC/MS procedure for the analysis of phosphonium ILs and, if possible, also

400 ppm Cyphos 101 + 700 ppm TPPO
 3 mg/mL Cr(acac)₃
 30 minute 31P NMR spectrum
 sino = 45:1

Limit of Quantitation = 100 ppm
 Limit of Detection = 10 ppm



A: IL101 (P4) B: TPPO, internal standard

Figure 3. Sensitivity of ³¹P NMR

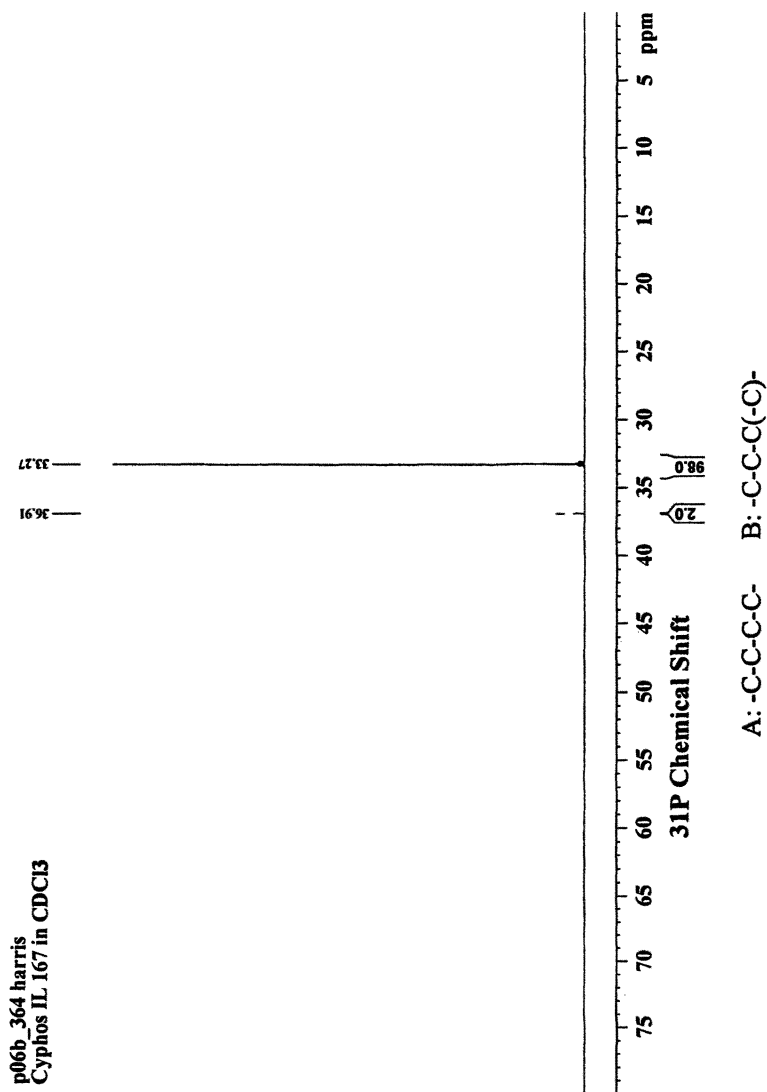


Figure 4. Detection of Impurity in IL167 (P3) by ³¹P NMR

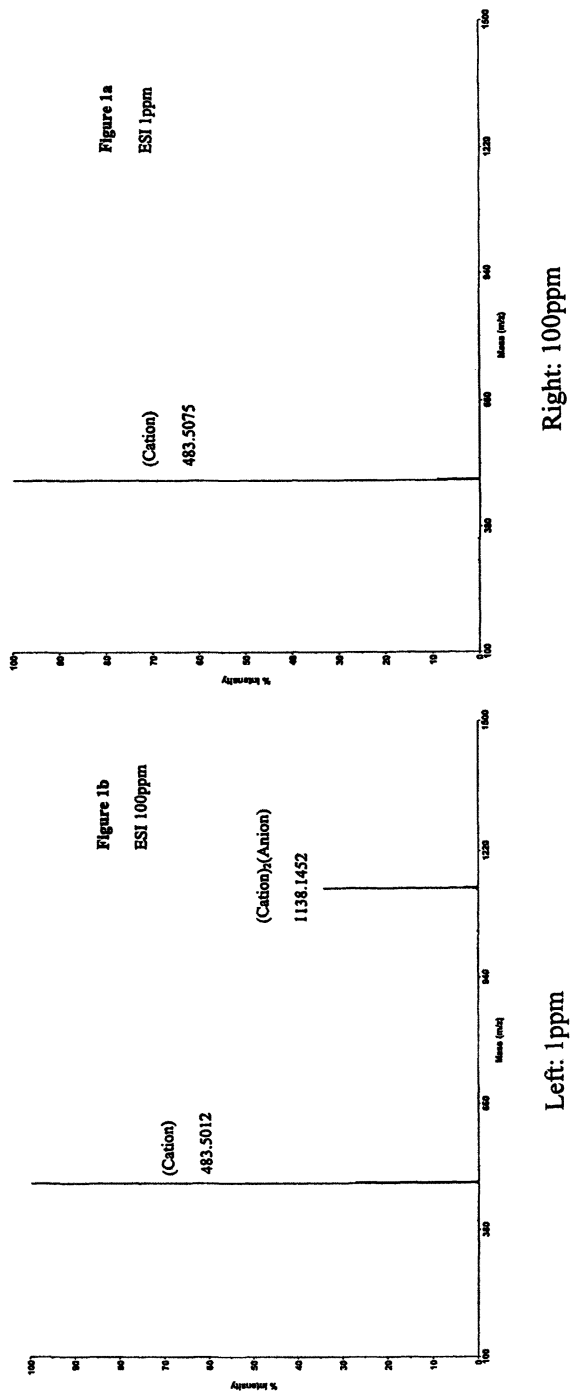
for the analysis of imidazolium ILs. The sensitivity of this technique is expected to be better than 0.1ppm. With such sensitivity, it is possible to analyze trace IL to the ppb level after sample enrichment. It is also possible to analyze impurities in IL at the <0.1% level using the commonly prepared 0.1% sample concentration used in HPLC analysis. The second objective is the analysis of the anionic counter ion. The third objective is the analysis of chloride. Many ILs are produced by using a chloride compound as the starting material and replacing the chloride with a desired anion. It is important to have an analytical procedure to analyze residual chloride accurately at the 10 ppm level in the sample.

Mass Spectrometry of Phosphonium ILs

All ILs show strong sensitivity in mass spec analysis. Figure 5-left is the ESI (Electrospray) mass spectrum of a 1 ppm IL101 solution obtained from positive mode operation. Intensity of the signal clearly indicates that the detection concentration is well below 0.1ppm. The observed ion is the phosphonium cation. Since the employed mass spectrometer is a high-resolution instrument, it is capable of determining the mass ion with accuracy of +/-5ppm. In this case, the measured cation is 483.5059 Daltons with mass accuracy of <+/-0.003 Daltons. This feature is very useful for trace analysis, because it can remove interfering compounds having the same nominal mass but not the same exact mass. The APCI (Atmospheric Pressure Chemical Ionization) ionization technique exhibits similar sensitivity as ESI. Both ionization techniques are used interchangeably in this study.

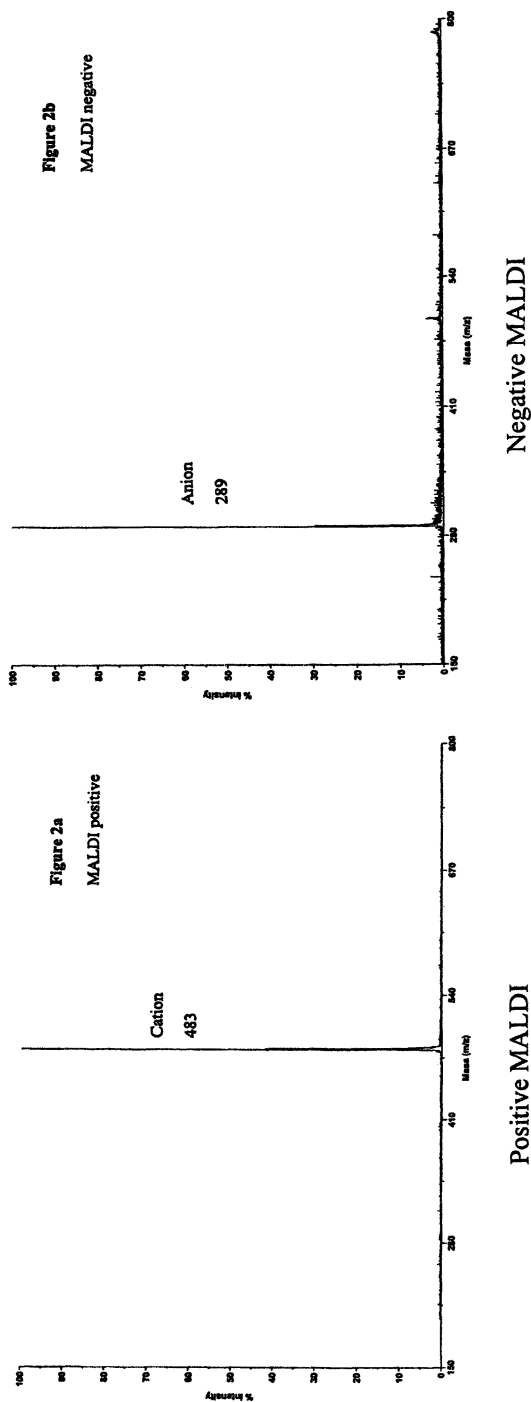
Cluster Ions

When the sample is introduced at a higher concentration, cluster ions begin to appear. Figure 5-right is the positive mode ESI mass spectra of a 100ppm IL101 solution. The cluster ions are [cation][molecule]_n. In negative mode, the formed cluster ions are [anion][molecule]_n. Cluster ion formation appears to be dependent on the ionization technique. In ESI and APCI ionization, the preferred cluster ion is the dimeric ion as shown. The trimeric ion is very weak even with a very high sample concentration. On the other hand, cluster ions up to 20 molecules have been observed by FAB (Fast Atom Bombardment) ionization in both positive and negative modes by Seddon's group²³. Contrary to expectation, MALDI (Matrix Assisted Laser Desorption Ionization) technique produces only the monomeric ion without cluster ions in both positive and negative mode operation as shown Figure 6. In this figure, the sample is L104. It is analyzed directly without a MALDI matrix agent.



Sample: IL 202 (P13)
 483.5059 C₃₂H₆₈P C₆,C₆,C₆,C₁₄-P+
 1138.1546 C₇₄H₁₅₅P₂O₂ = two C₃₂H₆₈P + C₁₀H₁₉O₂ = decanoate

Figure 5. Typical ESI Mass Spectra of Phosphonium IL at low and high concentrations



Sample: IL.104 (P6)
Cation: C₆C₆C₆C₁₄-P, m/z = 483
Anion: di(trimethylpentyl)phosphinate, m/z = 289

Figure 6. MALDI Mass Spectra of Phosphonium IL

Chromatography of Phosphonium ILs

Figure 7 shows our first attempt²⁴, and also the first reported attempt elsewhere, of chromatographic separation of ILs. The sample is a mixture of four phosphonium ILs and one imidazolium IL at 10 ppm level each. The figure shows that some ILs are separated nicely but others show strong adsorption effects. The positive outcome of this study is that it is feasible to analyze IL cations by LC/MS with high sensitivity. The drawback is the ill-defined peak shape from the adsorption effect.

The adsorption effect is caused by an interaction between the polar IL and the Si-OH sites of the HPLC column substrate. The conventional C18 column we employed apparently has too many residual un-derivatized Si-OH sites. An apparent solution is to replace the HPLC column with a high surface coverage column. Unfortunately, not all commercially available columns performed satisfactorily. The one column which gives minimal adsorption effects is the Varian MetaSil column. This column was successfully used by Stepnowski²⁵ for the separation of imidazolium ILs. The same column is employed in this study²⁶.

Figure 8 shows LC/MS results using the Varian MetaSil column for the separation of four phosphonium ILs and two imidazolium ILs. Four representative phosphonium ILs, covering the spectrum of Cytec ILs, are selected for this study. They are two small molecule phosphonium ILs (IL106 and IL164) and two large molecule phosphonium ILs (IL167 and IL 101). The total carbon numbers in these four phosphonium ILs are C13, C16, C26 and C32, respectively. Two imidazolium ILs (EMIm and BMIm) are included to show the universal applicability of the developed HPLC procedure.

Next to the column type, acidity of the mobile phase is also an important factor for successful separation of ILs. At higher pH, the peak shape of ILs is diffused, especially with the smaller ILs. As acidity of the aqueous phase increased to pH 6, the peak shape starts to become well defined. pH 4 is selected because it is easier to prepare as a buffered solution (HAc/NH₄Ac = 10/1).

Mobile Phase for HPLC

A methanol/water system is selected over the acetonitrile/water (ACN/H₂O) system used by Stepnowski. The acetonitrile/water system was found not suitable for phosphonium IL, especially for larger molecules. The following table lists the retention times of four phosphonium ILs obtained under isocratic conditions with different mobile phases. Two variables are pH and polarity. The first set of experiments changes the pH of the aqueous phase by setting water/acetonitrile at a 1/10 ratio. The effect of pH is as expected. The retention

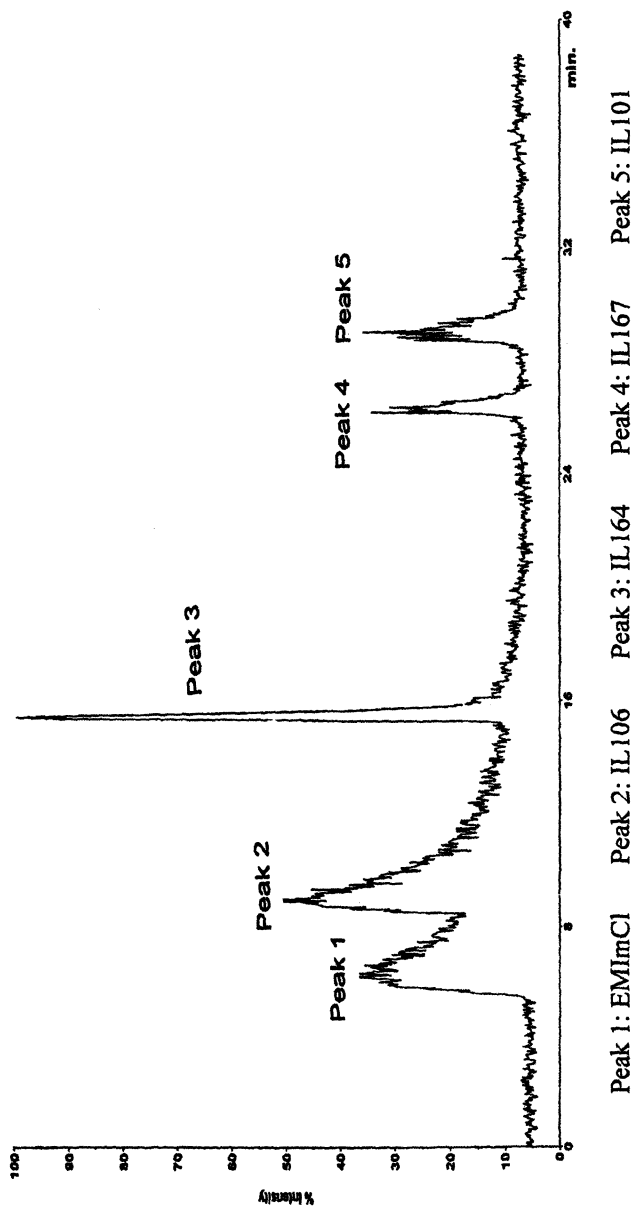
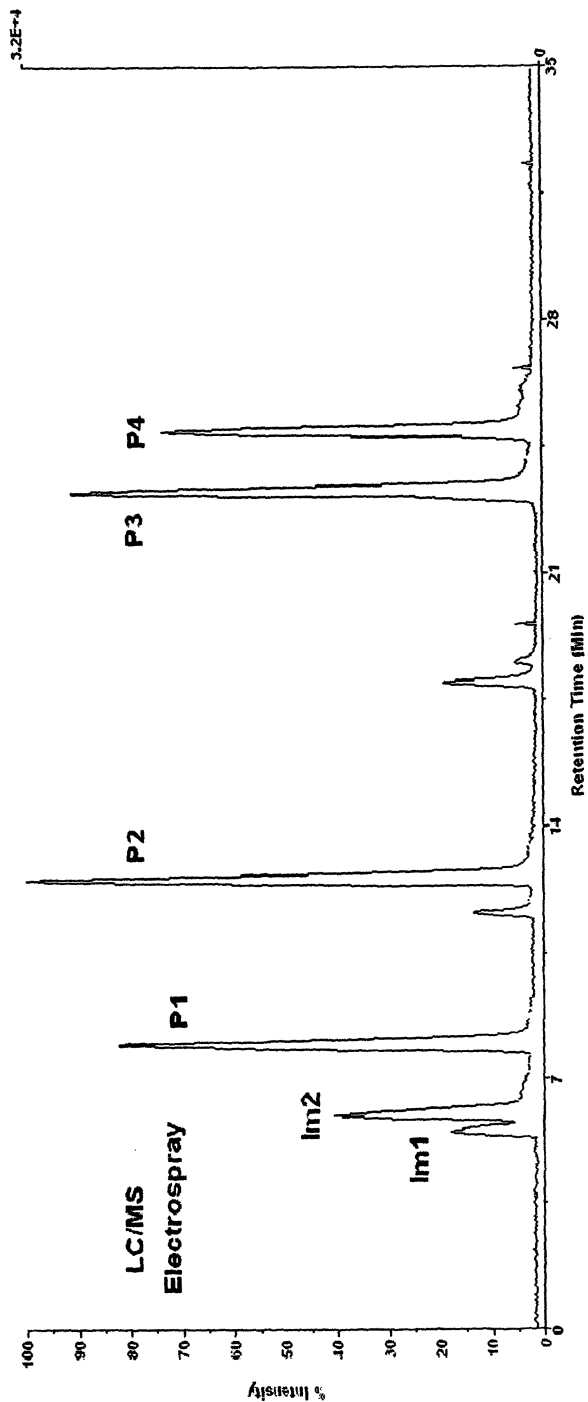


Figure 7. LC/MS Analysis of an IL Mixture using a conventional C18 HPLC column



P1: IL106, P2: IL164, P3: IL167, P4: IL101, Im1: EBImCl, Im2:BMImCl

Figure 8. LC/MS Analysis of IL Mixture using a high surface coverage HPLC column

times continue to decrease with the decrease of pH of the aqueous phase and become stable after aqueous acidity reaches $\text{pH} = 4$. The second set of experiments fixed the pH of aqueous phase at $\text{pH}=4$ and changes the methanol/acetonitrile ratio. Decreasing the water concentration (= increasing the acetonitrile concentration) means decreasing the polarity of the mobile phase. This, in principle, aids the elution of larger, less-polar compounds. The effect of polarity is less predictable. The retention times show a minimum at 90% acetonitrile and become larger again with increase of acetonitrile concentration. It appears that in high acetonitrile concentration mobile phases, pH, the other important factor, becomes less effective. This reversal of retention time indicates a bimodal separation mechanism. The water/methanol system shows no such effect. If large molecule ILs are the main concern, using a mixture of methanol and THF as the organic mobile phase will substantially reduce the retention time of these large ILs.

Sensitivity and Linearity of LC/MS

Figure 9 shows the excellent linearity between MS signals of ILs versus their concentrations. Analyzed samples include two small molecule ILs, IL106 (total C = 13) and IL164 (total C = 16), and two large molecule ILs, IL167 (total C = 26) and IL101 (total C = 32). Samples were examined with two ionization techniques, ESI and APCI. Both ionization techniques exhibit excellent linearity covering at least two orders of concentration range with sensitivity better than $<0.1\text{ppm}$. The non-linearity of IL167 and IL101 at higher concentrations is due to signal saturation of the detector. Table III compares the signal responses for four analyzed ILs normalized to the signal of IL164. It shows that the signal response varies from sample to sample and also different ionization techniques. A calibration curve is needed for each analyte with a specific ionization technique.

Identification of IL Anions from MS Cluster Ion

Attempts to develop an HPLC procedure universally applicable for IL anions were unsuccessful. Chemical and physical properties of IL anions are too dissimilar. Different HPLC procedures have to be developed for different IL anions.

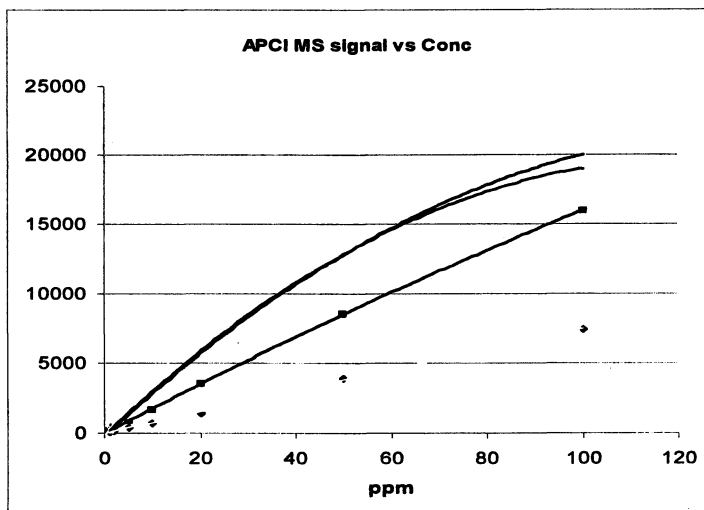
Qualitative identification of IL anions is a much simpler matter. As was discussed previously, in MS analysis of ILs, a high concentration sample tends to produce cluster ions. In positive mode MS, the dimeric cluster ion is composed of two cations and one anion. In negative mode MS, the dimeric cluster ion is composed of two anions and one cation. Anions can be easily identified after if the cation is known. Figure 10 shows the mass spectrum of

Table II. Effect of pH and Polarity on Retention Times in H₂O/ACN System. (ILs are listed based on their total carbon units)

ACN,%	pH	C13	C16	C26	C32
90	7.2	10.7	12.3	25.1	>40 min
90	5.8	8.0	9.0	17.0	31.5
90	3.8	7.5	8.4	15.1	24.6
90	2.7	7.3	8.2	15.1	24.8
70	3.8	5.7	7.2	29.1	>40
80	3.8	5.7	6.6	15.4	31.8
90	3.8	7.5	8.4	15.1	24.5
95	3.8	16.6	18.4	31.5	>40

Table III. Relative Signal Responses, normalized to IL164

Technique	IL106	IL164	IL167	IL101
APCI	0.42	1	1.57	1.67
Electrospray	0.85	1	0.86	0.67



From bottom to top: IL106(P1), IL164(P2), IL167(P4), IL101(P3)

Figure 9. Signal Linearity of LC/MS by APCI

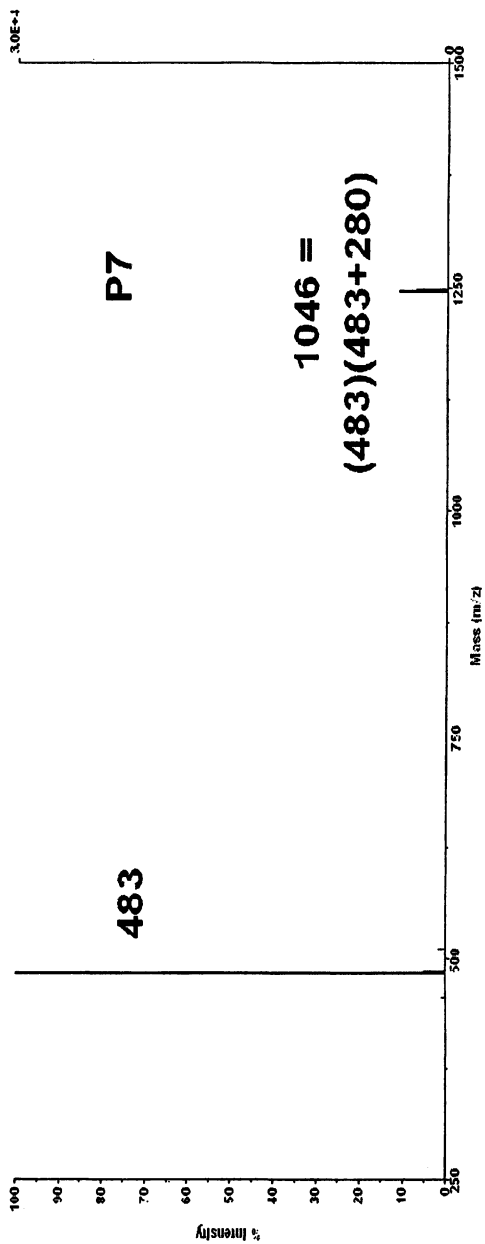
two phosphonium ILs, P7 (CYPHOS IL104) and P8 (CYPHOS IL109). Both ILs contain the same cation, trihexyl(tetradecyl)phosphonium ($m/z = 483$). The anion of P7 is easily determined as $m/z = 289$, confirming the anion as di(methylpentyl)phosphinate. Similarly, the anion of P8 is determined as $m/z = 66$, confirming the anion as dicyanamide.

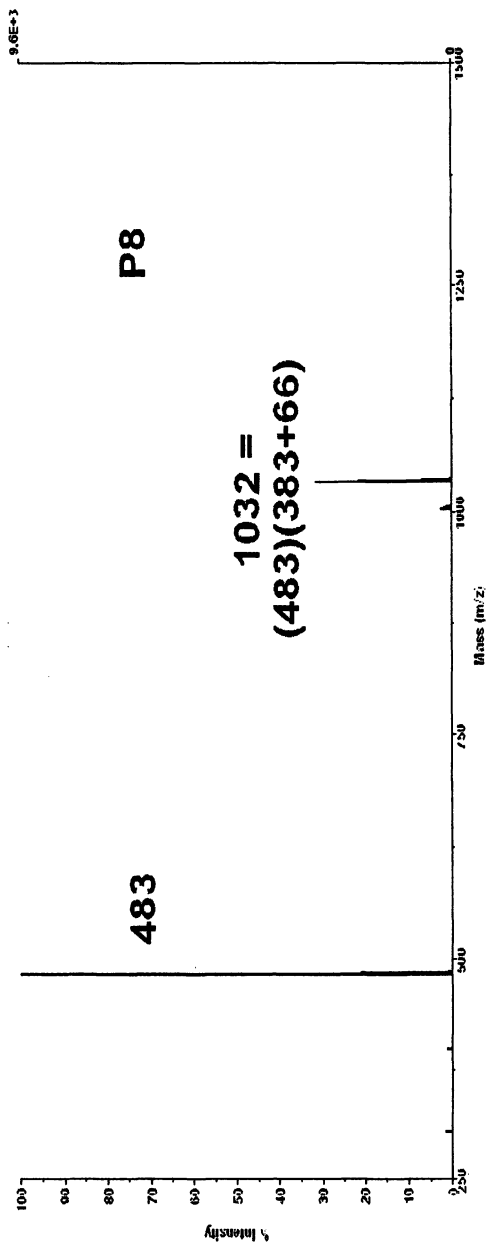
Residual Chloride Analysis

Many ILs use chloride salts as their starting material. Ion chromatography is an ideal technique for the analysis of residual chloride. Most commercial ion chromatographs have sensitivity for halides at the 0.1ppm level and a wide range of linear signal response. The sensitivity of 0.1ppm translates to a detection limit of 10ppm when the sample is prepared as a 1% aqueous solution. The following table lists residual chloride in ten ILs measured using an ion chromatograph.

Conclusion

An LC/MS procedure is established for phosphonium ILs. This procedure is also applicable for imidazolium ILs. The sensitivity of the procedure is





Upper: IL 104(P7): cation=483, anion=280
Lower: IL 109(P8): cation=483, anion=66

Figure 10. Identification of Anion

Table IV. Residual Chloride Analysis

<i>IL Abbr.</i>		<i>Residual Cl Anion</i>
P1	80 ppm	tosylate
P5	50	bromide
P6	160	(C8,C8)phosphinate
P8	630	dicyanamide
P9	890	bromide
P10	280	dibutylphosphate
P11	540	bromide
P12	170	hexafluorophosphate
Im3	10	trifluoromethanesulfonate
Py1	500	p-toluenesulfonate

0.1ppm or better. In mass spec analysis, higher concentration samples of ILs produce cluster ions. These cluster ions can be used to identify the anion portion of the IL. IC is a suitable technique for the analysis of residual chloride with 0.1ppm sensitivity.

Experimental

Instruments

The following instruments are used in this study.

Perkin Elmer Pyruis 1 TGA.

Bruker Avance 400 NMR

Applied Biosystems Mariner ToF LC/MS

Agilent HP1100 HPLC

Chromatographic conditions

The following chromatographic conditions are used in LC/MS analyses.

Column: Varian MetaSil Basic, 250 x 4.6mm

Aqueous mobile phase:

pH=3.9 1% HAc, 0.2% NH₄Ac

pH=2.8 1% HAc only

Organic mobile phase: Methanol

Flow rate: 0.5 mL/min.

Gradient: 50-100% MeOH (20min.) + 15 min.

Column temperature: 30°C

Sample size: 5 µL of 0.01% in MeOH

References

1. Seddon, K.; Stark, A.; Torres, M. *Pure Appl. Chem.*, **2000**, *62*(12), 2275-2287.
2. Bradaric, C.; Downard, A.; Kennedy, C.; Robertson, A.; Zhou, Y. *Green Chem.*, **2003**, *5*, 143-152.
3. Knifton, J. *J. Mol. Catal.*, **1987**, *43*, 65-77
4. Kaufmann, D.; Nouroozian, M.; Henze, H. *Synthetic Lett.*, **1996**, 1091-1092.
5. Gerritsma, D.; Robertson, A.; McNulty, J.; Capretta, A. *Tetrahedron Lett.*, **2004**, *45*(41), 7629-7631.
6. McNulty, J.; Capretta, A.; Wilson J.; Dyck, J.; Adjabeng, G.; Robertson, A. *Chem. Commun.*, **2002**, 1986-1987.
7. McNulty, J.; Cheekoori, S.; Nair, J.; Larichev, V.; Capretta, A.; Robertson, A. *Tetrahedron Lett.*, **2005**, *46*, 3641-3664.
8. Hutchings, J.; Fuller, K.; Heitz, M.; Hoffmann, M. *Green Chem.*, **2005**, *7*(6), 475-478.
9. Del Desto, R.; Dudis, D.; Ghebremichael, F.; Heimer, N.; Lowe, T.; Wilkes, J. *Ionic Liquids IIIB; Fundamentals, Progress, Challenges and Opportunities: ACS Symposium Series 902*, p144.
10. Del Desto, R.; Corley, C.; Robertson, A.; Wilkes, J. *J. Organomet. Chem.*, **2005**, *690*, 2536-2542.
11. Gorodetsky, B.; Ramnial, T.; Branda, N.; Clyburne, J. *Chem. Commun.*, **2004**, 1972-1973.
12. Ramnial, T.; Ino, D.; Clyburne, J. *Chem. Commun.*, **2005**, 325-327.
13. Pernak, J.; Stefaniak, F.; Wegewski, J. *Eur. J. Chem.*, **2005**, 650-652.
14. Frackowiak, E.; Grzegorz, L.; Pernak, J. *Appl. Phys. Lett.*, **2005**, *86*, 161404/1-161404/3.
15. Han, S.; Wong, H.; Livingston, A. *Chem. Eng. Res. and Des.*, **2005**, *83*(A3), 309-316.
16. Wong, H.; Han, S.; Livingston, A. *Chem. Eng. Sci.*, **2006**, *61*, 1338-1341.
17. Wong, H.; Pink, C.; Ferreira, F.; Livingston, A. *Green Chem.*, **2006**, *8*, 373-379.
18. Ohno, H. *231st ACS National Meeting*, Atlanta GA, March 2006.
19. Del Sesto, R.; McMcleskey, T.; Burrell, A.; Baker, G.; Wilkes, J. *ACS National Meeting*, Atlanta GA, 2006.
20. Cieniecka-Roslonkiewicz, A.; Pernak, J.; Kubis-Feder, J.; Ramani, A.; Robertson, A. Seddon K. *Green Chem.*, **2005**, *7*, 855-862.
21. Stock, F.; Hoffmann, J.; Ranke, J.; Stormann, R.; Ondruschuka, B.; and Jastorff, B. *Green Chem.*, **2005**, *6*, 286-290.

22. Wilkes, J. *231st ACS National Meeting*, Atlanta GA, March 2006.
23. Abdul-Sada, A.; Elaiwi, A.; Greenway, A.; Seddon, K. *Eur. J. Mass Spectrom.*, **1997**, 3(3), 245-247.
24. Chang, T.; Piquette, M. *DECHEMA Conference on Green Solvents*, Bruchsal, Germany, 2002.
25. Stepnowski, P.; Muller, A.; Behrend, P.; Ranke, J.; Hoffmann, J.; Jastorff, B. *J. Chromatog.*, **2003**, A, 993.
26. Chang, T.; Robertson, A. *1st Int'l Congress on Ionic Liquids*, Salzburg Austria 2005

Theory

Chapter 6

Force Field Refinement and Molecular Simulations of Imidazolium-Based Ionic Liquids

Zhiping Liu and Wenchuan Wang

Division of Molecular and Materials Simulation, Key Lab for Nanomaterials, Ministry of Education, Beijing University of Chemical Technology, Beijing 100029, People's Republic of China

Refined force fields for imidazolium ionic liquids, proposed recently by the authors, are summarized in this paper. The procedure to optimized the parameters is described. The performance of both the all-atom and united-atom force fields is verified by molecular dynamics simulation of pure ionic liquids and their mixtures with acetonitrile.

1. Introduction

Room temperature ionic liquids (RTILs) are organic salts with a melting point as low as room temperature. The major interactions in RTILs are coulombic, leading to their unique properties, compared with conventional molecular solvents. It is believed that RTILs are environmentally benign solvents with various potential applications. Furthermore, through different combinations of cations and anions, there is a tremendous variety of “designer” solvents. With great versatility of their chemical and physical properties, ionic liquids can be thus tailored and tuned for specific tasks.

Computer simulations have been playing an important role in molecular design, which is especially useful for RTILs because of their tremendous diversity. Nevertheless, success of molecular simulation mainly depends on the quality of the inter- and intra-molecular potential functions, i.e. the force fields.

Several force fields were proposed for the imidazolium-based RTILs by the groups of Lynden-Bell¹, Maginn², Stassen³, Padua^{4,5} and our group^{6,7}. More

recently, ab initio molecular dynamics were also performed for RTILs without any pre-defined force field^{8,9}, although it is much more expensive to implement such simulations. In this paper, we report our systematical work on the force fields development and atomistic molecular simulations of RTIL systems

2. Force Field Development

An all-atom (AA) force field is developed for RTILs containing dialkyl-imidazolium cations⁶ (for their schematic structures, see Figure 1a). To decrease the computational intensity without reducing the accuracy, we also proposed a united-atom (UA) force field⁷, being wholly consistent with the AA one.

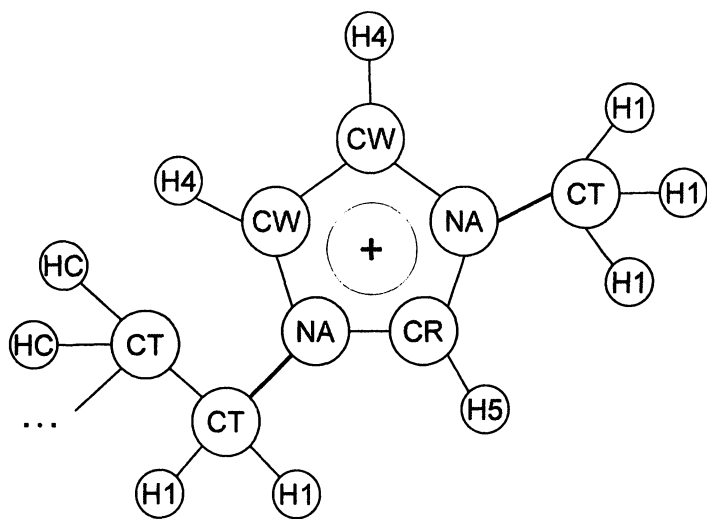
$$E = \sum_{\text{bonds}} K_r (r - r_0)^2 + \sum_{\text{angles}} K_\theta (\theta - \theta_0)^2 + \sum_{\text{dihedrals}} \frac{K_\phi}{2} [1 + \cos(n\phi - \gamma)] + \sum_{i < j} \left[4\epsilon_{ij} \left[\left(\frac{\sigma_{ij}}{r_{ij}} \right)^{12} - \left(\frac{\sigma_{ij}}{r_{ij}} \right)^6 \right] + \frac{q_i q_j}{r_{ij}} \right] \quad (1)$$

The first three terms represent the bonded interactions, i.e., bonds, angles and torsions. The non-bonded interactions are described in the last term, including van der Waals (VDW, in the Lennard-Jones (LJ) 6-12 form) and Coulombic interactions of atom-centered point charges. Electrostatic and VDW interactions are calculated between only the atoms in different molecules or for the atoms in the same molecule separated by at least three bonds. The non-bonded interactions separated by exactly three bonds (1-4 interactions) are reduced by a scale factor, which is optimized as 1/2 for VDW and 1/1.2 for electrostatic interactions. The LJ parameters for unlike atoms are obtained from the Lorentz-Berthelot (LB) combining rule:

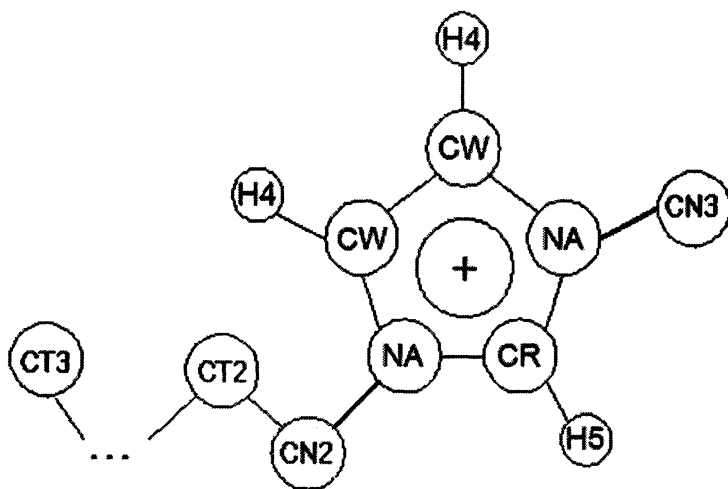
$$\epsilon_{ij} = \sqrt{\epsilon_{ii} \epsilon_{jj}} ; \quad \sigma_{ij} = (\sigma_{ii} + \sigma_{jj}) / 2 \quad (2)$$

2.1 All-atom (AA) force field

Most of the parameters in our force field are directly extracted from AMBER by atom type matching between the imidazolium cations and



(a)



(b)

Figure 1. Schematic structure and atom type notations of 1-alkyl-3-methylimidazolium cation (amim) in (a) all-atom (AA) force field, (b) united-atom (UA) force field, this work. (Reproduced with permission from reference 7. Copyright 2006 Royal Society of Chemistry.)

protonated histidine (HIP). The atom charges are obtained by the one-conformation two-step RESP¹⁰ method in AMBER. Besides, three major improvements are made to describe the RTILs more accurately⁶.

(1) The VDW diameter of H5 (see Figure 1) is adjusted according to the optimized geometries of cation-anion pairs by quantum calculations (QM). The value of 2.432 Å from AMBER results in the symmetric optimized geometry for [dmim][PF₆] pair (see Figure 2b for more details), while the optimized geometry by QM in HF/6-31+G(d) level is obvious asymmetric (see Figure 2a for more details). It is found that when the VDW diameter of H5 is reduced to 1.782 Å, the asymmetric geometry emerges (see Figure 2c for more details), which is consistent to the QM calculation. The similar results are obtained for the ion pairs of [emim][BF₄] and [bmim][PF₆]⁶.

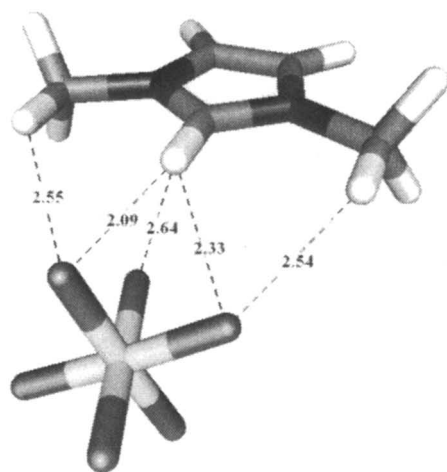
(2) Some of the force constants of the bonds and angles are adjusted by fitting the vibrational frequencies from QM calculations and IR experiments¹¹. For example, the frequency of the imidazolium ring stretching is predicted by the original AMBER as 1808 cm⁻¹, while the experimental value is 1574 cm⁻¹. After we reduced the bond force constants related to the imidazolium ring and the angle force constants of H4-CW-NA, H4-CW-CW and H5-CR-NA, an improved value of 1632 cm⁻¹ was obtained. For more details, the readers are referred to the Table 3 of the literature⁶.

(3) Four missing torsion parameters in AMBER related to the bond NA-CT are obtained by fitting the ab initio torsion energy profiles at MP2/6-31+G(d)//HF/6-31+G(d) level. Lopes et al.⁴ have been reported these missing parameters through a similar procedure. However, it is necessary to get a set of consistent parameters for our force field, because the atom charges between the two force fields are very different.

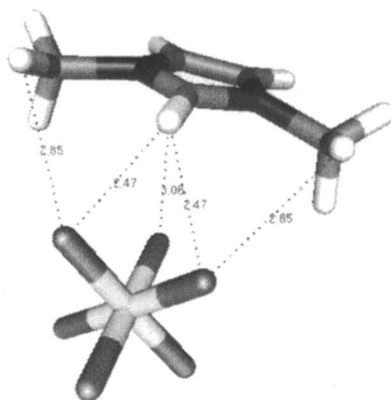
2.2 United-atom (UA) force field

The UA force field is derived from the above AA model⁷. It is essential to define the united atoms by using a coarse-grained method for the imidazolium cation. Because the three H atoms on the ring are very important to the hydrogen-bond formation in RTILs,⁶ the detailed structure between the cations and anions would be lost if the CH groups in the ring are treated as united atoms. Therefore, only CH₃ and CH₂ in alkyl chains can be treated as united atoms here (see Fig. 1). Consequently, four kinds of united atoms are defined in this work, i.e. CN₂, CN₃, CT₂ and CT₃ (see Fig. 1b), since there are two kinds of H on the alkyl chains, i.e. H₁ and H_C.

The VDW parameters of the united atoms are obtained by mapping the interaction energies of a pair of them. The energies between united atom pairs

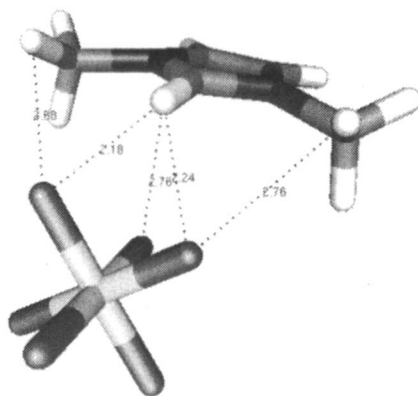


(a)



(b)

Figure 2. Optimized geometries of [dmim][PF₆] pair from (a) quantum calculation, (b) the original AMBER force field, and (c) the refined force field presented in this work. Use with permission from *J. Phys. Chem. B* 2004, 108, 12978 (Liu, Huang and Wang)



(c)

Figure 2. Continued.

were calculated by a Monte Carlo algorithm⁷, i.e., the UA groups are rotated randomly to obtain the average interaction energies.

It is noticed that in the published UA force fields^{1,12,13}, the charges of the united atoms were all obtained by simply adding the corresponding atom charges. In fact, the atom charges would be determined to reproduce the electric field around a molecule. Therefore, it is more reasonable to refit the charges in the UA force field. The method used is RESP¹⁰, the same algorithm used for the AA force field. The difference in the UA force field here is that all the H atoms in the alkyl chains were removed in the fitting procedure.

The parameters of our AA and UA force fields can be found in our previous work^{6,7}.

3. Molecular Dynamics Simulations

To obtain macro-properties of RTIL systems from the AA and UA force field developed by our group, the molecular dynamics simulations were performed by the package MDynaMix¹⁴. The typical systems include 128 ion pairs or more. The typical length of MD in this work is 400ps. More details of the simulations can be found in the literature^{6,7,15}. The results from UA force field agree well with those from AA force field. However, the computational cost of the former

decreases significantly. For example, the time for the simulations of [bmim][PF₆] by UA is about 1/4 of that by AA.

3.1 Pure ionic liquids

Some of the simulated results for pure RTILs are listed in Table 1. More results are referred to the literature [6] and [7]. For brevity, only the liquid densities and inter-molecular energies are presented here.

3.1.1 Densities

The densities of the ionic liquids are one of the most accurate sources of experimental data. Therefore, it is important to predict the densities by simulations for the validation of the proposed force field. The simulated results show that both our force fields can describe the densities of pure RTILs rather accurately, with the absolute relative deviations less than 2%^{6,7}. For example, the densities of [C_nmim][PF₆] are predicted from our UA force field, as is shown in Figure 3. Besides, a correlation between liquid density and the carbon atom number of [C_nmim][PF₆] is proposed by fitting our simulated data with n=5~7, given by

$$\rho = 1.483 - 0.0295n \quad (3)$$

where ρ is the liquid density of [C_nmim][PF₆], g/cm³, n is the carbon number of the alkyl chain in [C_nmim]⁺. Furthermore, the densities of [C₄mim][PF₆] and [C₈mim][PF₆] are predicted by the correlation. It is found in Figure 2 that the predicted densities for the two liquids are in good agreement with the experimental data.

3.1.2 Inter-molecular Energies

The inter-molecular energy, U_{int} , is another characteristic property for condensed phases. In addition, it can be directly extracted from the molecular simulation. It is shown by our calculations^{6,7} that the electrostatic interactions are about four times as large as the VDW interactions, indicating the “ionic feature” of these solvents.

Table 1. Densities (ρ), self diffusion coefficients (D), intermolecular energies (U^{int}), heats of vaporization (ΔH^{vap}) and the cohesive energy densities (c) for some pure room temperature ionic liquids (RTILs) simulated by using the AA and UA force field proposed in this work.

RTIL	ρ		$10^{11}D / \text{m}^2 \text{s}^{-1}$						exp.		
	UA	AA	exp.	UA		AA		cation	anion	cation	anion
[bmim][PF6]	1.365	1.350	1.363 ^a	1.2	0.6	1.2	1.2	1.0	0.7 ^d	0.5 ^d	
[hmim][PF6]	1.308		1.307 ^a	0.8	0.8						
[omim][PF6]	1.258		1.237 ^a	0.6	0.6						
[emim][BF4]	1.264	1.284	1.279 ^b	2.1	2.0	1.1	1.1	0.9	4.9 ^b	4.2 ^b	
[bmim][BF4]	1.208	1.194	1.211 ^c	0.9	0.6	1.2	1.2	0.8	1.4 ^d	1.3 ^d	
[omim][BF4]	1.126			0.8	0.6						

RTIL	$U^{\text{int}} / \text{kJ mol}^{-1}$		$\Delta H^{\text{vap}} / \text{kJ mol}^{-1}$		c / J cm ⁻³	
	UA	AA	UA	AA	UA	AA
[bmim][PF6]	-498.6	-493.8	190.4	186.7	902.6	875.0
[hmim][PF6]	-508.6		199.0		822.8	
[omim][PF6]	-519.8		208.2		765.9	
[emim][BF4]	-509.5	-509.6	175.8	175.9	1105.8	1124.6
[bmim][BF4]	-511.5	-506.8	179.1	174.7	937.4	906.2
[omim][BF4]	-533.0		198.7		782.4	

Notes: ^a from reference¹⁸, ^b from reference¹⁹, ^c from reference¹⁷, ^d from reference²⁰, ^e from reference¹⁶.

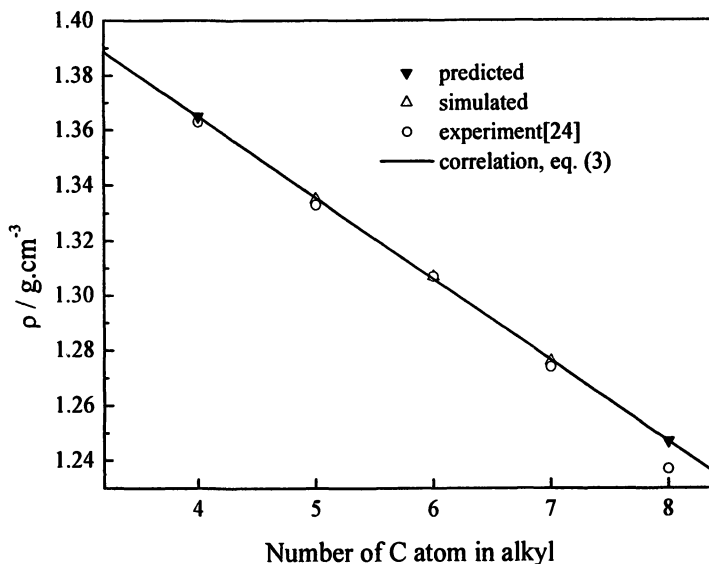


Figure 3. A correlation between the simulated liquid density and the carbon number of alkyl chain in $[C_n\text{mim}][\text{PF}_6]$ for $n=5-7$ (see equation (3) in section 3.1). The predictive liquid densities for $n=4$ and 8 are also presented. (Reproduced with permission from reference 7. Copyright 2006 Royal Society of Chemistry.)

The enthalpy of vaporization, ΔH_{vap} , and cohesive energy density, c , are calculated by⁶

$$\Delta H^{\text{vap}} = RT - (U^{\text{int}} - U^{\text{ion pair}}) \quad (4)$$

$$c = (U^{\text{ion pair}} - U^{\text{int}}) / V_m \quad (5)$$

where V_m is the molar volume of the liquid. R is the gas constant, $U^{\text{ion pair}}$ represents the average intermolecular energy of ionic pairs at the ideal gas state, which can be simulated in term of a single ion pair at the same temperature with a simulation box large enough^{2,15}.

It is difficult to measure the enthalpy of vaporization directly from experiment, since RTILs are all nonvolatile. However, Swiderski et al.¹⁶ reported the values for several ionic liquids estimated from the bimolecular rate constant experiments very recently. The internal energies of vaporization estimated for $[\text{bmim}][\text{PF}_6]$ and $[\text{bmim}][\text{BF}_4]$ are 189 ± 20 and 201 ± 20 kJ/mol, respectively,

which are in fair agreement with the simulated values of 190.4 and 179.1 kJ/mol from our UA force field. In addition, they also estimated the cohesive energy densities for [bmim][PF₆] and [bmim][BF₄], which are 912±100 and 998±100 J/cm³, respectively. The values coincide well with our simulated values, 902.6 and 937.4 J/cm³.

3.2 Mixtures of [bmim][BF₄] and acetonitrile (CH₃CN)

A rigorous test for our force fields is the interactions between RTILs and other molecules, therefore, we performed molecular dynamics of the mixtures of [bmim][BF₄] and acetonitrile¹⁵. Some of the simulation results for different concentrations of the mixtures are shown in Table 2. It is also noticed that the values from UA and AA force fields are very close.

3.2.1 Excess volumetric and energetic properties

The nonideality of mixture can be depicted by the excess properties. From our simulation, both the excess molar volume (see Figure 4) and excess molar enthalpy (see Figure 5) exhibit negative deviations and show a minimum in the concentration range of $x_1=0.3-0.4$, which is consistent with the corresponding experimental results¹⁷.

3.2.2 Viscosities

The experimental values of viscosity for both pure ionic liquids and the mixtures are frequently reported in the literature. In contrast, it is more difficult to measure the diffusion coefficients accurately by experiment. In molecular dynamics, it needs much longer time in simulation to calculate the viscosity than self-diffusion coefficient by either the Green-Kubo or Einstein methods. Here we assumed that the Stokes-Einstein relation² holds for the mixture, in which

$$\eta_i D_i = \eta_j D_j \quad (6)$$

where η_i , η_j , D_i and D_j represent the viscosity and self-diffusion coefficient of the two systems *i* and *j*, respectively, at the same temperature and pressure.

By using equation (6) and the simulated values of the self-diffusion coefficient, the viscosities of the mixture can be estimated. The calculation

Table 2. Sizes of the systems and the results of simulations for the mixture [bmim][BF₄](1) + CH₃CN (2) from the AA and UA force field presented in this work

System size	N ₁	N ₂	x ₁	V _m / cm ³ mol ⁻¹		U ^{int} / kJ mol ⁻¹		ΔH ^{vap} / kJ mol ⁻¹	
				AA	UA	AA	UA	AA	UA
0	210	0	0	54.86	54.86	-30.75	-30.75	33.22	33.22
52	204	0.20	0.20	79.52	79.00	-129.29	-130.23	63.82	64.48
77	179	0.30	0.30	92.30	91.60	-176.37	-177.69	78.24	79.13
102	154	0.40	0.40	105.61	104.60	-223.26	-224.98	92.46	93.62
118	78	0.60	0.60	133.87	131.99	-319.51	-322.93	120.57	123.17
102	52	0.80	0.80	161.77	158.98	-411.52	-415.75	147.45	150.55
256	0	1	1	190.57	187.35	-507.42	-512.59	175.40	179.15

Notes: V_m is the molar volume of the mixture; U^{int} is the intermolecular energy of the system; ΔH^{vap} is enthalpy of vaporization and c is the cohesive energy density of the system.

SOURCE: Reproduced with permission from reference 7. Copyright 2006 Royal Society of Canada.

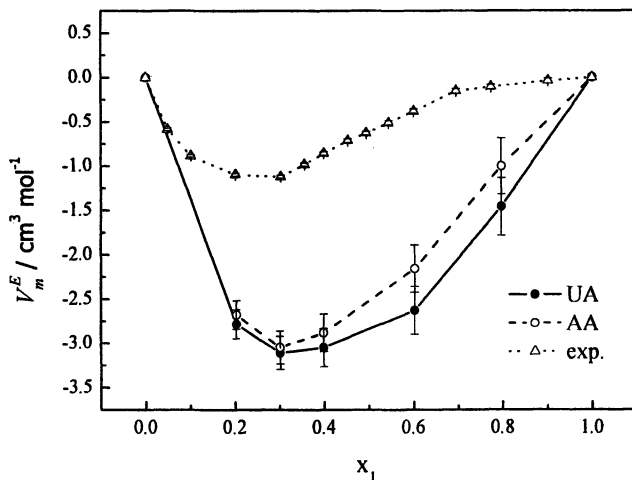


Figure 4. Excess molar volumes of the mixtures of [bmim][BF₄](1) - CH₃CN(2) from simulations by the all-atom (AA) and united-atom (UA) model. (Reproduced with permission from reference 7. Copyright 2006 Royal Society of Chemistry.)

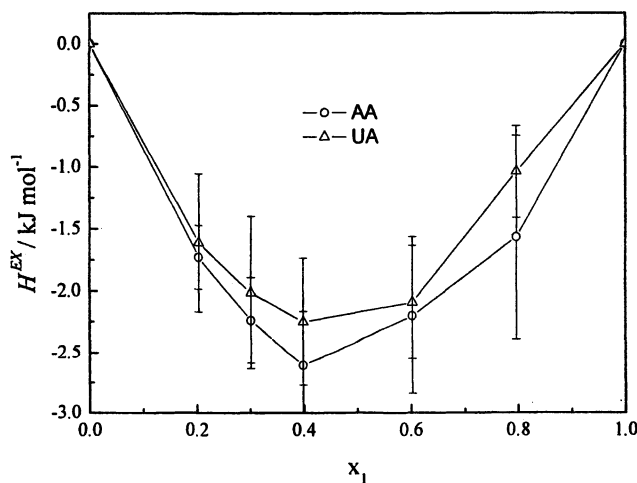


Figure 5. Excess molar enthalpies of the mixtures of [bmim][BF₄](1) - CH₃CN(2) from our simulations by the all-atom (AA) and united-atom (UA) model. (Reproduced with permission from reference 7. Copyright 2006 Royal Society of Chemistry.)

details can be referred to the the literature¹⁵. Impressively, as is shown in Figure 6, the UA force field even presents better results, especially for the viscosity at $x_i=0.8$.

3.2.3 Microscopic structures

The microscopic structural information of liquids can be extracted from molecular simulation. The radial distribution function (RDF) is often presented in the literature. However, it is difficult to describe the three-dimensional distribution of particles by RDF. In contrast, the space distribution function (SDF) is a more intuitive method to represent the distribution of particles around a central molecule⁶.

The distribution contour surfaces of the [bmim]⁺, [BF₄]⁻ and CH₃CN molecules around a CH₃CN molecule are shown in Figures 7a to 7c, respectively. The cations distribute like a cap adjacent to the N atoms of CH₃CN, while the anions and the N atoms in CH₃CN distribute like a ring surrounding the CH₃CN near the side of CH₃. In Figures 7a and 7b, both the distributions of cations and anions exhibit a minimum at $x_1=0.3$. As is seen in Figure 7c, the distribution of CH₃CN shows a maximum at the same concentration. These results coincide well with the analyses of the RDFs (see Figures 10-12 in the literature¹⁵). It is shown intuitively by the distributions of different species in the mixture that the liquid structure at $x_1=0.3$ is significant different, which causes the maximal negative deviation of excess properties of the mixtures near this concentration.

4. Conclusions

We developed a refined all-atom force field and the corresponding united-atom one for RTILs with imidazolium cations. Comprehensive tests on the force field were presented for the liquid densities, inter-molecular energies, transport properties. It is found that both the pure RTILs and mixtures can be described quite accurately by the force fields. This work provides a good start to the molecular design of RTILs. In future work, we will focus our attentions on the task-specific RTILs, such as ionic liquids with guanidinium cations²¹, the promising solvents in flue gas desulfurization.

Acknowledgements

This work was supported by the National Basic Research Program (No. G2000048010), the National Natural Science Foundation of China (No. 20236010) and the Postdoctoral Scientific Foundation of China (No. 2003033095).

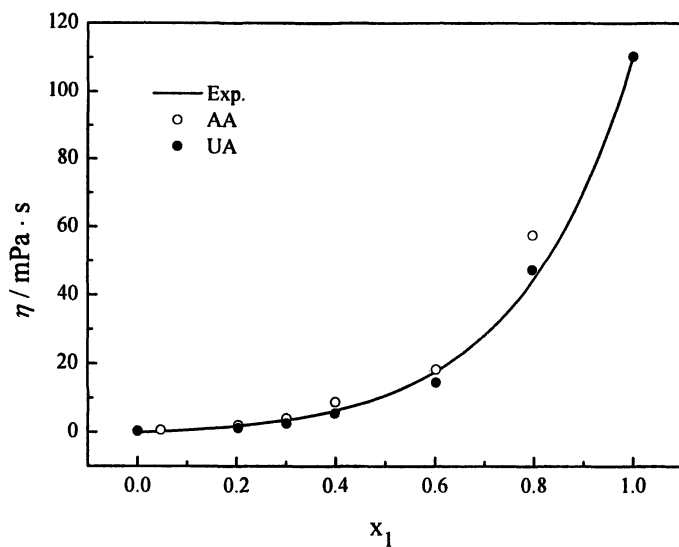


Figure 6. Viscosity of the mixtures of $[bmim][BF_4](1) - CH_3CN(2)$ at $T=298\text{ K}$, $P=0.1\text{ MPa}$. The solid line represents experimental data²⁷. The circles are estimated by the Stokes-Einstein relation and our simulations. (Reproduced with permission from reference 7. Copyright 2006 Royal Society of Chemistry.)

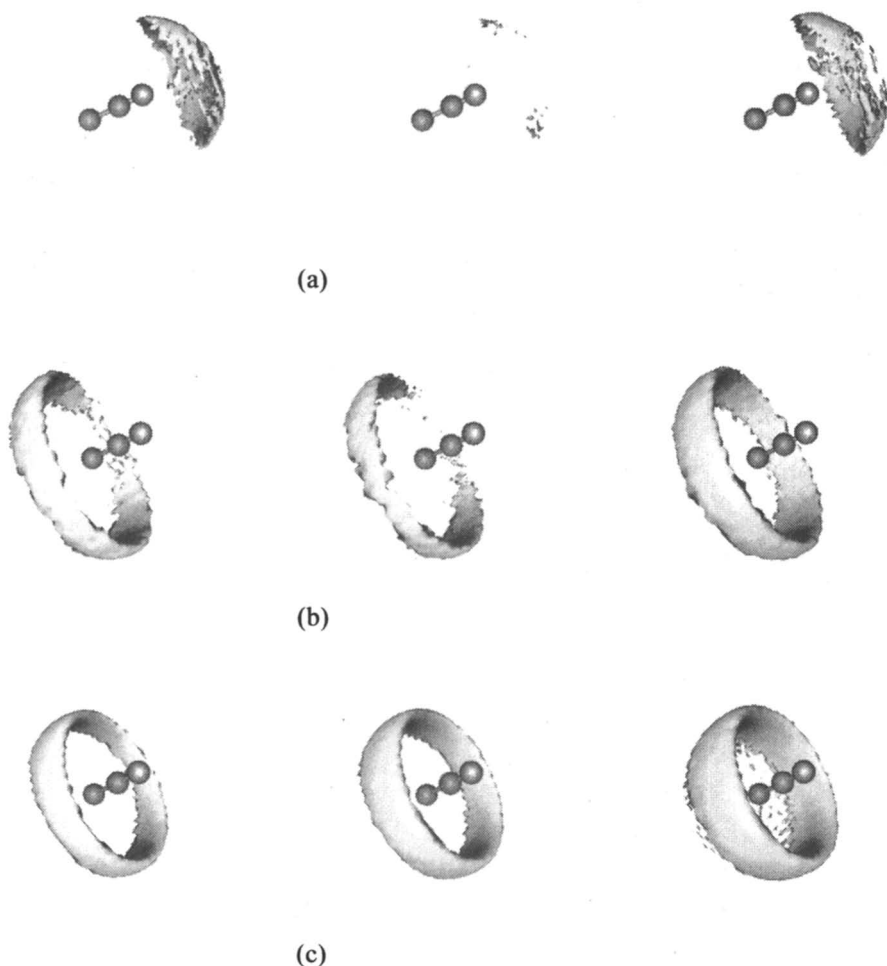


Figure 7. The orientational distributions of the CR atoms in cation (a), the B atoms in anion (b) and the N atoms in CH₃CN (c) around CH₃CN in the mixtures [bmim][BF₄](1) - CH₃CN(2). From left to right, the molar fractions of the mixture x_1 are 0.2, 0.3 and 0.4. The contour levels in (a), (b) and (c) are 2.5, 4.5 and 3.0, respectively. (Reproduced with permission from reference 15. Copyright 2005 Royal Society of Canada.)

References

1. Hanke, C. G.; Price, S. L.; Lynden-Bell, R. M. *Mol. Phys.*, **2001**, *99*, 801.
2. Morrow, T. I.; Maginn, E. J. *J. Phys. Chem. B*, **2002**, *106*, 12807.
3. de Andrade, J.; Boes, E. S.; Stassen, H. *J. Phys. Chem. B*, **2002**, *106*, 3546.
4. Lopes, J. N. C.; Deschamps, J.; Padua, A. A. H. *J. Phys. Chem. B*, **2004**, *108*, 2038.
5. Lopes, J. N. C.; Padua, A. A. H. *J. Phys. Chem. B*, **2004**, *108*, 16893.
6. Liu, Z. P.; Huang, S. P.; Wang, W. C. *J. Phys. Chem. B*, **2004**, *108*, 12978.
7. Liu, Z. P.; Wu, X. P.; Wang, W. C. *Phys. Chem. Chem. Phys.*, **2006**, *8*, 1096.
8. Del Popolo, M. G.; Lynden-Bell, R. M.; Kohanoff, J. *J. Phys. Chem. B*, **2005**, *109*, 5895.
9. Buhl, M.; Chaumont, A.; Schurhammer, R.; Wipff, G. *J. Phys. Chem. B*, **2005**, *109*, 18591.
10. Cornell, W. D.; Cieplak, P.; Bayly, C. I.; Kollman, P. A. *J. Am. Chem. Soc.*, **1993**, *115*, 9620.
11. Paulechka, Y. U.; Kabo, G. J.; Blokhin, A. V.; Vydrov, O. A.; Magee, J. W.; Frenkel, M. *J. Chem. Eng. Data*, **2003**, *48*, 457.
12. Shah, J. K.; Brennecke, J. F.; Maginn, E. J. *Green Chem.*, **2002**, *4*, 112.
13. Urahata, S. M.; Ribeiro, M. C. C. *J. Chem. Phys.*, **2004**, *120*, 1855.
14. Lyubartsev, A. P.; Laaksonen, A. *Comp. Phys. Comm.*, **2000**, *128*, 565-589.
15. Wu, X. P.; Liu, Z. P.; Wang, W. C. *Phys. Chem. Chem. Phys.*, **2005**, *7*, 2771.
16. Swiderski, K.; McLean, A.; Gordon, C. M.; Vaughan, D. H. *Chem. Comm.*, **2004**, 2178.
17. Wang, J. J.; Tian, Y.; Zhao, Y.; Zhuo, K. *Green Chem.*, **2003**, *5*, 618.
18. Chun, S.; Dzyuba, S. V.; Bartsch, R. A. *Anal. Chem.*, **2001**, *73*, 3737.
19. Noda, A.; Hayamizu, K.; Watanabe, M. *J. Phys. Chem. B*, **2001**, *105*, 4603.
20. Tokuda, H.; Ishii, K.; Hayamizu, K.; Susan, M. A. B. H.; Watanabe, M. *J. Phys. Chem. B*, **2004**, *108*, 16593.
21. Wu, W. Z.; Han, B. X.; Gao, H. X.; Liu, Z. M.; Jiang, T.; Huang, J. *Angew. Chem.-Int. Edit.*, **2004**, *43*, 2415.

Chapter 7

Intra- and Intermolecular Structure of Ionic Liquids: From Conformers to Nanostructures

Agílio A. H. Pádua¹ and José N. A. Canongia Lopes²

¹Laboratoire de Thermodynamique des Solutions et des Polymères,
Université Blaise Pascal Clermont-Ferrand/CNRS, France
(email: agilio.padua@univ-bpclermont.fr)

²Centro de Química Estrutural, Instituto Superior Técnico/Instituto
de Tecnologia Química e Bioquímica, Lisboa, Portugal
(email: jnlopes@ist.utl.pt)

Conformations of the alkyl side chains in 1-alkyl-3-methylimidazolium cations were studied for different dihedrals along the alkyl side chain in a given cation, and for different cations of the family. The ionic liquids were represented by an all-atom force field developed specifically for these compounds and the simulation results were compared with spectroscopic data. Nanometer-scale structuring in room-temperature ionic liquids is observed using molecular simulation. The ionic liquids studied belong to the 1-alkyl-3-methylimidazolium family with hexafluorophosphate or with bis(trifluoromethanesulfonyl)amide as the anions. For ionic liquids with alkyl side chains in the cation longer than or equal to butyl, segregation is observed between, on one side, the strongly charged parts of the cations and the anions, and on the other, the non-polar side chains of the cations. The alkyl chains aggregate in non-polar domains that permeate a three-dimensional network of ionic channels formed by the charged parts of the ions. The consequences of these nanostructural features on the solvation of nonpolar, polar, and associating solutes are discussed in the light of the solute-solvent radial distribution functions for systems containing between 0.1 and 0.2 mole fraction of solute.

Introduction

The development in the last few years of molecular models for ionic liquids, to be used within the framework of statistical mechanics simulations in condensed phases was received with great interest by many researchers who can use those models to study structural, energetic and dynamic properties of ionic liquids.

One of the most widely used and studied ionic liquid families is the one based on imidazolium cations, in particular 1-alkyl-3-methylimidazolium, $C_n\text{mim}^+$, combined with different (mainly inorganic) anions. The main differences between room-temperature ionic liquids and simple molten salts are the molecular asymmetry usually built into the cation, the conformational flexibility of the ions, and the spreading of electrostatic charge over relatively large groups of atoms. These attributes oppose the strong charge ordering due to the ionic interactions that normally would cause the system to crystallize, and thus a wide liquid range is obtained.

Molecular modeling is a powerful tool to access condensed-phase structure, but most of the simulation studies with ionic liquids carried out so far concentrated on the local intermolecular scale around a given cation or anion, providing results that agree with many of the structural features found in diffraction experiments. In this work we will focus on structural features that are present at an intramolecular level and at longer range intermolecular distances. The first concerns intramolecular conformation of the cations, and the second medium-range order in the liquid phase.

The presence of medium-range order in the ionic liquids has consequences on the solvation of different molecular species. The differences in the solvation of nonpolar and polar solutes in the ionic liquids will be discussed.

Conformational distributions of imidazolium cations in the liquid phase

In this section we will address ionic liquids based on the 1-alkyl-3-methylimidazolium cation family (alkyl=ethyl, butyl or hexyl) combined with anions such as hexafluorophosphate (PF_6^-), bistriflamide ($(\text{CF}_3\text{SO}_2)_2\text{N}^-$), tetrafluoroborate (BF_4^-) and triflate (CF_3SO_3^-). In Figure 1 we present the nomenclature used throughout this paper as well a color code for the different dihedral angles under discussion.

In a recent publication, Umebayashi and co-authors (1) confirmed using Raman spectroscopy and quantum chemical calculations that the 1-ethyl-3-methylimidazolium cation ($C_2\text{mim}^+$), present in several ionic liquids, exists as a mixture of two principal conformers, Figure 2. The two conformers are obtained by rotation around the C2–N1–C6–C7 dihedral angle (color-coded black in Figure 1). The results of these authors also supported the soundness of the

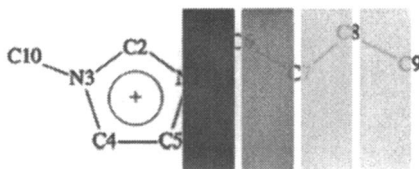


Figure 1. Nomenclature of the 1-alkyl-3-methylimidazolium cations.

approximations used when developing a systematic molecular force-field for ionic liquids by the authors of the present article (2), namely the careful mapping of the torsion profile around the above mentioned dihedral angle.

In other recent publications, Osawa et al. (3), Katayanagi et al. (4), and Berg et al. (5) also demonstrated the existence of conformers for the $C_4\text{mim}^+$ cation in ionic liquids containing BF_4^- (3), halides (4,5) and PF_6^- (5) anions, Figure 3. The conformations studied in $C_4\text{mim}^+$ were those around the C6–C7 bond (color-coded dark gray in Figure 1). Berg et al. (5) also extended their investigation to the $C_6\text{mim}^+$ cation and observed similar conformers around the C6–C7 bond.

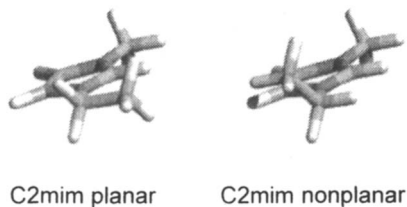


Figure 2. Main conformers of 1-ethyl-3-methylimidazolium.

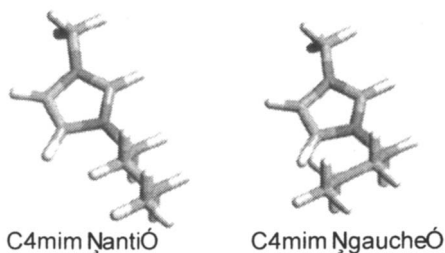


Figure 3. Main conformers of 1-butyl-3-methylimidazolium.

In this work we calculated the dihedral distribution along the alkyl chain of different $C_n\text{mim}^+$ cations using MD simulations. All of the ionic liquids studied were modeled by the all-atom molecular force field proposed by the authors in two previous publications (2,6). While developing the force field it was always our reasoning that accurate conformational energies and electrostatic charge distributions derived from high-level quantum calculations would be relevant to render subtle energetic or configurational features, such as those responsible for many of the particular properties of these large organic salts in the liquid phase. The computational details of the simulations are given elsewhere (7). Margulis et al. (8,9) also calculated dihedral distributions on similar ionic liquid systems using MD simulation data. However, the employed force field was not specifically developed to account for the torsional energy profiles of alkyl chains linked to imidazolium rings (OPLS parameters for normal alkyl chains were used).

The MD simulation results generated configuration data from which dihedral angle distributions were calculated. The results are shown in Figure 4.

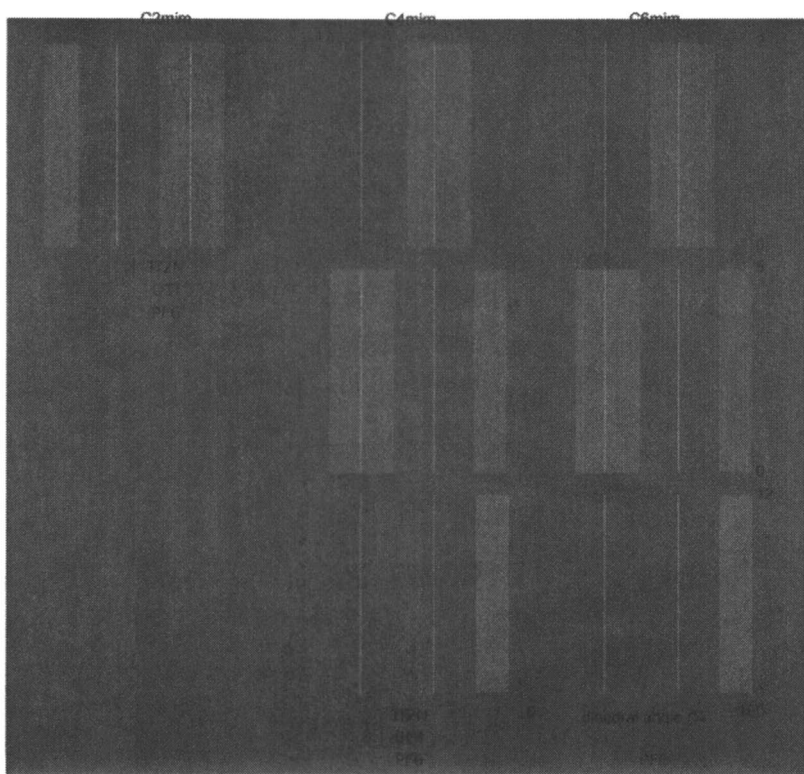


Figure 4. Dihedral distribution along the alkyl chain of 1-alkyl-3-methylimidazolium cations obtained by MD simulation.

For C_2mim^+ the histograms show (Figure 4, upper left corner) that there are two preferred conformers: the first corresponds to a C2–N1–C6–C7 dihedral angle of 0° giving a planar conformation, while the second corresponds to a non-planar conformation with a dihedral angle of approximately 120° , Figure 2. These results agree with both the ab initio calculations of Umebayashi et al. — that predict minima in the torsion energy profile around 0 and 110 degrees, (see Figure 3 of ref. 1) — and also with their Raman experimental data that give evidence for the two conformers in the liquid phase: the spectra exhibit peaks at 387 and 430 cm^{-1} characteristic of the non-planar conformation, and also at 448 cm^{-1} characteristic of the planar conformer (see Figure 2 of ref. 1).

Based on the Gaussian decomposition of the Raman spectrum of $[C_2mim][BF_4]$ (presented in Figure 4 of ref. 1) we estimated the ratio between the areas (a_1/a_2) and the heights (h_1/h_2) of the peaks characteristic of the planar and non-planar conformers. These values were then corrected by the ratio of the Raman intensities estimated ab initio, to yield the ratio between the populations of the two conformers, $NP/P(a)$ and $NP/P(h)$, respectively, and the corresponding fractions of the planar conformer, $x_p(a)$ and $x_p(h)$. These results, which are 0.10 and 0.22, respectively, are not entirely consistent, reflecting the crude approximations implied in the attempt to estimate relative amounts of the conformers from Raman spectra. The Raman intensities estimated ab initio refer to calculations performed on an isolated molecule at a given conformation, and not to the distribution of conformers that exist in the condensed phase. Moreover, the widening of the bands in the condensed phase is not taken into account. However, even if approximate, the calculations from the spectra provide a rough estimate that can be compared (semi-quantitatively) with the values obtained from the other two sets of data.

From the MD data, the ratio between the two conformers and the fraction of the planar one can be calculated from a Gaussian decomposition of the histograms presented in Figure 4. For all the ionic liquids simulated by MD, the fractions of the planar conformer range from 0.20 to 0.30.

The Gibbs free energy difference between the two isomers, ΔG , obtained ab initio (Table 1 from ref. 1) can also serve to derive the relative amounts of the two conformers. A $\Delta G = 2.3 \text{ kJ mol}^{-1}$ (the non-planar conformer is more stable) corresponds to a fraction of the planar conformer of 0.17. It must be stressed at this point that, since there are two possible enantiomeric non-planar conformations but only one planar conformation, a factor of two must be used when calculating the relative amounts of the two conformers.

The three sets of data yield similar results, showing that there is a larger amount of non-planar conformer (around 80%). The results are summarized in Figure 5. This is a remarkable, albeit semi-quantitative, agreement since the confrontation of data from single-molecule ab initio calculations (in some cases very sensitive to the choice of the basis sets and theoretical level) with condensed-phase results (MD and Raman) can sometimes lead to erroneous

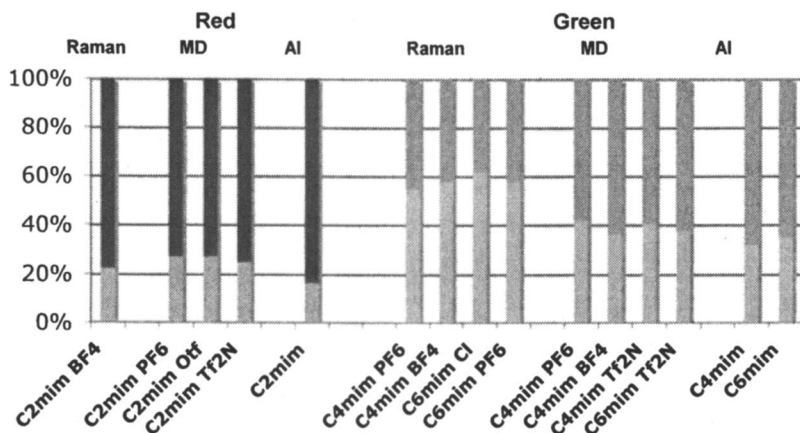


Figure 5. Comparison between Raman, MD and AI results for the proportion of the main conformers around the N1-C6 and C6-C7 bonds.

results. The same conclusion applies to the comparison between MD results, based on a semi-empirical force field, and the attempt to extract quantitative data from the intensity and width of peaks of a Raman spectra.

Two remaining issues concerning the C2-N1-C6-C7 must be addressed (cf. first row of histograms in Figure 4). First, when one moves from C₂mim⁺ to longer alkyl side chains, the peak at 0° (planar conformation) disappears. This means that from the energetic point of view, the local minimum in the torsion energy profile of this dihedral angle is overcome by the contribution of non-bonded interactions arising from atoms in the longer alkyl chain. Second, all C2-N1-C6-C7 histograms show non-negligible populations at all conformations, and not just for the values of the dihedral around the two energy minima. In the simulated liquid phase there is a wide distribution of conformers, with two peaks at the planar and non-planar conformations, implying a considerable freedom of rotation around the N1-C6 bond. This situation is also present when the cation contains a longer alkyl chain.

For the C₄mim⁺ and C₆mim⁺ cations this type of analysis can be extended to the N1-C6-C7-C8 (green-coded) dihedral. The histograms for this dihedral angle are shown in the 2nd row of Figure 4, and they exhibit two peaks: one at 180° corresponding to an anti conformer and one around 60° corresponding to a gauche conformer. These results agree with both our own ab-initio calculations performed when developing the force field — that predict minima in the torsion energy profile around the same angles (Figure 3 of ref. 6) — and also with the experimental Raman data of Berg et al. (5) that show evidence for the two conformers in the liquid phase: for instance, the liquid phase spectra exhibit peaks around 625 cm⁻¹ characteristic of the anti conformation and around 600 cm⁻¹ characteristic of the gauche conformers (Tables 2 and 6 of ref. 5).

Again, a more quantitative analysis of the three sets of data (MD, AI, Raman) was performed, the results of which are also given in Figure 5.

The *ab initio* calculations performed by Berg et al. predicted a relatively small difference between the Gibbs free energy of the two conformers: ΔG around only 0.2 kJ mol⁻¹, the anti and gauche conformers being the more stable in the case of C₄mim⁺ and C₆mim⁺, respectively. With such a low free energy difference the ratio of anti:gauche should be approximately 2:1, since there are two gauche and one anti conformers, corresponding to a fraction of anti conformer of about 0.33 (cf. last two bars in Figure 5). For this dihedral angle, the peak ratio measurements at the characteristic frequencies of the anti and gauche conformers, again by Gaussian decomposition of the appropriate portion of the Raman spectra, yield results that are inconsistent with this last result, giving a fraction of the anti conformer around 0.65. Nevertheless the Raman data clearly show the existence of both conformers in the ionic liquid. The inconsistency between the Raman spectra and the *ab initio* calculations of free energy can probably be assigned to the rather rudimentary approximations involved in the estimation of the relative amounts of each conformer from the Raman peaks, and also to the use in the *ab initio* calculations of just two conformations of one isolated molecule, and not of the continuous distribution that in fact exists in condensed phase, including the rather diffuse distribution of the C2–N1–C6–C7 dihedral angle.

The MD calculations yield two distinctive peaks, seen in the second row of Figure 4. The ratios (area and intensity) of these two peaks correspond to fractions of the anti conformer around 0.40 for C₄mim⁺ and 0.37 for C₆mim⁺, values that are comparable to the ones estimated *ab initio*. The N1–C6–C7–C8 dihedral angle distributions calculated by the MD simulations also show that, unlike for the C2–N1–C6–C7 distribution, the molecules in the liquid phase are clearly either in the anti or in the gauche conformation around the C6–C7 bond, with negligible amounts of intermediate conformations.

A final remark can be made about the dihedrals further away from the imidazolium ring along the alkyl side chain, whose histograms are presented in the last rows of Figure 4. The dihedral angle distributions in these cases exhibit pronounced peaks corresponding to anti conformers and much less intense ones associated with gauche conformers, as is typical of normal alkanes. This behavior is present for all C–C–C–C torsions, from the first of such dihedral angles in C₄mim⁺ to the one at the end of the side chain in C₁₂mim⁺ (lower right corner of Figure 4). The significant differences between the C–C–C–C and the N1–C6–C7–C8 dihedrals lead us to conclude that the latter must be parameterized in a specific manner for imidazolium cations and cannot be reliably extrapolated from other families of molecule.

As a conclusion one can say that the confrontation between simulation and liquid-phase spectroscopic evidence, apart from providing a partial validation of the force field used for the simulations, can also offer an overall view on the

arrangement of the alkyl chain in 1-alkyl-3-methylimidazolium cations composing ionic liquids. The MD results showed that, as one proceeds from the dihedrals closer to the imidazolium ring to those approaching the end of the alkyl chain, the conformations become defined in a sharper manner: the dihedral centered around N1–C6 exhibits a wide distribution of possible conformations, the one centered at C6–C7 exhibits two possible conformers (anti or gauche) whereas those centered on C–C bonds beyond are predominately in an anti conformation. The simulations also showed that the planar conformation of the C7 carbon of the side chain relative to the imidazolium ring, which corresponds to a relative probability maximum in C_2mim^+ , is no longer present as a preferred conformer in alkylmethylimidazolium cations with longer side chains. These conformational shifts along the imidazolium cation family as the alkyl chain is increased can help explain the complex and non-monotonous behavior in some of their properties, a theme that will be further developed in the next section.

Nanometer-scale structures in ionic liquids

As pointed out in the introduction, room temperature ionic liquids differ from simple molten salts in three respects: molecular asymmetry, conformational richness, and charge distribution. In this section we consider the differences in liquid state structure between room temperature ionic liquids and simple molten salts.

Liquid structure can be translated into radial distribution functions (rdfs), which measure the probability of finding a given pair of atomic sites as a function of separation. In liquids away from the critical point, rdfs tend to unity at large distances, meaning that there is no long range order. The overall picture of the structure in a liquid can be conveyed by centers-of-mass rdfs, such as those shown in Figure 6 for the ionic liquid $[C_6mim][PF_6]$. Simulation details and force field models can be found in the literature (10).

The center-of-mass rdfs of an ionic liquid are similar to those of a simple molten salt, with a structure determined principally by electrostatic charge ordering. It can be seen that the cation-cation and the anion-anion rdfs are in phase, and that the cation-anion rdf is in opposition of phase with the other two functions. The peaks and troughs in the cation-cation rdf are less pronounced than those in the anion-anion rdf because the cation has a flexible molecular skeleton whereas the anion is more rigid and almost spherical. As the cation explores different conformations, its center-of-mass is displaced over a region in space. In the PF_6^- anion the center-of-mass stays essentially on the P atom.

A more detailed image of the liquid structure can be formed by looking at site-site rdfs. In Figure 7 are shown atom-atom rdfs between the end-carbons of the alkyl side-chains of several imidazolium cations, in ionic liquids of the $[C_nmim][PF_6]$ family. A very significant difference appears in the first peak for

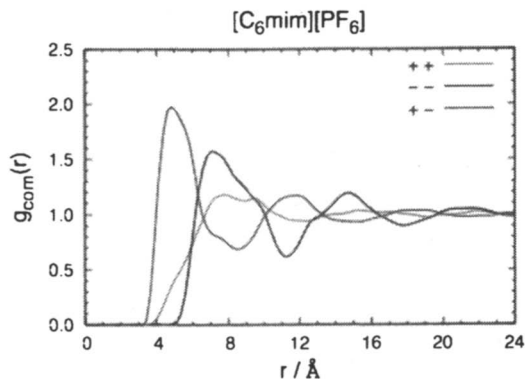


Figure 6. Center-of-mass ion-ion radial distribution functions at 300 K.

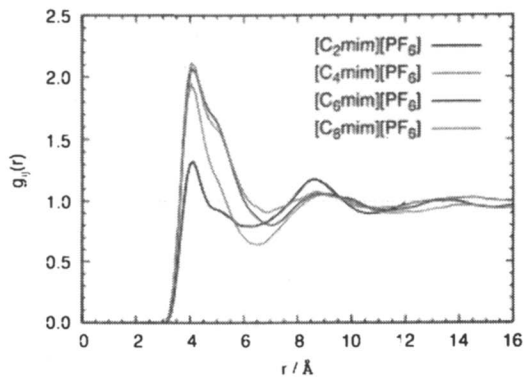


Figure 7. Radial distribution functions between the end carbons of the alkyl side chains in ionic liquids of the [C_nmim][PF₆] family.

[C₂mim][PF₆] when compared to the ionic liquids with longer side-chains. The strong correlation between end-carbons for $n \geq 4$ means that the side chains are coming into close contact. But for $n = 2$ the ethyl groups are found dispersed in the liquid, with loose mutual correlation. The same features are present in imidazolium ionic liquids with other anions such as bis(trifluoromethanesulfonyl)amide (2).

The end-carbon rdfs suggest clustering of the alkyl side-chains for $n \geq 4$, resulting in a segregation between the charged head-groups of the cations and the anions, and the nonpolar regions of the ions. In order to identify the atoms that will belong to the “charged” and the “nonpolar” regions, the partial charge distributions generated for the molecular force field (2,6) were inspected. Atoms that we assign to the charged regions are, in the imidazolium cations, those of the imidazolium ring, plus atoms bonded to these, and also hydrogens bonded to the first carbons of the alkyl chains (those connected to the imidazolium nitrogens); atoms that we identify as forming the nonpolar region of the cation are those from C2 in the alkyl chains onward. The rationale for such a division is illustrated in the electrostatic surface potential plot in Figure 8. The entire hexafluorophosphate anion is considered as a “charged” entity, but if the anion were for example an alkylsulphate it would also contain a nonpolar chain.

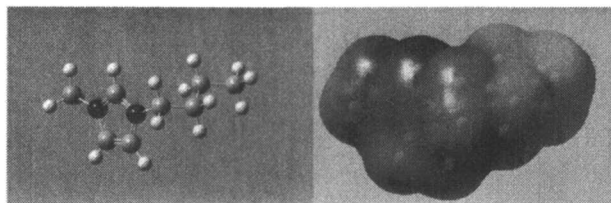


Figure 8. Charge density in C₄mim⁺ calculated *ab initio* at the MP2/cc-pVTZ(-f) level. The surface depicted is an isoelectron density surface; the color is related to the electrostatic potential: deeper blue corresponds to more positive.

In order to visualize clearly the arrangement of the nonpolar and charged parts of the ions in the liquid phase, a color code was adopted, according to which atoms belonging to the charged parts of the cation and the anion are distinguished from those of the nonpolar side chain of the cation. Representative simulation snapshots of ionic liquids are collected in Figure 9, where for alkyl side chains longer than butyl (inclusive) the formation of spatial domains containing the nonpolar and charged parts is evident. Ethyl side chains do not aggregate.

For alkyl side chains longer than C₁₂ ionic liquids of the [C_{*n*}mim][PF₆] family are known to form liquid-crystalline phases (11). According to our

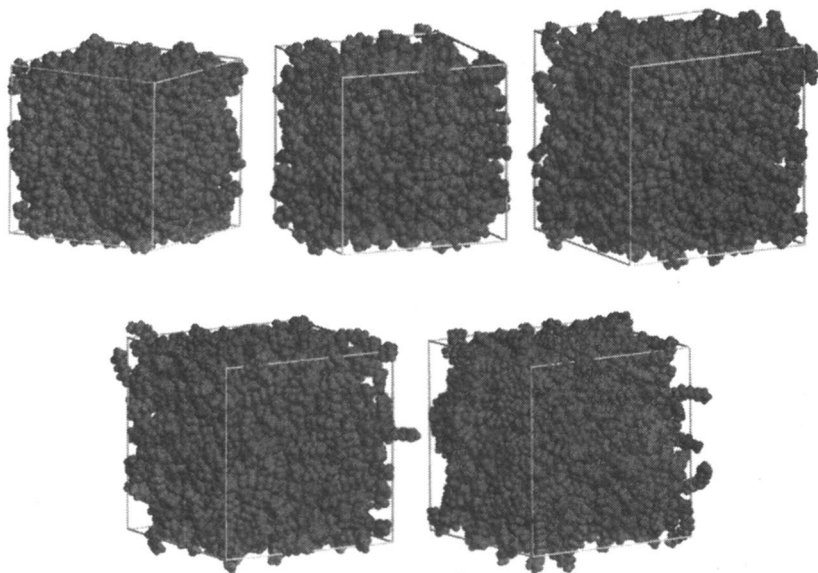


Figure 9. Snapshots of simulation boxes of $[C_n\text{mim}][\text{PF}_6]$, $n = 2, 4, 6, 8, 12$, in which atoms belonging to the charged parts of the cations (imidazolium ring and attached atoms, plus hydrogens bonded to the carbon atoms directly attached to the ring) and anions were colored in black, and atoms belonging to the nonpolar part (starting from the second carbon atom of the cations' chain) were colored gray.

simulations, those with shorter side chains have liquid structures analogous to simple molten salts, but those with intermediate length side chains, from C4 to C12, exhibit very interesting medium-range order, similar to microphase separation observed in certain diblock copolymers.

In $[\text{C}_4\text{mim}][\text{PF}_6]$ aggregation of the side chains in nonpolar spatial domains is evident, although those domains do not form a continuous microphase. In $[\text{C}_6\text{mim}][\text{PF}_6]$ the connectivity of the nonpolar domains is clearly more important, and in $[\text{C}_8\text{mim}][\text{PF}_6]$ and $[\text{C}_{12}\text{mim}][\text{PF}_6]$ it is established and percolates the entire fluid. The charged domain forms a network of ionic channels that, thanks to the strong electrostatic forces, show three-dimensional continuity in all cases studied.

The characteristic length scales of these medium-range heterogeneities could be quantified by calculating the static structure factor considering the centers of mass of the charged and nonpolar domains (2). Those structure factors show low wavelength peaks that correspond to periodicity at longer range than the oscillations in the rdfs shown in Figure 6. The spatial domains have

characteristic lengths ranging from 12 Å in [C₄mim][PF₆] to approximately 20 Å in [C₁₂mim][PF₆], thus in the nanometer scale.

The same kind of medium-range ordering reported here has been observed in other computer simulation studies, to our knowledge first by Urahata and Ribeiro using an united-atom model (12) and recently by Wang and Voth using a coarse grained model (13). A number of simulation studies on the microscopic dynamics in ionic liquids have also pointed out the slow dynamics of these liquids and the persistence of local environments, typical of the glassy state.

Several pieces of experimental evidence can be related to the nanostructuring. First, the behavior of viscosity, diffusion and ion mobility with the length of the alkyl side-chain in [C_nmim][PF₆], n = 1, 2, 4, 6, 8, reported by Watanabe et al. (14) has a striking feature: electric conductivity increases from C1 to C2, but then decreases for longer side chains. Diffusion shows the same behavior and viscosity the opposite. This is difficult to explain since, when the alkyl chain length increases, strong cohesive electrostatic forces become less dominant in the system when compared to weaker dispersive interactions between the alkyl chains. Ion mobility would be expected to increase. The fact that it doesn't may be interpreted as a result of the formation of the nonpolar spatial domains, that restrict ion mobility and confine conduction to the ionic channels.

Second, the fluorescence emission of probe molecules in some ionic liquids shows a red shift (15) analogous to that observed in nanostructured systems such as micelles and membranes, or in glassy states. Third, the fluorescence emission of ionic liquids themselves shows a long-wavelength band that disappears upon dilution of the ionic liquid in a solvent (16), a result attributable to the breaking of associative structures.

Forth, ionic liquids have been used as stationary phases for gas chromatography and separation of polar and nonpolar compounds was observed, as well as a good separation of homologous nonpolar molecules such as the series of *n*-alkanes (17). This dual selectivity towards both polar and nonpolar species is compatible with the existence of the two types of domain predicted in our simulations.

All these experimental properties are indirect and some of them would be compatible with simply a glassy nature of the ionic liquids. We hope the present simulation results stimulate experimental work aimed at investigating the structural heterogeneity of imidazolium ionic liquids with side chains ranging from butyl to dodecyl.

Solvation structure of nonpolar, polar and associating solutes

The results of using alkyimidazolium ionic liquids as stationary phases for gas chromatography indicate that polar and nonpolar species interact in their

own way with the different parts of the ions, notably the cation. This suggests that the solvation of nonpolar, polar, or associating solutes in the bulk ionic liquids could be very diverse in nature, given the presence of the segregated domains. This led us to investigate the solute-solvent structure of mixtures containing various solutes in an ionic liquid using molecular simulation. Solutes were represented by the OPLS_AA force field (18,19), and the technical details of the simulations were similar to those adopted to simulate pure ionic liquids (7).

A solution of cyclohexane in $[C_4mim][PF_6]$ with a mole fraction of cyclohexane of 0.1 was simulated at 330 K and 0.1 MPa. This composition lies in the one-phase region of the mixture, according to the experimental liquid-liquid phase diagram (20). Some illustrative site-site solute-solvent rdfs, accompanied by a snapshot of the simulation box, are shown in Figure 10.

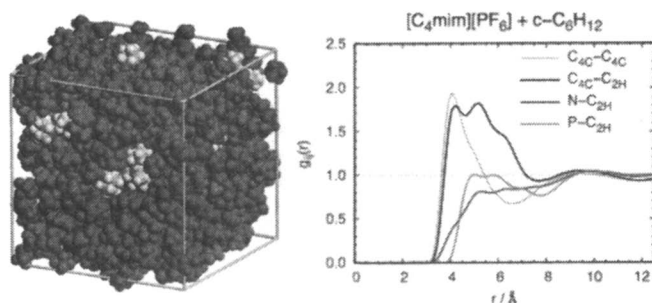


Figure 10. Snapshot of a simulation box containing 20 cyclohexane molecules and 200 ion pairs of $[C_4mim][PF_6]$ at 330 K. Site-site rdfs between selected atoms of the solute and solvent are shown, and compared to the end-carbon rdf of the cation (thin line).

It is observed that there is a marked correlation between the end carbon of the cation's alkyl chain and the carbon atoms of cyclohexane. The multiple peaks correspond to the different carbon atoms of the cyclohexane ring. There is an absence of correlation with the headgroup of the cation (here represented by the nitrogen atoms of the imidazolium ring) and with P atom of the anion. In other words, cyclohexane is solvated in the nonpolar domain of the ionic liquid.

A similar situation is observed for n-hexane, as seen in Figure 11. The composition is also 0.1 mole fraction in the alkane, again within the experimental one-phase region (20). The sole significant nuance is the distinction we have made between the end methyl carbons and the four methylene carbons in n-hexane. The correlation between the end carbon of C_4mim^+ is strong with both types of carbon atom from n-hexane.

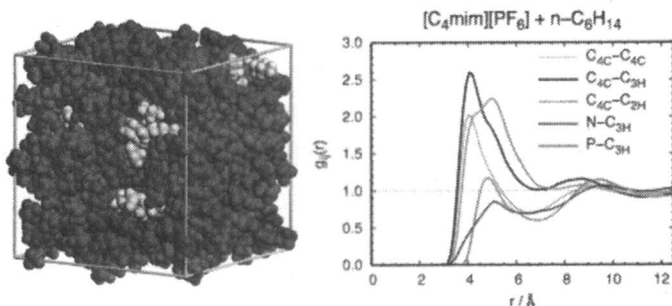


Figure 11. Snapshot of a simulation box containing 20 *n*-hexane molecules and 200 ion pairs of $[C_4mim][PF_6]$ at 330 K.

The results are quite different for a polar solute like acetonitrile. The snapshot and solute-solvent rdfs in Figure 12 were obtained at 330 K in a system with a 0.2 mole fraction in acetonitrile (acetonitrile and $[C_4mim][PF_6]$ are miscible in all proportions at the simulation temperature). Here there is a significant correlation between atoms in the imidazolium ring and the solute, and also between the anion and the solute. The atoms of the imidazolium ring chosen to illustrate the solvation structure were the hydrogen atoms connected to the carbons of the ring, since these are the acidic hydrogens that interact more closely with the negatively charged nitrogen of the nitrile group in the solute. It is seen that the first peak in the rdfs of the nitrile N with either H₂ or H₄ and H₅ are almost superimposed. There is also a strong peak in the rdf of the methyl carbon of acetonitrile with the end carbon of the alkyl side chain of the cation, demonstrating that acetonitrile is interacting with both types of domain in the ionic liquid.

Finally, methanol was studied in a similar way, and the results are shown in Figure 13. The remarkable feature here is the presence of a very sharp peak in the rdf between the hydroxyl hydrogen of methanol and the anion, indicating a hydrogen bond. Complementary hydrogen bonds between the acidic hydrogens of the imidazolium and the oxygen of methanol are much less conspicuous. Again, similarly to what was observed for acetonitrile, there is a significant peak in the rdf between the end carbon of the cation side chain and the methyl carbon in the solute. Methanol is not simply a polar solute but has an associating character with the ionic liquid.

Conclusion

In the present work several structural features of pure ionic liquids and of mixtures with different molecular solutes were interpreted using molecular simulation.

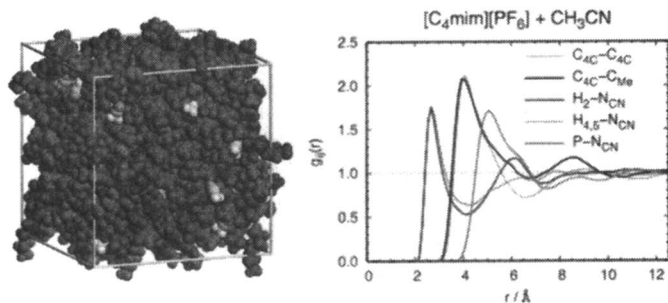


Figure 12. Snapshot of a simulation box containing 40 acetonitrile molecules and 200 ion pairs of $[C_4mim][PF_6]$ at 330 K.

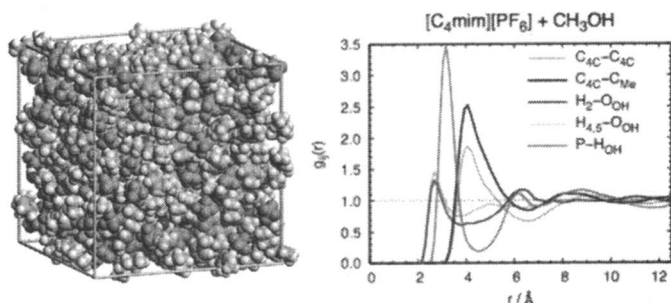


Figure 13. Snapshot of a simulation box containing 40 methanol molecules and 200 ion pairs of $[C_4mim][PF_6]$ at 330 K.

At an intramolecular level, the conformational behavior of 1-alkyl-3-methylimidazolium cations was studied using a specific force field, and the results compared with experimental spectroscopic data and also with quantum chemical calculations. The agreement obtained supports the use of the force field under discussion. The conformational characteristics around successive bonds change along the alkyl side chain of a given imidazolium cation, but also change when one member of the $C_n\text{mim}^+$ is compared to the next one.

Imidazolium ionic liquids with alkyl side chains longer or equal to butyl exhibit segregation between nonpolar and “charged” domains in the liquid phase, giving rise to medium-range ordering. Although no direct experimental evidence was found to support these predictions, several pieces of evidence indicate that such structures are likely to occur. Independent simulation work, using very different models from the ones used here, are in total agreement with the present results.

These nanostructures have consequences to the solvation of polar and nonpolar molecular species in the ionic liquids. Original results concerning the solvation structure of cyclohexane, n-hexane, acetonitrile and methanol were presented to illustrate the completely different solvation regimes around nonpolar, polar, or associating solutes.

References

1. Umebayashi, Y.; Fujimori, T.; Sukizaki, T.; Asada, M.; Fujii, K.; Kanzaki, R.; Ishiguro, S. *J. Phys. Chem. A* **2005**, *109*, 8976
2. Canongia Lopes, J. N.; Deschamps, J.; Pádua, A. A. H. *J. Phys. Chem. B* **2004**, *108*, 2038; *ibid.* **2004**, *108*, 11250.
3. Ozawa, R.; Hayashi S.; Saha, S.; Kobayashi, A.; Hamagushi, H. *Chem. Lett.* **2003**, *32*, 948
4. Katayanagi, H.; Hayashi, S.; Hamagushi, H.; Nishikawa, K. *Chem. Phys. Lett.* **2004**, *392*, 460
5. Berg, R.W.; Deetlefs, M.; Seddon, K. R.; Shim, I.; Thomson, J. M. *J. Phys. Chem. B* **2005**, *109*, 19018
6. Canongia Lopes, J. N.; Pádua, A. A. H. *J. Phys. Chem. B* **2004**, *108*, 16893
7. Canongia Lopes, J. N.; Pádua, A. A. H. *J. Phys. Chem. B* **2006**, *110*, 7485.
8. Margulis, C.; Stern, H. A.; Berne, B. J. *J. Phys. Chem. B* **2002**, *106*, 12017.
9. Margulis, C. *Mol. Phys.* **2004**, *102*, 829.
10. Pádua, A.A.H.; Canongia Lopes, J.N.C. *J Phys Chem B* **2006**, *110*, 3330.
11. Gordon, C. M.; Holbrey, J. D.; Kennedy, A. R.; Seddon, K. R. *J. Mater. Chem.* **1998**, *8*, 2627.
12. Urahata, S. M.; Ribeiro, M. C. C. *J. Chem. Phys.* **2004**, *120*, 1855.
13. Wang, Y.; Voth, G. A. *J. Am. Chem. Soc.* **2005**, *127*, 12192.
14. Tokuda, H.; Hayamizu, K.; Ishii, K.; Susan, M. A. B. H.; Watanabe, M. *J. Phys. Chem. B* **2005**, *109*, 6103.
15. Mandal, P.K.; Sarkar, M.; Samanta, A. *J. Phys. Chem. A* **2004**, *108*, 9048.
16. Paul, A.; Mandal, P.K.; Samanta, A. *J. Phys. Chem. B* **2005**, *109*, 9148.
17. Anderson, J. L.; Armstrong, D. W. *Anal. Chem.* **2003**, *75*, 4851.
18. Jorgensen, W.L.; Maxwell, D.S.; Tirado-Rives, J. *J. Am. Chem. Soc.* **1996**, *118*, 11225.
19. Price, M.L.P.; Ostrovsky, D.; Jorgensen, W.L. *J. Comput. Chem.* **2001**, *22*, 1340.
20. Domanska, U.; Marciniak, A. *J. Chem. Eng. Data* **2003**, *48*, 451.

Chapter 8

Molecular Simulation of Mixtures Containing Imidazolium- and Pyridinium-Based Ionic Liquids and 1-Butanol

Timothy I. Morrow and Edward J. Maginn*

Department of Chemical and Biomolecular Engineering, University of Notre Dame, South Bend, IN 46554

A molecular simulation study of mixtures containing 1-butanol and various imidazolium and pyridinium-based ionic liquids that form liquid-liquid equilibrium is reported. Solutions of 1-butanol and 1-*n*-butyl-3-methylimidazolium tetrafluoroborate ([bmim][BF₄]), 1-*n*-butyl-3-methylimidazolium bis(trifluoromethane-sulfonyl) imide ([bmim][Tf₂N]), 1-*n*-butyl-3-methylpyridinium tetrafluoroborate ([bmpy][BF₄]), and 1-*n*-butyl-3-methylpyridinium bis(trifluoromethane-sulfonyl) imide ([bmpy][Tf₂N]) are examined using isothermal-isobaric molecular dynamics simulations. Quantities computed include molar volumes, self-diffusivities, radial distribution functions, local composition functions, and interaction energies. The simulations help explain recent experimental results in which [bmpy][BF₄] was found to have a lower upper critical solution temperature (UCST) with 1-butanol than [bmim][BF₄]. This is due to weaker cation/anion association in the [bmpy] mixture, which in turn allows stronger alcohol/anion and alcohol/cation association in this system relative to [bmim][BF₄]. The simulations also help explain why [bmim][Tf₂N] has a lower UCST with 1-butanol than [bmpy][Tf₂N]. This behavior is attributed to weak cation/anion association in both systems and a stronger alcohol/cation interaction with the [bmim] cation relative to the [bmpy] cation.

Introduction

It has been noted experimentally (1) that liquid-liquid equilibrium (LLE) is formed below 50°C for 1-butanol mixed with 1-n-butyl-3-methylimidazolium tetrafluoroborate ([bmim][BF₄]), 1-n-butyl-3-methylimidazolium bis(trifluoromethane-sulfonyl) imide ([bmim][Tf₂N]), 1-n-butyl-3-methylpyridinium tetrafluoroborate ([bmpy][BF₄]), and 1-n-butyl-3-methylpyridinium bis(trifluoromethane-sulfonyl) imide ([bmpy][Tf₂N]). The temperature at which the mixture remains one phase regardless of composition is called the upper critical solution temperature (UCST). A high UCST generally indicates that self interactions (in this case, alcohol-alcohol and IL-IL) are more favorable than unlike (alcohol-IL) interactions in the mixture. Interestingly, the UCST of the mixture with [bmim][BF₄] is *higher* than that with [bmpy][BF₄], but the UCST for the mixture with [bmim][Tf₂N] is *lower* than that with [bmpy][Tf₂N]. This indicates that alcohol LLE behavior is not just governed by simple interactions between the alcohol and a particular cation or anion, but instead results from a complex interplay between alcohol, cation, and anion. These systems are therefore ideally suited for a molecular modeling study in which structure and energetic interactions can be directly calculated.

The present work is directed at understanding the molecular interactions for these mixtures through isothermal-isobaric (NPT) molecular dynamics (MD) simulations. The local fluid structure of the mixtures is studied via radial distribution functions and local composition functions. Interaction energies between each species are also computed. The simulation results provide insight into the nature of the alcohol-ionic liquid interactions that give rise to the observed liquid-liquid coexistence behavior.

Methodology

In this work we have used a standard molecular mechanics forcefield (2), with functional form

$$\begin{aligned}
 V_{tot} = & \sum_{bonds} k_b (r - r_o)^2 + \sum_{angles} k_\theta (\theta - \theta_o)^2 + \sum_{dihedrals} k_\chi [1 + \cos(n\chi - \delta)] \\
 & + \sum_{improper} k_\psi (\psi - \psi_o)^2 + \sum_{i=1}^{N-1} \sum_{j>i}^N \left\{ \epsilon_{ij} \left[\left(\frac{r_{min,ij}}{r_{ij}} \right)^{12} - 2 \left(\frac{r_{min,ij}}{r_{ij}} \right)^6 \right] + \frac{q_i q_j}{r_{ij}} \right\} \quad (1)
 \end{aligned}$$

to model the interactions in the fluid mixtures. The force constants, Lennard-Jones parameters, and partial atomic charges for eq 1 were all taken from the literature. The OPLS (3) all-atom (AA) model was used for 1-butanol, the parameters for the cations [bmim] and [bmpy] were taken from the work of Cadena, *et al.* (4), the parameters for the [BF₄] anion were taken from the work of de Andrade, *et al.* (5), and the parameters for the [Tf₂N] anion were taken from the work of Padua (6). The Lennard-Jones parameters for unlike atoms, ϵ_{ij} and $r_{min,ij}$, were obtained using the Lorentz-Berthelot combining rule. Coulombic interactions were modeled using fixed partial charges on each atom center. Figures 1a and 1b list the atom number conventions used for the [bmim] and [bmpy] cations, respectively.

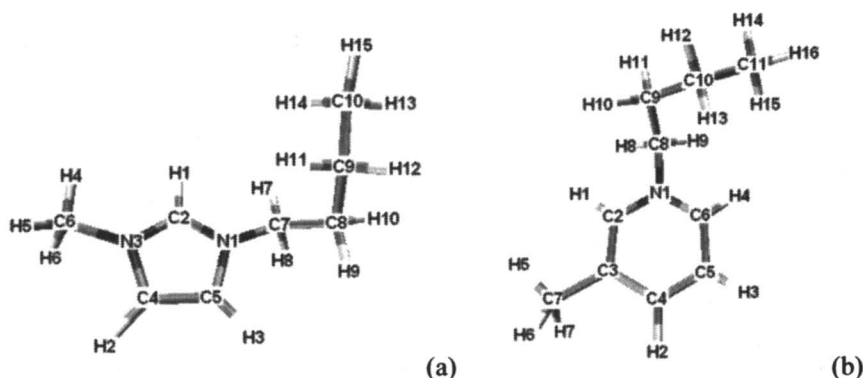


Figure 1. Atom numbering scheme used for [bmim] (a) and [bmpy] (b) cations.

Molecular dynamics simulations were performed with the program NAMD (7) version 2.5 using a cubic cell with standard periodic boundary conditions. The simulations were carried out in the isothermal-isobaric (NPT) ensemble using a modified Nosé-Hoover barostat with oscillation and decay periods of 250 fs each. The temperature was controlled via Langevin dynamics with a damping factor of 5 ps⁻¹. Simulations at two compositions were performed for each IL/butanol mixture, with one simulation consisting of a butanol-rich system (~4 mol% IL), and the other simulation consisting of an IL-rich system (~25-40 mol% IL). These compositions are all near the experimental coexistence compositions. The thermodynamic state points for all eight simulations are shown in Table 1. All eight simulations were performed at a reduced temperature, $T_r = T/T_{UCST}$ where T_{UCST} is the experimentally determined UCST, of 0.9836 and a pressure of 1 bar. A total of 1000 molecules were used for each

simulation of a butanol-rich phase, and a total of 700 molecules were used for each simulation of an IL-rich phase (a single IL ion pair is considered to be one molecule). The initial configuration for each system was generated by randomly inserting first the cations, then the anions, and finally the butanol molecules into the simulation box. To prevent overlap, an insertion was rejected if any of the newly inserted atoms were within 0.75 Å of any existing atoms. The initial cell volume was chosen such that the probability of molecule overlap during the random insertion stage was small. The initial cell volumes corresponded to a starting density of 0.05 g/cm³ for each simulation. The initial configurations were relaxed using a conjugant-gradient energy minimization scheme followed by NPT MD until the density was equilibrated. All of the C-H and O-H bonds were held rigid using the SHAKE (8) algorithm. The r-RESPA (9) multiple time-stepping algorithm was used with a timestep of 2 fs for bonded and van der Waals interactions, and 4 fs for electrostatic interactions. The dispersion interactions were cut off beyond 15.0 Å. A switching function (10), initiated at a distance of 10.0 Å, was used to bring the dispersion interactions smoothly to zero at the cutoff distance. Electrostatic interactions were computed using the particle mesh Ewald method (11,12).

Table 1. Thermodynamic state points investigated in this work and experimental¹ UCSTs.

IL	T (K)	T _{UCST}	x_{IL} butanol-rich (mol %)	x_{IL} IL-rich (mol %)
[bmim][BF ₄]	330.0	335.5	3.1	42.3
[bmpy][BF ₄]	316.7	322.0	3.6	31.3
[bmim][TF ₂ N]	295.0	300.0	3.91	30.1
[bmpy][TF ₂ N]	298.0	303.0	3.61	25.9

Equilibration runs for each system were conducted for 600 ps (or 300,000 timesteps), after which production runs lasting 600 ps were started. The thermodynamic properties of the system (total energy, pressure, temperature, kinetic and potential energy contributions) and the atomic coordinates were saved to disk every 100 timesteps.

Results and Discussion

Densities

Table 2 shows the computed densities of the IL/butanol mixtures. We are unaware of any experimental densities for these mixtures. The predicted densities of the IL-rich phases of the mixtures with the [BF₄] anion are ~25% more dense than their corresponding butanol-rich phases, and the predicted densities of the IL-rich phases of the mixtures with the [Tf₂N] anion are ~35% more dense than their corresponding butanol-rich phases. Also, the mixtures with the [Tf₂N] anion are more dense than the mixtures with the [BF₄] anion. Lastly, it is observed that the [bmpy][BF₄] mixtures are more dense than the [bmim][BF₄] mixtures, but the IL-rich phase of the [bmim][Tf₂N] mixture is more dense than the IL-rich phase of the [bmpy][Tf₂N] mixture. In the butanol-rich phase, there is no significant difference in the computed densities.

Table 2. Predicted densities of the IL/butanol mixtures studied in this work.

IL	ρ butanol-rich (kg m ⁻³)	ρ IL-rich (kg m ⁻³)
[bmim][BF ₄]	768.2 ± 4.7	977.3 ± 4.0
[bmpy][BF ₄]	794.8 ± 4.5	989.9 ± 4.3
[bmim][Tf ₂ N]	858.1 ± 3.9	1170.2 ± 3.9
[bmpy][Tf ₂ N]	856.3 ± 3.9	1161.9 ± 4.2

Fluid Structure and Local Composition

To obtain a better understanding of how the ions interact with each other and with the alcohol in these mixtures, radial distribution functions (RDFs or $g(r)$) and local composition functions (13) were computed at each of the state points. To compute the local composition within a sphere of radius L , we first define the coordination number of site j with respect to site i as

$$N_{ji}(L) = 4\pi\rho_j \int_0^L g_{ji} r^2 dr, \quad (2)$$

and the self-coordination number for site i is given by replacing j with i in eq 2.

Sites i and j can represent molecules or specific atom sites on a molecule. For a given L , the local composition of site j around a central reference site of type i is given by

$$x_{ji}(L) = \frac{N_{ji}(L)}{\sum_k N_{ki}(L)} = \frac{\rho_j \int_0^L g_{ji} r^2 dr}{\sum_k \rho_k \left(\int_0^L g_{ki} r^2 dr \right)} \quad (3)$$

where the sum extends over all sites. In addition, we define a local association factor (10)

$$\alpha_{ji}(L) = \frac{x_{ji}(L)}{x_j}, \quad (4)$$

where x_j is the bulk mole fraction of species j in the mixture. Physically, the α_{ji} factors, which are functions of the local environment radius L , indicate deviations from random mixing. If $\alpha_{ji} = 1$, then there is no preferential association of sites or species of type j with i . In other words, there is random mixing of j about i . When $\alpha_{ji} < 1$, it indicates that there is a tendency for site i to associate with sites other than j (including self-association) relative to the random mixing case. On the other hand, when $\alpha_{ji} > 1$, it indicates that there is an attraction between unlike sites i and j relative to that which site i feels with itself or other sites. For all of the α_{ji} curves reported here, the integrals in eq 3 were computed numerically using the trapezoid rule.

Mixtures with the [BF₄] anion

Radial Distribution Functions

In the discussion that follows, we will use the symbol O^{Al} to indicate the oxygen atom of a butanol molecule, O to indicate any oxygen atom of a [Tf₂N] anion, N to indicate the nitrogen atom of a [Tf₂N] anion, B to indicate the boron atom of a [BF₄] anion, and H-C_# to indicate a particular hydrogen atom of either an imidazolium or pyridinium ring. The notation $g_{ji}(r)$ refers to the distribution of site i about a central site of type j . Site-site RDFs for the IL-rich phase of the [bmim][BF₄]/1-butanol and [bmpy][BF₄]/1-butanol mixtures are shown in Figures 2 – 5. Figure 2 indicates that the C₂ position on the [bmim] cation shows the strongest association with O^{Al} , while for the [bmpy] cation, O^{Al} associates most strongly with C₂ and C₆. Figure 3 shows that the first solvation shell peaks for the $B - O^{Al}$ pair in both ILs are higher than the corresponding peaks in Figure 2, indicating that the alcohol localizes more strongly with the [BF₄] anion than with either of the [bmim] or [bmpy] cations. It is also observed in Figure 3

that the $B - O^{Al}$ first peak for the [bmpy] mixture is slightly higher than that for the [bmim] mixture, suggesting that the anion-butanol interaction is more localized in the [bmpy] mixture than the [bmim] mixture.

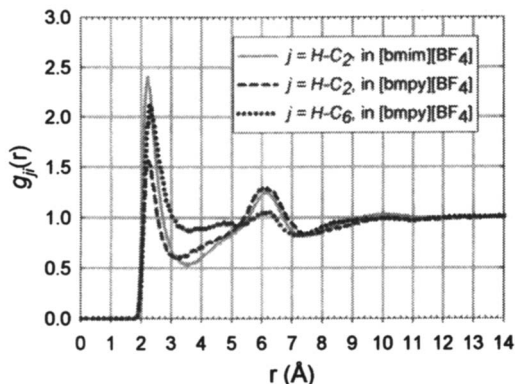


Figure 2. Atom-atom radial distribution functions for the $H-C_{\#} - O^{Al}$ atom pairs for the IL-rich phases of the [bmim][BF₄] and [bmpy][BF₄] mixtures with 1-butanol. For all the curves, site $i = O^{Al}$.

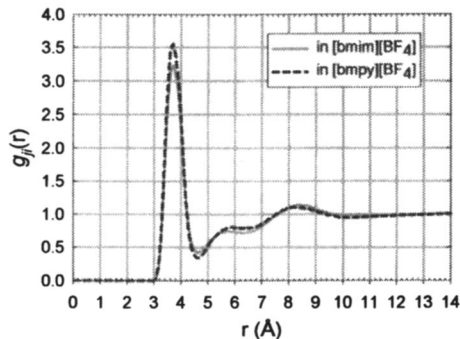


Figure 3. Atom-atom radial distribution functions for the $B - O^{Al}$ atom pairs for the IL-rich phases of the [bmim][BF₄] and [bmpy][BF₄] mixtures with 1-butanol.

Figure 4 shows the $H-C_{\#} - B$ RDFs for the IL-rich phases of the mixtures. The first peak for the $H-C_2 - B$ RDF in the [bmim] mixture is higher than that for the $H-C_6 - B$ in the [bmpy] mixture, and similar to that of the $H-C_2 - B$ in the [bmpy] mixture. In addition to interacting with the ions, butanol is able to self-

associate. Figure 5, shows that there is strong $O^{II} - O^{II}$ interaction for the IL-rich phases of the mixtures, and that the butanol self-association is slightly stronger in the [bmpy] mixture than the [bmim] mixture. These interactions are indicative of alcohol-alcohol hydrogen bonding. Similar behavior is observed in the butanol-rich phases of these mixtures. The information from the RDFs suggest the following hypothesis as to why the [bmpy][BF₄]/butanol mixture has a lower UCST than the [bmim][BF₄]/butanol mixture:

- Butanol interacts more strongly with [BF₄] than either cation.
- The cation/anion association is stronger for the [bmim][BF₄] mixture than for the [bmpy][BF₄] mixture.
- The weaker cation/anion association in [bmpy][BF₄] allows butanol to interact more strongly with the [BF₄] anion.
- The more favorable butanol/anion and butanol/butanol association in the [bmpy][BF₄] mixture explains why this mixture has the lower UCST.

While the structural information provided by RDFs can be used to assess the relative strength of various site-site interactions, the RDF is not always the best means of comparing interactions between two different mixtures and can even be misleading when comparing a particular site-site RDF between mixtures that vary significantly in composition. Although the difference in mixture compositions between similar phases of the [bmim][BF₄] and [bmpy][BF₄] mixtures (see Table 1) is small enough to make conclusions based upon comparisons between the site-site RDFs of the mixtures, we nevertheless seek to support these conclusions with information provided by local composition functions and system potential energies.

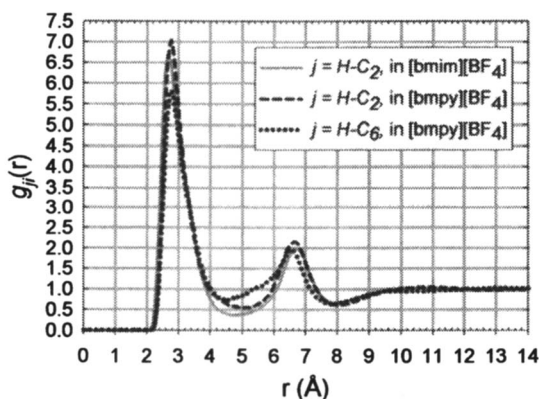


Figure 4. Atom-atom radial distribution functions for the H-C_# - B atom pairs for the IL-rich phases of the [bmim][BF₄] and [bmpy][BF₄] mixtures with 1-butanol. For all the curves, site *i* = B.

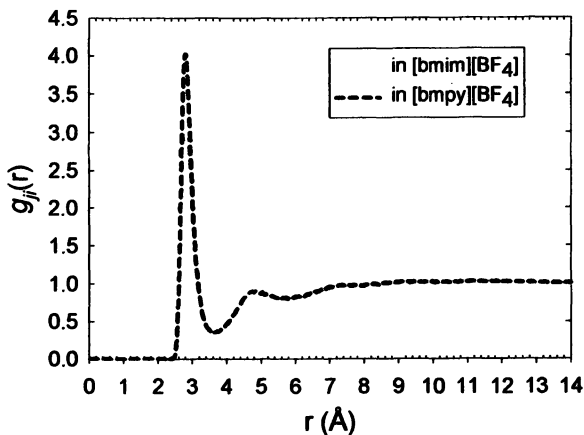


Figure 5. Atom-atom radial distribution functions for the $O^{Al} - O^{Al}$ atom pairs for the IL-rich phases of the $[bmim][BF_4]$ and $[bmpy][BF_4]$ mixtures with 1-butanol.

Local Composition Functions

As discussed above, the local association factor $\alpha_{ji}(r)$ can be used to assess the relative strength of site-site interactions between species with different compositions in a mixture because the dependence of the local composition $x_{ji}(r)$ upon the bulk mole fraction x_i is removed in eq 4. Thus, $\alpha_{ji}(r)$ can also be used to assess the relative strength of a particular site-site interaction between mixtures with different compositions.

Figure 6a shows the local association factors for the $B - O^{Al}$ atom pairs for the IL-rich phases of the mixtures. Recall that $\alpha_{B-O^{Al}}$ describes the local association of anion boron atoms about a central butanol oxygen atom, so Figure 6a figure describes solvation of the alcohol by the anion. It is observed that $\alpha_{B-O^{Al}} > 1$ at distances between ~ 3.6 and 6.7 Å, and that the association factor for the [bmpy] mixture is slightly higher than that of the [bmim] mixture. This shows that there is some solvation of the alcohol by the anion over $3.6 - 6.7$ Å, and that the butanol/anion association is slightly stronger in the [bmpy][BF_4] mixture than in [bmim][BF_4]. Figure 6b shows the association factors for the $H-C_{\#} - O^{Al}$ atom pairs. Interestingly, all three association factors in Figure 6b are > 1 at distances less than 3.8 Å, indicating that the alcohol is able to associate closely with the cation. Also, for the [bmpy] mixture, $\alpha_{HC_6-O^{Al}} > \alpha_{HC_2-O^{Al}}$ at distances up to 6.0 Å, indicating that the alcohol prefers to associate with the C_6 position of the pyridinium ring instead of the C_2 position. This is consistent with

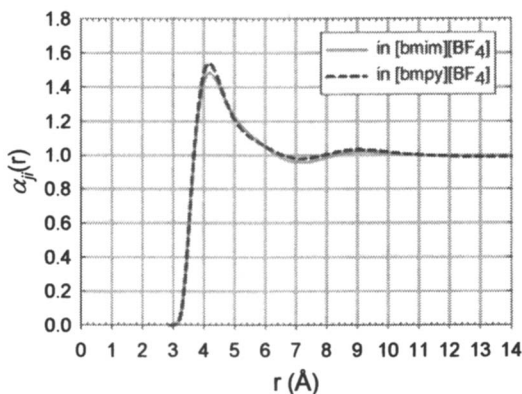


Figure 6a. Association factors for the $B - O^{Al}$ atom pairs for the IL-rich phases of the $[bmim][BF_4]$ and $[bmpy][BF_4]$ mixtures with 1-butanol.

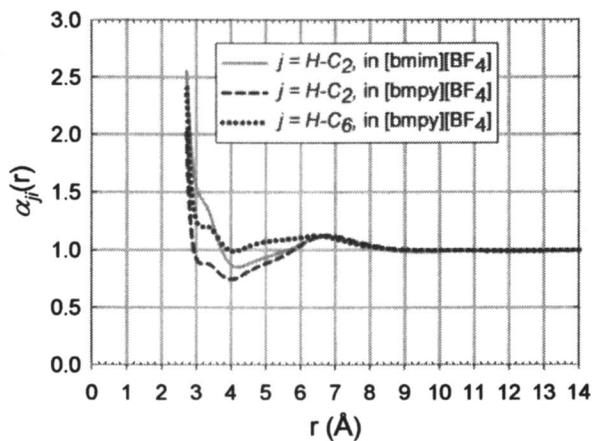


Figure 6b. Association factors for the $H-C_{\#} - O^{Al}$ atom pairs for the IL-rich phases of the $[bmim][BF_4]$ and $[bmpy][BF_4]$ mixtures with 1-butanol. For all the curves, site $i = O^{Al}$.

the RDFs of Figure 2, which show that there is a slight preference for the alcohol to associate with the C₆ position over the C₂ position.

Before moving on we wish to mention why the association factor plots in Figure 6b are not shown for distances less than 2.7 Å. This is because the association factors in Figure 6b become ill-behaved at distances less than 2.7 Å, and eventually become undefined as the distance r goes to zero. A closer look at eq 3 reveals why the association factors can become ill-behaved at short distances. At distances in which all the $g_{ji}(r)$ s in eq 3 are zero, the association factor is undefined (i.e. it is equal to zero divided by zero). As r is increased to the point in which one of the $g_{ji}(r)$ s in eq 3 becomes nonzero, the behavior of $\alpha_{ji}(r)$ will be determined by one of two cases: Case 1) The $g_{ji}(r)$ in the numerator remains zero while one or more $g_{ji}(r)$ s in the denominator are nonzero. This is the case in Figure 6a. By the time the numerator becomes nonzero, the denominator is considerably greater than zero and well-behaved, which leads to an association factor which begins at zero and rises up to a maximum and appears well-behaved at all distances for which it is defined. Case 2) The $g_{ji}(r)$ in the numerator becomes nonzero while all other $g_{ji}(r)$ terms in the denominator are zero. This is the case in Figure 6b. If the numerator's $g_{ji}(r)$ is the only nonzero term, then the association factor is equal to $1/x_i$ for all distances at which none of the other $g_{ji}(r)$ terms in the denominator are nonzero. As soon as a second $g_{ji}(r)$ term in the denominator becomes nonzero, the association factor will decrease from its maximum value of $1/x_i$. However, this decrease can be ill-behaved because the association factor will be very sensitive to any small fluctuations in this second $g_{ji}(r)$ term. These fluctuations typically arise due to high statistical uncertainties in the regions where this second $g_{ji}(r)$ term is very close to zero. The association factor will become better behaved as r approaches the first peak in the second nonzero $g_{ji}(r)$ term, and the statistical uncertainty in this term diminishes. In this work we have decided, somewhat arbitrarily, that we have confidence in a Case 2 association factor when the second nonzero $g_{ji}(r)$ term has reached one-half the maximum value of its first peak.

Lastly Figure 7a shows the center-of-mass $\alpha_{\text{BuOH}-\text{BF}_4}$, $\alpha_{\text{BuOH}-\text{bmim}}$ and $\alpha_{\text{BuOH}-\text{bmpy}}$ association factors for the IL-rich phases of the mixtures, and Figure 7b shows the same association factors for the butanol-rich phases of the mixtures. It is observed that all of these association factors are < 1 at all distances. Since these association factors describe the local association of butanol around a central cation or anion, this means that the individual ions *are not solvated by the butanol, even at a composition of ~4 mol% IL*. Instead, in both the IL-rich and alcohol-rich phases, the ions form into cation/anion pairs and it is these pairs which are solvated by butanol.

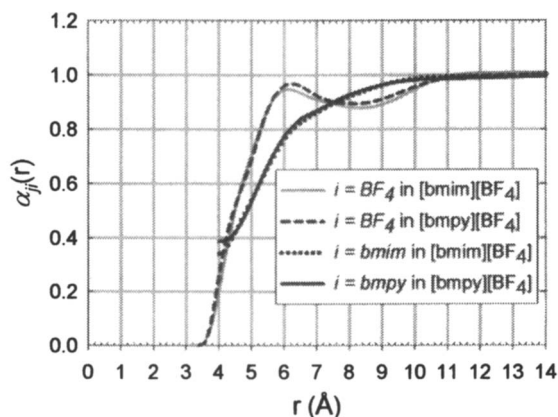


Figure 7a. Center-of-mass association factors for the BuOH- BF_4 , BuOH-*bmim*, and BuOH-*bmpy* pairs for the IL-rich phases of the $[bmim][BF_4]$ and $[bmpy][BF_4]$ mixtures with 1-butanol. For all the curves, site $j = BuOH$.

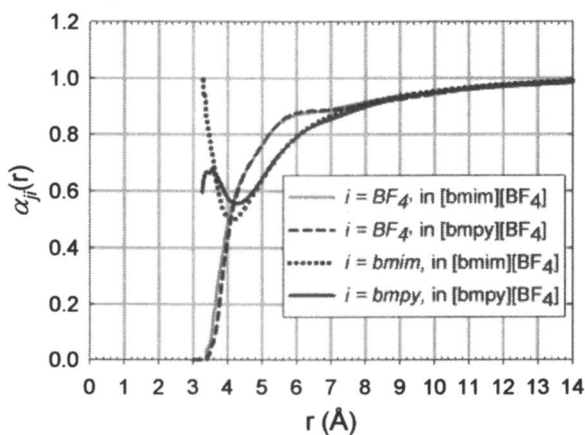


Figure 7b. Center-of-mass association factors for the BuOH- BF_4 , BuOH-*bmim*, and BuOH-*bmpy* pairs for the butanol-rich phases of the $[bmim][BF_4]$ and $[bmpy][BF_4]$ mixtures with 1-butanol. For all the curves, site $j = BuOH$.

Energetics

Further confirmation of our hypothesis can be gained from close examination of the potential energies of both mixtures. Table 3 shows the breakdown of the potential energies of the IL-rich phases into contributions from butanol-butanol, butanol-ion, and ion-ion interactions for [bmim][BF₄] and [bmpy][BF₄]. The energies in Table 3 are given on a per mol of butanol basis. The butanol-butanol interaction is 1.0 kcal / mol more favorable in the [bmpy] mixture than the [bmim] mixture. On the other hand, the ion-ion interactions are 12.7 kcal / mol more favorable in the [bmim] mixture, which confirms that the [bmim][BF₄] interaction is stronger than that of the [bmpy][BF₄] interaction. The butanol-ion interactions are only slightly (0.4 kcal / mol) more favorable in the [bmpy] mixture than in the [bmim] mixture, which is probably within the statistical uncertainty of the calculations. Altogether butanol experiences about 1.4 kcal / mol lower energy in the [bmpy][BF₄] mixture than in the [bmim][BF₄] mixture, consistent with the trend in UCST. Similar trends in the energies are observed for the alcohol-rich phase, and will not be discussed here.

Table 3. Comparison of the contribution of the butanol-butanol, butanol-ion, and ion-ion interactions to the system total potential energy for the IL-rich phases of the [bmim][BF₄] and [bmpy][BF₄] mixtures with 1-butanol.

Interaction	[bmim]	[bmpy]
	Energy (kcal / mol BuOH)	Energy (kcal / mol BuOH)
BuOH– BuOH	0.486	-0.514
BuOH – IL	-14.9	-15.3
IL – IL	-50.8	-38.1

Mixtures with the [Tf₂N] anion

Radial Distribution Functions

Site-site RDFs for the IL-rich phase of the [bmim][Tf₂N]/1-butanol and [bmpy][Tf₂N]/1-butanol mixtures are shown in Figures 8, 9 and 10. Figure 8 shows the $H-C_{\#} - O^{Al}$ RDFs, Figure 9 shows the $O - O^{Al}$ RDFs, and Figure 10 shows the $N - O^{Al}$ RDFs. The first solvation shell peaks for the $H-C_{\#} - O^{Al}$ pairs (Figure 8) in both ILs are higher than the corresponding peaks in Figures 9 and 10, indicating that the alcohol associates more strongly with the cation than with the [Tf₂N] anion. This is quite different from what was observed for the mixtures with the [BF₄] anion, in which the butanol/[BF₄] interaction was stronger than the butanol/cation interaction. In addition, the first peaks for the $O - O^{Al}$ atom pair are higher than the corresponding peaks for the $N - O^{Al}$ atom pair, even though the largest negative charge on the [Tf₂N] anion is located on the N atom. Finally, strong butanol self-association is observed in Figure 11, which shows the $O^{Al} - O^{Al}$ RDFs for the IL-rich phases of the mixtures. Similar behavior is observed in the butanol-rich phases of these mixtures, whose RDFs are not shown here. Lastly we note that the RDFs in Figures 9 – 11 show that the butanol self-interaction and the butanol-anion interaction are nearly independent of the type of cation present. To see any effect of the cation upon the relative strength of these interactions, we must examine the local composition functions.

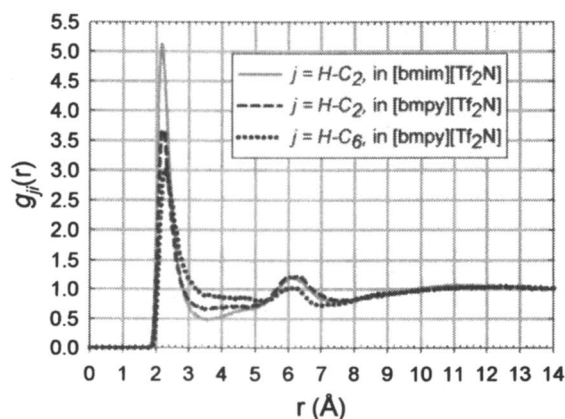


Figure 8. Atom-atom radial distribution functions for the $H-C_{\#} - O^{Al}$ atom pairs for the IL-rich phases of the [bmim][Tf₂N] and [bmpy][Tf₂N] mixtures with 1-butanol. For all the curves, site $i = O^{Al}$.

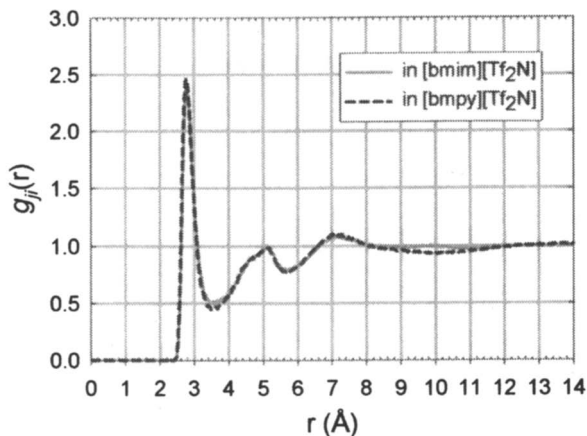


Figure 9. Atom-atom radial distribution functions for the $O^- - O^{Al}$ atom pairs for the IL-rich phases of the $[bmim][Tf_2N]$ and $[bmpy][Tf_2N]$ mixtures with 1-butanol.

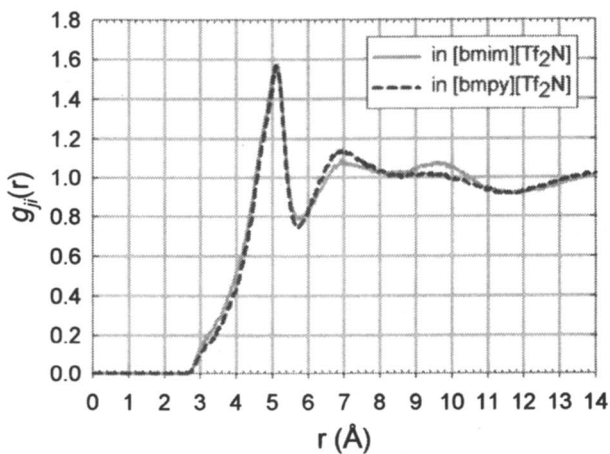


Figure 10. Atom-atom radial distribution functions for the $N - O^{Al}$ atom pairs for the IL-rich phases of the $[bmim][Tf_2N]$ and $[bmpy][Tf_2N]$ mixtures with 1-butanol.

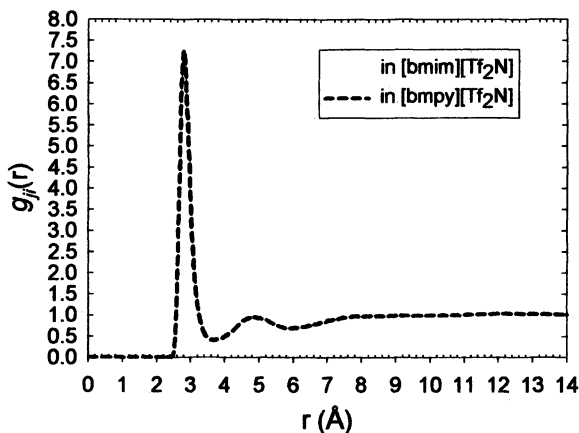


Figure 11. Atom-atom radial distribution functions for the $O^{II} - O^{II}$ atom pairs for the IL-rich phases of the [bmim][Tf₂N] and [bmpy][Tf₂N] mixtures with 1-butanol.

Local Composition Functions

Figure 12 shows the local association factors for the $O - O^{II}$ atom pairs for the IL-rich phases of the mixtures, and Figure 13 shows the association factors for the $H-C_{\#} - O^{II}$ atom pairs. It is observed that both $\alpha_{O-O^{II}}$ and $\alpha_{O^{II}-O}$ are less than one at distances less than 8 Å, and are approximately one beyond 8 Å. This further confirms that butanol is not preferentially associating with the anion as was the case for the mixtures with the [BF₄] anion. Figure 12 shows that the cation/butanol association factors $\alpha_{HC_2-O^{II}}$ for the [bmim] mixture and $\alpha_{HC_6-O^{II}}$ for the [bmpy] mixture are both > 1 at distances less than 2.9 Å, confirming that butanol is able to associate with the cation, and that in the [bmpy] mixture the alcohol prefers to associate with the C₆ position of the pyridinium ring instead of the C₂ position, as was the case for the [bmpy][BF₄] mixture. It is also observed, at distances less than 3.6 Å, that $\alpha_{HC_2-O^{II}}$ for the [bmim] mixture is slightly larger than the corresponding association factors for the [bmpy] mixture, indicating that butanol also associates with the [bmim] cation more strongly than it does with the [bmpy] cation.

Lastly, Figure 14a shows the center-of-mass association factors for the IL-

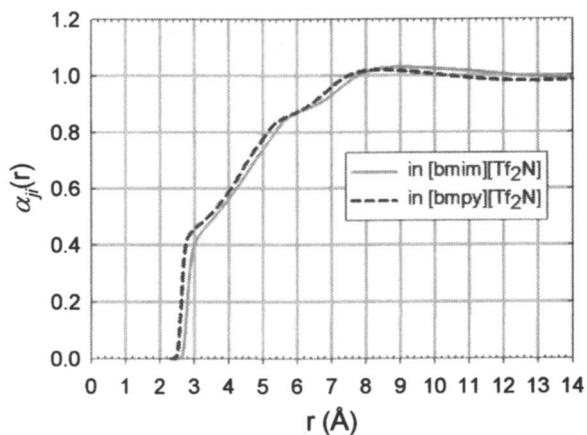


Figure 12. Association factors for the $O - O^{Al}$ atom pairs for the IL-rich phases of the $[bmim][Tf_2N]$ and $[bmpy][Tf_2N]$ mixtures with 1-butanol.

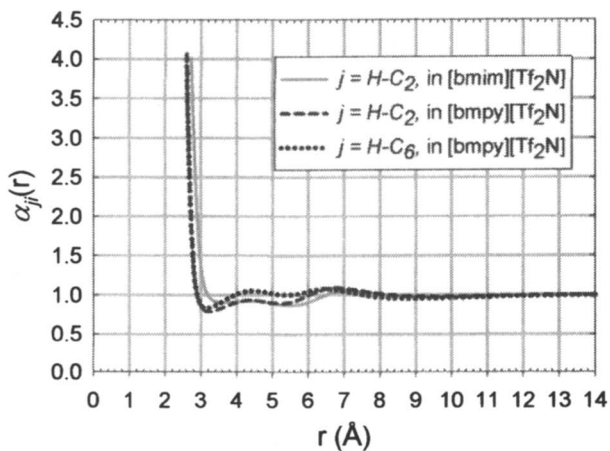


Figure 13. Association factors for the $H-C_{\#} - O^{Al}$ atom pairs for the IL-rich phases of the $[bmim][Tf_2N]$ and $[bmpy][Tf_2N]$ mixtures with 1-butanol. For all the curves, site $i = O^{Al}$.

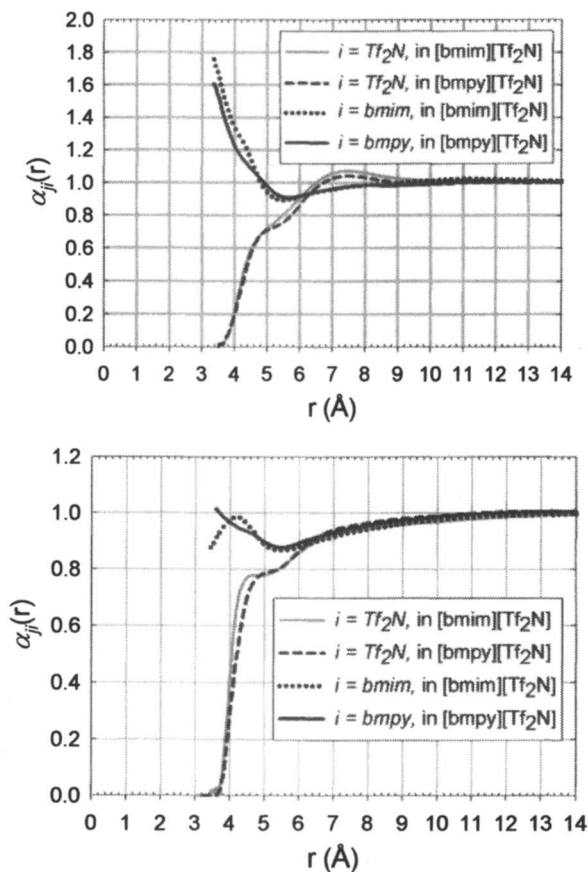


Figure 14. (a – top) Center-of-mass association factors for the BuOH- Tf_2N , BuOH-bmim, and BuOH-bmpy pairs for the IL-rich phases of the $[\text{bmim}][\text{Tf}_2\text{N}]$ and $[\text{bmpy}][\text{Tf}_2\text{N}]$ mixtures with 1-butanol. For all the curves, site $j = \text{BuOH}$; (b – bottom): Center-of-mass association factors for the BuOH- Tf_2N , BuOH-bmim, and BuOH-bmpy pairs for the butanol-rich phases of the $[\text{bmim}][\text{Tf}_2\text{N}]$ and $[\text{bmpy}][\text{Tf}_2\text{N}]$ mixtures with 1-butanol. For all the curves, site $j = \text{BuOH}$.

rich phases of the mixtures, and Figure 14b shows the same association factors for the butanol-rich phases of the mixtures. There is a qualitative difference between the association factors involving the cations and those involving the anions. For the anions, α_{ji} is small and only approaches 1 at approximately 6 Å or more. For the cations, α_{ji} is actually > 1 at short distances for the IL-rich phase (Figure 14a) and close to 1 for the butanol-rich phase (Figure 14b). This indicates that there is a preference for butanol to associate with the cation, which is qualitatively different from what was observed for the mixtures with the $[\text{BF}_4]$ anion. This difference stems from the fact that the negative charge on $[\text{Tf}_2\text{N}]$ is much more delocalized than on $[\text{BF}_4]$, thus enabling butanol to at least partially solvate the cation in the IL-rich phase. Figure 15 shows the center-of-mass $\alpha_{\text{BuOH}-\text{BuOH}}$ self association factor for the IL-rich phases of the mixtures. There is slightly greater tendency for butanol to self-associate in $[\text{bmim}][\text{Tf}_2\text{N}]$ than $[\text{bmpy}][\text{Tf}_2\text{N}]$.

The information from the RDFs and association factors suggest the following hypothesis as to why the $[\text{bmim}][\text{Tf}_2\text{N}]/\text{butanol}$ mixture has a lower UCST than the $[\text{bmpy}][\text{Tf}_2\text{N}]/\text{butanol}$ mixture:

- The alcohol interacts preferentially (aside from self-association) with the cation.
- The cation/butanol association is stronger for the $[\text{bmim}][\text{Tf}_2\text{N}]$ mixture than for the $[\text{bmpy}][\text{Tf}_2\text{N}]$ mixture because the butanol/ $[\text{bmim}]$ interaction at the C_2 position is stronger than the butanol/ $[\text{bmpy}]$ interactions at either the C_2 or C_6 positions.
- The more favorable butanol/cation and butanol/butanol association in the $[\text{bmim}][\text{Tf}_2\text{N}]$ mixture explains why this mixture has the lower UCST.

Energetics

Table 4 shows the breakdown of the potential energies of the IL-rich phases into contributions from butanol-butanol, butanol-ion, and ion-ion interactions on a per mol butanol basis. The butanol-ion interactions are 1.34 kcal / mol-butanol more favorable in the $[\text{bmim}]$ mixture than the $[\text{bmpy}]$ mixture, which confirms the structural observations that the cation/butanol interaction is stronger in the $[\text{bmim}]$ mixture. On the other hand, the butanol-butanol interaction is 0.35 kcal / mol more favorable in the $[\text{bmpy}]$ mixture than the $[\text{bmim}]$ mixture and the ion-ion interactions are 0.5 kcal / mol more favorable in the $[\text{bmpy}]$ mixture. Overall, butanol has ~ 1.0 kcal / mol more favorable interactions with $[\text{bmim}][\text{Tf}_2\text{N}]$ than $[\text{bmpy}][\text{Tf}_2\text{N}]$ due to the favorable cation/butanol energetics. This is in contrast to the case when $[\text{BF}_4]$ was the anion, and explains why for this system the UCST is lower for $[\text{bmim}][\text{Tf}_2\text{N}]$ than $[\text{bmpy}][\text{Tf}_2\text{N}]$. These differences are driven by the fact that the more localized charge on $[\text{BF}_4]$ makes

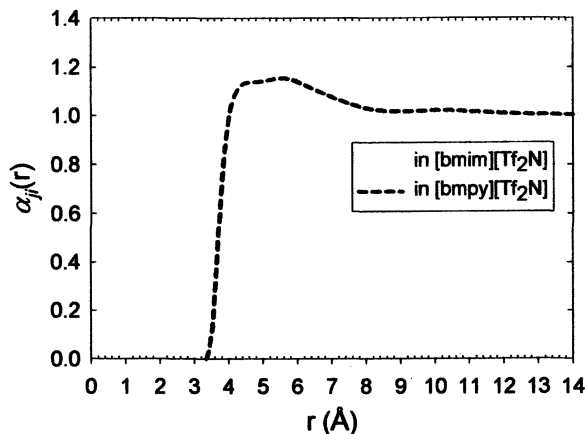


Figure 15. Center-of-mass association *BuOH-BuOH* self association factors for the IL-rich phases of the [bmim][Tf₂N] and [bmpy][Tf₂N] mixtures with 1-butanol.

the cation/anion interactions very favorable, thus inhibiting association between the alcohol and the IL. This is why the UCST is higher for each IL with a [BF₄] anion than for the [Tf₂N] ILs. On the other hand, the more delocalized charge on [Tf₂N] weakens the cation/anion interactions, enabling the alcohol to interact more directly with the ions. In this case, the butanol interacts most strongly with the localized charge on [bmim]. This tends to lower its UCST relative to [bmpy][Tf₂N].

Diffusion

The self-diffusion coefficient for a fluid can be calculated using the Einstein relation¹⁴

$$D_s = \frac{1}{6} \lim_{t \rightarrow \infty} \frac{d}{dt} \left\langle |\mathbf{r}_i(t) - \mathbf{r}_i(0)|^2 \right\rangle, \quad (6)$$

where the quantity in braces is the ensemble-averaged mean-square displacement (MSD) of the molecules and \mathbf{r}_i is the vector coordinate of the center of mass of molecule i . The computed self-diffusivities of the cation, anion, and butanol for each of the mixtures studied are listed in Table 5. For the butanol rich phase of the [bmim][BF₄] mixture, the cation self-diffusion coefficient is slightly larger than that of the anion, but for the other three mixtures with the [BF₄] anion, the anion self-diffusion coefficient is larger. For all the mixtures with the [BF₄]

Table 4. Comparison of the contribution of the butanol-butanol, butanol-ion, and ion-ion interactions to the system total potential energy for the IL-rich phases of the [bmim][Tf₂N] and [bmpy][Tf₂N] mixtures with 1-butanol.

Interaction	[bmim]	[bmpy]
	Energy (kcal / mol BuOH)	Energy (kcal / mol BuOH)
BuOH– BuOH	-1.21	-1.56
BuOH – IL	-15.12	-13.78
IL – IL	-5.8	-6.2

anion, the self-diffusion coefficient of butanol is anywhere from 2 to 4 times larger than the self diffusion coefficient of the anion. The self-diffusion coefficients of all species in the butanol-rich phases are 3-5 times larger than their corresponding values in the IL-rich phase. The self-diffusion coefficients of all species in the mixtures with the [bmpy] cation are lower than the corresponding values for mixtures with the [bmim] cation. For comparison, the self-diffusion coefficients of pure [bmim][BF₄] at 298K reported by de Andrade *et al.* (5) are 1.2×10^{-11} m²/s for [bmim] and 1.0×10^{-11} m²/s for [BF₄]. However, recent studies (4,15) suggest that computed self-diffusivities for pure ILs are highly dependent upon the length of the simulation, and previous results should be carefully scrutinized.

For mixtures with the [Tf₂N] anion, the cation has a slightly larger self-diffusion coefficient than the anion with the exception of the butanol-rich phase of the [bmim][Tf₂N] mixture, and the self-diffusion coefficient of butanol is anywhere from 2 to 3 times larger than the self-diffusion coefficient of the anion. The self-diffusion coefficients of all species in the butanol-rich phases are 2-3 times larger than their corresponding values in the IL-rich phase. Lastly, the self-diffusion coefficients of all species in the mixtures with the [bmim] cation are lower than the corresponding values for mixtures with the [bmpy] cation, which is the opposite of what was observed for the mixtures with the [BF₄]

Table 5. Self-diffusion coefficients of the cation, anion, and 1-butanol for each mixture studied.

IL	$D_+ \times 10^{11}$ ($m^2 \text{ sec}^{-1}$)		$D_- \times 10^{11}$ ($m^2 \text{ sec}^{-1}$)		$D_{BuOH} \times 10^{11}$ ($m^2 \text{ sec}^{-1}$)	
	butanol rich	IL rich	butanol rich	IL rich	butanol rich	IL rich
[bmim][BF ₄]	19.2	4.21	18.1	4.5 2	48.8	16.4
[bmpy][BF ₄]	13.4	2.90	14.6	3.1 4	32.7	11.8
[bmim][Tf ₂ N]	6.83	2.60	8.02	2.3 5	18.4	6.44
[bmpy][Tf ₂ N]	8.32	3.15	8.28	3.0 0	19.5	8.01

anion. The trend in self-diffusivities generally follows the trend in densities, with the highest density systems exhibiting the lowest self-diffusivities.

Conclusions

Results of molecular dynamics simulations of mixtures of 1-butanol with the ILs [bmim][BF₄], [bmpy][BF₄], [bmim][Tf₂N], and [bmpy][Tf₂N] are reported. Previously developed all-atom force fields are used for the ions and the OPLS all-atom model is used for butanol. Liquid structure is reported in the form of site-site radial distribution functions as well as association factors. It is observed that the individual cations and anions are not generally solvated by the butanol, even at a concentration of ~4 mol% IL. Rather, the ions exist as solvated ion pairs. The exceptions to this are the IL-rich phases of the [bmim][Tf₂N] and [bmpy][Tf₂N] mixtures, which showed partial solvation of the cation by butanol. The MD results show that [bmpy][BF₄] has a lower UCST with 1-butanol than [bmim][BF₄] because the alcohol interacts more strongly with the anions in the

presence of the [bmpy] cation. This is due to weaker cation/anion association in the [bmpy] mixture, which in turn allows stronger alcohol/anion and alcohol/cation association. The MD results also show that [bmim][Tf₂N] has a lower UCST with 1-butanol than [bmpy][Tf₂N] because the delocalized charge on [Tf₂N] enables butanol to interact more directly with the cations. The butanol thus favors the localized charge on [bmim] which lowers its UCST relative to [bmpy][Tf₂N].

Acknowledgements

Support for this work was provided by the Indiana 21st Century Fund.

References

1. J. Crosthwaite, PhD thesis, University of Notre Dame (2005).
2. MacKerell, A.D.; Bashford, D.; Bellott, M.; Dunbrack, R.L.; Evanseck, J.D.; Field, M.J.; Fisher, S.; Gao, J.; Guo, H.; Ha, S.; Joseph-McCarthy, S.; Kuchnir, L.; Kuczera, K.; Lau, F.T.K.; Mattos, C.; Michnick, S.; Ngo, T.; Nguyen, D.T.; Prodhom, B.; Reiher III, W.E.; Roux, B.; Schlenkrich, M.; Smith, J.C.; Stote, R.; Straub, J.; Watanabe, M.; Wiorkiewicz-Kuczera, J.; Yin, D; Karplus, M. *J. Phys. Chem. B*, **1998**, *102*, 3586.
3. W.L. Jorgensen, D.S. Maxwell, and J. Tirado-Rives, *J. Am. Chem. Soc.*, **1996**, *118*, 11225.
4. C. Cadena, Q.Zhao, R.Q. Snurr, and E.J. Maginn, *J. Physical Chemistry B.*, **2006**, *110*, 2821-2832.
5. J. de Andrade, E.S. Boes, and H. Stassen, *J. Phys. Chem. B*, **2002**, *106*, 13344.
6. A.A.H. Padua, *J. Phys. Chem. B*, **2004**, *108*, 16893.
7. Kale, L.; Skeel, R.; Bhandarkar, M.; Brunner, R.; Gursoy, A.; Krawetz, N.; Phillips, J.; Shinozaki, A.; Varadarajan, K.; Schulten, K.; *J. Comp. Phys.*, **1999**, *151*, 283.
8. Ryckaert, J.P.; Ciccotti, G.; Berendsen, H.J.C.; *J. Comp. Phys.*, **1977**, *23*, 327.
9. Tuckerman, M.; Berne, B.J.; Martyna, G.J.; *J. Chem. Phys.*, **1992**, *97*, 1990.
10. Morrow, T.I., and E.J. Maginn, *Fluid Phase Equilibria* **2004**, *217*, 97.
11. Darden, T.A.; York, D.M.; Pedersen, L.G.; *J. Chem. Phys.*, **1993**, *98*, 10089.
12. Essmann, U.; Perera, L.; Berkowitz, M.L.; Darden, T.; Lee, H.; Pedersen, L.G.; *J. Chem. Phys.*, **1995**, *103*, 8577.

13. R.L. Rowley, *Statistical Mechanics for Thermophysical Property Calculations*, Prentice-Hall, New York, **1994**.
14. D. Frenkel, B. Smit, *Understanding Molecular Simulation*, Academic Press, New York, **1996**.
15. Del Popolo, M.G.; Voth, G.A.; *J. Phys. Chem. B*, **2004**, *108*, 1744.

Applications

Chapter 9

Carbonylation in Ionic Liquids Using Vapor-Takeoff Reactors

Gerald C. Tustin, Regina M. Moncier, and Joseph R. Zoeller

Eastman Chemical Company, P.O. Box 1972, Kingsport, TN 37662

Ionic liquids allow the carbonylation of lower molecular weight alcohols and esters be operated in a continuous vapor takeoff mode resulting in higher reaction rates, with fewer units of operation, and negligible catalyst loss. For example, when the Rh catalyzed carbonylation of methanol to acetic acid is conducted in an ionic liquid, the process can be operated in a continuous vapor a take-off mode of operation, while still demonstrating improved reactor production rates (approaching 25 mol/L-h) and high methanol conversion (up to 100%) and no Rh loss.

Worldwide demand for acetic acid exceeds 6.9 million metric tons per year (2). The majority of acetic acid consumed in the world is made by the carbonylation of methanol, a process which has been extensively reviewed (3), and commercially the best systems employ a catalyst system composed of methyl iodide and a combination of either rhodium and lithium (4) or iridium and ruthenium (5). For an industrial process, the process operates under modest pressure (450-500 psig, 30-35 atm.) and temperature (175-195°C) while demonstrating very high conversions (99-100% methanol conversion) and selectivities (99-100% based on methanol, ca. 97% on CO), and excellent rates (>10 mol/l-h and possibly higher with specialized equipment.)

While these processes are well established and superior to any prior process, there are some key issues still faced by anyone commercially practicing this technology. Specifically, key issues are:

- *Product/Catalyst Separation.* Currently, the product is flashed from the catalyst by transferring to a separation unit and releasing the pressure. The flash is normally conducted adiabatically, or at best with only a moderate amount of heat addition, to avoid catalyst precipitation. This requires a separate unit of operation, only allows partial product removal per pass (implying extensive recycle streams), and represents a bottleneck in the process.
- *Heat Removal.* The reaction is highly exothermic ($\Delta H_{298^\circ\text{C}} = \text{ca. } -28.8 \text{ kcal/mol}$). Whereas much of the heat is removed in the adiabatic flash in the current operation, the reaction is subject to rapid exotherms and the high heat of reaction has hampered the development of vapor phase processes where heat removal is difficult.
- *Water Removal.* Most commercial processes use 4-5% water, but water is difficult and expensive to remove from the product, reduces the depth of flash in the adiabatic operation, and leads to CO yield losses as the CO is converted to CO₂ and hydrogen by water gas shift.

Similar problems, especially catalyst separation and heat removal, are encountered in related carbonylations such as the commercially practiced carbonylation of methyl acetate to acetic anhydride (3) and the potentially useful carbonylation of ethanol to propionic acid. A process that could circumvent some or all of these issues would be very useful in commercial practice.

While normally one would address the issue of product/catalyst separation using heterogeneous catalysts, the application of heterogeneous catalysts has been hampered by leaching when operated in the liquid phase. When operating in the vapor phase where leaching is reduced, one encounters either poor catalyst activity or difficulties with heat removal when active catalysts are found (6). While several methods around this problem have been under active examination in our laboratories (1,6,7), we have found that ionic liquids can play a particularly useful role since they permit the development of a useful vapor take-off reactor, which effectively resolves the issues of catalyst/product separation and heat removal while offering rate and cost advantages.

Development of Vapor Take-off Reactors with Ionic Liquids

Vapor take-off reactors, which combine the reaction and separation steps into the same vessel by distilling the product continuously from the reaction medium, are common in industrial practice. When operating vapor take-off reactors one needs a high boiling, non-reactive solvent or starting material and operating conditions are constrained to temperature and pressure regimes where the product can be distilled or entrained from the reactor. The first and obvious advantage is that there is a capital savings when the reaction and separation are

combined into a single unit of operation. However, there are further potential advantages.

In cases where a catalyst is unstable outside the reaction environment or where leaching may be an issue, vapor take-off reactors can be useful in maintaining the catalyst. In the specific case of methanol carbonylation, catalyst decomposition and precipitation occurs during separation as the catalyst is heated in the absence of stabilizing CO and iodide. However in a vapor take-off reactor the Rh catalyst is always in the presence of stabilizing carbon monoxide and iodide. Additionally, since heat transport in liquids is more efficient, when compared to heterogeneous catalysts employing vapor-solid reactions, it is possible to operate vapor take-off reactor at faster rates without losing temperature control.

Since ionic liquids are non-volatile, normally thermally stable, normally chemically inert, and effective heat transfer fluids they should represent ideal vapor take-off solvents regardless of the application. However, iodide based ionic liquids, which are easily generated by simple alkylation of the parent phosphine or amine with an alkyl iodide, were found to be especially suitable for the carbonylation of methanol with rhodium catalysts. When used in methanol carbonylation, the rhodium catalysts were not only very soluble in ionic liquids, but were stabilized by the iodide in the ionic liquid. The continued presence of CO in vapor take-off reactors and inherent higher catalyst stability in ionic liquids eliminated both catalyst precipitation and any Rh volatilization. This allowed operation at higher Rh concentrations (and therefore higher rates) than are achievable in the commercial liquid phase reactors without catalyst losses. Further, Rh was inherently more reactive in iodide based ionic liquids. When compared in batch reactions, Rh catalysts were found to be ca. 1.5X more active in iodide based ionic liquids than they are in conventional operations which use acetic acid solutions of rhodium and lithium. The only potential downfall was the virtual insolubility of CO in most ionic liquids.

In testing vapor take-off reactors, most of the initial work was conducted in a microreactor which consisted of an unstirred, gas stripped reactor which is visually depicted in Figure 1, but which is described in detail in the experimental section and in earlier work (1). This represents a classic design for vapor take-off reactors and agitation is accomplished in these units by the combination of gas addition and the boiling liquid. In practice, upon the introduction of reactants the liquid swelled to ca. 2X its original volume as starting material and products became dissolved in the ionic liquid. Figure 2 depicts the results of an extended run with 1-butyl-3-methyl-dimethylimidazolium iodide (BMIMI). As shown, the catalyst was stable over an extended period of time while operating at high conversion, at high selectivity, and at rates comparable to, or better than, currently operated in commercial processes.

While the primary focus was on rhodium catalyzed methanol carbonylation, the unstirred vapor take-off reactor was used to demonstrate the usefulness of vapor takeoff reactors in several additional carbonylation reactions, such as the

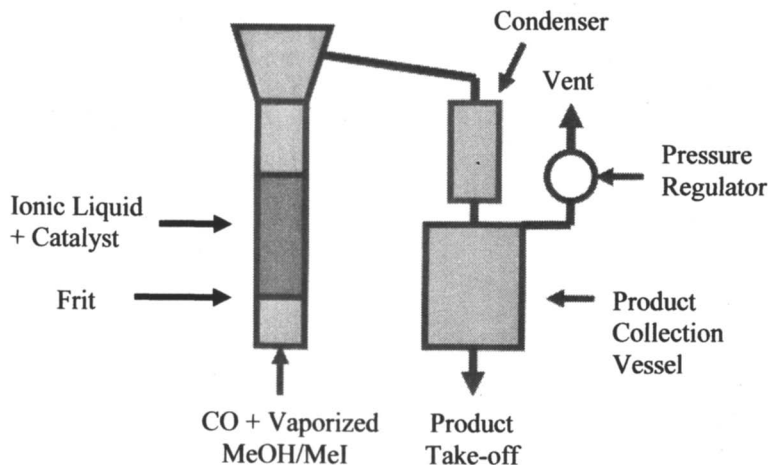


Figure 1. Diagram of Unstirred, Vapor Take-off Reactor.

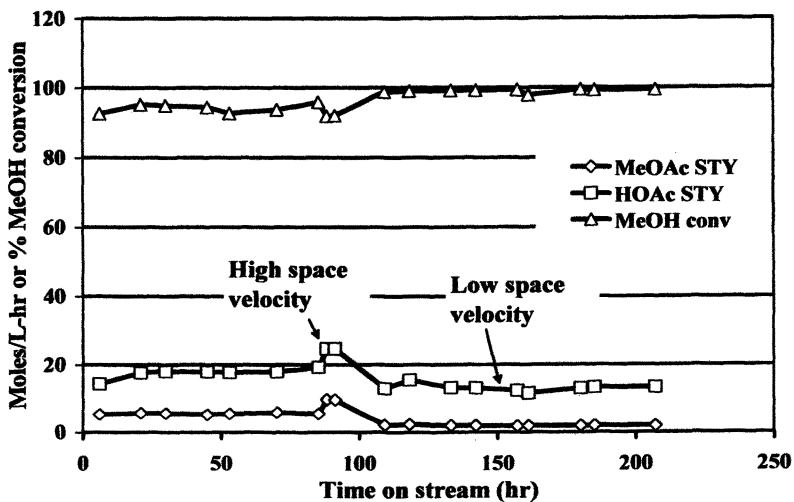


Figure 2. Continuous Vapor Take-Off Carbonylation of Methanol with MeI using BMIMI ionic liquid. (Conditions: Feed: 2.8:1:0.14 CO:MeOH:MeI; Catalyst: 0.32 mmol Rh in 10 mL BMIMI; 190°C, 200 psig; Space Velocity: Varied: 153, 302, 455 h⁻¹) (Reproduced from reference 1 with permission of author.)

carbonylation of methyl acetate to acetic anhydride and ethanol to propionate derivatives. (See Table I. All tests were performed with the same molar catalyst levels and volume (10 mL) as our Rh runs.) In addition, several additional methanol catalysts were demonstrated including Pd and Ir-Ru systems. (See Table I.) The palladium example is noteworthy in that, while Pd is normally a poor methanol carbonylation catalyst, it has been shown that Pd can operate in the presence of a large excess of iodide ions (8), a situation very consistent with an ionic liquid media. When examined in the vapor take-off mode where Pd is maintained in a very large excess of iodide, the methanol carbonylation with Pd catalysts, while not as fast as those with Rh, was surprisingly facile and could be operated for long periods of time with no noticeable deactivation.

Regarding the Ir catalyst and its design, it has been well established that excess iodide inhibits the Ir-Ru catalyst system (5). To bind the excess iodide, the ionic liquid was formed from a mixture of butyltridodecylphosphonium iodide (BTDPI) and zinc iodide to form butyltridoceylphosphonium triiodozincate as the ionic liquid. (The choice of the butyltridoceylphosphonium cation was based on the solubility of the resultant triiodozincate.) This led to an effective catalyst for the carbonylation of methanol with Ir-Ru based catalysts.

Table I. Results of carbonylation with other substrates and catalysts in the unstirred vapor phase reactor.

<i>Feed</i>	<i>Catalyst</i>	<i>Ionic Liquid</i>	<i>Conversion (based on)</i>	<i>Product 1 (Rate)</i>	<i>Product 2 (Rate)</i>
EtOH	Rh	BMIMI	66% (EtOH)	EtCO ₂ H (1.2 mol/L-h)	EtCO ₂ Et (1.3 mol/L-h)
Methyl Acetate	Rh	BMIMI	21% (MeOAc)	Ac ₂ O (1.4 mol/L-h)	-
MeOH	Pd	BMIMI	59% (MeOH)	AcOH (2.4 mol/L-h)	MeOAc (3.6 mol/L-h)
MeOH	Ru-Ir-Li (5:1:1)	BTDPI + 2 ZnI ₂	92% (MeOH)	AcOH (4 mol/L-h)	MeOAc (5 mol/L-h)
MeOH	Co	BMIMI	35% (MeOH)	AcOH (0.03 mol/L-h)	MeOAc (0.09 mol/L-h)
MeOH	Ni/ [MePPh ₃] ⁺ iodide	BMIMI	21% (MeOH)	AcOH (0.02 mol/L-h)	MeOAc (0.09 mol/L-h)

Nickel and cobalt are also known to be active catalysts for the homogeneous carbonylation of methanol, although they normally are less active than Rh or Ir and normally operate at high pressure (3). While they showed some marginal activity in the vapor take-off reactor, the activity was still very low. It is apparent that high iodide environments can not substitute for high CO pressures normally associated with Ni or Co catalysts.

Several additional ionic liquids were tested using Rh based catalysts in the unstirred vapor take-off reactor. Each of the ionic liquids tested demonstrated differing rates and different optimal operating conditions. Some exemplary results are shown in Table II, however the variable performance of these differing ionic liquids exposed an inherent difficulty in using ionic liquids for carbonylation. When performing carbonylations in ionic liquids, the viscosity is normally high and the carbon monoxide solubility very low. Further, both properties can vary significantly with the nature of the ionic liquid. The combination of high viscosity and low solubility often leads to mass transfer problems when conducting gas-liquid biphasic catalytic process. In the unstirred vapor take-off reactor, this represented a potentially serious limitation.

To test for mass transfer effects, an alternative reactor design was employed in which a standard stirred 300 mL autoclave was fitted with a vapor take-off outlet connected to a high pressure condenser and a collection vessel. (This represented a 10X scale up in reactor volume. None of the concentrations were changed.) Normally in homogeneous catalysis, if mass transfer is an issue one will see a rate effect with increasing stirring speed. As can be seen in Figure 3, which depicts the rate as a function of stirrer speed, there was a significant effect based on stirrer speed which implies a significant mass transfer barrier. At high stirrer speeds, the relative rates in the differing ionic liquids changed and

Table II. Summary of best behavior for several ionic liquids in unstirred vapor take-off reactor.

	<i>Ionic Liquid</i>		
	<i>BMIMI</i>	<i>BTDPI</i>	<i>MTBPI</i>
<i>Temp, °C</i>	180	210	220
<i>Pressure, psig</i>	210	210	210
<i>Rate (Mol HOAc/L-h)</i>	24.6	9.8	7.9
<i>% MeOH Conv.</i>	93.6	97.9	100
<i>% CO Conv.</i>	29	77	41
<i>HOAc/MeOAc</i>	2.5	3.0	38
<i>Wt % H2O</i>	7.4	5.3	0.58

MTBPI = methyltributylphosphonium iodide

eventually reached a plateau. The final rate order (MTBPI>BMIMI>BTDPI) is inversely related to the melt viscosities (MTBPI = 23-38 cp; BMIMI = 36-45 cp; BTDPI = 50-54 cp) for the three ionic liquids which further supports the importance of mass transfer in these reactions since higher viscosities result in lower diffusion rates and reduced mass transfer rates.

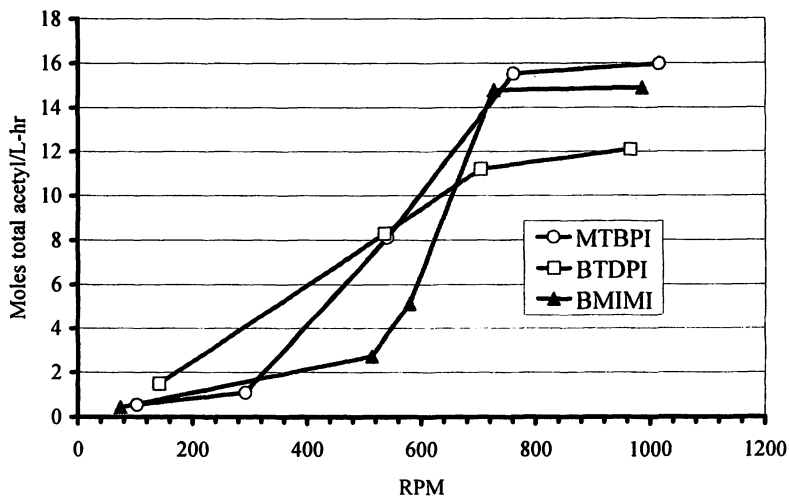


Figure 3. Reaction rate as a function of stirrer speed. (Reproduced from reference 1 with permission of author.)

In commercial operation, the most desirable reactions would have very high (>99%) methanol conversion, high rates, high AcOH/MeOAc ratios, and low water content. In Table III, results are shown for three ionic liquids operated at the high methanol conversions which would be required for useful operation. The highest rate process was obtained with MTBPI (methyltributylphosphonium iodide) and when optimized for the key variables, the Rh/MTBPI systems displayed rates of 17 mol/L-h at 100% methanol conversion and provided a product which had an AcOH/MeOAc ratio of 18 with only 1.1 wt.% water present in the effluent when operated at 225-230°C and 225 psig. The combination of low water content and high AcOH/MeOAc ratio translates into a simpler, lower cost product separation than conventional processes since there is less material to be recycled to the reactors.

The ionic liquids tested in this study demonstrated stable operation over the >300 hours of reaction time examined in the course of this study. NMR examination of the recovered solutions using the preferred MTBPI ionic liquid indicated that there was no detectable exchange of alkyl groups (monitored up to

Table III. Rh catalyzed reactions in stirred vapor takeoff reactor.

	<i>Ionic Liquid</i>		
	<i>BMIMI</i>	<i>BT DPI</i>	<i>MTBPI</i>
<i>Temp, °C</i>	190	220	230
<i>Pressure, psig</i>	135	225	225
<i>Rate (Mol HOAc/L-h)</i>	12.5	9.7	18.9
<i>% MeOH Conv.</i>	99.9	99.8	99.3
<i>% CO Conv^a.</i>	75	74	75
<i>Liquid Recycle</i>	Large	small	medium
<i>HOAc/MeOAc</i>	4.8	16.6	6.5
<i>Product Wt % H₂O</i>	3.4	1.2	3.0
<i>Product wt % Me^b</i>	17	16	17
<i>Product wt % MeOAc^b</i>	16	6	13
<i>Product Wt% AcOH^b</i>	64	74	68

NOTE: (a) CO:MeOH 1.33:1; (b) Wt % values are raw GC data for condensed liquid product; BMIMI operated near dew point.

200 hrs.) Further, when stripped of any reaction products (evacuation at 90°C, <2 mm Hg) the Rh remained completely in solution, although under these conditions infrared indicated that the Rh was completely in the form of Rh(CO)₅²⁻. The BMIMI ionic liquid was not as stable and small amounts of 1,3-dimethylimidazolium iodide could be detected indicating a small amount of alkyl exchange wherein the butyl group had been replaced with a methyl group, but there was no accompanying change in rate.

Conclusions

Ionic liquids can serve as very effective solvents in vapor take-off reactors for the carbonylation of methanol to acetic acid. In the case of rhodium catalyzed methanol carbonylation, methanol carbonylation to acetic acid has been shown to be operable at high rates (17 mol/L-h acetic acid) and high conversions (>99% methanol conversion) with:

- (1) no catalyst loss or deactivation over 300 hrs of operation,
- (2) no ionic liquid decomposition over 300 hours of operation,
- (3) and a purer reactor effluent (<2 wt% water; AcOH/MeOAc ratio = 18) than in conventional processes.

The key factor in obtaining high rates is achieving adequate mass transfer. Due to the combination of fewer units of operation, high rates, and advantaged

reactor effluent compositions, the ionic liquid based vapor take-off reactors may have significant advantages in the production of acetic acid. The process is applicable to other substrates and conversions as has been demonstrated for ethanol carbonylation to propionic acid and methyl acetate carbonylation to acetic anhydride.

Experimental

Materials

Rhodium trichloride hydrate was provided by Johnson Matthey. Iridium trichloride hydrate was provided by Strem Chemicals. Palladium acetate was obtained from Aldrich. Butyltridodecylphosphonium iodide (BTDPI) was obtained from Cytec. 1-butyl-3-methylimidazolium iodide (BMIMI) was synthesized by the following procedure. 1-butylimidazole (400 g, 3.22 moles) was dissolved in tetrahydrofuran (400 mL) in a 3-liter flask equipped with a magnetic stir bar, reflux condenser and a pressure-equilibrated dropping funnel with a nitrogen inlet. Methyl iodide (570 g, 4.0 moles) was added from the addition funnel with stirring under nitrogen over seven hours at ambient temperature. The mixture was stirred for 2 hours at room temperature then refluxed overnight. The solvent and excess methyl iodide were then removed by distillation on a steam bath to provide BMIMI as a red-brown oil (870.7g). Methyltributylphosphonium iodide (MTBPI) was synthesized in an analogous fashion from tributylphosphine and methyl iodide. Methanol (MeOH) and methyl iodide (MeI) were reagent grade and were used without further purification.

Carbonylation reactions

The carbonylation procedure has been described in detail in the patent literature.^{1b} A brief but sufficient description will be provided here. The basic reaction system consisted of Brooks 5850 Series E mass flow controllers for gas delivery and an Alltech 301 HPLC pump for liquid feed delivery. The gas and liquid streams were fed to an electrically heated Hastelloy C vaporizer. The vaporized reactants were fed to an electrically heated Hastelloy C reactor containing the ionic liquid and catalyst, and the vapor product directed to a Hastelloy C condenser and product receiver. Pressure was maintained using a Tescom Model 44-2300 backpressure regulator. Heating and gas flow feeds were controlled by a Camile® 3300 Process Monitoring and Control System. Most of the reactions were performed in an unstirred reactor consisting of a 1.60

cm I.D. X 15.9 cm long Hastelloy C reaction tube fitted with a 5 micron Hastelloy C filter at the base which acted as a gas dispersion device and support for the ionic liquid catalyst system. Typical ionic liquid charge to the unstirred reactor was 10 mL which contained 0.32 mmole Rh. Some reactions were performed in a stirred 300 mL Hastelloy C autoclave with subsurface gas feed using the same feed and condensation systems used with the unstirred reactor. A typical ionic liquid charge to the stirred autoclave was 100 mL containing 3.2 mmoles Rh. Typical reaction pressures ranged between 200 and 250 psig, and typical reactor temperatures ranged between 190 and 250°C. Feed rates varied widely and are provided in the Results and Discussion section. Condensed methanol carbonylation products from the receiver were weighed and analyzed by gas chromatography using a 30 m X 0.25 mm DB-FFAP capillary column (0.25 micron thickness) programmed at 40°C for 5 minutes, 25°C/minute to 240°C and holding at 240°C for 1 minute using a thermal conductivity detector held at 250°C (injector temperature = 250°C).

References

1. For preliminary reports on portions of this work see: (a) Tustin, G. C. *Prepr. Pap. – Am. Chem. Soc., Div. Fuel Chem.* **2005**, 50 (2), 494; (b) Tustin, G. C.; Moncier, R. M. US Patent 6,916,951 B1, 2005.
2. Anon., *Chemical Week*, June 30/July 7, 2004, p.40.
3. (a) Howard, M.J.; Jones, M.D.; Roberts, M.S.; Taylor, S.A. *Catalysis Today* **1993**, 18, 325. (b) Zoeller, J.R. in *Acetic Acid and Its Derivatives*, Agreda, V. H.; Zoeller, J. R., eds., Marcel-Dekker, New York, NY, 1993; pp. 35-52. (c) Gauthier-Lafaye, J; Perron, R., *Methanol and Carbonylation*, Rhone-Poulenc Recherches, Editions Technip, Paris, FR, 1987.
4. Smith, B.L.; Torrence, G.P.; Murphy, M.A.; Aguilo, A. *Journal of Molecular Catalysis* **1987**, 39, 115.
5. Sunley, G.J.; Watson, D.J. *Catalysis Today* **2000**, 58, 293.
6. Zoeller, J. R.; Singleton, A.H.; Tustin, G.C.; Carver, D.L. US Patent 6,452,043 B1, 2002 and references cited therein.
7. Tustin, G.C.; Zoeller, J.R.; Colberg, R.D. US Patent Application 2005/0049434 A1, 2005.
8. Yang, J.; Haynes, A.; Maitlis, P.M. *Chem. Commun.* **1999**, 179.

Chapter 10

Ionic Liquids for Space Propulsion

Yu-hui Chiu and Rainer A. Dressler

**Air Force Research Laboratory, Space Vehicles Directorate,
Hanscom Air Force Base, MA 01731**

The negligible vapor pressure, substantial conductivities, and thermal stability of ionic liquids make them ideal candidates for electrospray space propulsion applications. This chapter provides an introduction to current requirements in space propulsion, and summarizes the virtues of ionic liquid propelled electrospray thrusters. The physics associated with single cone-jet electrosprays is reviewed and recent developments with respect to ionic liquid ion sources are discussed. Specific examples of mass spectrometric measurements of charged particle emission from ionic liquid cone-jets are presented. The results include positive and negative ion emissions from [Emim][BF₄], [Emim][Im] and [Emim][NO₃].

Introduction

Space propulsion is a highest priority enabling technology of novel interplanetary and Earth orbiting vehicles. Not only must the propulsion system and associated propellant match the in-space mission needs, but it is also of critical importance that the propulsion system is integrated on a space vehicle in a way that minimizes contamination effects on the operational performance. Contamination hazards include surface depositions and sputtering, radio-frequency interference, and optical background generation. As mission requirements evolve, particularly with the push to accelerate access to space through space miniaturization technologies, new innovative forms of space propulsion are needed.

The negligible vapor pressure and significant conductivities of ionic liquids (ILs) make them ideal candidates for micro-electric propulsion, as first suggested by Fernández de la Mora (this was an early oral communication, published subsequently in (1)). ILs are now on the verge of ensuring the high precision positioning of a small spacecraft. The IL [Emim][Im] (1-ethyl-3-methylimidazolium bis(trifluoromethylsulfonyl)imide) has successfully passed the critical design review to propel a cluster of electrospray thrusters on the Jet Propulsion Laboratory ST7 Disturbance Reduction System mission (2-4). The objective of this mission is to position a spacecraft at the LaGrangian Point, L1, where the gravities of Earth and the sun almost cancel and the spacecraft is suspended in an orbit that rotates the Sun with the same orbital period of Earth. This point lies at approximately $1/100^{\text{th}}$ the distance between Earth and the sun where there is no significant atmosphere apart from the interplanetary solar wind plasma. Nevertheless, the position at L1 is not stable, and a spacecraft at L1 will be forced from this position in approximately 20 days. The main source of the perturbation is the solar radiation pressure which amounts to approximately 10 nN per cm^2 at the respective distance to the sun. Consequently, extended positioning of a small space vehicle requires a high precision propulsion system with μN range thrust and ~ 10 nN accuracy.

The electrospray thruster designed by Busek, Inc. (2), also referred to as a colloid thruster, has met all the stringent precision and noise specifications, and the propellant has survived space environmental test exposures (4). The ST7 mission, currently planned to launch in 2008, is a technology demonstration to support the Laser Interferometry Space Antenna (LISA) (5) mission in which an interferometer will be spanned between 3 spacecraft separated by ~ 5 million km. In that mission to measure extra-galactic gravity waves, the relative positioning between the spacecraft has to be maintained with a precision on the order of the wavelength of the laser light.

The IL electrospray thruster used on ST7, however, does not fully exploit the diverse physical attributes of ILs in these microelectric propulsion systems. While that thruster has a high precision thrust priority, it performs poorly in a second, equally important propulsion attribute, specific impulse, I_{sp} , which is a measure of thrust per unit propellant mass flow. As will be discussed later in this

chapter, with the proper choice of an IL and emitter design, very high specific impulses, close to an order of magnitude higher than that of typical chemical propulsion systems, can be obtained with available power resources. Meanwhile, micro-machined (MEMS) arrays of electrospray thrusters using an IL propellant have been tested successfully in a laboratory (6), suggesting that low thrusts associated with a single-emitter electrospray thruster can also be scaled up to higher thrusts of larger propulsion systems. Thus, it can be anticipated that microelectric thrusters operated with ILs will play an increasingly important role in space propulsion technology used for space exploration, the defense of national security, and monitoring the health of our planet.

In the present chapter, we first introduce the technical parameter space associated with space propulsion, provide a primer on the virtues of electric propulsion juxtaposed to chemical propulsion, and then briefly discuss the theory of electrosprays operated in a single cone-jet mode. The theory is then applied to interpret recent mass spectrometric measurements of the charge emission from 3 ILs, [Emim][BF₄], [Emim][Im], and [Emim][NO₃].

Space Propulsion

Space Propulsion Missions

Usually, space propulsion refers to “in-space” or “on-board” propulsion, and, therefore, excludes propulsion systems used for space launch. Obviously, the highest thrusts (thrust = force) are associated with the launch propulsion system of a rocket that needs to generate the extreme acceleration of the space vehicle payload(s) to a velocity and altitude that leads to a stable orbit or to the escape of Earth’s gravitational field. The space vehicle on-board propulsion system has multiple functions: orbit transfer corresponding to the maneuver that leads to a final orbit, repositioning, station keeping or orbital maintenance, and attitude control. Due to the significantly different thrust levels of these different missions, frequently a suite of thrusters, possibly using different propellants, are needed, each with specific missions of imparting velocity changes, Δv , to the space vehicle at specific moments of its journey.

The journey of a spacecraft can include an orbit with respect to a planet, in which case it can be referred to as a satellite, or, it can include travel to distant members of our solar system, eventually leaving it forever. In case of Earth orbit, the propulsion needs will change dramatically depending on the desired orbit. A low-Earth circular orbit at an altitude of 300 km will have significantly higher orbit maintenance propulsion requirements than a circular orbit at 800 km due to the much denser atmosphere at the lower altitude. The geostationary orbit at ~36,000 km altitude is in the equatorial plane, and is usually reserved for communications satellites that maintain a position over a specific location on the equator. Despite the very thin atmosphere at those altitudes – in fact, plasma densities exceed gas densities, there – the station-keeping propulsion require-

ments are significant due to orbital perturbations induced by the moon and sun. Thus, at launch, the geostationary satellite propellant mass fraction can be as high as 90%. This is significant because the cost of putting a pound in space is a key driver behind engineering the on-board propulsion system of a spacecraft. Consequently, propellant needs are precisely calculated to avoid paying for unnecessary lift. Meanwhile, considerable development is occurring in developing high I_{sp} engines that sacrifice thrust in favor of propellant utilization efficiency. Therefore, space vehicle designs are emerging that have separate high thrust and high I_{sp} engines to cover different Δv maneuvers.

Space Propulsion Performance Parameters

The critical parameters of space propulsion engines are thrust, F , specific impulse, I_{sp} , and efficiency, η . Thrust is also expressed in terms of impulse bits in the case of pulsed thrusters used for high precision maneuvers. The thrust is given by:

$$F = \dot{m}v_n + A_n(p_n - p_a), \quad (1)$$

where \dot{m} is the total propellant mass flow (in case of a bipropellant, this includes propellant and oxidizer), v_n is the propellant nozzle exit velocity, A_n is the nozzle aperture, and p_n and p_a are the nozzle and atmospheric pressures, respectively. The second term can generally be neglected in space propulsion applications. Chemical thrusters, such as the Space Shuttle monomethyl hydrazine/ N_2O_4 bipropellant engines, have exit velocities in the vicinity of 3 km s^{-1} . The thrust of different chemical thrusters, is, therefore, primarily determined by the propellant mass flow.

As mentioned earlier, I_{sp} is defined as the thrust per unit mass flow:

$$I_{sp} = \frac{F}{\dot{m}g} \quad (2)$$

According to most space propulsion conventions, I_{sp} is quoted in units of g (9.81 m s^{-2}), resulting in the somewhat counter-intuitive overall unit of seconds. If g is eliminated in Eq. (2), the unit of I_{sp} becomes that of velocity, providing a simple memory prop. The typically quoted value of I_{sp} for the Shuttle bipropellant engine mentioned earlier is $\sim 300 \text{ s}$. The importance of I_{sp} is expressed in the Newtonian rocket equation that relates the space vehicle liftoff propellant mass fraction to Δv of the propulsion mission and I_{sp} :

$$\frac{M_p}{M_0} = \left(1 - \exp \left(-\frac{\Delta v}{g I_{sp}} \right) \right), \quad (3)$$

where M_0 and M_p are the total space vehicle liftoff mass and the liftoff propellant mass, respectively. In the case of a chemical propulsion system with

$\Delta v = 1,000 \text{ m s}^{-1}$, 28% of the space vehicle liftoff mass will be attributed to propellant. The previously mentioned geostationary example with chemical propellant mass ratio, $M_p/M_0 = 0.9$, would correspond to a necessary $\Delta v = 6,900 \text{ m s}^{-1}$ for station keeping.

The efficiency, η , of a propulsion system is given by the ratio between the power associated with the propulsive force and the power input of the propulsion system. In case of chemical propellants, the input power corresponds to the free energy ΔG released to the system by the chemical reactions assuming complete combustion or chemical decay. Efficiencies are generally high and above 90% for chemical propulsion systems.

Electric Propulsion

The critical weakness of chemical propulsion systems are the relatively low specific impulse, leading to substantial propellant mass consumption for a specific Δv mission. In order to raise the specific impulse, the temperature in the stagnation chamber of the thruster needs to be raised, which is very challenging considering that the lift-off mass savings should not be lost to propulsion system mass increases due to new high-temperature materials. Higher stagnation temperatures are accomplished in thermal arcjets (7,8), in which case highly local heating occurs by striking an electric arc in the nozzle region. Arcjets are operated with propellants such as ammonia, hydrogen, and nitrogen/hydrogen mixtures, and depending on the propellant, the nozzle exit velocities are raised to achieve specific impulses between 500 and $>1,000 \text{ s}$. Arcjets, however, are not considered to be chemical thrusters, but are classified as electric thrusters. Arcjet efficiencies, however, are notoriously low at $\sim 30\%$.

Except for arcjets, electric thrusters achieve high I_{sp} through the electrostatic acceleration of charged particles (9,10). Eqs. (1) and (2) can be rewritten in terms of the mass-to-charge ratio of the accelerated particles. The thrust and I_{sp} associated with an individual, accelerated charged particle, i , is given by:

$$F = \dot{m}_i v_i = I_i (m_i / q) \sqrt{2V_{acc} (q / m_i)} \sim \sqrt{m_i / q}, \quad (4)$$

$$I_{sp} = \frac{F}{\dot{m}_i g} = (1 / g) \sqrt{2V_{acc} (q / m_i)} \sim \sqrt{q / m_i}, \quad (5)$$

where I_i is the output current associated with charged particle emission, v_i is the charged particle velocity, m_i is the charged particle mass, q is the particle charge, and V_{acc} is the electrostatic acceleration potential. Eqs. (4) and (5) express that thrust is proportional to the square root of m/q of the charged particles that are accelerated, while I_{sp} is proportional to the square root of the specific charge, q/m . Thus, at a given acceleration voltage, charged particles of high mass will lead to high thrust with a penalty in specific impulse, while charged particles of low mass will lead to high specific impulses with a penalty in thrust.

Eq. (4) and (5) raise the question why it is not possible to simply increase V_{acc} to augment thrust and I_{sp} ? A critical limitation of electric space propulsion is power, and its limited availability on a space vehicle. The power necessary to accelerate charged particles is given by:

$$P = \dot{m}_i v_i^2 / 2 \quad (6)$$

The power needed to accelerate a particle is thus proportion to I_{sp}^2 . Even if sufficient power is available, an electric propulsion system will reach an I_{sp} limit where the added mass of the larger high-voltage transformers will offset the gains of propellant utilization efficiency.

The electric propulsion efficiency is given by:

$$\eta = \frac{\bar{F}^2}{2\dot{m}V_{acc}I} = \frac{\bar{F}^2}{2V_{acc}I} \frac{q}{m}, \quad (7)$$

where I is the total output current of the thruster, \bar{F} is the average thrust given by the sum of thrusts of individual particles with mass-to-charge ratios m_i/q :

$$\bar{F} = \sum_i f_i \dot{m}_i v_i, \quad (8)$$

where f_i is the normalized fraction of the total accelerated current attributed to particles, i . Eq. (7) does not take inefficiencies such as incomplete ionization of propellant into account. Incorporation of Eq. (8) in Eq. (7) leads to the conclusion that if an electric thruster emits charged particles with a large range of mass-to-charge ratios, there is a considerable reduction in efficiency.

Table I compares the discussed propulsion parameters of selected electric propulsion models to those of common chemical engines. In pulsed plasma thrusters, a pulsed discharge is directed across a polymer surface, usually polytetrafluoroethylene. This generates a plasmoid that is then electrohydrodynamically accelerated. In ion and Hall effect thrusters, also referred to as electrostatic thrusters, a gas, preferably Xe, is ionized with high efficiency, and the resulting plasma consisting of xenon ions and electrons is accelerated. In ion thrusters, the acceleration is implemented with a set of grid lenses, while in Hall effect thrusters, the acceleration occurs in a grid-free plasma channel through a combination of magnetic and electric fields. Ion thrusters have been successfully operated in planetary missions (11). More recently, the European Space Agency (ESA) propelled the Smart 1 spacecraft from Earth to an orbit around the moon using a Hall effect thruster (12). As is seen in Table I, thrust of electric propulsion engines are typically low, and they cannot compete when mission time is an issue, as is the case during the traversal of a region of high radiation intensity. The 1,350 W Hall thruster on Smart 1 produces 70 mN thrust and it took just over a year to propel the ~300 kg spacecraft to the moon, during which 59 kg of Xe were used. The true value of electric propulsion, however, is appreciated when applying the typical Hall thruster I_{sp} of 1,800 s to the geostationary station-keeping example discussed

Table I. Representative propulsion parameters for selected space propulsion engines

<i>Thruster</i>	$I_{sp}(s)$	η (%)	F (N)
Solid Rocket Motor	185-300	90+	100+
Chemical Bipropellant	280-430	95+	2-→1000
Arcjet	500-800 >1,000 (H ₂)	30	0.1 – 1
Pulsed Plasma Thruster	200-1,500	45	10 ⁻⁶ – 10 ⁻²
Hall Effect Thruster	1,500-3,000	50-60	10 ⁻³ –0.5
Ion Thruster	1,700-3,900	65	10 ⁻³ –0.1

earlier. The 90% propellant mass fraction at liftoff in case of a chemical propulsion system is reduced to just 32% using Hall thrusters. Given the high cost of space lift, in particular into high geosynchronous orbits, electric propulsion can result in tremendous cost savings.

Discharge-Free Electric Thrusters: Electro spray Thrusters

The plasma-based thruster designs described above have an important drawback when miniaturized models are sought for micro and nanosatellite applications. Upon size reduction, plasmas lose efficiency due to the increase in the plasma surface-to-volume ratio. This problem is circumvented by highly promising micro-electric thrusters that are discharge free. The technology makes use of Taylor cones (13) that form when a surface of a conducting liquid is subjected to a high electric field. At the tip of the cone, the electric field strength is very high, leading to ion field evaporation and acceleration in the case of liquid metals, and the formation of a jet that eventually breaks up into saturation-charged droplets in the case of non-metallic conducting liquids. Liquid metal discharge-free thrusters are also referred to as field-emission electric propulsion thrusters (FEEPs), while the variants with non-metallic liquids have traditionally been called colloid thrusters. The conventional colloid thruster models used salt solutions in non-volatile solvents such as glycerol (14,15) and, more recently, formamide. As discussed below, electro spray thrusters using ILs can have properties that mimic either FEEP or colloid behavior. We will, therefore, refer to them as IL electro spray thrusters.

Figure 1 compares schematically a FEEP with a colloid thruster. At first sight the operation principles are very similar. A critical difference, however, is the need for a neutralizer in the FEEP system. The neutralizer is essentially a cathode that produces electrons to ensure that a neutral plasma leaves the spacecraft. This has two purposes: to prevent negative charging of the spacecraft which would cause the positive ion beam to return, and the reduction of space charge divergence of the emitted ion beam. The latter is less important

in the case of the low charge densities of some micro-electric thrusters. Colloid thrusters, on the other hand, can neutralize the current leaving the spacecraft by operating the engine in positive and negative ion emitting pairs. While negative ion emission can be effected using non-metallic conducting liquids, liquid metals emit electrons when subjected to a field of negative polarity. Thus, a FEEP expends considerable power in producing electrons that do not produce thrust. The specific power of a FEEP thruster is, therefore, significantly higher than that of a colloid thruster.

A second critical difference between the electro spray thruster models of Figure 1 is that colloid thrusters can emit both ions and charged droplets, while FEEPs are generally known to only emit atomic ions, although droplet emission, not necessarily charged, has been considered to pose problems with respect to contamination (4). As will be presented in the next section, the physics of colloid thrusters provide the means to control the droplet size and the ion/droplet ratio for a specific propellant. Consequently, colloid thrusters offer a significantly broader range of I_{sp} . A final important difference is that the propellant flow can be throttled in the case of colloid thrusters (16), while this ability has not yet been achieved for liquid metals.

The charge emission process of colloid thrusters clearly represents a form of electro spray ionization, originally referred to as electrohydrodynamic ionization (17). The electro spray ionization approach used in mass spectrometry of large biomolecules, however, occurs in an atmosphere with solutions involving volatile solvents. This critical difference will be emphasized further in the next section.

The performance parameter range of flight-ready FEEP models, colloid thruster models prior to the introduction of IL propellants, and research-level IL electro spray thrusters are listed in Table II. The table shows that FEEPs are unparalleled in I_{sp} since they produce more or less monodisperse atomic metal ion beams, and because the required extraction voltages in the current configurations are very high, thus leading to a high I_{sp} without the need for

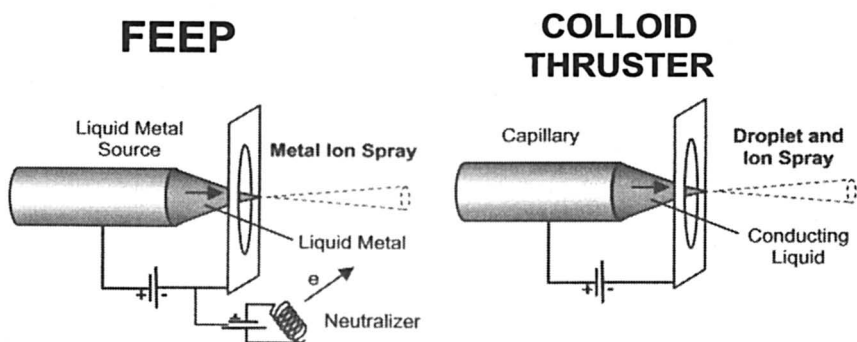


Figure 1. Schematic representation of field emission (FEEP) and colloid microthrusters.

Table II. Typical parameters for the most advanced FEEP, colloid and IL electrospray thrusters.

<i>Parameter</i>	<i>FEEP</i>	<i>Colloid Thrusters</i>	<i>IL Electro spray Thrusters</i>
Propellant	Cs, In	Salt Solutions	ILs
Thrust (μN)	1 – 1,400	<0.05 – 400	<0.05 – 20
I_{sp} (s)	4,000 – 11,000	450 – 1,500	200 – >3,000
Specific Power (W/mN) ^a	58 – 67	4	4 – 20
Extraction Voltage (kV)	4.5 – 12	4 – 19	1 – 2 kV
Efficiency (%)	>90	~70	60 – >90

^aBipolar operation assumed for colloid and IL electrospray thrusters

additional acceleration. Since the I_{sp} and thrust can always be raised with additional acceleration stages, the most pertinent parameter for comparison is the specific power, where the FEEP engines have a disadvantage. Particularly noteworthy is the significant improvement of anticipated performance of the IL electrospray thrusters in most categories in comparison to the colloid thrusters using non-volatile salt solutions.

Also worth noting are the much lower extraction voltages in the IL systems. This is not just a consequence of the use of ILs, since similar low voltages have been used in the study of formamide solutions (16,18). Rather, this can be attributed to operation in a single cone-jet mode, as depicted in Figure 1. The liquid cone is referred to as a Taylor cone (13). Different liquid jet geometries for varying field conditions are depicted in Figure 2. V_c represents the voltage range at which a stable cone-jet is formed. The earlier electrospray thruster models were operated at substantially higher voltages, at which the electrospray jet becomes stressed and is believed to break up in a number of smaller jets on the rim of the capillary edge (19). As the earliest studies of ions emitted from stressed jets attest, a multitude of solvated ions as well as multiply charged ions were observed including a significant fraction of metastable ions (14,15,20,21). The stressed jets are substantially less stable, and also are known to result in releases of uncharged droplets. In order to better understand the versatility of IL electrosprays operated in a single cone-jet, the physics associated with Taylor cones is discussed in the following section.

The comparison shown in Table II is not intended to express that eventually all space missions including FEEP propulsion plans will be replaced with IL electrospray thruster designs. There are missions that require the high I_{sp} performance and other attributes of FEEPs, such as noise, stability, and reliability. The LISA mission mentioned earlier (5) is exploring both FEEP and electrospray thrusters for the highly demanding positioning mission (4). In

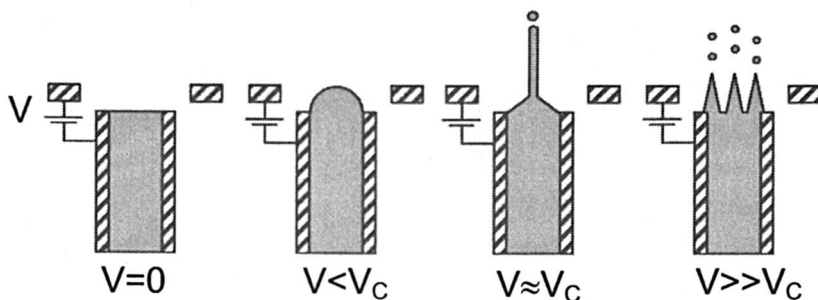


Figure 2. Behavior of conducting liquid subjected to different electric field strengths by applying a voltage between the liquid in a conducting capillary and an aperture. V_c is the extraction voltage range at which cone-jet formation is observed.

many instances, reliability supersedes performance when engineers put the finishing touches on a spacecraft design. A lot rides on the success of the IL electro spray thruster cluster on the ST7 mission (3). That engine, however, is run in a large-droplet emission mode corresponding to a low I_{sp} of less than 300 s. As will be discussed later, the same propellant, [Emim][Im], can be operated in a high I_{sp} , ion emission mode. A successful ST₇ mission, consequently, could dramatically increase the “market share” of IL electro spray thrusters.

Electrohydrodynamics of Taylor Cones

Taylor (13) showed that the meniscus of a non-conducting liquid under the influence of an electric field exceeding a critical value will deform into a cone where the balance between the surface tension and electrostatic forces due to partial charges at the surface creates a well-defined half-angle at the cone apex of 49.3°. Fernández de la Mora has derived a more general theory for Taylor cones of conducting liquids predicting a broader range of cone apex angles which was also confirmed experimentally (22). In case of conducting liquids at sufficiently high fields, the Taylor cone forms a jet that eventually breaks up into charged droplets. The lower extraction voltages needed to operate such a Taylor cone-jet mode, 1 to 2 kV, lead to a significantly gentler break-up of the jet.

In pioneering work, Fernández de la Mora and Loscertales (23) derived both theoretically and experimentally the proportionality between the parameters of a conducting liquid and the current emitted by the Taylor cone:

$$I \propto (\gamma K Q / \epsilon)^{\frac{1}{2}}, \quad (9)$$

where K and ϵ are the liquid conductivity and dielectric constant, respectively, γ is the surface tension, and Q is the volume flow rate. The electric field does not

appear in the equation. Its role is the generation of the Taylor cone and the associated surface-charge buildup which leads to the high electric fields that cause jet formation at the apex. Eq. (9) can be rearranged in terms of specific charge of the emitted droplets, q/m ,

$$\frac{q}{m} \propto \frac{1}{\rho} \sqrt{\frac{\gamma K}{\epsilon Q}}, \quad (10)$$

where ρ is the liquid density. Consequently, thrust and I_{sp} can be adjusted by the conductivity K and the volume flow rate, Q . Droplets formed in jet fission are expected to be charged near the Rayleigh limit (24):

$$q_R = (8\pi^2 \epsilon_0 \gamma d^3)^{\frac{1}{2}} \quad (11)$$

where ϵ_0 is the permittivity of vacuum, and d is the droplet diameter. Thus, since q/m is also a measure of the droplet diameter, Taylor cone-jets offer a means to control the droplet size.

Inspection of the cone-jet structure in Figure 2 allows the identification of 3 regions, the cone region, the jet and the intermediate neck region. In the cone region, there is an electrostatic nonequilibrium due to the narrowing cone diameter and the increasing flow velocity, leading to current flow in the liquid. The jet, on the other hand, represents a convective flow region that can be described in first approximation to be in electrostatic equilibrium. Rayleigh instabilities (charge density fluctuations) in the jet lead to the break-up. In the cone, the charge density on the surface increases as the tip is approached, while in the jet, the higher flow velocity causes the density to decrease with distance to the Taylor cone. Thus, the region of highest surface charge and normal electric field is in the intermediate neck region, where current flow and Ohmic losses are also expected to be high. Gamero-Castaño and Fernández de la Mora (25) derived expressions for the maximum normal electric field in this region:

$$E_{\max} = \frac{\gamma^{\frac{1}{2}}}{\epsilon_0^{\frac{2}{3}}} \left(\frac{K}{Q} \right)^{\frac{1}{6}}. \quad (12)$$

Using a concentrated NaI formamide solution, they succeeded in lowering the flow rate to a regime where the droplet diameters were estimated to be less than 100 nm. Below the respective flow rate of ~ 100 pl/s, the emission current was observed to rise precipitously. The rise was attributed to ion field evaporation, which has been postulated to occur at surface field strengths of approximately 1 V/nm (26-30). This generated considerable excitement in the colloid thruster community, since ion emission from Taylor cones represented a high I_{sp} mode at stable, well-described conditions.

Ion field evaporation figures prominently in the theory of the venerable electrospray ionization technique used in mass spectrometric studies of biomolecules (17). According to the theory first proposed by Iribarne and Thomson, (27,30) the charged droplets emitted into an atmosphere by the spray

diminish in size due to solvent evaporation. The large droplets will reach the Rayleigh limit with surface fields significantly below 1 V/nm, and will undergo Coulomb fission. As the droplets reach diameters in the vicinity of 10 nm, however, the surface fields are near 1 V/nm prior to reaching the Rayleigh limit, and ion field evaporation occurs. In a second model, the charged residue model, Dole (31) proposed that the ions are produced through complete evaporation of droplets, leaving an ionized, non-volatile residue of the solution. Dole's mechanism applies to solutions, where the diameter associated with the pure solute exceeds the diameter at which field evaporation occurs.

Chiu and coworkers conducted the first mass spectrometric analysis of ions field evaporated from a NaI formamide cone-jet (18). They observed $\text{Na}^+(\text{HCONH}_2)_n$ and $\text{I}(\text{HCONH}_2)_n$ solvated ions, where the distributions were consistent with thermal stability predictions at approximately 300 K. This is consistent with the notion that electrospray ionization and the associated field evaporation involving electrolyte solutions is a soft-ionization approach.

Fernández de la Mora was first to propose the use of ILs for the purpose of space propulsion. Shortly after, ion field evaporation was observed from ILs (1,18,32). An important drawback of ILs is their relatively high viscosity. The viscosity can be reduced to improve capillary flow by heating them. Another option has been demonstrated by Lozano and Martinez-Sanchez (33), who developed the methodology to emit stable ion currents from externally wetted metal needles with sharp tips. This method is not easily applied to electrolyte solutions because they tend to freeze without an electrohydrodynamic flow imposed on the droplet-vacuum interface. IL droplets, given their negligible vapor pressure, are unaffected by a vacuum. Figure 3 shows the principle of an externally wetted emitter. Success depends on the sharpness of the tip, which is obtained through an etching process (33). The surface properties of the emitter also need to be optimized for wetting the IL. Figure 3 shows a video microscope image of an externally wetted tungsten needle. An IL drop is applied to where a wire has been welded to the needle. The IL wets the needle including the tip, from which it emits an invisible ion beam. This method does not allow direct control of the propellant flow rate. The latter, however, is a function of the wire diameter and tip dimensions.

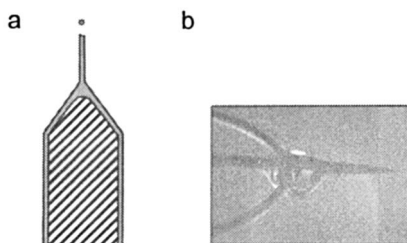


Figure 3. a: Schematic representation of an externally wetted emitter tip. b: Video microscope image of an ion emitting externally wetted tip in a vacuum. An IL droplet is applied at the junction between the needle and a spotwelded wire. The tip diameter of the emitter is 20 μm . (See page 1 of color inserts.)

Mass Spectrometric Measurements of Ions Field Evaporated from Ionic Liquids

Mass Spectrometric Experiment

Figure 4 is a schematic of the apparatus built by Chiu et al. (18,34) In conventional electrospray ionization experiments, the ions entering the mass spectrometer are thermalized, allowing a broad range of mass spectrometers to be used for the analysis. When studying ion field evaporation from cone-jets in a vacuum, the ions have keV kinetic energies, and in some instances broad, and structured energy distributions are observed (14). Severe retardation of the ions would result in significant losses. Thus, a mass spectrometer is needed that is relatively insensitive to the ion energy distribution. Quadrupole mass spectrometers are the simplest choice for this application. While the mass position is insensitive to ion energy, the resolution declines as the ion transmission energy increases. A compromise between resolution, signal-to-noise and angular and energy discrimination must, therefore, be found through the use of a retarding lens.

Ions are emitted either from a capillary or an externally wetted needle emitter. The ions encounter a linear translation stage where total emission current, I , and mass flow, \dot{m} , are measured with a Faraday cup and a quartz-crystal microbalance (QCM), respectively. Mass spectra are measured when the translation stage allows passage of ions. Following the quadrupole mass filter, ion energies can be measured using a retarding potential analyzer. A channeltron ion detector is used for counting both positive and negative ions.

The integration of thrusters on a spacecraft requires accurate knowledge of the angular spread of the exhaust in order to minimize contamination effects due to the exhaust. For this reason, the present emitter can be pivoted with respect to the emitter tip in order to measure the intensity as a function of the angle with

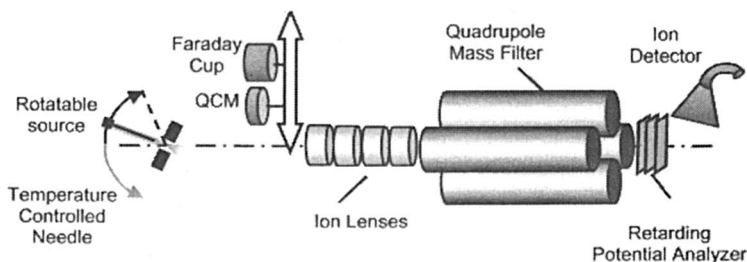


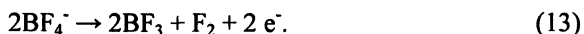
Figure 4. Schematic of mass spectrometric instrument used to study field evaporation from ILs. The retarding potential analyzer is used to measure mass-resolved energy distributions of the ions. Source rotation allows the study of ion angular distributions. Reproduced from reference (34).

respect to the thrust axis. As the results below show, the angular distributions are also symptomatic of the electrospray physics. The electrospray needle tip can also be heated to lower the viscosity, or to study ILs with melting points above room temperature.

In the examples discussed below, externally wetted tungsten needles were used. In all examples, extraction voltages of 1.0 ± 0.1 kV were necessary to establish a Taylor cone-jet.

[Emim][BF₄]

[Emim][BF₄] is a good example of the unique electrospray properties of ILs and their potential in micro-electric propulsion. Chiu et al. successfully operated both capillary and externally wetted emitters using this IL (18). Early on, it was found that operation was particularly unstable for a positive polarity. Emission intensity declined, and the IL exhibited brown discoloration. This was attributed to electrochemical fouling of the IL due to the conversion of BF₄⁻ to the reactive BF₃ and fluorine products at the anode (the emitter):



Lozano and Martinez-Sanchez developed an innovative way to mitigate electrochemical fouling (35). The approach exploits the unique electrochemical properties of ILs, in particular their large electrochemical windows that define the voltage above which electrochemical reactions occur. Lozano and Martinez-Sanchez proposed to switch the emitter polarity before the voltage across the growing electrochemical double layer at the interface exceeds the electrochemical window. Applying an alternating polarity at a sufficiently high frequency should, therefore, prevent electrochemical onset, and thus eliminate electrochemical fouling. In effect, charges are plucked from the IL without charge transfer across the emitter-IL interface to close the current loop. The capacitance associated with the double layers on the specific emitters was such that running [Emim][BF₄] with an alternating polarity frequency of 1 Hz allowed unlimited stable operation.

Figure 5 shows mass spectra recorded in such an alternating polarity mode using an etched tungsten tip. The mass spectrometric acquisition software is synchronized with the polarity alternating frequency, and gated to measure a single polarity. The mass spectra of both positive and negative ions are extremely sparse, showing only 2 peaks consisting of Emim⁺{[Emim][BF₄]}_n and BF₄⁻{[Emim][BF₄]}_n ions with $n = 0$ and 1. An additional ion, $n = 2$, was also observed when spraying the IL from a 5 μm inner diameter capillary tip (18). This may be attributable to the increased flow rate, which is prescribed by Eq. (10) to lead to the emission of larger ions. That equation, however, comes from continuum electrohydrodynamic theory, which may no longer be applicable at the conditions of the present electrojets with nano dimensions.

The parallel work by Chiu et al. (18) and Romero-Sanz et al. (1,32) on

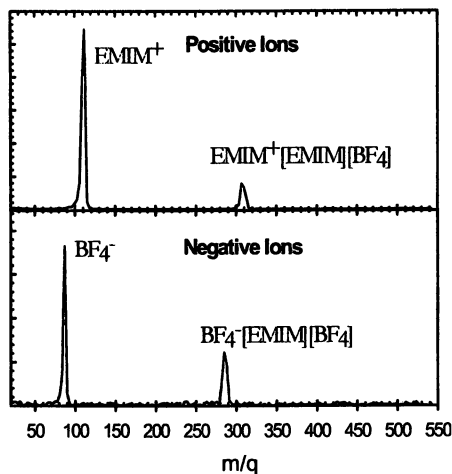


Figure 5. Positive and negative ion mass spectra of ions field evaporated from a needle externally wetted with [Emim][BF₄].

[Emim][BF₄] represented the first observation of pure ion emission from a prototype electrospray thruster. At higher flow rates, droplet emission was observed by Romero-Sanz et al. (1), consistent with Eq. (10). The pure ion emission suggests that ion field evaporation occurs directly at the Taylor cone tip, and that no jet exists when pure ion emission occurs, similar to liquid metal ion sources (36). This interpretation is consistent with the observed energy distribution of the ions, which is narrow and peaked at energies corresponding to the needle potential, implying that no ohmic losses are occurring. As stated in the previous section on Taylor cones, the ohmic losses occur primarily in the transition region between Taylor cone and jet.

Consequently, [Emim][BF₄] can be regarded as a highly efficient (>90%), high I_{sp} candidate for future missions. Chiu et al. (18) reported an I_{sp} of approximately 4,000 s based on an extraction voltage of 1.5 kV.

Figure 6 shows mass spectra as a function of emission angle for positive ions field-evaporated from [Emim][BF₄]. The distribution is peaked on axis and the mass spectra are more or less independent of the emission angle, consistent with observations by Lozano and Martinez-Sanchez (33). The present observation conflicts with results reported by Romero-Sanz et al. (32) whose measurements indicated peak emission at 20° for pure ion evaporation conditions.

[Emim][Im]

As mentioned earlier, [Emim][Im] is the propellant earmarked for the low I_{sp} ST7 DRS (3) mission. The thruster developed by Busek Inc. operates in an

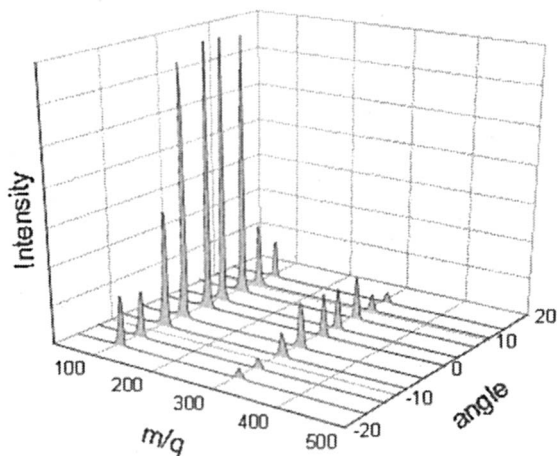


Figure 6. [Emim][BF₄] Positive ion mass spectra as a function of emission angle with respect to thrust axis.

almost pure droplet emission mode. Recently, however, Lozano (37) reported pure ion emission from [Emim][Im], implying that this IL offers a lot of flexibility to mission planners of future microsatellite missions. A critical component with respect to the mass of a small spacecraft is the electric propulsion power processing unit (PPU). The need to alternate polarities, as described in the previous section, adds sufficient complexity to the PPU that could significantly increase the mass of a microsatellite. The ST7 electro spray thruster will be operated in a dc positive only mode. The thruster has survived over 3,000 hours of uninterrupted operation with no stability problems (4). This raises the question why electrochemical propellant fouling is not affecting this engine. The most plausible explanation is that the electrochemical reaction products are flushed out of the system by the high propellant flow rates and the large charged droplets. To confirm this, Chiu and coworkers (34) embarked on comparing the ion emission of a high I_{sp} wetted 20 μm needle configuration in a dc and an ac (alternating polarity) mode. Electrochemical decay products should then appear in the mass spectrum of ions field evaporated in the dc configuration.

Figures 7 and 8 show the angular dependence of the [Emim][Im] positive and negative ion mass spectra emitted from an externally wetted tungsten tip. The spectra were both recorded in an alternating polarity mode of operation. As in the case of [Emim][BF₄], the mass spectra are sparse, represented by $\text{Emim}^+ \{[\text{Emim}][\text{Im}]_n\}$ and $\text{Im}^- \{[\text{Emim}][\text{Im}]_n\}$ ions with $n = 0-2$. The $n = 2$ ions are not shown and are significantly weaker in intensity. The angular dependence, however, is substantially different from that observed for [Emim][BF₄]. The intensity of the individual ions is peaked at an angle off axis, while on axis, a significant background is observed, in particular for negative

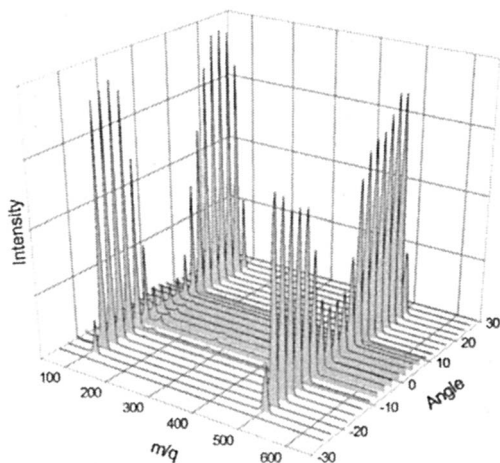


Figure 7. *[Emim][Im] positive ion mass spectrum as a function of emission angle. The main peaks consist of $Emim^+$ and $Emim^+[Emim][Im]$ ions. The emitter was run in an alternating polarity mode. The corresponding negative ion spectrum is shown in Figure 8. Reproduced from reference (34).*

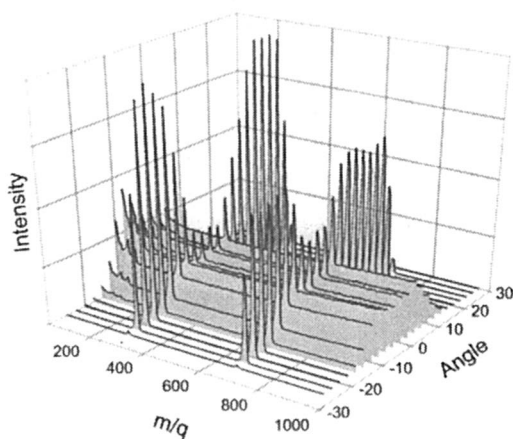


Figure 8. *[Emim][Im] negative ion mass spectrum as a function of emission angle. The main peaks consist of Im^- and $Im^-[Emim][Im]$ ions. The emitter was run in an alternating polarity mode. The corresponding positive ion spectrum is shown in Figure 7. Reproduced from reference (34).*

ions. The angular distribution of the background signal is consistent with the angular distribution of the mass flow registered on the QCM, which implies that the background is due to high m/q droplets which the quadrupole does not discriminate against. The registered mass flow is similar for both positive and negative polarity, and it is, therefore, concluded that the different relative intensities between ions and droplets for the negative and positive polarities can be attributed to different detector sensitivities for the droplets of different charge polarity. The average m/q derived from the ratio between QCM mass flow and Faraday cup current is approximately 24,000 and 17,000 amu per charge for positive and negative polarities, respectively. The low I_{sp} ST7 colloid thruster, on the other hand, operates at $>100,000$ amu per charge (4).

The observation of droplets on axis and ions off axis is fully consistent with the hydrodynamics of a Taylor cone-jet system operating in a mixed ion-droplet regime, where ions are predicted to be field evaporated primarily from the neck region where the highest surface-normal electric field strengths occur. The direction of the field gives the ions momentum away from the axis, consistent with the peaked distribution off axis. The droplets are produced on axis consistent with droplet formation at the tip of the jet. This interpretation is further confirmed by the observed mass-resolved energy distributions. When the mass filter is tuned to only pass signal attributable to droplets, a broad energy distribution is observed that is centered ~ 200 V below the emitter potential of 500 V with respect to the ground. Thus, droplets are formed at the jet end where the potential is lower due to ohmic losses that occur near the neck of the cone-jet. Figure 9 displays the energy distribution observed for Emim^+ ions at 17.5° , an angle of maximum intensity where no background due to droplets is evident. The ion distribution is peaked at the emitter potential. However, there is a weak tail that reaches ~ 300 V, the energy of the droplets. The distribution suggests that ions are emitted primarily from the neck region at a location upstream of where ohmic losses occur. Some ion evaporation, however, occurs in regions of ohmic dissipation as well as downstream thereof, producing the tail ions observed in Figure 9.

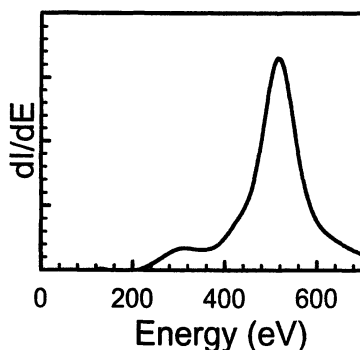


Figure 9. Retarding potential ion energy measurement of Emim^+ ions emitted at 17.5° with respect to the thrust axis.

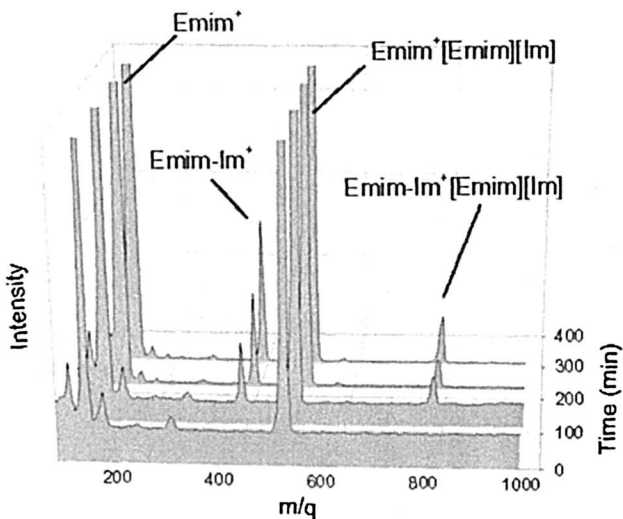


Figure 10. Time evolution of positive ion mass spectra observed on axis from an $[Emim][Im]$ vacuum electro spray operated at dc conditions.

As seen in Figures 7 and 8, when operated in the alternating polarity mode, the observed spectra are sparse, apart from minor trace peaks that are probably due to ion decay products that are difficult to assign without a second ion fragmentation experiment (e.g., MS-MS). Figure 10 illustrates the time evolution of positive ion mass spectra when the electro spray thruster is operated in a dc mode. After approximately 2 hours, new peaks at ~ 390 and ~ 780 amu appear. These are tentatively assigned to $Emim^+ \{ [Emim][Im] \}_n - Im$ adducts, with expected masses of 391 and 782 amu for $n = 0$ and 1. These products can be rationalized by the neutralization of Im at the emitter, which then binds with an ion, possibly through a proton or hydrogen-transfer complex.

Not apparent in the figure is that the output current declined dramatically during the respective experiment. The droplet fraction of the total current also decreased. This is again consistent with the hydrodynamics of a Taylor cone-jet (Eq. 10), where the specific charge of the emitted particles increases when the volume flow rate decreases. Very interesting is the observation that after several hours of operation in a dc mode, reverting to the ac polarity mode leads to instant recovery of the electro spray thruster to its original performance. These observations suggest that propellant fouling is not the main cause of the emission reduction, but that an electrochemical modification of the liquid-metal interface effectively throttles the flow. One envisioned scenario is a steady build-up of charge layers with alternating polarities in the liquid that extends beyond the double layer, thereby immobilizing a growing fraction of the liquid and increasing the flow resistance of the thin film. Once the polarity is reversed, the built-up interfacial structure disintegrates, and the layering of a new stack is

initiated starting with the opposite polarity. Indeed, “quasi-ternary layers” have been proposed to clarify the capacitive behavior of imidazolium based ILs (38). The same study also found evidence for bulky, rough interface layers due to ionic cluster pairs, fully consistent with the present observations and interpretation.

[Emim][NO₃]

There is considerable interest in energetic ILs. An IL that could be used both in a chemical as well as an electric engine would provide considerable mission flexibility. [Emim][NO₃] can be regarded as a generic energetic IL, the nitrate ion representing the oxidizer, and Emim⁺ being the propellant. Chiu et al. (34) conducted an analysis of the vacuum electro spray of [Emim][NO₃] externally applied to an etched tungsten emitter tip. The melting point of [Emim][NO₃] is 39°C, and it was necessary to heat the emitter to ~50°C. The angular distributions are comparable to those observed for [Emim][Im], however, the droplet emission is weaker, and therefore, the ion signals are not as depleted on axis for [Emim][NO₃]. Main peaks are attributable to Emim⁺{[Emim][NO₃]}_n and NO₃⁻{[Emim][NO₃]}_n ions with $n = 0$ and 1. Minor peaks due to $n = 2$ are also observed. The measured energy distributions of the charged particles on axis are bimodal, with one peak at the emitter potential, the other ~200 V lower. While the former is most likely due to ions field-evaporated at the neck, the latter can be either due to ion evaporation in jet regions following stages of ohmic dissipation, or due to droplets.

Figures 11 and 12 are positive and negative ion mass spectra, respectively, shown both for on and off-axis conditions, the latter taken at approximately 20°.

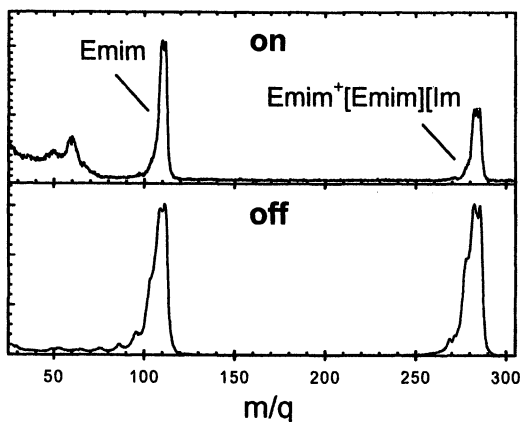


Figure 11. Field-evaporated positive ions observed on and off-axis for [Emim][NO₃].

On axis, a background is apparent for both polarities. The axial spectra, however, also exhibit broad, diffuse bands at low m/q in addition to the main ion peaks. The energy distributions of these diffuse bands, which are more intense in the case of the negative ion spectrum, and the narrow angular distributions suggest that they are associated with droplets. A higher resolution experiment is necessary in order to ascertain whether the bands are due to a dense mass spectrum or another phenomenon. A comparison with positive ion mass spectra observed following rapid thermolysis of $[\text{Emim}][\text{NO}_3]$ by Chowdhury and Thynell (39) provides no evidence that the diffuse bands are due to thermal decomposition events.

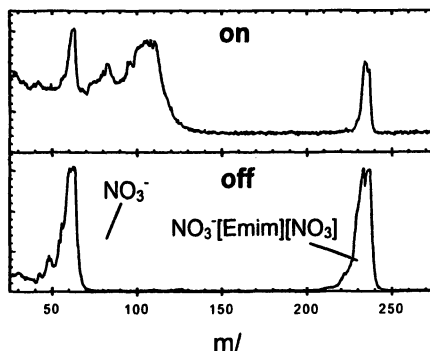


Figure 12. Field-evaporated negative ions observed on and off-axis for $[\text{Emim}][\text{NO}_3]$.

Conclusions

Significant progress has been made in understanding the electrosprays associated with Taylor cone-jets of ILs in a vacuum. Major hurdles have been cleared for IL use as propellants for both low (droplet acceleration) and high (ion acceleration) I_{sp} micro-electric spacecraft engines. Most significant among these is the innovative use of alternating polarity operation first introduced by Lozano and Martinez-Sanchez (35). The present studies show that a 1 Hz polarity switching frequency can suppress electro-chemical effects in $[\text{Emim}][\text{BF}_4]$. In the case of $[\text{Emim}][\text{Im}]$ emitted from a wetted tungsten needle, it is found that even if electrochemistry does not degrade the propellant significantly, the metal (electrode) IL interfacial properties change in a way to severely throttle the propellant flow on the wetted surface. While the ability to alternate the polarity adds complexity and mass to the PPU, most applications will require that no net current is emitted by the propulsion system. Thus, the

requirement of bipolar operation will exist for many missions. The envisaged configuration would then have half the emitters operated 180° out of phase with respect to the other half in an alternating polarity mode.

There is a concerted effort in developing arrays of electrospray thrusters to scale up the thrust. First successful demonstration of a micro-mechanically machined (MEMS) array of 1025 silicon emitters on a 0.64 cm² area has been reported (6). The silicon wetting was improved with a layer of black silicon that improved the wicking properties for an external wetting approach. Uniform emission was observed for an [Emim][BF₄] propellant. With these recent developments, it is likely that, as space technology progressively miniaturizes, IL-electrospray thrusters will play a prominent role in enabling future space missions.

Acknowledgments

This work has been supported by AFOSR through task 2303EP02 as part of the Space Miniaturization Theme (Program Manager, Michael R. Berman). The authors thank D. J. Levandier, G. Gaeta and 1Lt T. R. Heine for their laboratory contributions with respect to acquiring the data examples of this review. The authors are greatly indebted to P. Lozano for his assistance in preparing the etched emitter tips. This manuscript greatly benefited from many fruitful discussions with M. Martínez-Sánchez and J. Fernández de la Mora.

References

1. Romero-Sanz, I.; Bocanegra, R.; Fernández de la Mora, J.; Gamero-Castaño, M. *J. Appl. Phys.* **2003**, *94*, 3599.
2. Gamero-Castaño, M. *J. Prop. Power* **2004**, *20*, 736.
3. <http://nmp.jpl.nasa.gov/st7/>.
4. Ziemer, J. K.; Gamero-Castaño, M.; Hruby, V.; Spence, D.; Demmons, N.; McCormick, R.; Roy, T.; C. Gasdaska; Young, J.; Connolly, B., AIAA 2005-4265, 41st AIAA/ASME/SAE/ASEE Joint Propulsion Conference and Exhibit, Tucson, Arizona, 2005.
5. <http://lisa.jpl.nasa.gov/>.
6. Velásquez-García, L. F.; Martínez-Sánchez, M.; Akinwande, A. I., AIAA 2004-3595, 40th AIAA/ASME/SAE/ASEE Joint Propulsion Conference and Exhibit, Fort Lauderdale, Florida, 2004.
7. Birkan, M. *J. Prop. Power* **1996**, *12*, 1011.
8. M. Auweter-Kurtz; Gözl, T.; Habiger, H.; Hammer, F.; Kurtz, H.; Riehle, M.; Sleziona, C. *J. Prop. Power* **14**, *14*, 764.
9. Jahn, R. G.; Choueiri, E. Y., in *Encyclopedia of Physical Sciences and Technology, Third Edition, Volume 5* (Academic Press, 2002), pp. 125.

10. Martinez-Sanchez, M.; Pollard, J. E. *J. Prop. Power* **1998**, *14*, 689.
11. Marcucci, M. G.; Polk, J. E. *Rev. Sci. Instr.* **2000**, *71*, 1389.
12. <http://www.esa.int/esaMI/SMART-1/>.
13. Taylor, G. I. *Proc. Royal Soc. A* **1964**, *280*, 383.
14. Huberman, M. N. *J. Appl. Physics* **1970**, *41*, 578.
15. Huberman, M. N.; Rosen, S. G. *J. Spacecraft* **1974**, *11*, 475.
16. Gamero-Castaño, M.; Hruby, V. *J. Prop. Power* **2001**, *17*, 977.
17. Fenn, J. B.; Mann, M.; Meng, C. K.; Wong, S. F.; Whitehouse, C. M. *Science* **1989**, *246*, 64.
18. Chiu, Y.; Austin, B. L.; Dressler, R. A.; Levandier, D.; Murray, P. T.; Lozano, P.; Martinez-Sanchez, M. *J. Prop. Power* **2005**, *21*, 416.
19. Cloupeau, M.; Prunet-Foch, B. *J. Aerosol Sci.* **1994**, *25*, 1021.
20. Simons, D. S.; Colby, B. N.; C. A. Evans, J. *Int. j. Mass Spect. Ion Phys.* **1974**, *15*, 291.
21. Stimpson, B. P.; Simons, D. S.; Evans, C. A. *J. Phys. Chem.* **1978**, *82*, 660.
22. Fernández de la Mora, J. *J. Fluid Mech.* **1992**, *243*, 564.
23. Fernández de la Mora, J.; Loscertales, I. G. *J. Fluid Mech.* **1994**, *260*, 155.
24. Rayleigh, L. *Phil. Mag* **1882**, *14*, 184.
25. Gamero-Castaño, M.; Fernández de la Mora, J. *J. Chem. Phys.* **2000**, *113*, 815.
26. Fenn, J. B.; Rosell, J.; Meng, C. K. *J. Am. Soc. Mass Spectrom.* **1987**, *8*, 1147.
27. Iribarne, J. V.; Thomson, B. A. *J. Chem. Phys.* **1976**, *64*, 2287.
28. Katta, V.; Rockwood, A. L.; Vestal, M. L. *Int. J. of Mass Spectrometry and Ion Processes* **1991**, *103*, 129.
29. Loscertales, I. G.; Fernández de la Mora, J. *J. Chem. Phys.* **1995**, *103*, 5041.
30. Thomson, B. A.; Iribarne, J. V. *J. Chem. Phys.* **1979**, *7164*, 4451.
31. Dole, M.; Mack, L. L.; Hines, R. L.; Mobley, R. C.; Ferguson, L. P.; Alice, M. B. *J. Chem. Phys.* **1968**, *49*, 2240.
32. Romero-Sanz, I.; Bocanegra, R.; Fernández de la Mora, J.; Gamero-Castaño, M. *J. Appl. Phys.* **2004**, *95*, 2123.
33. Lozano, P.; Martinez-Sanchez, M. *J. Coll. and Interface Sci.* **2005**, *282*, 415.
34. Chiu, Y.; Gaeta, G.; Heine, T. R.; Dressler, R. A., 42nd AIAA/ASME/SAE/ASEE Joint Propulsion Conference & Exhibit, Sacramento, CA, 2006.
35. Lozano, P.; Martínez-Sánchez, M. *J. Coll. and Interface Sci.* **2004**, *280*, 149.
36. Prewett, P. D.; Mair, G. L. R., *Focused ion beams from liquid metal ion sources* Wiley, New York, 1991.
37. Lozano, P. *J. Phys. D* **2006**, *39*, 126.
38. Liu, H.; He, P.; Li, Z.; Liu, Y.; Li, J.; Zheng, L.; Li, J. *Electrochem. and Solid-State Lett.* **2005**, *8*, J17.
39. Chowdhury, A.; Thynell, S. T. *Thermochimica Acta* **2006**, *443*, 159.

Chapter 11

Columnar Liquid Crystalline Imidazolium Salts: Self-Organized One-Dimensional Ion Conductors

Masafumi Yoshio¹, Tomohiro Mukai², Hiroyuki Ohno²,
and Takashi Kato^{1,*}

¹Department of Chemistry and Biotechnology, School of Engineering,
The University of Tokyo, Hongo, Bunkyo-ku, Tokyo 113-8656, Japan

²Department of Biotechnology, Tokyo University of Agriculture
and Technology, Nakacho, Koganei, Tokyo 184-8588, Japan

A series of columnar liquid crystalline (LC) imidazolium tetrafluoroborate salts, 1-methyl-3-{3,4,5-tris(alkyloxy)-benzyl}imidazolium tetrafluoroborate (**Im-*n***; *n* = 6–18), where *n* is the carbon number of the aliphatic alkyl chains, have been prepared and studied as anisotropic ion-conductors. Their self-assembled structures in the fluid columnar LC states have been examined by X-ray diffraction measurements. In the columnar phases, the imidazolium portions self-assemble into the inner part of the columns through nano-segregation between the ionic and non-ionic parts driven by electrostatic interactions. The columns can be oriented macroscopically in two directions by different methods: the direction parallel to a glass surface by mechanical shearing; the direction perpendicular to the modified surface of a glass substrate with 3-(aminopropyl)triethoxysilane. Anisotropic ionic conductivities have been measured for columnar ionic liquids **Im-8** and **Im-12** that are aligned parallel to the surface of the glass substrate. These columnar ionic liquids have been found to function as one-dimensional ion-conductors.

Introduction

Ionic liquids are functional liquids that are non-volatile and highly ion conductive. They have advantages for applications as reaction solvents for organic syntheses (1-7) and as electrolytes for energy devices such as batteries and capacitors (8-13). For further functionalization of ionic liquids, introduction of self-organized structures such as liquid crystalline (LC) ordering would be important (14-16).

Two types of LC materials based on ionic liquids have been reported (17-35). The first example is the organic salts chemically modified with appropriate aliphatic and/or aromatic groups. A large variety of thermotropic ionic liquid crystals have been known (36-39). For thermotropic ionic liquid crystals exhibiting low melting temperatures, Seddon et al. reported on long-chain alkyl modified imidazolium and pyridinium salts containing perfluorinated anions such as tetrafluoroborate and hexafluorophosphate anions. They show smectic LC phases at room temperature range (19-21). These materials are called liquid crystalline ionic liquids. The second type is self-assembly of non-mesogenic ionic liquids with mesogenic molecules partially miscible with ionic liquids (33-35). We previously described that the mixing of a conventional ionic liquid, 1-ethyl-3-methylimidazolium tetrafluoroborate, and hydroxy-functionalized mesogenic molecules leads to the formation of nano-layered ionic liquids exhibiting two-dimensional ionic conduction (34,35). For these materials, liquid crystalline phases are induced by nano-segregation of block molecules (40,41). Intermolecular interactions such as hydrogen binding (42,43) and ion-dipolar interactions (44-48) play key roles in the formation of nanosegregated LC structures (14).

Here we report on self-assembled structures of columnar ionic liquids, a series of fan-shaped imidazolium tetrafluoroborate salts containing 3,4,5-tris(alkyloxy)benzyl groups (**Im-*n***; *n* = 6-18). In our previous communication (31), we reported on the LC and anisotropic ion-conductive properties of **Im-8** and **Im-12**.

No columnar LC ionic liquids based on imidazolium salts had been reported until we developed columnar ionic liquids (31) and a polymerizable columnar ionic liquid (32) as a new family of one-dimensional ion-conductors. In addition, one-dimensional ion transport was achieved for the columnar ionic liquids forming fluid columnar LC states. Such function may be useful for the development of energy devices with nanoscale order. For the preparation of these columnar materials showing anisotropic functions, molecular design (shape, interactions, and phase-segregation) and control of macroscopic columnar orientations is essential (14,15).

Results and Discussion

Synthesis and Liquid Crystalline Properties

Fan-shaped imidazolium salts **Im-*n*** (*n* = 6–18) shown in Figure 1 were prepared by a quaternization reaction of *N*-methylimidazole and 3,4,5-tris(alkyloxy)benzyl chloride, followed by anion exchange with silver tetrafluoroborate (31). All of **Im-*n*** show hexagonal columnar liquid crystalline phases (Col_h) both on heating and cooling. The phase transition behavior of **Im-*n*** is summarized in Table I. Figure 2 shows transition temperatures as a function of the aliphatic chain length (*n*) of **Im-*n*** on heating. Only **Im-6** and **Im-8** form glassy phases forming Col_h order. On the increase of the chain length (*n* = 10–18) the melting points increase from –10 to 88 °C. The clearing points show a maximum point for *n* = 14. It is found that the thermal temperature range of the Col_h phase is tunable by changing the alkyl chain length for the salts.

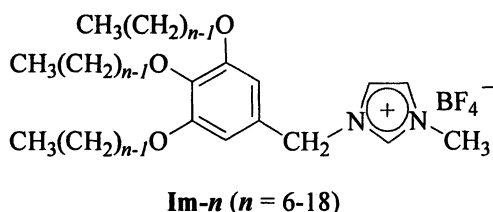


Figure 1. Molecular structure of 1-methyl-3-{3,4,5-tris(alkyloxy)benzyl}imidazolium tetrafluoroborate salts **Im-*n***, where *n* is the alkyl chain length (*n* = 6, 8, 10, 12, 14, 16, 18).

Self-assembled columnar structures were examined by X-ray diffraction measurements. The results are summarized in Table II. Three peaks with the ratio of 1: 1/√3: 1/2 and a broad halo were obtained for all of **Im-*n***, which indicate the formation of a disordered hexagonal columnar packing. The intercolumnar distance (*a*) was calculated with the following equation: $a = 2\langle d_{100} \rangle / \sqrt{3}$, $\langle d_{100} \rangle = (d_{100} + \sqrt{3}d_{110} + 2d_{200})/3$. The number (μ) of molecules per unit cell in a hexagonal lattice was estimated to be about 4, except for **Im-10** ($\mu = 5$), from $\mu = \sqrt{3}N_A a^2 h \rho / 2M$ (49), where N_A is Avogadro's number ($6.02 \times 10^{23} \text{ mol}^{-1}$), h is 3.74 Å of the layer thickness taken from the halo of X-ray in a wide angle region, and M is molecular weight. The material density (ρ) was determined by a flotation method in D-(+)-sucrose/H₂O at 20 °C.

Table I. Thermal properties of compounds **Im-n**

<i>n</i>	Phase transition behavior ^[a]				
6	G	-35	Col _h	32 (0.4)	I
8 ^[b]	G	-29	Col _h	133 (1.0)	I
10	Cr	-10 (6.1)	Col _h	162 (1.2)	I
12 ^[b]	Cr	17 (29.3)	Col _h	183 (1.3)	I
14	Cr	82 (61.8)	Col _h	185 (0.9)	I
16	Cr	74 (42.1)	Col _h	177 (1.5)	I
18	Cr	88 (87.4)	Col _h	148 (1.1)	I

^[a]Transition temperatures (°C) and enthalpies of transition (kJ mol⁻¹, in parentheses) determined by DSC (second heating scan, 10 °C min⁻¹). Col_h: columnar hexagonal; Cr: crystalline; G: glassy; I: isotropic. ^[b]Data are from reference 31.

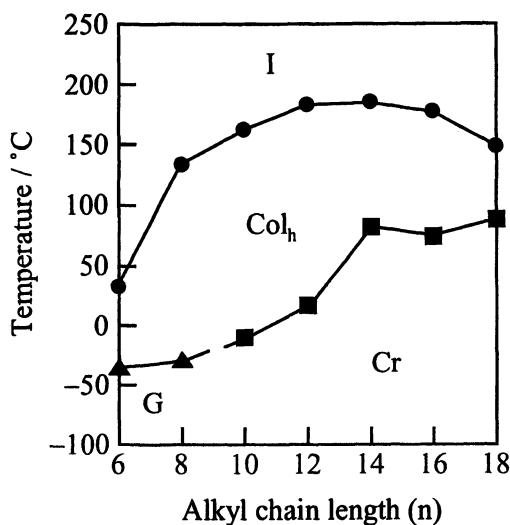


Figure 2. Transition temperatures of **Im-n** as a function of the alkyl chain length of imidazolium cation. Col_h: columnar hexagonal; Cr: crystalline; G: glassy, I: isotropic.

Table II. X-ray results of compounds **Im-n**

<i>n</i>	<i>T</i> (°C)	<i>d</i> ₁₀₀ (Å)	<i>d</i> ₁₁₀ (Å)	<i>d</i> ₂₀₀ (Å)	<i>a</i> ^[a] (Å)	<i>ρ</i> ^[b] (g cm ⁻³)	<i>μ</i> ^[c]
6	25	27.6	15.9	13.8	31.8	1.05	3.7
8 ^[d]	25	30.4	17.5	15.2	35.1	1.05	3.9
10	25	35.6	20.5	17.8	41.1	1.05	4.7
12 ^[d]	25	32.9	19.0	16.5	38.0	1.13	3.9
14	100	35.0	20.3	17.5	40.5	1.10	3.9
16	100	36.8	21.2	18.4	42.5	1.10	3.9
18	100	38.4	22.1	19.2	44.3	1.04	3.7

^[a]Hexagonal columnar lattice parameter $a = 2\langle d_{110} \rangle / \sqrt{3}$; $\langle d_{110} \rangle = (d_{100} + \sqrt{3}d_{110} + 2d_{200})/3$.

^[b]Experimental density at 20 °C. ^[c]Number of molecules per unit cell in a hexagonal lattice. ^[d]Data are from reference 31.

Fan-shaped molecules **Im-n** form supramolecular columnar structures through self-organization via nano-segregation (14) and electrostatic interactions (37), as schematically shown in Figure 3. In these structures, the imidazolium part forms ionic channels inside the columns (31).

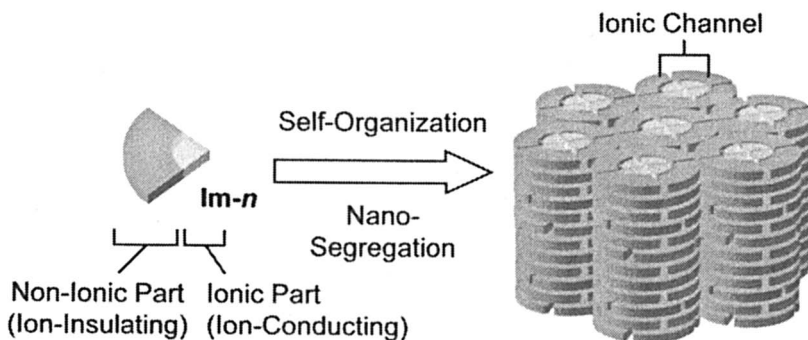


Figure 3. Schematic illustration of a columnar self-assembly of fan-shaped imidazolium salts **Im-n** ($n = 6-18$) through nano-segregation and electrostatic interactions.

Macroscopic Alignment of the Columns

These columnar ionic liquid crystals can be used as one-dimensional ion-conductors (31,32). For this approach, the formation of oriented monodomains in the macroscopic scale is important because the boundary in the randomly oriented polydomains disturbs high and anisotropic ion conduction.

These columnar materials are macroscopically aligned by shearing on the glass substrate. Figure 4 shows the polarizing microscope images of **Im-12** before and after shearing (31). The monodomain of the columnar phase is formed between Au electrodes after the polydomain material (Figure 4a) is mechanically sheared in the sandwiched glasses without rubbing treatment. One-dimensional ionic conductivities were measured by the cell with comb-shaped gold electrodes, which is described in the following section. In addition, we have achieved vertical alignment of the columns to the glass surface (homeotropic orientation) by using a chemically modified glass with 3-(aminopropyl)triethoxysilane as shown in Figure 5. This alignment has been confirmed by the conoscopic observation on a polarized microscope. A cross-shaped pattern is observed as shown in the inset of Figure 5a. A hexagonal diffraction pattern of X-ray is obtained for the homeotropic columns as seen in Figure 5b. This homeotropic alignment can be attributed to the interactions between the imidazolium moiety of **Im-*n*** and the amine-functionalized glass surface. We also reported (32) on the vertical alignment of the columns formed by a columnar ionic liquid having polymerizable groups on the surface modified with 3-(aminopropyl)triethoxysilane.

Anisotropic Ionic Conductivities of Columnar Ionic Liquids (31)

One-dimensional ion conduction is achieved for columnar ionic liquids **Im-8** and **Im-12** (31). Anisotropic ionic conductivities were measured by an alternating current impedance method for the samples forming oriented monodomains between comb-shaped gold electrodes. In the macroscopically oriented states of these columnar materials, ionic conductivities parallel to the columnar axis (σ_{\parallel}) are higher than those perpendicular to the axis (σ_{\perp}). For example, compound **Im-12** shows the conductivities of $3.1 \times 10^{-5} \text{ S cm}^{-1}$ (σ_{\parallel}), $7.5 \times 10^{-7} \text{ S cm}^{-1}$ (σ_{\perp}), and anisotropy ($\sigma_{\parallel}/\sigma_{\perp}$) of 41 at 100°C. No anisotropy of the ionic conductivity is seen when the compound forms the isotropic state. The formation of the columnar structures through the nano-segregation between ionic and non-ionic parts results in the spontaneous formation of anisotropic ion-conductive pathways with long range order. These materials function as self-organized electrolytes. They dissolve a variety of ionic species such as lithium salts. Compound **Im-12** containing LiBF_4 (molar ratio of LiBF_4 to **Im-12**: 0.25) exhibits the conductivities of $7.5 \times 10^{-5} \text{ S cm}^{-1}$ (σ_{\parallel}) and $8.0 \times 10^{-7} \text{ S cm}^{-1}$ (σ_{\perp}) at

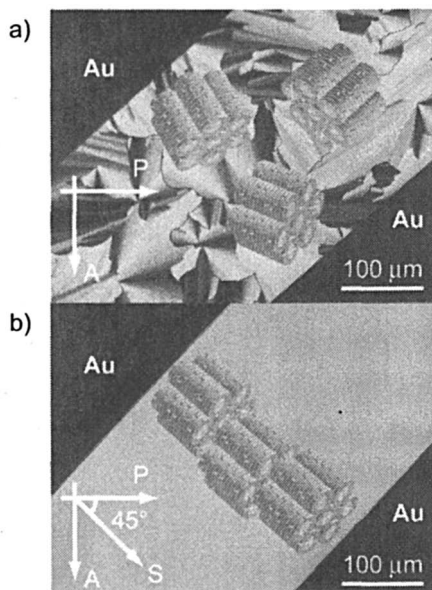


Figure 4. Polarizing optical microscopic images and schematic illustrations of the oriented and self-assembled structures of **1m-12** in the hexagonal columnar state: a) before shearing; b) after shearing the material along the direction perpendicular to the Au electrodes. Directions of A: analyzer; P: polarizer; S: mechanical shearing. (Reproduced with permission from reference 31. Copyright 2004 American Chemical Society.)

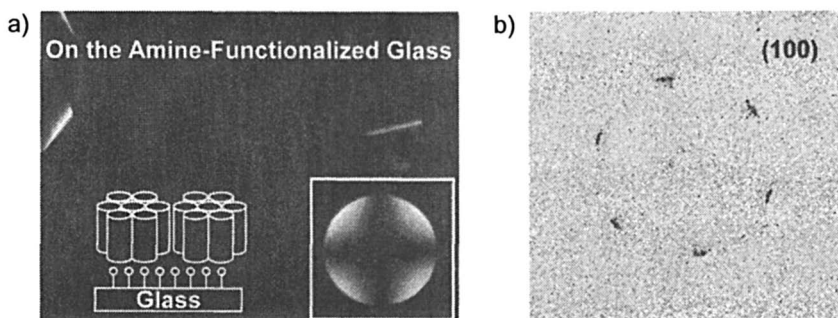


Figure 5. Polarizing optical microscopic image (a) and 2D X-ray diffraction pattern (b) of **1m-8** in the Col_h phase at 25 °C. The columns are aligned perpendicular to an amine-functionalized surface of a glass substrate.

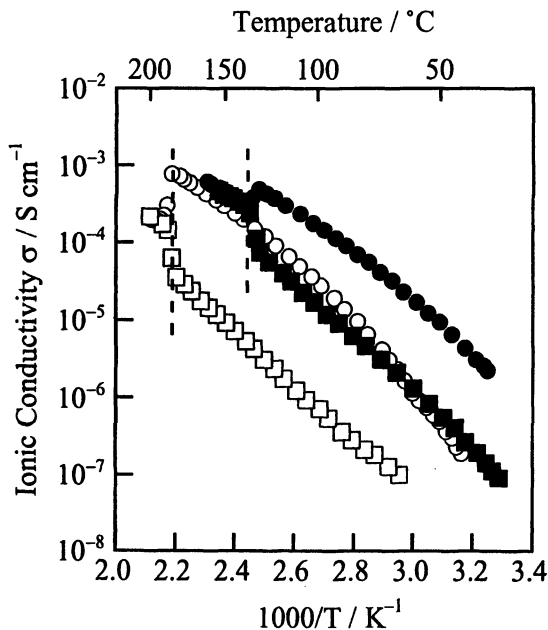


Figure 6. Anisotropic ionic conductivities of *Im-8* and *Im-12* as a function of temperatures: (●) parallel and (■) perpendicular to the columnar axis for *Im-8*; (○) parallel and (□) perpendicular to the columnar axis for *Im-12*. The broken lines denote the Col_h -I phase transition temperatures. (Reproduced with permission from reference 31. Copyright 2004 American Chemical Society.)

100 °C. The value of $\sigma_{\parallel}/\sigma_{\perp}$ at 100 °C is 94. It should be noted that the addition of the salts only enhance the conductivities of σ_{\parallel} .

Conclusion

In this paper, we have described the preparation of a series of fan-shaped imidazolium salts and their liquid crystalline properties. Two types of columnar orientation parallel and perpendicular to the surface of substrates have been achieved by different techniques. Anisotropic ionic conductivities have been demonstrated for columnar liquid crystals aligned parallel to the surface of glass substrate. These anisotropically ion-active materials have great potentials as ordered solvents for catalytic reactions as well as electrolytes that anisotropically transport ions at the nanometer scale. Introduction of liquid

crystalline nanostructures into ionic liquids may open a new avenue in the field of material science and supramolecular chemistry.

Acknowledgements

This study was partially supported by Grant-in-Aid for Creative Scientific Research of “Invention of Conjugated Electronic Structures and Novel Functions” (No. 16GS0209) (T.K.) and Grant-in-Aid for Scientific Research (B) (No. 17350065) (T.K.) from the Japan Society for the Promotion of Science (JSPS) and Grant-in-Aid for The 21st Century COE Program for Frontiers in Fundamental Chemistry (T.K.) from the Ministry of Education, Culture, Sports, Science, and Technology.

References

1. Seddon, K. R. *J. Chem. Tech. Biotechnol.* **1997**, *68*, 351–356.
2. Welton, T. *Chem. Rev.* **1999**, *99*, 2071–2083.
3. Rogers, R. D.; Seddon, K. R. *Science* **2003**, *302*, 792–793.
4. Wasserscheid, P.; Keim, W. *Angew. Chem. Int. Ed.* **2000**, *39*, 3772–3789.
5. Sheldon, R. *Chem. Commun.* **2001**, 2399–2407.
6. Wilkes, J. S. *Green Chem.* **2002**, *4*, 73–80.
7. Lee, S. *Chem. Commun.* **2006**, 1049–1063.
8. Ohno, H., Ed. *Electrochemical Aspects of Ionic Liquids*; Wiley, Hoboken, NJ, 2005.
9. Ohno, H.; Yoshizawa, M. In *Ionic Liquids IIIB: Fundamentals, Progress, Challenges and Opportunities: Transportations and Processes*; ACS Symposium Series 902, American Chemical Society: Washington, DC, 2005, 159–170.
10. Susan, M. A. B. H.; Kaneko, T.; Noda, A.; Watanabe, M. *J. Am. Chem. Soc.* **2005**, *127*, 4976–4983.
11. Buzzeo, M. C.; Evans, R. G.; Compton, R. G. *Chem. Phys. Chem.* **2004**, *5*, 1106–1120.
12. Bonhôte, P.; Dias, A.-P.; Papageorgiou, N.; Kalyanasundaram, K.; Grätzel, M. *Inorg. Chem.* **1996**, *35*, 1168–1178.
13. Forsyth, S. A.; Pringle, J. M.; MacFarlane, D. R. *Aust. J. Chem.* **2004**, *57*, 113–119.
14. Kato, T.; Mizoshita, N.; Kishimoto, K. *Angew. Chem. Int. Ed.* **2006**, *45*, 38–68.
15. Kato, T. *Science* **2002**, *295*, 2414–2418.
16. Kato, T.; Yoshio, M. Liquid Crystalline Ionic Liquids, In *Electrochemical Aspects of Ionic Liquids*; Ohno, H., Ed.; Wiley, Hoboken, NJ, 2005; Chapter 25, 307–320.

17. Bazuin, F.; Guillon, D.; Skoulios, A.; Nicoud, J.-F. *Liq. Cryst.* **1986**, *1*, 181–188.
18. Bowlas, C. J.; Bruce, D. W.; Seddon, K. R. *Chem. Commun.* **1996**, 1625–1626.
19. Gordon, C. M.; Holbrey, J. D.; Kennedy, A. R.; Seddon, K. R. *J. Mater. Chem.* **1998**, *8*, 2627–2636.
20. De Roche, J.; Gordon, C. M.; Imrie, C. T.; Ingram, M. D.; Kennedy, A. R.; Lo Celso, F.; Triolo, A. *Chem. Mater.* **2003**, *15*, 3089–3097.
21. Holbrey, J. D.; Seddon, K. R. *J. Chem. Soc., Dalton Trans.* **1999**, 2133–2139.
22. Merrigan, T. L.; Bates, E. D.; Dorman, S. C.; Davis Jr, J. H. *Chem. Commun.* **2000**, 2051–2052.
23. Lee, C. K.; Huang, H. W.; Lin, I. J. B. *Chem. Commun.* **2000**, 1911–1912.
24. Neve, F.; Francescangeli, O.; Crispini, A.; Charmant, J. *Chem. Mater.* **2001**, *13*, 2032–2041.
25. Bradley, A. E.; Hardacre, C.; Holbrey, J. D.; Johnston, S.; McMath, S. E. J.; Nieuwenhuyzen, M. *Chem. Mater.* **2002**, *14*, 629–635.
26. Hoshino, K.; Yoshio, M.; Mukai, T.; Kishimoto, K.; Ohno, H.; Kato, T. *J. Polym. Sci., Part A: Polym. Chem.* **2003**, *41*, 3486–3492.
27. Lee, K.-M.; Lee, Y.-T.; Lin, I. J. B. *J. Mater. Chem.* **2003**, *13*, 1079–1084.
28. Mukai, T.; Yoshio, M.; Kato, T.; Ohno, H. *Chem. Lett.* **2004**, *33*, 1630–1631.
29. Mukai, T.; Yoshio, M.; Kato, T.; Ohno, H. *Chem. Lett.* **2005**, *34*, 442–443.
30. Mukai, T.; Yoshio, M.; Kato, T.; Yoshizawa, M.; Ohno, H. *Chem. Commun.* **2005**, 1333–1335.
31. Yoshio, M.; Mukai, T.; Ohno, H.; Kato, T. *J. Am. Chem. Soc.* **2004**, *126*, 994–995.
32. Yoshio, M.; Kagata, T.; Koji, H.; Mukai, T.; Ohno, H.; Kato, T. *J. Am. Chem. Soc.* **2006**, *128*, 5570–5577.
33. Yoshio, M.; Mukai, T.; Kanie, K.; Yoshizawa, M.; Ohno, H.; Kato, T. *Chem. Lett.* **2002**, 320–321.
34. Yoshio, M.; Mukai, T.; Kanie, K.; Yoshizawa, M.; Ohno, H.; Kato, T. *Adv. Mater.* **2002**, *14*, 351–354.
35. Yoshio, M.; Kato, T.; Mukai, T.; Yoshizawa, M.; Ohno, H. *Mol. Cryst. Liq. Cryst.* **2004**, *413*, 99–108.
36. Ujiie, S.; Iimura, K. *Chem. Lett.* **1990**, 995–998.
37. Ujiie, S.; Iimura, K. *Macromolecules* **1992**, *25*, 3174–3178.
38. Kosaka, Y.; Kato, T.; Uryu, T. *Liq. Cryst.* **1995**, *18*, 693–698.
39. Binnemans, K. *Chem. Rev.* **2005**, *105*, 4148–4204.
40. Tschierske, C. *J. Mater. Chem.* **1998**, *8*, 1485–1508.
41. Tschierske, C. *J. Mater. Chem.* **2001**, *11*, 2647–2671.

42. Kato, T.; Mizoshita, N.; Kanie, K. *Macromol. Rapid Commun.* **2001**, *22*, 797–814.
43. Kato, T. *Struct. Bonding* **2000**, *96*, 95–146.
44. Ohtake, T.; Ito, K.; Nishina, N.; Kihara, H.; Ohno, H.; Kato, T. *Polym. J.* **1999**, *31*, 1155–1158.
45. Ohtake, T.; Ogasawara, M.; Ito-Akita, K.; Nishina, N.; Ujiie, S.; Ohno, H.; Kato, T. *Chem. Mater.* **2000**, *12*, 782–789.
46. Hoshino, K.; Kanie, K.; Ohtake, T.; Mukai, T.; Yoshizawa, M.; Ujiie, S.; Ohno, H.; Kato, T. *Macromol. Chem. Phys.* **2002**, *203*, 1547–1555.
47. Kishimoto, K.; Yoshio, M.; Mukai, T.; Yoshizawa, M.; Ohno, H.; Kato, T. *J. Am. Chem. Soc.* **2003**, *125*, 3196–3197.
48. Kishimoto, K.; Suzawa, T.; Yokota, T.; Mukai, T.; Ohno, H.; Kato, T. *J. Am. Chem. Soc.* **2005**, *127*, 15618–15623.
49. Percec, V.; Cho, W.-D.; Ungar, G.; Yeardley, D. J. P. *J. Am. Chem. Soc.* **2001**, *123*, 1302–1315.

Chapter 12

Ionic Liquids as Versatile Media in Lanthanide Chemistry

A.-V. Mudring

Institut für Anorganische Chemie, Universität zu Köln, Greinstrasse 6,
D-50939 Köln, Germany

Despite intense research in the field of ionic liquids, solvation processes even of simple inorganic salts like lanthanides halides are still poorly understood. A combination of absorption and emission spectroscopy together with single crystal X-ray structure analysis can help to elucidate these processes.

Lanthanides in ionic liquids may be interesting optical materials, as ionic liquids can be designed in such a way that the luminescent lanthanide centres are not only well shielded from any ligands containing low frequency oscillators but also from themselves. In consequence the probability of a radiationless decay is reduced so that high luminescence lifetimes even at unusually high lanthanide concentrations are achievable.

Furthermore, ionic liquids offer the possibility to generate, stabilize and work with highly reducing species like divalent lanthanides. Carefully chosen ionic liquids not only have a high electrochemical window, but can diminish the reducing power of divalent lanthanides compared to conventional organic solvents (VOCs). This should open the way to both, new inorganic coordination/organometallic chemistry as well as synthetic organic chemistry.

Trivalent lanthanides in ionic liquids – structural characterizations

The dissolution and solvation of simple inorganic compounds as for example halide salts in conventional inorganic solvents like water or liquid ammonia, or organic solvents like tetrahydrofuran or acetonitrile, is quite well understood and extensive studies have appeared in the past. In contrast, despite the large interest in ionic liquids as a new class of solvents, investigations of the solvent-solute interaction are still scarce especially when it comes to simple inorganic salts.¹ Considering the dissolution of an inorganic salt (**AB**) in a given ionic liquid (**XY**), the interaction of the cation **A** with the anion of the ionic liquid **Y** which is present in excess and the interaction of the anion **B** of the salt to be dissolved with the cation of the ionic liquid **X** has to be studied. From conventional solvent system studies and studies of molten salt systems it might be anticipated that the solvation of the cation **A** is generally the energetic driving force of the reaction and, hence, plays the most important role. Among tetrahaloaluminates, halides, and triflate ($\text{CF}_3\text{SO}_3^- = \text{OTf}$) bis(trifluoromethanesulfonyl)amide ($\text{N}(\text{SO}_2\text{CF}_3)^- = \text{Tf}_2\text{N}^-$) in particular is currently the most popular anion used in ionic liquids.

As for most metal cations the formation of halogeno-complexes is well described and structural data are readily available,² our research focuses on studying the interaction of cations with the triflate or the bis(trifluoromethanesulfonyl)amide anion. In order to investigate the solvation and coordination of lanthanide cations in ionic liquids various di- and trivalent lanthanide iodides, triflates and bis(trifluoromethanesulfonyl)amides as well as alkaline earth salts as model compounds for divalent lanthanides were dissolved in the respective ionic liquids. To obtain structural data single crystals of lanthanide complex compounds were grown out of the ionic liquid. Many traditional crystallization techniques, such as isothermal evaporation of the solvent, fail due to the unique properties of ionic liquids (negligible vapour pressure), but traditional solid state techniques are successful. By supersaturating the ionic liquid with the respective salt in the heat and cooling, the desired reaction products were obtained. Special attention has to be paid to a careful cooling procedure as the high conformational flexibility and charge delocalization of the ions, which are desired for an ionic liquid, often either lead to glass formation rather than crystallization or to a high degree of structural disorder in the crystals.

The results for the dissolution of simple iodides in pyrrolidinium bis(trifluoromethanesulfonyl)amides can be rationalized as follows:

All lanthanide triiodides form as the least soluble product in [bmpyr][Tf₂N] compounds of the general composition [bmpyr]₄[LnI₆][Tf₂N] containing the trivalent lanthanide cation in a nearly ideal octahedron of iodide anions. The

Ln³⁺ = Pr-Tb



Ln³⁺ = Pr-Tb



M²⁺ = Ca, Sr, Yb



mppypr = 1-methyl-1-propylpyrrolidinium; bmpyr = 1-butyl-1-methylpyrrolidinium

Figure 1. Lanthanide and alkaline earth iodides in pyrrolidinium bis(trifluoromethanesulfonyl)amides.

crystal structures show above each of the triangular faces of the $[\text{LnI}_6]$ octahedron a cation of the ionic liquid.³ Interestingly, this structural feature was predicted by molecular dynamical studies to be present in similar ionic liquid systems.⁴ In $[\text{bmpyr}]_4[\text{NdI}_6][\text{Tf}_2\text{N}]$ one formula unit of the ionic liquid itself is included in the compound to achieve optimal packing in the solid. This can be illustrated by rewriting the formula as $[\text{bmpyr}]_3[\text{NdI}_6] \cdot [\text{bmpyr}][\text{Tf}_2\text{N}]$. According to Figure 1, after formation of $[\text{bmpyr}]_4[\text{LnI}_6][\text{Tf}_2\text{N}]$ from LnI_3 the other half of the lanthanide ions that remain in solution have to be coordinated by bis(trifluoromethanesulfonyl)amide ligands. In order to obtain structural information on those species we have prepared in a first step the respective anhydrous compounds, $\text{Ln}(\text{Tf}_2\text{N})_3$, and subsequently grew crystals from the same ionic liquid ($[\text{bmpyr}][\text{Tf}_2\text{N}]$). Figure 2 shows the coordination environment for Pr-Tb in $[\text{bmpyr}]_2[\text{Ln}(\text{Tf}_2\text{N})_5]$ and Dy-Lu in $[\text{bmpyr}][\text{Ln}(\text{Tf}_2\text{N})_4]$, respectively.

In both cases, the trivalent lanthanide cations are exclusively coordinated by oxygen atoms belonging to the Tf_2N ligand.⁵ The larger lanthanide cations $\text{Ln}^{3+} = \text{Pr-Tb}$ exhibit a nine-fold oxygen coordination which can best be described as a monocapped square antiprism (Fig. 2, (1)). The oxygen surrounding of the lanthanide cation is formed by four bidentate bis(trifluoromethanesulfonyl)amide ligands and one monodentate ligand. While for the monodentate bis(trifluoromethanesulfonyl)amide ligand a *transoid* conformation (with respect to the S—N—S plane) is observed, for the bidentate ligands both conformations are observed. One of the four ligands adopts a *cisoid* conformation and another one a *transoid* conformation while the other two ligand positions show a mixed occupation by ligands in *cisoid* and *transoid* conformations. The smaller trivalent lanthanide cations Dy-Lu prefer an eightfold coordination by oxygen

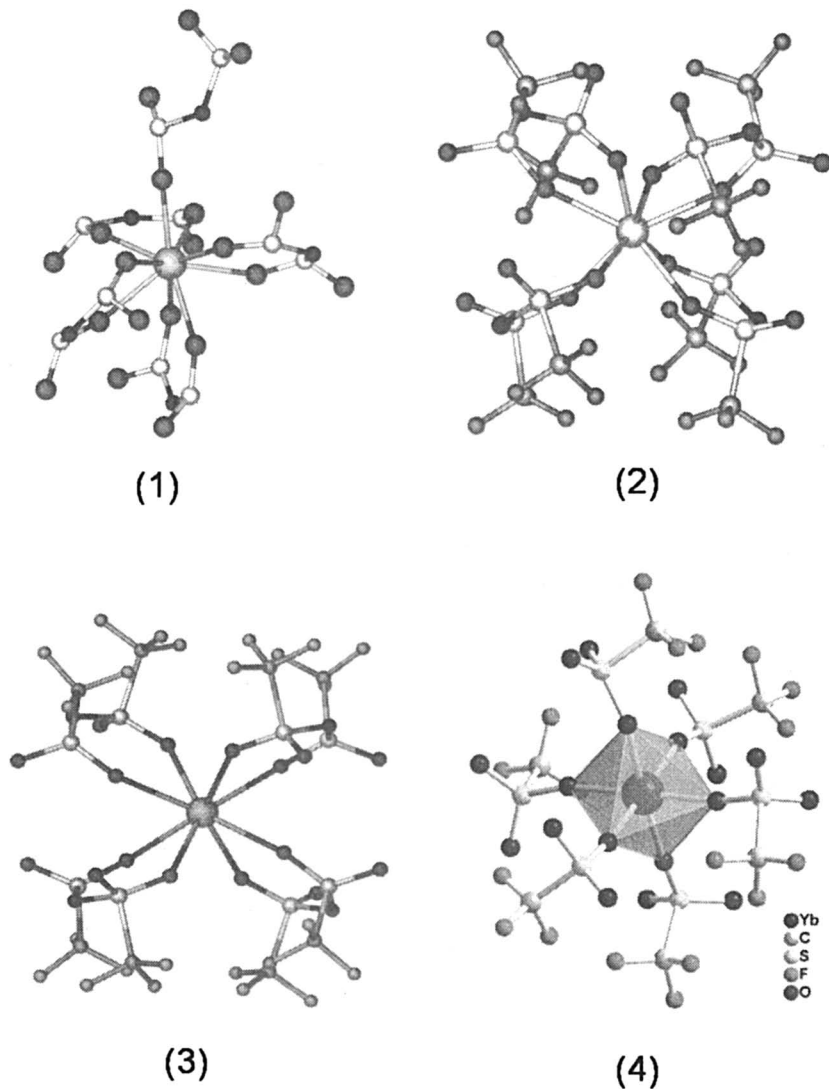


Figure 2. Lanthanide coordination in the compounds $[\text{bmpyr}]_2[\text{Ln}(\text{Tf}_2\text{N})_5]$ ($\text{Ln} = \text{Pr-Tb}$, CF_3 groups omitted for clarity) (1), $[\text{bmpyr}][\text{Ln}(\text{Tf}_2\text{N})_4]$ ($\text{Ln} = \text{Dy-Lu}$) (2), $[\text{mppyr}][\text{Yb}(\text{Tf}_2\text{N})_4]$ (3) and $[\text{bmpyr}]_3[\text{Yb}(\text{OTf})_4]$. $\text{bmpyr} = 1\text{-butyl-1-methylpyrrolidinium}$, $\text{mppyr} = 1\text{-methyl-1-propyl-pyrrolidinium}$, $\text{Tf}_2\text{N} = \text{bis}(\text{trifluoromethanesulfonyl})\text{amide}$.

(Fig. 2, (2)) which resembles a trigonal dodecahedron. This coordination polyhedron is generally preferred over a cube whenever ligand-ligand repulsion becomes important for coordination number eight. The oxygen coordination of the smaller lanthanide centers is accomplished by eight bidentately coordinating bis(trifluoromethanesulfonyl)amide ligands which adopt both, the *cisoid* and *transoid* conformations. In case of the trivalent Ln-Tf₂N complexes a small but distinct change of about 6 pm in the S—O interatomic distances within the bis(trifluoromethane-sulfonyl)amide ligand can be detected upon coordination. With only 2-3 pm this change in the S—O bond distance is far less pronounced in the complex compounds of divalent cations [mppyr]₂[M(Tf₂N)₄], M = Ca, Sr⁶ and Yb.⁷ Raman spectra of [mppyr]₂[M(Tf₂N)₄], M = Ca, Sr, Yb show how the S-O modes of the Tf₂N anion are affected upon coordination to the metal (Fig. 3).

The divalent metal cations in [mppyr]₂[M(Tf₂N)₄], M = Ca, Sr, Yb principally feature the same coordination environment as it is observed for the smaller trivalent lanthanides in [bmpyr][Ln(Tf₂N)₄] (Ln = Dy-Lu) with the major difference that all the Tf₂N ligands around the divalent cations adopt exclusively a *cisoid* conformation. It is noteworthy that ytterbium both in the divalent and the trivalent oxidation state shows nearly the same coordination by Tf₂N (c.f. Fig. 1 (2) and (3)). [bmpyr]₃[Yb(OTf)₆] (Fig. 1 (4)) represents the first example of a structure featuring a lanthanide in a (homoleptic) triflate environment. In this case Yb³⁺ is surrounded by an only slightly distorted octahedron of triflate ligands. The compound was obtained from solution of Yb(OTf)₃ in [bmpyr][OTf].⁸

Optical Properties of Lanthanides in Ionic Liquids

In order to correlate the solid state structure with structures present in the liquid state optical absorption and emission spectra of lanthanide ions have been studied in the liquid state and compared with the respective solid state structures.

Upon dissolution of lanthanide triiodides in a Tf₂N-based ionic liquid two lanthanide species form according to Figure 1 – one contains the lanthanide cation surrounded solely by iodide anions and in the other one the cation is exclusively coordinated by the oxygen atoms belonging to the Tf₂N-anions. Indeed, this finding is not only backed by single X-ray structure analysis but can also be confirmed by absorption spectroscopy. Fig. 4, left, shows the absorption spectrum of a solution of neodymium triiodide in [C₁₂mim][Tf₂N] (C₁₂mim = 1-dodecyl-3-methylimidazolium). Comparison of the shape of the ⁴I_{9/2} → ⁴G_{5/2} hypersensitive transition reveals that the line shape can be explained by a superposition of the absorption spectra of NdBr₃ in [hmim][Br] (hmim = 1-hexyl-3-methylimidazolium) where neodymium is exclusively found in a halide environment, and Nd(OTf)₃ in [emim][OTf] (emim = 1-ethyl-3-methyl-

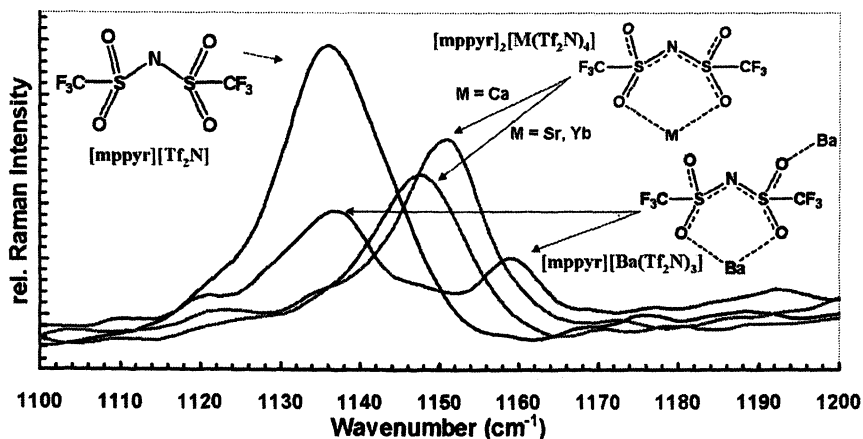


Figure 3. Raman spectra of $[mppyr][Tf_2N]$ and $[mppyr]_2[M(Tf_2N)_4]$, $M = Ca, Sr$ and Yb .

imidazolium), where neodymium is solely coordinated by oxygen atoms of the triflate ligands.

Spectroscopic investigations of trivalent lanthanides in ionic liquids cannot only help to establish the coordination environment but also show that these solvents are promising media for generating liquid or liquid crystalline luminescent materials. Evaluation of the luminescence spectra of NdI_3 in $[C_{12}mim][Tf_2N]$ show a luminescence lifetime of $15.3 \mu s$ for the most intense ${}^4F_{3/2} \rightarrow {}^4I_{11/2}$ transition. The quantum yield amounts to $1.5 \pm 0.2 \%$. While the quantum yield is in the typical range when the lanthanide ion itself is excited, the lifetime of the excited state is astonishingly high, especially when taking into account that the spectrum was recorded at room temperature in the liquid state for an ion that emits in the near-infrared. Especially these low energy transitions are prone to radiationless quenching by multiphonon relaxation processes. For the ${}^4I_{15/2} \rightarrow {}^4I_{13/2}$ emission of ErI_3 which also lies in the near infrared, a lifetime of $10.4 \mu s$ was measured. In case of DyI_3 which shows a green luminescence in the visible region of light, a lifetime of even $63.3 \mu s$ for the ${}^4F_{9/2} \rightarrow {}^4I_{11/2}$ transition could be determined.¹⁰ The reasons for the comparatively high lifetimes of excited states of lanthanide ions in the liquid state in Tf_2N -based ionic liquids compared to conventional solvents origins from a combination of different factors. First, the lanthanide ion in these systems is either coordinated by halide or Tf_2N ligands. In both cases no C-H, N-H and O-H oscillators are introduced into the inner coordination sphere of the lanthanide ion which would

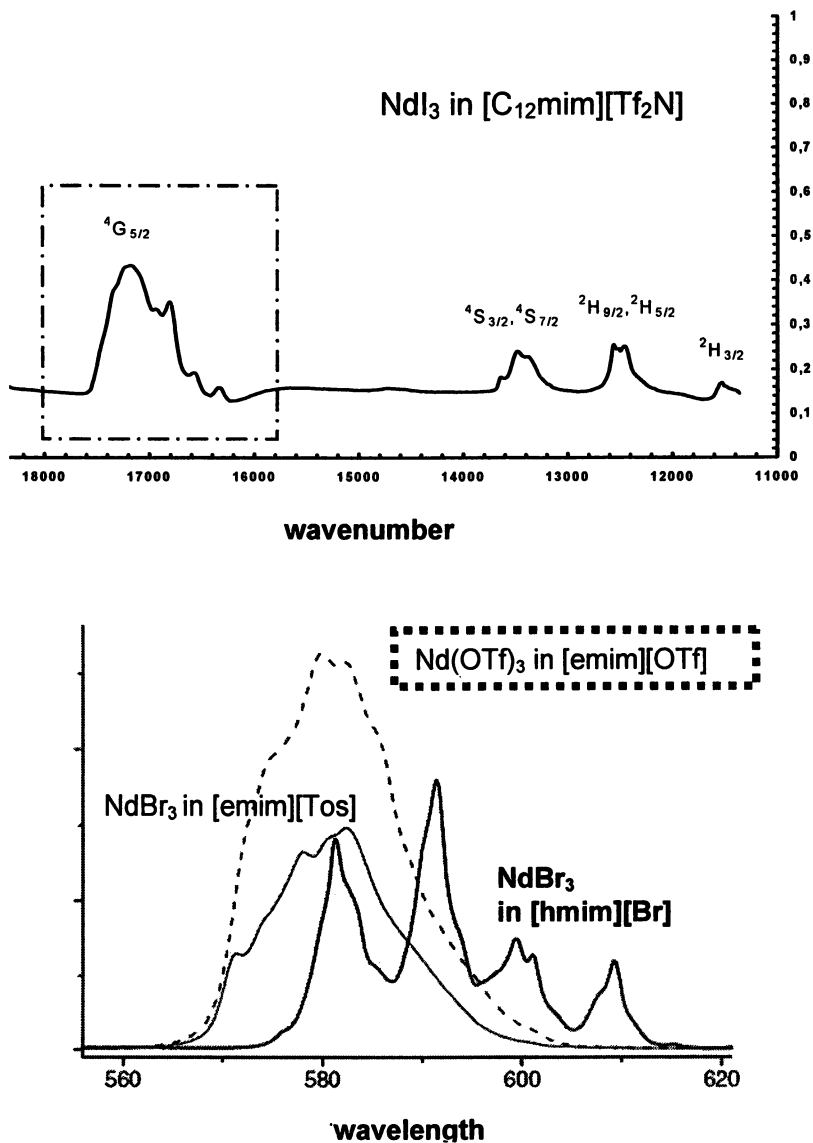


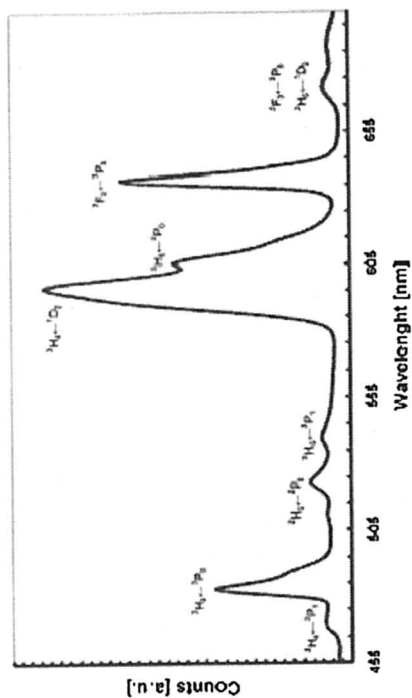
Figure 4. Absorption spectra of NdI₃ in [C₁₂mim][Tf₂N] (left). Absorption spectra of NdBr₃ in [hmim][Br], NdBr₃ in [emim][Tos] and Nd(OTf)₃ in [emim][OTf] according to K. Binnemans, K. Driesen, P. Nockemann, *Chem. Phys. Lett.* 2004, 4, 306.

readily lead to a quenching of the luminescence due to vibronic coupling. Furthermore, energy transfer between the lanthanide center and the ligand is minimized because of the weakly coordinating power of the bis-(trifluoromethanesulfonyl)amide anion and the heavy halide ligand. This also becomes evident when studying the emission spectra of both $\text{Pr}(\text{Tf}_2\text{N})_3$ and PrI_3 in $[\text{bmpyr}][\text{Tf}_2\text{N}]$ (Fig. 5). Comparatively well resolved and intense emissions from the ^3P levels in the low energy region of the spectrum (455 – 555 nm) can be observed in solution. In case of the solid compounds $[\text{bmpyr}]_2[\text{Pr}(\text{Tf}_2\text{N})_3]$ and $[\text{bmpyr}]_4[\text{PrI}_6][\text{Tf}_2\text{N}]$ these transition naturally become more intense as the lanthanide environment is more rigid in the solid. In case of solid $[\text{bmpyr}]_4[\text{PrI}_6][\text{Tf}_2\text{N}]$ where the iodide anions provide a rigid environment together with a high oscillator mass these transitions become even the most intense. Owing to the careful shielding of the lanthanide centres not only from X-H bonds but also from each other, unusually high dopant concentrations (both solid compounds have a lanthanide dopant concentration of 100%) can be achieved without observing any concentration quenching.¹¹

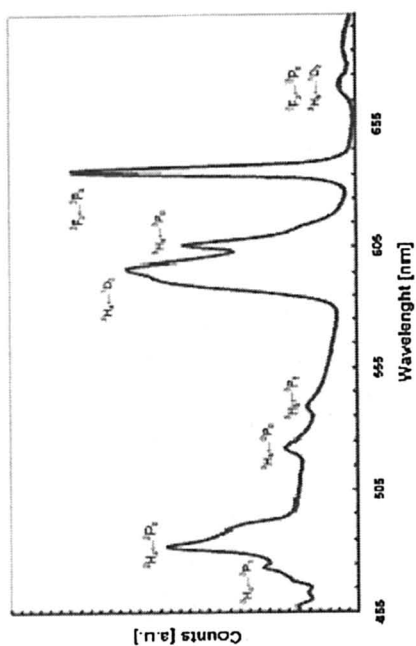
Low Valent Lanthanides in Ionic Liquids

Reduction reactions are one of the most basic types of chemical transformation reactions. For organometallic and especially for organic synthesis, reducing agents that can tolerate certain functional groups, but are still powerful reductants, are desirable. Kagan's reagent, SmI_2 , is a mild reducing agent which has the advantage that it can withstand certain functional groups. Because of this, it and its derivatives have found widespread application in organic synthesis for the selective reduction of functional groups and C-C bond formation.¹² To a lesser extent than $\text{Sm}(\text{II})$, $\text{Eu}(\text{II})$ and $\text{Yb}(\text{II})$ have found use as reducing agents. The application of divalent lanthanides other than $\text{Eu}(\text{II})$, $\text{Yb}(\text{II})$ and $\text{Sm}(\text{II})$ as reductants for chemical transformations appear promising as the reduction potential can be nearly continuously tuned by the choice of the lanthanide cation. Theoretical calculations together with thermodynamic estimations and optical measurements draw a coherent picture: The redox potentials of $\text{Ln}^{3+}/\text{Ln}^{2+}$ span a range of approximately 0.5 to 4 V vs. NHE.¹³ Many binary halides of divalent lanthanides are known to exist in the solid state and have been well characterized: the fluorides LnF_2 (Sm , Eu , Yb), the chlorides LnCl_2 (Nd , Sm , Eu , Dy , Tm , Yb), the bromides LnBr_2 (Nd , Sm , Eu , Dy , Tm , Yb) and the iodides LnI_2 (La , Ce , Pr , Nd , Sm , Eu , Gd , Dy , Tm , Yb).¹⁴ Although the divalent state has not been established for Tb , Ho , Er and Lu , subvalent compounds with metal-metal bonds like $[\text{Tb}_{10}(\text{C}_2)_2]\text{Br}_{18}$,¹⁵ $[\text{Ho}[\text{Ho}_6\text{C}]\text{I}_{12}]$,¹⁶ $\text{Cs}_2\text{Lu}[\text{Lu}_6\text{C}]\text{Cl}_{18}$ ¹⁷ and $[\text{Er}_{10}(\text{C}_2)_2]\text{Br}_{18}$ ¹⁸ are known. Consequently, valence states lower than the "traditional" oxidation state of +III have been identified for all

solution of PrI_3 in $[\text{bmpyr}][\text{Tf}_2\text{N}]$



solution of $\text{Pr}(\text{Tf}_2\text{N})_3$ in $[\text{bmpyr}][\text{Tf}_2\text{N}]$



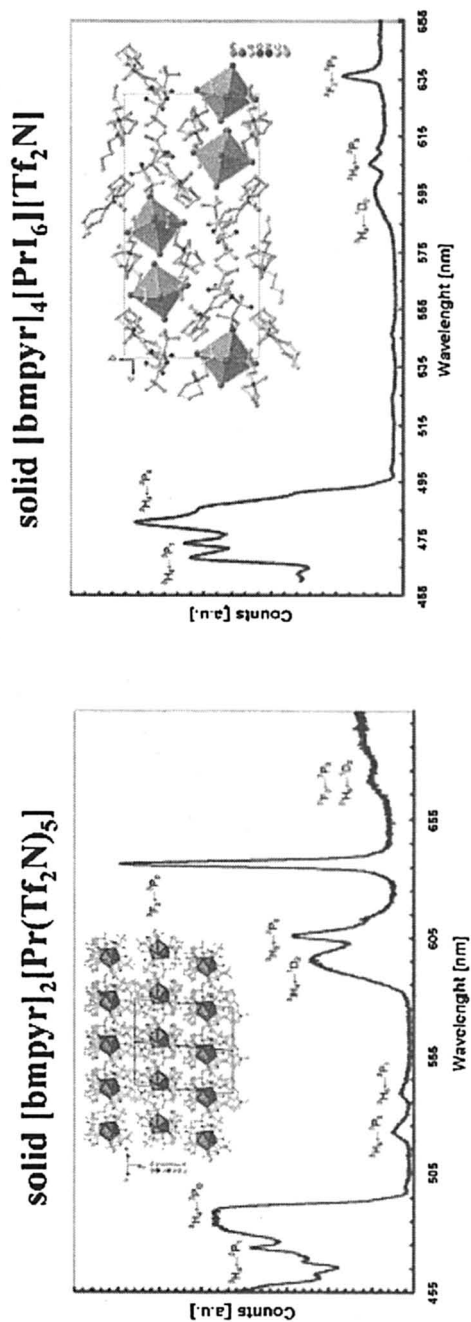


Figure 5. Emission spectra of a solution of Pr(Tf₂N)₃ (top left) and PrI₃ (top right) in [bmpyr][Tf₂N] as well as of the solid compounds [bmpyr]₂[Pr(Tf₂N)₅] and [bmpyr]₄[PrI₆][Tf₂N]. All spectra were recorded at room temperature.

(non-radioactive) lanthanides. So far solution chemistry is only known for the divalent lanthanide cations which form salt-like binary halides. Unfortunately, for the plethora of other divalent lanthanides (La, Ce, Pr, Nd, Gd, Dy, Tm), little to no solution chemistry and hence organometallic chemistry is known. Reasons for this can be found in the comparatively difficult synthesis and high reactivity of the divalent state of these lanthanides in solution. In the past few years, enormous advancements were made with the characterization of divalent Tm, Dy and Nd compounds in solution¹⁹. Recently it was shown that $\text{DyI}_2(\text{THF})_5$ is able to couple halogenoalkanes in contrast to SmI_2 due to its more negative redox potential.²⁰ $\text{DyI}_2(\text{DME})_3$ was also used as a reductant in organic synthesis.²¹ Similarly, TmI_2 can function as a much more powerful replacement for SmI_2/HMPA . Ketone coupling can be accomplished with NdI_2 .²² In order to perform this chemistry - which is already known in the solid state - also accessible in solution, we aim at the synthesis of specifically designed ionic liquids.

Cyclic voltammetry studies of the redox potential of the lanthanides in ionic liquids show that the reduction potentials are lower in bis(trifluoromethanesulfonyl)amide based ionic liquids in comparison to conventional solvents like THF. SmI_2 , the only lanthanide iodide for which reliable electrochemical data are available in various solvents, shows in the ionic liquid $[\text{mppyr}][\text{Tf}_2\text{N}]$ ($\text{mppyr} = N\text{-methyl-}N\text{-propyl-pyrrolidinium}$) a reduction potential of -0.222 V vs. Fc^+/Fc , Fig. 6. Upon addition of an equimolar amount of $[\text{mppyr}][\text{OTf}]$ ($\text{OTf} = \text{triflate}$) the potential is increased to -0.493 V . For comparison, SmI_2 exhibits in THF a reduction potential of -1.51 V . An increased reduction potential upon addition of triflate anions can also be observed in THF: $\text{Sm}(\text{OTf})_2$ has a reduction potential of -2.01 V in THF. An analogous shift of reduction potentials is observed for Eu^{2+} when comparing the reduction potentials of $\text{Eu}(\text{Tf}_2\text{N})_3$ in $[\text{bmpyr}][\text{Tf}_2\text{N}]$, $\text{Eu}(\text{OTf})_3$ in $[\text{bmpyr}][\text{Tf}_2\text{N}]$ and $\text{Eu}(\text{OTf})_3$ in $[\text{bmpyr}][\text{OTf}]$.²³ The weaker the ligand that coordinates to the divalent lanthanide the weaker its reducing power.

In summary, divalent lanthanides seem to be far less reducing in weakly coordinating ionic liquids based on Tf_2N than in THF. Thus it can be expected that it is possible to stabilize other, higher reducing low valent lanthanides in these media. Electrochemical measurements indicate that in the case of the trivalent lanthanide bis(trifluoromethanesulfonyl)amides $\text{Dy}(\text{Tf}_2\text{N})_3$ and $\text{Nd}(\text{Tf}_2\text{N})_3$ the lanthanide can be reduced to the metal in $[\text{bmpyr}][\text{Tf}_2\text{N}]$ and deposited as a thin film.²⁴ The use of triethylsulfonium based ionic liquids which were claimed by other groups to have a large stability towards reduction lead in the presence of SmI_2 and NdI_2 only to decomposition of the ionic liquid.²⁵

Acknowledgements

This research was supported by the Deutsche Forschungsgemeinschaft within the framework of the priority program "Lanthanide Specific

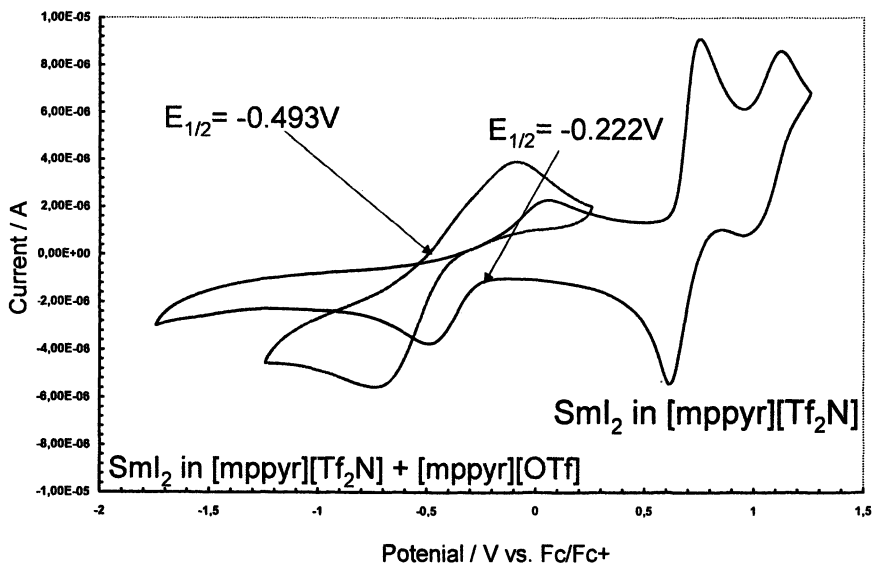


Figure 6. Dependence of the $\text{Sm}^{3+}/\text{Sm}^{2+}$ redox potential on the counterion of the ionic liquid.

Functionalities” and the Fonds der Chemischen Industrie. AVM thanks the Universität zu Köln and especially Prof. Dr. Gerd Meyer for generous support.

References

1. See for example: V. Gutmann, *Coordination Chemistry in Non-Aqueous Solutions*, Springer Verlag, Wien, New York, 1968; Ch. Reichard, *Solvents and Solvent Effects in Organic Chemistry*, Wiley-VCH, Weinheim, 2003.
2. ICSD data base.
3. A. Babai, A.-V. Mudring, *Chem. Mat.* **2005**, *17*, 6230 ;A. Babai, A.-V. Mudring, *J. Alloys Compd.* **2006**, *418*, 204; A. Babai, A.-V. Mudring, *Inorg. Chem.* **2006**, *45*, 4874.
4. A. Chaumont, G. Wipff, *Chem. Eur. J.* **2004**, *10*, 3919; A. Chaumont, G. Wipff, *J. Phys. Chem. B* **2004**, *108*, 3311; A. Chaumont, G. Wipff, *Inorg. Chem.* **2004**, *43*, 5891; A. Chaumont, G. Wipff, *Phys. Chem. Chem. Phys.* **2005**, *7*, 1926; C. Gaillard, I. Billard, A. Chaumont, S. Mekki, A. Ouadi, M.A. Denecke, g. Moutiers, G Wipff, *Inorg. Chem.* **2005**, *44*, 8355; N. Sieffert, G. Wipff, *J. Phys. Chem. A* **2006**, ASAP.
5. A. Babai, A.-V. Mudring, *Dalton Trans.* **2006**, 1828.
6. A. Babai, A.-V. Mudring, *Inorg. Chem.*, **2005**, *44*, 8168.

7. A. Babai, A.-V. Mudring, *Angew. Chem. Int. Ed.* **2005**, *44*, 5485.
8. A. Babai, A.-V. Mudring, publication in progress.
9. S. Arenz, A. Babai, K. Binnemans, K. Driesen, R. Giernoth, A.-V. Mudring, P. Nockemann, *Chem. Phys. Lett.*, **2005**, *402*, 75.
10. A. Babai, A.-V. Mudring, S. Arenz, R. Giernoth, P. Nockemann, *Z. Anorg. Allg. Chem.* **2004**, *630*, 1697; A.-V. Mudring, A. Babai, S. Arenz, R. Giernoth, K. Binnemans, K. Driesen, P. Nockemann, *J. Alloys Comp.* **2006**, *418*, 204.
11. A. Babai, A.-V. Mudring, *Chem. Mat.* **2005**, *17*, 6230.
12. A. Kreif, A.M. Laval, *Chem. Rev.* **1999**, *99*, 745; G.A. Molander, B. La Belle, B. Hahn, *J. Org. Chem.* **1986**, *51*, 5259; K. Otsubo, J. Inanaga, M. Yamaguchi, *Tetrahedron Lett.* **1987**, *28*, 4437; M. Miyashita, M. Hoshio, T. Suzuki, A. Yoshikoshi, *Chem. Lett.* **1988**, 507; P. Girard, J.-L. Namy, Kagan, *J. Am. Chem. Soc.* **1980**, *102*, 2963; M. Matsukawa, Tabuchi, J. Inanaga, M. Yamaguchi, *Chem. Lett.* **1987**, 2101; T. Tabuchi, J. Inanaga, M. Yamaguchi, *Tetrahedron Lett.* **1986**, *27*, 601; J. Inanaga, Ishikawa, Yamaguchi, *Chem. Lett.* **1987**, 1485; G.A. Molander, B. Hahn, *J. Org. Chem.* **1986**, *51*, 1125; B. Hamann-Gaudinet, J. L. Namy, H. B. Kagan, *J. Organomet. Chem.* **1998**, *567*, 39; J. Soupe, J.-L. Namy, H.-B. Kagan, *Tetrahedron Lett.* **1984**, *25*, 2869; J. Collin, J.-L. Namy, F. Dalemer, H.-B. Kagan, *J. Org. Chem.* **1991**, *56*, 3118; K. Kusuda, J. Inanaga, M. Yamaguchi, *Tetrahedron Lett.* **1989**, *30*, 2945; T. Imamoto, N. Takiyama, *Tetrahedron Lett.* **1987**, *28*, 1307; (b) B. Molander, L. S. Haring, *J. Org. Chem.* **1989**, *54*, 3525; H.-B. Kagan, J.-L. Namy, P. Girard, *Tetrahedron Lett. Suppl.* **1981**; *37*, 175; T. Tabuchi, K. Kawamura, J. Inanaga, M. Yamaguchi, *Tetrahedron Lett.* **1986**, *27*, 3889; G. A. Molander, J. B. Etter, *J. Am. Chem. Soc.* **1987**, *109*, 6556; Y. Kamochi, T. Kudo, *Chem. Lett.* **1991**, 893; A. S. Kende, J. S. Mendoza, *Tetr. Lett.* **1991**, *32*, 1699; J.-L. Namy, J. Soupe, H.-B. Kagan, *Tetrahedron Lett.* **1983**, *24*, 765; E. J. Enholm, D. C. Forbes, D. P. Holub, *Synth. Commun.* **1990**, *20*, 981; Imamoto, Nishimura, *Chem. Lett.* **1990**, 1141; Y. Kamochi, T. Kudo, *Tetrahedron Lett.* **2000**, *41*, 341; L. Lu, H. Y. Chang, J. M. Fang, *J. Org. Lett.* **1999**, *1*, 1989.
13. D.A. Johnson, *J. Chem. Soc. Dalton* **1974**, 1671; L.R. Morss, *Chem. Rev.* **1976**, *76*, 827; L.J. Nugent, R.D. Bayarz, J.L. Burnett, J.L. Ryan, *J. Phys. Chem.* **1973**, *77*, 1528; N.B. Mikheov, *Zh. Neorg. Khim.* **1984**, *29*, 450; P. Strange, A. Svane, W.M. Temmerman, Z. Szotek, H. Winter, *Nature* **1999**, *399*, 756; P. Dorenbos, *Chem. Mat.* **2005**, *17*, 6452.
14. G. Meyer, *Chem. Rev.* **1988**, *88*, 93.

15. F. Steffen, G. Meyer, *Z. Naturforsch.* **1995**, *50B*, 1570.
16. C. Hohnstedt, G. Meyer, *Z. Anorg. Allg. Chem.* **1993**, *619*, 1374.
17. H.M. Artelt, G. Meyer, *J. Chem. Soc., Chem. Comm.* **1992**, 460.
18. S. Uhrlandt, G. Meyer, *Z. Anorg. Allg. Chem.* **1994**, *620*, 1872.
19. M.N. Bochkarev, I.L. Fedushkin, A.A. Fagin, T.V. Petrovskaya, J.W. Ziller, R.N.R. Broohall-Dillard, W.J. Evans, *Angew. Chem. Int. Ed.* **1997**, *36*, 133; M. C. Cassani, M. L. Lappert, F. Saschi, *Chem. Commun.* **1997**, 1563; M. C. Cassani, D. J. Duncalf, M. L. Lappert, *J. Am. Chem. Soc.* **1998**, *120*, 12958; M.N. Bochkarev, A.A. Fagin, *Chem. Eur. J.* **1999**, *5*, 2990; W. J. Evans, N. T. Allen, *J. Am. Chem. Soc.* **2000**, *122*, 2118; W. J. Evans, N. T. Allen, J. W. Ziller, *J. Am. Chem. Soc.* **2000**, *122*, 11749; M. N. Bochkarev, I. L. Fedushkin, S. Dechert, A. A. Fagin, H. Schumann, *Angew. Chem.* **2001**, *113*, 3268; I.L. Fedushkin, M.N. Bochkarev, S. Dechert, H. Schumann, *Chem. Eur. J.* **2001**, *7*, 3558; W.J. Evans, N.T. Allen, J.W. Ziller, *J. Am. Chem. Soc.* **2001**, *123*, 7927; W.J. Evans, N.T. Allen, J.W. Ziller, *Angew. Chem.* **2002**, *114*, 369; W.J. Evans, *J. Organomet. Chem.* **2002**, *647*, 2; W.J. Evans, G. Zucchi, J. W. Ziller, *J. Am. Chem. Soc.* **2003**, *125*, 10; D. Turcitu, F. Nief, L. Richard, *Chem. Eur. J.* **2003**, *9*, 4916; M.N. Bochkarev, G.V. Khoroshenkov, H. Schumann, S. Dechert, *J. Am. Chem. Soc.* **2003**, *125*, 2894; W.J. Evans, D.S. Lee, J.W. Ziller, *J. Am. Chem. Soc.* **2004**, *126*, 454; M.N. Bochkarev, *Coord. Chem. Rev.* **2004**, *248*, 835; U. Groth, M. Jeske, *Synlett* **2001**, 129; U. Groth, M. Jeske, *Angew. Chem.* **2000**, *39*, 574.
20. W. J. Evans, *Coord. Chem. Rev.* **2000**, *206/207*, 263.
21. W.J. Evans et al., *J. Am. Chem. Soc.* **2000**, *122*, 11749.
22. W.J. Evans, P.S. Workman, N.T. Allen, *Org. Lett.* **2003**, *5*, 2041.
23. A. Babai, A.-V. Mudring, publication in progress.
24. A. Babai, A.-V. Mudring, publication in progress.
25. A. Babai, A.-V. Mudring, *Inorg. Chem.* **2005**, *44*, 8168.

Chapter 13

Electropolishing and Electroplating of Metals Using Ionic Liquids Based on Choline Chloride

Andrew P. Abbott*, Katy J. McKenzie, and Karl S. Ryder

Chemistry Department, University of Leicester,
Leicester LE1 7RH, United Kingdom

*Corresponding author: email: andrew.abbott@le.ac.uk;
fax: +44 116 252 3789

Eutectic based ionic liquids containing choline chloride are shown to be useful for electrochemical applications that currently use aqueous solutions. It is shown that an ionic liquid composed of ethylene glycol (HOCH₂CH₂OH) and choline chloride (HOC₂H₄N(CH₃)₃⁺Cl⁻) offers the first practical alternative to the use of phosphoric and sulphuric acid mixtures for the electropolishing of type 316 stainless steel. The mechanism has been elucidated and it is shown to be significantly different in an ionic liquid from that observed in aqueous solutions. Results from large-scale testing show, that for several types of steel, surface finishes at least as good as aqueous solutions can be obtained. A recycling protocol has been developed for the ionic liquid, which allows full metal recovery. We also demonstrate that these mixtures and the corresponding analogue with urea can be used for the deposition of a wide range of metals and alloys. Judicious choice of ionic liquid can, not only affect the morphology of the deposit obtained but also the composition of metals in the alloy.

Introduction

Over the last twenty years ionic liquids have been of considerable interest for a wide variety of electrochemical and synthetic applications. [1-4] Most of the studies have concentrated on imidazolium and pyridinium cations, however their high cost and sensitivity to water has made them of little practical use for large-scale metal finishing applications. We have developed a variety of eutectic type ionic liquids based on choline chloride. This salt is of particular interest because it is simple to make in a one-step, gas phase reaction with a quantitative yield from widely available precursors (trimethylamine, ethylene oxide and HCl). The salt is widely available, biodegradable and non-toxic. Eutectic mixtures of this quaternary ammonium salt with metal salts [5-7] or hydrated metal salts [8,9] can be used for the efficient electrodeposition of metals such as zinc and chromium.

The principle of forming an ionic liquid by complexation of the halide anion has been extended by mixing quaternary ammonium salts with compounds that form hydrogen bonds. This has been demonstrated with a range of hydrogen bond donors (HBDs) including amides such as urea [10] and carboxylic acids such as oxalic acid [11]. We have previously shown that these liquids can be used for the dissolution of metal oxides [12] and with a eutectic mixture of ethylene glycol as the hydrogen bond donor; choline chloride can be used for the electropolishing of stainless steel. [13] This process has the advantage that high current efficiencies are obtained with negligible gas evolution at the anode/solution interface. The liquid is comparatively benign and non-corrosive compared to the current aqueous phosphoric and sulphuric acid solutions used.

In the present study we use a.c. impedance, linear sweep voltammetry and chronoamperometry to investigate the mechanism of electropolishing in these glycol mixtures. The dissolution mechanism is complex making steady-state measurements difficult because the surface is etched up to 1 μm during the measurement timescale. We also show that choline chloride based ionic liquids can be used for the electrodeposition of zinc alloys.

Experimental

Choline chloride (ChCl) (Aldrich 99%) was recrystallised from absolute ethanol, filtered and dried under vacuum. Urea (Aldrich >99%) was dried under vacuum prior to use. Ethylene glycol (EG) (Aldrich 99+%) was used as received. The eutectic-based ionic liquid 'Ethaline 200' was formed by stirring the two components (1 ChCl: 2 EG) at 75°C until a homogeneous colourless liquid was formed. Voltammetry and impedance were carried out using an Autolab PGSTAT12 potentiostat fitted with an FRA impedance module and controlled using GPES software. Frequency spectra were collected in the range 10000 - 0.01 Hz. A three-electrode system consisting of a type 316 stainless steel (SS316) disc working electrode (0.5 mm radius), sealed in glass, a

platinum counter electrode and a silver wire reference electrode were used. The working electrode was abraded with 150 grit glass paper, rinsed and dried prior to all measurements to ensure reproducible voltammetric behaviour. Electrochemical measurements were performed at 20°C and a scan rate of 20 mVs⁻¹ was used in voltammetric experiments except where stated.

Surface analysis was carried out using scanning electron microscopy (SEM) (Philips XL30 ESEM). Atomic Force Microscopy (AFM) images were obtained using a Digital Instruments Nanoscope 4 run using contact mode in the ionic liquid. In the Hull cell experiments a stainless steel anode plate was used with a nickel plate as the cathode. Both electrodes were degreased using hexane and dried prior to use. Bulk electrolysis experiments were performed using a Thurlby Thandar power supply. Following electrolysis the anode was washed with deionised water and dried.

Results and Discussion

Electropolishing

Figure 1 (dotted line) shows the voltammetry of a type 316 stainless steel wire disc electrode abraded then immersed in a sulphuric, phosphoric acid and water mixture (volume ratio = 3:1:1). The current reaches a maximum at approximately 1.1 V before decreasing and then increasing again. This is due to the formation of a film at the electrode surface. The dissolution process has been described by two main models; the duplex salt model, which describes a compact and porous layer at the iron surface, [14] and an adsorbate-acceptor mechanism, which looks at the role of adsorbed metallic species and the transport of the acceptor which solubilises them. [15] Voltammetry of the same electrode, pre-treated by the same procedure, in an ionic liquid 1ChCl:2EG (Ethaline 200) shows negligible current over the voltage range suggesting that the metal does not dissolve. When the surface is abraded in-situ a peak shaped response is observed showing that the metal does dissolve once the oxide film is removed. Hence it can be concluded that oxide removal is vital to the electropolishing mechanism.

Impedance spectroscopy confirms that the dissolution mechanism in an ionic liquid is different from that in aqueous acidic solutions. Preliminary results suggest that a diffusion limited process in the viscous ionic liquid appears to be responsible for electropolishing [16]. Impedance spectroscopy has also shown that one of the main differences between the electropolishing mechanism in the ionic liquid and the aqueous solution is the rate at which the oxide is removed from the electrode surface.

A highly polished surface could be obtained with current densities between *c.a.* 70 and 50 mA cm⁻² with an applied voltage of 8 V. Below this current density a milky surface was obtained and above this range some pitting of the

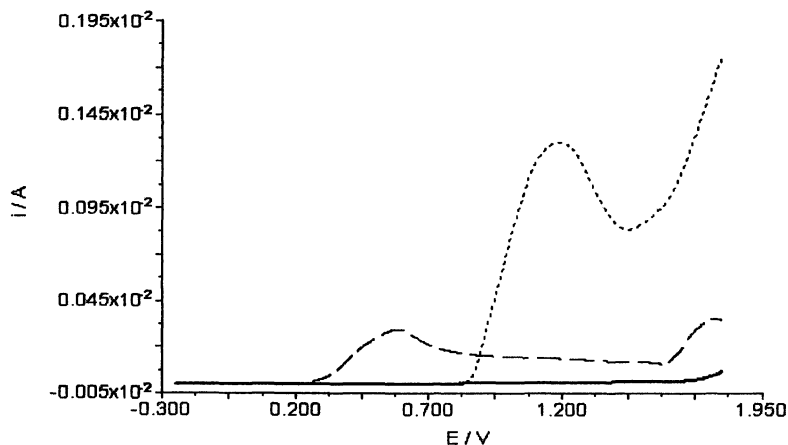


Figure 1. Linear sweep voltammograms (scan rate 20 mV s^{-1}) for a type 316 stainless steel wire disc electrode abraded then immersed in sulphuric/ phosphoric acid mixture (dotted line), and abraded in-situ in fresh 1ChCl: 2 EG mixture (dashed line).

surface was obtained on an otherwise bright surface. It should be noted that the polishing region was narrower than that in aqueous phosphoric/ sulphuric acid mixtures, however the current density requirements were considerably lower using the ionic liquid. In acidic solutions typical current densities are 100 mA cm^{-2} but much of this results in gas evolution at the anode. With the ionic liquid negligible gas evolution was observed suggesting that there are negligible side reactions occurring with the ionic liquid. The current efficiency of the 1ChCl: 2EG (Ethaline 200) electrolyte has been determined using coulometry and gravimetry and was found to be in excess of 90% which is significantly higher than the aqueous based electrolytes which are typically $\sim 30\%$. Given that the current density used for the 1ChCl: 2EG electrolyte is considerably lower than that used in the aqueous solution the slight difference in the conductivity of the two solutions does not lead to a significance in the ohmic loss through the solution. In fact preventing a passivating layer at the electrode surface during polishing decreases the overall ohmic resistance of the non-aqueous system. Hence the current going to metal dissolution is probably similar for the two systems explaining why the polishing process takes approximately the same time.

Similar experiments were carried out using different grades of stainless steel (410, 302, 304, 316 or 347) and it was found that the mechanism of metal dissolution and the oxidation potentials for the metals were very similar. The slight exception was the 410 series steel (which has no Ni unlike the 300 series

steels which have 8-14 %). The 410 steel required a more positive oxidation potential to break down the oxide in the ionic liquid whereas once the oxide was removed the metal was more easily oxidised than the other grades of steel. This shows why the 410 steel was more likely to pit during the polishing process. The pitting could be reduced, however, by chemically picking the steel with a proprietary phosphoric acid etch before electropolishing.

This technology has been scaled-up to a 1.3 tonne plant. Results have shown that the technology can be applied in a similar manner to the current technology. The ionic liquid has been found to be compatible with most of the materials used in current electropolishing equipment i.e. polypropylene, nylon tank and fittings, stainless steel cathode sheets and a titanium anode jig. The ionic liquid is kept at c.a. 50°C in an open facility, which is the same as that used for aqueous electropolishing. Figure 2 shows the adsorption of water into a sample of Ethaline 200 at 25 and 45 °C as a function of time. While the liquid is naturally hygroscopic (as is the current phosphoric acid/ sulphuric acid mixture) the composition of water is c.a. 5 wt % and under these conditions a good polish is obtained particularly on cast steel pieces. The quality of the finish is actually relatively unaffected until the water content reaches c.a. 10 wt %. This is common to most chloride based eutectics as the high charge around the anion decreases the activity of the water in the mixture. This contrasts strongly with ionic liquids with discrete, highly fluorinated anions where the presence of traces of water have a significant effect on the potential windows of the liquids.

The ionic liquid electropolishing process is a true drop in technology using the same power supply, tank, fittings and electrodes as the conventional process. The polishing time is also the same as the aqueous process *viz.* 10 minutes. The only parameter that changes is the current density. Figure 3 (overleaf) shows the test facility set up with an electropolishing company in Birmingham, U.K. (Anopol Ltd.)

Extended electropolishing using the same solution leads to a dark green/brown solution arising from the dissolved iron, chromium and nickel. The solubility of the metals in the ionic liquid is relatively high at 50 °C (Fe = 66746, Cr = 9150 and Ni = 3135 ppm). Metal in excess of this concentration precipitates as a dense sludge to the base of the tank. The metals are present as glycolate and chloride complexes and numerous solvents have been tested to determine their efficacy at precipitating the metal salts.

Figure 4 shows samples of the ChCl:2EG (Ethaline 200) ionic liquid saturated with electropolishing residue and the effect that various molecular solvents (in 1:1 volume ratios) have upon the phase behaviour of the metal complexes. It can be seen that acetone and acetonitrile are immiscible with the ionic liquid and while acetonitrile (ACN) brings about precipitation of some of the metal complexes, the solution is still intensely coloured with some of the iron entering the ACN phase.

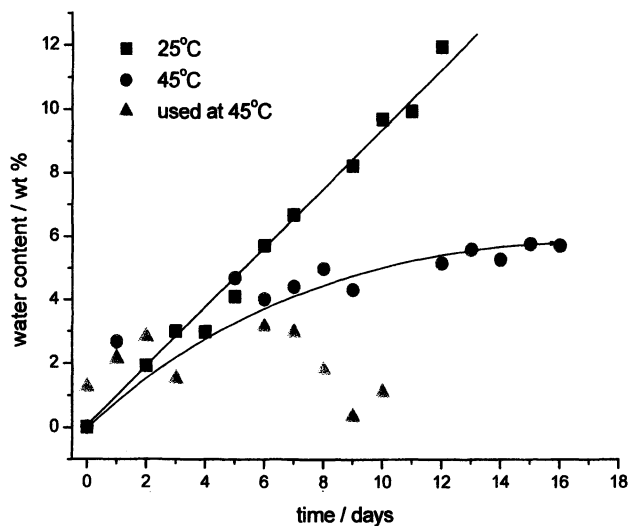


Figure 2: Absorption of water into Ethaline 200 as a function of time and temperature.

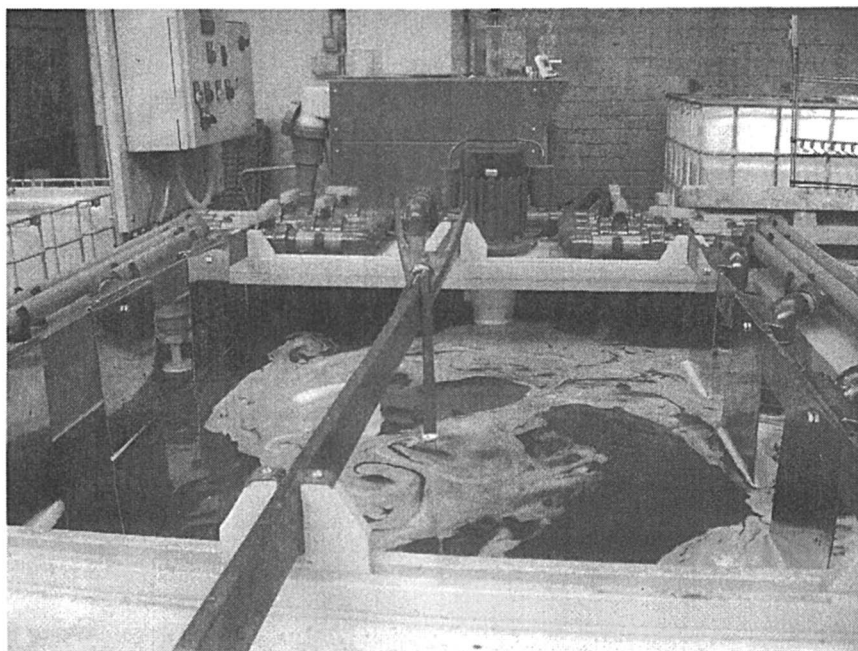


Figure 3. Pilot plant operating at Anopol Ltd using 1.3 tonnes of Ethaline.

The addition of water and ethanol both result in homogeneous liquids and in the case of water the resulting solution was completely transparent and almost all of the metal complex precipitates to the base of the cell. The water could be distilled from the mixture to leave a dry ionic liquid, which had lost only c.a. 15% ethylene glycol, mostly in the form of the metal complex. The residual concentration of each metal in the ionic liquid was less than 5 ppm. Hence not only has it been demonstrated that electropolishing can be carried out in this non-corrosive liquid, but also that the liquid can be completely recycled and all of the metal can be recovered.

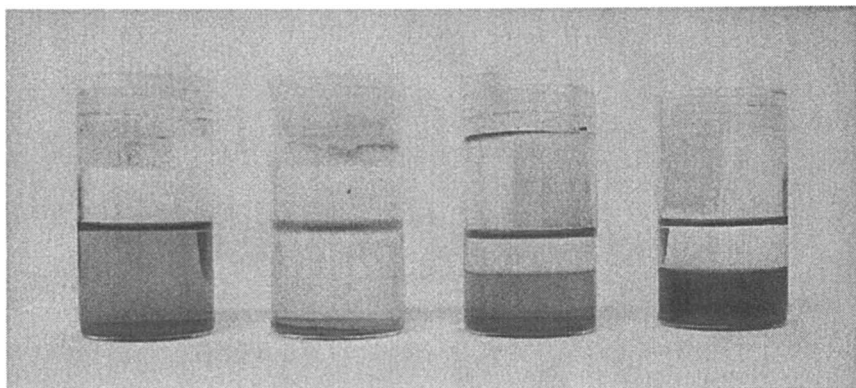


Figure 4. Samples of Ethaline 200 containing electropolishing residue to which equal volumes of (from l to r) ethanol, water, acetonitrile and acetone have been added

Electroplating of Alloys

Zinc and zinc alloys can be electrodeposited from eutectic mixtures of ChCl and ZnCl_2 . These liquids are, however, extremely viscous and have relatively low conductivities. The ethylene glycol (EG) and urea based eutectics have higher conductivities and demonstrate high metal solubilities. Alloys of zinc, particularly with tin are found to have better corrosion resistance than pure zinc, particularly in high humidity conditions and are superior to cadmium deposits in marine environments. It has recently been shown that ionic liquids formed with choline chloride and either urea or ethylene glycol can be used for the electrodeposition of zinc, tin, and zinc-tin alloys. Judicious choice of the hydrogen bond donor affects the type of alloy and the electrochemistry of the components in solution. [17]

Figure 5 shows the voltammetry of ZnCl_2 and SnCl_2 in both the urea and EG mixtures. It is interesting to note that the reduction potential for the tin salt is approximately constant in both liquids but the potential for zinc is shifted to

more negative overpotentials. When the two metal salts are combined in the same solution the electrochemical signal obtained is markedly different to the separate solutions. In EG the deposition of separate phases of Zn and Sn can be observed together with a signal, which appears to be the stripping of a tin rich alloy at c.a. 0 V. For urea, however, only one stripping and one main deposition process were observed.

FAB mass spectra showed no significant cationic metal-containing species are formed. The negative ion spectra showed that when just tin was present, $[\text{SnCl}_3]^-$ was the major species. For the zinc containing liquids a significant difference is observed between the urea and EG systems. In urea the only zinc containing species is ZnCl_3^- whereas in EG ZnCl_3^- , Zn_2Cl_5^- and Zn_3Cl_7^- were detected.

The most probable explanation for the observed differences between zinc chloride in these two liquids is the ligand properties of the two complexing agents. Urea is a stronger ligand than ethylene glycol for ZnCl_3^- . The absence of the HBD from the FAB-MS spectrum is not unexpected as it is rarely seen in metal complexes with this technique. No mixed metal complexes (e.g. ZnSnCl_5^-) were observed in either the urea or EG liquids, which is in contrast to what was found in the $\text{ZnCl}_2/\text{SnCl}_2/\text{ChCl}$ eutectic where it was the dominant species. [5,6] Eutectic mixtures between ChCl and ZnCl_2 are reported to contain ZnCl_3^- , Zn_2Cl_5^- and Zn_3Cl_7^- . The relative proportions of each species have been quantified using potentiometry. [6] It was found that Zn_2Cl_5^- was the predominant species. The observation that no Zn_2Cl_5^- was observed in the urea based liquid suggests that urea acts as a better complexing agent than ZnCl_2 for ZnCl_3^- .

The difference in the species present must change the thermodynamics of metal reduction. Figure 5 shows that the mixed zinc species present in 1ChCl:2EG are easier to reduce than ZnCl_3^- in urea, which supports these ideas. Figure 5 shows that when both metals are combined in the same solution the HBD has a significant effect on the voltammetry (or on the voltammetric response). In the ethylene glycol based ionic liquid, separate deposition and stripping signals are observed for tin and zinc. The zinc deposition response is not as sharp as that observed in Figure 5 for pure zinc, but this would be expected as the deposition of zinc is now occurring on a fresh tin surface rather than platinum. The two stripping potentials occurring on the anodic sweep occur at approximately the same potentials as the individual metals suggesting that this is stripping of the pure metals and that this is a two-phase alloy i.e. discrete zinc and tin phases. When the reductive limit is extended to more negative potentials a third stripping peak is observed at +50 mV which could be due to a third phase consisting of predominantly tin with some zinc. The relative areas under the oxidation peaks vary with the lower reduction limit. The data in Figure 5 compares favourably to the 2 ZnCl_2 / ChCl eutectic with 3 wt % SnCl_2 described previously. [18] However, the difference between the reduction potentials of the two metals in the 2 ZnCl_2 / ChCl eutectic is only 0.341 V which is less than that observed in either of the two solvents seen here and less than the standard

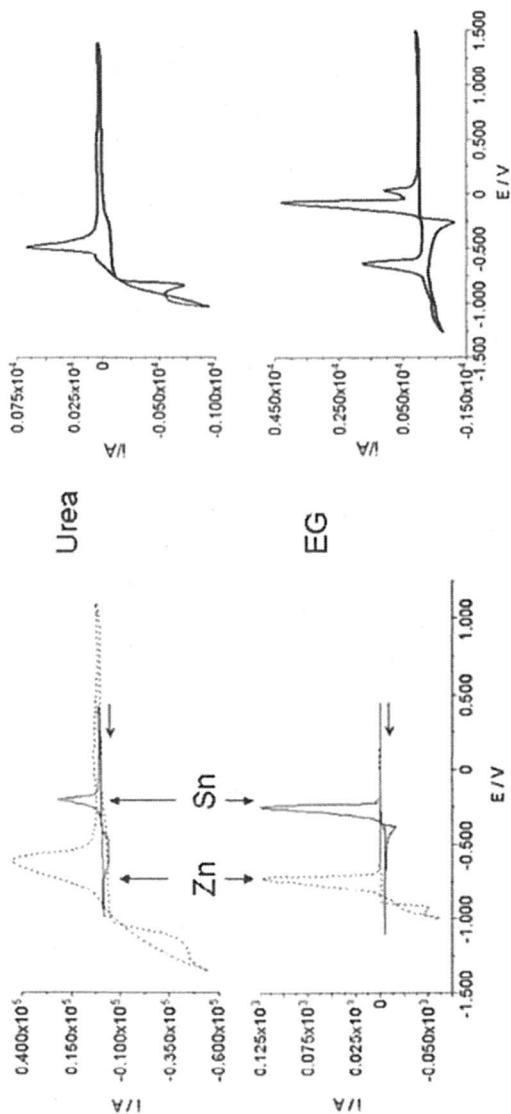


Figure 5. Cyclic voltammograms of ZnCl_2 and SnCl_2 in $\text{ChCl}:2\text{Urea}$ and $\text{ChCl}:2\text{EG}$ on a Pt electrode. Left: voltammograms of separate salts, Right: voltammograms of salts in the same solution.

aqueous reduction potentials (0.62 V). Interestingly, this could be due to the presence of mixed metal complexes i.e. ZnSnCl_5^- which are known to exist in these systems. [7]

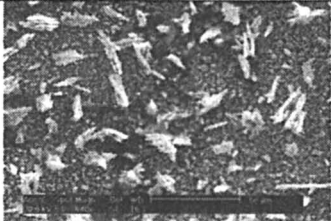
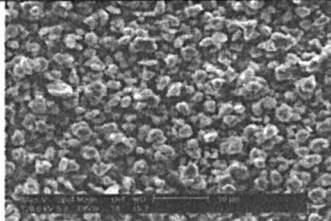
Using urea as a HBD, a single anodic process is observed at a voltage that is in between those for the zinc and tin processes. Interestingly no stripping of a tin rich phase is observed which probably means that the use of urea in the ionic liquid tends to lead to less of the separate zinc and tin phases and instead yields a zinc rich phase.

Bulk deposition of zinc from both EG and urea based liquids leads to zinc deposits with small crystallites (c.a. 5 μm) that have negligible residual chloride [17] and this was relatively unaffected by the current density. We have previously shown that zinc can be deposited as a crack free film with high current efficiency from a $1\text{ChCl}: 2\text{ZnCl}_2$ liquid. [7] These films are white in appearance and are made up of crystallites that are slightly larger (c.a. 10-25 μm). [7] The morphology is also similar to that obtained from deposition from the $2\text{ZnCl}_2/\text{ChCl}$ eutectic with 3 wt % SnCl_2 . [18] The issue associated with the use of these zinc eutectics is the low conductivity (36 $\mu\text{S cm}^{-1}$ at 40°C) whereas the two HBD eutectic mixtures used in this work have much higher conductivities ($\text{ChCl}:2\text{urea} = 1.8\text{ mS cm}^{-1}$ and $\text{ChCl}:2\text{EG} = 11\text{ mS cm}^{-1}$ both at 40°C). [10,12]

The deposition of tin from the urea and EG based eutectics produced more dendritic clusters, which are built up of simple cubic crystals. The deposition of whisker-like deposits, which is common for the deposition of tin from aqueous solutions, was not observed in either ionic liquid when the current density applied was 10 mA cm^{-2} .

Table 1 shows the morphologies and compositions of Zn/Sn alloys deposited from the solutions shown in Figure 5. It can be seen that the HBD changes both the morphology and composition of the alloy, which we propose is due to the change in metal speciation occurring in the two liquids.

Table 1. Morphologies and compositions of deposits obtained by deposition of the solutions shown in Figure 5.

HBD	Urea	EG
Morphology		
Composition Zn:Sn	89:11	55:45

Conclusions

This work has shown that eutectic mixtures based on choline chloride and hydrogen bond donors can be used in metal finishing applications. The use of chloride based mixtures makes the liquids relatively insensitive to water content and hence "drop-in" replacements for aqueous solutions can be produced. For the electropolishing process the application of ionic liquid technology to tonne scale processes has been demonstrated and a recycling protocol for the liquid has been developed. For electrodeposition applications it can be seen that this type of eutectic based ionic liquid can be used to control both deposit morphology and composition.

Acknowledgements

The authors would like to acknowledge the funding of this work by the DTI (ETREAT) and EU (IONMET).

References

1. P. Wasserscheid, T. Welton, *Ionic Liquids in Synthesis* Wiley-VCH Verlag, Weinheim, Germany 2003.
2. P. Wasserscheid, W. Keim, W., *Angew. Chem. Int. Ed.*, 39 (2000) 3772
3. F. Endres, *ChemPhysChem* 3(2002) 144
4. H. Ohno (ed.) *Electrochemical Aspects of Ionic Liquids*, John Wiley & Sons, New York, 2005
5. A. P. Abbott, G. Capper, D. L. Davies, H.L. Munro, R. K. Rasheed, V. Tambyrajah, *Chem. Commun.*, (2001) 2010
6. A. P. Abbott, G. Capper, D. L. Davies, R. K. Rasheed, *Inorg. Chem.*, 43 (2004) 3447
7. A. P. Abbott, G. Capper, D. L. Davies, H.L. Munro, R. K. Rasheed, V. Tambyrajah, "Ionic Liquids as Green Solvents: Progress and Prospects" R. D. Rogers and K. R. Seddon Eds. *ACS Symposium Series*, 2003, 439
8. A. P. Abbott, G. Capper, D. L. Davies and R. K. Rasheed, *Chem. Eur. J.*, 10 (2004) 3769
9. A. P. Abbott, G. Capper, D. L. Davies, R. K. Rasheed, J. Archer, C. John, *T. Inst. Met. Fin.*, 82 (2004) 14
10. A. P. Abbott, G. Capper, D. L. Davies, R. K. Rasheed, V. Tambyrajah, *Chem. Commun.*, (2003) 70
11. A. P. Abbott, D. Boothby, G. Capper, D. L. Davies, R. K. Rasheed, *J. Am. Chem. Soc.*, 126 (2004) 9142

12. A. P. Abbott, G. Capper, D. L. Davies, R. Rasheed and P. Shikotra, *Inorg. Chem.* 44 (2005) 6497
13. A. P. Abbott, G. Capper, B. G. Swain, D. A. Wheeler, *T. Inst. Met. Fin.*, 83 (2005) 51
14. R. D. Grimm, A. C. West, D. Landolt, *J. Electrochem. Soc.*, 139 (1992) 1622
15. M. Matlosz, S. Magaino, D. Landolt, *J. Electrochem. Soc.*, 141 (1994) 410
16. A.P. Abbott, G. Capper, K. J. McKenzie and K. S. Ryder, *Electrochim. Acta* 2006 in press
17. A.P. Abbott, G. Capper, K. J. McKenzie and K. S. Ryder, *J. Electroanal. Chem.* 2006 in press
18. A. P. Abbott, G. Capper, D. L. Davies, R. K. Rasheed and V. Tambyrajah, *T. Inst. Met. Fin.*, 79 (2001) 204

Chapter 14

Ionic Liquids as Vehicles for Reactions and Separations

**Jason P. Hallett¹, Philip G. Jessop², Charles A. Eckert¹,
and Charles L. Liotta^{1,*}**

¹Schools of Chemistry and Chemical Engineering and Specialty Separations
Center, Georgia Institute of Technology, 311 Ferst Drive,
Atlanta, GA 30332-0100

²Department of Chemistry, Queen's University, Kingston,
Ontario K7L 3N6, Canada

Ionic liquids possess interesting properties as reaction and processing solvents, but large-scale implementation is hampered by potential difficulties associated with product recovery. We have explored several applications of ionic liquids with a keen focus on the separations accompanying organic synthesis. One exciting new possibility involves the reversible formation of ILs using gaseous CO₂. This molecular “switch” allows us to turn the polarity of the solvent on and off. We have also developed applications utilizing ILs as phase-transfer catalysts for multiphase organic synthesis; this process enables us to use the solvent as a catalyst, enhancing the reaction efficiency. The solvatochromic behavior of CO₂/IL systems is also reported, providing insight into the effect of dissolved CO₂ on the solvent properties, an important consideration for designing CO₂-based processes using ILs.

Room temperature ionic liquids are an exciting class of solvents for chemical processes. Recent interest in the use of these media as solvents for organic reactions has led to the demonstration of a wide variety of chemical transformations in ILs (1), while somewhat less attention has been paid to the efficient recovery of products from these media. The use of supercritical CO₂ as an extraction solvent has been used to demonstrate the recovery of volatile organic compounds from ILs without detectable loss of the ionic reaction solvent (2). This paper highlights results pertinent to each of these issues: (1) the use of an ionic liquid as both solvent and catalyst for nucleophilic displacement; (2) the effect of pressurized carbon dioxide on the solvent properties of ionic liquids; and (3) the recent development of reversible ionic liquids as an exciting new class of solvents with built-in separation "switches."

Experimental

Nucleophilic Substitution Reactions

Materials. The ionic liquid, 1-n-butyl-3-methylimidazolium hexafluorophosphate, was provided by SACHEM, Inc. Of two bottles used, one indicated that it contained 3% water, and the other gave no information regarding its purity. The benzyl chloride (99%) and potassium cyanide (97%, ACS Reagent) were obtained from Aldrich Chemical Company. The acetonitrile and the benzyl cyanide (99+%) used for HPLC calibration were also from Aldrich.

Apparatus and Procedure. The nucleophilic substitution reactions were carried out in a 25 ml volumetric flask set in a temperature-controlled jacketed beaker and stirred with a magnetic stir bar. The fluid in the jacketed beaker was ethylene glycol recirculated through a heated bath with control (in reaction flask) of $\pm 0.5^\circ\text{C}$. The concentration of benzyl chloride in the ionic liquid was 1 M, and the amount of potassium cyanide was three times the stoichiometric amount of benzyl chloride. While all of the benzyl chloride was visually observed to be soluble, solid potassium cyanide was present in the systems at all times. Before introduction of benzyl chloride, the salt was stirred overnight in the ionic liquid so that particles of uniform size would form and the salt would reach an equilibrium concentration.

Analysis. After the introduction of benzyl chloride, samples of about 0.1 mL volume were drawn with a Pasteur pipette and dissolved in cold acetonitrile before being analyzed by HPLC equipped with a UV-Vis detector. The

wavelength monitored by the detector was 248 nm, where both the reactant and product absorb strongly.

Physical Property Measurements

Materials. The IL [bmim][PF₆] was provided by SACHEM (purity of 97%). To eliminate possible moisture, [bmim][PF₆] was held under vacuum at ambient temperature for approximately a week prior to use. Carbon dioxide was the product from Matheson (SFC grade, 99.99% purity). The solvatochromic indicator *N,N*-dimethyl-4-nitroaniline (Aldrich, 97%) and the fluorescence probe DCVJ (Molecular Probes) were used as received. All organic solvents were of the highest purity available from Sigma-Aldrich and used without further purification.

Apparatus. A stainless-steel vessel with three sapphire windows (6.4 mm-thick) was constructed for the UV-Vis and the fluorescence spectroscopy. The windows were sealed with Teflon gaskets capable of withstanding pressures exceeding 250 bar. The path length of the cell is 2.2 cm and the internal volume is 9.6 cm³ at room temperature. The temperature control unit (Omega) for the cell consists of heating cartridges inserted into the body, a microprocessor thermometer, and a temperature controller. The temperature variation was maintained within ± 0.1 °C of the setpoint. Pressure was monitored by a pressure transducer and a pressure readout (Druck) with an uncertainty of 0.01% in the range of 0-207 bar. A Teflon-coated spin bar constantly agitated the contents in the cell throughout measurements to facilitate equilibrium. The solvatochromic measurements and spectrum processing were performed on a Hewlett-Packard 8453 diode array UV-Vis spectrophotometer (1 nm resolution and ± 0.2 nm wavelength accuracy). A Shimadzu RF-5301PC spectrofluorophotometer provided all the fluorescence spectra with ± 1.5 nm wavelength accuracy.

Procedure. The dried [bmim][PF₆] solution with an indicator of an appropriate concentration was loaded into the high-pressure vessel and degassed under vacuum at a given temperature for at least 24 hours prior to measurement. The solution visible through the optical windows was the IL phase. Initial spectroscopic measurements were conducted in the absence of CO₂ and then CO₂ was pressurized into the cell with a syringe pump (ISCO). Phase equilibrium was ensured by observation that spectrum and pressure no longer changed with time (equilibration took longer to achieve at lower CO₂ pressures). CO₂ was added repeatedly until the highest pressure was reached at each temperature. Reproducibility was tested with continuously decreasing pressure for the same content by releasing CO₂ and conducting spectral measurements when each equilibrium was achieved. All the solvatochromic spectra were subtracted by with the spectrum of the corresponding pure solvent. The initial

concentrations of *N,N*-dimethyl-4-nitroaniline and DCVJ in [bmim][PF₆] without added CO₂ were 2.0×10^{-5} and 4.5×10^{-6} mol/L, respectively. The density of pure CO₂ was calculated by an equation of state (3). The viscosity and dielectric constant for conventional liquids were obtained from DIPPR 801 Thermophysical Properties Database (2002 Public Release).

Results and Discussion

Nucleophilic Substitution Reactions

Nucleophilic displacements are often carried out using phase-transfer catalysis (PTC) to facilitate reaction between nonpolar organic reactants and polar inorganic salts(4). The phase-transfer catalyst, often a tetraalkylammonium salt or a crown ether, acts as a shuttle to transfer the nucleophilic anion between the polar (liquid or solid) salt phase and the non-polar organic phase. This technique not only overcomes the problem of contacting the reactants, but also activates the nucleophilic anion, since it is much less tightly electrostatically bound to a tetraalkylammonium cation than it would be to a metal cation. In conventional PTC typical organic media are sometimes environmentally undesirable solvents such as methylene chloride or o-dichlorobenzene, and catalyst separation and recovery are significant challenges. Because ionic liquids are comprised of bulky organic cations, similar to tetraalkylammonium salts, they seem well suited for use as both solvent and catalyst in many traditional PTC applications. This would combine solvent and catalyst removal into one step, reducing the separations costs for the process. The ionic liquid cation might not be as effective a catalyst as most PTCs; however, as a solvent its high concentration should overcome this limitation, yielding a high reaction rate.

We demonstrated the utility of ionic liquids for PTC-type applications using a well-characterized (5-9) model reaction: the nucleophilic displacement of chloride ion by cyanide ion from benzyl chloride, shown in Figure 1 (10). The IL used in this application was 1-*n*-butyl-3-methylimidazolium hexafluorophosphate (Figure 1), often called [bmim][PF₆], one of the most widely used ILs.

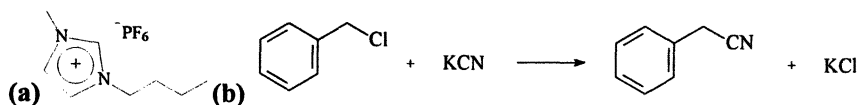


Figure 1. (a) The IL [bmim][PF₆]; (b) cyanide displacement on benzyl chloride

Reactions were carried out at 40, 60, and 80°C, and conversion vs. time is plotted in Figure 2. Reaction rates were high, with the reaction at 80°C reaching complete conversion in less than half an hour. Although the reactions at 60 and 80°C show the expected pseudo-first-order kinetic behavior (since the amount of cyanide available for reaction should be constant), the reaction at 40°C appears to be of zero order. This behavior indicates that mass transfer of CN⁻ into the solvent is probably the rate-limiting step at the lower temperature. This behavior is likely due to slow dissolution of the salt into the IL being the rate-controlling step at lower temperatures, rather than simple ion exchange within the solvent.

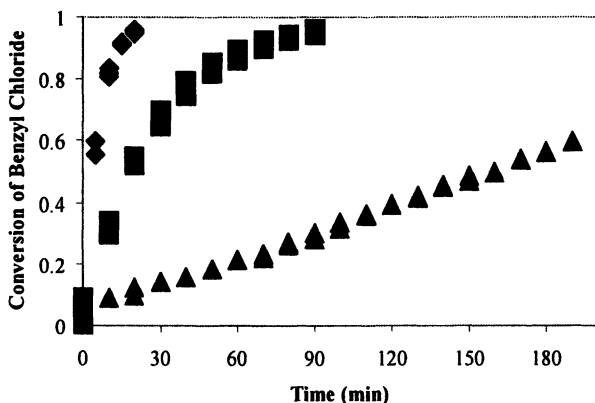


Figure 2. Conversion of benzyl chloride to benzyl cyanide (● 80°C, ■ 60°C, ▲ 40°C) (10)

The rate constants for each temperature are listed in Table I. Using the pseudo-first order rate constants obtained at 60 and 80°C, an effective activation energy of 19 kcal/mol is calculated. This activation energy includes several factors other than the temperature dependence of the intrinsic reaction rate, most especially the rate of solubilization of potassium cyanide in the IL.

Table I. Rate constants for reaction of benzyl chloride with KCN (10)

Temperature	Rate Constant ^a	Units
40°C	^b (4.76 ± 0.12) × 10 ⁻⁵	Mol L ⁻¹ s ⁻¹
60°C	^c (5.45 ± 0.38) × 10 ⁻⁴	s ⁻¹
80°C	^c (2.54 ± 0.10) × 10 ⁻³	s ⁻¹

^aUncertainty is represented by 95% confidence intervals

^bZero order

^cPseudo-first order

For the sake of comparison, the same reaction was run at 60°C using two dipolar aprotic solvents, dimethyl sulfoxide (DMSO) and propylene carbonate. In DMSO, the reaction was slightly faster than in the ionic liquid, with the rate at 60°C comparable to that at 80°C in the ionic liquid. In propylene carbonate, the reaction was very slow, with minimal conversion achieved in 24 hours. Thus, the ionic liquid compared favorably with these polar, aprotic organic solvents, even though cyanide salt solubility is much higher in those systems.

There are several points that are important to address. (1) The reaction in the ionic liquid is a heterogeneous reaction. Both the potassium cyanide reactant and the potassium chloride product have limited solubilities in the ionic liquid. In fact, most of the potassium cyanide remains as a solid phase and only a very small portion dissolves at the start of the reaction. As such there are at least three steps in the reaction process for the major portion of the reaction. The first step is the dissolution of the salt into the ionic liquid phase, the second step is the nucleophilic reaction, and the third step is the transport of the leaving group anion from the ionic liquid phase to the solid salt phase. The observations of pseudo-zero order kinetics at the lower temperature clearly indicates that the dissolution process must be rate controlling. The switch to pseudo-first order kinetics at higher temperatures suggests that now the rate controlling step must be the nucleophilic substitution process and that the rate of dissolution is fast compared to the rate of reaction. (2) Phase transfer catalysis requires at least three conditions. First, the quaternary cation must ion pair with the nucleophilic anion to transport it from one phase to another. In our case, the anion is being transported from the solid salt phase to the ionic liquid phase. Second, the nucleophilic anion in the ionic liquid phase must be ion paired with the quaternary cation in such a way that it is reactive toward the benzyl chloride. In general, bulky quaternary cations are quite good in separating the centers of positive and negative charges in order to activate the nucleophilic characteristics of the anion. Third, the chloride ion leaving group, derived from the benzyl chloride, should be transported from the ionic liquid phase into the solid salt phase in order to complete the phase transfer catalytic cycle. (See a detailed discussion of the entire process in reference 4.) (3) Finally, the rate of reaction in the ionic liquid compared with other solvent systems (Dimethyl carbonate, DMSO, etc.) is not an indication of PTC. PTC exists if the three steps discussed above are mechanistically operating. The observed kinetics indicates that this is the case. All this being said, what we have shown is a "PTC-type process"- a process somewhat different from the classical PTC processes described in the literature. Here the catalyst and the reaction phase are one and the same.

Physical Property Measurements

Mass transfer limitations, such as those exhibited by the nucleophilic displacement reaction, could potentially be overcome by reducing the viscosity

of ILs. Since CO₂ can be used to extract products out of the IL solution, the presence of CO₂ in the system to reduce viscosity would add a processing benefit at low cost. CO₂ dissolution in organics can often lead to antisolvent precipitations as high concentrations of CO₂ vastly lowers the polarity of organic solvents. In order to study these two effects in ILs we examined the Kamlet-Taft dipolarity/polarizability (π^*) and microviscosity of CO₂-expanded ionic liquids.

The Kamlet-Taft π^* parameter provides a comprehensive measure of the ability of a solvent to stabilize a solute molecule based on the dielectric effects (11). It is a quantitative index of solvent dipolarity/polarizability that also provides insight into the local solvent environment surrounding an indicator molecule. Figure 3 displays π^* parameters for [bmim][PF₆]/CO₂ mixtures as a function of CO₂ pressure at 35 °C and 50 °C (12). Similar measurements for other ILs were recently made by Aki *et al.* (13) The π^* of pure [bmim][PF₆] at 35 °C is higher relative to that at 50 °C, and agrees with the previously published temperature-dependence (14). With the isothermal addition of CO₂ to [bmim][PF₆], the π^* parameter undergoes minimal decrease at up to 200 bar at 35 °C (0.95 to 0.94) or 230 bar at 50 °C (0.92 to 0.90). This stands in stark contrast to the results of Wyatt *et al.* (15) for the π^* values of CO₂-expanded methanol and acetone. These solvents experienced an approximately 80% decrease in π^* at pressure around 80 bar. The results for CO₂-expanded ionic liquids would seem to indicate that local polarity in these systems is unaffected by the presence of CO₂. It is important to note in interpreting these results that preferential solvation of the IL around the indicator may be responsible for the insignificant effect of substantial amounts of CO₂ on the apparent polarity of [bmim][PF₆]. Baker and coworkers reported a decline in the value of the Py scale for fluorescent pyrene (nonpolar) in [bmim][PF₆]/CO₂ as the pressure of CO₂ increases (16). The Py scale measures the ratio of the first and third fluorescence bands (I_1/I_3) of pyrene and relates this quantity to local polarity. The existence of solute-specific solvent effect in IL/CO₂ could account for the discrepancy between these two studies.

Microviscosity using a fluorescent molecular rotor

The high viscosity of [bmim][PF₆] and many other ILs could be a limitation for practical application because multiphasic reaction processes (such as PTC-type reactions) may move into the transport-limited regime. CO₂ can act as an effective diluent to reduce the viscosity, thereby promoting mass transfer into the viscous ILs. We investigated the influence of CO₂ on the local viscosity of [bmim][PF₆] using the fluorescence probe DCVJ (Figure 4) (12). DCVJ is a well-described solvent-dependent molecular rotor characterized by two photophysical phenomena: a microviscosity-dependent fluorescence intensity and a polarity-dependent emission maximum (17-20).

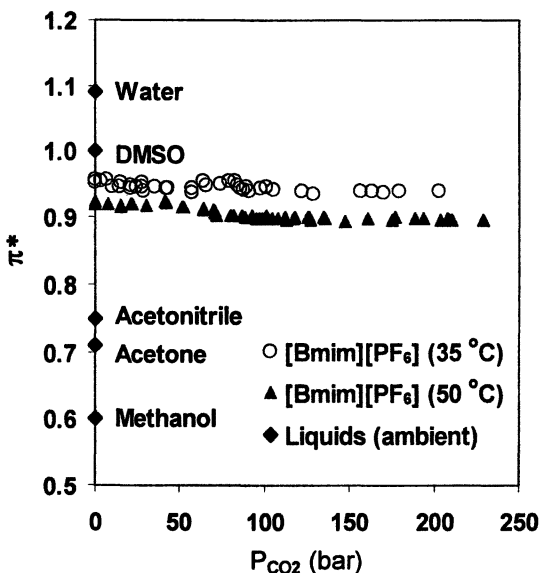


Figure 3. Kamlet-Taft π^* parameter (dipolarity/polarizability) for conventional organic solvents and for [bmim][PF₆]/CO₂ as a function of CO₂ pressure (Reproduced from reference 12. Copyright 2003.)

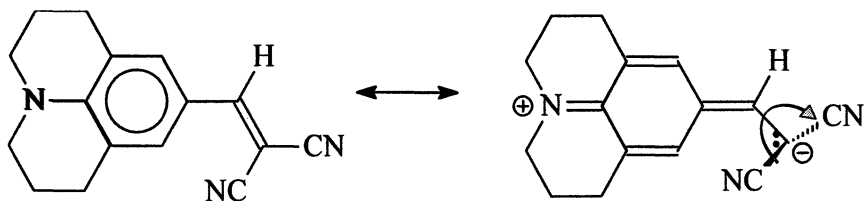


Figure 4. Chemical structure of DCVJ

The fluorescence quantum yield (ϕ_f) for DCVJ emission is expressed as

$$\phi_f = k_r / (k_r + k_{nr}) \quad (1)$$

where k_r and k_{nr} are the radiative rate and the nonradiative deactivation rate, respectively. The nonradiative deactivation of the singlet-excited-state can occur rapidly through intramolecular torsional relaxation about the donor-acceptor bond. An increase in rigidity and viscosity of surrounding medium tends to inhibit the internal molecular rotation and, as a consequence, the radiative decay

rate (k_r) increases. The resultant fluorescence quantum yield is enhanced in such a highly constrained microenvironment (i.e., high microviscosity).

The microviscosities were correlated to fluorescence intensity of DCVJ using a series of conventional liquids spanning a broad range of viscosity at 25 °C (Figure 5). We assume that negligible heterogeneity on a molecular scale exists in these incompressible liquids, thus microviscosity is assumed to be equivalent to the bulk viscosity. Figure 5 also shows an excellent correlation between relative fluorescence intensity (FI) of DCVJ and viscosity of these solvents (η). The same fluorescence spectral measurements were conducted for [bmim][PF₆]/CO₂ in the pressure range of 0–205 bar and at 35 °C. The fluorescence spectra were corrected by multiplying the expansion factor under corresponding conditions (obtained from the intensity reduction of the π^* probe) to ensure that all the intensities are evaluated for the same concentration of the probe.

Figure 6 shows several representative spectra for [bmim][PF₆]/CO₂ at several pressures, which reveal that the fluorescence intensity decreases remarkably with increasing CO₂ pressure. The pressure dependence is also depicted in Figure 6 and reveals that the microviscosity of [bmim][PF₆] is reduced significantly in the presence of CO₂. The local viscosity decreases from 425 cP to 65 cP as the pressure increases from 0 to 68 bar at 35 °C, and then flattens out as the pressure further increases. This result is in agreement with the work of Baker et al. who reported about 5-fold reduction in viscosity (16), although their estimated viscosity for neat [bmim][PF₆] is lower than our results and other published data (21). The added CO₂ appears to have the capability of “lubricating” the viscous IL even at moderate pressures, which could dramatically minimize transport resistance and facilitate separation in IL/CO₂ mixtures. For example, reductions in viscosity of ILs could reduce the time required for substrate dissolution, gas solubilization or product crystallization, as the time required to reach equilibrium in these types of processes is a function of viscosity. As a result, the reaction or crystallization kinetics of these processes would be markedly enhanced.

Local dielectric using a fluorescent molecular rotor

Because the π^* excited-state for DCVJ contains a considerable amount of charge transfer character, the excited-state and the ground-state have substantially different dipole moments ($\mu_e \approx 24$ Debyes, $\mu_g \approx 9$ Debyes) (20). As a result, the fluorescence emission maximum is strongly dependent on the polarity of the solvent, which allows for probing the “microscopic dielectric property” in the vicinity of the fluorophore. It is evident from Figure 5 that the emission maximum (λ_{em}) shifts to a longer wavelength with an increase in solvent polarity. The correlation of λ_{em} and the dielectric constant (ϵ) of the

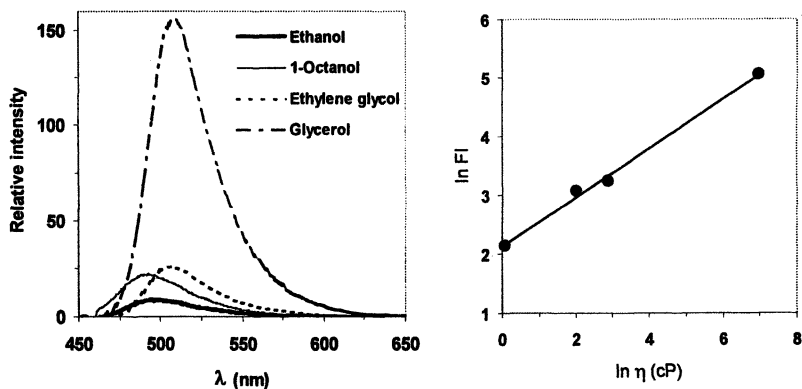


Figure 5. **Left:** Fluorescence emission spectra of DCVJ in several organic alcohols at 25 °C ($C_{DCVJ} = 4.5 \times 10^{-6}$ mol/L); **Right:** Viscosity-dependence of fluorescence intensity (FI) of DCVJ for the alcohols listed on the left (Reproduced from reference 12. Copyright 2003.)

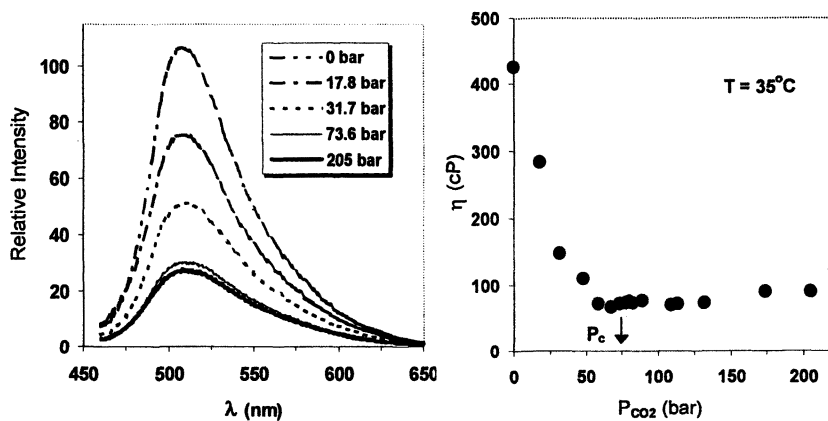


Figure 6. **Left:** Fluorescence spectra of DCVJ (corrected for volume expansion) in [bmim][PF₆]/CO₂ at different pressures and 35 °C ($C_{DCVJ} = 4.5 \times 10^{-6}$ mol/L); **Right:** Microviscosity for [bmim][PF₆]/CO₂ calculated from the peak maxima on the left. The arrow indicates the critical pressure of pure CO₂ (73.8 bar) (Reproduced from reference 12. Copyright 2003.)

corresponding solvent (Figure 7) shows a satisfactory linear relationship, from which the dielectric constant of [bmim][PF₆]/CO₂ at different pressures at 35 °C was calculated. The results shown in Figure 7 demonstrate that the local dielectric constant in the immediate surroundings of the probe is independent of the CO₂ solubility, with values from 41-44. The general shape of the local dielectric constant for [bmim][PF₆]/CO₂ is consistent with that of the Kamlet-Taft π^* parameters. Both methods show that the polarity of [bmim][PF₆]/CO₂ is slightly weaker than water and DMSO, but stronger than acetone and methanol, and nearly independent of CO₂ concentration.

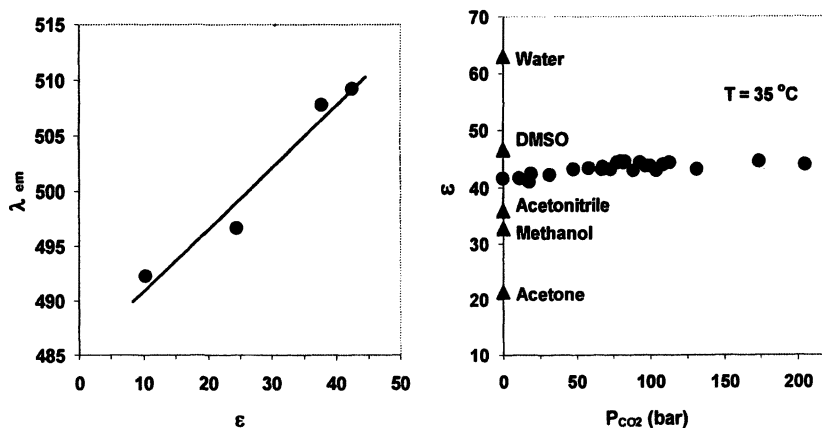


Figure 7. *Left:* Correlation of fluorescence emission maximum of DCVJ with dielectric constant for the same alcohols as in Figure 6 at 25 °C; *Right:* Estimated dielectric constants for [bmim][PF₆]/CO₂ as a function of pressure of CO₂ at 35 °C (Reproduced from reference 12. Copyright 2003.)

Reversible ionic liquids

Chemical production processes often involve multiple reaction and separation steps, and the type of solvent that is optimum for one step may not be viable for the next. This often necessitates removal of the solvent between each step in a multistep synthesis, greatly increasing the cost and the waste generated. This could be avoided if the properties of a solvent could be adjusted between reaction steps by a simple trigger, enabling use of the “same” solvent –with different properties- for several consecutive reaction or separation steps.

Moderate changes in temperature or pressure are incapable of triggering significant changes in the properties of conventional solvents, and the tunability of supercritical fluids (22) and CO₂/organic solvent mixtures (23) is only sufficient at substantial pressures.

As an alternative, we have developed a simple switch between nonionic organic solvents and a polar ionic liquid under very mild conditions. Exposure of a 1:1 mixture of the two non-ionic liquids DBU (1,8-diazabicyclo-[5.4.0]-undec-7-ene) and 1-hexanol to gaseous CO₂ at one atmosphere and room temperature causes conversion of the organic liquid mixture to an ionic liquid (Figure 8) (24). The resulting IL is readily converted back into a nonionic liquid by bubbling an inert gas, such as N₂ or argon, through the liquid. These changes were confirmed by chemical shifts in key protons, as revealed by 1H-NMR spectroscopy, and by a large solvatochromic shift characterized by the dye Nile Red. This dye suggests a switch in polarity from something similar to chloroform (before CO₂) to properties approximating dimethylformamide in the IL form. The reaction is exothermic and causes a marked increase in the viscosity of the liquid. The choice of alcohol is critical; for example the 1-hexylcarbonate salt is a viscous liquid at room temperature, whereas the bicarbonate and methylcarbonate salts are solids. The polarity changes in this switchable solvent system is exemplified by the dramatic reversal in solubility of nonpolar species such as decane, which is miscible with the liquid under N₂ but immiscible under CO₂. CO₂ is a useful "switching" agent because it is nonreactive, benign and easily removed. The use of "switchable" solvents could open up a wide range of new opportunities for simplified chemical processing.

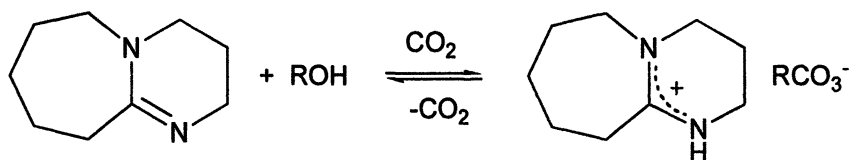


Figure 8. Reversible IL (right) formed from DBU, an alcohol and CO₂ at 1 atm and 25°C (24)

Conclusions

Chemical processing with ionic liquids represents an important step along the road to a more environmentally benign chemical industry. We report here several examples highlighting the important intersection of chemical reactions, physicochemical properties and separations in the development of processes

using these new solvents. We have shown a nucleophilic displacement reaction using an ionic liquid as both solvent and catalyst. The success of this reaction is somewhat hampered by mass transfer limitations at low temperatures. The transport and solvent properties of an ionic liquid were measured using solvatochromic techniques in order to better understand these limitations. We found that the viscosity of [bmim][PF₆] could be dramatically lowered using dissolved CO₂ without compromising the solvent strength. We also reported on the development of “reversible” ionic liquids that could be formed by bubbling CO₂ through a mixture of nonpolar organic liquids. This represents a potential “switch” for easy separation of ionic liquid solvents; making processes utilizing these solvents more facile.

References

1. Welton, T. *Chem. Rev.* **1999**, *99*, 2071.
2. Blanchard, L.A.; Hancu, D.; Beckman, E.J.; Brennecke, J.F. *Nature* **1999**, *399*, 28.
3. Ely, J. F.; Haynes, W. M.; Bain, B. C. *J. Chem. Thermodynamics* **1989**, *21*, 879.
4. Starks, C.M.; Liotta, C.L.; Halpern, M. *Phase-Transfer Catalysis: Fundamentals, Applications, and Industrial Perspectives*; Chapman and Hall: New York, 1994.
5. Cook, F.L.; Bowers, C.W.; Liotta, C.L. *J. Org. Chem.* **1974**, *39*, 3416.
6. Zubrick, J.W.; Dunbar, B.I.; Durst, H.D. *Tetrahedron Lett.* **1975**, 71.
7. Reeves, W.P.; White, M.R. *Synth. Commun.* **1976**, *6*, 193.
8. Liotta, C.L.; Burgess, E.M.; Ray, C.C.; Black, E.D.; Fair, B.E. In *Phase-Transfer Catalysis: New Chemistry, Catalysts, and Applications*; ACS Symp. Ser. 326; Starks, C.M., Ed.; American Chemical Society: Washington, D.C., 1987.
9. Liotta, C.L.; Berkner, J.; Wright, J.; Fair, B.E. In *Phase-Transfer Catalysis: Mechanisms and Syntheses*; ACS Symp. Ser. 659; Halpern, M.E., Ed.; American Chemical Society: Washington, D.C., 1997.
10. Wheeler, C.; West, K.; Liotta, C.; Eckert, C. *Chem. Commun.* **2001**, 887.
11. Kamlet, M.J.; Abboud, J.; Taft, R.W. *J. Am. Chem. Soc.* **1977**, *99*, 6027.
12. Lu, J.; Liotta, C. L.; Eckert, C. A. *J. Phys. Chem. A* **2003**, *107*, 3995.
13. Fredlake, C. P.; Muldoon, M. J.; Aki, S. N. V. K.; Welton, T.; Brennecke, J. F. *Phys. Chem. Chem. Phys.* **2004**, *6*, 3280.
14. Baker, S. N.; Baker, G. A.; Bright, F. V. *Green Chemistry* **2002**, *4*, 165.
15. Wyatt, V.T.; Bush, D.; Hallett, J.P.; Liotta, C.L.; Eckert, C.A. *J. Supercritical Fluids* **2005**, *36*, 16.
16. Baker, S. N.; Baker, G. A.; Kane, M. A.; Bright, F. V. *J. Phys. Chem. B* **2001**, *105*, 9663.
17. Kung, C. E.; Reed, J. K. *Biochemistry* **1986**, *25*, 6114.

18. Kung, C. E.; Reed, J. K. *Biochemistry* **1989**, *28*, 6678.
19. Loutfy, R. O.; Arnold, B. A. *J. Phys. Chem.* **1982**, *86*, 4205.
20. Loutfy, R. O. *Pure & Appl. Chem.* **1986**, *58*, 1239.
21. Huddleston, J. G.; Visser, A. E.; Reichert, W. M.; Willauer, H. D.; Broker, G. A.; Rogers, R. D. *Green Chemistry* **2001**, *3*, 156.
22. Jessop, P.G.; Leitner, W. (eds). *Chemical Synthesis using Supercritical Fluids*; VCH/Wiley: Weinheim, 1999.
23. Eckert, C.A.; Liotta, C.L.; Bush, D.; Brown, J.S.; Hallett, J.P. *J. Phys. Chem. B* **2004**, *108*, 18108.
24. Jessop, P.G.; Heldebrant, D.J.; Xiaowang, L.; Eckert, C.A.; Liotta, C.L. *Nature* **2005**, *436*, 1102.

Chapter 15

Mesoscopic Dye Sensitized Solar Cells Using Hydrophobic Ionic Liquid Electrolyte

Daibin Kuang, Seigo Ito, Shaik M. Zakeeruddin^{*},
and Michael Grätzel^{*}

Laboratory for Photonics and Interfaces, Swiss Federal Institute
of Technology, CH-1015 Lausanne, Switzerland

^{*}Corresponding authors: email addresses: shaik.zakeer@epfl.ch;
michael.graetzel@epfl.ch

A new binary ionic liquid electrolyte for dye sensitized solar cell was prepared by mixing 1-propyl-3-methylimidazolium iodide (PMII) with a low viscosity hydrophobic ionic liquid, 1-ethyl-3-methylimidazolium bis(trifluoromethyl sulfonyl) imide (EMITFSI). Using this new binary ionic liquid electrolyte in combination with amphiphilic sensitizer Z907Na we obtained 6.6 % photovoltaic energy conversion efficiency at full sunlight. These devices showed excellent stability after long-term acceleration test under visible light soaking at 60 °C. Electrochemical impedance spectroscopy was performed to analyze the photovoltaic parameters variations during visible light soaking.

Introduction

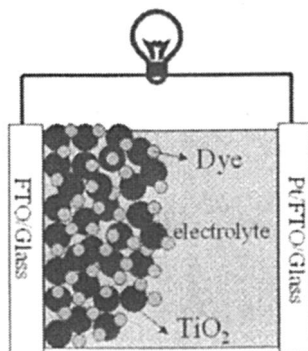
In recent years mesoscopic dye sensitized solar cell (DSC) has been paid intensive attentions as an alternative to silicon technology and progresses have been made in the development of efficient dyes, electrolytes and TiO₂ films to enhance the device performance.¹⁻⁵ Encapsulation and leakage of high vapor pressure organic solvents based electrolytes is a major challenge for the commercialization of DSC. A number of efforts have been paid to replace the volatile organic solvent of the electrolyte with hole conducting materials and solid electrolytes.^{6,7} Photovoltaic performance of solid-state devices are not high enough to compete with the organic solvent-based electrolytes.

Room temperature ionic liquids (ILs) are attractive alternative to replace the volatile organic solvents due to their negligible vapor pressure and high ionic conductivity.^{8,9} Imidazolium iodide ILs are very viscous and the high concentration of iodide ions in these electrolytes creates a loss channel through reductive quenching of the excited sensitizer and hampering device performance.¹⁰ Use of binary ionic liquid electrolytes for DSC reduces the viscosity of the electrolyte and the reductive quenching effect. Various binary ionic liquid electrolytes have recently been applied to DSC reaching over 7.0 % photovoltaic conversion efficiency with a good stability under accelerated light soaking tests at 60 °C.^{5, 10, 11} In this study, we applied a low viscous hydrophobic ionic liquid electrolyte for DSC and monitored the long-term stability of devices under light soaking at 60 °C.

Experimental

The amphiphilic sensitizer Z907Na was synthesized as reported earlier¹⁰ and the molecular structure is shown in Figure 1b. Ionic liquids including 1-propyl-3-methylimidazolium iodide (PMII), 1-ethyl-3-methylimidazolium bis-(trifluoromethylsulfonyl) imide (EMITFSI) were prepared according to literature methods and their purity confirmed by ¹H NMR spectra.¹² The co-adsorbents 3-phenylpropionic acid (PPA) and guanidinium thiocyanate (GuNCS) were purchased from Aldrich and Fluka, respectively were used as received. N-methylbenzimidazole (NMBI, from Aldrich) was recrystallized from diethyl ether before use.

The double layer structured mesoporous TiO₂ films and the DSC devices were fabricated as reported earlier.⁵ Film thickness was also optimized in the ionic liquid electrolyte system.⁵ Here, the photoanode consisting of a double layer structure, with a transparent layer (20 nm particle) of 6.8 μm and scattering layer (400 nm particle) of 4 μm thickness, respectively, was dipped into 300 μm Z-907Na dye solution or a mixture of 300 μm Z-907Na and 300 μm 3-phenylpropionic acid in a mixture of acetonitrile and *tert*-butyl alcohol (volume



Scheme 1. The structure of DSCs.

ration: 1:1) at room temperature for 14 h. Dye coated double layer films were assembled and sealed with counter electrode (Pt on FTO glass). The DSC investigated below employed a binary ionic liquid composed of 0.2 M I₂, 0.5 M N-methylbenzimidazole and 0.1 M guanidinium thiocyanate in a mixture of PMII and EMITFSI (volume ratio: 13:7), in combination with the amphiphilic sensitizer (Z-907Na). The typical structure of DSCs is shown in scheme 1.

Impedance spectra of DSCs were measured in the dark at -0.70 V applied forward bias using a computer controlled potentiostat (EG&G, M273) equipped with a frequency response analyzer (EG&G, M1025). The spectra were scanned in a frequency range of 0.005 Hz \sim 100 KHz at room temperature with alternating voltage amplitude set at 10 mV.

The measurement of current-voltage curves of the cells were obtained by using a Keithley model 2400 digital source meter (Keithley, USA) under an applied external potential bias as reported.⁵ Hermetically sealed cells were used to check the long-term stability under thermal stress (60 °C) and visible light soaking. The cells were covered with a polymer film of 50 μ m thickness (Preservation Equipment Ltd, UK), which acts as a UV cutoff filter and were illuminated at open circuit under a Suntest CPS lamp (ATLAS GmbH, 100 mW/cm², 60 °C). The cells were taken out at regular intervals to record the photocurrent-voltage curve measured over a period of 1000 h.

Results and Discussion

The molecular structure of 1-ethyl-3-methylimidazolium bis(trifluoromethylsulfonyl)imide, (EMITFSI) is shown in Figure 1a. EMITFSI is a hydrophobic ionic liquid having a viscosity of 35 cP at 20 °C, which is much lower than that of PMII viscosity. The low viscosity of EMITFSI is due to the

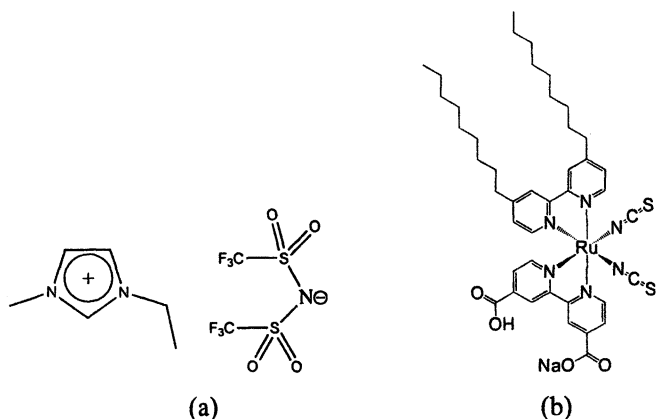


Figure 1. The molecular structures of (a) EMITFSI and (b) Z907Na.

extensive delocalization of negative charge on the TFSI anion, which is responsible in reducing the ion pair effect.

In a binary ionic liquid electrolyte by increasing the concentration of PMII in the electrolyte the dye regeneration increases and the photovoltaic efficiency increases. After increasing the concentration of PMII more than 65% by volume the efficiency goes down due to the reductive quenching of excited state of sensitizer, creating another loss channel of deactivation.¹⁰ Hence we prepared the new binary ionic liquid electrolyte with 65% of PMII and 35% of EMITFSI.

The short-circuit photocurrent density (J_{sc}), open-circuit photovoltage (V_{oc}), and fill factor (FF) of the device A with Z907Na alone are 12.1 mA cm⁻², 726 mV, and 0.725, respectively, obtaining a photovoltaic conversion efficiency of 6.3 %. In presence of 3-phenylpropionic acid (PPA) as co-adsorbent (device B), the corresponding photovoltaic parameters (J_{sc} , V_{oc} , FF, η) are 12.5 mA cm⁻², 743 mV, 0.712 and 6.6, respectively. The photocurrent density-voltage curves of device B under different light intensities are shown in Figure 2. At the lower light irradiance of 52 and 30 mW cm⁻², the efficiencies are 7.2 % and 7.5 %, respectively. The detailed photovoltaic parameters of the device A and B under various light intensities are shown in Table 1.

Devices employing Z907Na in conjunction with present binary ionic liquid electrolyte showed excellent long-term stability, when subjected to accelerated light soaking test at 60 °C. Figure 3 presents the stability data of the device containing Z907Na dye and PPA co-adsorbent which kept 91 % of the initial performance after the 1000 h light soaking test at 60 °C. During this aging, the V_{oc} decreased by 60 mV but this was compensated by a gain in fill factor without much change in the short circuit current density.

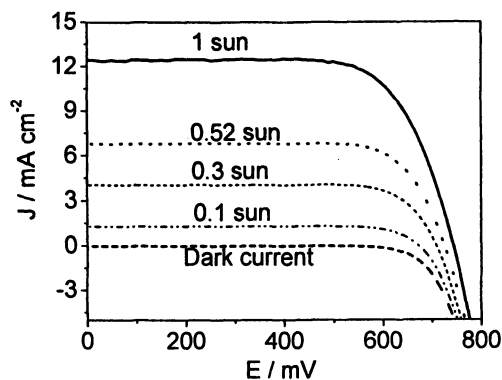


Figure 2. Photocurrent density-voltage curves of EMITFSI binary ionic liquid electrolyte at different light intensities with Z 907Na dye and PPA co-adsorbent.

Table 1 Photovoltaic parameters of DSC based on Z907Na with or without PPA co-adsorption under AM 1.5 simulated full sunlight (100 mW cm^{-2}) illuminations.^a

Sensitizer	Light intensity	$J_{sc}/\text{mA cm}^{-2}$	V_{oc}/mV	FF	$\eta/\%$
Z907Na	1.0 sun	12.1	726	0.725	6.3
	0.52 sun	6.74	710	0.765	6.9
	0.3 sun	3.96	694	0.783	7.1
Z907Na/PPA	1.0 sun	12.5	743	0.712	6.6
	0.52 sun	7.0	724	0.755	7.2
	0.3 sun	4.16	708	0.771	7.5

^a The spectral distribution of the xenon lamp simulates air mass 1.5 solar light. 1.0 sun corresponds to 100 mWcm^{-2} .

Recent studies have revealed electrochemical impedance spectroscopy (EIS) is a powerful technique for characterization of the electrochemical interface variation in DSC during the aging process.^{11, 13, 14} EIS investigation was performed on the fresh and aged cells after 1000 h acceleration test at 60 °C with 1 sun irradiance. A typical EIS spectrum exhibits three semicircles in the Nyquist plots or three characteristic frequency peaks in a Bode phase angle presentation as indicated in Figure 4a and Figure 4b. In the order of increasing frequency the features are attributed to the Nernst diffusion in electrolyte, electron transfer at the TiO₂/electrolyte interface and charge transfer at the counter electrode, respectively. Figure 4a and 4b shows the Nyquist plots and Bode phase diagrams of the DSC device measured in dark at -0.70 V bias before and after the aging at 60 °C with 1 sun irradiance for 1000 h. Upon aging, the middle-frequency peak position slightly shifts to higher frequency (Figure. 4b) revealing a decrease in the electron recombination time (τ) from 37.4 ms to 16.9 ms. The decrease of electron lifetime explains the drop of V_{oc} observed upon aging the cells. The position of high frequency peak corresponding to the charge transfer reaction at counter electrode ($I_3^- + 2e^- = 3I^-$) also shift to a little higher frequency for aged cell, indicating a faster charge transfer at the counter electrode. Hence, there was an increase in the fill factor of devices during the aging process.

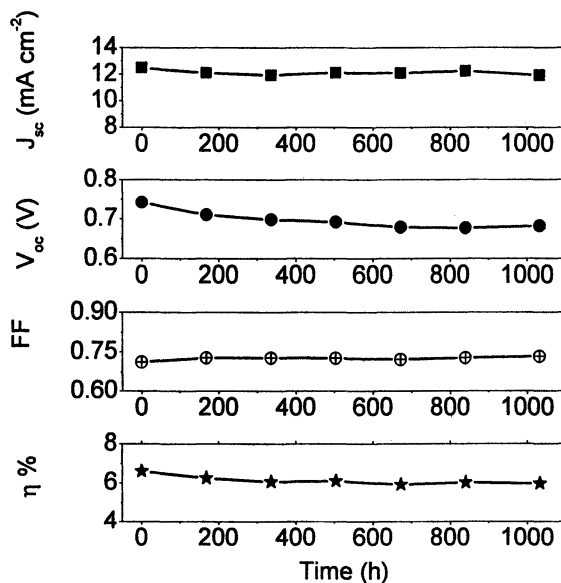


Figure 3. Evolution of photovoltaic parameter of device during continued aging under visible light at 60 °C

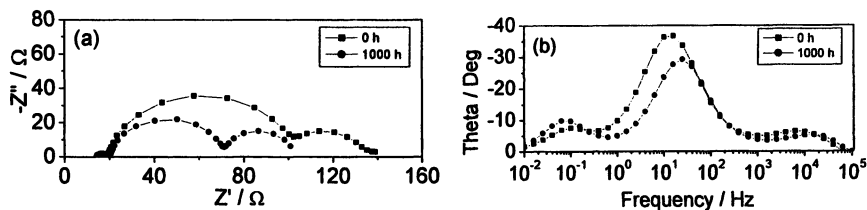


Figure. 4 Impedance spectra of the fresh cell (black) and aging cell (red) under light soaking at 60 °C for 1000 h, measured at -0.7 V bias in dark. (a) Nyquist plots; (b) Bode phase plots.

Conclusions

In conclusion, we have obtained 6.6% energy conversion efficiency at full sunlight by employing a novel ionic liquid electrolyte composed of PMII and EMITFSI. These devices show excellent stability when subjected to visible light soaking at 60 °C for 1000 h. EIS measurements of devices show that the decrease in the electron recombination time is responsible for the drop in the V_{oc} of device during 1000h light soaking test. The stable device performance of IL based DSC at accelerated light soaking test will stimulate the practical applications of DSC, particularly flexible devices.

Acknowledgement

We are grateful to R. T. Koyanagi (CCIC, Japan) for providing the 400 nm sized TiO_2 particles; The Swiss Science Foundation and Swiss Federal Office for Energy (OFEN) have supported this work.

References

1. O'Regan, B.; Grätzel, M. *Nature* **1991**, *353*, 737.
2. Grätzel, M. *Chem. Lett.* **2005**, *34*, 8.
3. Grätzel, M. *Inorg. Chem.* **2005**, *44*, 6841.
4. Kuang, D.; Klein, C.; Snaith, H. J.; Moser, J. E.; Humphry-Baker, R.; Comte, P.; Zakeeruddin, S. M.; Grätzel, M. *Nano Lett.* **2006**, *6*, 769.
5. Kuang, D.; Ito, S.; Wenger, B.; Klein, C.; Moser, J-E.; Humphry-Baker, R.; Zakeeruddin, S.M.; Grätzel, M. *J. Am. Chem. Soc.* **2006**, *128*, 4146.

6. Bach, U.; Lupo, D.; Comte, P.; Moser, J. E.; Weissörtel, F.; Salbeck, J.; Spreitzer, H.; Grätzel, M.; *Nature* **1998**, *395*, 583.
7. Wang, H. X.; Li, H.; Xue, B. F.; Wang, Z. X.; Meng, Q. B.; Chen, L. Q. *J. Am. Chem. Soc.* **2005**, *127*, 6394.
8. Wasserscheid, P.; Welton, T. *Ionic Liquids in Synthesis*; Wiley: Weinheim, **2002**.
9. Dupont, J.; de Souza, R. F.; Suarez, P. A. Z. *Chem. Rev.* **2002**, *102*, 3667.
10. Wang, P.; Bernard, W.; Humphry-Baker, R.; Moser, J. E.; Teucher, J.; Kantlehner, W.; Mezger, J.; Stoyanov, E. V.; Zakeeruddin, S. M.; Comte, P.; Charvet, R.; Grätzel, M. *J. Am. Chem. Soc.* **2005**, *127*, 6850.
11. Kuang, D.; Wang, P.; Ito, S.; Zakeeruddin, S.M.; Grätzel, M. *J. Am. Chem. Soc.* **2006**, *128*, 7732.
12. Bonhôte, P.; Dias, A. P.; Papageorgiou, N.; Kalyanasundaram, K.; Grätzel, M. *Inorg. Chem.* **1996**, *35*, 1168.
13. Bisquert, J. *J. Phys. Chem. B.* **2002**, *106*, 325.
14. Wang, Q.; Moser, J. E.; Grätzel, M. *J. Phys. Chem. B.* **2005**, *109*, 14945.

Chapter 16

The Application of Trialkyl-Imidazolium Ionic Liquids and Salts for the Preparation of Polymer–Clay Nanocomposites

Paul C. Trulove^{1*}, Douglas M. Fox¹, Walid H. Awad²,
Jeffrey W. Gilman², Cher D. Davis², Thomas E. Sutto³,
Paul H. Maupin⁴, and Hugh C. De Long⁵

¹Department of Chemistry, U.S. Naval Academy, Annapolis, MD 21402

²Fire Research Division, Building and Fire Research Laboratory, National Institute of Standards and Technology, Gaithersburg, MD 20899

³Naval Surface Warfare Center, Dahlgren Division, Dahlgren, VA 22448

⁴Office of Basic Energy Sciences, Office of Science, U.S. Department of Energy, Washington, DC 20585

⁵Directorate of Chemistry and Life Sciences, Air Force Office of Scientific Research, Arlington, VA 22203

Increasing the thermal stability of organically modified layered silicates (clays) is essential for the application of polymer-clay nanocomposites on the industrial scale. Trialkyl-imidazolium ionic liquids and salts were investigated as more thermally stable alternatives to the current alkyl ammonium clay treatments. Imidazolium treated montmorillonite clays were prepared by ion exchange and their thermal stabilities and structural properties evaluated. Tri-imidazolium treated clays were also melt blended with polystyrene (PS) and poly(ethylene terephthalate) (PET) to form nanocomposites. Results showed that the imidazolium treated clays have significantly higher thermal stabilities than current clay treatments, and they exhibit excellent compatibility with PS and PET.

Introduction

The significant flammability of many organic polymers has led to extensive work dedicated towards improving their fire retardant capabilities. For commodity polymers, cost considerations limit fire retardant solutions primarily to additive type approaches. These additives or fillers must be low cost, easily processed with the polymer to form a composite, not significantly degrade polymer performance properties in the resulting composite, and not create environmental problems at the time of final disposal or recycling. Unfortunately, current conventional additives often require loadings of 20 to 30 wt. %[†] to achieve significantly reduced polymer flammability, and at these loadings the reduced flammability is often at the expense of other polymer properties.

Recent nano-scale approaches to polymer composites, employing layered-silicate (clay) additives, have shown significant promise towards improving polymer properties at very low filler levels.^{1,2} These polymer layered-silicate nanocomposites exhibit the unusual combination of greatly enhanced flame-retardant properties^{3,4,5} in combination with considerable improvements in mechanical,⁶ thermal,⁷ and barrier⁸ properties. Furthermore, only 2 to 5 wt. % of organically modified clay is necessary to observe these property enhancements.

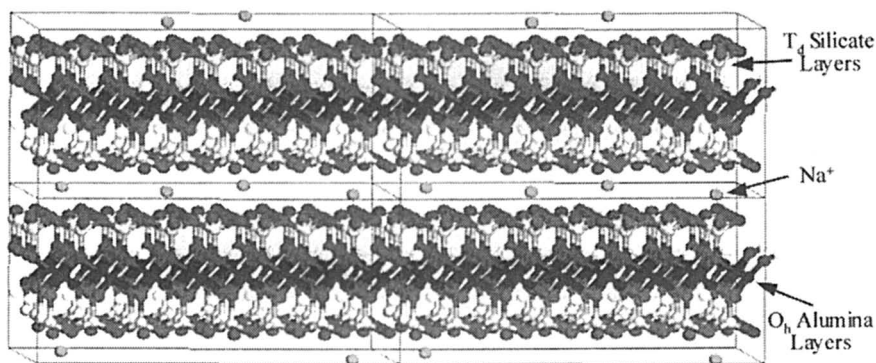


Figure 1. A molecular representation of sodium montmorillonite showing two aluminosilicate layers with Na^+ cations in the interlayer gallery⁵

Montmorillonite (MMT) is the most commonly used layered silicate in polymer-clay nanocomposites (Figure 1).⁹ MMT consists of clay layers stacked

[†] Wt. % is used here in this paper and is equivalent to mass fraction %

upon each other with a “deck of cards” like registry. Each layer is a sandwich of silica tetrahedra on the outside with aluminum oxide octahedra in the center. The gap between the clay layers is referred to as the gallery spacing and is dependent on the size of the species intercalated in the clay gallery. Isomorphic substitution within the clay layers (i.e. Fe^{2+} or Mg^{2+} replacing Al^{3+}) results in a net negative charge that is compensated by Na^+ or K^+ ions residing in the gallery space.

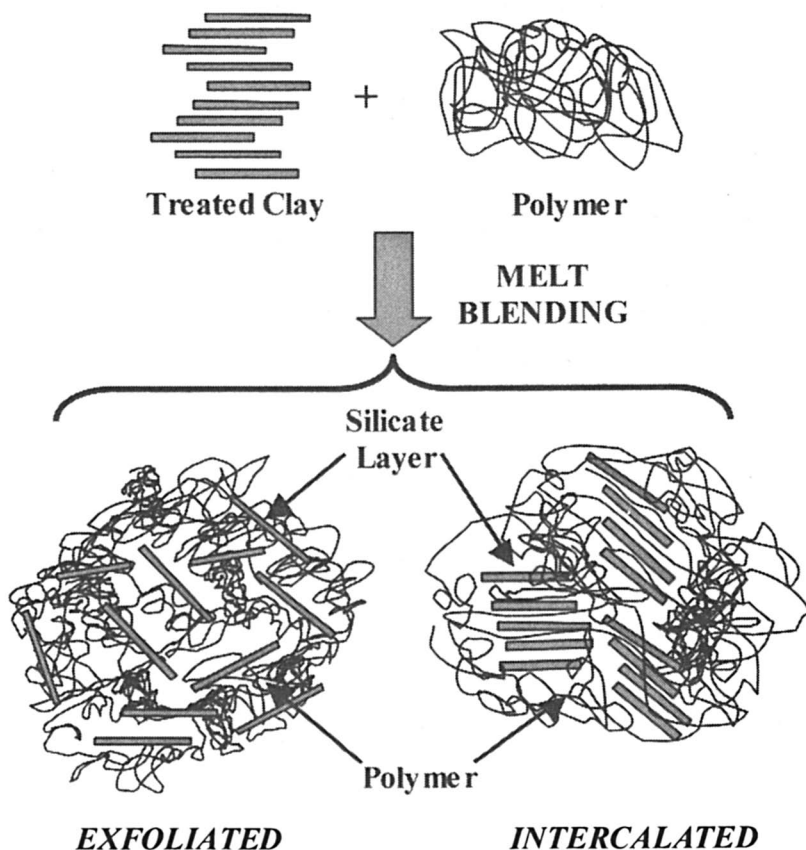


Figure 2. Schematic representation of the preparation of a polymer-layered silicate nanocomposite via melt blending.

A wide variety of methods have been employed by researchers to prepare polymer-clay nanocomposites. However, melt blending is the preferred method for large scale preparation of nanocomposites from thermoplastics (Figure 2).⁹ Melt blending involves the high-shear mixing of the neat polymer and clay at

temperatures above the polymer melt. The optimal properties of polymer-clay nanocomposites are generally obtained when the clay is fully dispersed into the polymer matrix. Two terms are often used to describe the relative dispersion of the clay in the polymer matrix, exfoliation and intercalation. Exfoliated clays are fully dispersed in the polymer matrix such that the clay particles have separated into single clay layers randomly oriented with respect to each other. Intercalated clays are less dispersed and exist as well ordered multi-layered structures where the extended polymer chains are inserted into the gallery spacing between the individual silicate layers.

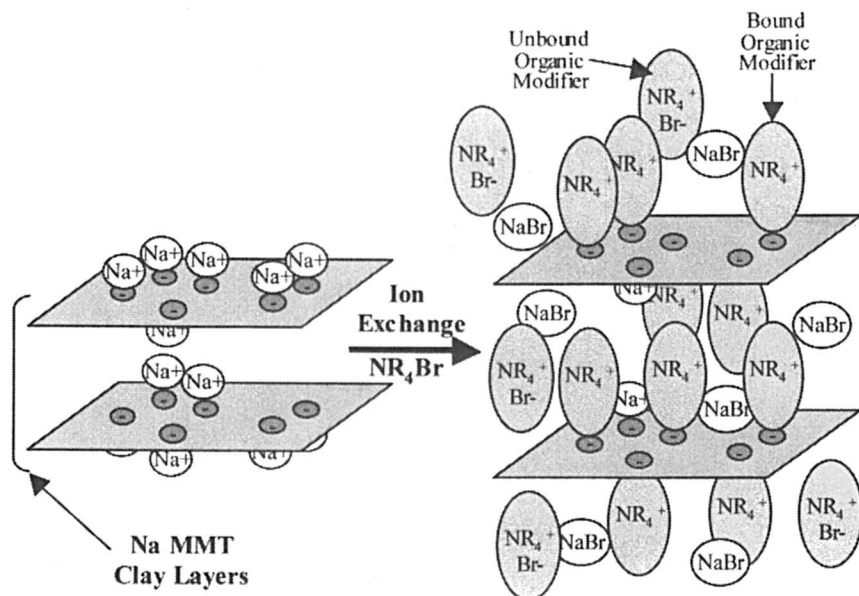


Figure 3. Schematic representation of the preparation of treated MMT clay via ion exchange with an organic modifier (quaternary ammonium bromide).

In its natural state, MMT clay does not exfoliate or intercalate in most polymers. Therefore, the clay must be treated with an "organic modifier" (commonly a quaternary alkylammonium salt) before it can be melt blended with a polymer to form a nanocomposite. Treatment most often consists of ion exchanging the natural cations in the MMT clay galleries with the organic cations (Figure 3) of the organic modifier. This gives rise to an increase in the gallery spacing (1.7 nm to 3.0 nm) of the treated clay due to the larger steric size of the organic cation. Furthermore, the organic cation improves the polymer and inorganic clay sheet interaction by acting, in essence, as a "surfactant" for the clay thus improving its compatibility with the polymer (Figure 4). Consequently,

the choice of organic modifier strongly impacts the degree of organoclay dispersion during melt blending, and, therefore, it strongly impacts the degree of property enhancement observed in the resulting polymer-clay nanocomposites.

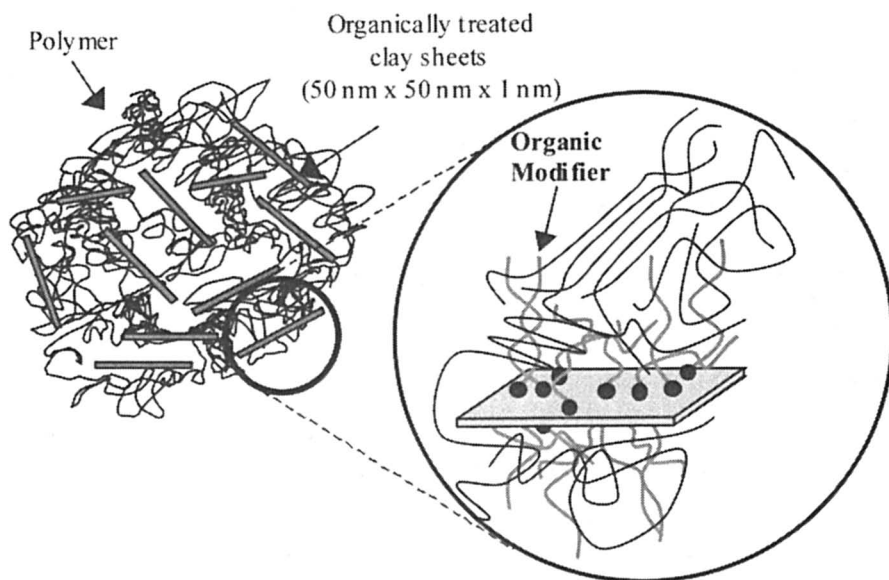


Figure 4. Diagram of the structure of a fully exfoliated polymer-clay nanocomposite

A significant limitation of the current quaternary alkylammonium treatments for MMT is their relatively low thermal stability. Most commercial alkylammonium treatments have an onset of thermal decomposition at or below 200 °C.¹⁰ The melt processing temperatures for many important engineering polymers such as polyamide-6 (PA-6), poly(ethylene terephthalate) (PET), and polycarbonate (PC) are significantly above this temperature. For example, PA-6 is generally processed in the lab (injection molded, extrusion, etc.) near 250 °C. However, industrially PA-6 is processed near 300 °C in order to increase product output. Current quaternary ammonium clay treatments are not stable at these elevated temperatures, and their decomposition appears to have a significant negative impact on the properties of the resulting nanocomposite.^{10,11,12} Consequently, there is a significant need for new organic cation treatments that will be stable at the elevated temperatures used for processing many engineering polymers.

Recent studies have shown that many imidazolium based ionic liquids and salts possess high thermal stabilities, often in excess of 300 °C.^{13,14,15,16,17,18,19,20} In the present work we evaluate several tri-alkylimidazolium salts as thermally stable alternatives to the current alkylammonium salts used for treating layered silicates. In this paper we will discuss the thermal stability of various tri-alkylimidazolium treated MMT clays, and we will present examples of the preparation and characterization of polymer/clay nanocomposites synthesized via melt blending from tri-alkylimidazolium treated MMT clays.

Experimental*

Materials

The tri-alkylimidazolium ionic liquids and salts were prepared as previously described.^{21,22,23,24,25} A total of five 1,2-dimethyl-3-R-imidazolium (R = alkyl groups from C3 to C18) treated montmorillonite organoclays were synthesized via a standard ion exchange procedure.²⁶ Either the BF_4^- or PF_6^- salt of the imidazolium cation were used for the ion exchange process. The nomenclature used for the alkylimidazolium cations in this study is given in Table I. The imidazolium-MMT clays were analyzed and then used to prepare polymer-clay nanocomposites. For comparison purposes, we also treated MMT with one of the most thermally stable organic modifiers, *N,N*-dimethyl-*N,N*-dioctadecylammonium bromide (DMDOdABr).²¹ In addition, because of the known negative effect of the Br^- ion on thermal stability we rigorously washed the DMDOdA/MMT to remove residual NaBr.¹² The 1,2-dimethyl-3-R-imidazolium-MMT clays were melt blended with polystyrene (PS) and poly(ethylene terephthalate) (PET) as previously described using a mini twin-screw extruder.^{21,27}

Instrumentation

Thermal gravimetric analysis (TGA) data were collected from 30 °C to 800 °C at 10 °C/min under N_2 and air atmosphere using a TA Instruments SDT 2960. Each sample was run in triplicate and the mean value was taken. The results are reported in terms of the onset decomposition temperature (5% mass fraction loss) and the peak decomposition temperature; both of them have an uncertainty

* The identification of any commercial product or trade name does not imply endorsement or recommendation by the National Institute of Standards and Technology or the Air Force Office of Scientific Research.

of 1.2 °C (2 sigma). X-ray diffraction data (XRD) were collected on a Philips diffractometer using Cu K α radiation, ($\lambda = 0.150\ 594\ 5\ \text{nm}$). The standard uncertainty in the d spacing was $\pm 0.03\ \text{nm}$ (2σ). Transmission electron microscopy (TEM) was performed on a Philips 400T electron microscope, using Kodak SO-161 film. TEM samples were ultra-microtomed at either room-temperature (PS) or $-110\ ^\circ\text{C}$ (PET) to cut 70-nm-thick sections. The sections were transferred onto carbon-coated Cu grids of 200 mesh.

Table 1: Nomenclature used in this study

<i>Abbreviation</i>	<i>Definition</i>
DMDOdA	<i>N,N</i> -dimethyl- <i>N,N</i> -dioctadecylammonium
DMPI	1,2-dimethyl-3-propylimidazolium
DMBI	1-butyl-2,3-dimethylimidazolium
DMDI	1-decyl-2,3-dimethylimidazolium
DMHDI	1-hexadecyl-2,3-dimethylimidazolium
DMEiI	1,2-dimethyl-3-eicosylimidazolium

Results and Discussion

Imidazolium treated layered silicates.

The 1,2-dimethyl-3-R-imidazolium treated MMT (IM-MMT) clays were analyzed by XRD to evaluate changes in interlayer spacing (d spacing) and these data are given in Table 2. In addition, Figure 5 shows XRD data from several representative IM-MMT clays. In all cases the d spacing for the IM-MMT clays is greater than that for the untreated sodium-MMT (1.12 nm, 7.8° 2-theta). Furthermore, the IM-MMT d spacing increases as the length of the imidazolium R group increases (C3 to C18). The lone exception to this trend is seen for the butyl and propyl derivatives of IM-MMT clays where approximately the same d spacing is found for both derivatives.

The results of TGA analysis of IM-MMT clays under N₂ and air atmosphere are given in Table 2. These data clearly show significant enhancement in the thermal stability of the IM-MMT clays over the DMDOdM/MMT. For example, the TGA peak decomposition temperature of all the IM-MMT clays shows an improvement of almost 100 °C over that of the DMDOdM/MMT.

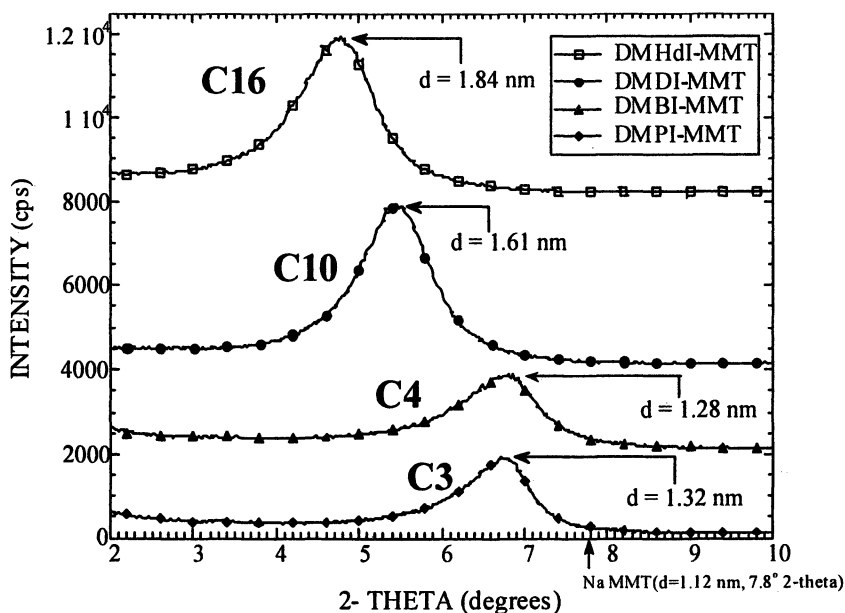


Figure 5. X-ray diffraction data showing the effect of imidazolium alkyl chain length on d spacing between layers for several treated MMT clays.

Table 2: XRD and TGA Data for 1,2-Dimethyl-3-R-Imidazolium and Quaternary Ammonium Treated Montmorillonite Clays.

Sample	TGA, °C (under N ₂)		TGA, °C (under air)		Organic content			d -spacing
	T _{onset}	T _{peak}	T _{onset}	T _{peak}	Theor.	Air	N ₂	
DMDOdA/MMT	280	308	226	299	34.11	34.43	31.15	2.61
DMPI/MMT	340	445	305	422	11.57	10.30	8.77	1.32
DMBI/MMT	340	448	303	381	12.59	11.60	9.17	1.28
DMDI/MMT	320	432	234	312	18.26	17.14	13.63	1.61
DMHdi/MMT	343	406	250	298	23.21	23.50	20.53	1.84
DMEii/MMT	308	409	250	317	26.20	27.10	26.09	2.06

Standard uncertainty ± 1.2 °C (2σ)

Table 2 shows the influence of oxygen on the thermal decomposition of the IM-MMT clays. The oxygen atmosphere significantly diminishes the thermal stability of the IM-MMT clays as evidenced by the decrease in both the onset decomposition temperature and the peak decomposition temperature. However, the thermal stabilities of the IM-MMT clays are still higher than that of quaternary ammonium treated montmorillonite under the same conditions. Table 2 also shows the theoretical and experimental organic fractions. The total organic content was lost in the temperature range 200-500 °C and was determined by accounting for the mass loss corresponding to the dehydroxylation process of montmorillonite. Good agreement was observed between the calculated values and those determined by oxidative decomposition. Nonetheless, the results also indicated that tri-alkylimidazolium and quaternary ammonium cations may be taken up in amounts exceeding cation exchange capacity. This is evident from the higher values for montmorillonite clay treated with DMDOdA, DMHdI, and DMEiI cations. A possible explanation is that for the polar cations (small R group), the excess salt accumulated in interlayer space may be easily extracted by washing with water or alcohol-water mixtures, but for less polar cations (long chain R group) the excess resists extraction.^{28,29}

Polymer Layered Silicate Nanocomposites

To investigate the ability of the new imidazolium treated clays to form nanocomposites, we synthesized several IM-MMT/polymer nanocomposites via melt blending. The polymers used for this study were polystyrene (PS) and poly(ethylene terephthalate) (PET). The PS and PET were melt blended with the IM-MMT in a twin-screw mini-extruder at 225 °C and 285 °C, respectively. Figure 6 shows the XRD data for DMBI-MMT and DMHdI-MMT clays before and after melt blending with PET. The XRD data for the DMBI-MMT shows no significant change upon melt blending with PET other than a decrease in x-ray intensity due to dilution by the polymer. This result is consistent with poor dispersion of the DMBI-MMT clay in the PET. In contrast, the XRD data for the DMHdI-MMT shows a complete loss of the peak for the treated clay upon melt blending. This result indicates good dispersion of the clay sheets in the nanocomposite. Overall observations from XRD analysis of melt blended IM-MMT/polymer indicated that the quality of clay dispersion improved as the length of the imidazolium R-group increased. Essentially no clay dispersion was observed for either PS or PET with $R < 10$, and the best clay dispersion was observed for $R \geq 16$.

The TEM image (Figure 7) of the DMHdI-MMT/PS nanocomposite shows that the 1,2-dimethyl-3-hexadecyl-imidazolium-MMT successfully dispersed and exfoliated in the PS matrix. Similar quality nanocomposites were synthesized under the same conditions using the quaternary ammonium-MMT, indicating that the DMHdI cation interacts as well with PS as the quaternary ammonium

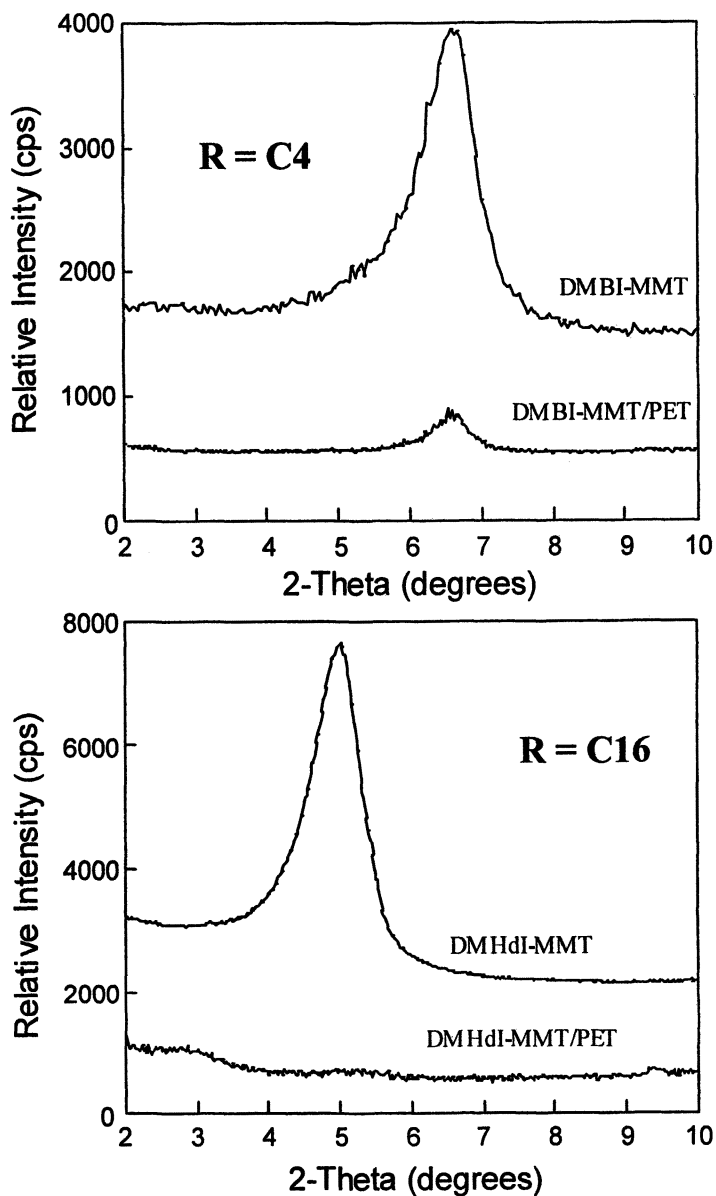


Figure 6. X-ray diffraction data for DMBI-MMT and DMHdI-MMT treated clays before and after melt blending with PET

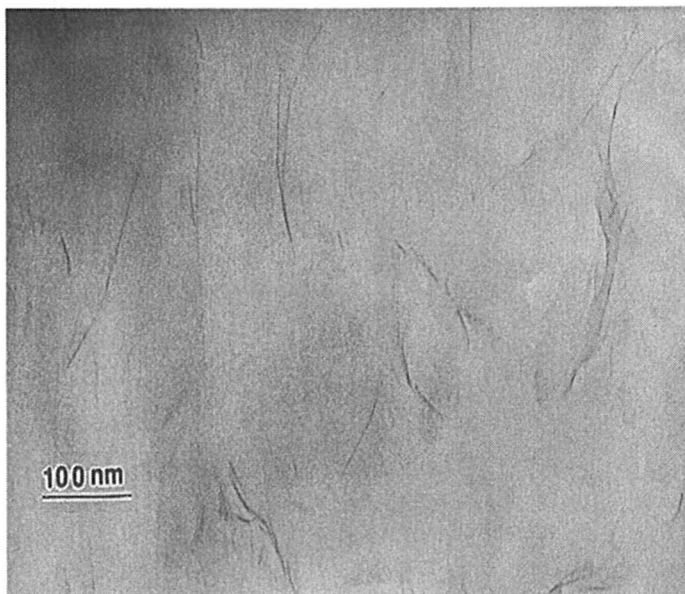


Figure 7. TEM image of PS/5 % DMHdl-MMT nanocomposite



Figure 8. TEM image of PET/5 % DMHdl-MMT nanocomposite

cation. PET is a more challenging polymer because it is moisture sensitive at elevated temperatures and quaternary ammonium clays degrade at 50 °C below the PET processing temperature (285 °C). Thus, there is no report of any PET/clay nanocomposite directly synthesized via melt mixing with an organo-clay in literature. The TEM image (Figure 8) shows that melt mixing DMHdIm-MMT in PET yields a highly dispersed and exfoliated nanocomposite. The average clay aggregate size was 2 to 4 MMT sheets, indicating this nanocomposite contains intercalated clay particles, therefore this nanocomposite would be referred to as a mixed exfoliated and intercalated system. Our previous attempts to prepare PET nanocomposites with quaternary ammonium-MMT gave black products,²⁷ with GPC analysis that indicated the PET molecular mass had significantly decreased, presumably resulting from the quaternary ammonium degradation. The DMHdIm-MMT/PET nanocomposite is evidence that with a more thermally stable organic modifier, new polymer/clay nanocomposites can be synthesized from polymers that require high temperature processing.

Conclusions

In this contribution we have discussed the oxidative and nonoxidative thermal stability of several tri-alkylimidazolium-treated MMT layered silicates. MMT clays treated with imidazolium salts showed superior thermal properties compared to the quaternary alkyl ammonium treated MMT. More importantly, MMT clays treated with tri-alkylimidazolium cations with longer alkyl (R) groups exhibited excellent compatibility with both PS and PET. Finally, these results show the significant promise of tri-alkylimidazolium ionic liquids and salts in terms of their potential application for the preparation of polymer-clay nanocomposites from polymers that require high temperature processing.

Acknowledgements

We thank Dr. Paul Stetzman for use of XRD facilities. We thank the following organizations for funding of this work: Federal Aviation Administration (DTFA 03-99-X-9009) and Air Force Office of Scientific Research.

References

* - The policy of the National Institute of Standards and Technology (NIST) is to use metric units of measurement in all its publications, and to provide statements of uncertainty for all original measurements. In this document however, data

from organizations outside NIST are shown, which may include measurements in non-metric units or measurements without uncertainty statements. The identification of any commercial product or trade name does not imply endorsement or recommendation by NIST or the United States Air Force (USAF). Opinions, interpretations, conclusions, and recommendations are those of the authors and are not necessarily endorsed by the USAF or NIST. This is a work of the US government and by statute not subject to copyright in the US.

1. Alexandre, M.; Dubois, P., *Mater. Sci. Eng. R: Reports* **2000**, 28, 1.
2. Pinnavaia, T.J.; Beal, G.W. Editors.; *Polymer-Clay Nanocomposites*, John Wiley and Sons: New York, (2000).
3. Gilman, J. W.; Kashiwagi, T.; Lichtenhan, J. D., *SAMPE Journal* **1997**, 33, 40.
4. Gilman, J. W., *App. Clay Sci.* **1999**, 15, 31.
5. Gilman, J. W.; Jackson, C. L.; Morgan, A.B.; Harris, R.; Manias, E.; Giannelis, E. P.; Wuthenow, M.; Hilton, D.; Philips, S.H., *Chem. Mater.* **2000**, 12, 1866.
6. Usuki, A.; Kojima, Y.; Kawasumi, M.; Okada, A.; Fukushima, Y.; Kurauchi, T.; Kamigaito, O., *J. Mater. Res.* **1993**, 8, 1179.
7. Tyan, H. L.; Liu, Y. C.; Wei, K. H., *Chem. Mater.* **1999**, 11, 1942.
8. Messersmith, P.; Giannelis, E.P., *J. Polym. Sci. A: Polym. Chem.* **1995**, 33, 1047.
9. Giannelis, E. P., *Adv. Mater.* **1996**, 8 (1), 29.
10. Xie, W.; Gao, Z.; Pan, W.; Hunter, D.; Singh, A.; Vaia, R., *Chem. Mater.* **13**, 2979 (2001).
11. Xie, W.; Gao, Z.; Liu, K.; Pan, W.P.; Vaia, R.; Hunter, D.; Singh, A., *Thermochimica Acta* **2001**, 367, 339.
12. Davis, R. D.; Gilman, J. W.; Sutto, T. E.; Callahan, J. H.; Trulove, P. C., De Long, H. D.; *Clay and Clay Minerals* in press.
13. Ngo, H. L.; LeCompte, K.; Hargens, L.; McEwen, A. B.; *Thermochim. Acta* **2000**, 357, 97.
14. Huddleston, J. G.; Visser, A. E.; Reichert, W. M.; Willauer, H. D.; Broker, G. A.; Rogers, R. D., *Green Chem.* **2001**, 3, 156.
15. Awad, W. H.; Gilman, J. W.; Nyden, M.; Davis, R. D.; Harris Jr., R. H.; Sutto, T. E.; Callahan, J.; De Long, H. C.; Trulove, P. C., In *Proceedings of the Thirteenth International Symposium on Molten Salts*, Trulove, P. C.; De Long, H. C.; Mantz, R. A.; Stafford, G. R.; Matsunaga, M. Eds.; 2002, 2002-19, The Electrochemical Society: Pennington NJ, 200 – 212.
16. Awad, W. H.; Gilman, J. W.; Nyden, M.; Harris Jr., R. H.; Sutto, T. E.; Callahan, J.; Trulove, P. C.; De Long, H. C.; Fox, D. M., *Thermochim. Acta* **2004**, 409 (1), 3.
17. Kosmulski, M.; Gustafsson, J.; Rosenholm, J. B., *Thermochimica Acta* **2004**, 412 (1-2), 47.

18. Fox, D. M.; Gilman, J. W.; De Long, H. C.; Trulove, P. C.; *J. Chem. Thermo.*, **2005**, 37(9), 900.
19. Wooster, T. J.; Johanson, K. M.; Fraser, K. J.; MacFarlane, D. R.; Scott, J. L., *Green Chem.*, **2006**, 8 (8), 691.
20. Katritzky, A. R.; Singh, S.; Kirichenko, K.; Smiglak, M.; Holbrey, J. D.; Reichert, W. M.; Spear, S. K.; Rogers, R. D., *Chem. – A Europ. J.*, **2006**, 12(17), 4630.
21. Gilman, J. W.; Awad, W. H.; Davis, R. D.; Shields, J.; Kashiwagi, T.; VanderHart, D. L.; Harris Jr., R. H.; Davis, C.; Morgan, A. B.; Sutto, T. E.; Callahan, J.; Trulove, P. C.; De Long, H. C., *Chem. Mater.* **2002**, 14(9), 3776.
22. Koch, V. R.; Nanjundiah, C.; Appetecchi, G. B.; Scrosati, B., *J. Electrochem. Soc.* **1995**, 142, L116.
23. Fuller, J.; Breda, A. C.; Carlin, R. T., *J. Electrochem. Soc.* **1997**, 144, L68.
24. Carlin, R. T.; Fuller, J., *Chem. Commun.* **1997**, 1345.
25. Fuller, J.; Breda, A. C.; Carlin, R. T., *J. Electroanalytical Chem.* **1998**, 459, 29.
26. Vaia, R. A.; Teukolsky, R. K.; Giannelis, E. P., *Chem. Mater.* **1994**, 6, 1017.
27. Davis, C. H.; Mathias, L. J.; Gilman, J. W.; Schiraldi, D. A.; Shields, J. R.; Trulove, P.; Sutto, T. E.; DeLong, H. C., *J. Polym. Sci., Poly. Phys.* **2002**, 40, 2661.
28. Garrett, W.G.; Walker G.F., *Clays Clay Miner.* **1962**, 9, 557.
29. Furukawa, T.; Brindley, G.W., *Clays Clay Miner.* **1973**, 21, 279.

Chapter 17

Ionic Liquids as Modifiers for Cationic and Anionic Nanoclays

Neung Hyun Kim¹, Sanjay V. Malhotra^{2,*}, and Marino Xanthos^{1,*}

¹Otto H. York Department of Chemical Engineering and ²Department of Chemistry and Environmental Science, New Jersey Institute of Technology, Newark, NJ 07102

*Corresponding authors: malhotra@njit.edu and xanthos@njit.edu

As part of a broader effort to develop nanoclays functionalized with different heterocyclic aromatic structures for novel applications, preliminary data are reported on the modification of sodium montmorillonite, a cationic clay, and hydrotalcite, an anionic clay, with four low molecular weight pyridinium and imidazolium-based ionic liquids. Commercially available unmodified montmorillonite was treated with aqueous solutions of three ionic liquids: N-ethyl pyridinium tetrafluoroborate, 1-ethyl 3-methyl imidazolium bromide and 1-hexyl 3-methyl imidazolium chloride. Commercially available hydrotalcite was treated with N-ethyl pyridinium tetrafluoroborate and its amorphous calcined version was regenerated in the presence of N-ethyl pyridinium tetrafluoroborate and N-ethyl pyridinium trifluoroacetate aqueous solutions. The modified materials were characterized qualitatively and quantitatively by FTIR, TGA, EDX, WXR and elemental analysis. The cationic clay data show an overall increase in interlamellar spacing as a result of sodium cation exchange with the cations of the ionic liquids (in spite of their relative small size) and improved thermal stability vs. commercial nanoclays modified with long chain quaternary ammonium salts. The effects were dependent on the type of the ionic liquid. The anionic clay data showed no anion intercalation for the commercial hydrotalcite and mostly surface absorption, rather than intercalation, for the calcined clay; this is possibly due to the relatively small size of the anions and the presence of a strongly bound carbonate anion, not easily amenable to exchange.

Introduction

Ionic Liquids (ILs) are organic salts with melting points below 100°C. They can be produced with a variety of cations and anions. The most common organic cations are imidazolium and pyridinium derivatives, but also phosphonium or tetra-alkyl-ammonium compounds. Anions are based on nucleophilic inorganic anions such as $[\text{BF}_4]^-$, $[\text{PF}_6]^-$, and organic anions such as $[\text{CF}_3\text{COO}]^-$, $[\text{CF}_3\text{SO}_3]^-$, etc.

Because of their insignificant vapor pressures, low melting points, good solvent characteristics for organic, inorganic and polymeric materials, adjustable polarity, selective catalytic effects, chemical and thermal stability, non-flammability and high ionic conductivity, ionic liquids have generated significant interest for a wide range of industrial applications. Examples include organic synthesis where they are employed as green solvents replacing volatile organic compounds (VOC) or substituting for various organic solvents, catalysis, polymerization, bio-processing operations (1,2), liquid-liquid extraction, gas separation, electrochemical processes, and heat transfer fluids. ILs have also the attractive benefits of easy recovery since organic molecules can be easily separated by direct distillation without loss of the ionic liquids (3).

Modification of nanoclays or nanofibers are among the emerging new applications for ionic liquids, due to their high thermal stability and ability to tune their structure as needed for a given application. Cationic nanoclays such as smectites (e.g. montmorillonite) and anionic nanoclays or layered double hydroxides (e.g. hydrotalcite), having expandable interlayer spacing, are known to be highly reactive to polar compounds containing exchangeable ions and, hence, are ideal candidates for modification with ionic liquids. The high thermal stability of ILs and the ability to tailor the structure of their cations/anions to match the application requirements have been in the center of recent research activities, mostly related to cationic clays.

Modification of montmorillonite (MMT) clay with imidazolium-based long aliphatic chain molten salts (4) showed significantly greater thermal stability (100°C improvement) than that of conventionally MMTs modified with long chain quaternary ammonium ions. The MMTs treated with alkyl-imidazolium also showed an expansion of the basal spacing (up to 1.49nm) by XRD analysis (5). MMTs modified with quaternary alkylphosphonium salts (trihexyl, tetradecyl, phosphonium tetrafluoroborate) also showed an expansion of the basal spacing (1.8nm compared to 1.1 nm in pristine MMT) and improved thermal stability up to 330°C (6,7). Incorporation of such MMTs modified with long chain aliphatic imidazolium cations (e.g. 1, 2-dimethyl-3-hexadecyl imidazolium) in polyamide or polystyrene matrices produced composites with better clay exfoliation, enhanced clay compatibility and superior thermal stability versus composites containing commercial MMTs modified with alkyl ammonium cations of limited thermal stabilities (4,7,8,9).

With respect to other nanofillers, ILs have been used as modifiers for carbon nanotubes (8). However, to our knowledge, no data have been reported

for IL modified anionic clays (e.g. hydrotalcite, HT) in spite of their potential to accommodate a variety of anions in its basal spacing from anionic surfactants (e.g. alkyl carboxylates, alkylsulfates or alkyl sulfonates) which modify their absorptive characteristics towards a variety of organic molecules including polymers (10).

In this Chapter, we report on the modification of a sodium montmorillonite, cationic clay and a hydrotalcite, carbonated anionic clay with four, low MW ionic liquids, based on imidazolium and pyridinium cations having relatively short chain length substituents, in combination with different anions. Emphasis is placed on the comparison of the ionic liquids in terms of their degree of modification of the clay interlayer spacing, their efficiency of cationic exchange/anchoring and thermal stability. The short alkyl lengths of the cations and the small size anions are not expected to significantly promote compatibility/dispersion of the modified clays with most polymer matrices in nanocomposites, where bulky cations or anions are required. However, a variety of potential applications exist in the pharmaceutical, medicinal, cosmetic, pesticide or catalysis industries where clay functionalization with small heterocyclic aromatic structures could be accomplished through exchange with appropriate, low molecular weight ionic liquids.

Experimental

Materials

Montmorillonite (MMT- Na^+), a hydrated aluminum silicate with sodium as the predominant exchangeable cation (trade name: Cloisite- Na^+ , CAS# 1318-93-0, Southern Clay Products Inc.) was obtained as a powder with typical particle size less than $2\mu\text{m}$. As per supplier's information, specific gravity of MMT- Na^+ is between 2.8-2.9, pH value of a 10% suspension is 10 and its cation exchange capacity (CEC) as reported by the supplier is 92.6meq/100g clay. In some experiments, commercial clays modified with tallow based quaternary ammonium salts [Cloisite 15A, modifier 2M2HT (Dimethyl, dehydrogenated tallow quaternary ammonium chloride); and Cloisite 30B, modifier MT2EtOH (Methyl tallow bis-2-hydroxyethyl quaternary ammonium chloride), Southern Clay Products Inc.] were used for comparison.

A synthetic hydrotalcite (HT), aluminum magnesium hydroxyl carbonate, with carbonate as the predominant exchangeable anion (trade name: Pural MG 61 HT, CAS#1344-28-1, Sasol) was obtained as a white powder with a reported average particle size of $2\mu\text{m}$ and a weight % ratio for MgO to Al_2O_3 of 61:39. The weight % of carbon in the hydrotalcite used is 2.04 wt % (10.2 wt% carbonate ion). pH value of a 10% suspension was reported to be in the range of 7-9 and the theoretical anion exchange capacity (AEC) was calculated as 340meq/100g. In some experiments a calcined hydrotalcite (CHT) produced by

heating HT at 450°C for 3 hrs to remove carbonate ions and water was used. This calcined hydrotalcite, which can be regenerated by hydration in an aqueous solution (10,11) was treated with solutions of ionic liquids.

Ionic liquids used for clay modification by ion exchange included two inidazolium based (1-ethyl-3-methylimidazolium bromide and 1-hexyl-3-methylimidazolium chloride), and two pyridinium based (N-ethyl pyridinium tetrafluoroborate and N-ethyl pyridinium trifluoroacetate) materials as shown in Table 1. IL-1 and IL-2 were obtained from Fluka whereas IL-3 and IL-4 were synthesized in our laboratories.

Table 1. Ionic Liquids used as Organic Modifiers

<i>Ionic liquid</i>	<i>Abbreviation</i>	<i>Formula</i>	<i>MW</i>	<i>State at R. T.</i>	<i>Used in ion exchange</i>
[EMIM] ⁺ [Br] ⁻	IL-1	C ₆ H ₁₁ BrN ₂	191.07	solid	Cationic
[HXMIM] ⁺ [Cl] ⁻	IL-2	C ₁₀ H ₁₉ ClN ₂	202.72	viscous liquid	Cationic
[Etpy] ⁺ [BF ₄] ⁻	IL-3	C ₇ H ₁₀ NBF ₄	194.80	solid	Cationic/ Anionic (HT, CHT)
[Etpy] ⁺ [CF ₃ COO] ⁻	IL-4	C ₉ H ₁₀ NF ₄ O ₂	221.01	liquid	Anionic (CHT)

Modification of Clays

Ionic exchange of MMT-Na⁺, HT and CHT was carried out with aqueous solutions of the ILs at different temperature/time conditions and at 1X (one equivalent) and 2X (two equivalent) concentrations of the clay based on the CEC or 1X based on the AEC. After filtration, all modified clays were repeatedly (more than 10 times) washed with distilled water. For MMTs modified with IL-1 and IL-2, washing was continued until no residual halogen anion was detected by adding 0.1M silver nitrate solution in the filtrate. It is to be noted that filtration time for all treated clays was significantly shorter than that for the unmodified one. After 24 hrs at room temperature, drying continued at 80°C for 24 hrs under vacuum. Sample designations and abbreviations are included in Tables 2 and 3.

Characterization

FTIR spectra of untreated clays, ionic liquids and modified clays were obtained using a Spectrum One FTIR Spectrometer[®] (Perkin Elmer

Table 2. Description of MMTs Modified with Ionic Liquid

<i>MMT abbreviation *</i>	<i>Modifier</i>	<i>Ionic Liquid *</i>	<i>Exchange Temp., °C/ Time, hrs/ CEC amount used</i>
MMT-0/(a)	-	-	-
MMT-1/(b)	only H ₂ O	-	80/6/ -
MMT-3/(c)	[EMIM] ⁺ [Br] ⁻	IL-1/(I)	80/6/1X
MMT-5/(d)	[EMIM] ⁺ [Br] ⁻	IL-1	80/6/2X
MMT-7/(e)	[HXMIM] ⁺ [Cl] ⁻	IL-2/(II)	80/6/2X
MMT-9/(f)	[Etpy] ⁺ [BF ₄] ⁻	IL3/(III)	80/6/2X
MMT-2/(g)	only H ₂ O	-	60/1/ -
MMT-4/(h)	[EMIM] ⁺ [Br] ⁻	IL-1	60/1/1X
MMT-6/(i)	[EMIM] ⁺ [Br] ⁻	IL-1	60/1/2X
MMT-8/(j)	[HXMIM] ⁺ [Cl] ⁻	IL-2	60/1/2X
MMT-10/(k)	[Etpy] ⁺ [BF ₄] ⁻	IL-3	60/1 /2X
MMT-15/(m)	2M2HT	-	N/A
MMT-30/(n)	MT2EtOH	-	N/A

* Letters and numbers in parentheses indicate respective designation in all subsequent Figures.

Table 3. Description of HTs and CHTs Modified with Ionic Liquids

<i>Hydrotalcite Abbreviations*</i>	<i>Modifier</i>	<i>Ionic liquid*</i>	<i>Exchange Temp., °C/ Time, hrs/ AEC amount used</i>
HT-0/(a)	-	-	-
HT-1/(b)	only H ₂ O	-	80/1
HT-3/(c)	[Etpy] ⁺ [BF ₄] ⁻	IL-3/(III)	80/1/1X
HT-2/(d)	only H ₂ O	-	60/1
HT-4/(e)	[Etpy] ⁺ [BF ₄] ⁻	IL-3	60/1/1X
CHT-0/(b)	-	-	-
CHT-1/(c)	[Etpy] ⁺ [BF ₄] ⁻	IL-3/(III)	RT/24/1X
CHT-2/(d)	[Etpy] ⁺ [CF ₃ COO] ⁻	IL-4/(IV)	RT/24/1X

* Letters and numbers in parentheses indicate respective designation in all subsequent Figures.

Instruments). Thermal stability of the untreated clays, ionic liquids and modified clays was studied by TGA (TA Instruments' QA 50 thermogravimetric analyzer) from room temperature to 500°C, at a heating rate of 15°C/min in a nitrogen atmosphere. Wide Angle X-Ray Diffraction (WXRDX) with a Philips PW3040 diffractometer (Cu K α radiation $\lambda=0.154$ nm, generator voltage = 45 kV, current = 40 μ A) was used to calculate *d*-spacing of unmodified and modified clays. Morphology and surface atomic analysis of clays were studied by SEM/EDX (LEO 1530VP Emission Scanning Electron Microscope). Quantitative elemental analysis of modified clays for nitrogen and fluorine was performed by standard analytical techniques.

Results and Discussion

Cationic clays

Figures 1-3 compare FTIR spectra of unmodified MMT-Na⁺ (MMT-0), pure ionic liquids IL-1, IL-2 and IL-3 and clays modified at 2X the clay's CEC concentration with IL-1 (MMT-5), IL-2 (MMT-7) and IL-3 (MMT-9). All compositions were prepared at 80°C/6hrs conditions. Not shown are spectra obtained at 1X the clay's CEC by using IL-1 (MMT-3) since the spectrum of the latter was identical to that of MMT-5. All spectra of the modified clays contain characteristic peaks of the ionic liquids (pyridinium and imidazolium cations) shown by arrows, an indication of anchoring or intercalation. Spectra obtained at 60°C/1hr conditions were very similar to the ones obtained at 80°C/6hrs and are not included here. This is an indication that cation exchange takes place fairly rapidly and that different treatment times and temperatures may not be important factors for the modification of MMTs.

Figures 4-5 show TGA data for pure ionic liquids and (Figure 4) and for modified clays (Figure 5). Thermal stability of the ionic liquids is ranked as IL-3>IL-1>IL-2. The same trends are followed in the stability of the modified clays, MMT-9>MMT-5>MMT-7. This may suggest that exchange with the Etpy ion results in more stable organoclays than exchange with EMIM or HXMIM, assuming, of course that the residual temperature stable BF₄ ion has been fully removed from our samples by washing. Note that the overall weight losses are lower for MMT-3 (produced at 1X the clay CEC) than MMT-5 (produced at 2X the clay CEC). Figures 4-5 also contain data for the unmodified MMT-0 and two commercial organoclays (MMT-15 and MMT-30) that are modified with large amounts of thermally unstable tallow based quaternary ammonium salts.

Figure 6 shows shifting of the *d*-spacing of the IL modified clays to lower diffraction angles by comparison to the unmodified MMT-0 (as received) or its washed version (MMT-1). The higher extent of intercalation corresponding to the largest interlayer distance of 1.41 nm in MMT-7 is obtained with IL-2, which has a relatively bulkier cation than the other two ionic liquids. Results are comparable with those reported in (4) for dimethyl imidazolium ionic liquids

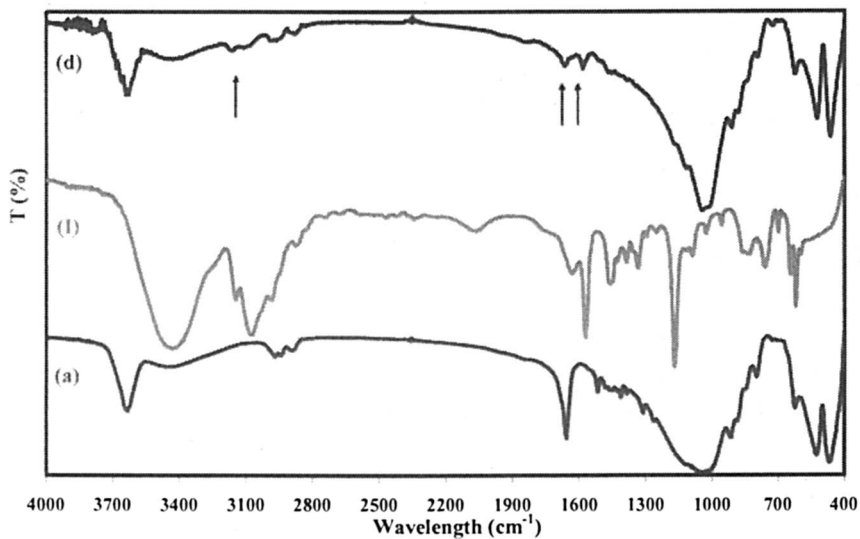


Figure 1. FTIR spectra of (a) MMT-0, (d) MMT-5, and (I) IL-1

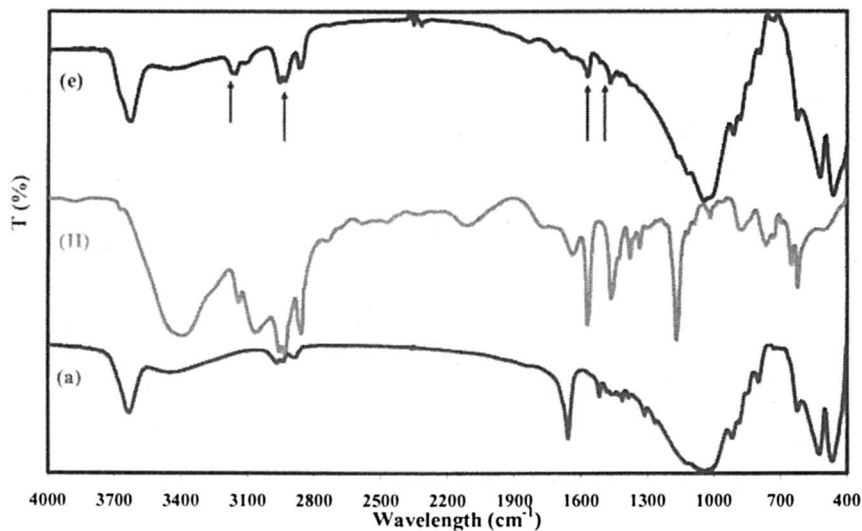


Figure 2. FTIR spectra of (a) MMT-0, (e) MMT-7, and (II) IL-2

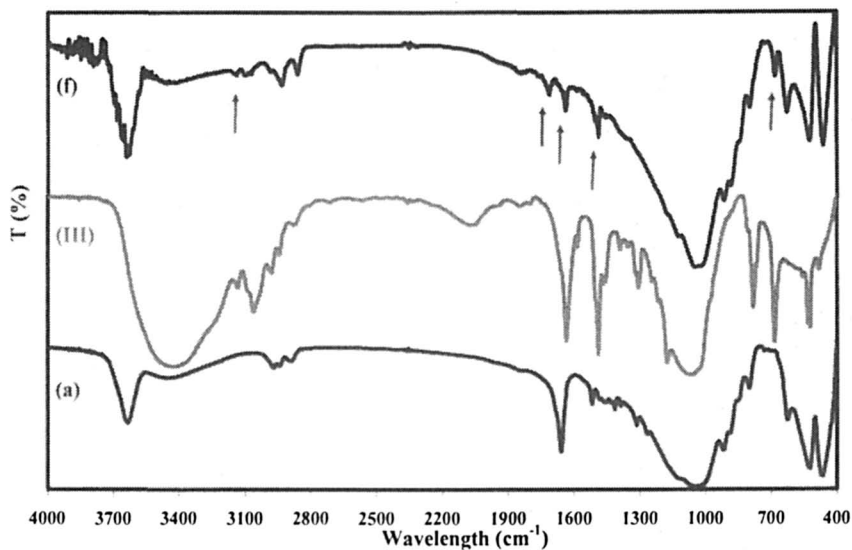


Figure 3. FTIR spectra of (a) MMT-0, (f) MMT-9, and (III) IL-3

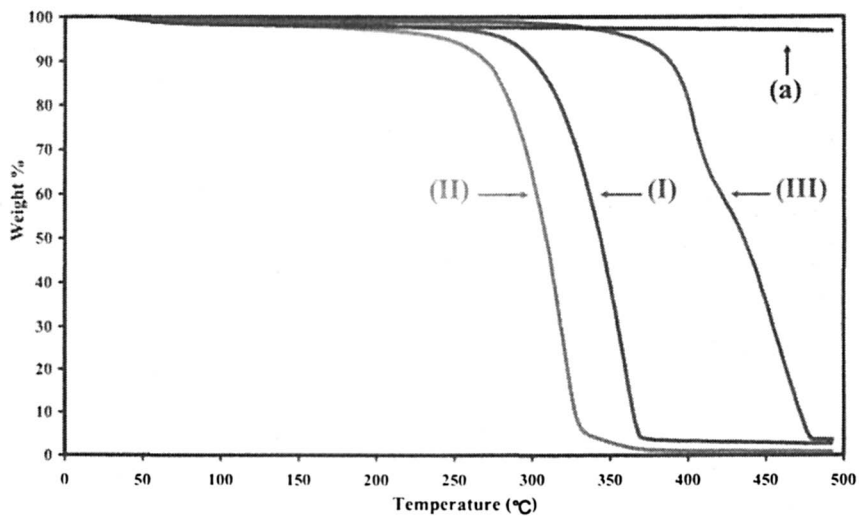


Figure 4. TGA results of (I) IL-1, (II) IL-2, (III) IL-3, and (a) MMT-0

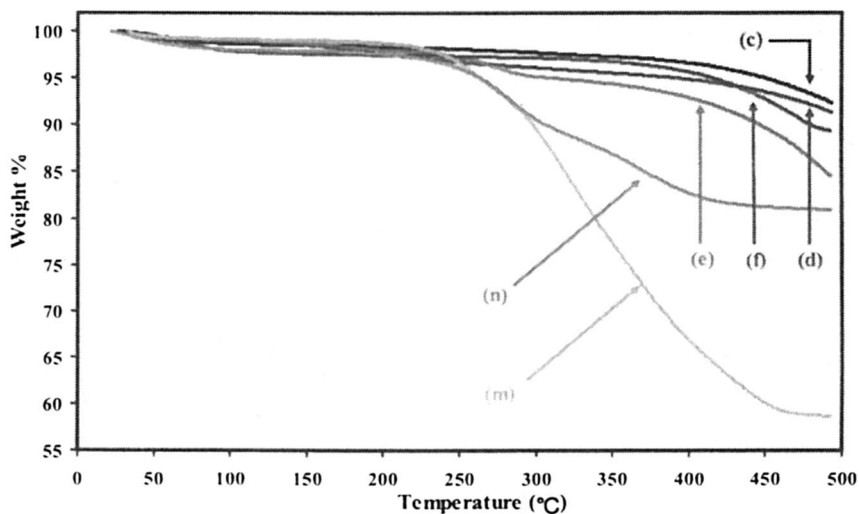


Figure 5. TGA results of (c) MMT-3, (d) MMT-5, (e) MMT-7, (f) MMT-9, (m) MMT-15, and (n) MMT-30

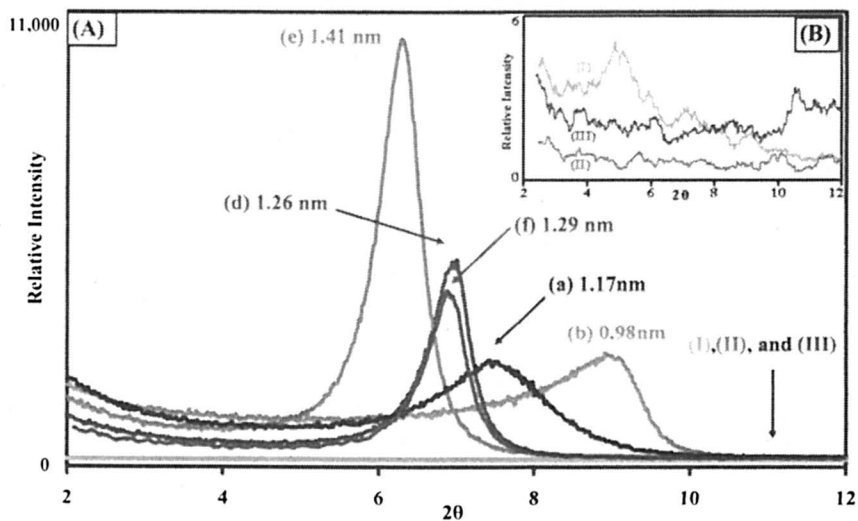


Figure 6. (A) WXR D results of (a) MMT-0, (b) MMT-1, (d) MMT-5, (e) MMT-7, (f) MMT-9, (I) IL-1, (II) IL-2, and (III) IL-3; (B) Insert of WXR D results of Ionic Liquids: (I) IL-1, (II) IL-2, and (III) IL-3

with variable alkyl chain length where MMT organoclay *d*-spacings increased from 1.28 nm for a propyl group to 1.61 nm for a butyl substituents. It should be noted that the *d*-spacing of a commercial organoclay (MMT-15) containing inorganic intercalants with long alkyl chain was found to be significantly higher (3.13 nm) than the spacings of all the IL modified clays.

Theoretical C:N weight ratios for the three ionic liquids used in this work as well as their cations were as follows: IL-1, 2.57; IL-2, 4.3; IL-3, 6.0. In the EDX results of MMTs modified with ionic liquids (Table 4) duplicate samples obtained at different surface locations show C:N weight ratios differing by 10-20% of the above values and total absence of the exchangeable sodium. These results indicate that MMTs modified with ionic liquids can be purified by washing and that the IL cations become part of the MMTs structure. Nitrogen content was determined on single organoclay samples and wt% cation was calculated as: MMT-5, 9.3%, MMT-7, 13.6%, MMT-9, 8.4%. These values are in reasonably good agreement with weight loss values obtained by TGA analysis: 7.96 wt % for MMT-5, 13.10 wt% for MMT-7, and 10.09 wt% for MMT-9 at 480°C (see Figure 5).

Table 4. EDX Results of MMTs Modified with Ionic Liquids.

<i>Clay</i>	<i>MMT-5</i>		<i>MMT-7</i>		<i>MMT-9</i>	
<i>Location</i>	<i>1</i>	<i>2</i>	<i>1</i>	<i>2</i>	<i>1</i>	<i>2</i>
<i>Element</i>	<i>Wt%</i>	<i>Wt%</i>	<i>Wt%</i>	<i>Wt%</i>	<i>Wt%</i>	<i>Wt%</i>
C	11.39	10.05	13.05	13.90	17.53	17.85
N	3.64	3.29	3.22	3.62	3.32	3.70
O	49.89	52.50	47.91	45.10	40.78	50.21
Mg	1.32	1.14	1.23	0.17	1.24	0.77
Al	9.33	9.07	9.00	9.68	9.13	7.32
Si	24.43	24.40	25.59	26.53	28.00	20.15

Anionic clays

Hydrotalcites treated with IL-3 under different conditions (see Table 3) were also characterized by FTIR, TGA, and WXR. The data did not show any differences from those of HT-0 (untreated HT-61), thus, confirming the difficulty in exchanging the strongly bound carbonate anion as reported by several authors (10).

FTIR data of calcined hydrotalcite treated with IL-3 and IL-4 indicated the presence of characteristic peaks due to the anions of the pure ionic liquids; this suggests their strong attachment to the hydrotalcite structure that was reconstituted during treatment with the ionic liquid solutions. TGA results in

Figure 7 confirmed the presence of ILs in CHT-1 and CHT-2. Note the similarities of the shape of the TGA curves of CHT-1 and CHT-2 with the curve of the non-calcined hydrotalcite and the absence of the first degradation step which corresponds to the removal of the carbonate ion in the CHT-0 (non-hydrated) curve. It appears that our treatment conditions did not prevent CO₂ from the atmosphere or from the aqueous solution to reenter in the hydrotalcite structure during reconstitution.

WXRd results shown in Figure 8 indicate the collapse of the hydrotalcite structure by calcination (compare HT-0 and CHT-0) and only slight shifts of the *d*-spacings of HT-0 after treatment with the solutions of the ionic liquids. This may be due to the relatively small anions of the ionic liquids used and/or the competing effects of hydroxyl groups absorbed from solution preventing intercalation.

EDX results of HT-0 indicated the presence of C, O, Mg, Al at the expected concentrations. Analysis of both CHT-1 and CHT-2 showed the presence of fluorine, an indication of absorption or intercalation of the IL anion into the interlayers of CHTs. Based on fluorine concentrations of 1.5-1.6 wt% obtained by elemental analysis, calculations showed that the wt% of the ionic liquids on the clay were about 1/3 of the theoretical anion exchange capacity. Carbon and nitrogen content analysis of CHT-1 and CHT-2 suggested that the cations were still part of the modified structure. Exact determination of the cation content from carbon and nitrogen analysis presented difficulties, since a small concentration of the carbonate anion reappearing in the reconstitution of the hydrotalcite structure could only be approximated; while in the case of IL-4 carbon was also present in its anion.

Conclusions

Cationic clays: Intercalation of three ILs containing small cations in MMT, through exchange with interlamellar sodium ions, was achieved and confirmed by qualitative and quantitative techniques. Highest thermal stability of the modified MMTs was obtained after treatment with N-ethyl pyridinium tetrafluoroborate. The highest degree of intercalation was obtained with the long side chain 1-hexyl, 3-methyl imidazolium cation.

Anionic clays: As received carbonated hydrotalcite, treated under different conditions with two N-ethyl pyridinium ionic liquids ([BF₄]⁻ and [CF₃COO]⁻) anions, showed no intercalation or even the presence of anions as confirmed by FTIR, TGA, and WXRd analysis. Calcined hydrotalcite having a amorphous structure was regenerated in its crystalline form by treatment with aqueous solutions of the ionic liquids to produce IL modified hydrotalcites. Characterization data and elemental analysis of such modified structures suggest mostly surface absorption of the anions of the ionic liquid rather than intercalation, but also the presence of the corresponding cations.

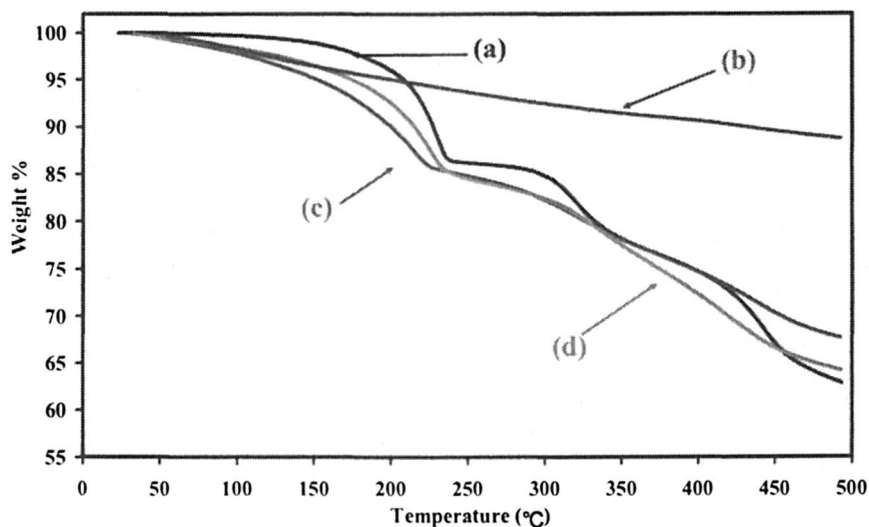


Figure 7. TGA results of (a) HT-0, (b) CHT-0, (c) CHT-1, and (d) CHT-2.

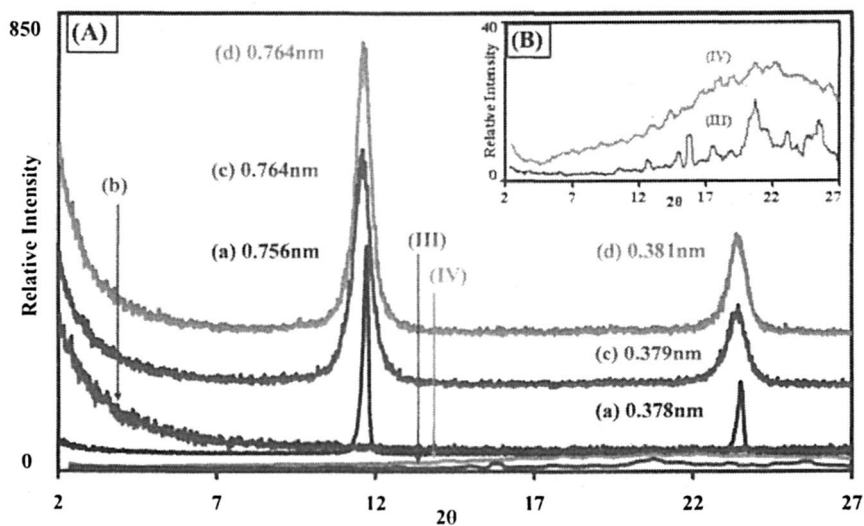


Figure 8. (A) WXR D results of (a) HT-0, (b) CHT-0, (c) CHT-1, (d) CHT-2, (III) IL-3, and (IV) IL-4. (B) Inset of WXR D results of Ionic Liquids: (III) IL-3, and (IV) IL-4.

References

1. Zhao, H., Malhotra, S. V., *Aldrichimica Acta*, **2002**, *35* (2), 75-83.
2. Zhao, H., Malhotra, S. V., and Luo, R. G., *Physics and Chemistry of Liquids*, **2003**, *41*(5), 487-492
3. Wasserscheid, P.; Welton, T. *Ionic liquids in Synthesis*, John-Wiley & Sons. New York, **2002**.
4. Gilman, J. W., Awad, W. H., Davis, R. D., Shields, J., Harris, R. H., Davis, C., Morgan, A. B., Sutto, T. E., Callahan, J., Trulove, P. C., and Delong, H. C., *Chem., Mater.*, **2002**, *14*, 3776-3785
5. Awad, W. H., Gilman, J. W., Nyden, M., Harris, R. H., Jr. Sutto, T. E., Callahan, J., Trulove, P. C., Delong, H. C., and Fox, D. M., *Thermochimica Acta*, **2004**, *409*, 3-11
6. Byrne, C., McNally, T., and Armstrong, C. G., "Thermally Stable Modified Layered Silicates for PET Nanocomposites", Proc. of Polymer Processing Society, PPS 2005, Americas Regional Meeting, Quebec, August, 2005.
7. Stoeffler K., Lafleur P.G., Denault J., Proc. Soc. Plast. Eng. Ann. Tech. Conf., 2006 p. 263.
8. Fox, D.M., Bellayer, S., Murariu, M., Gilman, J.W., Maupin, PH., De Long, H. C. and Trulove, P.C., Ch. 12 in "*Ionic Liquids in Polymer Systems*", C.S. Brazel and R.D. Rogers, Eds., ACS Symposium Series 913, American Chemical Society, Washington, DC, 2005, pp 175-188.
9. Morgan, A. B., Harris, J. D., *Polymer*, **2004**, *45*, 8695-8703.
10. Braterman, P. S., Xu, Z.P. and Yarberry, F. in Auerbach, M., Carrado, K. and Dutta, P.K., (Eds.), Ch. 8, "*Handbook of Layered Materials* ", Marcel Dekker, Inc, New York, NY, 2004, pp. 373-474.
11. Sasol Germany GmbH, Germany, Product Information Hydrotalcites-PuralMG6 IHT, (2005).

Chapter 18

Solution Chemistry of Cm(III) and Eu(III) in Ionic Liquids

S. Stumpf¹, I. Billard¹, and P. J. Panak²

¹Institut Pluridisciplinaire Hubert Curien, 23 Rue de Loess, P.O. Box 28,
67037 Strasbourg, France

²Forschungszentrum Karlsruhe, Institut für Nukleare Entsorgung,
P.O. Box 3640, 76021 Karlsruhe, Germany

Ionic liquids (ILs) are discussed to replace traditionally used organic solvents in view of reprocessing of radioactive waste. In this context the separation of lanthanides and actinides is of great importance. The objective of this work is to understand classical solution reactions in ILs in view of their application in actinide/lanthanide reprocessing and to answer the questions: “Do ILs behave as normal solvents?” OR “Do lanthanides behave different in ILs compared to actinides?” Time-resolved laser fluorescence spectroscopy (TRLFS) is used to clarify the influence of Cu(II) on the fluorescence emission of Eu(III) and Cm(III) comparatively in BumimTf₂N and in water. The investigations show that solvation chemistry has definitely a great influence on solution chemistry/reactivity of lanthanides and actinides in ILs.

The management of highly radioactive waste actually represents a very important concern and is discussed in terms of its ultimate disposal and/or its reprocessing by partitioning and further transmutation. In contrast to the traditionally used extracting phases, low melting organic salts known as Ionic Liquids (ILs) represent a new class of “green” solvents that are inherently safer (1). Because of their tunable physical properties ILs can be designed for specific tasks and therefore become a suitable extracting phase (2). By grafting extracting moieties on the organic skeleton new ILs can be synthesized that possess both the “green” aspect and the properties suited for a given actinide/lanthanide extraction/partitioning goal. It is clear that the potential for the use of ILs in extraction processes is great but there is a necessary yet missing fundamental understanding of the coordination chemistry and the extraction mechanisms. Especially the potential of ILs to be used in actinide/lanthanide separation schemes is largely unemployed. The intent of the presented studies is to clarify solution reactions (e.g. quenching processes) of the lanthanide Eu(III) and the actinide Cm(III) in BumimTf₂N (1-butyl-3-methylimidazolium-bis(trifluoromethylsulfonyl)imide) compared to the aqueous case.

Time resolved laser fluorescence spectroscopy (TRLFS) represents a well-known experimental method that is suited for studying chemical reactions of Eu(III) and Cm(III) in solution (3). The different Eu(III) and Cm(III) species that are formed by the dissolution in BumimTf₂N are characterized by their emission spectra and fluorescence emission lifetimes. The position and shape of the fluorescence emission spectra provides information on the ligand field of the Eu(III) and Cm(III) metal ions in solution. This makes the determination of different solution species possible. Moreover ligands that are coordinated to the fluorescing central ion can have an influence on the fluorescence emission lifetime by quenching processes. It is known from literature that water quenches the fluorescence by vibration transfer processes. Ligands with N-H oscillators, having vibronic frequencies similar to the O-H ones, are also effective as nonradiative de-activators of the Eu(III) and Cm(III) excited states (4). The resulting correlation between emission lifetime and the number of quenchers in the first coordination sphere of europium and curium allows a further characterization of different Eu(III) and Cm(III) species (5). In literature also the influence of cations like Fe(III), Cu(II) and Mn(II) on the fluorescence emission of Eu(III) and Cm(III) in aqueous solution has been reported (6). Here the quenching is primarily a result of dipole-dipole interactions between the donor and acceptor. This kind of interaction results in a decrease of fluorescence emission intensity as well as the fluorescence emission lifetime. In this study the latter described quenching reaction should serve as basis for understanding ‘simple’ solution reactions in ILs. The actual investigations of the interaction between the fluorophore Eu(III) and Cm(III) respectively and the quencher Cu(II) should give an idea of solvation of Eu(III) and Cm(III) in BumimTf₂N. Moreover the investigations should clarify the impact of solvation onto solution chemistry.

Experimental Section

Measurements in H₂O

To avoid hydrolyses of Eu(III) and Cm(III) quenching experiments in water (MilliQ) were performed at pH 1. Therefore all used solutions were acidified with HClO₄.

Eu(OTf)₃ (Sigma Aldrich) was dissolved in water. The final Eu(III) concentration was $1 \cdot 10^{-2}$ M. The concentration of Cm(III) in water was about $1.2 \cdot 10^{-7}$ M (stock solution composition: 89.68% ²⁴⁸Cm, 0.07% ²⁴⁷Cm, 9.38% ²⁴⁶Cm, 0.14% ²⁴⁵Cm, 0.30% ²⁴⁴Cm, and 0.43% ²⁴³Cm; concentration: $6 \cdot 10^{-6}$ mol/L Cm(ClO₄)₃).

Cu(OTf)₂ (Sigma Aldrich) solutions were prepared for further quenching experiments with different concentrations of Cu(II): $1 \cdot 10^{-4}$ M, $1 \cdot 10^{-3}$ M, $1 \cdot 10^{-2}$ M, $1 \cdot 10^{-1}$ M, 1 M, 2M.

For quenching investigations of the Eu(III) fluorescence the Cu(II) concentration in the Eu(OTf)₃ solution was raised in steps from 0 M to 0.25 M Cu(II). For each step the fluorescence emission and lifetime was measured by TRLFS. The same procedure was performed for the Cm(III) sample. Here the Cu(II) concentration was varied from 0 M up to a value of $5.35 \cdot 10^{-1}$ M.

Measurements in BumimTf₂N

Eu(OTf)₃ salt was dissolved in BumimTf₂N (Solvionics) ($1 \cdot 10^{-2}$ M Eu(III)). In order to dry the sample it was put to the vacuum line for 2 h at 70°C and 2 mbar.

Samples with different concentrations of Cu(OTf)₂ in BumimTUN were prepared as described above. The Cu(II) concentration was: $1 \cdot 10^{-3}$ M, $1 \cdot 10^{-2}$ M and $1 \cdot 10^{-4}$ M.

To perform a series of data points for the influence of Cu(II) on the Eu(III) fluorescence emission the Cu(II) concentration of the same Eu(III) sample was raised in several steps from 0 M Cu(II) up to a value of $1 \cdot 10^{-4}$ M Cu(II). For each concentration fluorescence emission spectra and lifetimes were recorded. The measurements were performed within a day.

In order to check that the water content of the samples stays constantly at its minimum, it was determined after each addition of Cu(II) solution by Karl Fischer titration (Mettler Toledo DL 32; detection limit $< 5 \times 10^{-3}$ M) and Infrared Spectroscopy (Bruker Equinox 55). No macroscopic uptake of water could be detected.

A droplet of the Cm(III) stock solution was put directly into a quartz cuvette and evaporated by heating on a heating surface at 100°C for 30 minutes. After evaporation dry BumimTf₂N was added. The final Cm(III) concentration of this

sample was 1.2×10^{-7} M. After the addition of BumimTf₂N the sample was put into an oven for 1 h at 70°C and 2 mbar to get it as dry as possible.

In order to record the quenching influence of Cu(II) onto the Cm fluorescence the concentration of added Cu(II) to the same Cm(III) sample was raised from 0 M up to 4.6×10^{-4} M. Before measuring the fluorescence emission and fluorescence emission lifetime the fluorescence sample was put in the oven for 1 h at 70°C and 2 mbar to avoid the influence of minimal amounts of absorbed water during opening the cuvette.

TRLFS

Emission spectra of all Eu(III) samples were recorded with a spectrofluorimeter (Photon Technology International). The measurements were not time resolved. Samples were excited at 394 nm and recorded in a range from 570 nm to 635 nm and a step size of 0.5 nm.

Lifetime measurements were performed using a Nd:YAG laser set up (10Hz, 6 ns pulse duration, 1.2 mJ, GCR 11, Spectra Physics). The fluorescence emission signal was detected by a monochromator (Jobin-Yvon, H20, precision ± 05 nm) connected to a photomultiplier (Philips, XP2254B) and an oscilloscope (Tektronik, 500 MHz, 10000 channels, 8 bit resolution). Eu(III) was excited at 266 nm. The decay was analyzed at 612 nm.

The Cm(III) speciation by TRLFS was performed using an excimer-pumped dye laser system (Lambda Physics, EMG 201 and FL 3002). Cm was excited at 375 nm and the resulting fluorescence emission was measured in the spectral range of 580 nm – 620 nm, using a delay time of 1.2 μ s at a gate width of 1.3 ms. An optical multichannel analyzer was used for detection, which consists of a polychromator (Jobin Yvon, HR 320) with a 1200 lines/mm grating and an intensified photodiode array (Spectroscopy instruments, ST 180, IRY 700G).

Results and Discussion

Eu(III) and Cm(III) Fluorescence Quenching by Cu(II) in H₂O

The most suited solution reaction that can be easily monitored by TRLFS is the quenching of fluorescence emission. The energy transfer by interaction of the fluorophore (e.g. Eu(III), Cm(III)) with metal ions like iron (7) or copper (8,9) is primarily a result of dipole-dipole interactions between the donor and acceptor caused by collisional encounters (dynamic quenching) (10). For the described process a decrease in fluorescence emission yield and lifetime occurs because the quenching rate depopulates the excited state without fluorescence emission. The quenching process can be described by the Stern-Volmer-equation (9):

$$\lambda = \lambda_0 + k_{SV}[Q] \quad (1)$$

[Q] concentration quencher

k_{SV} bimolecular quenching constant

λ decay rate of the fluorophore

λ_0 decay rate of the fluorophore in absence of a quencher

In the presented study the quenching influence of Cu(II) on the fluorescence emission has been comparatively performed for Eu(III) and Cm(III) in water at pH 1. The intend was to clarify if Eu(III) and Cm(III) can be considered as homologues in view of their solution chemistry. Moreover a comparison to the same reaction performed in BumimTf₂N should highlight a change of chemical behaviour of the lanthanide and actinide by changing the solvent. With this a characterization of ILs as a new solvent class is possible. Emission spectra of Eu(III) at different Cu(II) concentrations are presented in Figure 1a. In the absence of Cu(II) the Eu fluorescence emission with two maxima at 588 nm and 612 nm shows a monoexponential decay behaviour. That can be explained by the presence of only one Eu(III) species in the system. The calculated lifetime has a value of 116.9 μs which corresponds to the Eu(III) aquo ion coordinated by nine water molecules (5). With increasing copper concentration the fluorescence emission intensity and the fluorescence emission lifetime respectively are decreasing. The ratio of the two emission maxima as well as the monoexponential decay behavior of the fluorescence emission stay constant for the whole series. That is, the Eu speciation is not changing during the quenching process. From the data the Stern-Volmer has been determined to be $1.2 \cdot 10^4 \text{ M}^{-1} \text{ s}^{-1}$ (Figure 1b). The same reaction was performed with Cm(III). The peak maximum of the Cm fluorescence emission is at 593.8 nm. It's position does not change with increasing Cu(II) concentration. Also the fluorescence decay behaviour is monoexponential for the whole series. A lifetime of 66.2 μs determined for Cm(III) in water (pH 1) in absence of the Cu quencher corresponds to the curium aquo ion again coordinated by nine water molecules (5). The increase of copper concentration in this system again leads to a decrease of the Cm(III) fluorescence emission. The lifetime decreases to a value of 41.9 μs at a Cu(II) concentration of 0.5 mol/L. The calculated quenching constant (Figure 2) of this reaction is the same as it was determined for Eu(III) and has a value of $1.27 \cdot 10^4 \text{ M}^{-1} \text{ s}^{-1}$.

These results show that in an aqueous system solvation as well as solution chemistry of the lanthanide Eu(III) and the actinide Cm(III) are the same.

Eu(III) and Cm(III) solvation in BumimTf₂N

As it is already described in literature the water content of BumimTf₂N has a great influence on the speciation of Eu(III) in this IL because water can be

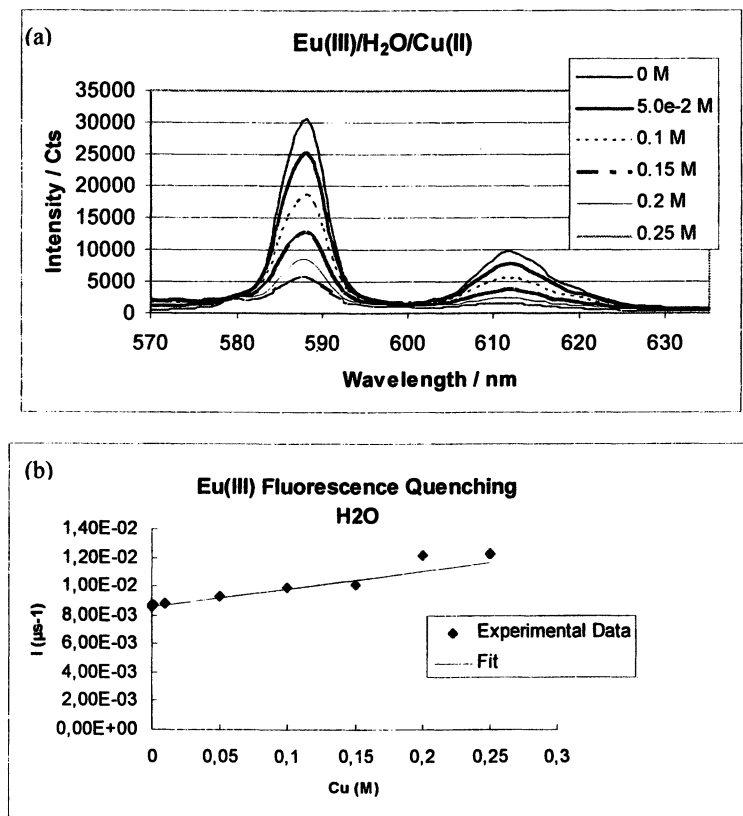


Figure 1. a) Eu(III) emission spectra in H₂O b) corresponding Stern-Volmer plot

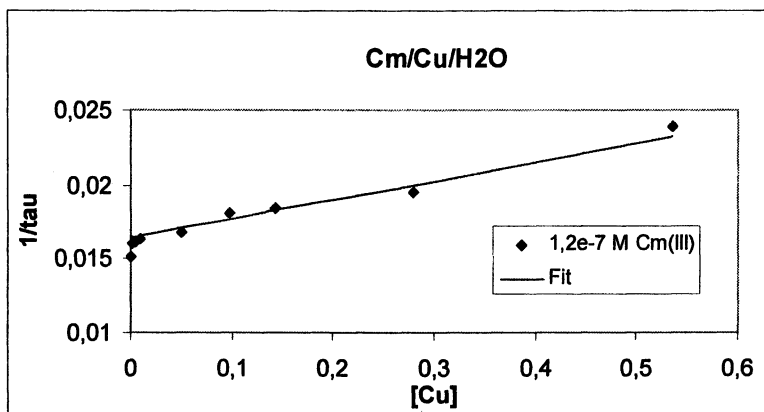


Figure 2. Stern-Volmer plot of the Cm(III) fluorescence quenching by Cu(II,)

considered as a competitive ligand for the first coordination sphere of Eu(III) (11). Lifetime measurements show that the solvation of Eu(III) and Cm(III) in BumimTf₂N always results in a biexponential decay behavior that is two species with two different lifetimes for each metal ion are formed in BumimTf₂N (Figure 3a and 3b). The fit of the biexponential decay of the Eu(III) fluorescence leads to a value of 2.5 ms for the first species and 1 ms for the second species. The value of 2.5 ms was already determined by Billard et al. (11) and corresponds to a Eu(III) species that is solely coordinated by the solvent ligands. A value of 1 ms for the second species indicates the Eu coordination by another ligand in the first Eu(III) coordination sphere which quenches the Eu fluorescence. The water content of the sample determined by Karl Fischer titration is < 50 ppm. That is to say, the maximum coordination of Eu(III) by water is 1. With this, the conclusion is allowed that an emission lifetime of 1 ms corresponds to an Eu(III)-BumimTf₂N species with one water molecule in the first coordination sphere resulting in an additional quenching effect.

The Cm(III) fluorescence decay behavior in dry BumimTf₂N is again biexponential. Lifetimes of 1 ms and 300 μs are determined. A comparison of these values with Cm(III) lifetimes cited in literature shows that 1 ms corresponds to a Cm(III) species without water in the first coordination sphere while 300 μs indicate a coordination of 1 water molecule (5).

At this point one can make a first statement. That is, europium and curium can be regarded as good homologues what solvation/coordination in BumimTf₂N is concerned.

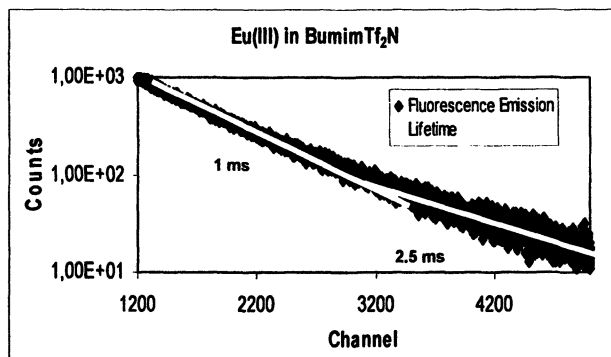


Figure 3a. biexponential decay behavior of the Eu(III) fluorescence emission in BumimTf₂N

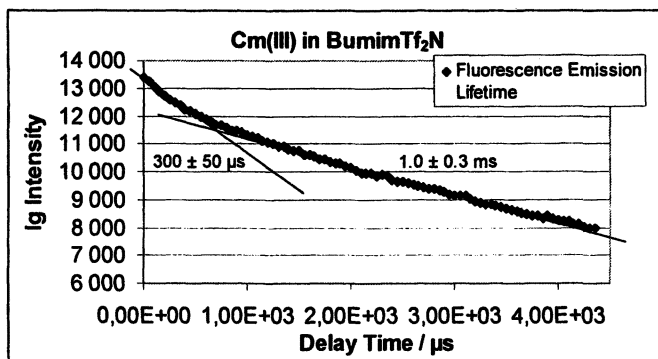


Figure 3b. biexponential decay behavior of the Cm(III) fluorescence emission in BumimTf₂N

Eu(III) and Cm(III) Fluorescence Quenching by Cu(II) in BumimTf₂N

After having characterized the different Eu(III) and Cm(III) species in BumimTf₂N it was our interest to investigate solution reactions of the lanthanide and actinide in this IL. The influence of Cu(II) on the europium fluorescence emission is shown in Figure 4a. With increasing copper concentration the fluorescence emission signal is decreasing. This effect can be again assigned to quenching by Cu(II). As expected for quenching reactions, Cu(II) also influences the fluorescence emission lifetime of the two different Eu(III)-BumimTf₂N species. A decrease from 2.46 ms to 1.73 ms and from 1.1 ms to 785 μs is detected. Figure 4b shows the Stern-Volmer plot of the described

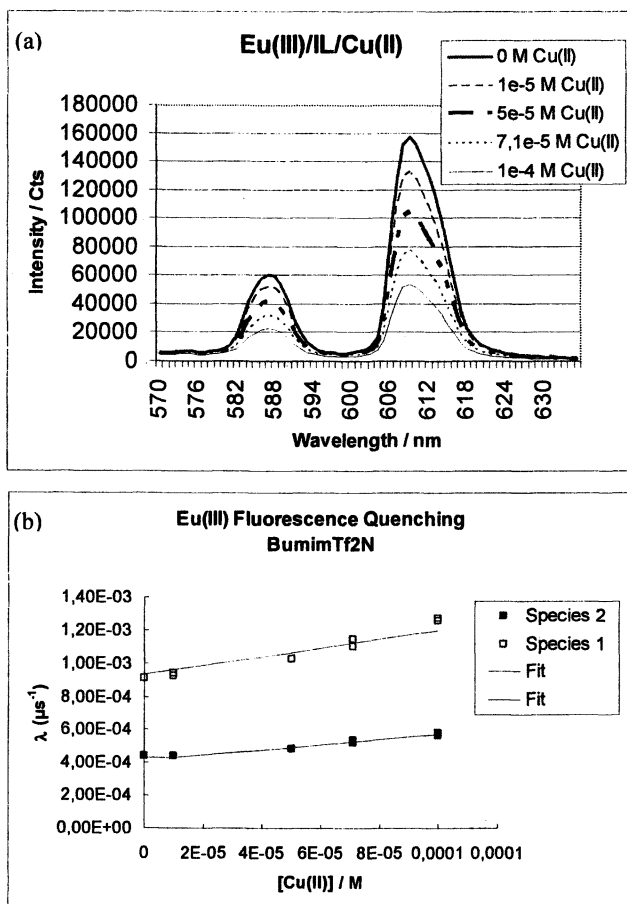


Figure 4. a) Influence of Cu(II) on the europium fluorescence emission
b) corresponding Stern-Volmer plot

process. According to the coexistence of two different Eu(III)-BumimTf₂N species two different slopes result from the fitting of the plotted data points. The calculated value of k_{SV} $1.54e^6 \text{ M}^{-1}\text{s}^{-1}$ corresponds to Eu(III) in BumimTf₂N without water in the first coordination sphere (species 1) while k_{SV} $2.70e^6 \text{ M}^{-1}\text{s}^{-1}$ is determined for the species additionally coordinated by one water molecule (species 2). A comparison of the calculated constants with the one determined for the same reaction in water shows that the interaction of Eu(III) and Cu(II) is accelerated in the IL even though this is the solvent with the higher viscosity. The accelerated quenching reaction in IL can be a result of the Eu(III) solvation

by BumimTf₂N which causes the shielding of positive charge and facilitates the approach of Cu(II).

The same quenching experiment has been performed with Cm(III) in BumimTf₂N. The TRLFS measurements show that Cu(II) has no influence on fluorescence emission intensities and lifetimes. According to this there is no quenching detectable. That is, solvation/coordination chemistry of Eu(III) and Cm(III) in BumimTf₂N is comparable but not solution chemistry. This result is of great importance regarding the separation of lanthanides and actinides in the nuclear fuel cycle.

In the abstract the question was raised: "Do ILs behave as normal solvents?" The presented results show that this is definitely not the case regarding Eu(III) and Cm(III) chemistry in BumimTf₂N compared to water. In the aqueous system Eu(III) and Cm(III) can be regarded as homologues. Coordination chemistry as well as solution chemistry is the same for both metal ions. The investigations performed in BumimTf₂N show that solvation chemistry has a great influence on solution chemistry and finally reactivity of lanthanides and actinides in ILs. This result represents a great step towards the separation of actinides and lanthanides in the nuclear fuel cycle which requires a difference in the chemical behaviour of both metal classes.

References

1. *Ionic Liquids: Industrial Application to Green Chemistry*; Rogers, R.D.; Seddon, K.R., Eds.; ACS symposium series 818; Washington, DC, 2002.
2. Wasserscheid, P.; Welton, T. *Ionic Liquids in Synthesis*; VCH Wiley, Weinheim, 2005.
3. Kimura, T.; Kato, Y.; Takeishi, H.; Choppin, G.R. *J. Alloys Comp.* **1998**, *271*, 719-722.
4. Lis, S. *J. Alloys Comp.* **2002**, *341*, 45-50.
5. Kimura, T., Choppin, G.R. *J. Alloys Comp.* **1994**, *213/214*, 313-317.
6. Zamochnick, S.B.; Rechnitz, G.A. *Z. Anal. Chem.* **1964**, *199*, 424-429
7. Stumpf, S.; Stumpf, Th.; Fanghünel, Th.; Klenze, R.; Bernhard, G.; Kim, J. I.; in preparation.
8. Kessler, M. A. *Anal. Chim. Acta* **1998**, *364*, 125-129.
9. Arakawa, T.; Akamine, M. *Sens. Actuator B-Chem.* **2005**, *108(1-2)*, 832-835.
10. J.R. Lakowicz *Principles of Fluorescence Spectroscopy* Plenum Press, New York/London, 1983.
11. Billard, I., Mekki, S., Gaillard, C., Hesemann, P., Moutiers, G., Mariet, C., Labet, A., Bünzli, J.-C. G., *Eur. J. Inorg. Chem.* **2004**, 1190-1197.

Synthesis and Properties

Chapter 19

New Ionic Liquids Based on Anion Functionalization

**Peter Wasserscheid, Dirk Gerhard, Simone Himmler,
Stefanie Hörmann, and Peter S. Schulz**

**Lehrstuhl für Chemische Reaktionstechnik, University
of Erlangen-Nuremberg, Egerlandstrasse 3, D-91058 Erlangen, Germany**

Introduction

Ionic liquids have gained wide popularity during the last decade because of their unique properties. More and more, ionic liquids are used as solvent substitutes and as innovative liquid materials in academic and industrial research laboratories. They have been applied in a broad variety of synthetic¹, catalytic², engineering³ and electrochemical applications.⁴ Other reported applications deal with the role of ionic liquids as active materials in sensors⁵ and analytical devices⁶ or as performance additives for paints⁷. In particular, their extremely low vapor pressure at ambient conditions makes ionic liquids extremely interesting for many technical purposes.

Given the wide variety of different ionic liquid materials, the selection of the right cation/anion combination is a key factor for success for all different applications. In recent years some of the traditionally used "working horses", namely tetrafluoroborates and hexafluorophosphates, have been found to be of restricted suitability in practical and industrial use due to their sensitivity vs. hydrolysis forming highly toxic and corrosive HF.⁸ Due to this reason bis(trifluoromethylsulfonyl)imide ([Tf₂N]⁻) is mostly used today if a hydrophobic and hydrolysis stable ionic liquid is required.⁹ However, the relatively high price of this anion and related fluorinated anions will limit the use of these systems in large scale applications. Also the presence of fluorine may still be problematic for an environmental friendly disposal.

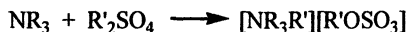
Given this importance of the anion's chemical nature on the practical applicability of an ionic liquid, one focus of our research group in recent years centered on the development of new synthetic approaches towards modified

anions in ionic liquid material development. Two different approaches that showed some promise will be presented in this paper. Both approaches allow and intend for a combinatorial research approach which means that the basic synthetic concept leads from a key-intermediate to a large number of different derivatives. With this strategy we have left the traditional reaction sequence for ionic liquid manufacturing (1. alkylation; 2. ion exchange). The latter was replaced by a sequence that includes the transformation of an ionic liquid key-intermediate in a reaction that forms one ionic liquid from another one.

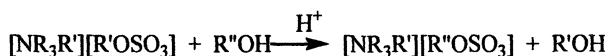
Synthesis of functionalized alkylsulfate ionic liquids

The proposed synthetic approach to functionalized alkylsulfate ionic liquids comprises two steps. First an amine is alkylated using a short chain alkylsulfate like dimethylsulfate or diethylsulfate, followed by a transesterification of the anion (see Scheme 1). This second transformation is performed by reacting the short chain alkylsulfate ionic liquid with an alcohol under slightly acidic conditions.

1. step: quaternization



2. step: transesterification



R'=Me, Et

Scheme 1. Two step synthesis of functionalized alkylsulfates ionic liquids.

Quaternization step

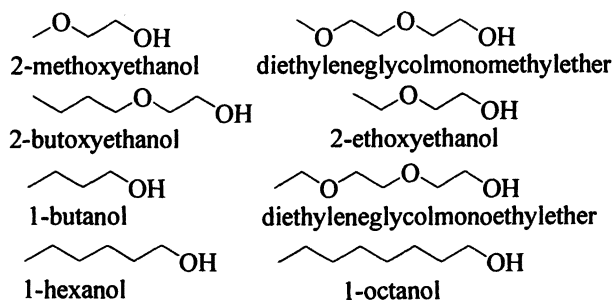
The first step of this synthesis is a classical quaternization reaction with dimethyl- or diethylsulfate, leading to ionic liquids. A wide variety of commercially available nucleophiles such as alkylimidazoles, substituted pyridines, tertiary phosphines or tertiary amines can be used.

Typically, the quaternization of 1-methylimidazole with diethylsulfate is carried out without a solvent under efficient temperature control in order to prevent hotspots, which would lead to a product of lower quality. By cooling the neat reaction mixture with a cold water- or ice bath nearly white products can be obtained¹⁰.

It is important to note in this context that 1-ethyl-3-methylimidazolium ethylsulfate ([EMIM][EtOSO₃]) is a commercial ionic liquid, produced on a ton-scale in excellent quality by Solvent Innovation/Degussa (marketed as ECOENG 212¹¹) and also from BASF. This ionic liquid proved a non-toxic nature in the registration process and must be regarded today as the most economic and reasonable access to ionic liquids carrying the [EMIM] cation.

Transesterification step

The key step of this strategy to functionalize the ionic liquid's anion is a transesterification reaction.¹² For this reaction, a long chain or functionalized alcohol is reacted under slightly acidic conditions with e.g. [EMIM][EtOSO₃]. Liquid acids, such as methanesulfonic acid, or solid acids, such as Dowex® MSC-1 can be used as transesterification catalysts. Alcohols that have been applied so far include primary alcohols (from *n*-butanol to *n*-octanol) and some ethyleneglycol based alcohols as depicted in Scheme 2.



Scheme 2. Alcohols applied so far for the transesterification of [EMIM][EtOSO₃].

The different alcohols have been found to lead to the formation of diverse functionalized alkylsulfate ionic liquids with different properties (e.g. viscosity, density). The motivation for choosing oligoether groups stems from the fact that the replacement of alkyl groups by oligoether groups at the ionic liquids cation has been shown to decrease the ionic liquids viscosity to a significant extent. Therefore, we were interested to look for similar effects on the anion side by replacing the alkyl group in higher alkylsulfate anions by different alkyloligoether groups. The properties of selected products are described later in this contribution.

In order to enable production of larger amounts (> 10 kg) of functionalized alkylsulfate ionic liquid, using the here described method, the reaction kinetics of the transesterification reaction were investigated in detail.

Kinetics of the transesterification reaction and concepts for scale-up

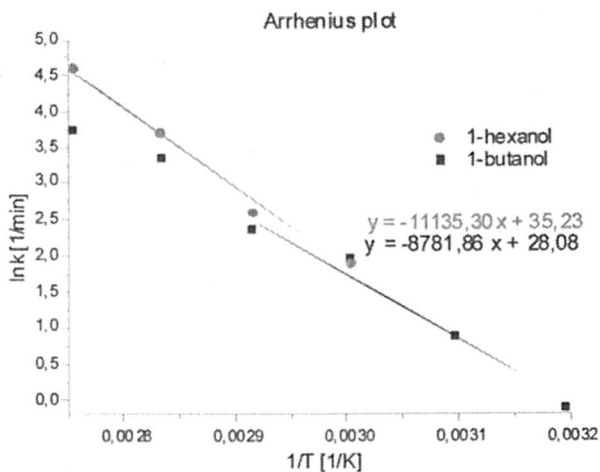
The transesterification reaction is a relatively fast reaction that is limited by equilibrium. For an equimolar mixture of [EMIM][EtOSO₃] and 1-butanol (1.4 mol-% methanesulfonic acid as catalyst) the equilibrium was fully reached at 40 °C within less than 3 hours, at 60 °C in 90 minutes, 70 °C in 50 minutes, 80 °C in 25 minutes and in only 15 minutes at 90 °C. The values for the equilibrium constants were between 0.95 and 1.01 for the temperatures mentioned above. For the reaction system [EMIM][EtOSO₃] and 1-hexanol (1.4 mol-% methanesulfonic acid as catalyst) the equilibrium was reached in 60 minutes at 60 °C, in 40 minutes at 70 °C, in 15 minutes at 80 °C and in only 10 minutes at 90 °C. Here the equilibrium constants were 0.96±0.03 for all temperatures between 60 °C and 90 °C.

In order to obtain complete conversion, the equilibrium has to be shifted towards the desired products. This can be done by removing the lower boiling alcohol constantly under reduced pressure and by adding a large excess of the high boiling alcohol. For example, a conversion higher than 90% was obtained within 4h by using a mixture of [EMIM][EtOSO₃] and 1-butanol in a ratio of 1:10 stirred at 60 °C under slightly reduced pressure. After removing the excess alcohol by an evaporation process, the desired product [EMIM][BuOSO₃] was obtained in quantitative yield (>99%) and high purity.

The transesterification reaction has been found to be a second order reaction, first order with respect to [EMIM][EtOSO₃] and the higher alcohol, respectively. The reaction has been carried out, under otherwise identical conditions, at different temperatures. The results of this set of experiments are displayed in form of an Arrhenius plot in Graph 1. From this plot the activation energies for the transformation of [EMIM][EtOSO₃] with 1-hexanol and 1-butanol can be easily obtained.

The activation energies were determined to be 73.01 KJ/mol for the reaction with 1-butanol and 92.58 KJ/mol for the reaction with 1-hexanol. The reaction enthalpies were 0.72 KJ/mol and 2.02 KJ/mol, indicating that the transesterification is a slightly endothermic reaction.

The described reaction of the commercial available [EMIM][EtOSO₃] and 1-butanol was carried out in lab-scale (~250 g product) using a rotavap as reaction vessel. Applying this equipment, the reaction mixture can easily be reacted at controlled temperature and reduced pressure with some film formation for improved evaporation of the low-boiling coupling product ethanol.



Graph 1. Arrhenius plot of transesterification of [EMIM][EtOSO₃] with 1-hexanol and 1-butanol.

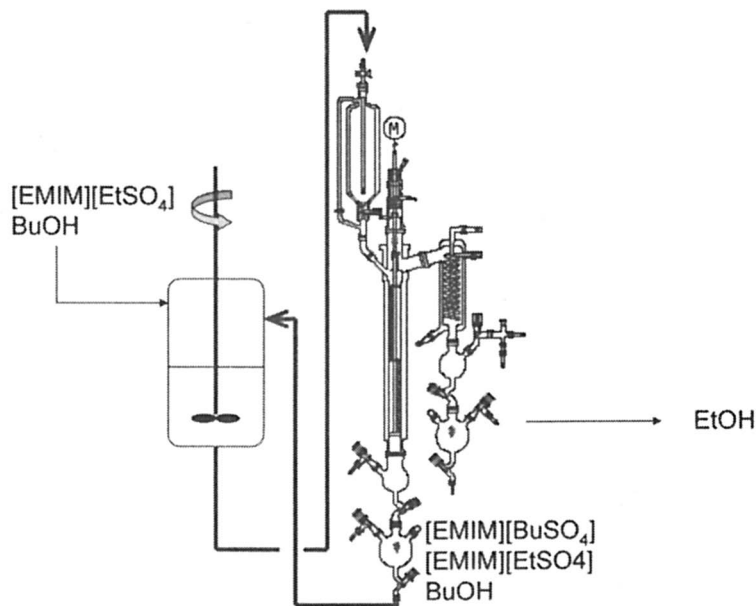


Figure 1. Proposed set-up for an up-scaling of the transesterification reaction combining a reaction vessel with a thin film condenser.

For the scale-up of the reaction we propose the combination of a reaction vessel with a thin film evaporator as displayed in Figure 1.

In such a set-up the transesterification reaction is carried out in the stirred tank reactor followed by continuous removal of the low boiling alcohol (e.g. ethanol) in the thin film evaporator. The starting material ([EMIM][EtOSO₃], BuOH) and the product ([EMIM][BuOSO₃]) are cycled between both apparatus of the overall set-up until full conversion is obtained and the remaining alcohols are completely removed.

The complete synthetic procedure can be regarded as very environmental benign. No volatile organic solvents are needed for both the quaternization and the transesterification step. Moreover, almost no waste is produced during the very atom-efficient synthesis as the excess of alcohol used can easily be recycled. With respect to many applications the fact that these novel substances do not contain any halides like chlorides or bromides (as the whole synthesis process is virtually halogen-free) is also a very important and attractive feature.

Selected physical-chemical properties of functionalized alkylsulfate ionic liquids

The physical-chemical properties of the following ionic liquid (produced according to the above described methodology) are presented.

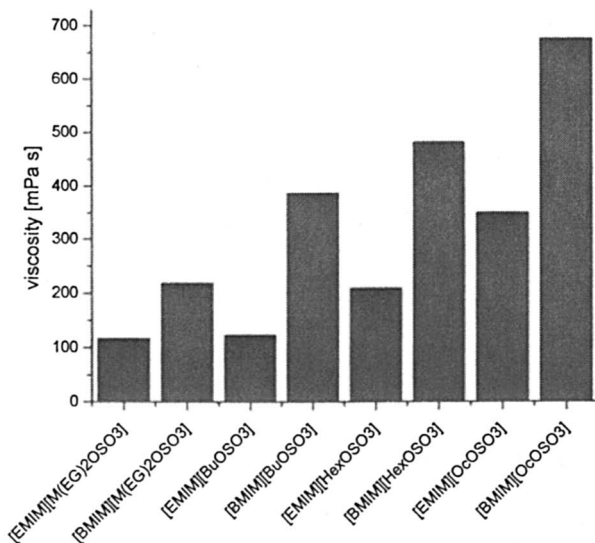
[EMIM][BuOSO₃], [EMIM][HexOSO₃], [EMIM][OcOSO₃], [EMIM] methoxyethylsulfate ([M(EG)OSO₃]), [EMIM] ethoxyethylsulfate ([E(EG)OSO₃]), [EMIM] butoxyethylsulfate ([B(EG)OSO₃]), [EMIM] 2-(2-ethoxyethoxy)-ethylsulfate ([E(EG)₂OSO₃]) and [EMIM] 2-(2-methoxyethoxy)ethylsulfate ([M(EG)₂OSO₃]). The properties of some corresponding 1-butyl-3-methylimidazolium ([BMIM]) based ionic liquids are given for comparison.

All properties were obtained using alkylsulfate melts with water content below 600 ppm as determined by Karl-Fischer-Titration.

Viscosity

The viscosity of the different ionic liquids were measured in a temperature range from 20 to 100 °C. Graph 2 summarizes the viscosities obtained at 30 °C.

A clear trend can be seen for all ionic liquids under investigation. The viscosity increases drastically with an increasing chain length of the alkylsulfate anion due to increasing van-der-Waals interactions.¹³ For example, [BMIM][BuOSO₃] shows a viscosity of 386 mPa s, whereas for [BMIM][HexOSO₃] a viscosity of 481 mPa s was measured. Comparing the same anion and different cations the same effect can be seen with an



Graph 1. Viscosities of different alkylsulfate ionic liquids at 30°C.

increasing chain length at the cation: [BMIM] based ionic liquids are always more viscous, e.g. ([EMIM][OcOSO₃] has a viscosity of 349 mPa s at 30°C while the viscosity of [BMIM][OcOSO₃] was determined to be 675 mPa s at the same temperature.

Concerning the ionic liquids with ethyleneglycol-functionalized anions, an interesting effect can be observed. By replacing CH₂-moieties by O-atoms (while keeping the overall chain length constant), the viscosity can be reduced to great extent. We assume that this effect has to do with the increasing flexibility of the side chain carrying the ether functionality.

For example, the viscosity at 30°C was determined to be 116 mPa s for [EMIM][E(EG)₂OSO₃] whereas the corresponding non-oxygen-functionalized [EMIM][OcOSO₃] shows a almost three times higher value at the same temperature.

These examples clearly illustrate the great role of anion modification on the viscosities of ionic liquids.

Density

The densities of all ionic liquids presented in Table 1 were measured at 25 °C using a pycnometer.

Table 1. Densities of different alkylsulfate ionic liquids at 25°C.

IL	Density [g mL ⁻¹]
[EMIM][EtOSO ₃]	1.22
[EMIM][BuOSO ₃]	1.18
[EMIM][HexOSO ₃]	1.13
[EMIM][OcOSO ₃]	1.10
[EMIM][M(EG)OSO ₃]	1.32
[EMIM][E(EG)OSO ₃]	1.30
[EMIM][B(EG)OSO ₃]	1.21
[EMIM][M(EG) ₂ OSO ₃]	1.23
[EMIM][E(EG) ₂ OSO ₃]	1.23
[BMIM][OcOSO ₃]	1.05
[BMIM][M(EG) ₂ OSO ₃]	1.19

As can be seen from the table, the density of [EMIM] based ionic liquid decreases with increasing alkyl chain length of the anion. For example, the density drops from 1.22 g mL⁻¹ for [EMIM][EtOSO₃] to 1.10 g mL⁻¹ for [EMIM][OcOSO₃].

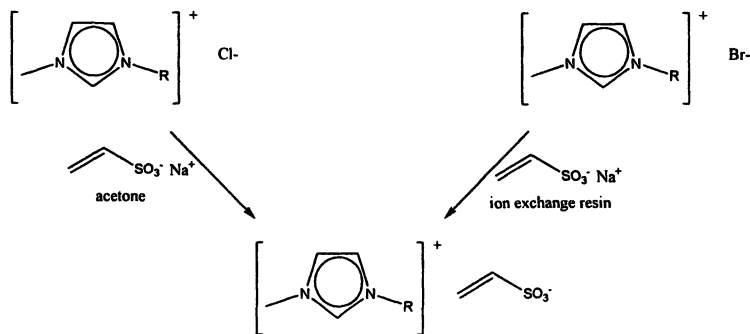
The comparison of functionalized with non-functionalized ionic liquids shows, that the substitution of carbon atoms by oxygen atoms leads to an increase of density. For example, [EMIM][OcOSO₃] has a density of 1.10 g mL⁻¹ whereas for the functionalized analogue [EMIM]-[M(EG)₂OSO₃] a value of 1.32 g mL⁻¹ was obtained. This behavior can be explained by the formation of inter- and intramolecular H-bonds. Therefore the molecules show a more dense arrangement of the molecules per volume unit.

Synthesis of vinylsulfonate ionic liquids and further functionalization

Introducing an ionic liquid with a double bound function either in the cation or in the anion offers the possibility of further functionalization reactions using standard catalytic transformations like hydroformylation, hydrosilylation or even polymerization. Using unsaturated alkylhalides as alkylating agents, a double bound can be easily introduced in the cation during the alkylation of a nucleophile. For example, vinyl iodide was used for quaternization of methylimidazole in order to synthesize a new iodide source for dye sensitized solar cells.¹⁴

In this paper we present the synthesis of vinylsulfonate ionic liquids which contain a double bond in the anion and thus can be further functionalized using different (catalytic) reactions. Sodium vinylsulfonate is a large scale industrial product which is commercially available in form of an aqueous solution. The corresponding acid was used by Yoshizawa *et al.* in a neutralization reaction with 1-vinylimidazol in order to form an ionic liquid monomer.¹⁵ A radical polymerization with AIBN yielded a polymer electrolyte which showed good electric conductivity.

To obtain dialkylimidazolium vinylsulfonate the aqueous solution of sodium vinylsulfonate was applied in metathesis reactions with e.g. [EMIM]Cl or [EMIM]Br. As shown in Scheme 3, two different synthetic approaches can be applied to obtain the desired product [EMIM][vinylsulfonate].



Scheme 3. Synthesis of vinylsulfonate ionic liquids.

Ion exchange in dry acetone

This synthetic approach uses the known very low solubility of sodium chloride in cold, dry acetone. Therefore, the aqueous solution of sodium vinylsulfonate is first dried under vacuum, obtaining the salt as a white powder. Together with [EMIM]Cl, dry sodium vinylsulfonate is suspended in the dry acetone in a 1:1 ratio. The whole mixture is stirred for 3 days at ambient temperature. Afterwards, the mixture is cooled down using an ice-bath and filtered over Celite. After evaporating the solvent, the ionic liquid was obtained as a clear, colorless liquid. The corresponding [BMIM][vinylsulfonate] has been obtained using the same procedure.

Ion exchange using an ion exchange resin

A commercial ion exchange resin has also been used for the synthesis of vinylsulfonate ionic liquids. This technique can be applied directly from the aqueous solution without drying. The ion exchange resin is placed in a column and is loaded by rinsing it with a diluted solution of sodium vinylsulfonate until the eluent is halide free (as checked by silver nitrate titration). Afterwards it is washed with a larger amount of distilled water to remove all sodium cation from the system. The so loaded resin is then slowly flushed with an aqueous solution of [EMIM]Br. The eluent is collected in small portions until first traces of bromides are found. The combined solutions are dried under reduced pressure yielding the desired ionic liquid as a clear, colorless liquid. Ion chromatography of the obtained product showed a halide content below 1000 ppm.

Selected physical-chemical properties of [EMIM]/[BMIM][vinylsulfonate]

All properties were obtained using [EMIM] and [BMIM][vinylsulfonate] with a water content below 1000 ppm as determined by Karl-Fischer-Titration. The ionic liquids were regarded to be halide-free as tested with a 1 M solution of aqueous silver nitrate and ion chromatography (halide content <1000 ppm).

Thermal properties

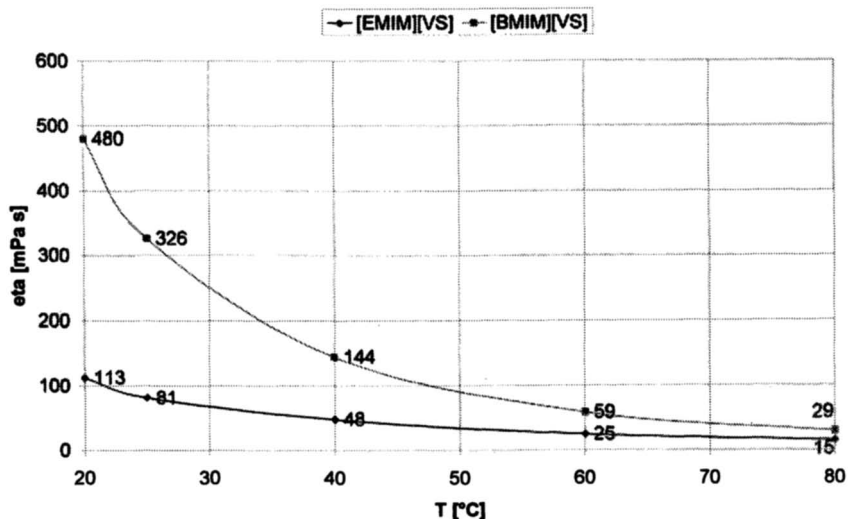
The temperatures of decomposition of both ionic liquids were investigated using a thermo gravimetric analysis with a heating rate of 10 K/min in an argon flushed chamber. The sample was heated from room temperature to 500 °C.

The temperatures of decomposition were obtained by the TG-onset method, which gave 310 °C for [EMIM][vinylsulfonate] and 306 °C for [BMIM]-[vinylsulfonate]. Though, the thermal stability seems to be rather independent of the cation structure. Obviously, the vinylsulfonate anion determines the temperature of decomposition.

It is worth notifying, that significant decomposition occurs in long-term measurements already approx. 50 °C below the measured TG-onset temperature as found for many other ionic liquids.¹⁶ The melting points of both ionic liquids were below 0 °C, exact values were not accessible by DSC measurements, as the substances formed super-cooled melts in this temperature range.

Viscosity

The viscosities of [EMIM]/[BMIM][vinylsulfonate] were measured between 20 and 80 °C. The results are given in Graph 3.



Graph 3. Viscosities of [EMIM][vinylsulfonate] and [BMIM][vinylsulfonate].

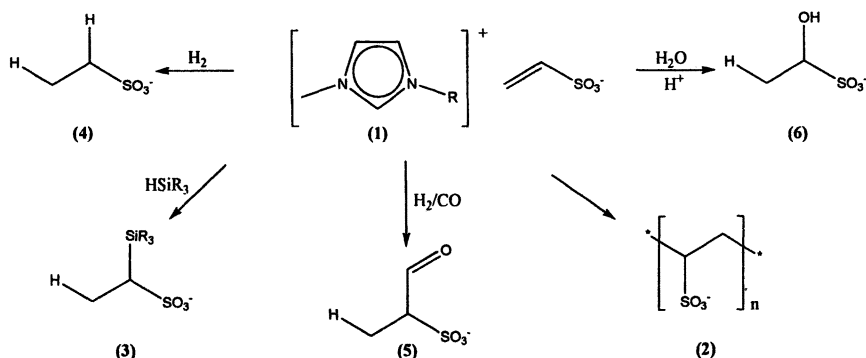
At 20 °C, [EMIM][vinylsulfonate] shows a viscosity of 113 mPa s, which is comparable to [EMIM][EtOSO₃]. Though, the double bond functionality does not have a great influence on the viscosity. As expected, the viscosity decreases with increasing temperature, reaching 16 mPa s at 80 °C.

As expected, the viscosity of [BMIM][vinylsulfonate] is always significant higher compared to that of the [EMIM] based ionic liquid.

Transformations of Vinylsulfonate Ionic Liquids

As mentioned above, double bond functionality in the ionic liquid's anion offers a wide variety of different catalytic and non-catalytic way for further structural modification. A selection of possible transformations of a vinylsulfonate ionic liquid is given in Scheme 4.

For example, vinylsulfonate ionic liquids (**1**) can be polymerized using a radical starter like AIBN. The so formed ionic gel (**2**) could have applications as



Scheme 4. Possible transformations of vinylsulfonate ionic liquids by anion modification.

electrolyte in electrochemical devices like dye-sensitized-solar-cells or lithium-ion batteries. So far, conductive gel electrolytes are mainly obtained by mixing poly(vinylidene fluoride-cohexa-fluoropropylene)(PVDF-HFP) polymers with an ionic liquid.¹⁷ Another possible transformation is the catalytic hydrosilylation, leading to an ionic liquid with silyl functionality in the anion (3).

In the following chapters, two catalytic reactions to further transform the vinylsulfonate anion of an ionic liquid will be described in more detail. Both, hydrogenation and hydroformylation are standard catalytic reactions.

Hydrogenation of vinylsulfonate

The hydrogenation of [EMIM][vinylsulfonate] (1) was carried out using methanol as a solvent and Ruthenium on active carbon as the heterogeneous catalyst. The reaction mixture was kept at 60 °C for 3 h with a hydrogen pressure of 80 bar. Afterwards, the catalyst was removed by filtration and the product was obtained after solvent evaporating as a colorless clear liquid in quantitative yield.

The ionic liquid [EMIM][ethylsulfonate] (4) was characterized by ¹H and ¹³C NMR-spectroscopy.

In comparison to the corresponding [EMIM][ethylsulfate], the ethylsulfonate ionic liquid is expected to be much more stable versus hydrolysis, due to the absence of the relatively labile carbon-oxygen-sulfur linkage. It is known that from the latter alcohol and hydrogensulfate can be liberated under aqueous, acidic conditions at elevated temperatures. Therefore, we anticipate that [EMIM][ethylsulfonate] may find use as an engineering fluid in applications where a halogen-free and highly hydrolysis stable ionic liquid is required.

Hydroformylation of vinylsulfonate

All hydroformylation experiments with [BMIM][vinylsulfonate] (**1**) were carried out in water as solvent using an Rh(acac)(CO)₂ precursor in combination with a TPPTS ligand as the homogenous catalyst. The reaction mixture was kept at 100 °C for 12 h with an overall pressure of 40 bar CO/H₂. After cooling to ambient temperature, the reaction mixture was filtered through Celite. Removing the solvent yielded the product as a highly viscous liquid. ¹H NMR-spectra showed complete conversion and a surprising *iso/n*-ratio of the produced aldehydes of greater than 18 indicating a highly selective formation of the branched aldehyde.

The obtained ionic liquid (**5**) can be directly used as a functionalized ionic liquid offering the new feature of a carbonyl group in the anion. The latter may be of use for selective coordination or even further anion reactions. As one example of such a further reaction the hydrogenation of the aldehyde function was already carried out leading to the corresponding hydroxysulfonate anion. The reaction was successfully carried out using again a heterogeneous hydrogenation catalyst under high pressure conditions.

Conclusion

The results discussed in this contribution demonstrate that a large variety of functionalized ionic liquids is indeed accessible by further chemical transformation of ionic liquid key-intermediates such as [EMIM][EtOSO₃] or [cation][vinylsulfonate].

The solvent-free synthesis of different, functionalized alkylsulfate melts by transesterification is an environmentally friendly way of producing large quantities of ionic liquids with a chance to tune properties like viscosity, density or solubility by the proper choice of the alcohol to be introduced. The cheap starting material and the possibility of an easy up-scale underline the potential of anion functionalized alkylsulfates in future bulk ionic liquid applications.

The new class of vinylsulfonate based melts is very interesting starting materials to generate new task-specific ionic liquids. The vinylsulfonate anion can be further transformed using standard reactions, such as hydrogenation, polymerization or hydroformylation opening-up a very attractive access to many new anion structures for ionic liquids.

References

1. (a) Welton, T.; Smith, P. J. *Advances in Organometallic Chemistry* **2004**, *51*, 251; (b) Sheldon, R. A.; Lau, R. M.; Sorgedraeger, M. J.; van Rantwijk, F.; Seddon, K. R. *Green Chem.* **2002**, *4*, 147.

2. (a) Gordon, C. M. *Appl. Catal. A: Gen.* **2001**, *222*, 101; (b) Jain, N.; Kumar, A.; Chauhan, S.; Chauhan, S. M. S. *Tetrahedron* **2005**, *61*, 1015.
3. (a) Beste, Y. A.; Schoenmakers, H.; Arlt, W.; Seiler, M.; Jork, C. *Ger. Offen.* **2005**, DE 10336555, WO 2005016484; (b) Esser, J.; Wasserscheid, P.; Jess, A. *Green Chem.* **2004**, *6*, 316.
4. (a) Papageorgiou, N.; Athanassov, Y.; Armand, M.; Bonhôte, P.; Pettersson, H.; Azam, A.; Grätzel, M. *J. Electrochem. Soc.* **1996**, *143*, 3099; (b) Matsumoto, H.; Matsuda, T.; Tsuda, T.; Hagiwara, R.; Ito, Y.; Miyazaki, Y. *Chem Lett.* **2001**, *26*; (c) Kubo, W.; Kitamura, T.; Hanabusa, K.; Wada, Y.; Yanagida, S. *Chem. Commun.* **2002**, 374; (d) Murai, S.; Mikoshiba, S.; Sumino, H.; Kato, T.; Hayase, S. *Chem. Commun.* **2003**, 1534; (e) Paulsson, H.; Hagfeldt, A.; Kloo, L. *J. Phys. Chem. B* **2003**, *107*, 13665; (f) Galinski, M.; Lewandowski, A.; Stepniak, I. *Electrochim. Acta* **2006**, *26*, 5567; (g) Endres, F.; El Abedin, S. *Z. Phys. Chem. Chem. Phys.* **2006**, *18*, 2101.
5. (a) Brinz, T.; Simon, U.; Application: DE 2002-10245337 10245337, (Robert Bosch G.m.b.H., Germany). **2004**; (b) Fukumoto, K.; Yoshizawa, M.; Ohno, H. *Journal Am. Chem. Soc.*, **2005**, *127*, 2398.
6. Bösmann, A.; Schubert, T. J. S. Application: GB 2005-10772, 2414553, (Germany). **2005**.
7. Weyershausen, B.; Lehmann, K. *Green Chem.* **2005**, *7*, 15.
8. Swatloski, R. P.; Holbrey, J. D.; Rogers, R. D. *Green Chem.* **2003**, *5*, 361.
9. (a) Lu, Q.; Wang, H.; Ye, C.; Liu, W.; Xue, Q. *Tribology International* **2004**, *37*, 547; (b) Endres, F. *Zeitschrift fuer Physikalische Chemie* **2004**, *218*, 255.
10. Große Böwing, A.; Jess, A.; Wasserscheid, P. *Chemie Ingenieur Technik* **2005**, *9*, 1430.
11. For more information see e.g. www.solvent-innovation.com.
12. Himmler, S.; Hörmann, S.; van Hal, R.; Schulz, P. S.; Wasserscheid, P. *Green Chem.* **2006**, (Advance Article).
13. Mantz, R. A.; Trulove, P. C. in *Ionic Liquids in Synthesis*; Wasserscheid, P., Ed.; Welton, T., Ed.; Publisher: Wiley-VCH, Weinheim, Germany, 2003. pp 56-68.
14. Mazille, F.; Fei, Z.; Kuang, D.; Zhao, D.; Zakeeruddin, S. M.; Grätzel, M.; Dyson, P. J. *Inorganic Chemistry* **2006**, *4*, 1585.
15. Yoshizawa, M.; Ogihara, W.; Ohno, H. *Polymers for Advanced Technologies* **2002**, *8*, 589.
16. Wooster, T. J.; Johanson, K. M.; Fraser, K. J.; MacFarlane, D. R.; Scott, J. L. *Green Chem.* **2006**, *8*, 691.
17. (a) Kim, K.; Park, S.; Choi, S.; Lee, H. *Journal of Power Sources* **2006**, *155*, 385; (b) Wang, P.; Zakeeruddin, S. M.; Exnar, I.; Grätzel, M. *Chem. Commun.* **2002**, 2972.

Chapter 20

Spatial Heterogeneity in Ionic Liquids

Yanting Wang, Wei Jiang, and Gregory A. Voth

Center for Biophysical Modeling and Simulation and Department
of Chemistry, University of Utah, 315 South 1400 East Room 2020,
Salt Lake City, UT 84112-0850

Electronically polarizable atomistic molecular dynamics models have been developed for the 1-alkyl-3-methylimidazolium nitrate ionic liquids with the alkyl-chain length ranging from 2 to 12. The molecular dynamics simulations with these models confirm the spatial heterogeneity previously discovered by the multiscale coarse-grained models (Wang & Voth, *J. Am. Chem. Soc.* 2005, 127, 12192). The global structures are monitored by a heterogeneity order parameter. The tail groups of cations are found to aggregate and distribute more heterogeneously than the headgroups of cations and the anions, forming discrete tail domains. The anions always stay close to the headgroups. The charged groups retain their local structures relatively unchanged, forming a continuous polar network, and leading to different global structures when varying the side-chain length. The ionic diffusion is slower with increasing alkyl-chain length. Based on these simulation results, a refined mechanism can be proposed, considering the competition among the Coulombic interactions, the collective short-range interactions, and the geometrical constraint from the intramolecular bonds. This mechanism can explain many experimental and simulation results, and is expected to be general for most kinds of ionic liquids. The finite size effects due to the limited simulation size are also discussed.

Introduction

Understanding the structural properties of ionic liquids is essential for the systematic design and application of ionic liquids.

Ionic liquids are room temperature molten salts which may be used as a potential substitute for the traditional environment-unfriendly organic solvents. They have a much lower melting point compared to the inorganic molten salts, which is achieved by involving a bulky organic cation (1). Generally most of the partial charges on the cation are distributed around its headgroup. When the side chain is short, the tail groups also have non-zero effective partial charges. With increasing side-chain length, the partial charges on the tail groups become smaller, and the amphiphilic feature for cations increases accordingly. Because there are numerous ionic liquid systems (2) to be chosen from to meet specific applications, a theoretical understanding of the "tunability" of ionic liquids, such as the changes of their physical properties with various side-chain lengths, is important for guiding their efficient design and applications.

Experiments have been done to investigate the behavior of ionic liquids with various cationic side-chain lengths. A liquid crystal phase has been observed for pure ionic liquids with long side chains (3-6). This mesophase affects the selectivity of the reaction products taken in ionic liquids (6). Tokuda *et al.* (7) reported for $[C_n\text{MIM}]^+(\text{CF}_3\text{SO}_2)_2\text{N}^-$ that the summations of the diffusion coefficients for the cations and the anions follow the order $C_2 > C_1 > C_4 > C_6 > C_8$. (Here and thereafter, C_n refers to the ionic liquid system having an imidazolium cation with n carbon groups on its side chain.) Seddon *et al.* (8) and Huddleston *et al.* (9) reported similar experimental results for the systems with different anions. The above three papers (7-9) have also found a decreasing mass density with increasing side-chain length. Wakai *et al.* (10) observed that the dielectric constant of ionic liquids decreases with increasing side-chain length of cations. Bonhôte *et al.* (11) also studied the importance of viscosity and ion size on conductivity of ionic liquids.

Molecular dynamics (MD) simulations have also been done to computationally investigate this issue. By MD simulations, Urahata and Ribeiro found that the diffusion increases from C_1 to C_4 , and then decreases when the side chain is longer (12). With static structure factor calculations, the same authors found a long-range ordering in their MD results (13). The MD simulations by Margulis (14) found that the systems are more structured with longer side chains. Del Pópolo and Voth (15) found evidence for dynamical heterogeneity, which should be indirectly related to spatial heterogeneity. Most recently Lopes and Pádua (16) used an all-atom model to report the microscopic separation of polar and nonpolar domains in ionic liquids. However, the authors did not give a clear mechanism to systematically explain their simulation results.

Recently we have successfully applied the multiscale coarse-graining (MS-CG) approach (17, 18) to the EMIM⁺NO₃⁻ (C₂) ionic liquid (19). The MS-CG model for EMIM⁺NO₃⁻ was then extended to qualitatively study the physical properties of ionic liquids with various lengths of side chains. By using these MS-CG models, we have revealed the spatial heterogeneity in ionic liquids formed by the aggregation of tail groups on side chains (20). The suggested mechanism is that the competition between the electrostatic interactions among the charged groups and the collective short-range interactions among the neutral tail groups results in the aggregation of tail groups, while the headgroups distribute as uniformly *as possible* (which does not mean completely uniformly). To verify the above mechanism, in this study polarizable atomistic models with full atomic detail have been developed for imidazolium cations with various side-chain lengths along with extensive MD simulations. In the past, we have shown (21) that electronic polarizability can be important to include in atomistic MD simulations.

In this work, our approach (21, 22) for developing the polarizable model for C₂ has been applied to develop the all-atom models for C₄, C₆, C₈, C₁₀, and C₁₂. Here only cations with even number carbons on the alkyl chain have been studied, because those with odd number carbons are more expensive to prepare in experiments, and they have different trends for some physical properties (5). The MD simulations have then been carefully carried out to ensure that the systems with 512 ion pairs have good equilibration at $T = 400$ K. It has been found that, with increasing cationic side-chain length, the system mass density and the diffusion of both the cations and the anions decrease; the tail groups aggregate to form isolated tail domains; and the charged groups retain their local structures relatively unchanged for different systems. By using a newly defined heterogeneity order parameter, the degrees of heterogeneous distribution have been quantified for different atom groups. With increasing side-chain length, both the headgroups and the tail groups distribute more heterogeneously. However, the tail groups distribute more heterogeneously than the headgroups of cations and the anions for all systems. Based on these observations, a mechanism is proposed to refine our previous one (20) based on the MD simulations using the MS-CG models.

Models and Methods

In this section the procedure of building the polarizable atomistic models is first described. A heterogeneity order parameter is then defined, designed to quantify the spatial heterogeneity in a finite-size simulation box. What follows are the definitions for diffusion constant and radial distribution function. Finally the MD simulation procedure for equilibration and sampling is given.

Polarizable atomistic models

A polarizable atomistic model (21, 22) has been developed for the EMIM⁺NO₃⁻ ionic liquid, based on the AMBER force field (23). In this model, a fast extended Lagrangian approach (24) similar in spirit to the Car-Parrinello method (25) has been used to treat the many-body polarizable model. In this method, the induced dipole degrees of freedom are coupled to a heat bath with a very low temperature (~ 0.1 K) separated from the system heat bath to help keep them evolving on the adiabatic surface. This algorithm leads to an increased simulation time (about a factor of two for C₂), but the polarization caused by the induced dipoles has been shown (21, 22) to have a significant influence on both the structural and the dynamical properties of ionic liquids, and is thus considered to be essential. The polarizable model also brings the atomistic simulation results into closer agreement with the experimental data in the cases we have examined (21, 22).

The total potential of the polarizable model V_{pol} is the sum of the bonded interaction, V_b , the short-range van der Waals interaction, V_{VDW} , the long-range Coulomb interaction, V_{el} , and an induction term, V_{ind} i.e.,

$$V_{pol} = V_b + V_{VDW} + V_{el} + V_{ind} \quad (1)$$

The bonded interaction V_b generally has the typical bond, valence angle, and dihedral angle terms among atoms

$$V_b = \sum_{bonds} \frac{1}{2} k_r (r - r_0)^2 + \sum_{angles} \frac{1}{2} k_\theta (\theta - \theta_0)^2 + \sum_{dihedrals} V_n \left[1 + \cos(n\phi - \gamma) \right] \quad (2)$$

where k_r , k_θ , V_n are force constants, r , θ , ϕ are bond length, valence angle, and dihedral angle, respectively, r_0 , θ_0 , and γ are equilibrium positions, and n is an integer number.

The short-range interaction generally takes the 12-6 Lennard-Jones potential form

$$V_{VDW} = \sum_i \sum_{j>i} 4\varepsilon \left[\left(\frac{\sigma}{r_{ij}} \right)^{12} - \left(\frac{\sigma}{r_{ij}} \right)^6 \right] \quad (3)$$

where ε is the depth of the energy minimum, σ is the minimum energy distance, r_{ij} is the distance between atom i and atom j .

In the Coulomb potential V_{el} , the charge q_i on atom i is the partial charge including the permanent dipole effect. The partial charges can be obtained from an *ab initio* study of the ions as described below, satisfying the constraint $\sum_i q_i = 1$ for cation, and $\sum_i q_i = -1$ for anion. With those partial charges, the Coulomb potential is written as

$$V_{el} = \sum_i \sum_{j>i} \frac{q_i q_j}{r_{ij}} \quad (4)$$

The induced term V_{ind} is expressed as

$$V_{ind} = -\sum_i \mu_i \cdot \mathbf{E}_i^0 - \sum_i \sum_{j>i} \mu_i \cdot \mathbf{T}_{ij} \cdot \mu_j + \sum_i \frac{\mu_i \cdot \mu_i}{2\alpha_i^2} \quad (5)$$

In the above equation $\mathbf{E}_i^0 = \sum_{j \neq i} q_j \mathbf{r}_{ij} / r_{ij}^3$ is the electric field on atom i , generated by the partial charges of all other atoms, excluding those within the same ion of atom i . The dipole field tensor \mathbf{T}_{ij} is calculated from the electrostatic potential $\varphi^f(\mathbf{r}_i - \mathbf{r}_j)$ at point j due to the charge at point i :

$\mathbf{T}_{ij} = \nabla_i \nabla_i \varphi^f(\mathbf{r}_i - \mathbf{r}_j)$. The induced dipole moment is

$$\mu_i = \alpha_i \left[\mathbf{E}_i + \sum_{j=1, j \neq i}^N \mathbf{T}_{ij} \cdot \mu_j \right], \text{ where } \alpha_i \text{ is the atomic polarizability of atom } i, \mathbf{E}_i \text{ is}$$

the electric field on atom i . The isotropic atomic polarizabilities $\{\alpha_i\}$ are determined by fitting the anisotropic molecular polarizabilities of the ions, which can be obtained by an *ab initio* simulation. Note that the induced dipole on each atom depends on the positions of all atoms, so the polarizability is a many-body effect.

The polarizable atomistic models for C_4 , C_6 , C_8 , C_{10} , and C_{12} were constructed by extending the force field parameters for C_2 . The methylene groups were added to the cationic side chains. The standard AMBER force field parameters (23) for the bonded (bond, angle, and dihedral) interactions and the VDW interactions were assigned to the new degrees of freedom accordingly. The isotropic atomistic polarizabilities fitted for C_2 (19, 22) were assigned to the added atoms on the cations. These parameters are given in the Appendix.

The standard one-configuration two-step procedure (26) of fitting partial charges for the AMBER force field was followed to obtain the partial charges for those cations. The Gaussian package (27) was first used to obtain the *ab initio* optimized structure of the cations at the theoretical level of mp2/6-31g*. The same theoretical level was then used to obtain the partial charges fitted to the electrostatic potential at points selected according to the Merz-Singh-Kollman scheme (28, 29). The RESP package as a part of the AMBER software was finally used to obtain the partial charges compatible to the AMBER force field parameters. Our fitted partial charges for C_4 are very close to those reported by de Andrade *et al.* (30). The fitted partial charges for the cations are also listed in the Appendix.

Heterogeneity Order Parameter

A new order parameter has been recently defined (31) to quantify the spatial heterogeneity continuously. This Gaussian-like *heterogeneity order parameter* (HOP) is defined for each site as

$$h_i = \sum_j \exp(-r_{ij}^2 / 2\sigma^2) \quad (6)$$

where r_{ij} is the distance between sites i and j , corrected with the periodic boundary conditions, $\sigma = L / N^{\frac{1}{3}}$ with L the side length of the cubic simulation box and N the total number of the sites.

For a given configuration, the average HOP is computed by averaging over all N_s sites of interest, such that

$$\hat{h} = \frac{1}{N_s} \sum_{i=1}^{N_s} h_i \quad (7)$$

The HOP is so defined that it is topologically invariant with the absolute distances between sites, thus independent of the simulation box size L . Because the weights of the sites far from the target site decrease quickly with distance, the HOP approaches a constant with increasing number of sites. Some ideal systems with $N = n^3$, $n = 1, 2, 3, \dots$, sites uniformly distributed in a cubic box were constructed, and the HOP was computed for these systems with periodic boundary conditions applied. The values for the ideal systems \hat{h}_0 are given in Table I. The HOP takes a fixed number of 15.7496 when the number of sites is larger than 1000.

In order to let the HOP take some values around zero when the sites distribute almost uniformly, a *reduced* HOP for each configuration is defined as

$$h = \hat{h} - \hat{h}_0 \quad (8)$$

The HOP defined above actually characterizes the instantaneous density of sites. To measure the ensemble-averaged density of sites, a *lattice HOP* is defined to calculate the average density for all configurations from one constant NVT trajectory. In order to calculate the lattice HOP, the cubic simulation box is divided into small cubic cells. For one configuration, in each cell i , the lattice HOP c_i is the HOP averaged over all sites of interest in this cell, such that

$$c_i = \frac{1}{M} \sum_{j=1}^M \hat{h}_{ij} \quad (9)$$

with M the number of sites in cell i , \hat{h}_{ij} the HOP of the j th site in cell i . Note that the regular HOP \hat{h}_{ij} , rather than the reduced HOP h_{ij} , is used here, so that the two cases of having no sites and having uniformly-distributed sites in a given cell are distinguishable.

Table I. Heterogeneity Order Parameter \hat{h}_0 for Uniformly Distributed Systems with Different Number of Sites N_s .

N_s	\hat{h}_0
1	1.0000
8	4.1464
27	10.8388
64	12.9513
125	15.3220
216	15.5285
343	15.7368
512	15.7431
729	15.7495
1000	15.7495
1728 and larger	15.7496

If a cell contains no sites of interest, the lattice HOP in this cell takes the average value of all neighboring cells, weighted by the inverse value of their center-center distance, such that

$$c_i = \frac{\sum_{j=1}^{M_c} \frac{1}{r_{ij}} c_{ij}}{\sum_{j=1}^{M_c} \frac{1}{r_{ij}}} \quad (10)$$

Here, M_c is the number of neighboring cells for cell i , c_{ij} is the lattice HOP for the j th neighbor of cell i , r_{ij} is the center-center distance from cell i to cell j . The neighboring cell is defined as the cells with their center-to-center distance from the target cell less than a cutoff of 5.9 Å, the same as that chosen in Ref. (31).

The ensemble-averaged lattice HOP $\langle c_i \rangle$ for cell i is the average value of instantaneous lattice HOP over all configurations for one trajectory, such that

$$\langle c_i \rangle = \frac{1}{N_t} \sum_{j=1}^{N_t} c_{ij} \quad (11)$$

where N_t is the number of configurations, c_{ij} is the lattice HOP for cell i in the

j th configuration. The ensemble-averaged lattice HOP for one trajectory is then obtained by averaging over all cells, given by

$$\langle c \rangle = \frac{1}{N_c} \sum_{i=1}^{N_c} \langle c_i \rangle \quad (12)$$

where N_c is the number of cells in the system.

Diffusion and local structure

The mean square displacement of particles is defined as $\langle \Delta r^2(t) \rangle = \langle |\mathbf{r}_i(t_0 + t) - \mathbf{r}_i(t_0)|^2 \rangle$, with $\mathbf{r}_i(t)$ the position of particle i at time t , averaged over all particles and initial times t_0 . The diffusion constant is then calculated (32) by fitting the linear part of the mean square displacement

$$D = \frac{\langle \Delta r^2(t) \rangle}{6t}. \text{ In this work, only the self-diffusivity of ions has been measured.}$$

So the term “diffusion” will be unambiguously used to refer to the self-diffusivity of ions.

One widely-used method of characterizing the local structure of a liquid is through the radial distribution function (RDF), which is defined as (32),

$$g(\mathbf{r}) = \frac{V}{N_s^2} \left\langle \sum_i \sum_{j \neq i} \delta(\mathbf{r} - \mathbf{r}_{ij}) \right\rangle \quad (13)$$

where V is the system volume, N_s is the total number of sites, \mathbf{r} is the radial distance, and \mathbf{r}_{ij} is the distance vector between sites i and j . When the side chain is long, calculating the RDFs for the center of mass of the cations has less meaning. Alternatively the partial site-site RDFs between the center of masses of the subgroups of cations and the anions were calculated for ionic liquid systems.

Molecular Dynamics Procedure

With increasing cationic side-chain length, the number of atoms is larger with a given number of ion pairs, and the diffusion is slower (7-9). On the other hand, systems with longer alkyl chains may have a more significant finite size effect in a finite simulation box, which may be big enough for systems with shorter chains. Considering the above facts, obtaining the fully equilibrated ionic liquid systems with a reasonably large simulation size is not an easy task. In this study, a strategy aimed at accelerating the equilibration in the MD simulations is taken, as described below. The integration time interval of 0.45 fs for each MD step was used for all MD simulations.

An initial configuration containing 64 ion pairs was first manually constructed, with the ions periodically placed on the lattice positions in a very large cubic simulation box. The initial configuration was then equilibrated at $T = 1000$ K by a Hoover barostat (33) with a pressure of $P = 1$ atm for 10^6 steps (450 ps). At such a high temperature the memory from the initial configuration was easily lost. The equilibrated configuration at $T = 1000$ K was then cooled down sequentially to 400 K, with an interval of 200 K. At each temperature the system was equilibrated with the constant NPT simulation with $P = 1$ atm for 10^6 steps (450 ps). The obtained configuration at $T = 400$ K was then equilibrated at this temperature with the constant NVT simulation by a Nosé-Hoover thermostat (34), with the system density fixed to be the one averaged from the previous constant NPT simulation. This equilibration was done for more than 5×10^6 steps (2.25 ns). The final configuration was confirmed to be fully equilibrated by observing that the diffusion of ions reaches a constant value.

The fully equilibrated configuration with 64 ion pairs at $T = 400$ K was then duplicated once in each dimension to get an initial configuration with 512 ion pairs. This initial configuration then went through a constant NPT simulation with $P = 1$ atm at $T = 400$ K for 10^6 steps (450 ps) to allow the system to relax from the periodic image interactions in the smaller-size simulation, and to eliminate the margin area between the duplicated images. With the system size fixed to be that averaged from the above constant NPT simulation, the system with 512 ion pairs then underwent a production run with a constant NVT simulation at $T = 400$ K for 10^6 steps (450 ps). During this production run 1000 configurations were sampled evenly with a time interval of 0.45 ps.

Results

The procedure described in last section was performed to obtain the MD data for the ionic liquid systems C_2 , C_4 , C_6 , C_8 , C_{10} , and C_{12} with 512 ion pairs at $T = 400$ K. The finite size effect was first evaluated based on the C_6 systems with 64 and 512 ion pairs. Analyses were then performed for the obtained data to get the structural, dynamical, and thermodynamical properties. The heterogeneity order parameter was applied to these systems to quantify the global heterogeneity in the liquids.

Below the term “headgroup” is used to specifically refer to the imidazolium ring of the cation, and the term “tail group” is used to refer to the terminal methyl group of the alkyl chain on the cation. The term “polar group” refers to the anion in addition to the headgroup and the adjacent methyl and methylene groups with non-negligible net partial charges, while the term “nonpolar group” refers to the methylene and methyl groups on the alkyl chain with negligible net partial charges. Here a net partial charge on a group of atoms is considered to be

negligible if its absolute value is smaller than 0.03 elementary charges, which, when apart about 5 Å from another group with the same type, roughly generates a Coulombic potential energy of less than 10% of the typical minimum short-range potential ~ 0.03 eV. The polar groups are dominated by the Coulombic interactions, while the nonpolar groups mainly have the collective short-range interactions. By this criterion, the third methylene group and other groups farther from the imidazolium ring on the side chain are considered nonpolar, while the remaining groups of the cation are considered polar.

Finite Size Effects

For ionic liquids, the quantities of interest are the physical and chemical properties of macroscopic samples containing $\sim 10^{23}$ molecules. In atomistic MD simulations with today's computers, however, only systems $\sim 10^3$ molecules with periodic boundary conditions can be studied. When the side length of the simulation box is smaller than twice the characteristic correlation length of interest, finite size effects will significantly distort the simulated properties. Generally the magnitudes of correlation lengths for different physical properties are not the same. Below the results for the C_6 systems with 64 and 512 ion pairs will be compared to show qualitatively different correlation lengths in ionic liquid systems.

In Figure 1 the RDFs between headgroups, tail groups, and anions for the C_6 systems with 64 and 512 ion pairs are compared. According to the four plots in Figure 1, while the peak positions remain the same, the finite size tends to suppress the peaks in the tail-tail RDF, but to raise the peaks in the head-head, anion-anion, and head-anion RDFs. This means that in an insufficiently large simulation box, the tail groups appear to distribute more uniformly, while the headgroups and anions appear to be more structured.

The mean square displacements for these two systems are shown in Figure 2. For both systems, the cations diffuse slower than the anions. This may be qualitatively understood by taking into account the fact that, besides the Coulombic interactions between the ions, the cations are also bound by the collective short-range interactions between the nonpolar groups. In contrast to the case of C_2 (22), the ions diffuse faster in the 64 ion-pair system than in the 512 ion-pair system. This is possibly due to the fact that the tail aggregation for C_6 in the smaller size system is reduced, as can be seen in Figure 1a.

Although quantitatively different, the RDFs and the diffusion for these two sizes give the same qualitative results for local structures and dynamics. In contrast, the finite size effect is so large for the global heterogeneity distributions in ionic liquids that the results from the small-sized systems would give a false impression. The reduced HOP defined in eq (8) was applied to these

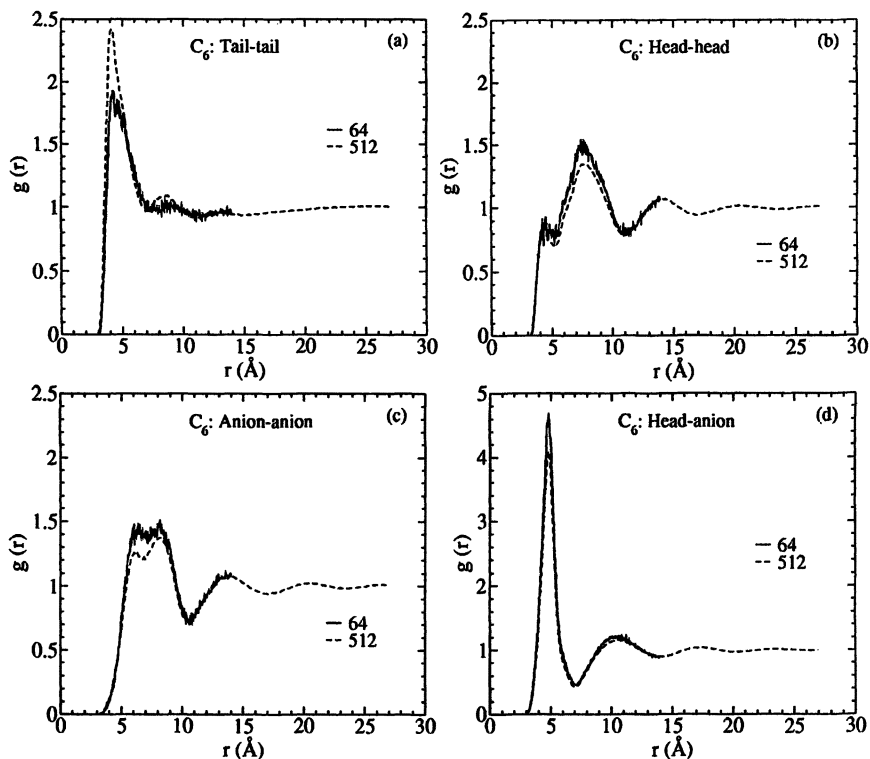


Figure 1. (a) Tail-tail, (b) head-head, (c) anion-anion, and (d) head-anion radial distribution functions for the C_6 systems with 64 and 512 ion pairs, respectively.

two C_6 systems, and their values are plotted in Figure 3. For the 64 ion-pair system, the HOPs fluctuate considerably and do not show much difference for the distributions of the tail groups from those for the headgroups and anions. For the 512 ion-pair system, however, the HOPs are stable and the tail groups take a value larger than those for the headgroups and the anions, indicating that the tail groups distribute more inhomogeneously. Thus the finite size effect has a large influence on the global heterogeneity of ionic liquids. It also likely suggests that the characteristic correlation length for global heterogeneity is longer than that for local structure and that for diffusion. It can be expected that, with increasing length of cations, the characteristic correlation length for heterogeneity becomes larger, and the required simulation size exhibiting little finite size effect should increase correspondingly.

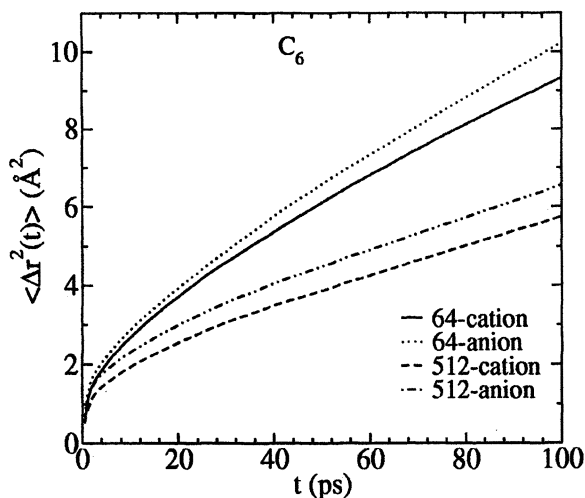


Figure 2. Mean square displacements for the C_6 systems with 64 and 512 ion pairs, respectively

In order to evaluate approximately the influence of the finite size effect on the systems with various lengths of the alkyl chain, the distributions of their cationic lengths d were calculated for 512 ion-pair systems. Here the cationic length d is defined as the distance from the center of mass of the methyl group not on the alkyl chain to the center of mass of the tail group. The distributions are shown in Figure 4. With increasing number of methylene groups on the alkyl chain, the most probable value of the cationic length d_M increases, but the probability of having this value decreases, and the distribution broadens, reaching very small values of d . This indicates that longer alkyl chains are more flexible and can bend to form many different shapes, so that the distance between the two terminals can range more widely.

The side length L of the cubic simulation box in the constant NVT simulations for the systems with 512 ion pairs was then divided by the most probable cationic length d_M . The plot of this ratio is drawn as the inset in Figure 4. The ratio decreases with increasing side-chain length, showing that, by taking the same simulation size of 512 ion pairs for all of the simulated systems, the finite size effect is more significant for the systems with longer side chain lengths. However, because no quantitative measurements have been done for the correlation lengths, no theoretical criterion can be used to gauge which systems are almost free of the finite size effect. Thus for the results shown below, the finite size effect is always considered in our data analyses.

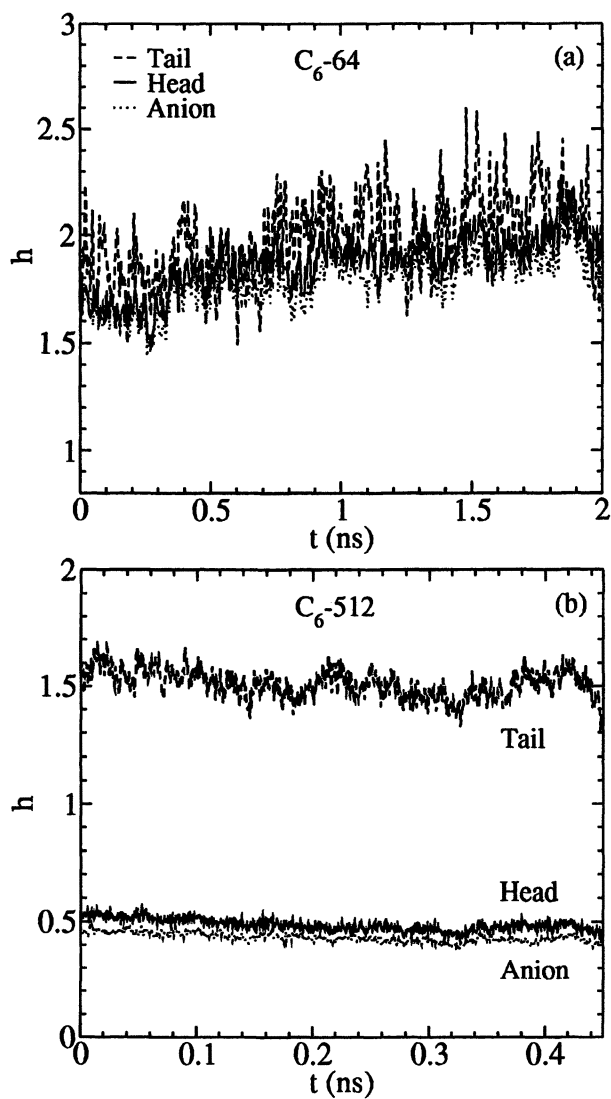


Figure 3. Instantaneous heterogeneity order parameter for the C_6 systems with (a) 64 and (b) 512 ion pairs, respectively.

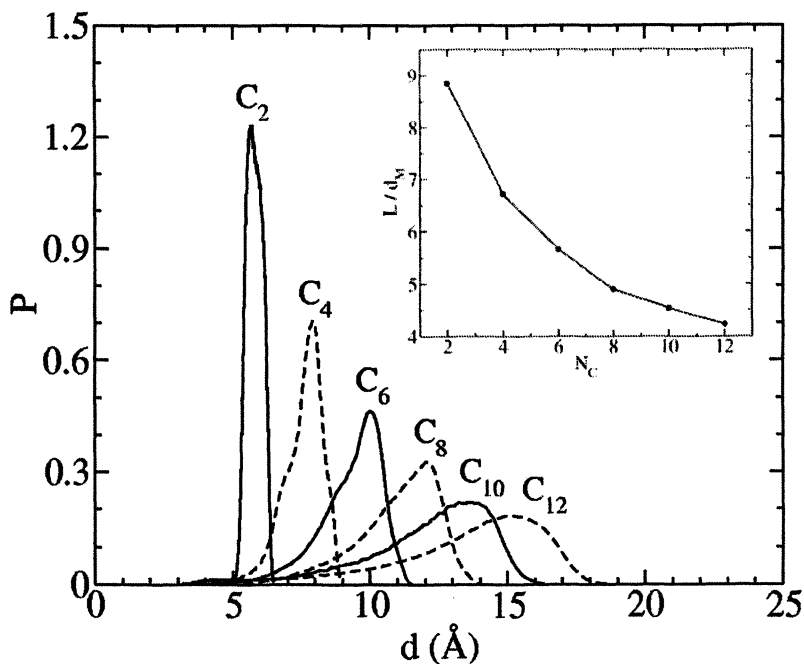


Figure 4. Distributions of cationic length for different ionic liquid systems. The inset is the ratio of the side length of the cubic simulation box with 512 ion pairs divided by the most probable cationic length, roughly showing the significance of the finite size effect.

Structural, Dynamical, and Thermodynamical Properties

The average mass densities obtained with 512 ion pairs are shown in Figure 5. Those obtained with 64 ion pairs are within 0.8% deviation from the data shown. The densities obtained for C_4 and C_6 are very close to the experimentally reported 1.1120 g/cm^3 for C_4 and 1.0769 g/cm^3 for C_6 at $T = 90 \text{ }^\circ\text{C}$ (8). Thus the finite size effect should have little influence on the mass density measurements. The density plot indicates that the mass density decreases as the alkyl chain length increases and approaches a constant value. This suggests that, at equilibrium, the methylene groups on the side chain have a larger space-to-mass ratio than the heavier head groups and anions. Increasing side-chain length includes more less-densely packed methylene groups in the cations. As the number of the methylene groups approaches infinity, the contribution from heavier atoms vanishes, and then the system density approaches a constant. The

monotonic decrease of mass density with increasing alkyl chain length is consistent with the experimental observations (7-9).

The diffusion constants for different ionic liquid systems are shown in Figure 6. Since the product runs are relatively short, the obtained diffusion constants may not be very accurate. They are shown here to illustrate the qualitative trend of the diffusion with various side-chain lengths. For all systems, the cations move slower than the anions. With increasing side-chain length, the ions move slower, except C_{12} and the anion of C_{10} , which we believe is due to the finite size effect. The slow down of the diffusion can be qualitatively understood by noting that the collective short-range attractive interactions increase with longer side-chain lengths, and the attractive interactions bind the cations more tightly than the systems with shorter side chains. The tendency that longer chain systems diffuse slower has also been found in experiments (7-9).

In order to reveal the characteristics of the local structures, the site-site RDFs for different ionic liquid systems are shown in Figure 7. For all of the systems studied, the main peak for the tail-tail RDF is higher than that for the head-head and anion-anion RDFs, indicating that the tail groups aggregate more than the headgroups and the anions. From C_4 to C_8 , with longer side chains, the main peak for the tail-tail RDFs is higher, showing that, for longer side-chain systems, more tail groups tend to aggregate. The characteristic second peak demonstrates an inhomogeneous distribution of the formed tail domains. Since the finite simulation size tends to lower the peak heights as shown in Figure 1a, the decrease of the peaks for C_{10} and C_{12} may be attributed to the finite size effect.

The head-head, anion-anion, and head-anion RDFs retain their shapes relatively unchanged for various systems. This means that the polar groups always retain their local structures, no matter how long the side chain is. We attribute this to the very strong Coulomb interactions between the headgroups and the anions. The peak heights for those RDFs grow with the length of the alkyl chain. This may correspond to the slower diffusion for a longer side-chain system, so the system appears more structured. Nevertheless, the finite size effect might also contribute at this feature, since the finite system tends to increase the peak heights for those RDFs, as shown in Figure 1b-d. In Figure 7d the head-anion RDFs have a high peak at a short distance of about 5 Å. This is strong evidence that the anions are always distributed very closely to the headgroups, and the polar groups containing the headgroups and the anions are more localized in the longer side-chain systems.

Spatial Heterogeneity

The above site-site RDFs reflect the local structures in the ionic liquids. The local distributions should in some ways relate to the global structures. Below

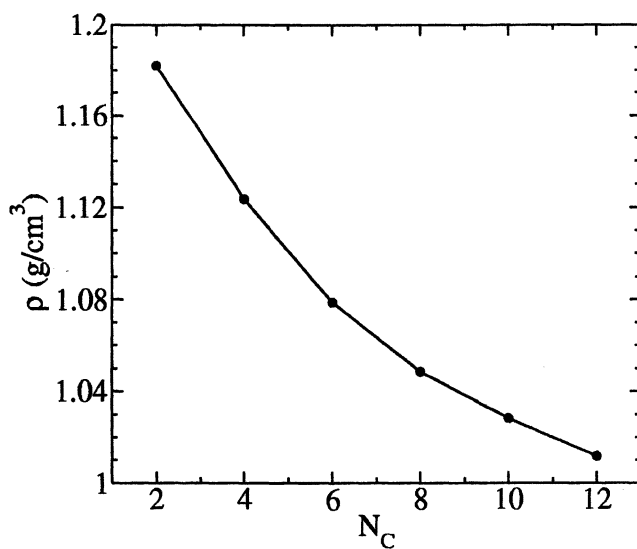


Figure 5. Mass densities for ionic liquids with various side-chain lengths.

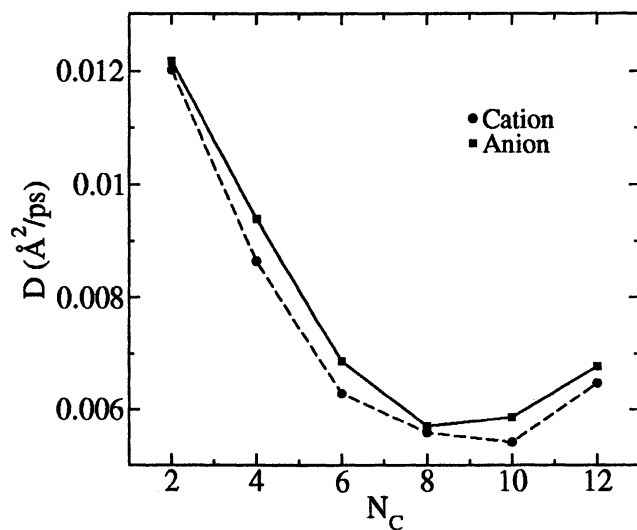


Figure 6. Diffusion constants for ionic liquids with various side-chain lengths.

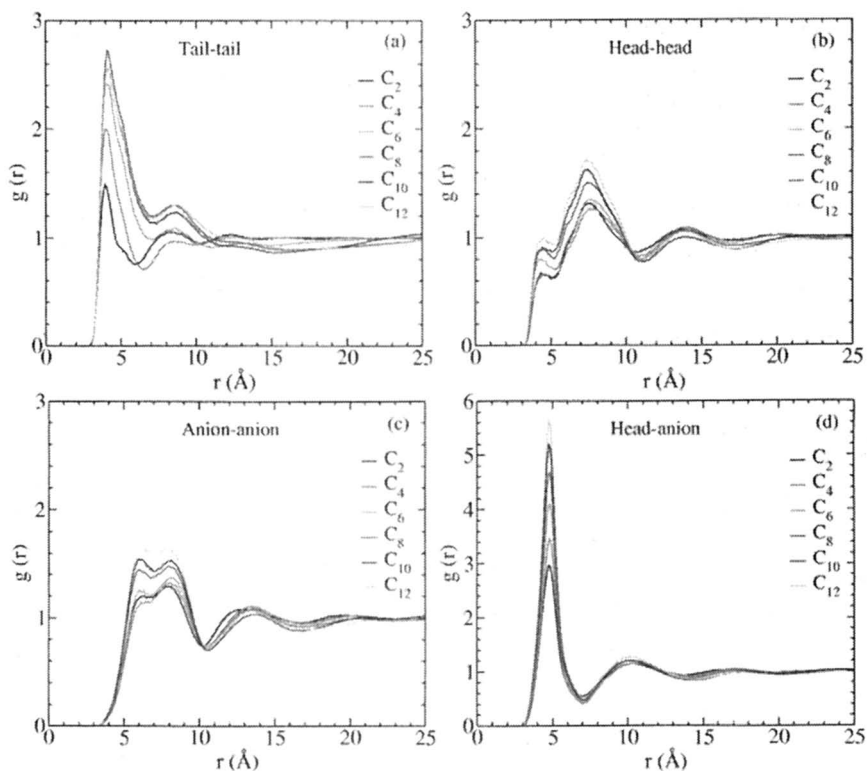


Figure 7. (a) Tail-tail, (b) head-head, (c) anion-anion, and (d) head-anion radial distribution functions for ionic liquids with various side-chain lengths.

one representative configuration of C_8 is taken as an example to show the global heterogeneous distributions for different sites in a visual way. The heterogeneity order parameter is then calculated for all the systems to show the tendency of the global heterogeneous distributions with various cationic alkyl-chain lengths.

One instantaneous configuration of C_8 is shown in Figure 8. Consistent with the head-anion RDFs shown in Figure 7d, the anions always stay close to the headgroups. In order to retain their local structures, when the alkyl chain is long, the headgroups and the anions can not distribute as uniformly as they do in the C_2 system, but span to form an inhomogeneous network with vacancies, such that the nonpolar groups connected with the headgroups by the chemical bonds can fill in.

By visual examination of Figure 8b and c, the tail groups form tail domains, and distribute more heterogeneously than the headgroups, due to the collective short-range interactions. Although both the tail groups and the headgroups distribute heterogeneously, the mechanisms they follow are different. The tail groups “actively” take a heterogeneous distribution due to the collective short-range interactions between the nonpolar groups, while the polar groups “passively” distribute heterogeneously due to the Coulomb interactions retaining their local structures and the geometrical constraint coming from the long alkyl chains. The degree of heterogeneity for tail groups is always larger than that for polar groups. Looking back to Figure 4, it can be seen that the cations curl in some complicated ways to satisfy the equilibrium requirements for both the tail groups and the headgroups.

Figure 8d shows the same snapshot including the tail groups, the headgroups, and the anions. Because the headgroups and the anions are attracted by the strong electrostatic interactions to maintain their local structures, they form a continuous polar network, as observed previously by Lopes and Pádua (16). In contrast, the tail groups aggregate to form several discrete tail domains, surrounded by the continuous polar network.

The reduced HOP has been performed on all of the systems to get the instantaneous HOP values for tail groups, headgroups, and anions, similar to those shown in Figure 3b. The average values and their standard deviations for these instantaneous HOPs are plotted in Figure 9. For all of the systems, the average HOP for the tail groups is larger than that for the headgroups. This demonstrates that the tail groups always globally distribute more inhomogeneously than the headgroups. The average HOP for anion is very close to that for headgroups, because the anions are always very close to the headgroups. Except C_{10} and C_{12} , for which the finite size effect appears to be significant, the average HOPs for both the tail groups and the headgroups increase. However, the reasons for this increase are different. With increasing side-chain length, the tail groups distribute more heterogeneously because of the

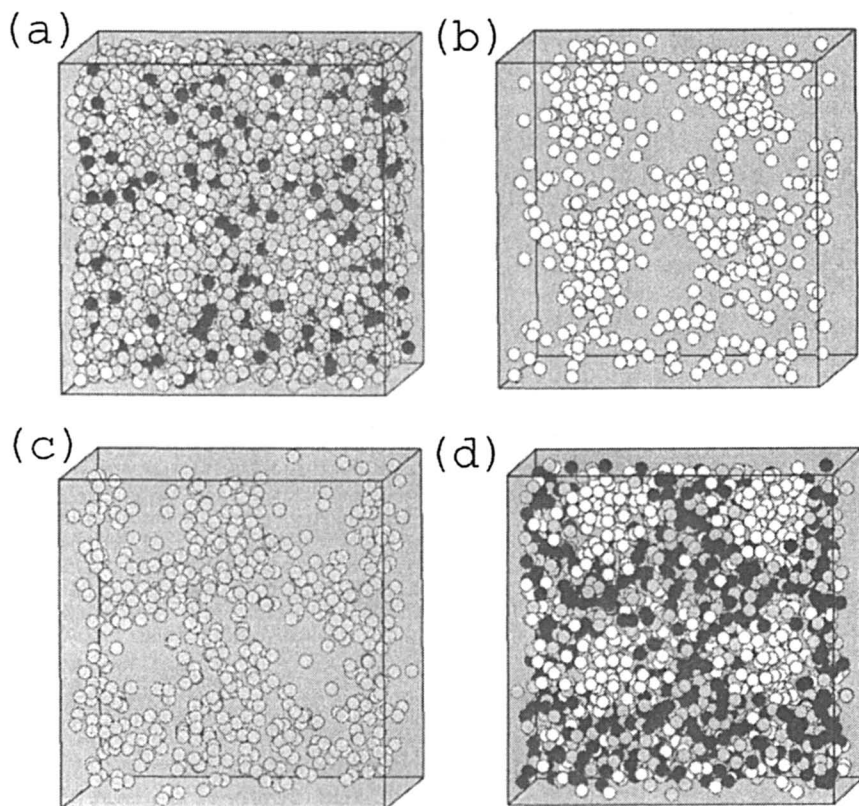


Figure 1. One instantaneous configuration showing the heterogeneous distribution of tail, head, and anion groups for the C_8 system with 512 ion pairs. (a) All atoms. (b) Tail groups only. (c) Headgroups only. (d) Tail groups (white), headgroups (light), and anions (dark).

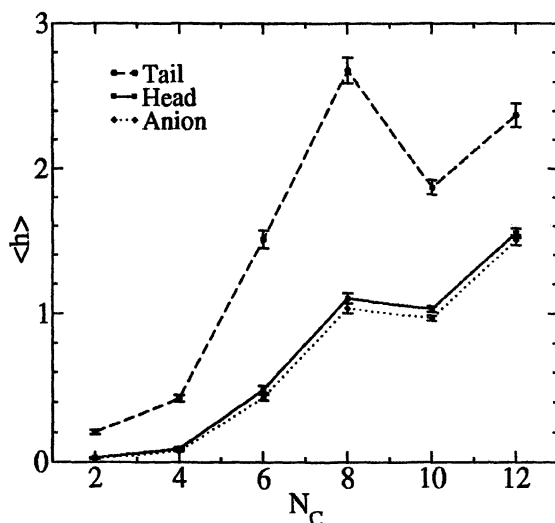


Figure 9. Average heterogeneity order parameters for the ionic liquid systems with various alkyl-chain lengths. The error bars are the standard deviations.

stronger collective short-range attractive interactions between the nonpolar groups. On the other hand, the more heterogeneous distribution of the headgroups is due to the fact that the growing size of the alkyl chains requires more space, so the requirement of maintaining the local structures forces the distribution of the polar groups to be more localized.

The behavior of the methylene groups on the side chain between the headgroups and the tail groups were then investigated. The methylene groups on the side chain of C_8 are denoted by M_n , where n is the position of the methylene group away from the headgroup. The RDFs between the same groups are drawn for M_2 , M_4 , and M_6 in Figure 10a. The RDFs for the headgroups and the tail groups are also plotted in the same figure for comparison. The main peak of the RDFs grows as the methylene groups come closer to the tail groups, showing that more groups aggregate. However, the RDFs are in no way similar to the RDFs for the tail groups of C_2 , C_4 , and C_6 , as shown in Figure 7a.

The HOPs have also been calculated for M_2 , M_4 , and M_6 and are plotted in Figure 10b. The HOPs grow from M_2 to M_4 to M_6 . They are all smaller than those for the tail groups, and only M_6 has larger HOPs than the headgroups. This suggests that the methylene groups in the middle of the side chains seem to act globally in a way compromising the heterogeneities in the two ends. It is interesting that the HOPs are very close to the values for the corresponding tail groups, i.e., M_2 takes the HOP values close to the tail groups of C_2 , and vice

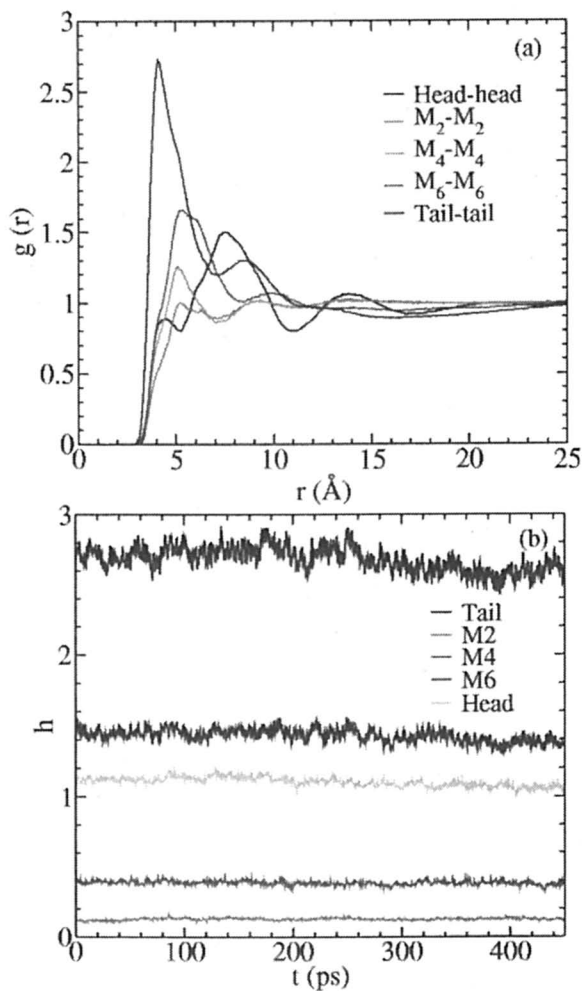


Figure 10. (a) Radial distribution functions and (b) instantaneous heterogeneity order parameter values for several atomic groups on the cations in the C_8 system.

versa, although their RDFs are quite different. This seems to suggest that, with a growing side chain, although the system volume expands, the existing groups on the side chain topologically retain their global heterogeneity. The additional nonpolar groups fill in the added space in a more aggregating manner. At the same time, the polar groups change their global distributions with their local structures unchanged. Below more analysis will be presented to make this point clear.

The HOP calculations shown above characterize the *instantaneous* spatial heterogeneity of individual atom groups. In order to see how the *ensemble-averaged* domains behave, the lattice HOP ($\langle c_i \rangle$) was performed on the ionic liquid systems with different side-chain lengths. The three dimensional illustration of the lattice HOPs for the tail groups and the headgroups for C₂ and C₈ systems are shown in Figure 11. In these pictures, each small sphere represents the lattice HOP value in the corresponding cell. The warmer is the color, the larger the lattice HOP value. Figure 11a and b shows that, on average, both the tail groups and the headgroups in C₂ distribute almost uniformly, despite the fact that the tail groups have some instantaneous spatial heterogeneity, as seen in Figure 9. Nevertheless, Figure 11c and d have many highly populated cells as well as many poorly populated cells. This means that, even on average, the polar and tail domains in C₈ are distributed very non-uniformly.

By using the lattice HOP calculations, with the MS-CG models, we have qualitatively investigated (31) the phase transition of tail domains with increasing temperature. It has been found that, below the tail-domain-diffusion transition temperature, the tail domains formed have relatively unchanged positions; above the transition temperature, although the tail domains still form instantaneous domains, on average they distribute uniformly. In the all-atom simulations reported here, because the tail aggregation is stronger with longer side chain, it seems reasonable to assume that the longer-chain system has a higher domain-diffusion transition temperature. The pictures in Figure 11a and c are very likely to suggest that the C₂ system at $T = 400$ K is above its tail-domain-diffusion transition temperature, while the C₈ system at $T = 400$ K is below its transition temperature. Although Figure 11b and d seem to suggest the same phenomena for headgroups, more work will be required to understand the phase behavior of the polar groups in ionic liquids.

The average lattice HOP averaging over all cells was calculated to show the trend of ensemble-averaged spatial heterogeneity with increasing side-chain length. The average lattice HOPs for tail groups, headgroups, and anions are shown in Figure 12. The error bar on each point indicates its standard deviation. From C₂ to C₈, the standard deviations grow for all three groups, meaning that the lattice HOP values are more different for longer side-chain systems. This indicates that, with increasing side-chain length, both the tail groups and the

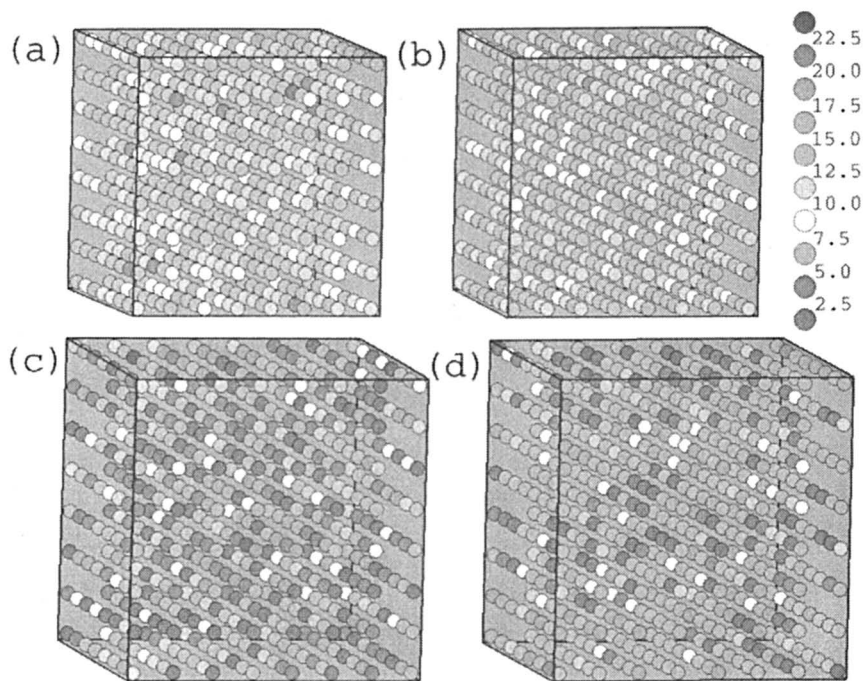


Figure 11. Three dimensional illustration of the lattice heterogeneity order parameters $\{c_i\}$ for (a) tail groups of C_2 , (b) headgroups of C_2 , (c) tail groups of C_8 , and (d) headgroups of C_8 . The spheres are colored according to the scale shown in this figure.

polar groups form more stationary domains. For the C_{10} and C_{12} systems, the finite size effect surely suppresses their standard deviations.

Mechanism

The results obtained by the all-atom polarizable models qualitatively agree with those by the primitive MS-CG models, but coincide more quantitatively with experimental results. A refined mechanism is thus proposed here to explain the behavior of ionic liquids with various lengths of cationic side chain. The main difference of this mechanism from our previous one (20) is the behavior of the polar groups. In this study the headgroups are found to retain their local structures, due to the very strong Coulombic interactions with the anions, rather than to push each other away as far as possible. Similar behavior has been suggested by the simulations of Lopes and Pádua (16).

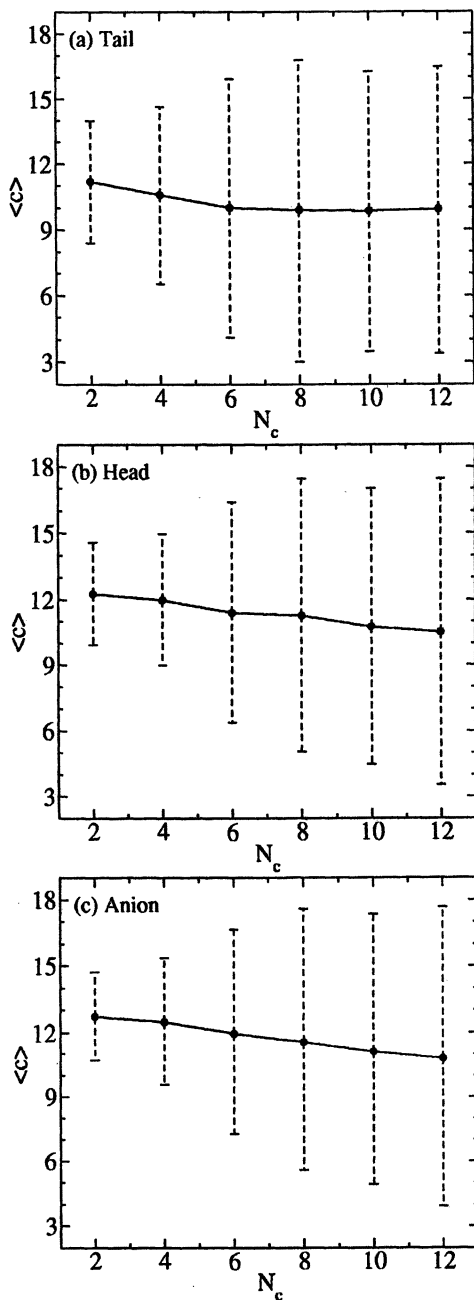


Figure 12. The average lattice HOP $\langle c \rangle$ for (a) tail groups, (b) headgroups, (c) anions for different systems. The error bars are the standard deviations.

There are mainly two kinds of competing non-bonded interactions between ions in ionic liquids: The Coulombic interactions and the collective short-range interactions. For the polar groups, the Coulomb interactions are very strong, such that the short-range interactions are only significant when the groups come very close and the short-range interactions are repulsive. The Coulomb interactions dominate the local behavior of the polar groups. These interactions are so strong that the polar groups retain their local structures and form continuous polar domains in different ionic liquid systems with various side-chain lengths (16). By contrast, the Coulomb interactions on the nonpolar groups are negligible compared to their collective short-range interactions. The tail groups distribute with their average distance around the equilibrium distance of the collective short-range interactions. Because the headgroups and the tail groups are connected by chemical bonds, the competition of these two groups leads to a balanced spatial distribution of ionic liquids, in which the tail groups of cations tend to aggregate to form isolated tail domains, while the polar groups adjust their global behavior to retain their local structures. The methylene groups between the headgroups and the tail groups adjust their structures in some complicated ways to compromise the different requirements from the two ends but, in general, the closer they are to the tail groups, the more heterogeneously they distribute. However, they do not necessarily distribute more heterogeneously than the headgroups. Also due to the very strong attractive Coulomb interactions between the headgroups and the anions, the anions always distribute closely around the polar headgroups.

With longer side-chain length, the collective short-range interactions from the nonpolar groups are larger, leading to more aggregated domains of the tail groups. On the other hand, more methylene groups on the side chains require larger portions of the space to be filled in by them. Along with the requirement that the local structures of the polar groups remain unchanged, the distribution of the headgroups is more localized, resulting in a more localized continuous polar network. Nevertheless, the distribution of the tail groups is more heterogeneous than the headgroups, no matter how long the side chain is.

It should be noted that the above mechanism should be somehow modified to describe the C_2 system, in which the tail groups still have a non-negligible partial charge distribution, such that the short-range interactions do not dominate. Nevertheless, by calculating the average HOPs as shown in Figure 9, the tail groups in C_2 have also been found to distribute more heterogeneously than the headgroups. This may result from a subtle balance between the repulsive and attractive Coulombic interactions between the whole cations and the anions, considering the tail groups have a much smaller partial charge than the headgroups. The short-range interactions between the tail groups, which are comparable to the Coulombic interactions, might have some influence as well.

Our all-atom simulations with the polarizable models also give more evidences to support the tail aggregation (20) and domain diffusion mechanism

(31) based on the primitive MS-CG models. They also suggest that the domain-diffusion transition temperatures are higher for longer side-chain systems. Atomistic simulations at different temperatures will likely be necessary to quantitatively investigate in detail the phase behavior of the polar and nonpolar domains in ionic liquids.

With this tail aggregation mechanism, some experimental results can immediately be rationalized, despite the fact that many experiments were done for ionic liquids with anions other than nitrate. The competition between the different distributions of tail groups and headgroups results in a liquid crystal-like structure similar to those observed in experiments (3-6). The experimentally observed heterogeneity, however, is at mesoscopic scales and with longer side chains ranging from C_{12} — C_{18} . More quantitative comparisons can only be obtained when simulations are performed at a much larger scale with longer side chains than the current study.

When the alkyl chain is short, the cations distribute almost uniformly in the space, so the diffusing behavior of the ions is similar to simple isotropic liquids. With a longer alkyl chain, the heterogeneously distributed domains formed by the tail groups bind groups of cations together instantaneously, effectively adding an energy barrier between cation groups. Thus the ions move in a more hop-like fashion (15) rather than the free style in a simple liquid. The longer the alkyl chain is, the higher the energy barrier, and the slower the diffusion. The contribution from the polar groups is almost fixed since their local structures remain relatively unchanged. This explains the experimentally observed diffusion decrease, or equivalently, viscosity increase, with longer alkyl chains (7-9). The diffusion of the anions is somehow associated with that of the cations, since they are attracted to be around the headgroups of the cations.

Wakai *et al.* (10) observed experimentally that the dielectric constant of ionic liquids decreases with increasing side-chain length of cations. This can be understood by noting that, with increasing side-chain length, the portion of nonpolar groups on the cations increases. Consequently the ionic liquid is more difficult to polarize.

One interesting experimental observation is that, for the ionic liquids with the different anion BF_4^- , the C_2 to C_9 systems have a very strong tendency to form glasses, and are very difficult to crystallize. In contrast, the C_{10} and longer side-chain systems are easier to crystallize. This phenomenon might be interpreted by our mechanism as follows: When the side-chain length is not very long, the Coulombic interactions dominating the polar groups and the collective short-range interactions dominating the nonpolar groups are comparable; the competition between these two different interactions leads to the self-generated glassy state independent of the cooling rate (35). When the side chain is long enough, the charged groups are greatly localized, so the global behavior of the system is dominated by the collective short-range interactions. The competition

between these two interactions with different length scales is weaker, so the tendency of self-generation of the glassy state is attenuated.

Discussion and Conclusions

By using the newly developed all-atom polarizable models (21, 22) based on the AMBER force field, the spatial heterogeneity in ionic liquids previously investigated (20) by the MS-CG models (17-19) has been confirmed. The tail groups are found to aggregate, while the polar groups retain their local structures relatively unchanged. A refined mechanism coming from the contribution from the Coulomb interaction, the collective short-range interaction, and the geometrical constraint from the chemical bonds has been proposed. The simulation results are quantitatively consistent with experimental ones, and the proposed mechanism can explain many experimental observations. Although our simulations have only been for the ionic liquid systems containing cations with an imidazolium ring and a nitrate anion, the mechanism should be applicable to most organic ionic liquids, independent of the specific choice of cation and anion species.

Our mechanism can also be reconciled with the MD simulation results of other researchers. Urahata and Ribeiro (12) found that the diffusion increases from C_1 to C_4 , and then decreases when the side chain is longer. This is qualitatively consistent with the experiments and our simulations. The difference for C_2 and C_4 might be explained by the differences of the anions and the simulation model used. The MD simulations performed by Margulis (14) and Urahata and Ribeiro (13) found that the systems are more structured with longer side chains. These are also consistent with our simulations, and can be explained by the inhomogeneous distribution of tail groups and slower diffusion with increasing side-chain length due to the tail aggregation mechanism. Our spatial heterogeneity mechanism may also closely relate to the dynamical heterogeneity (15, 36).

Lopes and Pádua (16) have reported some all-atom MD simulation results similar to ours for ionic liquids with different anions, which can also be interpreted by the refined mechanism proposed here. They imply that the continuous polar network is due to the hydrogen bonding. Although hydrogen bond network exists in both solid and liquid phases (37-41), our results suggest that it is the large ionic net charges, rather than the hydrogen bonds, that bind the polar groups together. The hydrogen bonds should instead have some influence on the details of the local structures of ions. Although these authors showed some evidences of tail aggregation, they did not investigate the isolated tail domains. The statistical characteristics of the tail and polar domains have been quantified in the present study by ensemble-average calculations using a recently defined heterogeneity order parameter. It should also be noted that

finite size effect may also exist in their results, since they used smaller simulation sizes up to 350 ion pairs. Since Lopes and Pádua used a non-polarizable atomistic MD model, it seems clear that the many-body polarization effect does not have a significant influence on the global spatial heterogeneity, although it does have an effect on the local structures and diffusion for ionic liquids.

With increasing alkyl-chain length, the diffusion at a given temperature is slower. On the other hand, ionic liquids with longer cationic side-chain lengths require larger simulation sizes to eliminate the finite size effect. In addition, the formation of tail domains may further complicate the phase diagram of ionic liquid systems. The complete phase diagram of ionic liquids along with the formation of a mesoscopic liquid crystal-like phase can only be studied with MD simulations in very large scales. Such simulations using all-atom models are far beyond the current computational capabilities. The MS-CG approach (19) for ionic liquids is therefore expected to be a powerful tool for the large scale simulations for ionic liquids. The phase diagram of ionic liquids may also be investigated by some analytical theories, similar to the methods used by Wolyne and co-workers (35, 42) to study systems with competing interactions. This research is currently underway in our group.

Acknowledgments

This research was supported by the Air Force Office of Scientific Research (FA9550-04-1-0381). The authors thank Dr. Tianying Yan for useful discussions. Allocations of computer time from the National Center for Supercomputing Applications (NCSA), the Cray XT3 system at the Pittsburgh Supercomputing Center, and the Center for High Performance Computing at the University of Utah are gratefully acknowledged.

Appendix

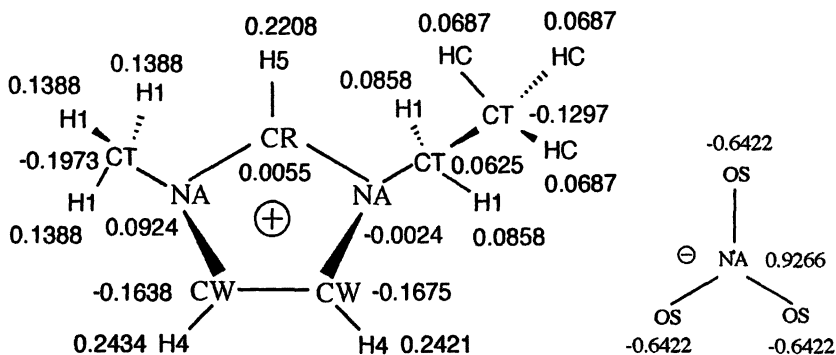
A1. Isotropic Atomic Polarizabilities

The isotropic atomic polarizability α takes an identical value for the same type of atoms in one ion.

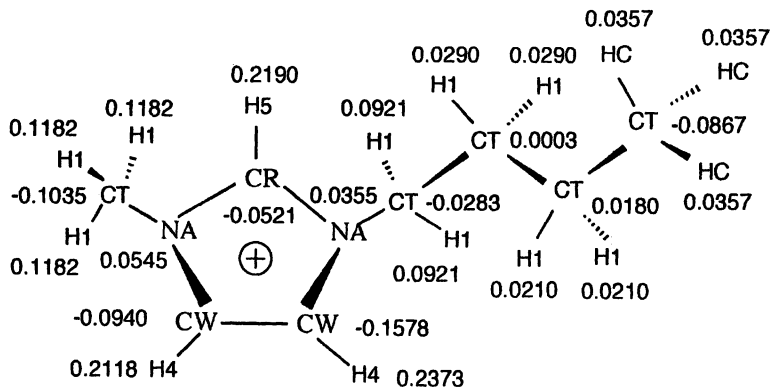
Atom	Cation			Anion	
	N	C	H	N	O
α	0.680	1.209	0.289	1.901	1.079

A2. Partial Charges of Atoms

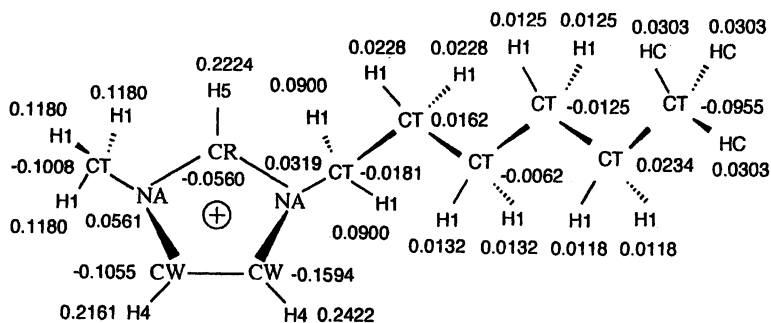
A2.1. C2 and Nitrate



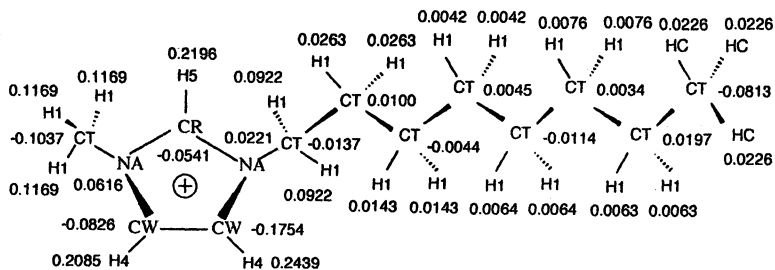
A2.2. C4



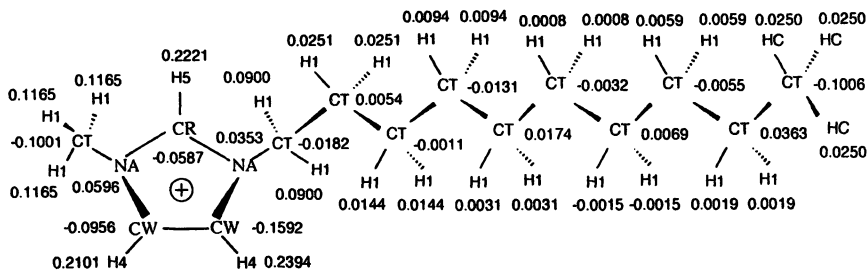
A2.3. C6



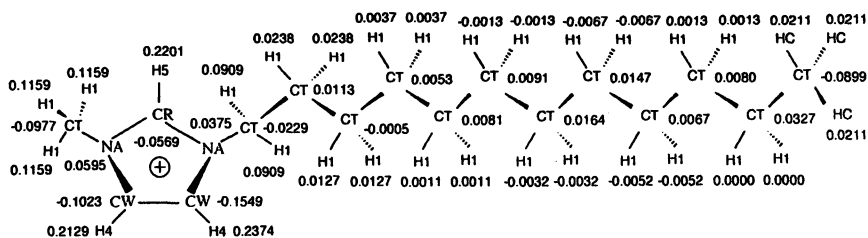
A2.4. C8



A2.5. C10



A2.6. C12



A3. Force Field Parameters

Bond parameters [k_r in kcal/(mol Å²) and r_{eq} in Å].

bond	k_r	r_{eq}	bond	k_r	r_{eq}
CR-NA	954.0	1.343	CW-NA	854.0	1.381
CT-NA	674.0	1.475	CT-CT	620.0	1.526
CW-H4	734.0	1.080	CT-H1	680.0	1.090
CW-CW	1040.0	1.370	CR-H5	734.0	1.080
CT-HC	680.0	1.090	NA-OS	600.0	1.260

Angle parameters [k_θ in kcal/(mol radian²) and θ_{eq} in degree].

angle	k_θ	θ_{eq}	angle	k_θ	θ_{eq}
CR-NA-CW	140.0	120.0	CW-NA-CT	140.0	125.8
NA-CR-NA	140.0	120.0	NA-CR-H5	70.0	120.0
NA-CW-H4	70.0	120.0	CW-CW-H4	70.0	128.2
NA-CT-H1	70.0	109.5	CT-CT-H1	100.0	109.5
H1-CT-H1	70.0	109.5	HC-CT-HC	70.0	109.5
CR-NA-CT	140.0	125.8	NA-CW-CW	140.0	120.0
NA-CT-CT	160.0	111.2	CT-CT-HC	100.0	109.5
CT-CT-CT	80.0	109.5	OS-NA-OS	300.0	120.0

Dihedral angle parameters [V_n in kcal/mol and γ in degree].

dihedral	V_n	γ	n	dihedral	V_n	γ	N
HC-CT-CT-NA	0.156	0.0	3	HC-CT-CT-H1	0.156	0.0	3
CT-NA-CR-H5	2.325	180.0	2	CT-NA-CR-NA	2.325	180.0	2
CT-NA-CW-CW	1.500	180.0	2	CT-NA-CW-H4	1.500	180.0	2
NA-CR-NA-CW	2.325	180.0	2	CR-NA-CW-H4	1.500	180.0	2
CW-NA-CR-H5	2.325	180.0	2	CR-NA-CW-CW	1.500	180.0	2
NA-CW-CW-NA	5.375	180.0	2	NA-CW-CW-H4	5.375	180.0	2
CT-CT-CT-H1	0.156	0.0	3	CT-CT-CT-CT	0.156	0.0	3
H1-CT-CT-H1	0.156	0.0	3	NA-CT-CT-CT	0.156	0.0	3
NA-CT-CT-H1	0.156	0.0	3	HC-CT-CT-CT	0.156	0.0	3
H1-CT-NA-CW	0.0	0.0	2	H1-CT-NA-CR	0.0	0.0	2
CW-NA-CT-CT	0.0	0.0	2	CR-NA-CT-CT	0.0	0.0	2
H4-CW-CW-H4	5.375	180.0	2	H5-CR-NA-NA ^a	1.100	180.0	2
CR-CW-NA-CT ^a	1.100	180.0	2	H4-CW-CW-NA ^a	1.100	180.0	2
OS-OS-NA-OS ^a	50.000	180.0	2				

^aImproper torsions.

Van der Waals parameters [ϵ in kcal/mol and σ in Å].

pair	ϵ	σ	pair	ϵ	σ
CW--- CW ^b	0.0860	3.400	CW--- NA	0.121	3.325
CW---H5	0.0359	2.911	CW--- HC	0.0371	3.025
CT---CT	0.109	3.400	CT---H1	0.0418	2.936
CT---HC	0.0418	3.025	CT---H4	0.0404	2.955
CT---CW	0.0968	3.400	H1---H1	0.0160	2.471
H1---HC	0.0160	2.560	H1---H4	0.0155	2.491
H5---H5	0.0150	2.422	H5---HC	0.0155	2.536
H5---NA	0.0505	2.836	HC---HC	0.0160	2.650
HC---NA	0.0522	2.950	H4---H4	0.0150	2.511
CW---H1	0.0371	2.936	CW---H4	0.0359	2.955
CT---H5	0.0404	2.911	CT---NA	0.136	3.325
H1---H5	0.0155	2.446	H1---NA	0.0522	2.861
H5---H4	0.0150	2.466	HC---H4	0.0155	2.580
H4---NA	0.0505	2.880	OS---OS	0.170	3.001
NA---NA	0.170	3.250	NA---OS	0.170	3.125
H1---OS	0.0522	2.736	H4---OS	0.0505	2.756
CW---OS	0.121	3.200	CT---OS	0.136	3.200
H5---OS	0.0505	2.711	HC---OS	0.0522	2.825

^bCR type atom has the same van der Waals parameters as CW atom.

References

1. Wasserschied, P.; Keim, W., *Angew. Chem., Int. Ed.* **2000**, *39*, 3772.
2. Seddon, K. R., The International George Papatheodorou Symposium: Proceedings. In *Institute of Chemical Engineering and High Temperature Chemical Processes*, Boghosian, S., Ed. Patras, Greece, 1999.
3. Lee, K. M.; Lee, C. K.; Lin, I. J. B., *Chem. Commun.* **1997**, 899.
4. Gordon, C. M.; Holbrey, J. D.; Kennedy, A. R.; Seddon, K. R., *J. Mater. Chem.* **1998**, *8*, 2627.
5. Holbrey, J. D.; Seddon, K. R., *J. Chem. Soc., Dalton Trans.* **1999**, 2133.
6. Lee, C. K.; Huang, H. W.; Lin, I. J. B., *Chem. Commun.* **2000**, 1911.
7. Tokuda, H.; Hayamizu, K.; Ishii, K.; Bin Hasan Susan, M. A.; Watanabe, M., *J. Phys. Chem. B* **2005**, *109*, 6103.
8. Seddon, K. R.; Stark, A.; Torres, M.-J., Alternative Media for Chemical Reactions and Processing. In *Clean Solvents*, Abraham, M.; Moens, L., Eds. American Chemical Society: Washington D. C., 2002; Vol. ACS Symp. Ser. 819.
9. Huddleston, J. G.; Visser, A. E.; Reichert, W. M.; Willauer, H. D.; Broker, G. A.; Rogers, R. D., *Green Chemistry* **2001**, *3*, 156.
10. Wakai, C.; Oleinikova, A.; Ott, M.; Weingärtner, H., *J. Phys. Chem. B* **2005**, *109*, 17028.
11. Bonhôte, P.; Dias, A.-P.; Papageorgiou, N.; Kalyanasundaram, K.; Grätzel, M., *Inorg. Chem.* **1996**, *35*, 1168.
12. Urahata, S. M.; Ribeiro, M. C. C., *J. Chem. Phys.* **2005**, *122*, 024511.
13. Urahata, S. M.; Ribeiro, M. C. C., *J. Chem. Phys.* **2004**, *120*, 1855.
14. Margulis, C. J., *Molec. Phys.* **2004**, *102*, 829.
15. Del Pópolo, M. G.; Voth, G. A., *J. Phys. Chem. B* **2004**, *108*, (5), 1744.
16. Lopes, J. N. A. C.; Pádua, A. A. H., *J. Phys. Chem. B* **2006**, *110*, 3330.
17. Izvekov, S.; Voth, G. A., *J. Chem. Phys.* **2005**, *123*, 134105.
18. Izvekov, S.; Voth, G. A., *J. Phys. Chem. B* **2005**, *109*, 2469.
19. Wang, Y.; Izvekov, S.; Yan, T.; Voth, G. A., *J. Phys. Chem. B* **2006**, *110*, 3564.
20. Wang, Y.; Voth, G. A., *J. Am. Chem. Soc.* **2005**, *127*, 12192.
21. Yan, T.; Burnham, C. J.; Del Pópolo, M. G.; Voth, G. A., *J. Phys. Chem. B* **2004**, *108*, (32), 11877.
22. Yan, T.; Burnham, C. J.; Wang, Y.; Gao, X.; Voth, G. A., *J. Phys. Chem. B* (submitted) **2006**.
23. Cornell, W. D.; Cieplak, P.; Bayly, C. I.; Gould, I. R.; Merz, K. M.; Ferguson, D. M.; Spellmeyer, D. C.; Fox, T.; Caldwell, J. W.; Kollman, P. A., *J. Am. Chem. Soc.* **1995**, *117*, 5179.
24. Sprik, M., *J. Phys. Chem.* **1991**, *95*, 2283.
25. Car, R.; Parrinello, M., *Phys. Rev. Lett.* **1985**, *55*, 2471.

26. Case, D. A.; Pearlman, D. A.; Caldwell, J. W.; Cheatham, T. E., III; Ross, W. S.; Simmerling, C. L.; Darden, R. A.; Merz, K. M.; Stanton, R. V.; Cheng, A. L.; Vincent, J. J.; Crowley, M.; Tsui, V.; Radmer, R. J.; Duan, Y.; Pitera, J.; Massova, I.; Seibel, G. L.; Singh, U. C.; Weiner, P. K.; Kollman, P. A., *Amber 6*. University of California: San Francisco, CA, 1999.
27. Frisch, M. J.; Trucks, G. W.; Schlegel, H. B.; et al., *Gaussian 03*. Gaussian Inc.: Wallingford CT, 2004.
28. Besler, B. H.; Merz Jr., K. M.; Kollman, P. A., *J. Comp. Chem.* **1990**, *11*, 431.
29. Singh, U. C.; Kollman, P. A., *J. Comp. Chem.* **1984**, *5*, 129.
30. de Andrade, J.; Böes, E. S.; Stassen, H., *J. Phys. Chem. B* **2002**, *106*, 13344.
31. Wang, Y.; Voth, G. A., *J. Phys. Chem. B* **2006**, In preparation.
32. Allen, M. P.; Tildesley, D. J., *Computer Simulation of Liquids*. Clarendon Press: Oxford, 1987.
33. Melchionna, S.; Ciccotti, G.; Holian, B. L., *Molec. Phys.* **1993**, *78*, 533.
34. Hoover, W. G., *Phys. Rev. A* **1985**, *31*, 1695.
35. Schmalian, J.; Wolynes, P. G., *Phys. Rev. Lett.* **2000**, *85*, (4), 836.
36. Hu, Z.; Margulis, C. J., *Proc. Natl. Acad. Sci. USA* **2006**, *103*, (4), 831.
37. Fannin, A. A.; Floreani, D. A.; King, L. A.; Landers, J. S.; Piersma, B. J.; Stech, D. J.; Vaughn, R. L.; Wilkes, J. S.; Williams, J. L., *J. Phys. Chem.* **1984**, *88*, 2614.
38. Dieter, K. M.; Dymek, C. J.; Heimer, N. E.; Rovang, J. W.; Wilkes, J. S., *J. Am. Chem. Soc.* **1988**, *110*, 2722.
39. Hardacre, C.; Holbrey, J. D.; McMath, S. E. J.; Bowron, D. T.; Soper, A. K., *J. Chem. Phys.* **2003**, *118*, (1), 273.
40. Hayashi, S.; Ozawa, R.; Hamaguchi, H.-o., *Chem. Lett.* **2003**, *32*, (6), 498.
41. Ozawa, R.; Hayashi, S.; Saha, S.; Kobayashi, A.; Hamaguchi, H.-o., *Chem. Lett.* **2003**, *32*, (10), 948.
42. Wu, S.; Westfahl Jr., H.; Schmalian, J.; Wolynes, P. G., *Chem. Phys. Lett.* **2002**, *359*, 1.

Chapter 21

Taylor Cones of Ionic Liquids as Ion Sources: The Role of Electrical Conductivity and Surface Tension

C. Larriba¹, D. Garoz¹, C. Bueno¹, I. Romero-Sanz¹, S. Castro¹,
J. Fernandez de la Mora^{1,*}, Y. Yoshida², G. Saito², R. Hagiwara³,
K. Matsumoto³, and J. Wilkes⁴

¹Mechanical Engineering Department, Yale University, 9 Hillhouse Avenue,
P.O. Box 208286, New Haven, CT 06520-8286

²Division of Chemistry, Graduate School of Science, Kyoto University,
Sakyo-ku, Kyoto 606-8502, Japan

³Department of Fundamental Energy Science, Graduate School of Energy
Science, Kyoto University, Sakyo-ku, Kyoto 606-8502, Japan

⁴Department of Chemistry, U.S. Air Force Academy, CO 80840

A purely ionic regime (PIR) of charge emission from Taylor cones of ionic liquids (ILs) held in a vacuum exists, giving ion beams of high quality. This regime is favored by ionic liquids of high electrical conductivity K and high surface tension γ . The present search for such ILs relies on an improved form of the *capillary rise method* using sample volumes smaller than 0.1 cm^3 . Prior and new observations are used to confirm the important role of both γ and K for PIR operation from conventional capillary electrospray sources.

Introduction

When the meniscus of a conducting liquid is charged to a high voltage with respect to surrounding electrodes, it becomes conical and its sharp tip emits charged particles (1, 2, 3, 4, 5). For liquids having electrical conductivities typically below 1 S m^{-1} the cone apex ejects a jet that breaks into a spray of charged drops. The drops have diameters of a few microns in the case of deionized water or other liquids having electrical conductivities in the range of 10^{-4} S m^{-1} . For this reason the phenomenon is commonly named an *electrospray*, though one should appropriately distinguish between the spray and the meniscus, often denoted a *Taylor cone* (4). The more precise term *cone-jet* has been introduced by Cloupeau and Prunet-Foch (5) to refer to the special regime of greatest practical interest, where a steady jet issues from the cone apex. In the case of liquids with exceptionally high electrical conductivities such as liquid metals held in a vacuum, regimes exist where the emissions are essentially in the form of metal ions, so that the conventional long and unstable jet is replaced by a short stable tip from which metal ions are field evaporated. Such systems are referred to as liquid metal ion sources (LMIS) and are in wide use in applications such as writing and etching on electrical circuits (6), as well as electrical propulsion (7). In between ion-emitting metals having electrical conductivities K of many thousands of S m^{-1} and drop-producing dilute electrolytes with K values below 10^{-3} S m^{-1} , a transition from one behaviour to the other would be expected. It does indeed arise at conductivities in the range of 1 S m^{-1} (8), but its investigation has been hampered by several difficulties. One is that the ions generated in the presence of high electric fields accelerate to sufficient energies to ionize the surrounding gas, leading to electrical discharges that disrupt the process. This problem may be overcome by operating under a vacuum. But a second difficulty then arises due to the lack of good solvents with the low vapor pressure required to withstand the vacuum. Some polar but viscous solvents such as glycerol have been widely used as sources of drops and ions (9) in a vacuum, but they can barely reach K values approaching 0.02 S m^{-1} , which are insufficient to produce high quality ion beams. Only two neutral solvents capable of withstanding a vacuum and forming electrolytes reaching conductivities of 1 S m^{-1} have been identified to date: formamide (FM) (8) and propylene carbonate (PC) (10). Their Taylor cones in vacuum produce a mixture of ions and drops, where the current of ions may be up to ten times higher than the drop current. These electrolytes, however are unsatisfactory because their finite volatility limits their practical value as electrical propellants in space applications, and precludes also well controlled terrestrial experiments. The presence of a finite fraction of drops also leads to poor performance in electrical propulsion devices and other ion sources.

Taylor cones of ionic liquids as sources of ions in vacuum

In view of these difficulties, and encouraged by the promising results reported long ago with H_2SO_4 (11), we have been studying the emissions from Taylor cones of similar (though less corrosive) purely ionic materials. Room temperature ionic liquids offer obvious advantages over salts melting at much higher temperature. For this reason, and also because most ionic liquids are essentially involatile and a fair number among them are known with room temperature electrical conductivities in excess of 1 S m^{-1} , we undertook their study (12) prior to that of high temperature molten salts. A first exploration (13) showed that the ionic liquid 1-ethyl-3-methylimidazolium bis(trifluoromethanesulfonyl)imide (EMI-Tf₂N) produced an undesirable mixture of ions and drops at comparable currents (mixed regime). However tests of the more conductive ionic liquid EMI-BF₄ (14) revealed for the first time the existence of the sought purely ionic regime (PIR). Subsequent investigations have confirmed this point with greater generality, and further shown a narrow ion energy distribution centered very close to the voltage of the emitting needle (15, 16, 17). However, the behavior of EMI-BF₄ was not easily generalized to other ionic liquids. Among the considerable number of those studied by I. Romero (18, 19), included in Table I together with EMI-TfO (studied subsequently by C. Bueno), only EMI-BF₄ exhibited the purely ionic regime at room temperature. Nonetheless, most of these liquids did reach the PIR at the temperatures indicated in Table I. Note that these measurements sampled few temperatures, so the value reported in Table I is a relatively rough upper bound (18, 19). Although raising the temperature decreases the surface tension and even more the exponential term associated to the field in the ion evaporation rate ($\sim E^{1/2}/kT$), the corresponding thermal activation effect ($-\Delta G/kT$) apparently dominates the picture, facilitating ion evaporation at increasing temperatures.

Subsequently, Garoz (20) synthesized, characterized and tested as ion emitters several new ionic liquids based on reactions of amines with acids, including $\text{R}_n\text{NH}_{4-n}\text{-COOH}$ ($n = 1-3$; R = ethyl and methyl), with some physical properties shown in Table II (note, however, that the water content was not measured, and most salts contained a slight excess of base). This work was inspired by an earlier study by Xu and Angell (21), showing very high conductivities in such salts. These ionic liquids, however, are somewhat volatile, and this poses limitations to their use in a vacuum. Furthermore, none of these formates reached the purely ionic regime at room temperature, even though several had singularly high electrical conductivities, well above that of EMI-BF₄. Garoz studied a few other nonvolatile ionic liquids whose properties are also included at the bottom of Table II. These turned out to be less conducting, and none achieved PIR operation.

Table I. Ionic Liquids studied in (18), including key physical constants at room temperature from the literature, and an upper bound to the temperature T_{PIR} at which their Taylor cones achieve the purely ionic regime.

Liquid	γ dyn cm ⁻¹	ρ g cm ⁻³	μ cP	K S m ⁻¹	Reference	T_{PIR} °C
EMI-BF ₄	45.2 ^f	1.24 ^g	43	1.3	(22) 26°C	23
EMI-TfO ^b	35.8 ^f	1.39	45	0.86	(23) 20°C	~ 23
EMI-Tf ₂ N	34.9 ^a	1.52	34	0.88	(23) 20°C	82
EMI-(C ₂ F ₅ SO ₂) ₂ N	31.2 ^{a,c}	1.6 ^a	61	0.34	(22) 26°C	119
EMI-Tf ₃ C	32.4 ^a	1.5 ^a	195 ^d	0.13	(24)	216
BMI-(C ₂ F ₅ SO ₂) ₂ N	27.6 ^a	1.51	87	0.19	(38) 30°C	204
DMPI-(C ₂ F ₅ SO ₂) ₂ N	29.7 ^a	1.51 ^a		0.252	(25) 25°C	212
DMPI-Tf ₃ C	37.8 ^a	1.55	726 ^d	0.046	(25) 25°C	None
Cyphos-Tf ₂ N	27.4 ^a	1.07 ^e	429 ^e			None
Cyphos-N(CN) ₂	29.2 ^a	0.90 ^h				None
PMI-PF ₃ (C ₂ F ₅) ₃	33.3 ^{a,c}	1.59 ^e	140 ^e	0.166	(26) 20°C	157

Cations: EMI = 1-ethyl-3-methylimidazolium; DMPI = 1,2-dimethyl-3-propylimidazolium; BMI = 1-butyl-3-methylimidazolium; PMI = 1-pentyl-3-methylimidazolium; Cyphos = trihexyltetradecylphosphonium. **Anions:** TfO = CF₃SO₃; Tf₂N = (CF₃SO₂)₂N; Tf₃C = (CF₃SO₂)₃C

^a Rough measurements of (18) without drying precautions; ^b This liquid was not studied by Romero. Its PIR operation was later discovered by C. Bueno. ^c See revised values in Table IV. ^d Private communication, V. Koch, Covalent. ^e Merck home page. ^f New measurements with dry samples. ^g Fuller, J.; Carlin, R. T.; Osteryung, R. A.. J. Electrochem. Soc. 1997, 144, 3881-3886. ^h home page of Sigma Aldrich.

This early work provided clear evidence that the electrical conductivity was not the only parameter distinguishing between purely ionic or mixed regime at room temperature. This was evident from a variety of observations, including the fact that the low surface tension ILs EMI-Tf₂N ($\gamma = 35.8$ dyn cm⁻¹; Table IV) and (CH₃)₂NH₂-COOH ($\gamma = 37.3$ dyn cm⁻¹; Table IV) do not reach the PIR at temperatures at which their electrical conductivity is substantially larger than the room temperature conductivity of EMI-BF₄.

Subsequent investigations by C. Bueno contributed further indications that the singular behavior of EMI-BF₄ was partly due to its relatively high surface tension. He first discovered that EMI-TfO operated also fairly near the PIR, while having the highest γ value following EMI-BF₄ in Table I. He also studied mixtures of the low and high surface tension liquids (C₂H₅)₃NH-Tf₂N and EMI-BF₄ as a function of EMI-BF₄ concentration. His results are summarized in Table III, and show an almost discontinuous transition to PIR conditions at a

Table II. Room temperature properties of the ILs studied in (20) ^c

Liquid	ρ (g cm ⁻³)	γ (dyn cm ⁻¹)	K (S m ⁻¹)
CH ₃ NH ₃ -COOH	1.12±0.01		2.9±0.3
(CH ₃) ₂ NH ₂ -COOH	1.06±0.02	37.6 ^b	6.7±0.9
(CH ₃) ₃ NH-COOH	1.092±0.002		3.8±0.8
C ₂ H ₅ NH ₃ -COOH	1.1±0.02	43.8 ^a ;39.5 ^b	1.4±0.1
(C ₂ H ₅) ₂ NH ₂ -COOH	1.02±0.02		0.96±0.09
(C ₂ H ₅) ₃ NH-COOH	1.061±0.005		1.04±0.09
(C ₈ H ₁₇) ₃ NH-COOH	0.84±0.01		0.014±0.001
(C ₂ H ₅) ₃ NH-TfO	1.19±0.01		0.46±0.06
(CH ₃) ₂ NH ₂ -Tf ₂ N	1.48±0.01		0.61±0.04
(C ₂ H ₅) ₃ NH-Tf ₂ N	1.41±0.01	30.2 ^b	0.52±0.06

^a Garoz's data without drying the sample. ^b New data with dry samples.

^c For the properties of a large number of related ILs see T. L. Greaves, A. Weerawardena, C. Fong, I. Krodziewska, C. J. Drummond, *J. Phys. Chem. B* (Web edition, Aug. 2006)

Table III: Room temperature characteristics of mixtures of (C₂H₅)₃NH-Tf₂N + EMI-BF₄ as a function of EMI-BF₄ concentration.

Vol %	0	10	30	50	60	65	70	80	100
K(S m ⁻¹)	0.39	0.53	0.65	0.66	0.74	0.72	0.82	0.99	1.3
γ (dyn cm ⁻¹)	30.19		35.3	37.7					45.2
Regime	M	M	M	M	M	both	PIR	PIR	PIR

M = mixed regime; PIR = purely ionic regime; M& PIR means that both regimes are attainable at low and high Taylor cone voltages, respectively.

volume concentration of about 65%. Although the surface tension of these mixtures was unknown then, we have now measured it for several having low concentration of EMI-BF₄, and found them to be relatively small (Table II).

All these early studies strongly suggested the proposition that both high surface tension and high electrical conductivity favor PIR operation. This hypothesis is also in accord with what one would expect on purely theoretical grounds. The scaling laws for the structure of cone-jets indicate that the maximum electric field on the surface of the meniscus varies as (δ)

$$E_{\max} = \varphi(\varepsilon) \gamma^{1/2} \varepsilon_0^{-2/3} (K/Q)^{1/6}, \quad (1)$$

where ε_0 is the electrical permittivity of vacuum, γ is the surface tension of the charged interface, K is the electrical conductivity of the conducting liquid and Q

is the flow rate of conducting liquid pushed through the meniscus tip and the jet. $\varphi(\epsilon)$ is a proportionality coefficient of order unity that depends on the dielectric constant ϵ . This law (1) has been recently confirmed numerically (10) with a value of $\varphi = 0.76$ for propylene carbonate ($\epsilon = 65$). Q cannot be arbitrarily small due to the finite range of stability of Taylor cones. The smallest value it can take scales as $1/K$ (27), whence $E_{\max} \sim \gamma^{1/2} K^{1/3}$, confirming the role expected of both γ and K to attain high surface electric fields. The importance of the surface electric field itself follows of course from its reduction of the activation barrier for an ion to evaporate. Because this barrier is typically 1.8 eV, in the absence of intense electric fields, ion evaporation rates are astronomically small at room temperature (28).

In conclusion, both theory and observations suggests that PIR operation requires liquids with high surface tension and high electrical conductivity. The goal of this study is therefore to identify ionic liquids with such characteristics, which in turn has required selecting materials having high electrical conductivities, and measuring their surface tensions. Since the ionic liquids in most cases were available only in relatively small quantities, we have introduced improvements over the capillary rise technique to minimize the volume of the sample used for an accurate measurement.

Surface tension measurement

The surface tension measurement method is essentially that of (29), with several improvements. Briefly, the ionic liquids are dried at room temperature for several hours under vacuum, and a small volume (typically less than 0.1 cm^3) is put inside a small vial into which a capillary tube with a radius of 0.27 mm (ACE glass microcapillary) is introduced (Figure 1). The liquid then rises inside the capillary to a certain equilibrium height h , and wets the glass surface at a certain wetting angle θ . θ and h are measured with a cathetometer (h directly, θ indirectly through the shape of the meniscus) providing the ratio of the surface tension over the liquid density γ/ρ . The liquid transfer and the measurement are done under atmospheric (humid) conditions. However, the active gas-liquid interface at the top of the capillary is kept dry by a gentle flow of dry gas. Because small levels of hydration tend to produce substantial increases in surface tension, this precaution is of even greater importance than pre-drying the liquid, particularly in the case of hydrophilic salts. The reason is that the surface is dried (or humidified) much faster than the bulk due to the higher diffusivity of water in the vapor than in the liquid phase. This point is readily seen because the height measured for dry liquids rises steadily when the meniscus is kept in ambient air, while that of an imperfectly dried liquid decreases upon bathing the meniscus in a dry gas. Such changes occur within a time frame of the order of ten minutes. Note that all the data shown in Table I except for those in rows 1

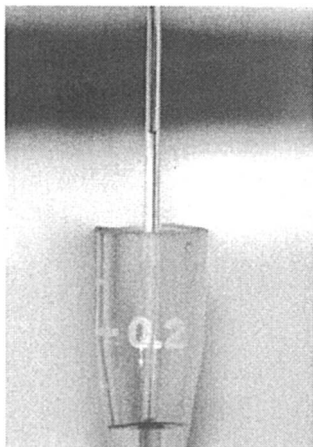


Figure 1. Illustration of the shape of the wetting meniscus at the liquid-glass capillary interfaces (internal, top and external, bottom), and the non-wetting meniscus at the polypropylene reservoir (bottom). The volume of sample is less than 0.1 cm^3

and 2 were taken in the open atmosphere without drying gas. However, all the liquids below row 2 are hydrophobic, and only rather modest humidity effects are expected for them (29).

The main source of measurement error in Martino et al. (29) was the imperfectly defined origin of heights on the small liquid reservoir below the capillary. This problem was caused by wetting of the liquid both on the outer capillary wall and the inner wall of the glass reservoir. Due to the small diameter of this reservoir (necessary to minimize sample consumption), these two menisci merged with each other allowing for no intermediate region of negligible curvature from which to define precisely the origin of heights. The associated error was estimated at 5%. This problem has been greatly reduced in our new measurements by use of commercial polypropylene vials with a conical bottom, of the type used to hold samples during centrifugation. As shown in the photograph of Figure 1, the wetting angle at the polypropylene surface is about 90° , leading to negligible uncertainty in the origin of heights. The improved method has been used to revise some of the prior data of (29), as well as those for EMI-($\text{C}_2\text{F}_5\text{SO}_2$)₂N and PMI-(C_2F_5)₃PF₃, all of which are reported in the bottom rows of Table IV. The most significant revision is the surface tension of DMI-N(CN)₂. In this case one sees an initial reduction of the meniscus height, clearly showing that the vacuum drying method is not adequate, perhaps due to the fact that this salt melts above room temperature. The relative error inferred from repeated measurements is at most 3%, probably associated to errors in the measurement of the wetting angle and to slight variations in the diameter of the capillary diameter. The improved measurement technique has been used to obtain the surface tension of a new group of materials described in the following section (Table IV).

Ionic Liquids

EMI-F(HF)_{2,3} was synthesized by the reaction of EMI-Cl with a large excess HF gas (30), and EMI-NbF₆ and EMI-TaF₆ were synthesized by the reaction of the EMI-F(HF)_{2,3} and appropriate MF₅ (M: Nb and Ta) (31). EMI-SbF₆ was prepared by the metathesis of EMI-Cl and K-SbF₆ in anhydrous acetone (32). Also the metathesis of each RMI-Cl and K-Au(CN)₂ in anhydrous acetone gave pale yellow liquids RMI-Au(CN)₂ [R = butyl (B), hexyl (C₆) and octyl(C₈)] (33). The FeCl₄ and FeBr₄ salts were prepared by the neat reaction of equivalent amount of RMI-X and appropriate FeX₃ (X: Cl, Br) (34). BMI-N(CN)₂ and C₆MI-N(CN)₂ were prepared by the metathesis of RMI-Br and Ag-N(CN)₂ in distilled water, in the same manner as earlier publication for EMI-N(CN)₂ (35).

Performance of the ionic liquids as ion sources

The experimental system is essentially that of Gamero and Hruby (18), where the Taylor cone is located inside a vacuum chamber and is charged at a certain high voltage *V*. Facing perpendicularly the meniscus is a grounded electrode (the extractor) with a perforation coaxial with the Taylor cone, through which the beam of ions and charged drops emitted pass into a larger chamber in the vacuum system. The charge over mass ratio *q/m* of the various particles produced is determined by time of flight mass spectrometry (TOF-MS), by interrupting the spray at time *t* = 0 and recording the arrival time distribution of current *I(t)* received at a collector electrode located a distance *L* along the axis away from the Taylor cone. On the assumption that all the particles have a kinetic energy per unit charge equal to the voltage difference *V*, the *I(t)* curve yields the distribution of *q/m*, providing in particular the masses and associated current of each ion.

Our work described above was carried out with conventional electrospray sources, with the Taylor cone supported at one open end of a capillary tube fed through its other end with a steady liquid flow rate *Q* externally imposed. The conclusions on the type of emission (PIR or mixed) discussed so far relate exclusively to this type of source. However, Lozano (36) has recently discovered that the emission regime depends on the characteristics of the ion source. Lozano and Martinez-Sanchez (15) have in particular introduced what they refer to as ionic liquid ion sources (ILIS), inspired by their liquid metal ion source (LMIS) analogs (6). Remarkably, although EMI-Tf₂N had in all prior work produced a mixture of ions and drops at comparable currents, Lozano (37) reports that it produces only ions from their ILIS system. These sources are externally wetted tungsten needles with sharp tips (radius ~ 1 μm), and with electrochemically roughened surfaces that facilitate arrival of the liquid to the tip by capillary

Table IV. Surface tensions for the new liquids studied, including in the bottom rows revisions of previously reported values

Liquid	γ (at 23°C) (dyn cm ⁻¹)	ρ (g cm ⁻³)	K (S m ⁻¹)	T _m (°C)	Ref
EMI-NbF ₆	51.7	1.67	0.85	-1	(31)
EMI-TaF ₆	51.3	2.17	0.71	2	(31)
EMI-F(HF) _{2,3}	48.0	1.13	10	-65 ^b	(30)
EMI-SbF ₆	47.8	1.85	0.62	10	(32)
BMI-FeBr ₄	47.1	1.98	0.55	-2	(34)
BMI-N(CN) ₂ ^d	46.6	1.06	1.1	-10	^d
C ₆ MI-FeBr ₄	42.0	1.86	0.28	-82(T _g)	(34)
C ₆ MI-N(CN) ₂ ^d	40.5	1.04	0.51	-90(T _g)	^d
C ₆ MI-FeCl ₄	39.4	1.33	0.47	-86(T _g)	(34)
C ₆ MI-Au(CN) ₂	39.3	1.65	0.081 ^e	13	(33)
C ₈ MI-FeBr ₄	38.1	1.74	0.14	-81(T _g)	(34)
C ₈ MI-FeCl ₄	37.2	1.28	0.22	-84(T _g)	(34)
C ₈ MI-Au(CN) ₂	36.0	1.59	0.056 ^e	-61(T _g)	(33)
EMI-GaCl ₄	48.6(50) ^{a, b}	1.53	2.2	11	(39)
EMI-FeCl ₄	47.3(47.7) ^{a, b}	1.42	2.0	18	(39)
BMI-GaCl ₄	43.6(41.5) ^a	1.43 ^c	0.95 ^c	-88(T _g)	(39)
EMI-(C ₂ F ₅ SO ₂) ₂ N	28.7 ^b	1.6 ^c	0.34	-1(37)	(22,36)
PMI-(C ₂ F ₅) ₃ PF ₃	30.3	1.59 ^h	0.166	<-50	(26)
EMI-TfO	38.3(39.2) ^a	1.39	0.86	-9	(23)
EMI-BF ₄	45.2(44.3) ^a	1.24 ^f	1.36	11	(22)
EMI-Tf ₂ N	35.8(35.2) ^a	1.52	0.88	-1	(23)
DMI-N(CN) ₂ ^d	54.9(61.6) ^a	1.14	3.6	34	^d

^a γ values in brackets are from (29) and are less reliable than the new values. ^b 21°C; ^c Rough measurements without drying precautions. ^d See Y. Yoshida, O. Baba, G. Saito, to be submitted to J. Phys. Chem. B. ^e Y. Yoshida, unpublished data. ^f Fuller, J.; Carlin, R. T.; Osteryung, R. A.. J. Electrochem. Soc. 1997, 144, 3881-3886. ^g R. Hagiwara, K. Matsumoto, Y. Nakamori, T. Tsuda, Y. Ito, H. Matsumoto, K. Momota, J. Electrochem. Soc. 2003, 150 (12), D195-D199. ^h Merck home page

action. In this system the flow Q of liquid cannot be controlled independently of the applied voltage (at least not for a fixed source), though it can be inferred from the TOF traces (13).

The details of our tests will be published elsewhere. However, we can advance here a complete confirmation of the hypothesis that both high K and high γ do favor PIR operation in capillary electrospray sources. For instance, EMI-N(CN)₂ behaves similarly as EMI-BF₄, while EMI-GaCl₄ behaves even better.

A more extensive series of tests in collaboration with P. Lozano (MIT) has been completed with externally wetted ILIS sources. Pending a more detailed report, we confirm that EMI-Tf₂N emits nothing but ions. Interestingly, the same behavior is found for more viscous liquids such as EMI-(C₂F₅SO₂)₂N (commercialized by Covalent) and PMI-(C₂F₅)₃PF₃ (commercialized in Europe by Merck), which emit ion beams of high quality (sharply defined energy distributions), confirming and extending the prior findings of Lozano (37). However, the currents emitted at room temperature are rather small, and decrease with increasing viscosity, taking values in the range of 20 nA in the case of EMI-(C₂F₅SO₂)₂N and PMI-(C₂F₅)₃PF₃.

Acknowledgments

We are grateful to Profs. Francisco Higuera (Polytechnical University, Madrid), Paulo Lozano and Manuel Martinez-Sanchez (MIT) for their many contributions to our studies. Our work has been possible through funding from the AFOSR via Yale grants F-49620-01-1-1416 and FA-9550-06-1-0104, as well as through several subcontracts from AFOSR contracts to the companies Busek and Connecticut Analytical.

References

1. Zeleny, J. *Phys. Rev.* **1914**, *3*, 69-91
2. Zeleny, J. *Proc. Cambridge Philosophical Soc.* **1915**, *18*, 71-93
3. Zeleny, J. *Phys. Rev.* **1917**, *10*, 1-6
4. Taylor, G. I. *Proc. Roy. Soc. A* **1964**, *280*, 383-397.
5. Cloupeau, M.; Prunet-Foch, B. *J. Electrostatics*, **1989**, *22*, 135-159
6. Prewett, P. D.; Mair, G. L. R. *Focused ion beams from liquid metal ion sources*, John Wiley, New York (NY), 1991
7. Tajmar M.; Wang J. J. *Propul. Power*, **2000**, *16*, 536-544
8. Gamero-Castaño, M.; Fernández de la Mora, J. J. *Chem. Phys.* **2000**, *113*, 815-832.
9. Cook, K. D. *Mass Spectr. Rev.* **1986**, *5*, 467-519

10. Guerrero, I.; Bocanegra, R.; Fernandez de la Mora, J.; Higuera, F. J. Ion evaporation from Taylor cones of propylene carbonate mixed with ionic liquids. Submitted to *J. Fluid Mech.*, 2006.
11. Perel, J.; Mahoney, J. F.; Moore, R. D.; Yahiku A.Y. *AIAA J.* **1969**, *7*, 507.
12. Fernandez de la Mora, J.; Gamero-Castaño, M., US patent, 6,768,119, 27 July 2004
13. Gamero-Castaño, M.; Hruby V. J. *Prop. Power* **2001**, *17*, 977-987
14. Romero-Sanz, I.; Bocanegra, R.; Fernández de la Mora, J.; Gamero-Castaño, M. *J. Appl. Phys.* **2003**, *94*, 3599-2005
15. Lozano, P.; Martínez-Sánchez, M. J. *Coll. Interface Sci.* **2005**, *282*, 415-421
16. Chiu, Y. H.; Austin, B. L.; Dressler, R. A.; Levandier, D.; Murray, P. T.; Lozano, P.; Martínez-Sánchez, M. J. *Prop. Power* **2005**, *21*, 416-423
17. Romero-Sanz, I.; Fernandez de la Mora, J. *J. Applied Phys.* **2004**, *95*, 2123-2129
18. Romero-Sanz, I. Master's Thesis. 2002. Universidad Carlos III de Madrid. Spain. An expanded version is included in Romero's PhD Thesis, *Propulsión y iónica y coloidal por atomización electrostática*, Universidad Carlos III, Madrid, Spain, 2006
19. Romero-Sanz, I.; Aguirre-de-Carcera, I.; Fernandez de la Mora, J. *J. Prop. & Power*, **2005**, *21*, 239-242
20. Garoz, D. Synthesis, study and mixtures of new ionic liquid-based propellants for electrical propulsion from Taylor cones in vacuo), Proyecto fin de carrera (Senior Thesis), Universidad Politecnica de Madrid, Marzo 2004.
21. Xu, W.; Angell, C. A. *Science*, **2003**, *302*, 422-425
22. McEwen, A. B.; Ngo, H. L.; LeCompte, K.; Goldman, J. L. *J. Electrochem. Soc.* **1999**, *146*, 1687-1695.
23. Bonhôte, P.; Dias, A. P.; Armand, M.; Papageorgiou, N.; Kalyanasundaram, K.; Grätzel, M., *Inorg. Chem.* **1996**, *35*, 1168-1178.
24. Nanjundiah, C.; McDevitt, S. F.; Koch, V. R. *J. Electrochem. Soc.* **1997**, *144*, 3392-3397.
25. Koch, V. R.; Nanjundiah, C.; Appetecchi, G. B.; Scrosati, B. *J. Electrochem. Soc.* **1995**, *142*, L116-L118.
26. Ignat'ev, N. V.; Welz-Biermann, U.; Kucheryna, A.; Bissky, G.; Willner, H. *J. Fluorine Chem.* **2005**, *126*, 1150-1159
27. Fernández de la Mora, J.; Loscertales, I. G. *J. Fluid Mech.*, **1994**, *260*, 155-184.
28. Iribarne, J. V.; Thomson, B. A. *J. Chem. Phys.* **1976**, *64*, 2287-2294
29. Martino, W.; Fernández de la Mora, J.; Yoshida, Y.; Saito, G.; Wilkes, J. *Green Chem.*, **2006**, *8*, 390-397
30. Hagiwara, R.; Hirashige, T.; Tsuda, T.; Ito, Y. *J. Electrochem. Soc.* **2002**, *149*, D1-D6

31. Matsumoto, K.; Hagiwara, R.; Ito, Y. *J. Fluor. Chem.*, **2002**, *115*, 133-135
32. Matsumoto, K.; Hagiwara, R.; Yoshida, R.; Ito, Y.; Mazej, Z.; Benkič, P.; Žemva, B.; Tamada, O.; Yoshino, H.; Matsubara, S. *Dalton Trans.*, **2004**, *1*, 144-149.
33. Yoshida, Y.; Fujii, J.; Saito, G.; Hiramatsu, T.; Sato, N. *J. Mater. Chem.* **2006**, *16*, 724-727.
34. Yoshida, Y.; Saito, G. *J. Mater. Chem.* **2006**, *16*, 1254-1262.
35. Yoshida, Y.; Muroi, K.; Otsuka, A.; Saito, G.; Takahashi, M.; Yoko, T. *Inorg. Chem.* **2004**, *43*, 1458-1462.
36. Ngo, H. L.; LeCompte, K.; Hargens, L.; McEwen, A. B. *Thermochim. Acta* **2000**, *357-358*, 97-102.
37. Lozano, P. C. *J. Phys. D: Appl. Phys.* **2006**, *39*, 126-134
38. Tokuda, H.; Tsuzuki, S.; Susan, Md. A. B. H.; Hayamizu, K.; Watanabe, M. *J. Phys. Chem. B* **2006**, *110*, 19593-19600
39. Yoshida, Y.; Otsuka, A.; Saito, G.; Natsume, S.; Nishibori, E.; Takata, M.; Sakata, M.; Takahashi, M.; Yoko, T. *Bull. Chem. Soc. Jpn.* **2005**, *78*, 1921-1928

Chapter 22

How to Make Ionic Liquids More Liquid

Nikolai V. Ignat'ev^{1*}, A. Kucheryna², G. Bissky², and H. Willner²

¹Merck KGaA, PLS R&D LSS, Frankfurter Strasse 250,
D-64293 Darmstadt, Germany

²University of Wuppertal, FB C, Inorganic Chemistry, Gaußstrasse 20,
D-47097, Wuppertal, Germany

The syntheses of new room temperature ionic liquids (ILs) possessing low viscosity are described. The strong influence of the nature of the anions on the viscosity of ionic liquids is demonstrated. A model, which rationalizes the influence of intra-ionic interactions on the viscosity of ionic liquids, is presented.

Room temperature ionic liquids were intensively studied in the last decade as potentially new reaction media for chemical synthesis (*1*), and they are attractive for applications in electrochemistry. These new materials exhibit unique properties: they are liquid over a wide temperature range, non-volatile, non-flammable, and show high thermal and electrochemical stability. Ionic liquids dissolve many organic and inorganic compounds, but they are much more viscous than conventional organic solvents (see Table I). During flow of ionic liquids the friction between the ions are in general stronger than between neutral molecules, because the interionic Coulomb forces are in general stronger than van der Waals or hydrogen bonding forces. On the basis of this approach, we developed a model, which may estimate the influence of the nature of the ions on the viscosity of ionic liquids.

Table I. Viscosity of Common Ionic Liquids

<i>Ionic Liquid</i>	<i>Viscosity</i>	<i>Density</i>
	$mm^2 \cdot s^{-1}$ (20° C)	$g \cdot cm^{-3}$
1-Hexyl-3-methylimidazolium Chloride	7453	1.05
1-Hexyl-3-methylimidazolium [PF ₆] ⁻	548	1.30
1-Hexyl-3-methylimidazolium [BF ₄] ⁻	195	1.15
Water	1.0	1.0
Methanol	0.73	0.79

Results and Discussion

The high viscosity of ionic liquids results in low current response in electrochemical processes and causes low bimolecular reaction rates, controlled by diffusion. In accordance to the Fick's first law (2), the diffusion (J) depends on the diffusion coefficient (D) and gradient of concentration (c):

$$J_{\text{dif}} = -D \frac{dc}{dx} \quad (1)$$

The diffusion coefficient (D) of the solute in common solvents depends on the viscosity of medium as demonstrated by the Stokes-Einstein equation 2.

$$D = \frac{kT}{c \cdot \pi \cdot \eta \cdot r_s} \quad (2)$$

k – Boltzmann constant

T – abs. Temperature

η – dynamic viscosity

r_s – hydrodynamic (Stokes) radius

c – coefficient, typically 6 for the solute in common solvents

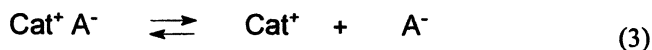
Furthermore the diffusion coefficient depends on the geometry (size) of the diffusing particles in the liquid medium, assuming that they are spheres with the radius (r). By the diffusion in liquid media the solute involves part of the solvent

into the motion and forms a sphere with the hydrodynamic (Stokes) radius (r_s). Typically, for common solvents r_s is $> r$. However, ionic liquids consist in anionic and cationic species, which do not have a solvation shell. From this point of view, it is not clear, which radius (r) we should consider to calculate the diffusion coefficient (D) of ions in ionic liquids. Can we apply the Stokes-Einstein equation in its classical form to calculate the viscosity of ionic liquids? Probably not, because in ionic liquids several types of moveable ion or ion-pairs are present.

Practically, an IL is a solute of ions in ionic media. Typically, the cationic part of ILs is a bulky organic cation with low charge density on the outer sphere due to the good charge delocalization (imidazolium, pyridinium, guanidinium, ammonium, phosphonium *etc.* cations). If the counter-anion is sufficiently nucleophilic (for instance chloride), it can coordinate on the cation to form contact ion-pairs, ion-clusters or even solid salts. In this case we should take into account a co-operative diffusion of anion and cation in the liquid state, and we should consider such ion-pairs as single particle (Model 1, Figure 1). According to Model 1, calculation of the self-diffusion coefficient (D_s) of these particles should be made in this case with the radius ($r_{C,A}$) of the sphere which encloses both cation and anion.

If the counter-anion belongs to the group of weakly coordinating anions (for instance tetrafluoroborate), with distinctly delocalized negative charge and low charge density on the outer sphere, we can consider such anions as independently moving particles (Model 2, Figure 1). In this case the radius (r_A) and (r_C) are much smaller than ($r_{C,A}$) and consequently the self-diffusion coefficient (D_s) and mobility of the ions are much higher. Practically, in ionic liquids we have three different kinds (probably more, if the anions and cations are able to form cluster structures) of moveable particles; ion-pairs, cations and anions, having different self-diffusion coefficients (D_s) and different mobility, which determine the viscosity of whole system (ionic liquid).

The number of free ions in an ionic liquid depends on the dissociation rate of the ion-pairs (equation 3).



The equilibrium constant (K) and rate of dissociation (ion separation) in ionic liquids strongly depends on the nature of anions and cations. We can assume that in the case of weakly coordinating anions and well stabilized cations (for example, imidazolium) the equilibrium is strongly shifted to the right side. But in any case, to estimate the fluidity of ionic liquids, we should take into account the mobility of different species: cations, anions, ion-pairs (or clusters). To understand the influence of all these particles on the macroscopic viscosity of

about 3.5 for imidazolium cations (in between 2.9 and 3.8, depending on the nature of counter anion) and of about 4.5 for $[(CF_3SO_2)_2N]^+$, $[CF_3SO_3]^+$, $[PF_6]^+$ and $[BF_4]^+$ anions in corresponding ionic liquids. We have used these values in equation 4, but additional studies are still required to obtain accurate factor (c) for different species in ionic liquids.

The transfer number (n) depends on the rate of ion separation in ionic liquid and can be estimated from the ratio of $\Lambda_{imp}/\Lambda_{NMR}$ (3-6), which can provide quantitative information about ion dissociation/association in ionic liquids according to equilibrium 3. For different room temperature ionic liquids (RTILs) this ratio ("ionicity" of ionic liquids (4)) was found to be in between 0.55 – 0.75, depending on the nature of the cations and anions forming an ionic liquid (3,6). Taking into account the average value of 0.65 and assuming that $(n_A) + (n_C) + (n_{A,C}) = 1$, we can estimate the transfer number of ion-pairs ($n_{A,C}$) in RTILs equal to 0.35 (or in between 0.25 and 0.45 depending on the "ionicity" rate of ionic liquid). The remaining 0.65 can be divided between the anionic (n_A) and cationic (n_C) transfer number in proportion approximately 2 : 3, found by Tokuda et al.(3,4,6) from the relation $D_{cation}/(D_{cation} + D_{anion})$. That gives the average values $(n_A) = 0.26$ and $(n_C) = 0.39$. All these estimations are based on the data available in the literature for limited number of RTILs. For precision quantization of (n_A), (n_C) and ($n_{A,C}$) further studies are required.

Of course, even in the case of Model 2, both cations and anions are interacting by their electric fields (according to the Debye-Hückel theory), and their diffusion (motion) is influenced by Coulombic forces. As a result of this interaction, the diffusion of the ions in ionic liquids is not an uniform motion. The motion of an ion can be accelerated if it is approaching the ion of opposite charge (counter-ion) or leaving the sphere of influence of an ion with the same charge. On the other hand, an ion will be slowed down upon approaching an ion of the same charge or moving away from an ion with the opposite charge. Consequently, the motion of the ions in ionic liquids is chaotic – their velocities being modulated by their local environment. That is probably the reason for a relatively low value of self-diffusion coefficients (for the room temperature ionic liquids the sum of self-diffusion coefficients of the cations and anions are in between 1.6 to $6.0 \times 10^{-7} \text{ cm}^2 \text{ s}^{-1}$), which were determinate recently by H. Tokuda *et al.* (6) via PGSE-MNR method.

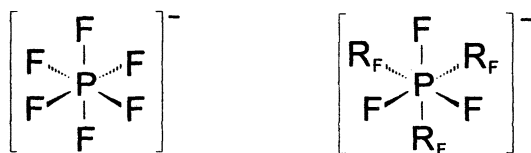
The greater the distance between two ions, the lower (in quadratic relation) are the forces between these ions. The Coulombic law describes the interaction between two point charges. Thus, the interaction between the ions in ionic liquids is strongly dependent on the delocalization of the charge over their outer spheres. The more localized the negative charge in an anionic species, the stronger they can interact with cations. Opposite, the anions with well delocalize charge (weakly coordinating anions, for example $[PF_6]^-$ and $[BF_4]^-$) form ionic

liquids with high “ionicity” rate. From the equation 4 we can conclude, that in this case the influence on the viscosity of RTILs from the side of ion-pairs or clusters, which presumably have a much smaller self-diffusion coefficient in comparison to free cations or anions, is limited and we can expect ionic liquids with relatively low viscosity.

All molecular impurities (polar organic solvents, water, *etc.*) increase the dissociation rate of ion-pairs or clusters (equation 3) via solvation (7). According to equation 4, this also leads to decrease in viscosity. The influence of water on the viscosity of hydrophilic ionic liquids (for example in the case of thiocyanate’s IL) is well known.

In our study we have compared the viscosity of room temperature ionic liquids having anions with the same central atom (phosphorus or boron) and possessing similar shape which is roughly spherical. In the case of spherical symmetry, the charge density on the outer sphere of the anions is a decisive factor for the formation of contact ion-pairs with cations (Model 1, Figure 1).

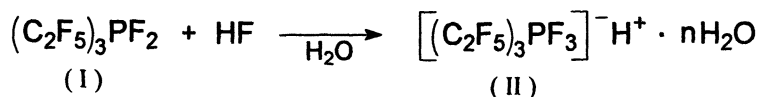
Table I presents the viscosity data for three commonly used, room temperature ionic liquids having the same cation but different anions: chloride, hexafluorophosphate and tetrafluoroborate. Remarkably, in spite of the significantly bigger ion’s radius of the hexafluorophosphate anion (0.254 nm (3)), ionic liquids with this anion show a much lower viscosity than chloride based ionic liquids. This is due to the relatively weak coordinating properties of the hexafluorophosphate anion. Nevertheless, the hexafluorophosphate, $[\text{PF}_6]^-$ anion is sensitive to attack by strong electrophiles such as protons. That explains the hydrolytic instability of the hexafluorophosphate anion by protonation of a fluorine atom and HF elimination upon reaction with water (8,9). To increase the hydrolytic stability and decrease the coordination ability of fluorophosphates, the replacement of some fluorine atoms in the hexafluorophosphate anion by hydrophobic perfluoroalkyl-groups is a promising approach to new weakly coordinating anions (10-14).



Scheme 1

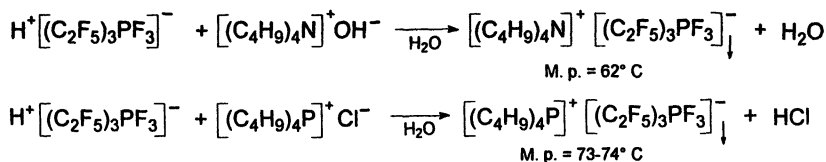
Ionic liquids with (perfluoroalkyl)fluorophosphate (FAP) anions were developed by Merck KGaA (Darmstadt, Germany) (15-20) and has been described recently (21). They can be prepared in three separate steps starting

with the industrially available trialkylphosphines, which are converted via electrochemical fluorination into tris(perfluoroalkyl)-difluorophosphoranes (I) (22-23). The second step is the formation of tris(perfluoroalkyl)-trifluorophosphoric acid (II) by the addition of HF to tris(perfluoroalkyl)difluorophosphoranes (15, 16).



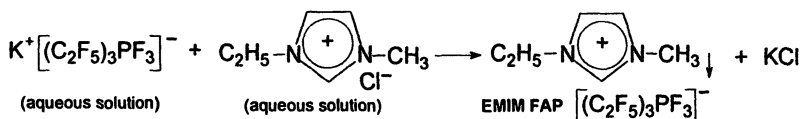
Scheme 2

Tris(perfluoroalkyl)trifluorophosphoric acid (II) is a strong acid, which is able to form salts by neutralization with organic or inorganic bases or via interaction with salts of other, weaker acids (15).



Scheme 3

Not only the acid (II), but also the alkali metal salts of tris(perfluoroalkyl)trifluorophosphoric acid (II) are convenient starting materials for the synthesis of ionic liquids with the FAP anion (20). For example, 1-ethyl-3-methylimidazolium tris(pentafluoroethyl)trifluoro-phosphate (EMIM FAP) is formed in high yield simply by mixing aqueous solutions of potassium tris(pentafluoroethyl)trifluorophosphate and 1-ethyl-3-methylimidazolium chloride.



Scheme 4

EMIM FAP is a hydrophobic room temperature ionic liquid with low viscosity, $44 \text{ mm}^2\text{s}^{-1}$ at 20°C (density: $1.71 \text{ g}\cdot\text{cm}^{-3}$). The kinematic viscosity of this ionic liquid is comparable to those of EMIM SCN; $41 \text{ mm}^2\text{s}^{-1}$ at 20°C (density: $1.15 \text{ g}\cdot\text{cm}^{-3}$), in spite of the big difference in the van der Waals radii of FAP and SCN

anions. Viscosity and density data were obtained for the samples of EMIM SCN and EMIM FAP with 160 ppm and 20 ppm of residual water correspondingly.

Table II presents a comparison of the viscosity data of room temperature ionic liquids with FAP anions to that of hexafluorophosphate and chloride based IL.


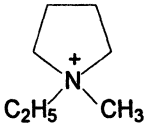
Table II. Viscosity of FAPs Ionic Liquids

<i>Ionic Liquid</i>	<i>Viscosity</i>	<i>Density</i>
	$\text{mm}^2 \cdot \text{s}^{-1}$	(20°C) $\text{g} \cdot \text{cm}^{-3}$
1-Hexyl-3-methylimidazolium Chloride	7453	1.05
1-Hexyl-3-methylimidazolium [PF ₆] ⁻	548	1.30
1-Hexyl-3-methylimidazolium [(C ₂ F ₅) ₃ PF ₃] ⁻	74	1.56
1-Hexyl-3-methylimidazolium [(C ₃ F ₇) ₃ PF ₃] ⁻	227	1.62
1-Pentyl-3-methylimidazolium [(C ₄ F ₉) ₃ PF ₃] ⁻	594	1.69

Despite the molecular weight and large ion radius of the tris(pentafluoroethyl)trifluorophosphate anion, the ionic liquid with this anion shows much lower kinematic viscosity than ionic liquids with the hexafluorophosphate anion; 74 and 548 $\text{mm}^2 \cdot \text{s}^{-1}$ respectively. This low viscosity can be explained by equation 4. The FAP ion is much weaker associated with the imidazolium cation than [PF₆]⁻, that increase the “ionicity” of RTILs with the FAP anion. The value ($n_{A,C}$) becomes smaller and reduce the influence of ion-pairs with low self-diffusion coefficient ($D_{A,C}$) on the viscosity of whole system. The mobility of ions, which is generally much higher than that of ion-pairs or clusters, determines now the macroscopic viscosity of the ionic liquid. Even ionic liquids containing the bulky tris(heptafluoropropyl)trifluorophosphate anion is less viscous than that of hexafluorophosphate (Table II). These results clearly demonstrate that, the coordination ability of the anion is the crucial point for the viscosity of ionic liquids. The same approach was used by W. Kantlehner et al. (24) to explain the low viscosity of ionic liquids with the tricyanomethanide anion.

The Table II also shows that with increasing radius of ions of the same nature (with similar coordinating ability) leads to increasing viscosity of RTILs in accordance with equation 4. We have observed this phenomenon not only in the case of RTILs with FAP anions, but also for alkylsulfate’s ionic liquids (Table III). The data presented in Table III are very interesting. Increase in the chain length of alkylsulfates (from C₁ to C₄) leads to higher viscosity of imidazolium and pyrrolidinium ionic liquids due to increase in the anion radius. That is in agreement with equation 4. Tokuda et al. (4) have observed the same phenomenon in the case of imidazolium ionic liquids having the same anion

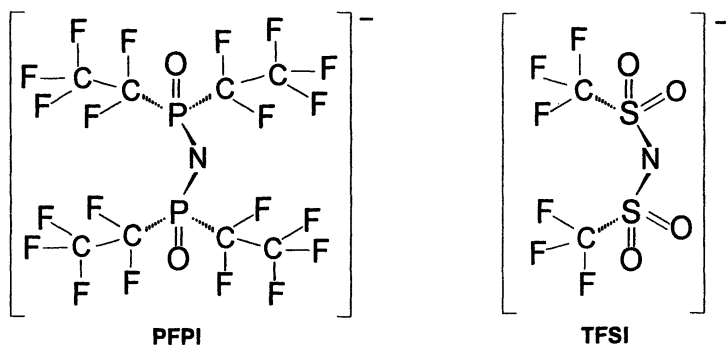
Table III. Viscosity of Alkylsulfates Ionic Liquids

Cation	Anion	Viscosity, mPa·s			
		20 °C	40 °C	60 °C	80 °C
	CH ₃ OSO ₃ ⁻	84	37	20	12
	C ₂ H ₅ OSO ₃ ⁻	117	47	24	14
	C ₄ H ₉ OSO ₃ ⁻	261	90	40	22
	CH ₃ OSO ₃ ⁻	221	84	40	22
	C ₄ H ₉ OSO ₃ ⁻	625	193	78	39

([(CF₃SO₂)₂N]), but different alkyl groups (C₁ to C₈) bonded at position 1 of imidazolium. Again, the increase of ion radius (of cation in this case) increase the viscosity of ionic liquids. That is also in agreement with equation 4.

Another interesting point is the difference in the viscosity of imidazolium and pyrrolidinium ionic liquids with the same anion (Table III). Imidazolium RTILs are less viscous than pyrrolidinium ones with the same alkyl substituents at nitrogen. Tokuda et al. (6) have reported the same observation for 1-butyl-3-methylimidazolium and N-butyl-N-methyl-pyrrolidinium ionic liquids with [(CF₃SO₂)₂N] anion. It seems that better delocalization of the positive charge over the conjugated system of the imidazolium ring reduces its coordination ability and increase the “ionicity” of imidazolium RTILs, which in accordance with equation 4 leads to a less viscous system. Again, the coordination ability of ions, or tendency to form ion-pairs and clusters, has major impact on the viscosity of ionic liquids. The van der Waals radius of ions, their symmetry (or asymmetry) and tendency to form hydrogen bonding have only the secondary influence on the viscosity of ionic liquids. Below is one more example.

Recently (25), we have synthesized new room temperature ionic liquids with, the bis[bis(pentafluoroethyl)phosphonyl]imide, {[(C₂F₅)₂P(O)]₂N}⁻ anion. This anion is much bigger than the well known bis(trifluoromethylsulfonyl)imide, [(CF₃SO₂)₂N]⁻ anion (see Scheme 5) or bis(pentafluoroethylsulfonyl)imide, [(C₂F₅SO₂)₂N]. Nevertheless, the viscosity of 1-butyl-3-methylimidazolium (BMIM) {[(C₂F₅)₂P(O)]₂N} (76 mPa·s) is comparable to the viscosity of BMIM [(CF₃SO₂)₂N], and well below the viscosity of BMIM [(C₂F₅SO₂)₂N] (146 mPa·s) (see Table IV).



Scheme 5

Table IV. Viscosity of Bis[bis(pentafluoroethyl)phosphonyl]imides Ionic Liquids

<i>Cation</i>	<i>Anion</i>	<i>Viscosity, mPa·s (20 °C)</i>
 $C_4H_9-N \text{ (ring) } N-CH_3$	$[CF_3SO_2]_2N^-$	63 (3) ; 61
	$[C_2F_5SO_2]_2N^-$	146 (3)
	$[(C_2F_5)_2P(O)]_2N^-$	76

It seems, that bis[bis(pentafluoroethyl)phosphonyl]imide, $\{[(C_2F_5)_2P(O)]_2N\}^-$ is much less coordinating than bis(trifluoromethylsulfonyl)imide, $[(CF_3SO_2)_2N]^-$.

Tetrafluoroborate based ionic liquids have been intensively studied in last years. Syntheses of these ionic liquids are well developed (1) and they are commercially available from different companies. Room temperature ionic liquids with the tetrafluoroborate anion are less viscous than corresponding IL with $[PF_6]^-$ (Table I), but the viscosity and limited hydrolytical stability of tetrafluoroborate based ionic liquids still restrict their broad practical applications. We have improved the properties of the RTILs by replacement of some fluorine atoms in $[BF_4]^-$ with perfluoroalkyl groups.

The data, listed in the Table V, show that replacement of the first fluoro ligand in $[BF_4]^-$ by a perfluoroalkyl group reduces dramatically the viscosity of imidazolium ionic liquids. Remarkably, the influence of the C_2F_5 group on the



Scheme 6

viscosity is stronger than that of the CF_3 group. Again, the coordination ability of the anion over compensates the influence of ion radius.

Table V. Viscosity of Perfluoroalkylborates Ionic Liquids

Ionic Liquid	Viscosity	Density
	$\text{mm}^2 \cdot \text{s}^{-1}$	(20° C) $\text{g} \cdot \text{cm}^{-3}$
1-Hexyl-3-methylimidazolium $[\text{BF}_4]^-$	195	1.15
1-Hexyl-3-methylimidazolium $[\text{CF}_3\text{BF}_3]^-$	80	1.21
1-Butyl-3-methylimidazolium $[\text{BF}_4]^-$	120	1.21
1-Butyl-3-methylimidazolium $[\text{C}_2\text{F}_5\text{BF}_3]^-$	47	1.47
1-Butyl-3-methylimidazolium $[(\text{C}_2\text{F}_5)_3\text{BF}]^-$	31	1.51

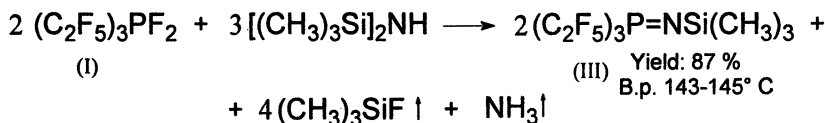
Furthermore, three pentafluoroethyl groups in the borate anion decrease the viscosity of ionic liquids more effectively than one C_2F_5 group (Table V).

The syntheses of ionic liquids with $[\text{CF}_3\text{BF}_3]^-$ and $[\text{C}_2\text{F}_5\text{BF}_3]^-$ anions were described recently (26-30). The method is based on ion exchange with $\text{K}[\text{CF}_3\text{BF}_3]$ or $\text{K}[\text{C}_2\text{F}_5\text{BF}_3]$ (26-31). Both salts can be synthesized via application of Ruppert's reagent $(\text{CH}_3)_3\text{SiCF}_3$ (32-34) or $(\text{CH}_3)_3\text{SiC}_2\text{F}_5$ (35). For the syntheses of these compounds, chemicals are required, which are restricted by the Montreal Protocol.

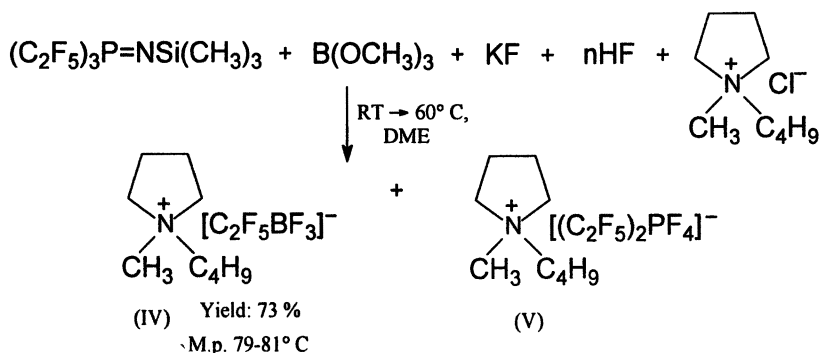
Recently, we have found that tris(perfluoroalkyl)phosphines (36,37) tris(perfluoroalkyl)phosphineoxides (37,38) or tris(perfluoroalkyl)-trimethylsilylphosphazenes (37,39) can be used as convenient perfluoroalkyl transfer reagents. The last compound appears to be especially suitable for the synthesis of perfluoroalkyltrifluoroborates. It can be obtained in a very simple way from tris(perfluoroalkyl)trifluorophosphoranes (39).

Compound (III) is a stable liquid material, which can be stored for a long time and used as convenient reagent for the synthesis of ionic liquids with pentafluoroethyltrifluoroborate anion, $[\text{C}_2\text{F}_5\text{BF}_3]^-$ (39).

Compounds (IV) and (V) have a different solubility in organic solvents and water, and they can be separated via extraction processes. They also can be used



Scheme 7



Scheme 8

in the mixture as a two component's ionic liquid. It is interesting to note that, introduction of only one C_2F_5 -group completely changes the nature of the fluoroborate anion. The $[\text{C}_2\text{F}_5\text{BF}_3]^-$ anion makes the ionic liquids of type (IV) hydrophobic and thermally more stable.

The properties of tetrafluoroborate based ionic liquids can be improved not only by the replacement of fluorine atoms with perfluoroalkyl groups but also via introduction of the cyano group to boron. Ionic liquids with tetracyanoborate anion (40) are hydrophobic and show high thermal and electrochemical stability and low viscosity (see Table VI).

Table VI. Viscosity of Tetracyanoborate Ionic Liquid

Ionic Liquid	Viscosity	Density
	$\text{mm}^2 \cdot \text{s}^{-1}$	(20° C) $\text{g} \cdot \text{cm}^{-3}$
1-Hexyl-3-methylimidazolium Chloride	7453	1.05
1-Hexyl-3-methylimidazolium $[\text{PF}_6]^-$	548	1.30
1-Hexyl-3-methylimidazolium $[\text{BF}_4]^-$	195	1.15
1-Hexyl-3-methylimidazolium $[\text{B}(\text{CN})_4]^-$	65	0.99

Again, delocalization of negative charge over four cyano groups reduces the coordination ability of $[\text{B}(\text{CN})_4]^-$ anion and reduces the viscosity by a factor of three in comparison to the BF_4^- based IL (Table VI).

The examples described above demonstrate that viscosity of room temperature ionic liquids can be significantly reduced by incorporating a new generation of weakly coordinated anions, such as $[(\text{C}_2\text{F}_5)_3\text{PF}_3]^-$, $[\text{C}_2\text{F}_5\text{BF}_3]^-$ or $[\text{B}(\text{CN})_4]^-$. These low viscosity ionic liquids should serve as a new reaction media for the different applications, for instance in organic synthesis. For example, the kinetics of palladium catalyzed Heck coupling between *p*-methoxyphenyldiazonium and 2-ethylhexylacrylate is much faster in FAP ionic liquids than in $[\text{PF}_6]^-$ based IL (41).

Experimental

Chemicals

Ionic liquids with FAP-anions were prepared in accordance with the procedures, described in the patents (15,17-20) and in the article (21). Syntheses of ionic liquids with perfluoroalkyl- and tetracyano-borate anions were carried out by the methods, described in the patents (39,40).

Analytical procedures

^1H , ^{19}F and ^{11}B NMR spectra were measured on a Bruker Avance 250 (250.13 MHz for ^1H , 235.36 for ^{19}F and 80.25 for ^{11}B) in acetonitrile- D_3 . CCl_3F and TMS were used as internal references for ^{19}F NMR and the proton spectra correspondingly. ^{11}B NMR spectra were recorded with BF_3 -Etherat as external standard.

The purity (quality) of ionic liquids was checked by measuring the residual water (Karl-Fischer titration; 831 KF-Coulometr, Metrohm) and chloride or bromide (ion-chromotography, Metrohm Advanced IC System; stationary phase: Metrosep A SUPP4 – 150). Residual water in FAP, perfluoroalkylborates and alkylsulfates ionic liquids was below 60 ppm and chloride content was below 40 ppm.

Viscosity and density of ionic liquids were measured with the use of Viscosimeter SVM 3000 (Anton Paar).

Acknowledgement

Authors thank Dr. O. Korbout for the measurements of ionic liquids viscosity.

References

1. *Ionic Liquids in Synthesis*, Wasserscheid, P.; Welton, T., Eds.; Wiley-VCH Verlag: Weinheim, 2003.
2. *Chemie Lexikon*; Römpp, 9 Auflage; Georg Thieme Verlag: Stuttgart, N. Y., 1955.
3. Tozuda, H.; Hayamizu, K.; Ishii, K.; Abu Bin Hasan Susan, Md.; Watanabe, M. *J. Phys. Chem. B*, **2004**, *108*, 16593-16600.
4. Tozuda, H.; Hayamizu, K.; Ishii, K.; Abu Bin Hasan Susan, Md.; Watanabe, M. *J. Phys. Chem. B*, **2005**, *109*, 6103-6110.
5. Noda, A.; Hayamizu, K.; Watanabe, M. *J. Phys. Chem. B*, **2001**, *105*, 4603-4610.
6. Tokuda, H.; Ishii, K.; Abu Bin Hasan Susan, Md.; Tsuzuki, S.; Hayamizu, K.; Watanabe, M. *J. Phys. Chem. B*, **2006**, *110*, 2833-2839.
7. Cammarata, L.; Kazarian, S.G.; Salter, P.A.; Welton, T. *Phys. Chem. Chem. Phys.*, **2001**, *3*, 5192-5200.
8. Swatloski, R.P.; Holbrey J.D.; Rogers, R.D. *Green Chemistry*, **2003**, *5*, Nr. 4, 361-363.
9. Plakhotnyk, A.V.; Ernst, L.; Schmutzler, R. *J. Fluorine Chem.*, **2005**, *126*, 27-32.
10. Pavlenko, N.V.; Yagupolskii, L.M. *Zh. Obshch. Khim.*, **1989**, *59*, 528-534.
11. Sartori, P.; Ignatiev, N. EP 0 929 558 B1, 2001.
12. Schmidt, M.; Kühner, A.; Jungnitz, M.; Ott F.; Ignatyev, N. WO 02/085919 A1, 2002.
13. Schmidt, M.; Heider, U.; Kühner, A.; Oesten, R.; Jungnitz, M.; Ignatyev, N.; Sartori, P. *J. Power Sources*, **2001**, *97-98*, 557-560.
14. Yagupolskii, L.M.; Yagupolskii, Yu.L. *J. Fluorine Chem.*, **1995**, *72*, 225-229.
15. Ignatyev, N. V.; Schmidt, M.; Kuehner, A.; Hilarius, V.; Heider, U.; Kucheryna, A.; Sartori, P.; Willner, H. WO 03/002579, 2003.
16. Ignat'ev, N.V.; Welz-Biermann, U.; Schmidt, M.; Weiden, M.; Heider, U.; Kucherina, A. I.; Willner, H.; Proceedings of the 16th Winter Fluorine Conference, St. Pete Beach, FL, 2003.
17. Ignatyev, N.; Welz-Biermann, U.; Bissky, G.; Willner, H. WO 04/106288, 2004.
18. Ignatyev, N.; Welz-Biermann, U.; Bissky, G.; Willner, H. WO 04/106287, 2004
19. Ignatyev, N.; Welz-Biermann, U.; Bissky, G.; Willner, H. DE 10325050, 2004.
20. Schmidt, M.; Heider, U.; Geissler, W.; Ignatiev, N.; Hilarius, V. EP 1 162 204 A1, 2001.

21. Ignat'ev, N.V.; Welz-Biermann, U.; Kucheryna, A.; Bissky, G.; Willner, H. *J. Fluorine Chem.*, **2005**, *126*, 1150-1159.
22. Ignat'ev, N.; Sartori, P. *J. Fluorine Chem.*, **2000**, *103*, 57-61.
23. Heider, U.; Hilarius, V.; Sartori, P.; Ignatiev, N. WO 00/21969, 2000.
24. Wang, P.; Zakeeruddin, S.M.; Grätzel, M.; Kantlehner, W.; Mezger, J.; Stoyanov E.V.; Scherr, O. *Appl. Phys. A*, **2004**, *79*, 73-79.
25. Ignatyev, N.; Welz-Biermann, U.; Bissky, G.; Heckmeier M.; Willner, H. DE 10 2005 025 315, 2006.
26. Zhou, Z.-B.; Takeda M.; Ue, M. *J. Fluorine Chem.*, **2003**, *123*, 127-131.
27. Zhou, Z.-B.; Takeda M.; Ue, M. *J. Fluorine Chem.*, **2004**, *125*, 471-476.
28. Zhou, Z.-B.; Matsumoto, H.; Tatsumi, K. *Chem. Lett.*, **2004**, *33*, 886-887.
29. Zhou, Z.-B.; Matsumoto, H.; Tatsumi, K. *Chem. Eur. J.*, **2004**, *10*, 6581-6591.
30. Zhou, Z.-B.; Matsumoto, H.; Tatsumi, K. *Chem. Eur. J.*, **2005**, *11*, 752-766.
31. Frohn, H.-J.; Bardin, V.V. *Z. Anorg. Allg. Chem.* **2001**, *627*, 15-16.
32. Prakash, G.K.S.; Mandal, M. *J. Fluorine Chem.*, **2001**, *112*, 123-131.
33. Prakash, G.K.S.; Yudin, A. *Chem.Rev.*, **1997**, *97*, 757-786.
34. Singh, R.P.; Shreeve, J.M. *Tetrahedron*, **2000**, *56*, 7613-7632.
35. Sosnovskikh, V.Ya.; Sevenard, D.V.; Usachev, B.I.; Rösenthaller, G.-V. *Tetrahedron Letters*, **2003**, *44*, 2097-2099.
36. Welz-Biermann, U.; Ignatyev, N.; Weiden, M.; Schmidt, M.; Heider, U.; Miller, A.; Willner, H. WO 03/087113 A1, 2003.
37. Ignatyev, N.; Welz-Biermann, U.; Miller, A.; Bissky, G.; Kucheryna, A.; Willner, H. Proceedings of the 17th Winter Fluorine Conference, St. Pete Beach, FL, 2005.
38. Ignatyev, N.; Welz-Biermann, U.; Schmidt, M.; Weiden, M.; Heider, U.; Sartori, P.; Willner, H.; Miller, A. WO 03/087020 A1, 2003.
39. Ignatyev, N.; Welz-Biermann, U.; Bissky, G.; Kucheryna, A.; Willner, H. WO 05/105815, 2005.
40. Welz-Biermann, U.; Ignatyev, N.; Bernhardt, E.; Finze, M.; Willner, H.; WO 04/072089 A1, 2004.
41. Ignat'ev, N.V.; Pitner, V.-R.; Welz-Biermann, U. In *Ionic Liquids in Organic Synthesis*; Ed. Malhotra, S.; ACS Symposium Series 950 (acp.)

Chapter 23

Molecular Dynamics Study of the Mechanism of Cellulose Dissolution in the Ionic Liquid 1-*n*-Butyl-3-methylimidazolium Chloride

Zhiwei Liu^{1,2}, Richard C. Remsing², Preston B. Moore^{1,2},
and Guillermo Moyna^{1,2}

¹West Center for Computational Chemistry and Drug Design
and ²Department of Chemistry and Biochemistry, University of the Sciences
in Philadelphia, 600 South 43rd Street, Philadelphia, PA 19104-4495

N,N'-Dialkylimidazolium ionic liquids (ILs) show promise as non-derivatizing 'green' solvents for the dissolution and processing of cellulose. To better understand how these ILs solvate this and other polysaccharides at the molecular level, we have performed molecular dynamics (MD) simulations of neat 1-*n*-butyl-3-methylimidazolium chloride ([C₄mim]Cl) at 298, 313, 333, 343, 353, 363, and 373 K, as well as 5 and 10 wt% cellobiose solutions in [C₄mim]Cl at 363 K. Static, dynamic, and thermodynamic quantities have been derived from the collected data. Our findings agree well with experimental data from various sources. In particular, analysis of structural features and hydrogen bonding patterns between [C₄mim]Cl and cellobiose are consistent with results from NMR relaxation studies which indicate that the IL Cl⁻ ions interact with the carbohydrate OH groups in a ~ 1:1 ratio.

1. Introduction

In addition to their now well-established role as alternative reaction and extraction media with 'green' potential (1), it has been shown that certain ionic liquids (ILs) can dissolve polysaccharides very efficiently (2-4). Perhaps the most salient results in this regard have been those obtained with 1-*n*-butyl-3-methylimidazolium chloride ([C₄mim]Cl, Figure 1), an IL which dissolves cellulose in concentrations of up to 300 g/L (2). In a recent report, we studied the solvation of cellulose models, such as cellobiose (Figure 1), in [C₄mim]Cl by means of ¹³C and ^{35/37}Cl NMR relaxation measurements (5). Our results indicate that the solvation of carbohydrates in this IL involves the formation of hydrogen bonds between the non-hydrated chloride ions of the IL and the sugar hydroxyl protons in a ~ 1:1 stoichiometry (5). In the case of cellulose, these interactions disrupt the extensive hydrogen bonding network of the polymer and lead to its dissolution. However, a detailed model of this dissolution mechanism is still unavailable. Knowledge of this process at the atomic level is critical in the development of new IL-based solvents for the processing of polysaccharides. As evidenced by the growing number of reports on the subject, many of which are referenced in this chapter or appear elsewhere in this volume, molecular dynamics (MD) simulations can provide this atomistic depiction of ILs and IL-based systems. In this chapter we describe the application of this methodology to the study of cellulose solvation by [C₄mim]Cl using the cellobiose model system. As detailed below, results from our MD simulations agree with previous theoretical and experimental studies, and, more importantly, corroborate the solvation model proposed by us in earlier reports.

2. Simulation Details

Classical MD simulations of neat [C₄mim]Cl and cellobiose/[C₄mim]Cl solutions were carried out using the CM3D package and the OPLS-AA force field modified as described in Section 3.1 (6,7). Partial charges were computed from fits to the electrostatic potential (ESP) derived from *ab initio* calculations at the B3LYP/6-311+G* level performed using Gaussian 03 (8). The geometries of an isolated [C₄mim]Cl pair and cellobiose, respectively, were optimized at the same level of theory prior to charge calculations. The optimized geometry of the single [C₄mim]Cl pair agrees well with results from *ab initio* MD simulations on [C₂mim]Cl (9), and shows that the chloride ion is localized above the plane of the imidazolium ring in close proximity to the C2 carbon. The charges computed for the cation and anion are +0.73 and -0.73, respectively. Following the approach employed in a reported MD study of [C₄mim]PF₆ (10), these partial charges were used to approximate the polarization of the ions in the liquid state in all our simulations. The disadvantage of this set of charges is that their distribution on the atoms of the cation is based on its gas phase geometry, which is likely to differ from its structure in the liquid state. However, and as pointed

out by Morrow and co-workers (10), this charge distribution gives no preferential orientation of the anions relative to the cations. Furthermore, the extent of polarization of the $[\text{C}_4\text{mim}]\text{Cl}$ cation in the ion pair *in vacuo* relative to that of the isolated cation seen by us is similar to that observed for $[\text{C}_4\text{mim}]\text{PF}_6$ (10). Therefore, we tentatively conclude that the charges derived from *ab initio* calculations on the $[\text{C}_4\text{mim}]\text{Cl}$ pair *in vacuo* are suitable for liquid phase simulations. While further tests will be conducted to verify this charge model, the results presented below validate these assumptions.

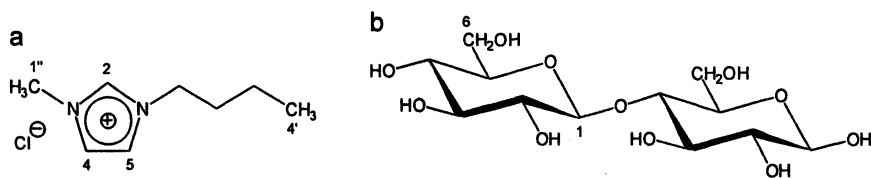


Figure 1. Structure and numbering of $[\text{C}_4\text{mim}]\text{Cl}$ (a) and cellobiose (b).

The neat IL systems were simulated at seven temperatures, including 298, 313, 333, 343, 353, 363, and 373 K. The cellobiose/IL solution simulations were performed at 363 K with disaccharide concentrations of ~ 5 and ~ 10 wt%. These temperatures and sugar concentrations correspond to those from our previous NMR studies (5). Each system contained 216 ion pairs, totalling 5616 atoms. In addition, there were 6 and 12 cellobiose molecules for the 5 and 10 wt% cellobiose/IL systems, respectively. Periodic boundary conditions were employed, using the Ewald method to treat long-range electrostatic interactions (11,12). The reversible reference system propagator algorithm (r-RESPA) with time steps of 0.5 and 2 fs was employed to evaluate short-range intramolecular forces and long-range interactions, respectively (13). The neat $[\text{C}_4\text{mim}]\text{Cl}$ system was constructed using the *ab initio* optimized ion pair as seed to create a cubic lattice with a final density of 1.0 g/cm³. The system was then simulated at high temperature for at least 100 ps to randomize the ions in the cell. Constant temperature and pressure (NPT) simulations ranging from 100 ps to 1 ns were then carried out at each of the above temperatures and 1 atm to stabilize cell sizes. The cellobiose/IL model systems were created by patching the disaccharides on the sides of the equilibrated neat IL simulation box, and the resulting cells were randomized and their sizes stabilized as described above. The different systems were equilibrated at constant temperature (NVT) for times ranging from 700 ps to 1.5 ns. The neat IL systems were then simulated for an additional 2 ns at each temperature. For each cellobiose/IL system, 6 ns simulations were carried out. Coordinate files were saved every 0.1 ps in all cases, leading to 20,000 and 60,000 conformations used for the analysis of structural and dynamic properties of the neat IL and cellobiose/IL systems,

respectively. In addition, simulations for both cellobiose/IL systems were performed in duplicate from different initial configurations.

3. Neat [C₄mim]Cl Simulations

3.1. Optimization of Non-bonded Parameters

Our exploratory studies were carried out using default OPLS-AA parameters for the chloride ion (6,14). The density computed from NPT simulations at 298 K using these parameters was 0.80 g/cm³, considerably lower than the value of 1.08 g/cm³ determined experimentally at this temperature (15). We thus investigated the factors affecting the calculation of non-bonded interactions, which for two species *a* and *b* are represented by the sum of Coulomb and Lennard-Jones energy terms as shown in Equation 1 (14),

$$E_{ab} = \sum_i^a \sum_j^b \left\{ \frac{q_i q_j e^2}{r_{ij}} + 4\epsilon_{ij} \left[\left(\frac{\sigma_{ij}}{r_{ij}} \right)^{12} - \left(\frac{\sigma_{ij}}{r_{ij}} \right)^6 \right] \right\} \quad (1)$$

where combining rules are used such that $\sigma_{ij} = (\sigma_i \sigma_j)^{1/2}$ and $\epsilon_{ij} = (\epsilon_i \epsilon_j)^{1/2}$. Simulations starting from different initial configurations and various ion charge sets led only to minor changes on the density of the system. However, variations of the chloride ion Lennard-Jones parameters, σ and ϵ , had a pronounced effect on the computed densities. Not surprisingly, low densities were obtained by using default chloride ion OPLS-AA parameters ($\sigma = 4.42$ Å and $\epsilon = 0.12$ kcal/mol), as these were optimized to fit interaction energies of ion-water complexes assuming an anion charge of -1.0. Based on our *ab initio* calculations, the partial charge for chloride in an ion pair has dropped to -0.73, indicating a reduction in the anion electron density and size. Similar reductions in size are likely for chloride ions in the IL, and thus Lennard-Jones parameters optimized for carbon-bound chlorine, $\sigma = 3.40$ Å and $\epsilon = 0.30$ kcal/mol (14), could in principle be better suited to represent the free anion in molten [C₄mim]Cl. Indeed, repeating the NPT simulations at 298 K using these non-bonded parameters yields a density of 1.05 g/cm³, which agrees well with the experimental density at this temperature. Figure 2 shows the simulated densities of neat [C₄mim]Cl as a function of temperature. As expected, the density decreases linearly with temperature, and volume expansions of less than 5% are observed as the system goes from 298 to 373 K (10).

As described in the following sections, the structural and dynamic properties obtained from our MD simulations for neat [C₄mim]Cl agree well with experimental as well as classical and *ab initio* MD studies on similar systems. This has further validated our choice of force field and simulation conditions.

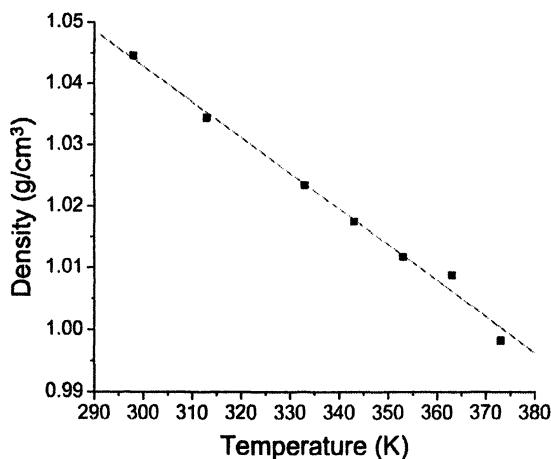


Figure 2. Density of neat $[C_4mim]Cl$ as a function of temperature computed from MD simulations.

The detailed analyses of the data summarized below are too vast to be presented here in full and will be made available elsewhere.

3.2. Structural Features of Neat $[C_4mim]Cl$

Figure 3 shows the cation-anion and cation-cation isotropic radial distribution functions (RDFs) computed from the center of mass of the imidazolium ring, $g_{ca}(r)$ and $g_{cc}(r)$, at the seven temperatures considered in our study. Their general characteristics agree well with those from previously reported MD simulations of ILs (9,10,19-23). Namely, $g_{ca}(r)$ and $g_{cc}(r)$ are out of phase, and also reveal that weak ordering due to long-range Coulombic interactions persists beyond 20 Å, which is approximately half of the unit cell and includes up to three coordination shells.

The first peak in the cation-anion RDF, located around 4.5 – 4.8 Å, represents the first coordination shell of chloride anions and is consistent with results from experimental and theoretical studies (16,19-23). The coordination number is 3 when the RDF is integrated up to 5 Å, and 5 when integrated up to 6.5 Å, which corresponds to the first minimum of $g_{ca}(r)$. The sharpness of the peak indicates that the local structure is well defined, and coordination numbers of 3 to 5 point to the formation of ion clusters rather than pairs. This agrees with a structural model for N,N' -dialkylimidazolium salts based on an overview of experimental data proposed recently by Dupont (17). This author suggests that these ILs are hydrogen-bonded polymeric supramolecules, in which each cation

is surrounded by three anions that are approximately coplanar with the imidazolium ring and forming hydrogen bonds with its H2, H4, and H5 hydrogens. Similarly, each anion has three cations in its first coordination shell.

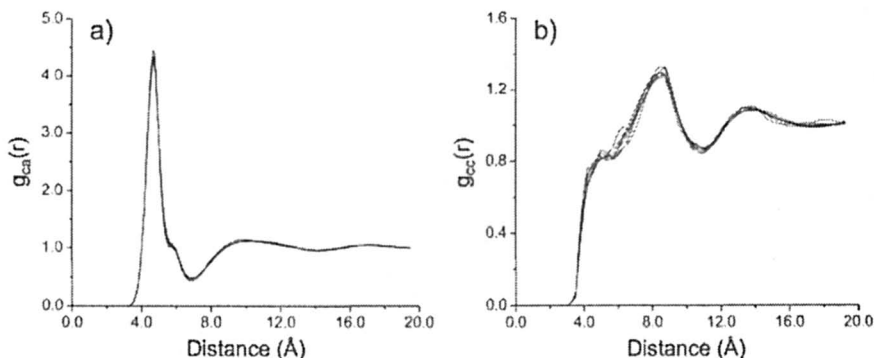


Figure 3. Cation-anion (a) and cation-cation (b) RDFs for neat $[C_4mim]Cl$ at temperatures ranging from 298 to 373 K.

The cation-cation RDFs show a broad peak at 8 – 8.5 Å, and a clear shoulder, or ‘bump,’ around 4 – 6 Å with coordination numbers ranging from 1 to 2. A similar feature in the cation-cation RDF was detected experimentally and observed in theoretical studies for $[C_2mim]Cl$ (16,20,23). While detailed 3D structural analyses of this salt in the liquid phase have not been reported, it has been postulated that these ‘bumps’ on $g_{cc}(r)$ are the result of π - π stacking interactions between imidazolium cations (17). Based on our analyses of the 3D distribution and angular distribution functions (ADFs) of cations (*vide infra*), we have indeed confirmed that the imidazolium rings π - π stack in $[C_4mim]Cl$.

As evidenced in Figure 3, the RDFs remain virtually unchanged as the system goes from 298 to 373 K. Similarly, there is only a minor decrease in the coordination numbers as the temperature increases, consistent with a slight decrease in the ordering of the system. This minimal increase in randomness agrees well with experimental findings which show that the ordering observed in crystals of N,N' -dialkylimidazolium salts is conserved in the liquid phase (17).

The RDFs provide short- and long-range structural features of the systems, but information regarding the spatial arrangement of ions is lost upon integration over angular space. To gain insights into the 3D structure of neat $[C_4mim]Cl$ in the liquid phase, we computed 3D configuration probability distribution isosurfaces of ions relative to the center of a reference imidazolium ring. Figures 4a and 4b show, respectively, the chloride ion distribution isosurface drawn at 5 times the average anion density, and the imidazolium ion distribution isosurface drawn at 1.5 times the average cation density.

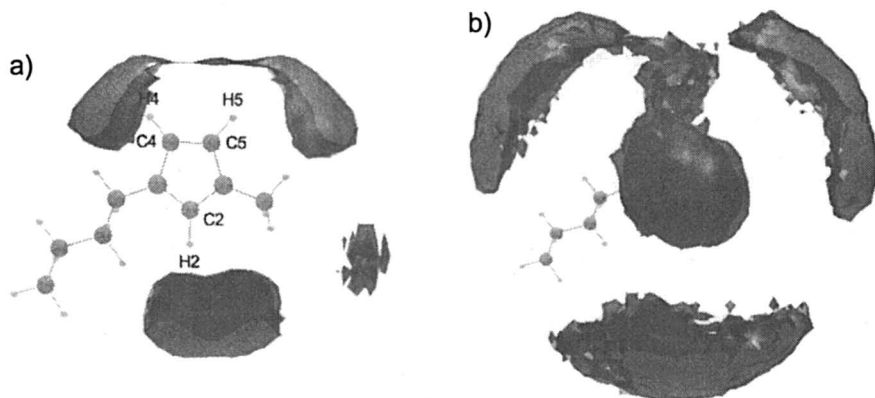


Figure 4. 3D configuration probability distribution isosurfaces of $[C_4mim]Cl$ anions (a) and cations (b) relative to the center of an imidazolium ring.

In addition to 3D distribution isosurfaces such as the ones shown above, the ion ADFs with respect to a reference cation were analyzed in detail (data not shown). By combining the visual inspection of the distribution isosurfaces with quantitative analyses of RDFs and ADFs, the 3D structural features of $[C_4mim]Cl$ can be summarized as follows. The ordering of the first coordination shells of an imidazolium cation is highly directional for anions and somewhat directional for cations. While the cation-anion and cation-cation RDFs indicate that weak ion ordering persists up to 20 Å, there is little preference in their angular distribution beyond the first coordination shells. The first anion coordination shell consists, on average, of five chloride ions, three of which are at less than 5 Å from the center of the ring and form hydrogen bonds with its H2, H4, and H5 hydrogens. These correspond with the three major lobes directed roughly along the C2-H2, C4-H4, and C5-H5 bonds observed in the anion distribution isosurface (Figure 4a). The probability of forming hydrogen bonds with H2 is significantly larger than with H4 and H5. The two additional anions in the first shell, located between 5 and 6.5 Å from the ring center, interact with the *N*-alkyl group hydrogens. The coordination number for the first shell of cations is 14.5. The majority of these cations coordinate to chloride ions in the first anion shell. Therefore, the cation distribution isosurface also shows three large lobes directed roughly along the C2-H2, C4-H4, and C5-H5 bonds, but at nearly twice the distance from the center of the ring than the first anion shell (Figure 4b). Finally, there are on average two cations whose rings lie parallel to that of the reference imidazolium ion located at only 4 to 6 Å from the ring center. These give rise to two lobes on the isosurface located above and below the ring, and reveal clearly that the imidazolium cations in $[C_4mim]Cl$ are involved in π - π stacking interactions.

3.3. Dynamic Properties of Neat [C₄mim]Cl

The ability of our simulations to reproduce the dynamic behavior of the neat [C₄mim]Cl systems was assessed by comparing ion self-diffusion coefficients measured by PFG-NMR techniques to those computed from the MD trajectories using the Einstein relation (Equation 2):

$$D = \frac{1}{6} \lim_{t \rightarrow \infty} \frac{\langle |\Delta \mathbf{r}(t)|^2 \rangle}{t} \quad (2)$$

$\langle |\Delta \mathbf{r}(t)|^2 \rangle$ represents the average mean square displacements (MSDs) of the ions, which were calculated from the MD trajectories using the center of mass of the cation or anion (Figure 5). Cations and anions show similar diffusive behaviors and three distinct dynamic regimes. At very short times (< 0.1 ps) their motion is ballistic. Between 1 and 300 – 500 ps, the ions are sub-diffusive or ‘caged,’ with $\langle |\Delta \mathbf{r}(t)|^2 \rangle \propto t^\beta$ ($\beta < 1$). After 500 ps, anions and cations display normal self-diffusivity, with $\langle |\Delta \mathbf{r}(t)|^2 \rangle \propto t$. The dynamic behavior described here has been observed for other ILs studied by MD simulations (10,19-21,24). It is worth noting that the current study reveals that ions in [C₄mim]Cl are trapped in a super-cooled sub-diffusive regime for at least 100 ps even at temperatures nearly 40 K above its melting point.

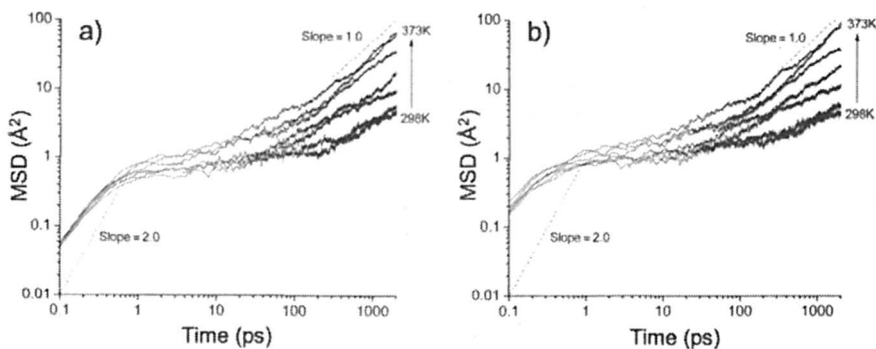


Figure 5. Average MSDs for cations (a) and anions (b) versus time for neat [C₄mim]Cl at temperatures ranging from 298 to 373 K.

Diffusion coefficients were estimated by fitting the linear self-diffusive regions of the MSDs to Equation 2 (10,19,20). Figure 6 shows a comparison of computed diffusion coefficients with those measured by NMR between 298 and 363 K. Below ~ 343 K (70 °C), our estimations for the imidazolium ion agree

remarkably well with experiment. As expected, measured and computed diffusion coefficients increase markedly after 343 K, slightly above the melting point of [C₄mim]Cl. While the computed values overestimate experiment above this temperature, the two sets of data remain in good semi-quantitative agreement. These results indicate that long-time quantities such as diffusion coefficients can be computed with reasonable accuracy in the simulation times considered in our study (10), and further validate our choice of force field parameters and simulation conditions for these systems.

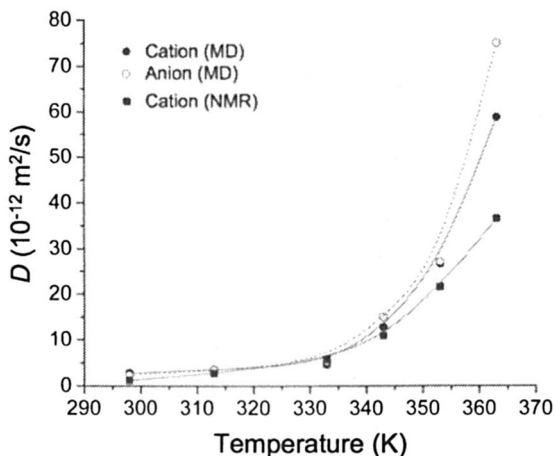


Figure 6. Computed and experimental diffusion coefficients for ions in neat [C₄mim]Cl as a function of temperature.

4. Cellobiose/[C₄mim]Cl Simulations

4.1 Solute-Solvent Interactions

The results presented in Section 3 indicate that our MD simulations are capable of reproducing structural and dynamic features of neat [C₄mim]Cl adequately, and we therefore turned our attention to the study of 5 and 10 wt% cellobiose/[C₄mim] solutions. As stated earlier, two independent 6 ns MD trajectories at 363 K were carried out for these systems. These parallel simulations led to virtually identical predictions, and therefore the analyses described here are based on results obtained for one of them.

The cellobiose-anion and cellobiose-cation center-of-mass RDFs show that the coordination shell closest to the disaccharide is within 4 – 6 Å of its center and contains mostly chloride ions. The first peak in the cellobiose-cation RDF is located at approximately 8 Å. This is in agreement with results from our recent NMR studies, which reveal that anions have a more important role than cations

in the dissolution of carbohydrates by this IL (5). However, the center-of-mass RDFs alone are ill-suited to describe the distribution of solvent ions around functional groups of the carbohydrate or specific solvent-solute interactions. Thus, we computed the RDFs from the hydroxyl protons to the chloride anions ($g_{\text{OH}\cdots\text{Cl}}(r)$, Figure 7a). Since the mobilities of the secondary and primary hydroxyl groups of the sugar are different, their $g_{\text{OH}\cdots\text{Cl}}(r)$ functions were considered separately. However, normalization over the number of equivalent hydroxyl groups yields RDFs that can be readily compared.

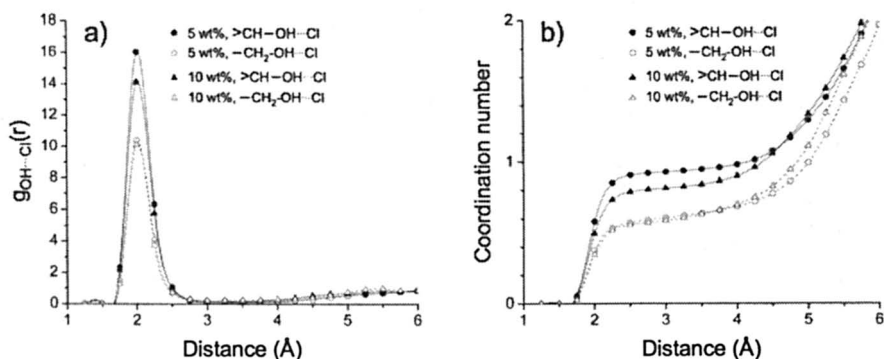


Figure 7. $\text{OH}\cdots\text{Cl}$ RDFs (a) and coordination numbers (b) for 5 and 10 wt% cellobiose/[C_4mim]Cl solutions at 363 K.

Irrespective of the type of hydroxyl group or sugar concentration, a single sharp peak at ~ 2 Å was observed in all $g_{\text{OH}\cdots\text{Cl}}(r)$ functions, strongly suggesting the formation of hydrogen bonds between the disaccharide hydroxyl protons and the chloride anions. Although their intensities are lower for primary hydroxyl groups, the position of the peaks is identical in all cases. Similarly, the coordination numbers of chloride ions to either primary or secondary hydroxyl protons plateau at ~ 2.3 Å and remains almost constant up to ~ 4 Å (Figure 7b). Beyond that distance, the coordination numbers increase due to interactions between ions in the first anion shell and protons in neighboring hydroxyl groups. For the 5 wt% cellobiose/[C_4mim]Cl solution, the coordination numbers of secondary and primary hydroxyl groups to chloride ions in the first shell are 0.93 and 0.60, respectively. In the 10 wt% solution these values are 0.82 and 0.59, consistent with the decrease in anion supplies at higher carbohydrate concentrations. The variations in coordination numbers observed for the different types of hydroxyl groups indicate that the chloride ions have a higher probability of forming hydrogen bonds with secondary hydroxyl protons. Additionally, the anion to primary hydroxyl proton coordination numbers

remain nearly constant at both sugar concentrations, revealing that the average number of hydrogen bonds between these two species is not affected by changes in the supplies of chloride ions.

The geometry of the hydrogen bonds formed between hydroxyl protons and anions was investigated by analysis of the probability distribution of O–H \cdots Cl angles. Since the OH \cdots Cl coordination numbers are less than 1 in all cases, the O–H \cdots Cl angles were calculated using the chloride ions located closest to the hydroxyl protons. As shown in Figure 8, almost all O–H \cdots Cl angles are within 150 and 180°, and thus in near-perfect hydrogen-bonding geometry. Combined with the analysis of OH \cdots Cl RDFs presented above, these results confirm conclusively that medium to strong hydrogen bonds form between the sugar hydroxyl protons and the chloride ions of the IL.

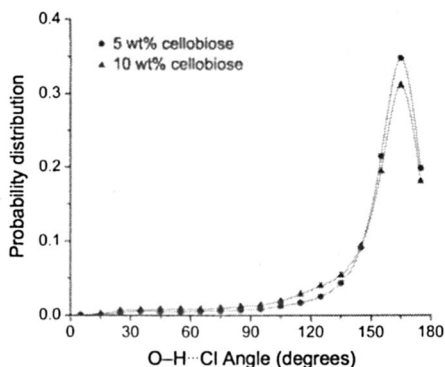


Figure 8. Probability distribution of O–H \cdots Cl angles in 5 and 10 wt% cellobiose/[C₄mim]Cl solutions at 363 K

Averaging the anion to hydroxyl proton coordination numbers over all types of hydroxyl groups yields OH \cdots Cl hydrogen-bonding stoichiometries of 1:0.85 and 1:0.76 for the 5 and 10 wt% cellobiose/[C₄mim]Cl solutions, respectively. These values depart slightly from the ideal 1:1 ratio expected for these systems. Analysis of several saved conformations from the MD trajectories indicates that this is due to the occasional formation of intra- or inter-molecular hydrogen bonds between sugar hydroxyl protons and oxygen atoms on other hydroxyl or ether groups. Both types of hydroxyl groups can do this, but the added flexibility of the hydroxymethyl side chains allows for more intra-molecular hydrogen-bonding interactions, and thus lower coordination numbers for these groups.

As shown in the next sections, the cellobiose/IL systems have slower dynamics than the neat IL systems. Thus, the minor deviations in our predicted OH \cdots Cl hydrogen-bonding stoichiometries from the theoretical 1:1 ratio could be due to insufficient sampling times. However, it should also be noted that this

ideal OH:Cl ratio can only be achieved in solutions with a large excess of chloride ions (i.e., infinite dilution), which is not the case in these systems. Despite this, our predictions are in excellent agreement with results from earlier NMR relaxation measurements on the cellobiose/[C₄mim]Cl system, which also indicate that OH⁺Cl interactions are nearly stoichiometric (5). Combined, our previous experimental findings and those presented here demonstrate conclusively that hydrogen-bonding interactions between non-hydrated chloride ions and sugar hydroxyl protons play a key role in the dissolution of carbohydrates in [C₄mim]Cl.

4.2. Solvent Structuring in Cellobiose/[C₄mim]Cl Solutions

The effects on the structuring of [C₄mim]Cl due to the presence of sugar solutes was also investigated. The overall structural features of the solvent are very similar to those of the neat ILs in terms of positions of the first anion and cation coordination shells, coordination numbers, angular distributions, and hydrogen-bonding patterns between anions and imidazolium ring protons. Anion-cation and cation-cation coordination numbers decrease slightly relative to neat [C₄mim]Cl, which is reasonable if the solute-solvent interactions described in the previous section are taken into account.

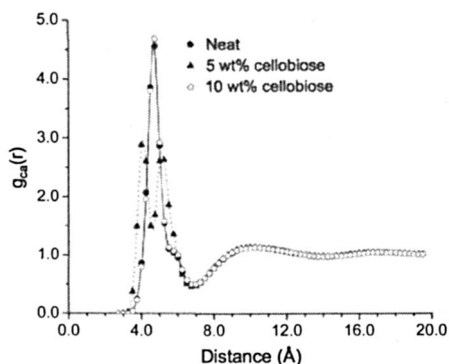


Figure 9. Cation-anion RDFs for neat [C₄mim]Cl and cellobiose/[C₄mim]Cl solutions at 363 K.

Although the overall solvent structuring in the systems is similar, the cation-anion RDF for the 5 wt% cellobiose/[C₄mim]Cl solution exhibits a feature that distinguishes it from the neat IL and 10 wt% cellobiose/IL systems. As shown in Figure 9, the first peak of cation-anion RDF in this system is split in two. Detailed analysis of the MD trajectories shows that this is caused by an

uneven distribution of disaccharides in the simulation box that leads to a cellobiose-rich region and one in which no sugars are present. By increasing the number of solutes in the unit cell from 6 (5 wt%) to 12 (10 wt%) their distribution becomes uniform, leading to a unique peak in the RDF. While these results could reflect the formation of solute clusters at lower sugar concentrations, they are more likely artifacts caused by inadequate equilibration and/or conformational sampling of the systems. Additional simulations are currently being carried out to address these issues.

4.3. Dynamic Properties of Cellobiose/[C₄mim]Cl Solutions

The MSDs of the cellobiose/[C₄mim]Cl solutions at 363 K are very similar to those presented in Section 3.3 for the neat [C₄mim]Cl systems, and display ballistic, sub-diffusive, and normal self-diffusive regimes. The cation, anion, and cellobiose self-diffusion coefficients were computed by fitting the linear regions of the MSDs in the normal diffusive regime to Equation 2 as described above. As mentioned earlier, two independent simulations for both cellobiose/[C₄mim]Cl solutions were carried out. Since their differences are negligible, the diffusivities presented here are averages from both MD trajectories recorded for each system. Not surprisingly, the dynamics of the cellobiose/IL solutions are considerably slower than for the neat [C₄mim]Cl systems. The diffusion coefficient for the cation drops from $58.8 \times 10^{-12} \text{ m}^2/\text{s}$ for the neat IL to 19.8×10^{-12} and $10.4 \times 10^{-12} \text{ m}^2/\text{s}$ at 5 and 10 wt% cellobiose, respectively. Similarly, the anion diffusion coefficient decreases from 75.1×10^{-12} in the neat IL to $21.9 \times 10^{-12} \text{ m}^2/\text{s}$ at 5 wt% cellobiose, and to $13.2 \times 10^{-12} \text{ m}^2/\text{s}$ at 10 wt% cellobiose. Consistent with its size, the self-diffusivities computed for the disaccharide are 4.1×10^{-12} and $2.6 \times 10^{-12} \text{ m}^2/\text{s}$ at 5 and 10 wt% concentration, respectively. These results agree qualitatively with reported variations in the viscosity of cellobiose/[C₄mim]Cl solutions versus sugar concentration (5), as well as with cation diffusion coefficients measured for these systems using PFG-NMR methods. However, the changes in diffusivities predicted from the MD simulations are nearly three-fold larger than those determined experimentally. As stated in the previous sections and discussed below, we believe that these deviations are due to improper and/or insufficient sampling of the conformational space available to the systems.

5. Conclusions

In this paper, MD simulations of neat [C₄mim]Cl at various temperatures and of cellobiose/[C₄mim]Cl solutions were performed in an attempt to better understand how this IL dissolves carbohydrates at the molecular level. The calculated properties of the neat IL derived from our simulations agree well with those from previously reported experimental and theoretical studies on similar systems. Structural analysis shows long-range ordering of ions as well as

directional ordering of the first anion and cation coordination shells. Anions in the first shell form hydrogen bonds with the ring hydrogen atoms and also interact with hydrogens in the alkyl chains. Most of the first cation shell is located well outside the first shell of anions, but a small portion of it stays above and below the ring, revealing that the imidazolium cations in [C₄mim]Cl participate in π - π stacking interactions. The calculated self-diffusion coefficients at various temperatures agree semi-quantitatively with results from PFG-NMR measurements, indicating that the dynamic properties of the neat IL are described with reasonable accuracy by the MD simulations.

MD simulations of cellobiose/[C₄mim]Cl solutions reveal the formation of medium to strong hydrogen bonds between the disaccharide hydroxyl protons and the IL chloride ions in a near 1:1 ratio, in excellent agreement with results from previous NMR studies. More importantly, our findings demonstrate clearly that these hydrogen-bonding interactions are responsible for the high solubility observed for many carbohydrates and polysaccharides in this IL. While a recent report speculates that interactions between the imidazolium cations and the sugar hydroxyl oxygens play a critical role in the dissolution process (25), our experimental and theoretical studies provide no evidence in support of these claims. On the contrary, they show that the cations are far from the solute and interact solely with chloride ions in the first solvation shell of the sugar.

The results presented here also indicate that while our current simulations reproduce trends in the dynamics of the cellobiose/[C₄mim]Cl systems, they cannot yet predict these properties quantitatively. Although MD simulations of similar lengths have been used successfully to investigate dynamic properties of IL solutions (26,27), the solutes considered in these studies were small weakly-coordinating molecules such as acetonitrile or CO₂. In our case, the solvated molecule is significantly larger, flexible, and interacts strongly with the solvent, and as a result the dynamics of the systems are considerably slower. Thus, the sugar/IL solutions are likely to require more extensive system equilibration and conformational sampling times to yield accurate atomistic dynamic models. Work on the improvement of these aspects of our simulations is underway. Ultimately, the information gathered from our ongoing experimental and theoretical studies should facilitate the rational development of new, and potentially 'greener,' IL-based solvent systems for the dissolution and processing of polysaccharides with industrial applications.

Acknowledgment

The authors acknowledge the H. O. West Foundation, the NSF CCLI-A&I and MRI programs (grants DUE-9952264 and CHE-0420556), and the Camille and Henry Dreyfus Foundation for financial support. We also thank Dr. Gonzalo Hernandez for performing the PFG-NMR measurements of cation diffusivities in neat [C₄mim]Cl and cellobiose/[C₄mim]Cl solutions.

References

1. *Ionic Liquids IIIA/B: Fundamentals, Progress, Challenges, and Opportunities*; Rogers, R. D., Seddon, K. R., Eds.; ACS Symposium Series 901/902; American Chemical Society: Washington, DC, 2005.
2. Swatloski, R. P.; Spear, S. K.; Holbrey, J. D.; Rogers, R. D. *J. Am. Chem. Soc.* **2002**, *124*, 4974-4975.
3. Liu, Q. B.; Janssen, M. H. A.; van Rantwijk, F.; Sheldon, R. A. *Green Chem.* **2005**, *7*, 39-42.
4. Fort, D. A.; Swatloski, R. P.; Moyna, P.; Rogers, R. D.; Moyna, G. *Chem. Commun.* **2006**, 716-718.
5. Remsing, R. C.; Swatloski, R. P.; Rogers, R. D.; Moyna, G. *Chem. Commun.* **2006**, 1271-1273.
6. <http://hydrogen.usip.edu/moore/code/code.html>.
7. Jorgensen, W. L.; Maxwell, D. S.; Tirado-Rives, J. *J. Am. Chem. Soc.* **1996**, *118*, 11225-11236.
8. Frisch, M. J.; Trucks, G. W.; Schlegel, H. B.; Scuseria, G. E.; Robb, M. A.; Cheeseman, J. R.; Montgomery, Jr., J. A.; Vreven, T.; Kudin, K. N.; Burant, J. C.; Millam, J. M.; Iyengar, S. S.; Tomasi, J.; Barone, V.; Mennucci, B.; Cossi, M.; Scalmani, G.; Rega, N.; Petersson, G. A.; Nakatsuji, H.; Hada, M.; Ehara, M.; Toyota, K.; Fukuda, R.; Hasegawa, J.; Ishida, M.; Nakajima, T.; Honda, Y.; Kitao, O.; Nakai, H.; Klene, M.; Li, X.; Knox, J. E.; Hratchian, H. P.; Cross, J. B.; Bakken, V.; Adamo, C.; Jaramillo, J.; Gomperts, R.; Stratmann, R. E.; Yazyev, O.; Austin, A. J.; Cammi, R.; Pomelli, C.; Ochterski, J. W.; Ayala, P. Y.; Morokuma, K.; Voth, G. A.; Salvador, P.; Dannenberg, J. J.; Zakrzewski, V. G.; Dapprich, S.; Daniels, A. D.; Strain, M. C.; Farkas, O.; Malick, D. K.; Rabuck, A. D.; Raghavachari, K.; Foresman, J. B.; Ortiz, J. V.; Cui, Q.; Baboul, A. G.; Clifford, S.; Cioslowski, J.; Stefanov, B. B.; Liu, G.; Liashenko, A.; Piskorz, P.; Komaromi, I.; Martin, R. L.; Fox, D. J.; Keith, T.; Al-Laham, M. A.; Peng, C. Y.; Nanayakkara, A.; Challacombe, M.; Gill, P. M. W.; Johnson, B.; Chen, W.; Wong, M. W.; Gonzalez, C.; Pople, J. A. *Gaussian 03*; Gaussian, Inc.: Wallingford, CT, 2004.
9. Del Pópolo, M. G.; Lynden-Bell, R. M.; Kohanoff, J. *J. Phys. Chem. B* **2005**, *109*, 5895-5902.
10. Morrow, T. I.; Maginn, E. J. *J. Phys. Chem. B* **2002**, *106*, 12807-12813; **2003**, *107*, 9160.
11. Darden, T. A.; York, D. M.; Pedersen, L. G. *J. Chem. Phys.* **1993**, *98*, 10089-10092.
12. Essmann, U.; Perera, L.; Berkowitz, M. L.; Darden, T.; Lee, H.; Pedersen, L. G. *J. Chem. Phys.* **1995**, *103*, 8577-8593.
13. Tuckerman, M.; Berne, B. J.; Martyna, G. *J. Chem. Phys.* **1992**, *97*, 1990-2001.

14. Chandrasekhar, J.; Spellmeyer, D. C.; Jorgensen, W. L. *J. Am. Chem. Soc.* **1984**, *106*, 903-910.
15. Huddleston, J. G.; Visser, A. E.; Reichert, W. M.; Willauer, H. D.; Broker, G. A.; Rogers, R. D. *Green Chem.* **2001**, *3*, 156-164.
16. Hardacre, C.; Holbery, J. D.; McMath, S. E. J.; Bowron, D. T.; Soper, A. K. *J. Chem. Phys.* **2003**, *118*, 273-278.
17. Dupont, J. *J. Braz. Chem. Soc.* **2004**, *15*, 341-350.
18. Hanke, C. G.; Price, S. L.; Lynden-Bell, R. M. *Mol. Phys.* **2001**, *99*, 801-809.
19. Margulis, C. J.; Stern, H. A.; Berne, B. J. *J. Phys. Chem. B* **2002**, *106*, 12017-12021.
20. Yan, T.; Burnham, C. J.; Del Pópolo, M. G.; Voth, G. A. *J. Phys. Chem. B* **2004**, *108*, 11877-11881.
21. Del Pópolo, M. G.; Voth, G. A. *J. Phys. Chem. B* **2004**, *108*, 1744-1752.
22. Bühl, M.; Chaumont, A.; Schurhammer, R.; Wipff, G. *J. Phys. Chem. B* **2005**, *109*, 18591-18599.
23. Bhargava, B. L.; Balasubramanian, S. *Chem. Phys. Lett.* **2006**, *417*, 486-491.
24. Hu, Z.; Margulis, C. J. *Proc. Natl. Acad. Sci.* **2006**, *103*, 831-836.
25. Zhang, H.; Wu, J.; Zhang, J.; He, J. *Macromolecules*, **2005**, *38*, 8272-8277.
26. Wu, X.; Liu, Z.; Huang, S.; Wang, W. *Phys. Chem. Chem. Phys.* **2005**, *7*, 2771-2779.
27. Huang, X.; Margulis, C. J.; Li, Y.; Berne, B. J. *J. Am. Chem. Soc.* **2005**, *127*, 17842-17851.

Chapter 24

New Class of Ionic Liquids Synthesized from Amino Acid and Other Bioderived Materials

Hiroyuki Ohno, Kenta Fukumoto, and Junko Kagimoto

Department of Biotechnology, Tokyo University of Agriculture and Technology, Koganei, Tokyo 184-8588, Japan

A new series of ionic liquids have been synthesized from bio-related compounds and their characteristics have been analyzed. Amino acid ionic liquids (AAILs), which contain amino acids as the anions, enable us to study the effect of substituent groups on the properties of ionic liquids. The mixing of different AAILs improved the polarity of the AAILs. This is attributable to interactions between the amino acids. Chiral amino acid derived cations have also been synthesized via regio-specific alkylation of histidine. These prepared imidazolium cations were mixed with lithium bis(trifluoromethane sulfonyl)imide (LiTf_2N) to construct lithium cation conductor. Equimolar mixture of these gave an ionic conductivity of about $1 \times 10^{-4} \text{ Scm}^{-1}$ at 50°C . Mixture of zwitterions with LiTf_2N provided effective dissociation of lithium ion in the mixture. Ionic liquids composed of choline and amino acids were newly prepared. Those AAILs with alanine or serine showed glass transition temperature at -53°C , and -46°C , respectively.

Since ionic liquids are composed of organic ions, there are potential possibilities to control physico-chemical properties, solvent properties, and even function (1,2). Nevertheless their possibility as designer liquids, the relationship between component ion structure and physico-chemical properties has not been clarified. One of factors to suppress the development of such research is the difficult steps to prepare pure ionic liquids. We have proposed a conventional method to prepare model salts by mixing equimolar amount of tertiary amine and acid (3). This reaction, called neutralization method, generally gave salt without any byproduct. Also, cations having hydroxide anions were used to prepare salts by mixing corresponding acids. This research produced the desired salts and water (4). Purification of starting materials is much easier than that of synthesized salts. These procedures are convenient to prepare pure salts. Based on these procedures, we have prepared a variety of different salts. One of our target salts is a ionic liquid based on bio-related ions. There have been a few studies on the preparation of ionic liquids with bio-related ions. Ions in our body are great candidates to prepare new ionic liquids. In addition, these ions should be effective starting materials for functionalized ionic liquids. Some practical advantages of these bio-related ionic liquids is bio-degradability (5), decreased toxicity (6), and possibility of chirality (7). Amino acids are good models to study the relationship between ionic structure and properties. Recently, functional ionic liquids prepared from the amino acids have been reported (8-10). Before these reports, we first reported the successful preparation of ionic liquids from 20 different natural amino acids (11). Most amino acids contain functional groups, therefore they are regarded as excellent starting materials for task-specific ionic liquids.

Room temperature ionic liquids composed of amino acid anions

Amino acids are good starting materials for designer ionic liquids because they possess a variety of side chains. However, intricate modification processes make it difficult to synthesize pure ionic liquids that retain their chirality. We have suggested ionic liquids containing an amino acid anion, hereafter AAILs (11). The synthetic process is very simple and the neutralized amino acids were easily obtained by the mixing corresponding amino acids with imidazolium hydroxide solution (Figure 1). All the amino acids were mixed with equimolar amount of cation, regardless of side chain structure. Thus the obtained AAILs are not only halogen-free but also designer ionic liquids.

By the combination with the [emim] cation, 20 different natural amino acids produced room temperature ionic liquids. Although prepared the AAILs had the same carboxylate anions, the difference between the lowest T_g for

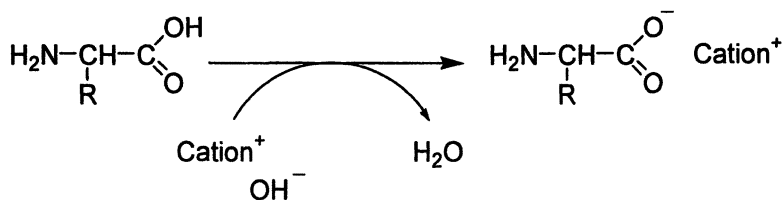


Figure 1. Preparation of amino acid ionic liquids.

([emim][Gly]) and the highest T_g for ([emim][Glu]) were over 70 °C. It is clear that the amino acid side chain affected the T_g considerably. In addition, these AAILs exhibited different solubility to organic solvents. For example, the AAILs prepared from amino acids containing two carboxyl groups, such as glutamic acid and aspartic acid, were insoluble in chloroform. There are amino acid species which depend on several physico-chemical factors such as melting point, glass transition temperature, viscosity, etc. These amino acids are useful to analyze the relationship between structure and physico-chemical properties of the corresponding ionic liquids.

Although imidazolium based AAILs have fascinating characteristics, viscosity and thermal stability need improvement. AAILs that have strong hydrogen bonding such as carboxyl generally showed high viscosity. This high viscosity is attributed to the hydrogen bonding among the amino acid anions and hydrogen atom on the 2 position of imidazolium cation ring. To find an effective cation structure to decrease the viscosity of AAILs, ammonium (N_{4444}), pyrrolidinium (P_{14}), pyridinium (Py_4), and phosphonium (P_{4444}) cations were investigated (Table 1). These ammonium cations are known to be suitable components of general RTILs. AAILs composed of ammonium cations and alanine were obtained as a solid at room temperature, and the thermal stability was not sufficient (below 200 °C). On the contrary, phosphonium-based ionic liquids exhibited a lower melting point and a lower viscosity than imidazolium-based ionic liquids (12). In spite of their excellent thermal and chemical stability (13,14), the phosphonium cation is generally not superior to the imidazolium cation to provide thermal stability and low viscosity. Additionally, the symmetric structure of the cation also tends to elevate the melting point of ILs due to easier crystallinity. For example, $[\text{P}_{4444}][\text{Tf}_2\text{N}]$ exhibited a relatively high melting point at 86 °C in spite that the $[\text{Tf}_2\text{N}]$ anion is known to give a less viscous ILs. Amino acid anions are revealed to be good partners to phosphonium cations. Generally, in case of imidazolium-based ionic liquids, hydrogen bonding between hydrogen atom on the 2 position of imidazolium ring and anion affect the physico-chemical properties. On the other hand, $[\text{P}_{4444}]$ was a moderately large cation and the weakened electrostatic interaction among ionic liquids was expected. In addition, there are no effective hydrogen bonding

Table 1. Physico-chemical properties of prepared onium-alanine salts.

		$T_m/^\circ\text{C}$	$T_g/^\circ\text{C}$	$T_{dec}/^\circ\text{C}$
[emim]		-57	ND	212
[N ₄₄₄₄]		ND	76	162
[P ₁₄]		-64	77	176
[Py ₄]		-	-	-
[P ₄₄₄₄]		-70	ND	286

ND; not detected, - not stable.

SOURCE: Data from references 3 and 12.

with the anions. The x-ray structure of [P₄₄₄₄][Glu] indicated no specific interaction, including hydrogen bonding, between cation and anion.

Furthermore, AAILs are confirmed to be more polar liquids than conventional ionic liquids by the polarity measurement using Kamlet-Taft parameters (15,16). Hydrogen bond basicity is stronger than that of chloride anion. Since hydrogen bond basicity mainly dominates the solvation of ionic liquids to bio-polymers such as cellulose (17), these AAILs are expected to be polar solvents for bio-polymers.

Binary mixtures of amino acid ionic liquids

Although the mixing with volatile organic solvents induced a large change of solution properties, the AAILs lost normal advantages of ILs such as non-flammability, non-volatility, and so on. On the other hand, when mixing different ILs is often difficult to change their properties dramatically (18,19). The mixtures of general ionic liquids such as [emim][Tf₂N], [emim][BF₄] exhibited a linear change of physico-chemical properties such as melting point, viscosity, and polarity. We expected that the additional interaction between ions could shift the physico-chemical properties of the ionic liquids. Therefore, prepared binary mixtures of these AAILs to improve the ionic conductivity and polarity. We studied three mixtures i.e., ([emim][Asp]+[emim][Lys], [emim][Asp]+[emim][His], and [emim][Ala]+[emim][Val]) to understand the effect of mixing on the ionic conductivity, phase transition temperature and polarity of the above mixtures. Although these mixtures showed linear changes of the ionic conductivity with their composition, the [emim][Asp]+[emim][Lys] systems showed dramatic increase of polarity (π^* ; polarity/dipolarity parameter

in Figure 2). These results show that the physico-chemical property is tunable and can be improved by mixing specific anion species.

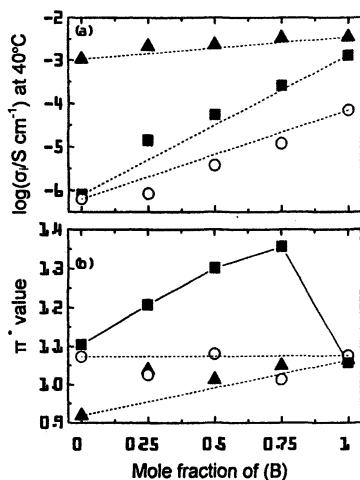
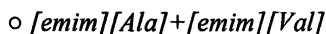
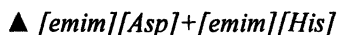
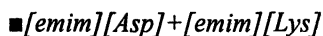
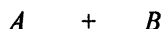


Figure 2. Ionic conductivity (a) and polarity (b) of amino acid ionic liquid mixtures.



Zwitterions derived from amino acid

As one derivative of AAILs, we synthesized novel zwitterions based on amino acids. We have already reported some imidazolium based zwitterions and their mixtures with $LiTf_2N$ and HTf_2N (20-22). These mixtures formed transparent liquids at room temperature, and we confirmed that the zwitterions accelerated the dissociation of additives in the mixture. Mixtures with lithium salt have been expected as a matrix for lithium ion conduction because of their high transport number of lithium ions. These mixtures with a Brønsted acid

were expected to be Brønsted acidic ionic liquids (23), and they are applicable as catalysts as well as matrix for selective proton conduction. Although amino acids are natural zwitterions, they are melting salts even after mixing with lithium salts because of the short distance between the cation and anion. A zwitterion needs a longer space between cation and anion to lower the melting point. Furthermore, aliphatic ammonium-based zwitterions exhibited a relatively high melting point in our previous studies. Therefore, among various natural amino acids, we focused on a histidine because of the imidazole side chain. The alkylation of the imidazole unit expected to provide zwitterions with low melting points. Furthermore, by the addition of Brønsted acid, the zwitterion derived from histidine was expected to be chiral Brønsted acidic ionic liquid. However, the histidine derived zwitterion is difficult to prepare from histidine by direct alkylation of the imidazole side chain (24): The carboxyl group and the amino group on α -carbon of histidine would disturb the alkylation of imidazole group, and the pure zwitterion could not be obtained.

We synthesized novel zwitterions by the quaternization of the imidazole unit on the histidine by blocking both the amino and carboxylic groups as seen in Figure 3. The zwitterions were synthesized by regio-specific alkylation (25) of the imidazole via intermediate cyclic urea. The regio-specific alkylation of the imidazole units provides some advantages. For example, this systematic alkylation provides homogeneous zwitterion. In addition the asymmetric alkyl chains on the imidazolium cation should produce zwitterions with lower melting point.

Histidine-derived zwitterion 1 ($R_1=Me$, $R_2=Et$) was obtained as white crystals with a melting point of a 183 °C. The melting point was similar to that of zwitterion containing carboxyl group reported previously. On the other hand, zwitterion 2 ($R_1=Me$, $R_2=Allyl$) provided no effective melting point. The

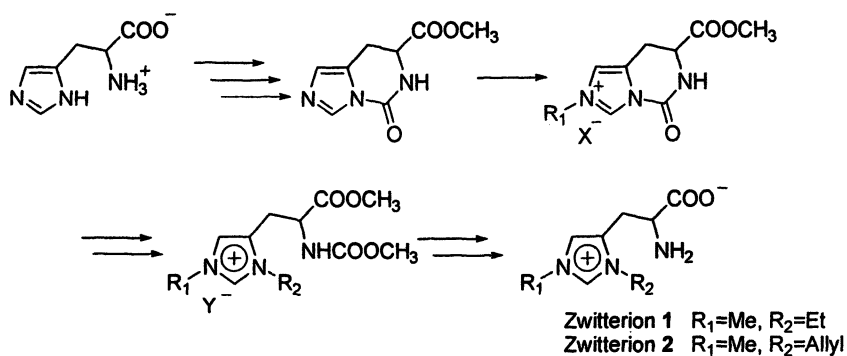


Figure 3. Synthesis of histidine-based zwitterion by regio-specific alkylation.

effectiveness of the allyl group(s) on the imidazolium cation ring has already been discussed in our previous paper (26).

Then, the performance of the zwitterion as an ion conductive matrix was evaluated after mixing with LiTf_2N . The mixtures with LiTf_2N provided transparent ionic liquids, and exhibited no melting point but a glass transition temperature. By adding equimolar amount of LiTf_2N , T_g of the mixture was found at 20 °C. By increasing the concentration of LiTf_2N in the mixtures, induced gradual lowering was observed in T_g . On the other hand, the ionic conductivity of these mixtures did not obey the values expected from their T_g (Figure 4).

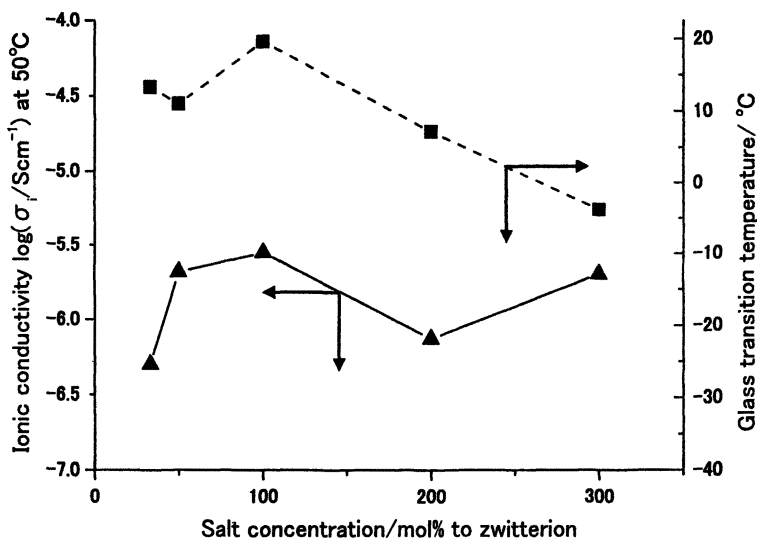


Figure 4. Effect of LiTf_2N concentration on σ_i (triangle) and T_g (square) of zwitterion 1 / LiTf_2N mixtures.

To analyze the dissociation degree of LiTf_2N in the mixture, Raman spectra of the mixtures was recorded. A scattering at 740 cm^{-1} represents the CF_3 symmetric deformation vibration of the dissociated Tf_2N anion (27). Up to equimolar addition of LiTf_2N , Tf_2N anions were confirmed to be dissociated efficiently by the peak at 740 cm^{-1} (Figure 5).

On the other hand, excess LiTf_2N increased the scattering intensity at 745 cm^{-1} , this peak was attributed to associate salts like solid state LiTf_2N . Therefore, relatively low ionic conductivity was attributed to the insufficient degree of dissociation of LiTf_2N . The lowering of the ionic conductivity seen in Figure 4 was attributed to the insufficient degree of dissociation of LiTf_2N .

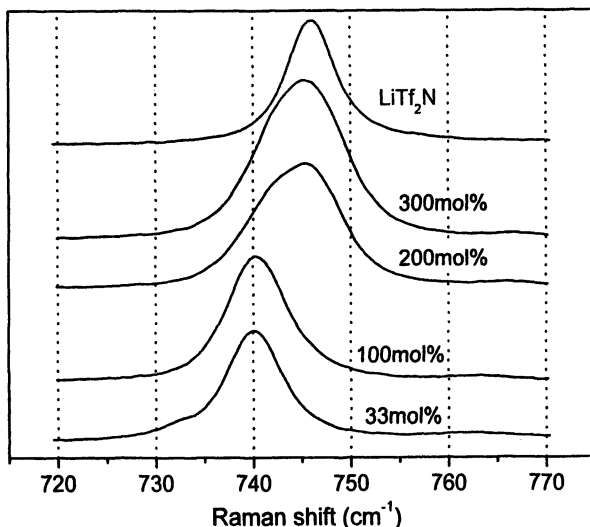


Figure 5. Raman spectra for zwitterion 1 /LiTf₂N mixtures.

Zwitterions derived from histidine exhibited suitable performance similar to conventional imidazolium-based zwitterions (28). Furthermore, these zwitterions have the potential to be chiral Brønsted acidic ionic liquids as well as reaction solvents. Viscosity is still a serious drawback, and efforts will be made to decrease it.

Fully natural ionic liquids containing amino acids

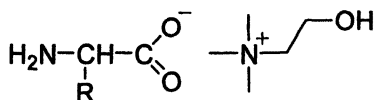
Since AAILs already have bio-related anions, we expected to prepare completely bio-related ionic liquids using amino acids. If both cation and anion were bio-derived materials, fully natural ionic liquids would be less toxic, biodegradable ILs and even though they would be applicable for medical science. Although these ILs have many applications, fully bio-related ILs have not been reported previously. The difficulty to prepare ILs is the selection of component ions from various bio-related materials. Generally these ions have functional groups to contribute hydrogen bonding, which increase T_m and/or T_g of the ILs. Different from conventional ILs, AAILs sometimes prefer to unsuitable cation such as the symmetrical phosphonium cation (12). Among various natural cations, we selected the choline cation to form AAILs. There are several choline derivatives in our body. For example, dipalmitoyl-phosphatidylcholine is a typical cell membrane lipid. Phosphorylcholine shows soft interaction on the membrane surface. Since these choline derivatives have some degree of

motility, choline may be used as a suitable cation to achieve lower T_g and toxicity. Some choline-based ionic liquids have already been reported (29,30). In spite of their expectation that choline should be better component of ionic liquids, choline salts exhibited higher melting point than those having conventional cations. Even if TF_2N was used as an anion, the choline salt became solid at room temperature. This relatively high melting point should be the effect of hydroxyl group, which induce hydrogen bonding with the component ion, and the short alkyl chains on the nitrogen atom.

As a further study of amino acid ionic liquids, we prepared novel fully natural ionic liquids by the combination of amino acid with choline. The preparation method is almost the same that of AAILs we have reported. Choline hydroxide ([Ch][OH]) was prepared by anion exchange column, and was reacted with amino acids in an aqueous media. Most amino acids gave liquid salts except for glycine. [Ch][Gly] exhibited melting point at 90 °C. Other salts, e. g. [Ch][Ala] and [Ch][Ser], had no melting point but a T_g about -50 °C (Table 2). Other amino acids gave liquid salts by the combination with choline. All these [Ch][amino acid] were revealed to decomposed below 200 °C. In addition to less thermal stability, these ionic liquids exhibited higher T_g than conventional imidazolium based amino acid ionic liquids. These characteristics should be attributable to the terminal hydroxide group. However, these choline-based AAILs are first case of ILs composed of only natural materials as far as we know. We started couple other bio-related ions, in order to prepare less viscous fully natural ionic liquids.

Table 2. Thermal properties of choline-based amino acid ionic liquids

	R	$T_g / ^\circ\text{C}$	$T_m / ^\circ\text{C}$	$T_{\text{dec}} / ^\circ\text{C}$
[Ch][Gly]	H	-73	90	186
[Ch][Ala]	CH_3	-53	-	181
[Ch][Ser]	CH_2OH	-46	-	187



Conclusions

We have prepared various ionic liquids using amino acid and other bio-related materials, and demonstrated that amino acids and bio-derived materials are potential candidates to prepare ionic liquids. The combination of symmetric

phosphonium cation and amino acids improved viscosity and thermal properties than those of conventional imidazolium-based AAILs. The modification of the amino acid enables us to provide novel functionalized ionic liquids. Regio-specific alkylation of imidazole on histidine also produced novel zwitterions. Raman spectra suggested that these zwitterions dissociated to generate free lithium ions in the mixture. Furthermore, fully natural ILs composed of amino acid and choline were prepared, and these showed lower T_g than imidazolium based AAILs. These bio-related ionic liquids should be useful for many scientific fields.

Acknowledgements

This study was supported by a Grand-in-Aid for Scientific Research from the Ministry of Education, Culture, Sports, Science and Technology, Japan (No. 17205020 and 17073005), and the 21st Century COE program of "Future Nano-Materials". LiTf_2N and HTf_2N were gift from Sumitomo 3M and Morita Chem. Co. Ltd, respectively. Tetrabutylphosphonium hydroxide was a gift from Hokko Chem. Ind. Co. Ltd.

References

1. Wasserscheid, P.; Welton, T. *Ionic Liquids in Synthesis*, Wiley-VCH, Weinheim, Germany, 2003.
2. Bonhôte, P.; Dias, A. P.; Papageorgiou, N.; Kalyanasundaram, K.; Grätzel, M. *Inorg. Chem.* **1996**, *35*, 1168.
3. Hirao, M.; Sugimoto, H.; Ohno, H. *J. Electrochem. Soc.* **2000**, *147*, 4168.
4. Ogihara, W.; Yoshizawa, M.; Ohno, H. *Chem. Lett.* **2004**, *33*, 1022.
5. Gathergood, N.; Garcia, M. T.; Scammells, P. J. *Green. Chem.* **2004**, *6*, 166
6. Pretti, C.; Chiappe, C.; Pieraccini, D.; Gregori, M.; Abramo, F.; Monni, G.; Intorre, L. *Green. Chem.* **2006**, *8*, (ASAP)
7. Wasserscheid, P.; Bösmann, A.; Bolm, C. *Chem. Commun.* **2002**, 200.
8. Bao, W.; Wang, Z.; Li, Y. *J. Org. Chem.* **2003**, *68*, 591.
9. Clavier, H.; Boulanger, L.; Audic, N.; Toupet, L.; Maudiot, M.; Guillemin, J.-C. *Chem. Commun.* **2004**, 1224.
10. Tao, G. H.; He, L.; Sun, N.; Kou, Y. *Chem. Commun.* **2005**, 3562.
11. Fukumoto, K.; Yoshizawa, M.; Ohno, H. *J. Am. Chem. Soc.* **2005**, *127*, 2398.
12. Kagimoto, J.; Fukumoto, M.; Ohno, H. *Chem. Commun.* **2006**, 2254.
13. Del Sesto, R. E.; Corley, C.; Robertson, A.; Wilkes, J. S. *J. Organomet. Chem.* **2005**, *690*, 2536.

14. Ramnial, T.; Ino, D. D.; Clyburne, J. A. C. *Chem. Commun.*, **2005**, 325.
15. Crowhurst, L.; Mawdsley, P. R.; Perez-Arlandis, J. M.; Salter, P. A.; Welton, T. *Phys. Chem. Chem. Phys.* **2003**, *5*, 2790.
16. Poole, C. F. *J. Chromatogr. A* **2004**, *1037*, 49.
17. Swatloski, R. P.; Spear, S. K.; Holbrey, J. D.; Rogers, R. D. *J. Am. Chem. Soc.* **2002**, *124*, 4974.
18. Fletcher, K. A.; Baker, S. N.; Bakear, G. A.; Pandey, S. *New. J. Chem.* **2003**, *27*, 1706.
19. Sun, J.; Forsyth, M.; MacFarlane, D. R. *J. Phys. Chem. B* **1998**, *102*, 8858.
20. Yoshizawa, M.; Ohno, H. *Chem. Commun.* **2004**, 1828.
21. Yoshizawa, M.; Ohno, H. *Chem. Lett.* **2004**, *33*, 1594.
22. Yoshizawa, M.; Hirao, M.; Ohno, H. *J. Mater. Chem.* **2001**, *11*, 1057.
23. Cole, A. C.; Jensen, J. L.; Ntai, I.; Tran, K. L. T.; Weaver, K. J.; Forbes, D. C.; Davis, J. H., Jr. *J. Am. Chem. Soc.*, **2002**, *124*, 5962.
24. Hannig, F.; Kehr, G.; Fröhlich, R.; Erker, G. *J. Organomet. Chem.* **2005**, *690*, 5959.
25. Jain, R.; Cohen, L. A. *Tetrahedron* **1996**, *52*, 5363.
26. Mizumo, T.; Marwanta, E.; Matsumi, N.; Ohno, H. *Chem. Lett.* **2004**, *33*, 1360.
27. Jo, S. I.; Lee, S. I.; Jeong, Y. B.; Kim, D. W.; Sohn, H. J. *Electrochimica Acta* **2004**, *50*, 327.
28. Ohno, H.; Washiro, S.; Yoshizawa, M. in *ACS Symp. Ser. 913*, Brazel, C. S., Rogers, R. D. Eds, American Chemical Society: Washington, DC, **2005**, 89-102.
29. Abbott, A. P.; Boothby, D.; Capper, G.; Davies, D. L.; Rasheed, R. K. *J. Am. Chem. Soc.* **2004**, *126*, 9142.
30. Abbott, A. P.; Capper, G.; Davies, D. L.; Rasheed, R. K.; Tambyrajah, V. *Green. Chem.* **2002**, *4*, 24.

Chapter 25

Hydrophobic *n*-Alkyl-*N*-isoquinolinium Salts: Ionic Liquids and Low Melting Solids

Ann E. Visser^{1,2}, Jonathan G. Huddleston^{1,3}, John D. Holbrey^{1,4},
W. Matthew Reichert¹, Richard P. Swatloski¹,
and Robin D. Rogers^{1,*}

¹Department of Chemistry and Center for Green Manufacturing,
The University of Alabama, Tuscaloosa, AL 35487

²Current address: Savannah River National Laboratory, Aiken, SC 29808

³Current address: Millipore Bioprocessing Ltd., Medomsley Road, Consett,
County Durham DH8 6SZ, United Kingdom

⁴Current address: QUILL, The Queen's University of Belfast,
Belfast BT9 5AG, Northern Ireland, United Kingdom

A series of hydrophobic *n*-alkyl-*N*-isoquinolinium ionic liquids (ILs) with a linear alkyl-chain substituent containing from 4-18 carbon atoms in combination with hexafluorophosphate, bis(trifluoromethylsulfonyl)amide, and bis(perfluoroethylsulfonyl)amide have been synthesized and characterized (water content, density, DSC, TGA, and LSER). The crystal structures of [C₂isoq][PF₆] (prepared and isolated only for the comparative X-ray diffraction study), [C₄isoq][PF₆], and [C₁₀isoq][PF₆] illustrate the underlying interactions in the higher melting salts. The isoquinolinium-based ILs studied here are interesting due to their highly aromatic nature and physical and solvent properties.

Introduction

The search for new ionic liquids (ILs) with the potential to interact with aromatic hydrocarbons for separation purposes, led us to the study of a new class of cations based on the isoquinoline molecule (*I*). Our previous study focused on bis(perfluoroethylsulfonyl)amide ($[\text{N}(\text{SO}_2\text{CF}_2\text{CF}_3)_2]^-$ or [BETA]) salts of the *n*-alkyl-*N*-isoquinolinium ($[\text{C}_n\text{isoq}]^+$) cation with alkyl chain lengths ranging from 4-18. We found that these ILs have an affinity over $[\text{C}_4\text{mim}][\text{PF}_6]$ for aromatic solutes as demonstrated by their increased distribution ratios in IL/water biphasic systems.

Here we expand this work with additional data for $[\text{C}_n\text{isoq}]^+$ salts of hexafluorophosphate ($[\text{PF}_6]^-$) and bis(trifluoromethylsulfonyl)amide ($[\text{NTf}_2]^-$). Partitioning data was collected to study solvent properties based on interpretation of Abraham's linear solvation energy relationships (LSER) (2) and provides insight into how subtle changes in the cation, not only the anion, can affect the solvent properties. Solid-state analyses of the $[\text{PF}_6]^-$ salts of $[\text{C}_2\text{isoq}]^+$, $[\text{C}_4\text{isoq}]^+$, and $[\text{C}_{10}\text{isoq}]^+$ were carried out to gain insight into the interactions responsible for the physical and solvent properties of these ILs (3).

Experimental

All aqueous solutions were prepared with deionized water that was purified with a Barnstead NANOpure water system (Dubuque, IA) and polished to 18.3 MΩ/cm. All salt and acid solutions were prepared as molar concentrations by transferring a known amount of material to a volumetric flask and diluting to the specified volume with deionized water. When needed, pH adjustments of the aqueous phase were made using HNO₃ or NaOH. HPF₆ was supplied by Ozark Mahoning (Tulsa, OK) and was used as received. Li $[\text{N}(\text{SO}_2\text{CF}_3)_2]$ (Li[NTf₂]) and Li $[\text{N}(\text{SO}_2\text{CF}_2\text{CF}_3)_2]$ (Li[BETA]) were obtained from 3M (Minneapolis, MN) and used as received. All other chemicals were of reagent grade, obtained from Aldrich (Milwaukee, WI), and used without further purification.

Synthesis of $[\text{C}_n\text{isoq}]\text{Cl}$ Salts

The *n*-alkyl-*N*-isoquinolinium chloride salts were prepared by alkylation of isoquinoline with an appropriate chloroalkane using a procedure developed for the alkylation of imidazoles to form 1-alkyl-3-methylimidazolium ILs described in the literature (4). Approximately 100 g batches were prepared by reaction of a 1:1 molar ratio of chloroalkane and isoquinoline with magnetic stirring at 70 °C for 72 h. After 72 h, two phases had formed with the top layer being the

unreacted starting material and the bottom layer being the isoquinolinium IL. The top layer was decanted and the bottom layer washed with ethyl acetate. The wash was repeated two more times and the IL dried under vacuum with heating at 70 °C to remove any remaining ethyl acetate.

Synthesis of $[C_n\text{isoq}][X]$ ($X = [\text{PF}_6]^-$, $[\text{NTf}_2]^-$, and $[\text{BETA}]^-$) Salts

$[C_n\text{isoq}][\text{PF}_6]$: The salts below were prepared by metathesis from the appropriate *n*-alkyl-*N*-isoquinolinium chlorides following the procedure described by Huddleston, et al. (4) for the preparation of 1,3-dialkylimidazolium salts. Approximately 100 g of $[C_n\text{isoq}][\text{Cl}]$ was transferred to a 2 L container lined with a perfluorinated material followed by the addition of 500 mL deionized water. An aqueous solution of 60% HPF_6 in a 1.1:1 molar ratio of $\text{HPF}_6:[C_n\text{isoq}]\text{Cl}$ was added. Caution: the addition of HPF_6 should be done slowly to minimize the amount of heat generated. As HPF_6 was added, two phases formed, where $[C_n\text{isoq}][\text{PF}_6]$ formed the brown bottom phase and aqueous HCl the top phase. The upper phase was decanted and 500 mL of water was added followed by vigorous shaking and mixing. After the mixture settled, the upper aqueous phase was decanted and the lower ionic liquid phase was washed again with deionized water. This procedure was repeated until the pH of the upper phase was ~ 7 .

$[C_n\text{isoq}][\text{NTf}_2]$: Approximately 100 g of $[C_n\text{isoq}]\text{Cl}$ was transferred to a 250 mL plastic bottle and a 1.1:1 molar ratio of $\text{Li}[\text{NTf}_2]:[C_n\text{isoq}]\text{Cl}$ was added, followed by 50 mL of deionized water. After mixing, two phases formed where the brown bottom phase was $[C_n\text{isoq}][\text{NTf}_2]$ and the colorless top phase was aqueous LiCl. After decanting the top phase, 50 mL of fresh deionized water was added and the solution was thoroughly mixed. This washing step was repeated twice.

$[C_n\text{isoq}][\text{BETA}]$: Approximately 100 g of $[C_n\text{isoq}]\text{Cl}$ was transferred to a 250 mL plastic bottle and a 1.1:1 molar ratio of $\text{Li}[\text{BETA}]:[C_n\text{isoq}]\text{Cl}$ was added, followed by 50 mL of deionized water. After mixing, two phases formed where the brown bottom phase was $[C_n\text{isoq}][\text{BETA}]$ and the colorless top phase was aqueous LiCl. After decanting the top phase, 50 mL of fresh deionized water was added and the solution was thoroughly mixed. This washing step was repeated twice.

Physical Property Measurements

After initial synthesis, the ILs were purified and dried. Since these ILs were prepared to study liquid/liquid partitioning from water, the physical properties of the hydrophobic ILs were studied after equilibration with an equal volume of water over a 24 h period.

The water content of each IL (Table I) was determined by Karl Fischer titration using a volumetric Aquastar Karl Fischer titrator (EM Science, Gibbstown, NJ) with Composite 5 solution as the titrant and anhydrous methanol as the solvent. Each sample was water equilibrated before measurements were taken. Sample weights were at least 1 g and duplicate measurements were performed on each sample with results agreeing to within 5%.

The density of each water-equilibrated IL was determined by gravimetric analysis. After calibrating a 1 mL pipet (Rainin, Woburn, MA) to dispense 1.0 g of water, that pipet was used to transfer 1.0 mL of each IL to determine the mass of that volume of liquid. Each measurement was repeated 10 times and the average value is reported. All measurements were taken at room temperature (25 ± 1 °C).

Melting point and glass transition temperatures were determined by differential scanning calorimetry (DSC) using a TA Instruments (New Castle, DE) model 2920 differential scanning calorimeter. Temperature calibration was performed on a sample of indium. Each sample was approximately 10 mg and analyzed in a hermetically-sealed aluminum pan. For each experiment, an empty hermetically-sealed pan was referenced as the blank. A ramp temperature of 10 °C/min was employed over the temperature range of -150 to 100 °C. To ensure properly equilibrated transition temperatures, the samples were cycled through this cooling/heating method once before temperatures were assigned to transition peaks. Transition temperatures were recorded at the peak maximum of the thermal transition.

X-ray Diffraction Studies

Crystals suitable for single crystal X-ray diffraction of $[\text{C}_2\text{isoq}][\text{PF}_6]$, $[\text{C}_4\text{isoq}][\text{PF}_6]$, and $[\text{C}_{10}\text{isoq}][\text{PF}_6]$ were obtained by recrystallization of the salts by heating above the melting point and allowing the ILs to slowly cool to room temperature. The $[\text{C}_2\text{isoq}][\text{PF}_6]$ salt was prepared and crystallized only for the comparative X-ray diffraction study. Single crystals of each salt were mounted on a glass fiber and transferred to the goniometer of a Siemens SMART diffractometer equipped with a CCD area detector and graphite monochromated Mo-K α radiation. The crystals were cooled to -100 °C with a stream of nitrogen gas. The data were corrected for absorption using SADABS (5) and SHELXTL Version 5 was used for structure solution and refinement (6).

In each structure, the atoms were readily located and the positions of all non-hydrogen atoms were refined anisotropically. In the $[\text{C}_2\text{isoq}]^+$ salt, the $[\text{PF}_6]^-$ anion was found to be disordered. Four fluorine positions in one plane were modeled with alternate positions of 70%/30% occupancy. The two fluorine atoms (axial to the disordered atoms) are ordered.

The hydrogen atoms in the disordered $[C_2\text{isoq}]^+$ salt were added in geometrically appropriate positions and refined constrained in a riding model. The hydrogen atoms in the two other salts were added in geometrically appropriate positions and then fully refined isotropically.

Partitioning Studies

^{14}C -labeled solutes were obtained from Sigma (St. Louis, MO). Liquid scintillation analyses were performed using Ultima Gold scintillation cocktail (Packard Instrument, Downers Grove, IL) and a Packard Tri-Carb 1900 TR Liquid Scintillation Analyzer. For each study, 1 mL of IL and 1 mL of an aqueous phase were mixed followed by vortexing (2 min) and centrifuging (2000 g, 2 min) to equilibrate the phases. When using ionizable solutes, the aqueous phase pH was adjusted (using either NaOH or HNO_3) to a pH where the solutes would be neutral. Addition of the organic tracer (ca. 0.005 μCi , 5 μL) was followed by two intervals of vortexing (2 min) and centrifuging (2000 g, 2 min) to ensure that the phases were fully separated. 100 μL of each phase was removed for radiometric analysis. Since equal volumes of both phases were removed for analysis, the distribution ratios for the organic solutes were determined as in eq. 1:

$$D = \frac{\text{Activity in the IL lower phase}}{\text{Activity in the aqueous upper phase}} \quad (1)$$

Each experiment was carried out in duplicate and the results agreed to $\pm 5\%$.

Results and Discussion

Physical Properties

We have synthesized a series of IL salts by straight chain *N*-alkylation ($C_n = 4-18$, all even) of isoquinoline followed by metathesis of the chloride salts resulting in pairing with $[\text{PF}_6]^-$, $[\text{NTf}_2]^-$, and $[\text{BETA}]^-$ anions (Figure 1). All $[\text{PF}_6]^-$ salts were obtained as low melting solids, whereas the salts containing either of the fluorinated sulfonylamide anions ($[\text{NTf}]^-$ or $[\text{BETA}]^-$) were liquid at room temperature. Since these salts were prepared for possible use in I/I extraction, the reported water contents and densities (Table I) are for the salts after equilibration with water.

The water contents of the saturated $[C_n\text{isoq}]^+$ salts are in general higher than those reported for the same Ca-substituted methylimidazolium ($[C_n\text{mim}]^+$) derivatives (4). As observed with other cation classes, the trend in water content

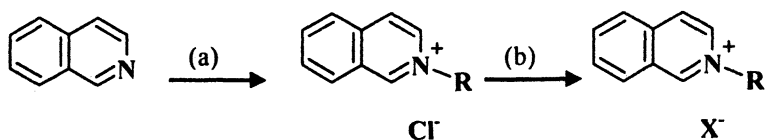


Figure 1. The general synthesis and metathesis of the *n*-alkyl-*N*-isoquinolinium salts ($n = 4-18$ all even, $X = [\text{PF}_6]^-$, $[\text{NTf}_2]^-$, or $[\text{BETA}]^-$): (a) $\text{C}_n\text{H}_{2n+1}\text{Cl}$; (b) HPF_6 , $\text{Li}[\text{NTf}_2]$, or $\text{Li}[\text{BETA}]$.

Table I. Water Content and Density of Water-Equilibrated $[\text{C}_n\text{isoq}]^+$ ILs

n	Anion	Water content (ppm)	Density (g/mL)
4	$[\text{PF}_6]^-$	-	-
4	$[\text{NTf}_2]^-$	18600	1.26
4	$[\text{BETA}]^-$	17700	1.23
6	$[\text{PF}_6]^-$	-	-
6	$[\text{NTf}_2]^-$	16900	1.23
6	$[\text{BETA}]^-$	16200	1.20
8	$[\text{PF}_6]^-$	18500	1.19
8	$[\text{NTf}_2]^-$	15600	1.19
8	$[\text{BETA}]^-$	14900	1.17
10	$[\text{PF}_6]^-$	-	-
10	$[\text{NTf}_2]^-$	7300	1.13
10	$[\text{BETA}]^-$	6900	1.09
12	$[\text{PF}_6]^-$	-	-
12	$[\text{NTf}_2]^-$	6800	1.11
12	$[\text{BETA}]^-$	6600	1.08
14	$[\text{PF}_6]^-$	-	-
14	$[\text{NTf}_2]^-$	6100	1.09
14	$[\text{BETA}]^-$	6100	1.07
16	$[\text{PF}_6]^-$	-	-
16	$[\text{NTf}_2]^-$	4800	1.06
16	$[\text{BETA}]^-$	4700	1.05
18	$[\text{PF}_6]^-$	-	-
18	$[\text{NTf}_2]^-$	4200	1.05
18	$[\text{BETA}]^-$	4100	1.05

follows the order $[\text{PF}_6]^- > [\text{NTf}_2]^- \approx [\text{BETA}]^-$. Table I also indicates that, for a series of cations with a particular anion, increasing the length of the alkyl chain appended to the cation decreases the water content of the IL phase (also as previously observed (4)). For the series $[\text{C}_n\text{isoq}][\text{BETA}]$, a noticeable change in water content occurs at $n = 10$, suggesting a change in internal liquid structure due to the interdigitation of the alkyl chains, as has been observed for imidazolium cations (7,8). Such interdigitation allows for the closer packing of the ions and establishes a charge-rich region and a hydrophobic region in the liquid, which increases the overall hydrophobicity.

The DSC-determined glass transition temperatures and melting points are summarized in Figure 2. While cooling, no crystallization events were observed, and the ILs cooled directly to a glassy state. The glass transition temperatures generally increase progressively with increasing alkyl chain length with the $[\text{BETA}]^-$ salts uniformly having the lowest T_g .

Melting points also vary with the alkyl chain length as shown in Figure 2b. The trends of decreasing melting points with increasing alkyl chain length to a minimum at $[\text{C}_6\text{isoq}][\text{BETA}]$, $[\text{C}_6\text{isoq}][\text{NTf}_2]$, and $[\text{C}_8\text{isoq}][\text{PF}_6]$, followed by increasing melting points for longer alkyl chain derivatives has been observed as a general feature of ILs containing an alkyl-chain substituent on quaternized imidazolium cations (9). Increasing chain lengths can lead to the formation of layered structures, often with the observation of thermotropic liquid crystalline phases on melting (10).

Thermal decomposition of the salts was determined by TGA (Figure 3). Figure 3a illustrates the change in thermal stability of the $[\text{PF}_6]^-$ salts as the alkyl chain length is varied. In all cases there was a 2-3% weight loss prior to 100 °C, which is attributed to the loss of water in the sample. After the initial loss of water, the weight of the sample remains relatively constant until a catastrophic weight loss between 325-375 °C corresponding to the decomposition of the cation.

The effects of the anion on the decomposition of the $[\text{C}_{10}\text{isoq}]^+$ salts is shown in Figure 3b. The Cl^- salt has the lowest decomposition temperature, which is consistent with the literature where halide-containing ILs have been shown to exhibit low decomposition temperatures (4,12) due to nucleophilic $\text{S}_{\text{N}}2$ attack of Cl^- on the N-C bond (11). The increase in anion size and nucleophilicity from Cl^- to $[\text{PF}_6]^-$ to $[\text{NTf}_2]^-$ and $[\text{BETA}]^-$, results in an increase in the decomposition temperature, which produces more thermally stable ILs. The TGA results are similar to those of $[\text{1-alkyl-3-methylimidazolium}]^+$ salts (4,12,14).

Single Crystal X-ray Diffraction Studies

Details regarding the collection and treatment of the data and the structure solution and refinement are included in Table II. ORTEP illustrations of the three salts examined, $[\text{C}_2\text{isoq}][\text{PF}_6]$, $[\text{C}_4\text{isoq}][\text{PF}_6]$, and $[\text{C}_{10}\text{isoq}][\text{PF}_6]$ are

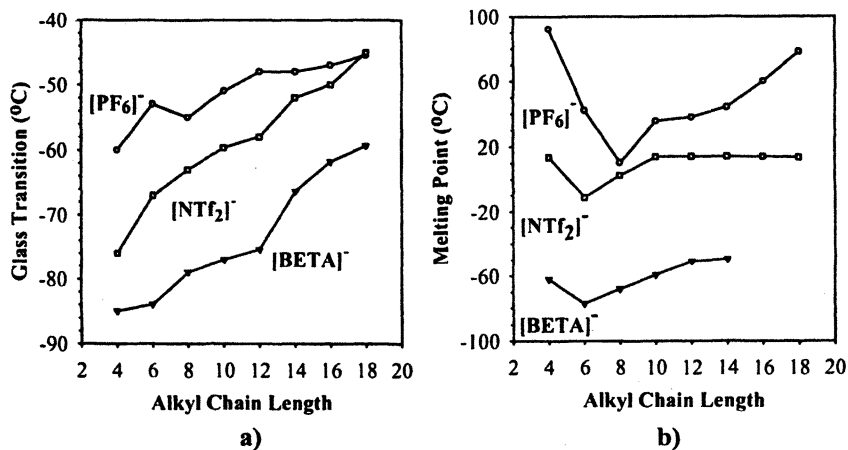


Figure 2. Glass transition temperatures (a) and melting point temperatures (b) for $[C_n,isoq]^+$ ILs as a function of increasing alkyl chain length.

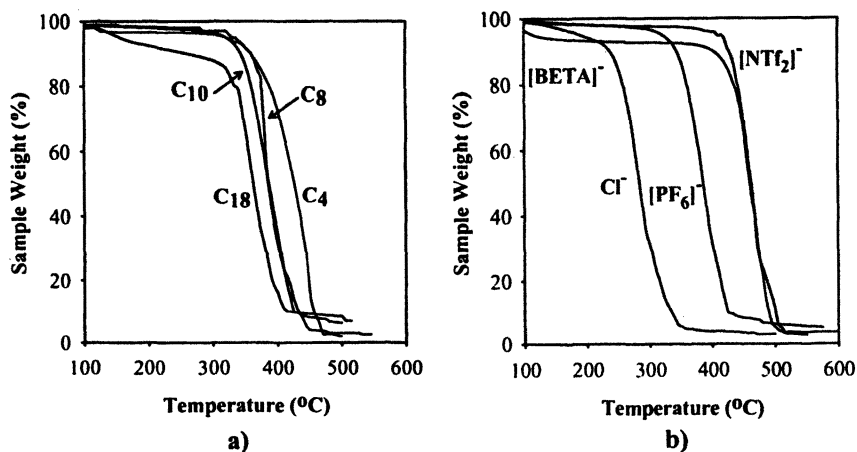


Figure 3. TGA for $[C_n,isoq][PF_6]$ (a) and $[C_{10},isoq]^+$ (b) ILs.

Table II. Summary of Crystallographic Data (15)

	[C ₂ isoq][PF ₆]	[C ₄ isoq][PF ₆]	[C ₁₀ isoq][PF ₆]
Formula	C ₁₁ H ₁₂ F ₆ NP	C ₁₃ H ₁₆ F ₆ NP	C ₁₉ H ₂₈ F ₆ NP
Formula Weight	303.19	331.24	415.39
Crystal Dimensions	0.42×0.20×0.18	0.32×0.22×0.10	1.10×0.50×0.30
T(K)	173	173	173
Crystal System	Triclinic	Triclinic	Triclinic
Space group	P-1	P-1	P-1
a (Å)	7.1750(9)	9.2078(10)	6.821(3)
b (Å)	9.3151(12)	9.2084(10)	7.923(3)
c (Å)	10.4638(14)	10.3028(12)	18.985(7)
α (°)	75.276(2)	104.173(2)	90.733(7)
β (°)	70.407(2)	111.701(2)	94.716(5)
γ (°)	87.602(2)	103.753(2)	97.942(6)
V (Å ³)	636.50(14)	732.84(14)	1012.3(6)
Z	2	2	2
D _{calc} (g cm ⁻³)	1.582	1.501	1.363
μ(MoKα) (mm ⁻¹)	0.274	0.245	0.193
F(000)	308	340	436
θ _{min-max} (°)	2.3, 23.2	2.3, 23.3	2.2, 23.3
Reflections collected	2867	3405	4457
Unique reflections, R _{int}	1815, 0.0997	2103, 0.0170	2882, 0.0262
[I > 2σ(I)] data	1221	1666	1838
Transmission factors	0.1355, 0.9703	0.6664, 0.9702	0.6466, 0.9703
Parameters varied	229	255	349
GOF ^a	1.313	0.949	0.919
R, ^b wR ₂ ^c [I > 2σ(I)]	0.1279, 0.3048	0.0334, 0.0843	0.0470, 0.1158
R, wR ₂ (all data)	0.1509, 0.3161	0.0447, 0.0894	0.0799, 0.1266

^aGOF = {Σ[w(F_o²-F_c²)²]/(n-p)}^{1/2} where n is the number of data and p is the number of parameters refined. ^bR = Σ||F_o-|F_c||/Σ|F_o|; ^cwR₂ = {Σ[w(F_o²-F_c²)²]/Σ(w(F_o²))}^{1/2}

provided in Figure 4. Even though the majority of the $[C_n\text{isoq}][\text{PF}_6]$ salts melt above room temperature, finding suitable crystals was a challenge, complicated by formation of microcrystals, multiple crystals, etc. Nonetheless, in the three structures studied, all of the ions are ordered except for the anions in the $[C_2\text{isoq}]^+$ salt, which showed typical disorder for the spherical $[\text{PF}_6]^-$ anion.

The close contacts and packing diagrams of the three structures are shown in Figure 5. These interactions illustrate the dominant nature of the Coulombic interactions in these salts and the increasing hydrophobic effect as the alkyl chain length increases; observations previously reported for a larger series of dialkyl-imidazolium $[\text{PF}_6]^-$ salts (3,16).

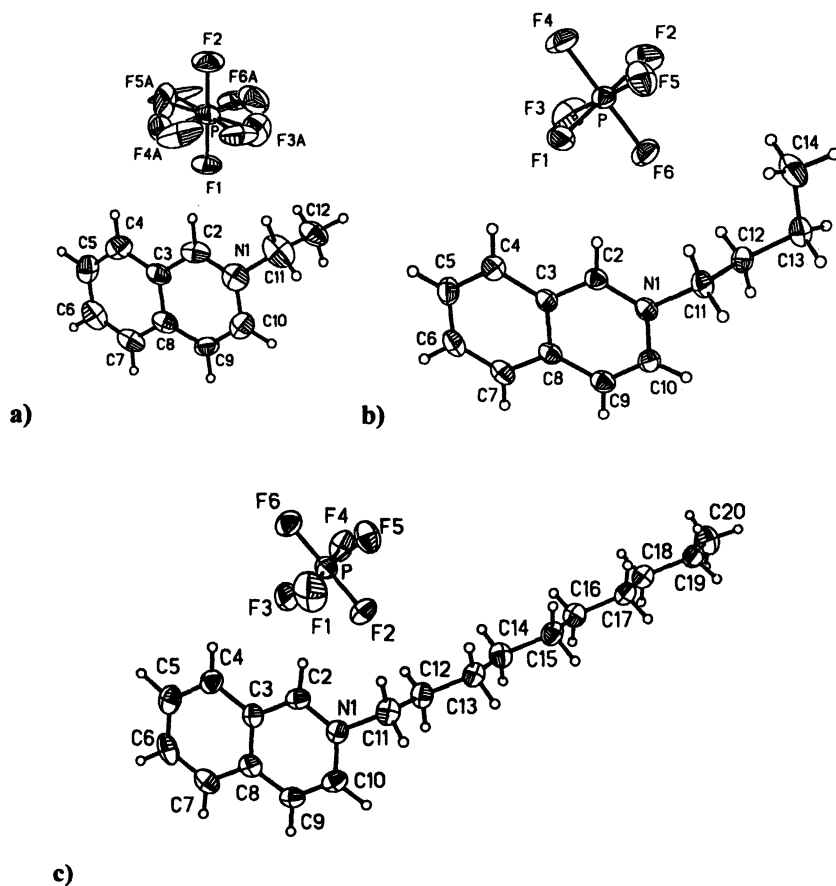


Figure 4. Asymmetric units of (a) $[C_2\text{isoq}][\text{PF}_6]$, (b) $[C_4\text{isoq}][\text{PF}_6]$, and (c) $[C_{10}\text{isoq}][\text{PF}_6]$.

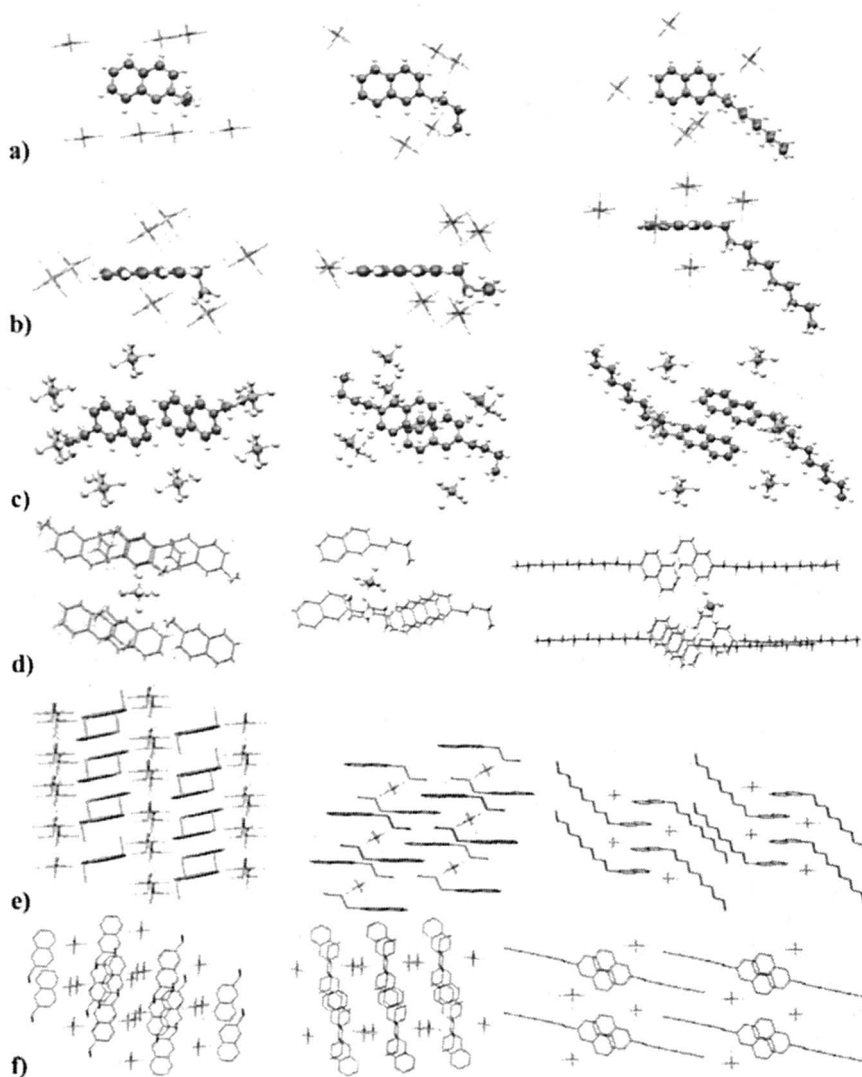


Figure 5. Close contact and packing diagrams of the cation environments top views (a), the cation environments side views (b), the π - π stacking (c), the anion environments (d), and packing diagrams (e, f).

With cation-anion interactions centered near the charge rich region of the cation (i.e., the carbon atoms nearest the nitrogen), the cations can and do pack with π - π interactions, something much less common in the imidazolium salts. In $[\text{C}_2\text{isoq}][\text{PF}_6]$, the π - π interactions occur on the back side between $\text{C5}\cdots\text{C6}$ at a distance of 3.54 Å (Figure 5c), while $[\text{C}_4\text{isoq}][\text{PF}_6]$ exhibits a more eclipsed interaction with partial overlap of the cations between $\text{C5}\cdots\text{C9}$ and $\text{C3}\cdots\text{C7}$ at 3.53 Å and with the C6 carbon residing over the nitrogen containing ring of the isoquinolinium cation at a distance of 3.74 Å. In $[\text{C}_{10}\text{isoq}][\text{PF}_6]$, the overlap is along the long edge between the $\text{C6}\cdots\text{C9}$ and $\text{C7}\cdots\text{C8}$ positions at a distance of 3.47 Å.

Solvent Properties

Liquid/liquid partitioning of a series of organic solutes between water and the series of ILs consisting of $[\text{C}_n\text{isoq}][\text{BETA}]$ (where $n = 6, 8, \text{ or } 14$) and, separately, $[\text{C}_8\text{isoq}]^+$ combined with $[\text{PF}_6]^-$, $[\text{NTf}_2]^-$, or $[\text{BETA}]^-$ (Figure 8) was carried out in order to determine the free energy of transfer of a methylene group (17,18) ($-\Delta G_{\text{CH}_2}$, a measure of the relative hydrophobicity of the phases) and linear solvation energy relationships (19,21) (LSERs, to describe the intermolecular forces in the form of solvent-solute interactions that control solute partitioning in various liquid/liquid systems). Previously, we (22,23) and others (24,25) have reported that solute partitioning in IL/aqueous systems generally follows the 1-octanol/water log P value with the most hydrophobic solutes having the highest affinity for an IL, and that in a series of [1-alkyl-3-methylimidazolium][PF_6] ($[\text{C}_n\text{mim}][\text{PF}_6]$) IL, the most hydrophobic IL will exhibit the highest distribution ratios for hydrophobic solutes.

Distribution ratio data can also be used to further evaluate the solvent properties, the underlying interactions, and the polarity of ILs. $[\text{C}_n\text{mim}][\text{X}]$ salts have been investigated with solvatochromatic dyes which give insight into specific interactions such as polarity and hydrogen bond character (14,26,27,28,29). Others have used the LSER method to model IL behavior using GC and HPLC (24,30,31). Literature reports suggest a range of polarity for the $[\text{C}_n\text{mim}]^+$ IL from more polar than acetonitrile (28) to similar to that of short chain alcohols (26). Variations in the $[\text{C}_n\text{mim}]^+$ cation and choice of anion also affect the polarity where, as observed by Carmichael, et al. (26), ILs with short alkyl chains ($n < 6$ or 8) are most affected by the anion, whereas the cation has more of an influence for longer alkyl chains where hydrophobic interactions tend to dominate.

The free energy of transfer of a methylene group ($-\Delta G_{\text{CH}_2}$), as developed by Zaslavsky (17,18,32), has also been proposed as a means to describe the relative hydrophobicity of biphasic systems and describes the cohesiveness of the solvent. It is a measure of the energy requirement involved in making a cavity in the non-aqueous phase. Traditionally, the partitioning of a series of dinitro-

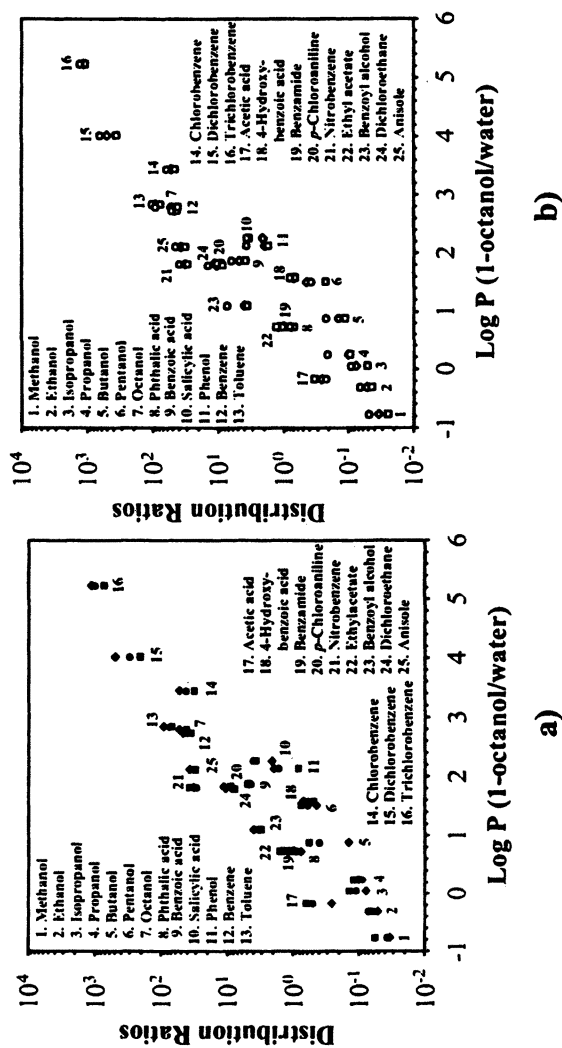


Figure 8. Distribution ratios for ¹⁴C-labeled organic solutes in a) [C₈isoq][X]/water (X = [PF₆]⁻, [NTf₂]⁻, [BETA]⁻, [NTf₂]⁺, [BETA]⁺, [NTf₂]⁺, [BETA]⁺), and b) [C₈isoq][BETA]/water (n = 6, □; n = 8, ○; n = 14, ◇) as a function of the solute's 1-octanol/water log P value.

phenylated amino acids with aliphatic appendages has been used in the calculations. We have previously used a series of normal alcohols with increasing numbers of methylene groups to characterize IL phase behavior (33).

The partitioning of a series of aliphatic alcohols (methanol, ethanol, propanol, isopropanol, butanol, pentanol, and octanol) is shown as part of the data in Figure 8. This subset of the data was plotted as $\ln D$ vs. the chain length of the n -alkyl substituent, and the slopes (E) of the resulting linear fits were used to calculate $-\Delta G_{\text{CH}_2}$ using eq. 2:

$$-\Delta G = RTE \quad (2)$$

where R is the universal gas constant and T is 298 K (Table III).

The data indicate that neither a change in the length of the alkyl chain appended to the cation, nor a change in the anion has a significant affect on the relative hydrophobicity of the system as measured in this fashion. The data do, however, seem to indicate that the magnitudes of the $-\Delta G_{\text{CH}_2}$ values for $[\text{C}_n\text{isoq}]^+$ ILs are larger than those for $[\text{C}_n\text{mim}]^+$ ILs, and thus the $[\text{C}_n\text{isoq}]^+$ ILs appear to be significantly more hydrophobic, as measured by the ease of relative cavity formation between the IL and water.

Table III. Extracting solvent systems compared by $-\Delta G_{\text{CH}_2}$

<i>Solvent system</i>	$-\Delta G_{\text{CH}_2}$ (kcal/mol)	<i>Water content</i> (ppm)
Hexane (32)	1.02	
Chloroform (32)	0.85	
Benzene (32)	0.84	
Octanol (32)	0.73	
Xylene (32)	0.64	
Methylethyl ketone (32)	0.43	
$[\text{C}_4\text{mim}][\text{PF}_6]$ (22)	0.45	11700
$[\text{C}_6\text{mim}][\text{PF}_6]$ (22)	0.50	8837
$[\text{C}_6\text{isoq}][\text{BETI}]$	0.62	16200
$[\text{C}_8\text{isoq}][\text{PF}_6]$	0.58	18500
$[\text{C}_8\text{isoq}][\text{NTf}_2]$	0.60	15600
$[\text{C}_8\text{isoq}][\text{BETI}]$	0.62	14900
$[\text{C}_{14}\text{isoq}][\text{BETI}]$	0.59	6100

While the $-\Delta G_{\text{CH}_2}$ values are an indication of the relative energy needed to create a cavity in the respective phases, the interactions that actually occur between solute and solvent are complex. A more detailed model of these interactions can be obtained by using linear solvation energy relationships

(LSERs). Although a more complete set of solutes would be desirable, the distribution ratios of all the organic solutes given in Figure 8 were used in an LSER model with Abraham's generalized solvation equation (19,20,21), eq. 3:

$$\text{Log } D = c + rR_2 + s\pi_2^H + a\Sigma a_2 + b\Sigma\beta_2 + vV_x \quad (3)$$

where D is the partition coefficient, R_2 is the solute's molar refractivity, π_2^H is a measure of the polarity/dipolarity of the solute, Σa_2 is the solute's hydrogen bond acidity, $\Sigma\beta_2$ is a measure of the solute's hydrogen bond basicity, and V_x is the solute's McGowan volume. The properties of the IL relative to water are obtained from multiple linear regression analysis which provides the coefficients: r , the ability of the IL to interact with π and non-bonding electrons, s , the IL's ability to interact with polar and dipolar solutes, a , the IL's hydrogen bond acceptor character, b , the IL's hydrogen bond donor character, and v , which can be thought of as the IL's molecular cohesion or the energy required to create a cavity in the solvent. The coefficient c is a constant. The sign and magnitude of the regression coefficients obtained from eq. 3 reflect the relative solvent properties of the two phases corresponding to the appropriate solute descriptors.

This analysis for the IL/aqueous systems studied here and select other systems is given in Table IV. The results indicate that the b coefficient, corresponding to the relative hydrogen bond acidity between the two phases, is the most important contributor to the overall fit (Table V). A comparison of these results to traditional organic solvents reveals that these ILs have similar hydrogen bond donor characteristics to octanol and chloroform.

The b term, a measure of the hydrogen bond donor ability of the IL, is the most important parameter in the LSER equation for the isoquinolinium ILs which exhibit higher values than the imidazolium ILs. Since these coefficients are negative, solutes with hydrogen bond acceptor character will partition to the water phase over the IL. The increase in these values for the isoquinolinium ILs indicate that they are poorer hydrogen bond donors than the corresponding imidazolium ILs. Solvents with similar b coefficients include hexadecyltrimethylammonium bromide and a non-ionic surfactant Brij-35 (36).

The volume parameter, v , is a measure of the relative energy needed to create a cavity in the solvents. A comparison of these values shows that the energy required to create a cavity in ILs, moderately structured liquids, is less than that of water, a highly ordered complex hydrogen bonded solvent. Based on the results presented here, the isoquinolinium ILs are less structured than their imidazolium counterparts, and an increase in anion size, $[\text{PF}_6]^- < [\text{NTf}_2]^- < [\text{BETA}]^-$, results in an increase in the volume parameter; indicating it is easier to form a cavity in the [BETA] ILs vs. the [PF₆] ILs.

Lastly, but no less significant is the increase in the s parameter. A comparison with other IL/water partitioning systems, shows an increase in this parameter for the isoquinolinium ILs over the imidazolium ILs indicating the

Table IV. Abraham's solvent descriptors for various solvent systems

<i>Solvent</i>	$r(R)$	$s(\pi_2^H)$	$a(\Sigma a_2^H)$	$b(\Sigma \beta_2^H)$	$v(V_x)$
Hexane (34)	0.58	-1.72	-3.60	-4.76	4.34
Octanol (20)	0.56	-1.05	0.03	-3.46	3.81
Benzene (35)	0.49	-0.60	-3.01	-4.63	4.59
Chloroform (34)	0.16	-0.39	-3.19	-3.42	4.19
[C ₄ mim][PF ₆] (22) ^b	0.63	-0.004	-1.82	-1.63	2.14
[C ₆ mim][PF ₆] (22) ^b	0.14	0.27	-1.48	-2.15	2.31
[C ₄ mim]Cl (31) ^c	0.24	2.24	7.03	-0.36	
[C ₄ mim][BF ₄] (31) ^c	0	1.65	2.22	-0.102	
[C ₄ mim][PF ₆] (31) ^c	0	1.91	1.89	0	
[C ₄ mim][NTf ₂] (31) ^c	0	1.89	2.02	0.36	
[C ₄ mim][PF ₆]/water (24) ^d	1.29	-0.73	-0.76	-2.39	0.64
[C ₄ mim][PF ₆]/heptane (24) ^d	3.28	-0.75	2.77	2.46	-2.80
[C ₈ isoq][PF ₆]	0.29	0.58	-1.03	-3.28	2.77
[C ₈ isoq][NTf ₂]	0.06	0.45	-0.87	-3.64	2.79
[C ₈ isoq][BETA]	0.24	0.29	-0.96	-3.73	2.93
[C ₆ isoq][BETA]	0.16	0.51	-0.97	-3.77	2.85
[C ₁₄ isoq][BETA]	0.61	0.11	-0.96	-3.52	2.81

^a Terms are defined in eq. 3. ^b Data obtained from solvent/water partitioning data. ^c Data obtained using GC at 40 °C. ^d Data obtained using a HPLC method to detect solutes partitioned in a liquid/liquid system.

Table V. Contribution of LSER coefficients to the overall fit and R²

<i>Coefficients</i>	[C ₆ isoq]- [BETA]	[C ₈ isoq]- [PF ₆]	[C ₈ isoq]- [NTf ₂]	[C ₈ isoq]- [BETA]	[C ₁₄ isoq]- [BETA]
<i>b</i>	0.590	0.573	0.608	0.604	0.613
<i>b + v</i>	0.907	0.901	0.928	0.929	0.924
<i>b + v + a + s + r</i>	0.925	0.924	0.942	0.946	0.934

increased ability of the isoquinolinium ILs to interact with non-bonding and π electrons. This increase is a reflection of the increase π system of the isoquinolinium cation and it is this increase in π interactions that make these ILs interesting as solvents for the separation of aromatic molecules.

A comparison of methods shows that in the GC method, the ILs have strong interactions with solutes possessing non-bonding or π electrons. The differences in magnitudes in the parameters may be indicative if the different relative interactions that are present between the IL and a gas phase in the GC method vs. between the IL and an aqueous phase in our liquid/liquid method.

Conclusions

Three series of hydrophobic IL based on a homologous series of *n*-alkyl-*N*-isoquinolinium cations and the anions [PF₆]⁻, [NTf₂]⁻, and [BETA]⁻ have been synthesized and characterized. All the salts are hydrophobic and melt below 100 °C and below room temperature for [C₈isoq][PF₆] and the [C_{*n*}isoq][NTf₂] and [C_{*n*}isoq][BETA] series, rendering them suitable candidates for further study in separations and synthetic chemistry.

Crystal structures of [C₂isoq][PF₆], [C₄isoq][PF₆], and [C₁₀isoq][PF₆] indicate Coulombic solids with enhanced π - π stacking over similar *N*-alkylmethylimidazolium salts. The cation-anion interactions tend to be localized to the charge bearing portion of the cation, which allows for the π - π interactions between the second aromatic ring of the isoquinolinium group. It is this type of interaction that offers unique opportunities for the separation of aromatic compounds in liquid/liquid systems of isoquinolinium ILs.

Not surprisingly, $-\Delta G_{\text{CH}_2}$ and LSER analyses indicate that the ILs present an environment more hydrophobic than water and that the ILs are much weaker hydrogen bond donors or acceptors than water. While there are small variations in the hydrophobicities, the data collected here, does not appear to have sufficient resolution to quantify these differences, and specific trends with IL cation or anion are difficult to discern. Thus, a change in either the alkyl chain length on the cation or the anion identity readily affects the measurable physical properties, while the chemical properties and molecular-level interactions are either much less affected or appear nearly the same because of the lack of resolution of the techniques used to study them.

Acknowledgements

This research has been supported by the U.S. Environmental Protection Agency's STAR program through grant number R-83143201 (Although the research described in this article had been funded in part by EPA, it has not been

subjected to the Agency's required peer and policy review and therefore does not necessarily reflect the views of the Agency and no official endorsement should be inferred.) and the U.S. Department of Energy, Division of Chemical Sciences, Geosciences, and Bioscience, Office of Basic Energy Research, (Grant DE-FG02-96ER14673). The authors would like to thank Merck KGaA/EMD Chemicals for support of the Center for Green Manufacturing.

References

1. Visser, A. E.; Holbrey, J. D.; Rogers, R. D. *Chem. Commun.* **2001**, 2484-2485.
2. Abraham, M. H. *Chem. Soc. Rev.* **1993**, *22*, 73-83.
3. Reichert, W. M.; Holbrey, J. D.; Swatloski, R. P.; Gutowski, K. E.; Visser, A. E.; Nieuwenhuyzen, M.; Seddon, K. R.; Rogers, R. D. *Cryst. Growth Des.* **2006**, submitted.
4. Huddleston, J. G.; Visser, A. E.; Reichert, W. M.; Willauer, H. D.; Broker, G. A.; Rogers, R. D. *Green Chem.* **2001**, *3*, 156-164.
5. Sheldrick, G. M., *Program for Semiempirical Absorption Correction of Area Detector Data*, University of Göttingen: Göttingen, Germany, 1996.
6. Sheldrick, G. M., SHELXTL, version 6.14; Siemens Analytical X-Ray Instruments Inc., 1996.
7. Gordon, C. M.; Holbrey, J. D.; Kennedy, A. R.; Seddon, K. R. *J. Mater. Chem.* **1998**, *8*, 2627-2636.
8. De Roche, J.; Gordon, C. M.; Imrie, C. T.; Ingram, M. D.; Kennedy, A. R.; Lo Ceslo, F.; Triolo, A. *Chem. Mater.* **2003**, *15*, 3089-3097.
9. Holbrey, J. D.; Seddon, K. R. *Clean Prods. Processes.* **1999**, *1*, 223-236.
10. Holbrey, J. D.; Seddon, K. R. *J. Chem. Soc., Dalton Trans.* **1999**, 2133-2139.
11. Chan, K. M. B.; Chang, N.; Grimmett, M. R. *Aust. J. Chem.* **1977**, *30*, 2005-2013.
12. Ngo, H. L.; LeCompte, K.; Hargens, L.; McEwen, A. B. *Thermochim. Acta*, **2000**, *357*, 97-102.
13. Holbrey, J. D. Seddon, K. R. *J. Chem. Soc., Dalton Trans.*, 1999, 2133-2140.
14. Bonhôte, P.; Dias, A-P.; Papageorgiou, N.; Kalyanasundaram, K.; Grätzel, M. *Inorg. Chem.*, **1996**, *35*, 1168-1178.
15. CCDC 629221 [C₂isoq][PF₆], 629222 [C₄isoq][PF₆], and 629223 [C₁₀isoq][PF₆], contain the supplementary crystallographic data for this paper. These data can be obtained free of charge from The Cambridge Crystallographic Data Centre via www.ccdc.cam.ac.uk/data_request/cif.
16. Rogers, R. D.; Visser, A. E.; Swatloski, R. P.; Hartman, D. H. In *Metal Ion Separations Technologies Beyond 2000. Integrating Novel Chemistry with*

- Processing*; Liddell, K. C.; Chaiko, D. J., Eds. The Minerals, Metals, and Materials Society Warrendale, PA 1999, 139-147. Gordon, C. M.; Holbrey, J. D.; Kennedy, A. R.; Seddon, K. R. *J. Mater. Chem.* 1998, 8, 2627-2636. De Roche, J.; Gordon, C. M.; Imrie, C. T.; Ingram, M. D.; Kennedy, A. R.; Lo Ceslo, F.; Triolo, A. *Chem. Mater.* 2003, 15, 3089-3097.
17. Zaslavsky, B. Y.; Gulaeva, N. D.; Djafarov, S.; Masimov, E. A.; Miheeva, L. M. *J. Colloid Interface Sci.* 1990, 137, 147-156.
 18. Zaslavsky, B. Y.; Miheeva, L. M.; Rogozhin, S. V. *J. Chromatogr.* 1981, 216, 13-22.
 19. Abraham, M. H. *Chem. Soc. Rev.* 1993, 22, 73-83.
 20. Abraham, M. H.; Chanda, S. H.; Whiting, G. S.; Mitchell, R. C. *J. Pharm. Sci.* 1994, 83, 1085-1100.
 21. Abraham, M. H.; Andonian-Haftvan, J.; Whiting, G. S.; Leo, A.; Taft, R. S. *J. Chem. Soc., Perkin Trans. 2* 1994, 8, 1777-1791.
 22. Huddleston, J. G.; Broker, G. A.; Willauer, H. D.; Rogers, R. D. In *Ionic liquids: Industrial Applications to Green Chemistry*; Rogers, R. D.; Seddon, K. R., Eds.; ACS Symposium Series 818; American Chemical Society: Washington, DC, 2002; pp 270-288.
 23. Abraham, M. H.; Zissimos, A. M.; Huddleston, J. H.; Willauer, H. D.; Rogers, R. D.; Acree Jr, W. E. *Ind. Eng. Chem. Res.* 2003, 42, 413-418.
 24. Carda-Broch, S.; Berthod, A.; Armstrong, D. W. *Anal. Bioanal. Chem.* 2003, 375, 191-199.
 25. Berthod, A. Carda-Broch, S. *Anal Bioanal Chem* 2004, 380, 168-177.
 26. Carmichael, A. J.; Seddon, K. R. *J. Phys. Org. Chem.* 2000, 13, 591-595.
 27. Baker, S. N.; Baker, G. A.; Bright, F. V. *Green Chem.* 2002, 4, 165-169.
 28. Aki, S. N. V. K.; Brennecke, J. F.; Samanta, A. *Chem. Commun.* 2001, 413-414.
 29. Oehlke, A.; Hofmann, K.; Spange, S. *New J. Chem.*, 2006, 30, 533-536.
 30. Anderson, J. L.; Armstrong, D. W. *Anal. Chem.* 2003, 75, 4851-4858.
 31. Anderson, J. L.; Ding, J.; Welton, T.; Armstrong, D. W. *J. Am. Chem. Soc.* 2002, 124, 14247-14254.
 32. Zaslavsky, B. Yu; Miheeva, L. M.; Rogozhin, S. V. *J. Chromatogr.* 1981, 216, 103-113.
 33. Gutowski, K. E.; Broker, G. A.; Willauer, H. D.; Huddleston, J. G.; Swatloski, R. P.; Holbrey, J. D.; Rogers, R. D. *J. Am. Chem. Soc.* 2003, 125, 6632-6633.
 34. Abraham, M. H.; Platts, J. A.; Hersey, A.; Leo, A. J.; Taft, R. W. *J. Pharma. Sci.* 1999, 88, 670-679.
 35. Abraham, M. H.; Chadha, H. S. In *Lipophilicity in Drug Action and Toxicology*; Pliska, V., Testa, B., van de Waterbeemb, H., Eds.; VCH: Weinheim, 1996; p 311-337.
 36. Rodrigues, M. A.; Alonso, E. O.; Yihaw, C.; Farah, J. P. S.; Quina, F. H. *Langmuir* 1999, 15, 6770-6774.

Author Index

- Abbott, Andrew P., 186
Awad, Walid H., 220
Billard, I., 247
Bissky, G., 320
Borissova, Maria, 35
Brennecke, Joan F., xi
Bueno, C., 308
Canongia Lopes, José N. A., 86
Carper, W. R., 21
Castro, S., 308
Chang, Ted, 47
Chiu, Yu-hui, 138
Crutchfield, Christopher, 47
Davis, Cher D., 220
De Long, Hugh C., 220
Dressler, Rainer A., 138
Du, Liying, 47
Eckert, Charles A., 198
Fernandez de la Mora, J., 308
Fox, Douglas M., 220
Fukumoto, Kenta, 351
Garoz, D., 308
Gerhard, Dirk, 258
Gilman, Jeffrey W., 220
Grätzel, Michael, 212
Hagiwara, R., 308
Hallett, Jason P., 198
Harris, Douglas, 47
Heimer, N. E., 21
Himmler, Simone, 258
Holbrey, John D., 362
Hörmann, Stefanie, 258
Huddleston, Jonathan G., 362
Ignat'ev, Nikolai V., 320
Ito, Seigo, 212
Jessop, Philip G., 198
Jiang, Wei, 272
Kagimoto, Junko, 351
Kaljurand, Mihkel, 35
Kamenetzky, Eduardo, 47
Kato, Takashi, 161
Kim, Neung Hyun, 234
Koel, Mihkel, 35
Kuang, Daibin, 212
Kucheryna, A., 320
Larriba, C., 308
Liotta, Charles L., 198
Liu, Zhiping, 70
Liu, Zhiwei, 335
Maginn, Edward J., 102
Malhotra, Sanjay V., 234
Matsumoto, K., 308
Maupin, Paul H., 220
McKenzie, Katy J., 186
Moncier, Regina M., 128
Moore, Preston B., 335
Morrow, Timothy I., 102
Moyna, Guillermo, 335
Mudring, A.-V., 172
Mukai, Tomohiro, 161
Nucciarone, Donato, 47
Ohno, Hiroyuki, 161, 351
Pádua, Agílio A. H., 86
Panak, P. J., 247
Piquette, Michael, 47
Reichert, W. Matthew, 362
Remsing, Richard C., 335
Rivera, Chermeine, 47
Robertson, Allan, 47
Rogers, Robin D., 362
Romero-Sanz, I., 308
Ryder, Karl S., 186

- Saito, G., 308
Schulz, Peter S., 258
Seddon, Kenneth R., xi
Stepnowski, Piotr, 2, 10
Stumpf, S., 247
Sutto, Thomas E., 220
Swatloski, Richard P., 362
Trulove, Paul C., 220
Tustin, Gerald C., 128
Visser, Ann E., 362
Voth, Gregory A., 272
- Wahlbeck, P. G., 21
Wang, Wenchuan, 70
Wang, Yanting, 272
Wasserscheid, Peter, 258
Wilkes, J. S., 21, 308
Willner, H., 320
Xanthos, Marino, 234
Yoshida, Y., 308
Yoshio, Masafumi, 161
Zakeeruddin, Shaik M., 212
Zoeller, Joseph R., 128

Subject Index

A

Ab initio calculations

- charge density in C₄mim⁺, 95*f*
- comparing main conformers around N1–C6 and C6–C7 bonds, 91*f*
- conformers, 90, 92

Abiotic conversions, ionic liquids, 15

Acetic acid

- demand, 128
- See also* Carbonylation of methanol

Acetonitrile

- excess molar enthalpies of 1-butyl-3-methylimidazolium tetrafluoroborate ([bmim][BF₄]) mixtures, 81*f*
- mixtures with [bmim][BF₄], 79, 80*t*, 82
- solvation structure of, in [bmim][PF₆], 98–99, 100*f*

Acetonitrile (ACN), additives 1-butyl-

- 3-methylimidazolium heptafluorobutanoate and 1-butyl-3-methylimidazolium trifluoroacetate, 41–42, 45

Actinide chemistry. *See* Solution chemistry of Cm(III) and Eu(III)

Aggregates, ionic liquids forming supramolecular, 21–22

Algal assays, ecotoxicology of ionic liquids, 16–17

1-Alkyl-3-methylimidazolium [PF₆]

- family, end-carbon radial distribution functions, 93, 94*f*, 95

1-Alkyl-3-methylimidazolium cation (amim)

- force field development, 71
- nomenclature, 87, 88*f*
- structure and atom type notations, 72*f*

n-Alkyl-*N*-isoquinolinium salts. *See*

- Hydrophobic *n*-alkyl-*N*-isoquinolinium ionic liquids

Alkylsulfate ionic liquids

- density, 264–265
- kinetics of transesterification and scale-up, 261–263
- physical-chemical properties of functionalized, 263–265
- proposed set-up for up-scaling transesterification, 262*f*
- quaternization step, 259–260
- synthesis of functionalized, 259–263
- transesterification step, 260–261
- viscosity, 263–264
- See also* Functionalized ionic liquids

Alkylsulfates ionic liquids, viscosity, 327, 328*t*

All-atom (AA) force field

- model, 71, 73
- schematic structure and atom type notations, 72*f*
- See also* Force field development; Molecular simulations of ionic liquids

Amino acid ionic liquids (AAILs)

- advantages of bio-related ionic liquids, 352
- ammonium cations, 353
- binary mixtures of, 354–355
- designer liquids, 352
- fully natural ionic liquids containing amino acids, 358–359
- histidine-derived zwitterion, 356–358
- imidazolium based, 353

- ionic conductivity and polarity of, mixtures, 355*f*
 - performance of zwitterion as ion conductive matrix, 357
 - physico-chemical properties of prepared onium-alanine salts, 354*t*
 - preparation, 353*f*
 - room temperature ILs composed of amino acid anions, 352–354
 - thermal properties of choline-based, 359*t*
 - zwitterions derived from amino acid, 355–358
 - Ammonium cations, amino acid ionic liquids, 353
 - Angle parameters, force field, 303
 - Anion functionalization. *See* Functionalized ionic liquids
 - Anionic clays. *See* Nanoclays
 - Anisotropic ionic conductivities, columnar ionic liquids, 166, 168
 - Arcjets, space propulsion, 142–143, 144*t*
 - Atomic polarizabilities, isotropic, 300
 - Atoms, partial charges, 300–302
- B**
- Binary mixtures, amino acid ionic liquids, 354–355
 - Bioavailability, ionic liquids, 14
 - Biodegradation, ionic liquids, 15
 - Bio-derived materials. *See* Amino acid ionic liquids (AAILs)
 - Bis[bis(pentafluoroethyl)phosphonyl]imides ionic liquids, viscosity, 329*t*
 - Bond parameters, force field, 303
 - 1-Butanol. *See* Molecular simulations of mixtures
 - 1-Butyl-3-methylimidazolium, main conformers, 88*f*
 - 1-Butyl-3-methylimidazolium bis(trifluoromethylsulfonyl)imide) (BumimTf₂N). *See* Solution chemistry of Cm(III) and Eu(III)
 - 1-*n*-Butyl-3-methylimidazolium chloride ([C₄mim]Cl)
 - 3D configuration probability distribution isosurfaces of anions and cations, 341*f*
 - cation-anion and cation-cation radial distribution functions (RDFs) for neat, 340*f*
 - cellobiose/[C₄mim]Cl simulations, 343–347
 - computed and experimental diffusion coefficients for ions in neat vs. temperature, 343*f*
 - density as function of computed temperature, 339*f*
 - dynamic properties in cellobiose/[C₄mim]Cl solutions, 347
 - dynamic properties of neat, 342–343
 - neat, simulations, 338–343
 - optimization of non-bonded parameters, 338–339
 - simulation details, 336–338
 - solute-solvent interactions, 343–346
 - solvent structuring in cellobiose/[C₄mim]Cl solutions, 346–347
 - structure and numbering of, and cellobiose, 337*f*
 - structure features of neat, 339–341
 - See also* Molecular dynamics (MD)
 - 1-Butyl-3-methylimidazolium tetrafluoroborate [bmim][BF₄]
 - excess molar volumes of mixtures with acetonitrile, 81*f*
 - mixtures with acetonitrile, 79, 80*t*, 82

C

Capillary electrophoresis

- analysis of ionic liquids, 6–7
- capillary coating procedure, 38–39
- electropherogram of 1-butyl-3-methyl-imidazolium ionic liquid, 8*f*
- ionic liquid-silica interaction, 36
- method for phenolic compound separation, 36

See also Silica gel modification

Carbonylation of methanol

- acetic acid, 128
- continuous vapor take-off, 131*f*
- experimental, 136–137
- heat removal, 129
- industrial process, 128
- issues for technology, 128–129
- nickel and cobalt catalysts, 133
- procedure, 136–137
- product/catalyst separation, 129
- rhodium catalysts, 130, 132
- water removal, 129

See also Vapor take-off reactors

Cationic clays. *See* Nanoclays

Cellobiose

- simulations of dissolution, 343–347
 - structure and numbering, 337*f*
- See also* 1-*n*-Butyl-3-methylimidazolium chloride ([C₄mim]Cl); Molecular dynamics (MD)

Center-of-mass, ion-ion radial

- distribution functions, 93, 94*f*

Charges, partial, of atoms, 300–302

Chemical modification, silica surface, 37–38

Chemical processes. *See* Solvents for chemical processes

Chemical shift anisotropy (CSA)

- aliphatic carbons, 24
- definition, 25

- evidence in cation and anion of 1-ethyl-3-methylimidazolium butanesulfonate, 29–30, 31*f*
- mechanism, 23–24

Choline-based, amino acid ionic liquids, 358–359

Choline chloride. *See* Metal electrodepositionChromatography. *See* Liquid chromatographyClays. *See* Nanoclays; Polymer-clay nanocomposites

"Clean" technology, chemicals, 11

Cluster ion formation, phosphonium ionic liquids, 55, 56*f*, 57*f*

Cobalt catalysts, methanol carbonylation, 133

Cohesive energy density, simulations of ionic liquids, 77*t*, 78–79

Colloid thruster

- electrospray thruster, 139
- parameters, 146*t*
- schematic, 145*f*

Columnar liquid crystalline

- imidazolium salts
- anisotropic ionic conductivities, 166, 168

illustration of columnar self-assembly of fan-shaped salts, 165*f*

- Im-*n* [1-methyl-3-{3,4,5-tris(alkyloxy)}benzylimidazolium tetrafluoroborate salts]
- molecular structure, 163*f*

macroscopic alignment of columns, 166

polarizing optical microscopic image and X-ray diffraction pattern of Im-8 in columnar hexagonal phase, 167*f*

polarizing optical microscopic images of oriented and self-assembled structures of Im-12 in hexagonal state, 167*f*

- synthesis and LC properties, 163, 165
- thermal properties of compounds
Im-*n*, 164*t*
- transition temperatures of Im-*n* vs. alkyl chain length of cation, 164*f*
- X-ray results of Im-*n* compounds, 165*t*
- Column packings
liquid chromatography, 5–6
separation of six ionic liquids, 6, 7*f*
- Composition, local, ionic fluid-butanol mixtures, 106–107
- Cones
cone-jet structure, 147*f*, 148
cone-jet term, 309
electrohydrodynamics of Taylor, 146–149
- Conformers. *See* Structures of ionic liquids
- Coordination, lanthanides in ionic liquids, 173–176
- Copper(II) cations
Eu(III) and Cm(III) fluorescence quenching in 1-butyl-3-methylimidazolium bis(trifluoromethylsulfonyl)imide [BumimTf₂N], 254–256
influence on Eu(III) fluorescence emission and Stern–Volmer plot, 255*f*
influence on fluorescence emission of aqueous Eu(III) and Cm(III), 248
See also Solution chemistry of Cm(III) and Eu(III)
- Coulombic interactions, atom-centered point charges, 71
- Coulombic law, interaction between ions in ionic liquids, 324–325
- Curium(III) chemistry. *See* Solution chemistry of Cm(III) and Eu(III)
- Cyanide displacement. *See* Nucleophilic substitution reactions
- Cyclic voltammetry studies, redox potential of lanthanides in ionic liquids, 182, 183*f*
- Cyclohexane, solvation structure of, in [C₄mim][PF₆], 98
- Cyclotella meneghiniana*, ecotoxicological assessment of ionic liquids, 17–18
- D**
- Degradation, phosphonium ionic liquids, 47–48
- Densities
n-alkyl-*N*-isoquinolinium ionic liquids, 367*t*
correlation between simulated, and carbon number of alkyl chain, 78*f*
ionic fluid-butanol mixtures, 106
mass, for ionic liquids, 287*f*
neat 1-*n*-butyl-3-methylimidazolium chloride vs. computed temperature, 339*f*
simulations of ionic liquids, 76, 77*t*
- Designer liquids
ionic liquids, 352
See also Amino acid ionic liquids (AAILs)
- Designer solvents, chemical industry, 11
- Diffusion
constants for various ionic liquids, 287*f*
Fick's first law, 321
local structure and, of ionic liquids, 279
mixtures of 1-butanol with ionic liquids, 121–123
See also Spatial heterogeneity in ionic liquids
- Diffusion coefficient, geometry of diffusion particles, 321–322

- Dihedral angle parameters, force field, 304
- Distribution ratios, *n*-alkyl-*N*-isoquinolinium ionic liquids, 366, 373, 374*f*
- Dye sensitized solar cell (DSC)
 amphiphilic sensitizer Z907Na, 213, 215*f*
 electrochemical impedance spectroscopy (EIS), 215, 217, 218*f*
 1-ethyl-3-methylimidazolium bis(trifluoromethyl sulfonyl)imide {EMITFSI}, 214, 215*f*
 experimental, 213–214
 impedance spectra of fresh cell and aging cell under light soaking, 218*f*
 mesoscopic, 213
 molecular structure of EMITFSI and Z907Na, 215*f*
 photocurrent density-voltage curves of EMITFSI with Z907Na and 3-phenylpropionic acid (PPA), 216*f*
 photovoltaic parameters of, based on Z907Na with or without PPA, 216*t*
 stability data of device with Z907Na and PPA during aging, 215, 217*f*
 structure, 214
- Dynamical properties, ionic systems, 285–286
- E**
- Ecotoxicology, ionic liquids, 16–18
- Efficiency
 electric propulsion, 143
 space propulsion performance, 141–142
- Electric propulsion
 discharge-free, 144–146
 electro spray thrusters, 144–146
 space, 142–143
- Electrochemical impedance spectroscopy (EIS)
 dye sensitized solar cells (DSC), 215, 217, 218*f*
 method, 214
- Electrohydrodynamics, Taylor cones, 146–149
- Electroosmotic flow (EOF), mobility, 41
- Electrophoretic mobility, effect of 1-butyl-3-methylimidazolium heptafluorobutanoate and 1-butyl-3-methylimidazolium trifluoroacetate on, of phenols, 43*f*
- Electrospray thruster, space propulsion, 139–140
- Energetics
 butanol and ionic fluids with [BF₄] anion, 114
 butanol and ionic fluids with bis(trifluoromethane-sulfonyl)imide [Tf₂N] anion, 120–121, 122*t*
- Enthalpies, excess molar, ionic liquids and mixtures, 79, 81*f*
- Enthalpy of vaporization, simulations of ionic liquids, 76, 77*t*, 78–79
- Environment
 risks of ionic liquids, 11
 sorption and stability of ionic liquids, 13–15
- Environmental samples, solid phase extraction of ionic liquids, 7–8
- Environmental systems, molecular interaction of ionic liquid cations, 12–13
- Error
 sources in relaxation analysis, 26
 surface tension measurement, 314
- 1-Ethyl-3-methylimidazolium alkylsulfates [EMIM][EtOSO₃]

- Arrhenius plot of transesterification with 1-hexanol and 1-butanol, 262*f*
- densities, 264–265
- kinetics of transesterification and scale-up, 261–263
- quaternization step, 259–260
- synthesis, 259–263
- transesterification step, 260–261
- viscosities, 263–264
- See also* Functionalized ionic liquids
- 1-Ethyl-3-methylimidazolium bis(trifluoromethyl sulfonyl)imide (EMITFSI)
- hydrophobic ionic liquid, 214
- structure, 215*f*
- See also* Dye sensitized solar cell (DSC)
- 1-Ethyl-3-methylimidazolium bis(trifluoromethylsulfonyl)imide [Emim][Im]
- causes of emission reduction, 156–157
- mixed ion-droplet regime, 155
- positive and negative ion mass spectra as function of emission angle, 153, 154*f*, 155
- propellant, 152–157
- retarding potential ion energy measurement, 155*f*
- time evolution of positive ion mass spectra on axis from vacuum electrospray, 156*f*
- See also* Ion field evaporation; Space propulsion
- 1-Ethyl-3-methylimidazolium butanesulfonate ([EMIM]BO₃)
- chemical shift values and carbon positions, 27*f*
- ¹³C NMR correlation times, 28–29, 30*f*
- ¹³C NMR total relaxation rates, 28, 29*f*
- evidence of chemical shift anisotropy in cation and anion, 29–30, 31*f*
- evidence of phase changes, 31
- initial successive approximation process, 27, 28*f*
- NMR correlation time relationship with viscosity, 32, 33*f*
- NMR relaxation measurements, 27
- 1-Ethyl-3-methylimidazolium cation, main conformers, 87, 88*f*
- 1-Ethyl-3-methylimidazolium nitrate [Emim][NO₃]
- field-evaporated negative ions, 158*f*
- field-evaporated positive ions, 157*f*
- propellant, 157–158
- See also* Ion field evaporation; Space propulsion
- 1-Ethyl-3-methylimidazolium tetrafluoroborate [Emim][BF₄]
- characteristics of mixtures of (C₂H₅)₃NH–Tf₂N and, vs. [Emim][BF₄], 312*t*
- potential in propulsion, 151–152
- See also* Ion field evaporation; Space propulsion
- Ethylene glycol. *See* Metal electrodeposition
- Europium(III) chemistry. *See* Solution chemistry of Cm(III) and Eu(III)
- Excess molar enthalpies, ionic liquids and mixtures, 79, 81*f*
- Excess molar volumes, ionic liquids and mixtures, 79, 81*f*

F

- Fick's first law, diffusion, 321
- Field-emission electric propulsion thrusters (FEEPs)
- discharge-free, 144–146
- parameters, 146*t*
- schematic, 145*f*

- Field evaporation. *See* Ions field evaporation
- Fluid structure, ionic fluid-butanol mixtures, 106–107
- Fluorescence. *See* Solution chemistry of Cm(III) and Eu(III)
- Fluorescent molecular rotor
 local dielectric using, 206, 208
 microviscosity using, 204–206, 207*f*
See also Nucleophilic substitution reactions
- Force field development
 all-atom (AA), 71, 73
 optimized geometries of [dmim][PF₆], 74*f*, 75*f*
 room temperature ionic liquids containing dialkylimidazolium cations, 71, 72*f*
 united-atom (UA) force field, 73, 75
See also Molecular simulations of ionic liquids
- Force field parameters
 angle, 303
 bond, 303
 dihedral, 304
 van der Waals, 305
- Fragmental methodology, predicting lipophilicity, 16, 17*f*
- Functionalized ionic liquids
 alcohols for transesterification of 1-ethyl-3-methylimidazolium ethylsulfate [EMIM][EtOSO₃], 260
 concepts for transesterification scale-up, 262*f*, 263
 density of functionalized alkylsulfates, 264–265
 hydroformylation of vinylsulfonate, 270
 hydrogenation of vinylsulfonate, 269
 ion exchange in dry acetone, 266
 ion exchange using ion exchange resin, 267
 kinetics of transesterification, 261, 262*f*
 physical-chemical properties of [EMIM] and [BMIM] vinylsulfonates, 267–268
 physical-chemical properties of functionalized alkylsulfates, 263–265
 quaternization step to functionalized alkylsulfates, 259–260
 synthesis of functionalized alkylsulfates, 259–263
 synthesis of vinylsulfonate ionic liquids, 265–267
 thermal properties of [EMIM] and [BMIM] vinylsulfonates, 267
 transesterification step to functionalized alkylsulfates, 260–261
 transformations of vinylsulfonate ionic liquids, 268–270
 viscosity of [EMIM] and [BMIM] vinylsulfonates, 268
 viscosity of functionalized alkylsulfates, 263–264
- ## G
- Geometry, diffusing particles, 321–322
- Gibbs free energy, planar and non-planar conformers, 90
- Glass transition temperature, *n*-alkyl-*N*-isoquinolinium ionic liquids, 368, 369*f*
- Green chemistry, goal, 11
- ## H
- Headgroup
 term, 280–281

- See also* Spatial heterogeneity in ionic liquids
- Heat removal, carbonylation of methanol, 129
- Heterogeneity order parameter (HOP)
 average HOP for ionic liquid systems with various alkyl-chain lengths, 291*f*
 average lattice HOP for tail groups, headgroups, and anions for different systems, 295*f*
 instantaneous HOP for atomic groups on cations in C₈ system, 292*f*
 instantaneous HOP for C₆ systems, 284*f*
 theory, 277–279
 three dimensional illustration of lattice HOP for tail groups and headgroups of C₂ and C₈, 294*f*
 uniformly distributed systems, 278*t*
See also Spatial heterogeneity in ionic liquids
- Heterogeneous way, capillary coating procedure, 38–39
- n*-Hexane, solvation structure of, in [C₄mim][PF₆], 98, 99*f*
- Histidine-derived zwitterion, 356–358
- Homogeneous way, capillary coating procedure, 39
- Hydrogen bond donors, mixing quaternary ammonium salts with, 187
- Hydrogen bonding, polar network in ionic liquids, 298–299
- Hydrophobic *n*-alkyl-*N*-isoquinolinium ionic liquids
 Abraham's solvent descriptors for solvent systems, 377*t*
n-alkyl-*N*-isoquinolinium ([C_{*n*}isoq]⁺) cation, 363
 asymmetric units of [C₂isoq][PF₆], [C₄isoq][PF₆], and [C₁₀isoq][PF₆], 371*f*
- close contact and packing diagrams, 372*f*
 crystallographic data, 370*t*
 density, 367*t*
 distribution ratios, 366, 374*f*
 experimental, 363–366
 extraction solvent systems compared by $-\Delta G_{\text{CH}_2}$, 375*t*
 free energy of transfer to methylene group ($-\Delta G_{\text{CH}_2}$), 373, 375
 general synthesis and metathesis, 367*f*
 glass transition temperatures, 369*f*
 interactions by linear solvation energy relationships (LSERs), 375–376
 LSER coefficients contribution, 377*t*
 melting point temperatures, 369*f*
 partitioning studies, 366
 physical properties, 366, 368
 physical property measurements, 364–365
 single crystal X-ray diffraction (XRD) studies, 368, 371, 373
 solvent properties, 373, 375–378
 synthesis of [C_{*n*}isoq][BETA], 364
 synthesis of [C_{*n*}isoq][NTf₂], 364
 synthesis of [C_{*n*}isoq][PF₆], 364
 synthesis of [C_{*n*}isoq]Cl salts, 363–364
 thermogravimetric analysis, 369*f*
 water content, 367*t*
 X-ray diffraction methods, 365–366
- Hypotalcite (HT)
 anionic clays, 243–244
 calcined HT (CHT), 236–237
 ionic liquids as organic modifiers of, 237*t*
 modification with ionic liquids, 237, 238*t*
 thermal stability, 245*f*
 wide angle X-ray diffraction, 245*f*
See also Nanoclays

I

Imidazolium ionic liquids

- amino acid ionic liquids, 353
- analysis by capillary electrophoresis, 6–7
- analysis by liquid chromatography (LC), 3–6
- atom number scheme for 1-butyl-3-methylimidazolium [bmim] cations, 104*f*
- biodegradation and abiotic conversions, 15
- chromatogram of [bmim] entity and degradation products, 6*f*
- chromatogram of separation of six, on SG–C4 stationary phase, 6, 7*f*
- clay modification, 235–236
- common examples, 11*f*
- electropherogram of [bmim] ionic liquid, 8*f*
- ion chromatography, 5
- isocratic separation of, cations, 4*f*
- packings with cholesterol ligands chemically bonded to silica and mixed stationary phases, 5–6
- solid phase extraction from environmental samples, 7–8
- See also* Molecular simulations of ionic liquids; Molecular simulations of mixtures; Nanoclays

Imidazolium salts. *See* Columnar liquid crystalline imidazolium salts

Impedance spectroscopy

- dye sensitized solar cells, 215, 217, 218*f*
- method, 214

Impurity detection, phosphonium

- ionic liquid by ^{31}P NMR, 52, 54*f*

Inter-molecular energies, simulations

- of ionic liquids, 76, 77*t*, 78–79

Intermolecular structure. *See*

- Structures of ionic liquids

Intramolecular structure. *See*

- Structures of ionic liquids

Ion chromatography

- ionic liquid separation, 5
- residual chloride analysis of phosphonium ionic liquids, 63, 66*t*

Ion exchange, preparation of

- montmorillonite clay, 223*f*

Ion field evaporation

- causes of emission reduction, 156–157

1-ethyl-3-methylimidazolium

- bis(trifluoromethylsulfonyl)imide [Emim][Im], 152–157

1-ethyl-3-methylimidazolium

- nitrate [Emim][NO₃], 157–158

1-ethyl-3-methylimidazolium

- tetrafluoroborate [Emim][BF₄], 151–152

field-evaporated negative ions on

- and off-axis for [Emim][NO₃], 158*f*

field-evaporated positive ions on

- and off-axis for [Emim][NO₃], 157*f*

instrument to study, from ionic

- liquids, 150*f*

mass spectrometric experiment,

- 150–151

mixed ion-droplet regime, 155

- positive and negative ion mass spectra of [Emim][Im] as function of emission angle, 153, 154*f*, 155

positive ion mass spectra of

- [Emim][BF₄] as function of emission angle, 153*f*

retarding potential ion energy

- measurement of Emim⁺ ions, 155*f*

theory, 148–149

- time evolution of positive ion mass spectra on axis from

- [Emim][Im] vacuum electro spray, 156*f*
See also Space propulsion
- Ionic character. *See* Viscosity of ionic liquids
- Ionic liquid ion sources (ILIS), Taylor cones, 315, 317
- Ionic liquids
 abiotic conversions, 15
 algal assays, 16–17
 alternative solvents, 11
 bioavailability, 14
 biodegradability, 15
 capillary electrophoresis, 6–7
 cation/anion selection, 258
 common examples, 11*f*
 green algae in ecotoxicological assessment, 17*f*, 18
 ideal candidates for micro-electric propulsion, 139
 lipophilicity and ecotoxicology, 16–18
 liquid chromatography, 3–6
 liquid crystalline materials, 162
 molecular interactions in environmental systems, 12–13
 neoteric solvents, 3
 photodegradation, 14
 physical constants and temperature for Taylor cones, 311*t*
 potential molecular interactions of cations, 12*f*
 reversible, 208–209
 room temperature properties, 312*t*
 side chain length effect, 16
 solid phase extraction from environment, 7–8
 sorption and stability in environment, 13–15
 sorption coefficients and desorption characteristics, 14*t*
 supramolecular aggregates, 21–22
 theoretical prediction of lipophilicity using fragmental methodology, 16, 17*f*
 vapor take-off solvents, 130
See also Amino acid ionic liquids (AAILs); Carbonylation of methanol; Functionalized ionic liquids; Molecular simulations of ionic liquids; Solution chemistry of Cm(III) and Eu(III); Space propulsion; Spatial heterogeneity in ionic liquids; Structures of ionic liquids; Viscosity of ionic liquids
- Ion sources. *See* Taylor cones
- Iridium catalysts, methanol carbonylation, 132
- Isoquinolinium-based ionic liquids. *See* Hydrophobic *n*-alkyl-*N*-isoquinolinium ionic liquids
- Isotropic atomic polarizabilities, 300
- ## L
- Lanthanide chemistry
 absorption spectra of NdBr₃ and Nd(OTf)₃ in ionic liquids, 178*f*
 absorption spectrum of NdI₃ in [C₁₂mim] bis(trifluoromethanesulfonyl) imide [Tf₂N], 178*f*
 cisoid and transoid conformations, 174, 176
 coordination environment for Pr–Tb in [bmpyr]₂[Ln(Tf₂N)₅] and Dy–Lu in [bmpyr][Ln(Tf₂N)₄], 175*f*
 dependence of Sm³⁺/Sm²⁺ redox potential on counterion of ionic liquid, 183*f*
 dissolution and solvation of simple inorganic compounds, 173
 emission spectra of solution of Pr(Tf₂N)₃ and Pfl₃ in ionic liquid and solid compounds, 180*f*, 181*f*

- lanthanide and alkaline earth iodides in pyrrolidinium bis(trifluoromethanesulfonyl)amides, 174*f*
- low valent lanthanides in ionic liquids, 179, 182
- luminescence spectroscopy, 177, 179
- optical properties, 176–177, 179
- oxygen atoms of Tf_2N ligand coordinating trivalent cations, 174, 175*f*
- reduction reactions, 179, 182
- solvation and coordination of lanthanide cations in ionic liquids, 173
- trivalent lanthanides in ionic liquids, 173–176
- See also* Solution chemistry of Cm(III) and Eu(III)
- Lipophilicity, ionic liquids, 16–18
- Liquid chromatography
- analysis of ionic liquids, 3–6
 - column packings, 5–6
 - effect of pH and polarity on retention times in water/acetonitrile, 62*t*
 - isocratic separation of imidazolium cations, 4*f*
 - mobile phase for HPLC, 58, 61
 - phosphonium ionic liquids, 58, 59*f*, 60*f*
 - sensitivity and linearity of LC/MS, 61, 62*t*, 63*f*
- Liquid crystalline (LC) materials
- ionic liquids, 162
 - See also* Columnar liquid crystalline imidazolium salts
- Liquid metal ion source (LMIS), metal systems, 309, 315
- Local composition, ionic fluid-butanol mixtures, 106–107
- Local composition functions
- butanol and ionic fluids with $[BF_4]$ anion, 110, 111*f*, 112, 113*f*
 - butanol and ionic fluids with bis(trifluoromethane-sulfonyl) imide $[Tf_2N]$ anion, 117, 118*f*, 119*f*, 120, 121*f*
- Local structure
- diffusion and, of ionic liquids, 279
 - See also* Spatial heterogeneity in ionic liquids
- Low melting solids. *See* Hydrophobic *n*-alkyl-*N*-isoquinolinium ionic liquids
- Luminescence spectroscopy, lanthanides in ionic liquids, 177, 178*f*, 179

M

- Mass spectrometry (MS)
- experiment studying field evaporation from ionic liquids, 150–151
 - identification of IL anions from MS cluster ion, 61, 63, 64*f*, 65*f*
 - phosphonium ionic liquids, 55, 56*f*
 - See also* Ion field evaporation
- Mass transfer effects, vapor take-off reactor, 133–134
- Mechanism
- behavior of ionic liquids with varying lengths of cationic side chain, 294, 296–298
 - See also* Spatial heterogeneity in ionic liquids
- Melt blending, polymer-clay nanocomposites, 222–223
- Melting point temperature, *n*-alkyl-*N*-isoquinolinium ionic liquids, 368, 369*f*
- Metal electrodeposition
- absorption of water into choline chloride/ethylene glycol (Ethaline 200) vs. time and temperature, 191*f*

- application of Ethaline 200, 187, 189
- bulk deposition of zinc from ethylene glycol (EG) and urea based liquids, 195
- cyclic voltammograms of $ZnCl_2$ and $SnCl_2$ in choline chloride/urea and EG mixtures, 194*f*
- electroplating of alloys, 192–195
- electropolishing, 188–192
- Ethaline 200 samples containing electropolishing residue, 192*f*
- experimental, 187–188
- impedance spectroscopy, 188
- linear sweep voltammograms for stainless steel wire disc electrode immersed in sulphuric/phosphoric acid and abraded in choline chloride/EG, 189*f*
- morphologies and compositions of deposits by urea and EG solutions, 195*t*
- pilot plant operation, 190, 191*f*
- scale-up of electropolishing, 190, 191*f*
- surface analysis methods, 188
- Methanol
- commercial carbonylation, 128, 134
- solvation structure of, in $[C_4mim][PF_6]$, 99, 100*f*
- See also* Carbonylation of methanol
- Micro-machined (MEMS) arrays, electrospray thrusters, 139–140
- Microscopic structures, ionic liquids, 82, 84*f*
- Missions, space propulsion, 140–141
- Mixtures. *See* Molecular simulations of mixtures
- Molecular dynamics (MD)
- 3D configuration probability distribution isosurfaces of $[C_4mim]Cl$ anions and cations, 341*f*
- average mean square displacements (MSDs) for cations and anions vs. time for neat $[C_4mim]Cl$, 342*f*
- cation-anion and cation-cation radial distribution functions (RDFs) for neat $[C_4mim]Cl$, 340*f*
- cation-anion RDFs for neat $[C_4mim]Cl$ and cellobiose/ $[C_4mim]Cl$ solutions, 346*f*
- cellobiose/ $[C_4mim]Cl$ simulations, 343–347
- comparing main conformers around N1–C6 and C6–C7 bonds, 91*f*
- computed and experimental diffusion coefficients for ions in neat $[C_4mim]Cl$ vs. temperature, 343*f*
- conformers, 89, 92
- density of neat $[C_4mim]Cl$ vs. temperature computed from, 339*f*
- dihedral distributions along alkyl chain of 1-alkyl-3-methylimidazolium cations, 89, 92
- dynamic properties of cellobiose/ $[C_4mim]Cl$ solutions, 347
- dynamic properties of neat $[C_4mim]Cl$, 342–343
- geometry of hydrogen bonds, 345
- neat $[C_4mim]Cl$ simulations, 338–343
- OH \cdots Cl RDFs and coordination numbers for cellobiose/ $[C_4mim]Cl$ solutions, 344*f*
- optimization of non-bonded parameters for neat $[C_4mim]Cl$, 338–339

- probability distribution of O–H···Cl angles in cellobiose/[C₄mim]Cl solutions, 345*f*
- procedure, 279–280
- simulation details, 336–338
- solute-solvent interactions, 343–346
- solvent structuring in cellobiose/[C₄mim]Cl solutions, 346–347
- structural features of neat [C₄mim]Cl, 339–341
- structure and numbering of [C₄mim]Cl and cellobiose, 337*f*
- See also* Molecular simulations of ionic liquids; Spatial heterogeneity in ionic liquids; Structures of ionic liquids
- Molecular interactions, ionic liquid cations in environmental systems, 12–13
- Molecular modeling. *See* Structures of ionic liquids
- Molecular simulations of ionic liquids
- cohesive energy density, 77*t*, 78
- densities, 76, 77*t*, 78*f*
- distribution contour surfaces of [bmim]⁺, [BF₄][−] and CH₃CN molecules, 82, 84*f*
- enthalpy of vaporization, 77*t*, 78
- excess volumetric and energetic properties, 79, 81*f*
- inter-molecular energies, 76, 77*t*, 78–79
- macro-properties from all-atom (AA) and united-atom (UA) force field, 75–76
- microscopic structures, 82, 84*f*
- mixtures of [bmim][BF₄] and acetonitrile, 79, 82
- pure ionic liquids, 76, 77*t*
- sizes of systems and results for [bmim][BF₄] and acetonitrile mixture, 80*t*
- viscosities, 79, 82, 83*f*
- Molecular simulations of mixtures
- association factors for B – O^{Al} atom pairs, 111*f*
- association factors for H-C_# – O^{Al} atom pairs, 111*f*
- association factors for H-C_# – O^{Al} atom pairs, 118*f*
- association factors for O[−] – O^{Al} atom pairs, 118*f*
- atom-atom radial distribution functions (rdfs) for B – O^{Al} atom pairs, 108*f*
- atom-atom rdfs for H-C_# – B atom pairs, 109*f*
- atom-atom rdfs for H-C_# – O^{Al} atom pairs, 108*f*, 115*f*
- atom-atom rdfs for N[−] – O^{Al} atom pairs, 116*f*
- atom-atom rdfs for O[−] – O^{Al} atom pairs, 116*f*
- atom-atom rdfs for O^{Al} – O^{Al} atom pairs, 110*f*, 117*f*
- atom numbering scheme for [bmim] and [bmpy] cations, 104*f*
- [bmim][BF₄] and acetonitrile, 79, 82
- center-of-mass association BuOH–BuOH self association factors, 121*f*
- center-of-mass association factors for BuOH–BF₄, BuOH–bmim, and BuOH–bmpy pairs for IL-rich and butanol-rich phases, 113*f*
- center-of-mass association factors for BuOH–Tf₂N, BuOH–bmim, and BuOH–bmpy pairs, 119*f*
- contribution of butanol–butanol, butanol–ion, and ion–ion interactions to total potential energy for IL-rich phases, 114*t*, 122*t*
- densities, 106

diffusion, 121–123
 energetics, 114, 120–121
 fluid structure and local
 composition, 106–107
 isothermal-isobaric (NPT)
 ensemble, 103, 104
 local composition functions, 110,
 112, 117, 120
 methodology, 103–105
 mixtures with [BF₄] anion, 107–
 114
 mixtures with bis(trifluoromethane-
 sulfonyl) imide [Tf₂N] anion,
 115–121
 radial distribution functions (rdfs),
 107–109, 115
 self-diffusion coefficients for
 cation, anion and 1-butanol,
 123*t*
 thermodynamic state points,
 105*t*
 upper critical solution temperature
 (UCST), 103
Montmorillonite (MMT)
 characterization, 237, 239
 commonly used silicate, 221–
 222
 EDX results of MMTs modified
 with ionic liquids, 243*t*
 Fourier transform infrared spectra
 of modified, 240*f*, 241*f*
 ion exchange, 223*f*
 ionic exchange of, 237, 238*t*
 modification, 235–236
 modified MMTs with ionic liquids,
 238*t*
 schematic, 222*f*
 thermal stability of modified, 239,
 241*f*, 242*f*
 wide angle X-ray diffraction of
 modified, 239, 242*f*
See also Nanoclays; Polymer-clay
 nanocomposites

N

Nanoclays

anionic clays, 243–244
 cationic clays, 239, 243
 characterization of clays and ionic
 liquids (ILs), 237, 239
 description of hydrotalcite (HT)
 and calcined HT (CHT)
 modified with ILs, 238*t*
 d-spacing of IL modified clays,
 239, 242*f*
 EDX results of MMTs modified
 with ILs, 243*t*
 experimental, 236–239
 Fourier transform infrared (FTIR)
 spectra of modified clays and
 ILs, 240*f*, 241*f*
 ILs as modifiers, 235–236, 237*t*
 materials, 236–237
 modification, 235
 modification of clays, 237
 montmorillonites (MMTs)
 modified with IL, 238*t*
 TGA (thermogravimetric analysis)
 of HT and CHT, 243–244, 245*f*
 TGA of modified clays and ILs,
 241*f*, 242*f*
 thermal stability, 239
 wide angle X-ray diffraction
 (WXRD), 239
 WXRD of modified MMTs and
 ILs, 242*f*
 WXRD results for HT, CHT, and
 ILs, 244, 245*f*
Nanocomposites. *See* Polymer-clay
 nanocomposites
Nanostructures
 aggregation of [C₄mim][PF₆] side
 chains, 96
 experimental evidence, 97
 ionic liquids, 93, 95–97
 medium-range ordering, 96–97

- simulation boxes of $[C_n\text{mim}][PF_6]$, 96*f*
See also Structures of ionic liquids
- Natural ionic liquids, amino acid-based, 358–359
- Nickel catalysts, methanol carbonylation, 133
- Nuclear magnetic resonance (NMR)
 basic assumptions, 26
 ^{13}C NMR correlation times for 1-ethyl-3-methylimidazolium butanesulfonate ([EMIM]BSO₃) cation and anion, 28–29, 30*f*
 ^{13}C NMR chemical shift anisotropy (CSA) for [EMIM]BSO₃ vs. temperature, 31*f*
 ^{13}C NMR relaxation studies, 22
 ^{13}C NMR total relaxation rates for [EMIM] cation and anion, 28, 29*f*
 chemical shift values and C positions for [EMIM]BSO₃, 27*f*
 CSA, 23–24, 25
 error sources in NMR relaxation analysis, 26
 evidence of CSA in cation and anion of [EMIM]BSO₃, 29–30
 evidence of phase changes from viscosity and NMR data, 31
 initial successive approximation process for C2 carbon in [EMIM]BSO₃, 27, 28*f*
 measurements, 22
 NMR correlation time relationship with viscosity, 32, 33*f*
 nuclear Overhauser effect (NOE), 23
 relaxation measurements, 27
 relaxation via CSA mechanism, 23–24
 solution of combined dipolar and NOE equations, 24–25
 sources of error, 26
 spectral densities, 23
- Nuclear Overhauser effect (NOE), theory, 23
- Nucleophilic substitution reactions
 1-butyl-3-methylimidazolium hexafluorophosphate [bmim][PF₆], 201*f*
 conversion of benzyl chloride to benzyl cyanide, 202*f*
 cyanide displacement on benzyl chloride, 201*f*
 experimental, 199–200
 ionic liquids, 201–203
 local dielectric using fluorescent molecular rotor, 206, 208
 microviscosity using fluorescent molecular rotor, 204–206
 physical property measurements, 200–201, 203–204
 rate constants for reaction of benzyl chloride with KCN, 202*t*
 reversible ionic liquids, 208–209
See also Solvents for chemical processes
- O**
- Oocystis submarina*, ecotoxicological assessment of ionic liquids, 17–18
- Optical properties
 lanthanides in ionic liquids, 176–177, 179
 luminescence of NdBr₃ and Nd(OTf)₃, 177, 178*f*
 luminescence of NdI₃, 177, 178*f*
- Organically modified silicates. *See* Polymer-clay nanocomposites
- P**
- Partial charges, atoms, 300–302
- Partitioning studies, *n*-alkyl-*N*-isoquinolinium ionic liquids, 366, 373, 375–378

- (Perfluoroalkyl)fluorophosphate (FAP) ionic liquids, viscosity, 325–326, 327*t*
- Perfluoroalkylborates ionic liquids, viscosity, 330*t*
- Phase changes, evidence from viscosity and NMR, 31
- Phenol compounds
effect of 1-butyl-3-methylimidazolium heptafluorobutanoate and 1-butyl-3-methylimidazolium trifluoroacetate on electrophoretic mobility, 43*f*
performance of, separation in uncoated and coated capillaries, 44*f*
- Phenolic compounds, capillary electrophoresis for separation, 36
- Phosphonium ionic liquids
applications, 47, 48
cluster ions, 55, 56*f*, 57*f*
commercial availability, 48, 49*t*
degradation studies, 47–48
demand, 47
effect of pH and polarity on retention times in water/acetonitrile system, 62*t*
experimental, 66–67
identification of IL anions from MS cluster ion, 61, 63, 64*f*, 65*f*
liquid chromatography/mass spectrometry (LC/MS), 58, 59*f*, 60*f*
mass spectrometry of, 55, 56*f*
mobile phase for high performance liquid chromatography (HPLC), 58, 61
³¹P nuclear magnetic resonance (NMR) spectroscopy, 52, 53*f*, 54*f*
residual chloride analysis, 63, 66*t*
sensitivity and linearity of LC/MS, 61, 62*t*, 63*f*
thermogravimetric analysis (TGA), 49, 50*f*, 51*f*, 52
- Phosphorus-31 nuclear magnetic resonance (NMR)
detection of impurity in phosphonium ionic liquid, 52, 54*f*
phosphonium ionic liquids, 52, 53*f*
- Photodegradation, ionic liquids, 14
- Polarizable atomistic models
theory, 275–276
See also Spatial heterogeneity in ionic liquids
- Polar networks, hydrogen bonding, 298–299
- Polymer-clay nanocomposites
experimental, 225–226
imidazolium treated layered silicates, 226, 228
instrumentation, 225–226
ion exchange with organic modifier for preparation of treated montmorillonite (MMT) clay, 223*f*
materials, 225
melt blending preparation of polymer-layered silicate nanocomposite, 222–223
molecular representation of sodium MMT, 221*f*
montmorillonite (MMT), 221–222
nomenclature, 226*t*
polymer treated silicate nanocomposites, 228, 231
preparation methods, 222–223
structure of fully exfoliated, 224*f*
thermal stability, 224
transmission electron microscopy (TEM) images of modified-MMT nanocomposites, 230*f*
X-ray diffraction (XRD) of effect of imidazolium alkyl chain length on d spacing, 227*f*
XRD and TGA data for 1,2-dimethyl-3-R-imidazolium and

quaternary ammonium treated
MMT clays, 227*t*
XRD data for modified-MMT
treated clays before and after
melt blending, 229*f*
Prediction, lipophilicity using
fragmental methodology, 16,
17*f*
Product/catalyst separation,
carbonylation of methanol, 129
Propulsion. *See* Space propulsion
Pyridinium-based ionic liquids
atom numbering scheme for
pyridinium cations, 104*f*
clay modification, 235–236
See also Molecular simulations of
mixtures; Nanoclays

R

Radial distribution functions (rdfs)
butanol and ionic fluids with [BF₄]
anion, 107–109, 110*f*
butanol and ionic fluids with
bis(trifluoromethane-sulfonyl)
imide [Tf₂N] anion, 115, 116*f*,
117*f*
liquid structure, 93, 94*f*
Radioactive waste
management, 248
See also Solution chemistry of
Cm(III) and Eu(III)
Raman spectroscopy
comparing main conformers around
N1–C6 and C6–C7 bonds,
91*f*
planar and non-planar conformers,
90
Reactions. *See* Solvents for chemical
processes
Reactors. *See* Vapor take-off reactors
Reduction reactions, low valent
lanthanides in ionic liquids, 179,
182

Relaxation studies
combined dipolar and nuclear
Overhauser effect (NOE)
equations, 24–25
error sources, 26
See also Nuclear magnetic
resonance (NMR)
Residual chloride analysis,
phosphonium ionic liquids, 63, 66*t*
Reversed phase chromatography, ionic
liquid analysis, 5
Rhodium catalysts
experimental, 136–137
methanol carbonylation, 130, 132
reactions in stirred vapor takeoff
reactor, 135*t*
See also Vapor take-off reactor
Room temperature ionic liquids. *See*
Molecular simulations of ionic
liquids

S

Self-assembled structures
columnar ionic liquids, 162
See also Columnar liquid
crystalline imidazolium salts
Self-diffusion coefficients
cation, anion, and 1-butanol of
mixtures, 123*t*
equation, 121
Side chain length effect, ionic liquid
cations and anions, 16
Silica gel modification
apparatus, 37
capillary coating procedure, 38–39
capillary electrophoresis (CE) of
ionic liquid (IL)-silica
interaction, 36
chemical modification of surface,
37
coating, 36
comparing capillaries by
homogeneous and

- heterogeneous modifications, 40*t*
- effect of 1-butyl-3-methylimidazolium heptafluorobutanoate and 1-butyl-3-methylimidazolium trifluoroacetate on electrophoretic mobility of phenols, 43*f*
- effect of IL concentration in buffer, 41–42, 45
- electroosmotic flow (EOF) mobility, 41
- EOF measurements and zeta-potentials in HO coated capillary, 41
- experimental, 37–39
- heterogeneous way (HE), 38–39
- homogeneous way (HO), 39
- masking negative charge of fused capillary surface, 36
- performance of phenols separation in uncoated and HO coated capillary, 44*f*
- permanent coatings, 37
- physiochemical properties of organic solvents, 42*t*
- surface characterization, 40–41
- traditional physical methods for measuring changes, 36
- xerogels, 35
- Simulations**
- boxes of [C_nmim][PF₆], 96*f*
- solvation of acetonitrile in [C₄mim][PF₆], 98–99, 100*f*
- solvation of cyclohexane in [C₄mim][PF₆], 98
- solvation of methanol in [C₄mim][PF₆], 99, 100*f*
- solvation of *n*-hexane in [C₄mim][PF₆], 98, 99*f*
- See also* Molecular dynamics (MD); Molecular simulations of ionic liquids; Structures of ionic liquids
- Solar cells. *See* Dye sensitized solar cell (DSC)
- Solid phase extraction, ionic liquids from environment, 7–8
- Solids, low melting. *See* Hydrophobic *n*-alkyl-*N*-isoquinolinium ionic liquids
- Solution chemistry of Cu(III) and Eu(III)
- biexponential decay behavior of Cm(III) fluorescence emission in 1-butyl-3-methylimidazolium bis(trifluoromethylsulfonyl)imide [BumimTf₂N], 254*f*
- biexponential decay behavior of Eu(III) fluorescence emission in BumimTf₂N, 254*f*
- comparing aqueous and reactions in BumimTf₂N, 248
- emission spectra of Eu(III) at different Cu(II) concentrations, 252*f*
- Eu(III) and Cm(III) fluorescence quenching by Cu(II) in BumimTf₂N, 254–256
- Eu(III) and Cm(III) fluorescence quenching by Cu(II) in water, 250–251
- Eu(III) and Cm(III) solvation in BumimTf₂N, 251, 253
- experimental, 249–250
- experimental method time resolved laser fluorescence spectroscopy (TRLFS), 248
- influence of Cu(II) on Eu fluorescence emission, 255*f*
- measurements in BumimTf₂N, 249–250
- measurements in water, 249
- Stern–Volmer equation describing quenching process, 250–251

- Stern–Volmer plot for Eu(III) emission spectra, 252*f*
- Stern–Volmer plot of Cm(III) fluorescence quenching by Cu(II), 253*f*
- Stern–Volmer plot of Cu(II) influence on Eu fluorescence emission, 255*f*
- TRLFS method, 250
- Solvation, lanthanides in ionic liquids, 173–176
- Solvation structure
- acetonitrile in [C₄mim][PF₆], 98–99, 100*f*
 - cyclohexane in [C₄mim][PF₆], 98
 - n*-hexane in [C₄mim][PF₆], 98, 99*f*
 - methanol in [C₄mim][PF₆], 99, 100*f*
- Solvent properties, *n*-alkyl-*N*-isoquinolinium ionic liquids, 373, 375–378*f*
- Solvents for chemical processes
- 1-butyl-3-methylimidazolium hexafluorophosphate [bmim][PF₆], 201*f*
 - conversion of benzyl chloride to benzyl cyanide, 202*f*
 - cyanide displacement on benzyl chloride, 201*f*
 - dipolarity/polarizability for organic solvents and [bmim][PF₆] vs. CO₂ pressure, 205*f*
 - estimated dielectric constants for [bmim][PF₆]/CO₂ vs. CO₂ pressure, 208*f*
 - experimental, 199–201
 - fluorescence emission maximum of fluorescent molecular rotor (DCVJ) correlation with dielectric constant for alcohols, 208*f*
 - fluorescence emission spectra of DCVJ, 207*f*
 - fluorescence quantum yield for DCVJ emission, 205
 - fluorescence spectra of DCVJ in [bmim][PF₆]/CO₂, 207*f*
 - local dielectric using DCVJ, 206, 208
 - microviscosity for [bmim][PF₆]/CO₂, 207*f*
 - microviscosity using DCVJ, 204–206
 - nucleophilic substitution reactions, 201–203
 - physical property measurement methods, 200–201
 - physical property measurements, 203–204
 - procedure for nucleophilic substitutions, 199–200
 - rate constants for reaction of benzyl chloride with KCN, 202*t*
 - reversible ionic liquids, 208–209
 - structure of DCVJ, 205*f*
 - viscosity-dependence of fluorescence intensity of DCVJ for alcohols, 207*f*
- Sorption, ionic liquids in environment, 13–15
- Space propulsion
- behavior of conducting liquid subjected to different electric field strengths, 147*f*
 - colloid thruster, 139
 - discharge-free electric thrusters, 144–146
 - efficiency, 141–142
 - electric propulsion, 142–143
 - electrohydrodynamics of Taylor cones, 146–149
 - electrospray thrusters, 139, 144–146
 - [Emim][Im] [1-ethyl-3-methylimidazolium bis(trifluoromethylsulfonyl)imidate], 152–157
 - [Emim] nitrate ([Emim][NO₃]), 157–158

- [Emim] tetrafluoroborate
 ([Emim][BF₄]), 151–152
- emitting stable ion currents from
 metal needles, 149
- ionic liquids as ideal candidates,
 139
- mass spectrometric experiment,
 150–151
- micro-machines (MEMS) arrays,
 139–140
- missions, 140–141
- performance parameters, 141–142
- principle of externally wetted
 emitter, 149
- propulsion parameters for selected,
 engines, 144*t*
- schematic of field emission (FEFP)
 and colloid microthrusters, 145*f*
- specific impulse, 141
- technology, 139
- thrust, 141
- typical parameters for FEFP,
 colloid, and ionic liquid (IL)
 electrospray thrusters, 146*t*
- See also* Ion field evaporation
- Spatial heterogeneity in ionic liquids
 behavior of methylene groups of
 side chains between head and
 tail groups, 291, 293
- diffusion and local structure, 279
- diffusion constants for ionic liquids
 (ILs) with various side-chain
 lengths, 287*f*
- distributions of cationic length for
 different ionic liquids, 285*f*
- finite size effects, 281–283
- force field parameters, 303–305
- "headgroup" term, 280–281
- heterogeneity order parameter
 (HOP), 277–279
- HOP calculations characterizing
 instantaneous, 293
- HOP for uniformly distributed
 systems with different number
 of sites, 278*t*
- instantaneous configuration
 showing heterogeneous
 distribution of tail, head, and
 anion for C₈ system, 289, 290*f*
- instantaneous HOP for C₆ systems,
 284*f*
- isotropic atomic polarizabilities,
 300
- lattice HOP calculations, 293–294
- lattice HOP for tail groups,
 headgroups, and anions for
 different systems, 295*f*
- mass densities for ILs with various
 side-chain lengths, 287*f*
- mean square displacements for C₆
 systems, 283*f*
- mechanism, 294, 296–298
- models and methods, 274–280
- molecular dynamics (MD)
 simulations, 273
- molecular dynamics procedure,
 279–280
- partial charges of atoms, 300–
 302
- polarizable atomistic models, 275–
 276
- polar network and hydrogen
 bonding, 298–299
- radial distribution functions (RDFs)
 and instantaneous HOP values
 for atomic groups on cations in
 C₈ system, 292*f*
- reconciling mechanism and MD
 simulation results, 298
- reduced HOPs for IL systems with
 various alkyl-chain lengths, 289,
 291*f*
- structural, dynamical, and
 thermodynamical properties,
 285–286
- "tail group" term, 280–281
- tail-tail, head-head, anion-anion,
 and head-anion radial
 distribution functions for C₆
 systems, 282*f*

- tail-tail, head-head, anion-anion, and head-anion radial distribution functions for ILs with various side-chain lengths, 288*f*
- three dimensional illustration of lattice HOPS for tail and head groups of both C₂ and C₈, 294*f*
- varying cationic side-chain lengths, 273
- Specific impulse
 - electric propulsion, 142
 - space propulsion performance, 141
- Spectral densities, theory, 23
- Stability, ionic liquids in environment, 13–15
- Stern–Volmer equation, quenching process, 250–251
- Stokes–Einstein equation, viscosity, 321, 322–323
- Structural properties, ionic systems, 285–286
- Structures of ionic liquids
 - ab initio* (AI) calculations, 90, 92
 - AI calculated charge density in C₄mim⁺, 95*f*
 - 1-alkyl-3-methylimidazolium cations [C_nmim⁺], 87
 - center-of-mass ion-ion radial distribution functions, 94*f*
 - comparison between Raman, molecular dynamics (MD), and AI results for main conformers around N1–C6 and C6–C7 bonds, 91*f*
 - conformational distribution of imidazolium cations in liquid phase, 87–93
 - dihedral distribution along alkyl chain of C_nmim⁺ cations using MD simulations, 89, 92
 - Gibbs free energy difference between isomers, 90
 - main conformers of 1-butyl-3-methylimidazolium, 88*f*
 - main conformers of 1-ethyl-3-methylimidazolium, 87, 88*f*
 - MD calculations, 89, 92
 - molecular modeling, 87
 - nanometer-scale, 93, 95–97
 - nomenclature of 1-alkyl-methylimidazolium cations, 88*f*
 - radial distribution functions between end carbons of alkyl side chains in [C_nmim][PF₆] family, 94*f*
 - Raman spectrum for planar and non-planar conformers, 90
 - simulation vs. liquid spectroscopic evidence, 92–93
 - snapshot of simulation box with 20 cyclohexane and 200 ion pairs of [C₄mim][PF₆], 98*f*
 - snapshot of simulation box with 20 *n*-hexane and 200 ion pairs of [C₄mim][PF₆], 99*f*
 - snapshot of simulation box with 40 acetonitrile and 200 ion pairs of [C₄mim][PF₆], 100*f*
 - snapshot of simulation box with 40 methanol and 200 ion pairs of [C₄mim][PF₆], 100*f*
 - snapshots of simulation boxes of [C_nmim][PF₆], 96*f*
 - solvation, of nonpolar, polar, and associating solutes, 97–99
- Substitution reactions. *See* Nucleophilic substitution reactions; Solvents for chemical processes
- Supramolecular aggregates, ionic liquids, 21–22
- Surface tension
 - measurement, 313–314
 - measurement error, 314
 - new ionic liquids, 316*t*
 - non-wetting meniscus, 314*f*
 - wetting meniscus, 314*f*
 - See also* Taylor cones

T

Tail groups

term, 280–281

See also Spatial heterogeneity in ionic liquids

Take-off reactors. *See* Vapor take-off reactors

Taylor cones

cone-jet structure, 147*f*, 148

cone-jet term, 309

electrohydrodynamics, 146–149

electrospray, 309

ionic liquid ion sources (ILIS), 315, 317

ionic liquids, 315

liquid metal ion sources (LMIS), 309, 315

measurement error of surface tension, 314

non-wetting meniscus at propylene reservoir, 314*f*

performance of ionic liquids as ion sources, 315, 317

physical constants and purely ionic regime (PIR) temperatures, 311*t*

purely ionic regime (PIR), 310, 312*t*, 315, 317

sources of ions in vacuum, 310–313

surface tension measurement, 313–314

surface tensions for new liquids, 316*t*

wetting meniscus at liquid-glass capillary interfaces, 314*f*

Tetracyanoborate ionic liquids,

viscosity, 331*t*

Tetrafluoroborate based ionic liquids,

viscosity, 329–330

Thermal properties, *n*-alkyl-*N*-

isoquinolinium ionic liquids, 368, 369*f*

Thermal stability, phosphonium ionic liquids, 49, 50*f*, 51*f*, 52

Thermodynamical properties, ionic systems, 285–286

Thermodynamic state points, ionic fluid-butanol mixtures, 105*t*

Thrust

electric propulsion, 142

space propulsion performance, 141

Time resolved laser fluorescence spectroscopy (TRLFS)

method for studying Eu(III) and Cm(III) reactions in solution, 248, 250

See also Solution chemistry of Cm(III) and Eu(III)

U

United-atom force field

model, 73, 75

schematic structure and atom type notations, 72*f*

See also Force field development; Molecular simulations of ionic liquids

Upper critical solution temperature (UCST)

mixtures, 103

thermodynamic state points, 105*t*

See also Molecular simulations of mixtures

Urea. *See* Metal electrodeposition

V

van der Waals (VDW)

all-atom force field, 71, 73

non-bonded interactions, 71, 73

parameters of united atoms, 73, 75

van der Waals parameters, force field, 305

Vapor take-off reactors

best behavior of ionic liquids in unstirred, 133*t*

- carbonylation in unstirred vapor phase reactor, 132*t*
- carbonylation reactions, 136–137
- commercial operation, 134
- continuous, carbonylation of
 - methanol with MeI using ionic liquid, 131*f*
- diagram of unstirred, 131*f*
- experimental, 136–137
- industrial practice, 129–130
- ionic liquids, 130
- Ir catalyst and design, 132
- mass transfer effects, 133–134
- nickel and cobalt catalysts, 133
- NMR examination of recovered solutions, 134–135
- Rd catalyzed reaction in stirred, 135*t*
- reaction rate vs. stirrer speed, 134*f*
- rhodium catalyzed methanol carbonylation, 130, 132
- testing, 130
- See also* Carbonylation of methanol
- Vinylsulfonate ionic liquids
 - hydroformylation, 270
 - hydrogenation, 269
 - ion exchange in dry acetone, 266
 - ion exchange using ion exchange resin, 267
 - possible transformations, 269
 - synthesis, 265–267
 - See also* Functionalized ionic liquids
- Viscosity of ionic liquids
 - analytical procedures, 332
 - bis[bis(pentafluoroethyl)phosphonyl]imides ILs, 328, 329*t*
 - common ILs, 321*t*
 - comparing anions chloride, hexafluorophosphate, and tetrafluoroborate, 325
 - co-operative diffusion of anion and cation in liquid state, 322, 323*f*
 - Coulombic law describing interaction between ions, 324–325
 - diffusion coefficient, 321–322
 - dissociation rate of ion-pairs, 322
 - evidence of phase changes, 31
 - experimental, 332
 - Fick's first law, 321
 - ILs and mixtures, 79, 82, 83*f*
 - ILs with
 - (perfluoroalkyl)fluorophosphate (FAP) anions, 325–326, 327*t*
 - ILs with alkylsulfates anions, 327, 328*t*
 - imidazolium and pyrrolidinium ILs with same anion, 328
 - independent moving particles, 322, 323*f*
 - "ionicity", 324
 - "ionicity" rate, 325
 - models describing, 322, 323*f*
 - molecular impurities and solvation, 325
 - NMR correlation time relationship with, 32, 33*f*
 - perfluoroalkylborates ILs, 329, 330*t*
 - replacing fluorine with cyano groups on tetrafluoroborates, 331
 - Stokes–Einstein equation, 321, 322–323
 - syntheses of ILs with $[\text{CF}_3\text{BF}_3]^-$ and $[\text{C}_2\text{F}_5\text{BF}_3]^-$ anions, 330
 - tetracyanoborate ILs, 331*t*
 - tetrafluoroborate based ILs, 329, 330
 - transfer number, 323, 324
- Volumes, excess molar, ionic liquids and mixtures, 79, 81*f*

W

Water content, *n*-alkyl-*N*-
isoquinolinium ionic liquids, 367*t*

Water removal, carbonylation of
methanol, 129

X

Xerogels, silica, 36

X-ray diffraction

n-alkyl-*N*-isoquinolinium ionic
liquids, 365–366, 368, 371, 373
columnar hexagonal phase, 167*f*
self-assembled columnar structures,
163, 165*t*

Z**Zinc**

electroplating alloys, 192–195

See also Metal electrodeposition

Zwitterions, amino acids, 355–358

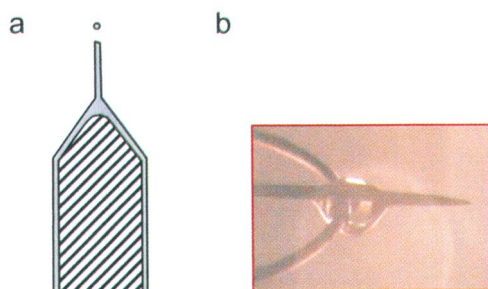


Figure 10.3. a: Schematic representation of an externally wetted emitter tip. b: Video microscope image of an ion emitting externally wetted tip in a vacuum. An IL droplet is applied at the junction between the needle and a spotwelded wire. The tip diameter of the emitter is 20 μm .